AN INVESTIGATION TO RESOLVE THE INTERACTION BETWEEN FUEL CELL, POWER CONDITIONING SYSTEM AND APPLICATION LOADS

Topical Report

Period Start Date: 10/01/2002 Period End Date: 09/30/2003

Sudip K. Mazumder, Ph.D. (Point of Contact)
Power Electronics Research Center
Department of Electrical and Computer Engineering
University of Illinois, MC: 154
1020 SEO, 851 South Morgan Street
Chicago, IL: 60607-7053
E-mail: mazumder@ece.uic.edu
Phone : 312-355-1315
Fax : 312-996-6465

Comas Haynes, Ph.D.
Center for Innovative Fuel Cell and Battery Technologies
Georgia Tech Research Institute
Atlanta, Georgia 30332-0853
E-mail: comas.haynes@gtri.gatech.edu
Phone: 770-528-7578
Fax: 770-528-7028/7083

Chuck Mckintyre, Ph.D. and **Dan Herbison, Ph.D.**
Systems Modeling Research and Development
Synopsys Inc.
9205 SW Gemini Drive, Beaverton
OR 97008
E-mails: herbison@synopys.com
Phone: 503-520-4391
Fax: 503-643-3361

Michael von Spakovsky, Ph.D.
Energy Management Institute
Mechanical Engineering Department
MC 0238, Virginia Tech
Blacksburg, VA 24061
E-mail: vonspako@vt.edu
Phone: 540-231-6684/7190
Fax: 540-231-9100

Doug Nelson, Ph.D.
Center for Automotive Fuel Cell Systems
Mechanical Engineering Department
Virginia Tech
Blacksburg, VA 24061-0238
Email: Doug.Nelson@vt.edu
Phone: 540-231-4324
Fax: 540-231-9100

Joseph Hartvigsen and S. Elangovan, Ph.D.
Ceramatec, Inc.
2425 South 900 West
Salt Lake City, Utah 84119
Emails: jjh@ceramatec.com, elango@ceramatec.com
Phone: 801-978-2163
Fax: 801-972-1925

Student Participants
Kaustuva Acharya – University of Illinois
Rajnikant Burra – University of Illinois
Diego F. Rancruel – Virginia Tech
Saravanan Subramanian – Virginia Tech.
Robert Williams – Georgia Tech.

July, 2004

DOE Award Number: DE-FC26-02NT41574

DISCLAIMER

Abstract

Solid-Oxide Fuel Cell (SOFC) stacks respond quickly to changes in load and exhibit high part- and full-load efficiencies due to its rapid electrochemistry. However, this is not true for the thermal, mechanical, and chemical balance-of-plant subsystem (BOPS), where load-following time constants are, typically, several orders of magnitude higher. This dichotomy diminishes the reliability and performance of the electrode with increasing demand of load. Because these unwanted phenomena are not well understood, the manufacturers of SOFC use conservative schemes (such as, delayed load-following to compensate for slow BOPS response or expensive inductor filtering) to control stack responses to load variations. This limits the applicability of SOFC systems for load-varying stationary and transportation applications from a cost standpoint. Thus, a need exists for the synthesis of component- and system-level models of SOFC power-conditioning systems and the development of methodologies for investigating the system-interaction issues (which reduce the lifetime and efficiency of a SOFC) and optimizing the responses of each subsystem, leading to optimal designs of power-conditioning electronics and optimal control strategies, which mitigate the electrical-feedback effects. Equally important are "multiresolution" finite-element modeling and simulation studies, which can predict the impact of changes in system-level variables (e.g., current ripple and load-transients) on the local current densities, voltages, and temperature (these parameters are very difficult or cumbersome, if not impossible to obtain) within a SOFC cell. Towards that end, for phase I of this project, sponsored by the U.S. DOE (NETL), we investigate the interactions among fuel cell, power-conditioning system, and application loads and their effects on SOFC reliability (durability) and performance.

A number of methodologies have been used in Phase I to develop the steady-state and transient nonlinear models of the SOFC stack subsystem (SOFCSS), the power-electronics subsystem (PES), and the BOPS. Such an approach leads to robust and comprehensive electrical, electrochemical, thermodynamic, kinetic, chemical, and geometric models of the SOFSS, PES and application loads, and BOPS. A comprehensive methodology to resolve interactions among SOFCSS, PES and application loads and to investigate the impacts of the fast- and slow-scale dynamics of the power-conditioning system (PCS) on the SOFCSS has been developed by this team. Parametric studies on SOFCSS have been performed and the effects of current ripple and load transients on SOFC material properties are investigated. These results are used to gain insights into the long-term performance and reliability of the SOFCSS. Based on this analysis, a novel, efficient, and reliable PES for SOFC has been developed. Impacts of SOFC PCS control techniques on the transient responses, flow parameters, and current densities have also been studied and a novel nonlinear hybrid controller for single/parallel DC-DC converter has been developed.

TABLE OF CONTENTS

LIST OF FIGURES

LIST OF TABLES

LIST OF ACRONYMS

AFR	Air to Fuel Ratio
APU	Auxiliary Power Unit
BGE	Baltimore Gas and Electric Territory
BOPS	Balance-Of-Plant Subsystem
CFD	Computational Fluid Dynamics
CSI	Current-Source Inverter
DLLS	Dynamic Link Library
DMFCS	Direct Methanol Fuel Cells
DOE	Department Of Energy
EES	Engineering Equation Solver
FEA	Finite Element Analysis
FEM	Finite Element Method
FPS	Fuel Processing Sub-System
FRR	Fuel Reformate Ratio
FU	Fuel Utilization

HF	High Frequency
IP	Initial Net Power
IVSC	Integral-Variable-Structure Control
LMTD	Log Mean Temperature Difference
MINLP	Mixed Integer and Non-Linear Programming
MSSC	Multiple-Sliding-Surface Control
NETL	National Energy Technology Laboratory
NTU	Number of Transfer Units
ORNL	Oak Ridge National Laboratory
PEM	Proton-Exchange Membrane
PES	Power-Electronics Subsystem
PESS	Power-Electronics Subsystems
PNNL	Pacific Northwest National Laboratory
PRS	Power Recovery Sub-System
PSE	Process Systems Enterprise
PSE&G	Public Service Electric & Gas Territory,
PWM	Pulse Width Modulation
SCE	Southern California Edison Territory
SECA	Solid State Energy Conversion Alliance
SLAP	Sparse Linear Algebra Package
SMR	Steam Methane Reformer
SMR	Steam to Methane Ration
SOFC	Solid-Oxide Fuel Cell
SOFCS	Solid-Oxide Fuel Cells
SOFCSS	SOFC Stack Subsystem
SPWM	Sinusoidal Pulse Width Modulation
SS	Stack Subsystem
SVM	Space-Vector Modulation
TMS	Thermal Management Sub-System
TSOFC	Tubular SOFC
VSI	Voltage-Source Inverter
WRS	Work Recovery and Air Supply Sub-System
YSZ	Yttrium Stabilized Zirconia
ZRBC	Zero-Ripple Boost Converter

1. INTRODUCTION

Renewable energy sources (such as fuel cell) are expected to provide 15% of the world energy demand in the near future (International Energy Agency Report, Ellis et al. 2001, Raissi 1997). Solid-oxide fuel cells (SOFCs) are expected to play a significant role in helping to meet the demands of power quality and reliability of distributed power generation. SOFCs have already demonstrated high quality of power output and are potentially simpler and more reliable than conventional power-generation utility technology. However, certain challenges remain before SOFCs can be applied to real-world applications. These challenges include the issues of reliability and lifetime of the SOFC stacks. For SOFCs to be used commercially, it is essential that SOFC technology be demonstrated to achieve long life (> 40000 hours for stationary applications and > 5000 hours for transportation applications).

Development of high-performance and durable solid-oxide fuel cells (SOFCs) and a SOFC power-generating system requires knowledge of the feedback effects from the power-conditioning electronics and from application-electrical-power circuits that may pass through or excite the power-electronics sub-system (PES)[1]. It is thus important to develop analytical models and methodologies to investigate the effects of the feedback from the PES and the application loads on the reliability and performance of SOFC systems for stationary and mobile applications. The behavior of a PES has a direct impact on the stack performance and the lifetime of the SOFC[2] (Gemmen, 2001; Hartvigsen, 2002; Mazumder et al., 2003, Acharya et al., 2003). For example, a dc-dc converter will impose its own time-varying load on the fuel cell, apart from that due to variations in the application loads and other effects from dc-ac and dc-dc converters. If the peak-current levels from these loads are high, it can lead to a low-reactant condition within the SOFC. As such, there is a need for analytical models and methodologies, which can be incorporated into a system tool to investigate the issues of safe load-fluctuation and effective load-following, and explore how to manage each of SOFC sub-system's response optimally[3]. Furthermore, such an analytical tool could also help determine how much current and voltage ripples a SOFC can acceptably withstand, how does the slow-(line) and fast-(switching) scale ripple (Mazumder et al., 2001a) affect the performance and operating life of the SOFC stack, and how should the power electronics be designed and operated to mitigate these problems. Filters are typically specified to reduce ripple current to "perceived" low risk levels. Understanding of the electrical impact of the PES on SOFCs allows the design of more cost-effective and reliable power electronics for SOFC based system. Equally important is the understanding of the impact of SOFC output voltage variations on PES network transients and stability for fixed and dynamic/perturbing application load (Mazumder et al., 2001a-d). Padulles et al. (2000) have shown that, if the output voltage of a SOFC stack drops beyond a certain point, the PES loses synchronism with the output electrical network and hence, the whole power plant needs to be disconnected.

Thus, there is a need to develop analytical tools and investigative methodologies to address the issues outlined earlier, and design and development of cost-effective, reliable, and optimal PESs. However,

---

[1] SOFC power-generating systems may provide direct or alternating current (ac or dc) to satisfy application specific power needs. The current, voltage, and power quality are controlled by electronic power conditioning systems. Generally, voltage regulators, dc-dc converters, and chopper circuits are used to control and adjust the fuel cell dc output voltage to a useful value. Inverters are used to convert this dc voltage to a useful ac voltage for stationary applications.

[2] NETL guidelines specify SOFC operating lifetime as >40,000 hours for stationary applications and >5000 hours for mobile applications.

[3] For example, by matching the optimal power-electronics sub-system to a particular SOFC system and application, such a system tool provides a designer with sufficient knowledge of both system and sub-system topologies. Additionally, sub-system and component response times are known to enable her or him to make the most judicious, as opposed to the most conservative choice of components.

any such attempt to resolve the electrical impacts of PES on SOFC would be incomplete unless one utilizes a comprehensive analysis, which takes into account the interactions of SOFC, PES, balance-of-plant sub-system (BOPS), and application loads as a whole. SOFC stacks respond quickly to changes in load, because of rapid electrochemistry. This is not true, however, for the thermal, mechanical, and chemical BOPS components and particularly for the fuel-processing sub-system, where load-following time constants are typically several orders of magnitude higher. Differences in response times between the electrochemical/electrical and thermal/mechanical/chemical sub-systems of the overall SOFC system can lead to undesirable effects, given significant variations in load.

SOFC manufacturers, traditionally model the PES as constant impedance, while manufacturers of PES, model the SOFC as stiff voltage sources for their analysis. Both these approaches yield inaccurate results. To overcome the lack of comprehensive analytical tools to model SOFC based systems, manufacturers of SOFC (utility) PES have so far implemented conservative (and expensive) schemes for managing stack response to application load variations (i.e., controls tactics for delayed load-following to allow for balance-of-plant response, expensive inductor filtering, etc.). SOFC systems are thus less practical from an applications and cost standpoint. Therefore, to comprehensively analyze these multiple-scale effects[4], analytical models are needed to perform system and component engineering studies to evaluate how an entire integrated fuel cell system works, to optimize designs, and to determine the best design approach to achieve the highest performance at least-cost. Finally, accurate dynamic modeling is critical to employing well thought-out and optimized control schemes, which respond reliably to operating conditions across an entire load profile and are applicable to a wide variety of SOFC stack and system configurations. Recently, Gemmen et al. (2001) attempted to estimate the effects of electrical loads and inverter ripple on the durability and performance of PEM fuel cells using a simple first order model for the PES. A preliminary understanding of the effect of inverter loads on conditions near the electrolyte surface was achieved. Our study resolves these issues using comprehensive and reduced-order models of the SOFC power system.

[4] One of the biggest problems to the comprehensive simulation is the issue of multiple-time scales associated with the vastly different response times of SOFC and BOPS dynamics as compared to that of the PES. While the PES time scale is in microsecond, the response times of SOFC and BOPS is in seconds (if not in minutes); the minimum ratio is a staggering million! *For the first time, in phase I, we have addressed this issue using a hybrid approach.*

2. EXECUTIVE SUMMARY

Development of high-performance and durable solid-oxide fuel cells (SOFCs) and a SOFC power-generating system requires knowledge of the feedback effects from the power-conditioning electronics and from application-electrical-power circuits that may pass through or excite the power-electronics subsystem (PES). It is, thus, important to develop analytical models and methodologies, which can be used to investigate the effects of the feedbacks from the PES and the application loads on the reliability and performance of SOFC systems for stationary and mobile applications. However, any such attempt to resolve the electrical impacts of the PES on the SOFC would be incomplete unless one utilizes a comprehensive analysis, which takes into account the interactions of SOFC, PES, balance-of-plant system (BOPS), and application loads as a whole. SOFC stacks respond quickly to changes in load and exhibit high part- and full-load efficiencies due to its rapid electrochemistry, which is not true for the thermal, mechanical, and chemical BOPS, where load-following time constants are, typically, several orders of magnitude higher. This dichotomy affects the lifetime and durability of the SOFC stacks and limits the applicability of SOFC systems for load-varying stationary and transportation applications.

To investigate the above-mentioned issues of reliability and performance, we investigate the interaction between fuel cell, power conditioning system and application loads and its effect on SOFC reliability and performance. Nonlinear, component- and system-level, steady-state and transient electrical, electrochemical, thermodynamic, kinetic, chemical, and geometric models of the SOFC stack subsystem (SOFCSS), the power-electronics system (PES), and the BOPS have been developed and validated. First, a transient SOFC model has been successfully developed for characterizing the performance (quantitative) and reliability (qualitative thus far) response of a multi-kW SOFC power module subject to electrical stimuli (i.e., load-following and load fluctuation). The specific design studied during this proof-of-concept has actually been reduced to practice and field tested extensively. Secondly, dynamical nonlinear models of three commonly used PESs have been implemented using an advanced PES simulation platform and the results were validated using previously published results. These topologies have different current ripple characteristics and hence allow a detailed analysis of the effect of PES on the SOFC reliability and performance. Finally, a mathematical model of the BOPS consisting of a set of equations that describe the mass and associated energy flows in each of the lines of the sub-systems is developed based on the chemical reactions inside each reactor and on the laws of conservation of mass and energy for each component in the sub-system.

A number of methodologies have been used to investigate the system-interaction issues (which reduce the lifetime and efficiency of a SOFC) and optimizing the responses of each sub-system. A comprehensive system-level model, using a multi-software simulation platform, has been developed. To overcome the computational difficulties with such a model, a novel hybrid two-step algorithm has been developed for parametric analysis and to study the effects of current ripple and load transients on SOFC material properties investigated. These results are used to gain insight into the long-term performance and reliability of the SOFCSS. “Multiresolution” finite-element modeling and simulation studies have been performed, which can be used to predict the impact of changes in system-level variables (e.g., current ripple and load-transients) on the local current densities, voltages, and temperatures (these parameters are very difficult or cumbersome, if not impossible to obtain) within a SOFC cell. The team has established pilot dependencies of stack response to load variations. Specific to load-following, pertinent time constants have been established which are functions of stack geometry and flow-field characteristics. Investigations on the effects of these time constants on the material properties of the SOFC stack have been initiated. Using these results, SOFC system reliability and performance have been investigated over a domain of transient

conditions, typical of stationary and mobile power applications for which SOFC based APUs are being considered.

We investigate the effects of variations in the SOFC output voltage on the PES transients and stability by using the hybrid-analysis methodology. Initially, we emulate the SOFC output voltage (by incorporating the effect of the BOPS) as a current-dependent harmonic voltage source and then, using this source conduct stability analyses. Because the PES is a nonlinear discontinuous system, conventional averaged small-signal analysis is not sufficient and hence, nonlinear methodologies such as bifurcation algorithms have been developed. Bifurcation analyses reveal when and why instability occurs and post-instability dynamics. Advanced bifurcation algorithms have been used to predict the global dynamics, which is important analyzing the effectiveness of control design, effects of parametric variations, and disturbance-rejection capability of the SOFC PCS.

Based on these analyses, University of Illinois has developed a novel low-cost, zero-ripple, energy-efficient, and high-power-density PES, which can meet SECA price target of $40/kW in volume production and enhances the durability of a SOFC stack.. The proposed PES achieves[5] i) 98% efficiency for dc-dc boost converter at 5 kW (full load), ii) over 94% (> 93%) efficiency at full load for single-phase (three-phase) output, iii) elimination of the ripple current drawn from the SOFC stack without using any bulky input filter, thereby significantly enhancing the life and energy efficiency of the SOFC stack iv) 50% reduction in voltage stresses for the intermediate inverter, which leads to higher reliability, v) direct power conversion, i.e., does not require any intermediate energy-storage bulk capacitors, thereby increasing power density. Thus, the proposed PES address several key SECA industry issues for power-conditioning electronics: i) cost, ii) durability and reliability of SOFC stack, and iii) energy efficiency and power density. The novel PES design has recently received a provisional patent from the University of Illinois.

Impact of SOFC PCS control techniques on the transient response, flow parameters and current density has been studied. Poor transient response of the controller is shown to result in current-overshoot during load-transients that may lead to electrically induced thermal effects in the SOFC stack due to high fuel utilization. SOFC output voltage variations (due to change in load demand or due to low bandwidth of BOPS) are also shown to act as a feedforward disturbance on the PES, which can destabilize the electronic subsystem. To address these issues, a novel nonlinear hybrid controller for single/parallel dc-dc boost converter has been developed. The concept can also be extended to the single/three phase dc-ac converter stage.

Finally, fuel and air buffering, which are practical and efficient ways of reducing the time delay due to the fuel processing sub-system, have been studied. In the same way electrical energy buffering to compensate the PES imbalance due to load perturbations, especially during start-up, is investigated. This ensures that the current ripple, load changes and difference in transient response between the electrical-electrochemical components of the subsystems doesn't affect the performance of the SOFC PCS.

[5] Based on preliminary-design calculations. Two additional design issues pertaining to the integration of output-filter-inductors and transformer magnetics to reduce the PES size and cost and robust hybrid nonlinear control of the DC-DC and DC-AC converters, will be two of our PES design focuses in Phase II.

3. METHODOLOGIES, ISSUES AND RESULTS

3.1 MODELING

SOFC electrochemical and thermal-transport-phenomena and methodologies have been, and continue to be, investigated by the team and are used to characterize the stack behavior under load-varying conditions. The resulting algorithms and code can be integrated with power-electronics and system model codes to simulate "real world" changes in current and voltage ripples, load following, start up/shut down, etc. Fuel cell reliability and performance can then be tested over a domain of transient conditions typical of the distributed generation and mobile power markets targeted within SECA. Ultimately, the goal is to resolve design approaches that enable SOFCs to be tolerant to variations in load in a cost-effective and efficient way. Towards this end, this project develops and integrates dynamic models of each of these sub-systems (i.e. power-electronics, SOFC stack, and balance-of-plant) into a comprehensive analytical tool, which can then be used through sensitivity parametric studies and/or dynamic optimization to create a variety of control strategies for stationary and transportation applications.

Fuel cell power conditioning system (PCS) (as shown in Fig. 1) consists of three components: (a) fuel-cell stack, (b) balance-of-plant system (BOPS), and (c) power-electronics system (PES). The chemical reactions responsible for producing electricity take place in the fuel cell stack. The BOPS acts as a fuel processor and converts hydrocarbon-based fuel to hydrogen. It is also responsible for maintaining the temperature of the fuel/air supply and their flow rates. The PES is responsible for processing the SOFC stack output to useful voltage/current levels. The sub-system modeling was divided among our team of investigators, who have proven theoretical and practical expertise in the component- and system-level modeling, interaction analysis, and optimization of these types of distributed and vehicular sub-systems and systems, that is,

(a) SOFC Stack: Georgia Tech. and Ceramatec, Inc.
(b) Power Electronics: University of Illinois and Synopsys Inc.
(c) Balance of Plant: Virginia Tech.
(d) System Integration: University of Illinois, Synopsys Inc., Georgia Tech., and Virginia Tech.

The following sub-sections describe in detail the approach to model each of the sub-systems. Sub-section 3.1.1 describes the model to characterize SOFC stack behavior under load-varying conditions. The resulting algorithms and code were integrated with the PES model (described in section 3.1.2) to simulate SOFC current and voltage dynamics. The BOPS model is then described in section 3.1.3. Section 3.1.4 goes on to describe the integration of the sub-system models using the comprehensive model developed on a multi-simulation platform. Fuel cell reliability and performance is then analyzed over a domain of transient conditions typical of stationary applications (discussed in section 3.2).

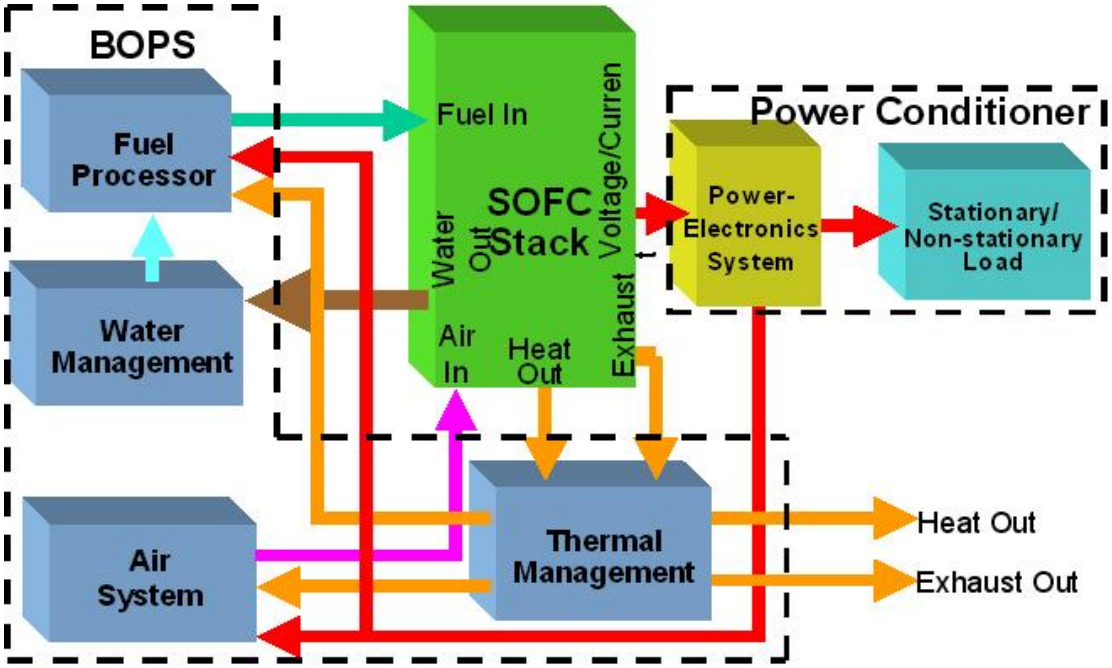

Fig. 1: SOFC power conditioning system block diagram showing the fuel cell stack, the power electronic circuit, and the balance of plant system.

3.1.1 SOFC Stack Sub-system (SOFCSS) Model

3.1.1.1 Establishment and Enhancement of a Validated SOFC Stack Model

The pilot effort's focus has been to realize a proof-of-concept systems integration that affords maximum validation within the scope of the Phase I award. Available published results on tubular multi-kW bundle row design were thus used as a "test bed" technology in order to leverage extensive demonstration and field data and insights into the exercise.

3.1.1.1.1 Electrochemistry

The investigators have published a model of the current tubular SOFC (TSOFC) design (Haynes and Wepfer, 2000). The model is based on fundamental electrochemistry (as opposed to curve fit correlations and "black box" simplifications). The attempt to simulate the TSOFCs was an extension of the work of Bessette (1994) and Kanamura et al. (1989). Specifically, all three models incorporate the "slice technique".

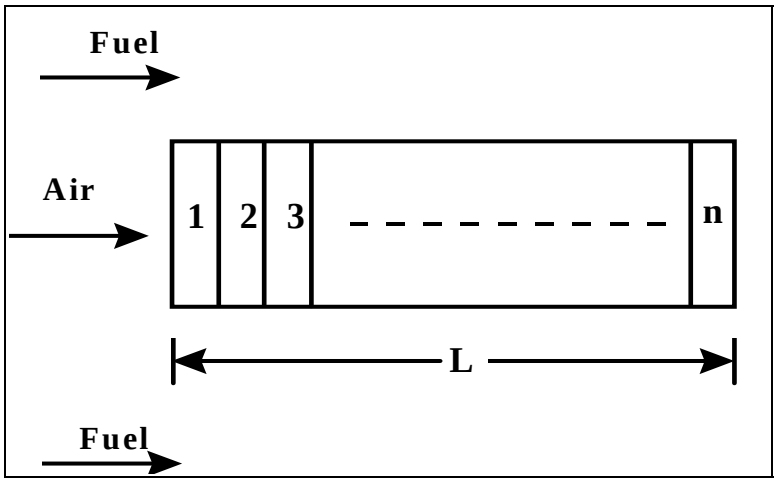

Fig. 2: Axial division of TSOFC.

The technique, illustrated in Fig. 2, divides the cell into a preset number of subdivisions (or slices). Mass and energy balances for fuel oxidation are made on each slice in an axial march. Each slice has an equilibrium voltage (i.e., Nernst potential), depending on constituent partial pressures at the slice:

$$E = \frac{1}{nF}\left\{-\Delta G^{o}_{steam,1000^{o}C} - R_u T * \ln \frac{p_{H2O}}{p_{H2} p_{O2}^{1/2}}\right\} \qquad (1)$$

The equilibrium voltage represents the largest possible potential difference, from a thermodynamic standpoint. The actual cell voltage is a common value among the slices and is dictated as an operating parameter. It is less than the equilibrium potential due to electrochemical irreversibilities.

Fuel cells cause ions and valence electrons to complete a circuit; hence, current is produced. Any finite rate process, however, also generates irreversibilities. In the case of fuel cells, these irreversibilities manifest as polarizations or losses in potential difference. The three types of polarization are activation, concentration and ohmic. Fuel-cell reactions require a certain "activation energy" in order for them to occur. The activation energy, which depends on how ions are transferred and the rate at which they are transferred, must be subtracted from the energy theoretically available (i.e., the Nernst potential). Fortunately, the high operating temperature of present TSOFCs promotes fast reaction kinetics, and activation polarization may be considered small (Minh and Takahashi, 1995), (Maskalick, 1989)[6]. Reactants are transported from their respective (i.e., fuel and air) streams to the fuel cell; thus, mass transfer irreversibility, or concentration polarization, occurs. Bagotsky (1993) gives the following relation for quantifying concentration polarization.

$$\Delta V_{polarizaton,conc} = \frac{R_u T}{nF} * \sum \ln\left\{\Pi_{reactants}\left[1 - \frac{i}{i_{l,j}}\right]^{\nu_j}\right\} \qquad (2)$$

The most significant loss is that due to ohmic resistance to current flow:

$$\Delta V_{polarization,ohmic} = iR_{eff} \qquad (3)$$

[6] As the ratio of charge transfer to ohmic resistances (i.e., effectively a Wagner number (Prentice, 1991)) lower with design advancement, activation polarization can be characterized either via the Butler-Volmer relations or simplifications thereof (i.e., "ohmic" activation resistances or Tafel relations).

The effective resistance of the TSOFC was developed from consideration of the "transmission line" model (Nisancioglu, 1989). The following electrochemical governing equation thus resulted:

$$\Delta V_{polarization,total} = \mathrm{E}_{slice} - V_{operate} \quad (4)$$

The first term is the sum of the concentration and ohmic losses and is current dependent. Once the current was converged upon for a given slice, constituent mole fractions and partial pressures for the next slice were calculated. These calculations were based on the stoichiometric relationship between current and reaction constituents (hydrogen, oxygen and steam), as well as shift reaction equilibrium (carbon monoxide combining with steam to form hydrogen and carbon dioxide). The power generated in each slice is given by:

$$Power_{slice} = i_{slice} V_{operate} \quad (5)$$

Successive slices are "marched" through until the current and power distributions for the entire cell are known. The total current and power are then accumulations of the slice values. As alluded to, the operating voltage must be lower than the lowest equilibrium potential, which occurs at the last slice due to reactant use. The model was applied to the recent generation, one and one-half meter electroactive TSOFC design, and there was good agreement between model and experiment, as shown below.

Fig. 3 is a sample of model and experiment agreement across a domain of pressure ratios. The model transitions from small over predictions of current to slight under predictions as operating voltage increases. This is attributable to error in calculating polarization. Actual concentration polarization phenomena have minor impact at low current densities (higher voltages) and are critical at high current densities (lower voltages). As more experimental data is released and modeling theory is developed, the polarization terms will be refined. Predictions are, however, consistently within 3%-5% of the experimental values. A foundational steady state model enabled the development of transient simulation capabilities.

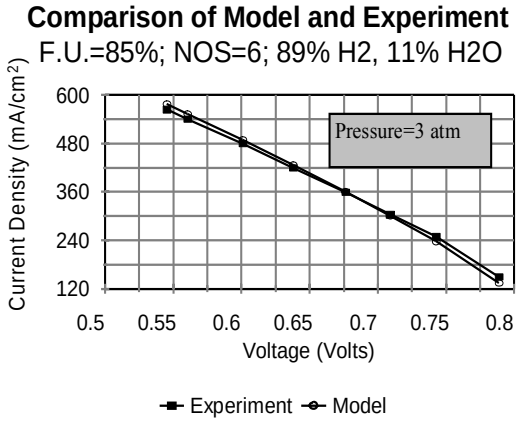

(a)

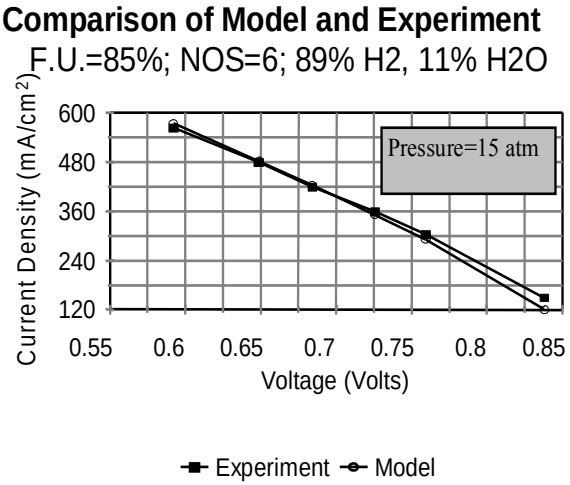

(b)

Fig. 3: Validation of model for (a) 15 atm and (b) 3 atm.

3.1.1.1.2 Electrical Transient Response Model

Although *electrochemical* transient responses are fast in comparison to thermal-hydraulic transients, finite *electrical* transient effects still arise due to changes in constituent concentrations.

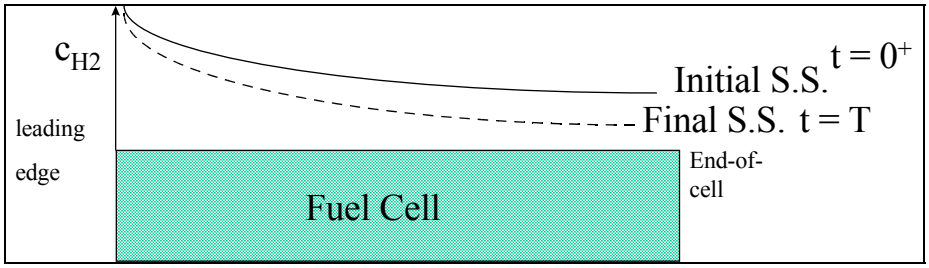

Fig. 4: Illustration of fuel stream transient dynamics.

Fig. 4 is a schematic of the hydrogen concentration profile along the fuel cell. The solid curve concentration profile corresponds to the cell's initial steady state. At "t = 0^+", the operating voltage idealistically decreases (i.e., cell potential behaves as a perfect step function) to accommodate an increase in load demand. The reactants supply, however, is predicated upon the prescribed fuel utilization and initial current. In accordance with Faraday's Law, there is a decline in reactant concentrations when the load increases. This decrease continues until a new electrical steady state is reached (at t=T). Transient analyses are facilitated by focusing attention on individual fluid elements as they travel along the cell; this method is called a Lagrangian approach.

Fig. 5 illustrates the Lagrangian approach. For the present, consider an idealistic step change (e.g., decrease) in cell potential. During the cells' transient response to load change, each fuel element approaches the cell with the same inlet characteristics, approximating invariant reactants supply[7] (e.g., load fluctuating scenarios). The exit properties of each fluid element, however, depend upon its location at the time of the load hike, $t=0^+$. Element 2 of Fig. 5, in the given example of a sudden decrease in cell potential, will have greater reactant depletion than element 1. This is because element 2 has longer exposure to electroactive area at the lower operating voltage. The *electrical* transient episode ensues until each fluid element approaching the cell again experiences an identical change in constituents. This occurs when element 3 reaches the end of the cell (note element 3 is at the beginning of the cell when the cell potential decreases). After element 3, every subsequent fluid element (e.g., element 4) *enters* at the new operating voltage; these elements then experience the same reaction phenomena. *The time of the electrical episode is thus nearly the length of the cell divided by the fuel velocity in this idealized, yet physically pertinent, scenario.* Note that this streamlined computational approach has two major assumptions with respect to the fuel stream which are now discussed.

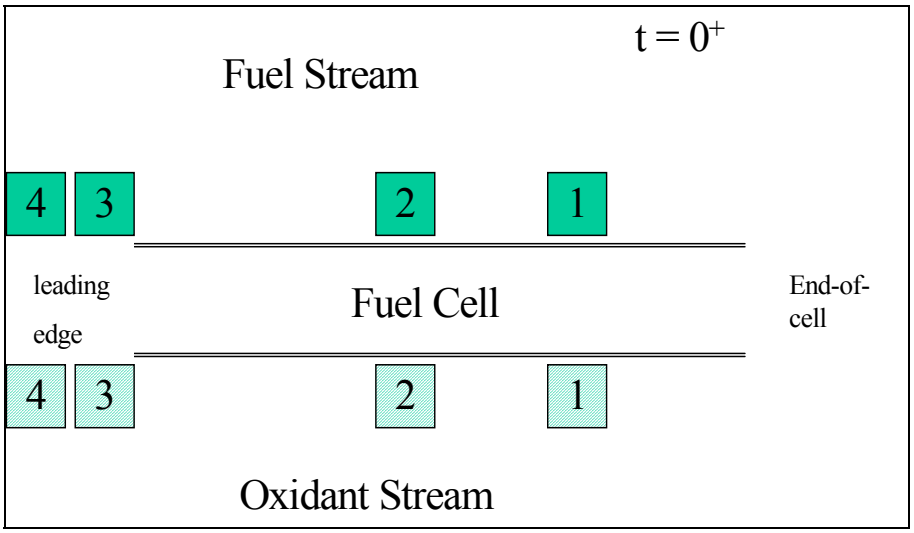

Fig. 5: Individual fuel element locations at the time of the electrical change (Lagrangian approach).

The first assumption is that the fuel stream effects dominate those of the oxidant stream. Note that the oxidant stream is not considered in the transient analysis. Typically oxidant is supplied in large excess

[7] Depending upon fuel flowrate, the timeframe of the electrical transients is a fraction of a second. Note that fuel processors have response times on the orders of seconds (e.g., partial oxidation/authothermal units) and minutes (e.g., steam reformers).

quantities for thermal management of the cell. A key result is that changes in current will not have nearly the impact upon oxidant utilization as they will the fuel utilization. In fact, as will be shown, the reactant utilization effect of changes in load is a dominant factor in resolving the SOFC response; so a mitigated change in oxidant utilization due to the capacity of the oxidant stream precludes the computational burden required for simultaneously characterizing both fuel and oxidant streams (which will flow at differing velocities, further compounding difficulties). Additionally, electrode transient effects are not quantified; specifically within the anode. The given test case tubular design is cathode-supported and has relatively thin anodes, hence minimizing the need for analyzing transient chemical/electrochemical behavior within a porous medium. At an extreme, a zero-thickness anode would have no capacitive effects upon the transient system. *The team, however, realizes that such capacitive effects may occur with pertinence within the other prevalent designs such as anode-supported SOFCs.* The given approach and the transient electrode characterization spearheaded by (Gemmen et al., 2003) can thus complement each other, and again a collaboration within the SECA Infrastucture is motivated.

The fluid elements involved in the transient episodes were computationally "tracked." This was done via two-dimensional arrays containing *field variable* information (i.e., axial position and time). The Lagrangian basis is that a fluid element occupies a certain location at a given time.

$$\eta_{element,\,fluid} = \eta(\vec{x}, t) \qquad (6)$$

The symbol η represents the properties of the fluid element in question (e.g., constituent partial pressures). The electrical power produced along the cell depends upon these properties. In accord with the Lagrangian methodology, the axial discretization (i.e., slice length) is compliant with the flows' velocity and the temporal discretization (i.e., desired simulation time step) of the cell. Equation (7) and Fig. 6 illustrate principle.

$$\Delta\vec{x} = \vec{v}\Delta t \qquad (7)$$

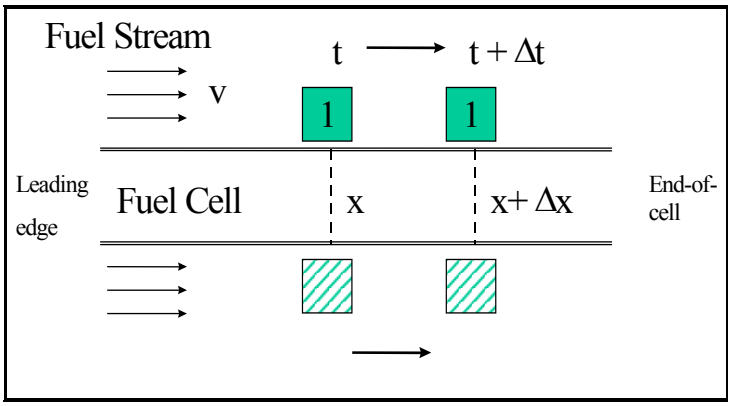

Fig. 6: Correlation between temporal and spatial discretizations.

The following relation results.

$$\eta_{fluid,element}(t + \Delta t) = \eta(\vec{x} + \Delta\vec{x}, t + \Delta t) \qquad (8)$$

The quasi-steady state electrochemistry assumption is incorporated, meaning that electrochemical phenomena occur as if at steady state, at the given instant. This is primarily based upon the large exchange current densities that SOFCs often engender. The Reynolds Transport Theorem is then utilized.

$$\dot{n}_{\mathrm{j,intermed}}\left(\vec{x}+\Delta\vec{x},t+\Delta t\right)=\dot{n}_{j,entering,slice}\left(\vec{x},t\right)+\Delta\dot{n}_{j}\left(\vec{x},t\right) \quad (9)$$

The "*j*" subscript represents hydrogen, oxygen and steam, and equation (9) accounts for the temporal change in constituents due to electrochemical oxidations.

$$\dot{n}_{k}\left(\vec{x}+\Delta\vec{x},t+\Delta t\right)=\dot{n}_{\mathrm{k,intermed}}\left(\vec{x}+\Delta\vec{x},t+\Delta t\right)+\dot{n}_{k,shift,change}\left(\vec{x},t\right) \quad (10)$$

The "*k*" subscript represents hydrogen, steam, carbon monoxide and carbon dioxide. Equation (10) accounts for the temporal change in constituents due to the shift reaction, which was modeled via equilibrium chemistry due to the hot fuel stream and nickel catalyst within the anode. These temporal expressions of mass conservation enabled the transient electrochemical model to "march out" in time.

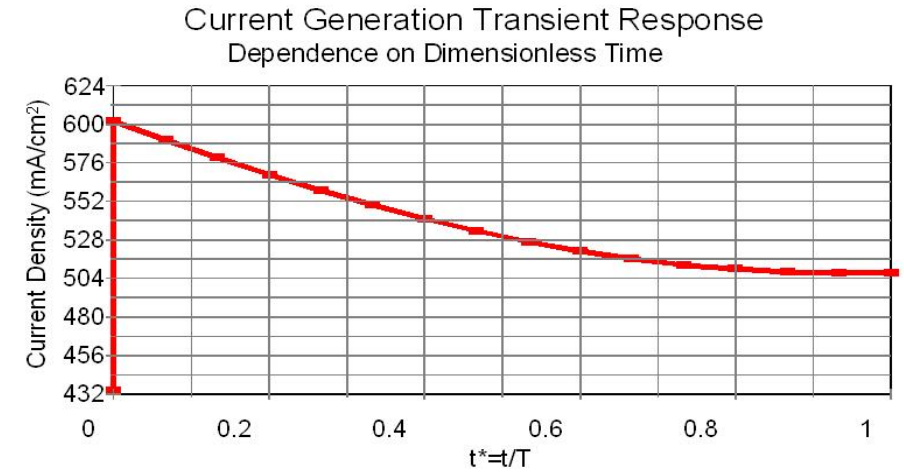

(a)

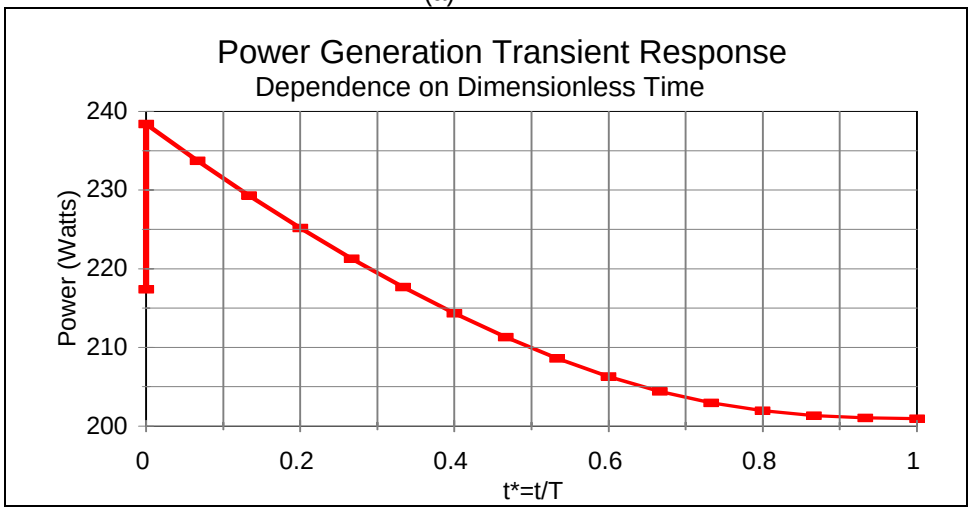

(b)

Fig. 7: Variation of (a) power and (b) current, with dimensionless time.

3.1.1.1.3 Load-Following Initial Analysis/Case Study - Idealized Potentiostatic-Control Step Change

A number of the settings are a compilation of test conditions reported in the literature as list in the Table I.

Table I: Baseline conditions used in the transient case study.

Pressure (atm)	3
Stoichiometric number	3
Fuel utilization (%)	85
Operating voltage (Volts)	0.6
Inlet methane mole fraction	5.e-5
Inlet hydrogen mole fraction	0.67
Inlet carbon monoxide mole fraction	0.22
Inlet steam mole fraction	0.11
Inlet carbon dioxide mole fraction	1.e-4

An idealistic 0.1V decrease (to 0.5V) occurs at "$t = 0^+$". Besides fuel utilization (discussed shortly) and corresponding NOS, all other baseline conditions remain fixed (including reactants supply rate). The changes in electricity are first discussed.

The voltage drop *event* corresponds to the spikes shown in Fig. 7. The percentage increase in power is not as great as that of the increase in current density. Although current density increases, it was simultaneous with a voltage decrease. The result is a dampened rise in power. Subsequent to these initial spikes, current and power decrease. Over half of the gain in current is lost, and the final power output is *less* than its initial value. These undesired effects stem from the decreased reactant concentrations along the cell. An explanation follows.

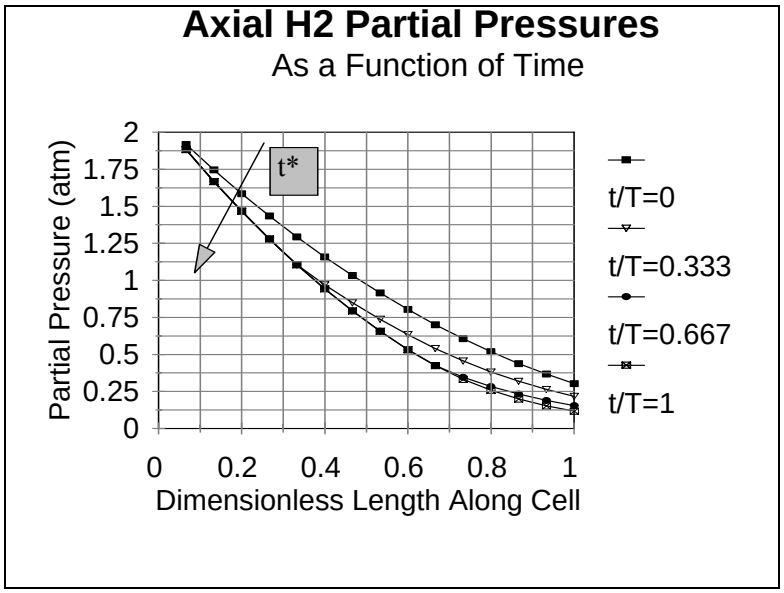

Fig. 8: Axial profiles of hydrogen partial pressure as functions of time.

Fig. 8 shows the decrease in hydrogen partial pressures throughout the time period (T) of the electrical response. The initial increase in current, shown in Fig. 8 consumes an excess of the fuel stream's hydrogen content. An effect-and-counter-effect then develops between current generation and fuel utilization.

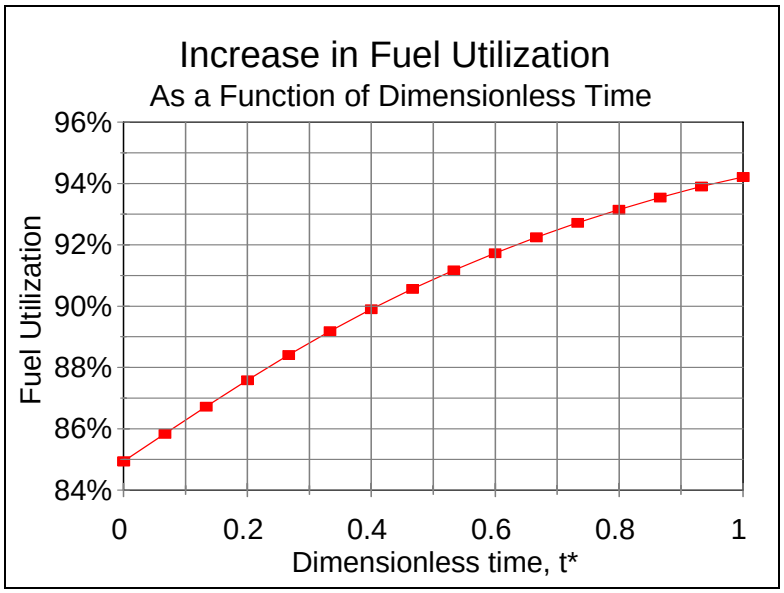

Fig. 9: Increase in fuel utilization during electrical transient episode.

Fig. 9 illustrates the rise in fuel utilization during the transient episode. The additional invariant fuel supply results in an *increase* in fuel utilization. The increase in fuel utilization, in turn, promotes current

reduction, because reactant depletion issues (e.g., concentration polarization, smaller Nernst potentials) become more pronounced. The effects of each upon the other cause current and fuel utilization to change accordingly until current electrochemically "matches" the original reactants supply rate and the new operating voltage. Fuel utilization then reaches a terminal value, and changes in electricity cease; this is neglecting second order effects of diminutive temperature rise during the timescale of *electrical* transients.

The current reduction here causes the power to fall below its initial value, because the decrease in operating voltage supersedes the *net* increase in current. *An attempt at rapidly increasing the power output of a cell stack, via independent load response, may actually lead to a rapid decrease in power generation; additionally, too large an increase in current may lead to dangerously high fuel utilizations (e.g., greater than 95%).* As will be shown, however, appropriate process settings facilitate using this rapid response controls scheme.

The potentiostatic methodology, wherein load-following is presumed to occur with change in cell potential as the stimulus is not the actual means of PES (current demand) control, but this pilot approach was used for various reasons. First, it enabled the establishment of fundamental time constants that can be used

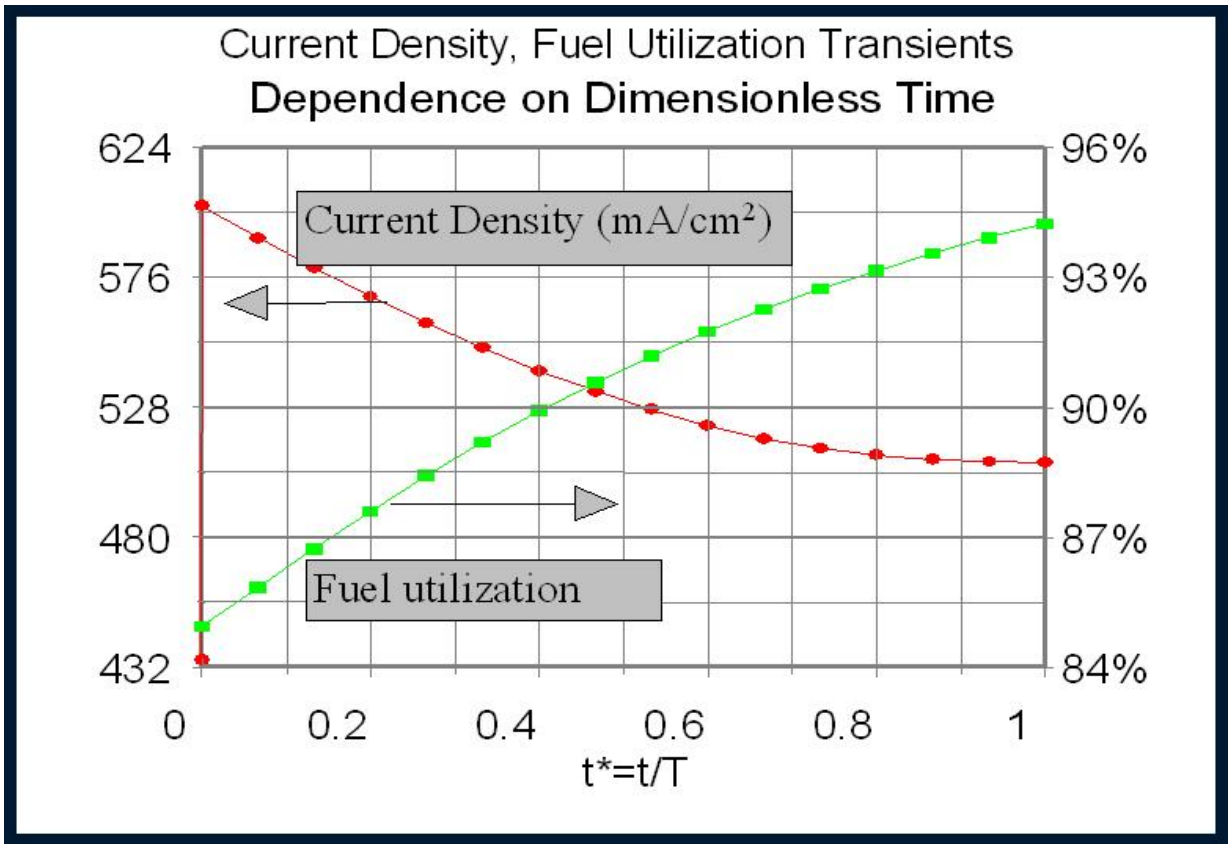

Fig. 10: Current and fuel utilization transients during transient episode.

Fig. 10 illustrates the trends in current density and fuel utilization caused by an idealized step decrease in cell potential. The additional current density and invariant fuel supply results in an *increase* in fuel utilization. The increase in fuel utilization, in turn, promotes current *reduction*, because reactant depletion issues (e.g., concentration polarization, smaller Nernst potentials) become more pronounced. The effects of each, upon the other cause current density and fuel utilization to change accordingly until current density

electrochemically “matches” the original and invariant reactants supply rates and the new operating voltage. Fuel utilization then reaches a terminal value, and changes in electricity cease; this is neglecting second order effects of diminutive temperature rise during the timescale of *electrical* transients and, again, porous media capacitive transients within the thin TSOFC anode of the present case study.

The current density reduction here causes the power to fall below its initial value, because the decrease in operating voltage supersedes the *net* increase in current density. *An attempt at rapidly increasing the power output of a cell stack, via independent load response, may actually lead to a rapid decrease in power generation; additionally, too large an increase in current may lead to dangerously high fuel utilizations (e.g., greater than 95%). It is thus imperative that simulations well-characterize the viable domains for timely and effective cell response to load variation*.

3.1.1.1.4 Response Characteristics to Load Current Variation

The potentiostatic methodology, wherein load-following was presumed to occur with change in cell potential as the stimulus is not the actual means of PES (current demand) control, but this pilot approach was used for various reasons. First, it enabled the establishment of a fundamental, yet viable, time constant (i.e., the quotient of fuel flow passage length divided by fuel velocity) that can be used to help characterize the transients associated with electrical stimuli (especially if it is clearly resolved that electrode transients occur relatively fast). Secondly, cell potential is a more suitable fuel cell control condition, regarding simulation, than is current demand, because an established cell potential allows for a dirichlet boundary condition to be imposed. This is as opposed to a current (density) wherein this Neumann boundary condition will invariably have non-uniformities. This isopotential modeling approach inherent within the potentiostatic transient methodology was thus incorporated as a “kernel” algorithm of the enhanced model, wherein variation in current demand (as opposed to cell potential) was the stimulus to allow for PES design studies.

Again the PES systems integration emphasis required the model accommodate Fig. 11 illustrates a sudden increase in current demand at time $t=0^+$, for three different scenarios of initial fuel utilization for a developmental TSOFC. Voltage decreases correspondingly in two stages. The first decline is a sharp decrease corresponding to a sudden movement along the right of the polarization curve (i.e., toward increasing current density). This is modeled to occur fairly instantaneously due to the fast nature of electrochemical transients. The additional, more gradual, decrease in cell potential is the accumulated effect of reactant depletion. Fig. 12 further illustrates this phenomenon.

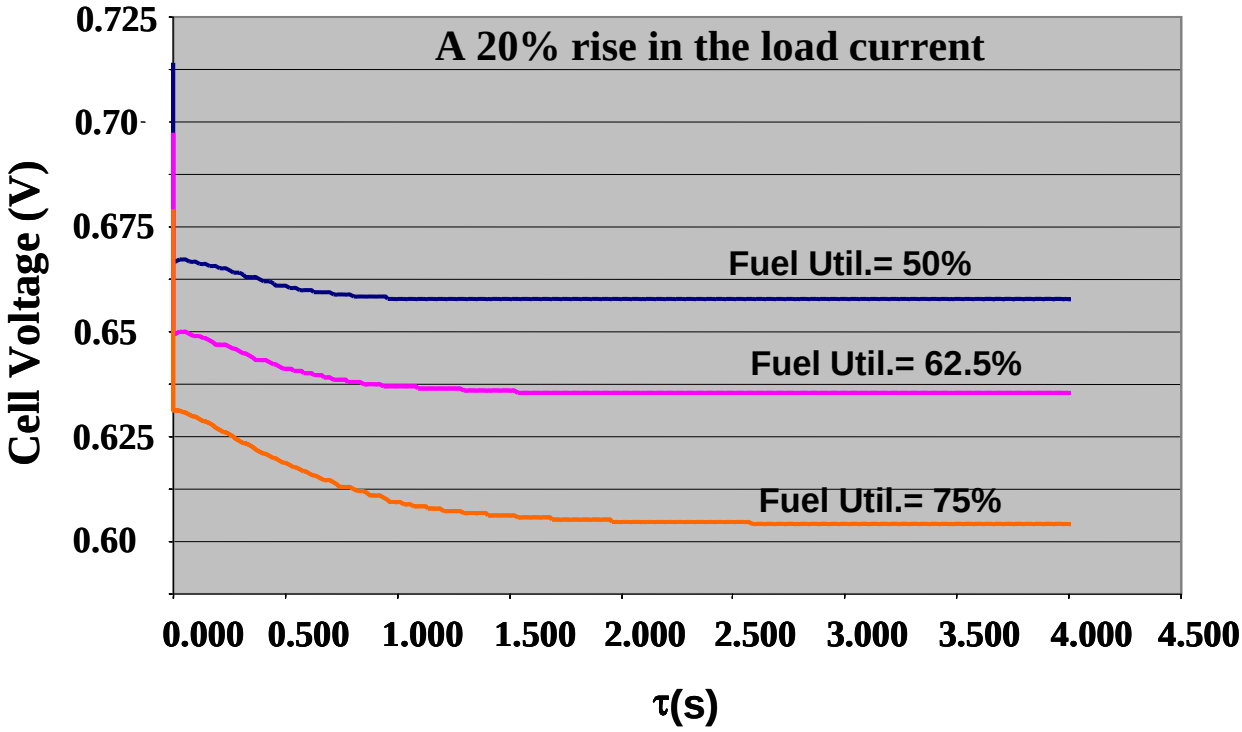

Fig. 11: Illustration of a TSOFC response to a galvanostatic control.

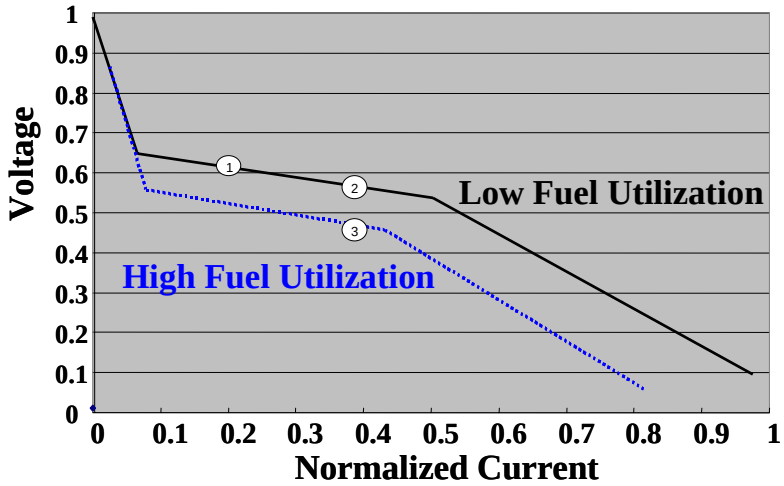

Fig. 12: Duality of cell potential drop due to polarization curve and fuel depletion effects.

Graphical movement from state 1 to state 2 (i.e., the "polarization curve" effect) corresponds to the initial spike in cell potential. This path is constrained to occur along the initial condition, lower fuel utilization polarization curve; subsequently, the reactant depletion effect causes a vertical decline to state 3 (i.e., the "reactant depletion/accumulation" effect), which corresponds to the final steady state point for the same current but higher fuel utilization. Referring again to Fig. 12, note that there are staged decreases in cell potential, as a result of progressive reactant depletion and the requirement to maintain the new current demand. The transient episode is thus multiples of the time constant (here denoted as τ), since the point of steady state attainment is that wherein each fuel parcel enters the cell electroactive area and "sees" a fairly stable cell potential. *One then denotes that a potentiostatic step change, as opposed to a galvanostatic step change, control capability results in shorter electrical transients.* Notice that larger initial fuel utilizations prolong the relative transient due to enhanced fuel depletion effects. This is further illustrated in Fig. 13.

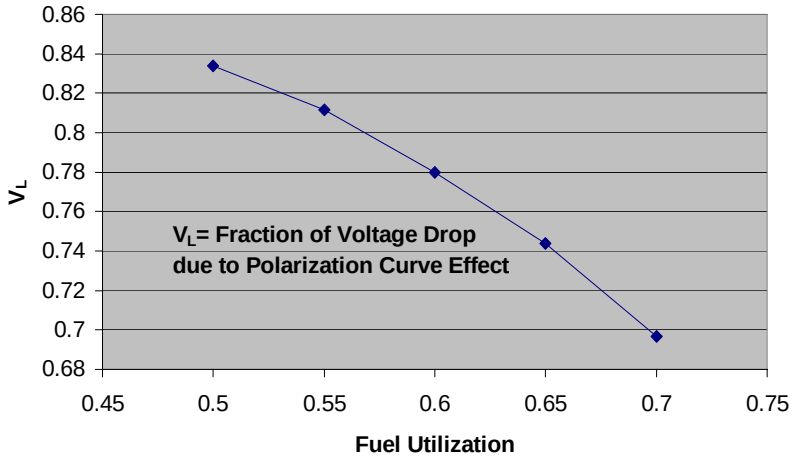

Fig. 13: Impact of initial fuel utilization upon fractional voltage drop due to "polarization curve" effect.

The larger the initial fuel utilization, the more prevalent the reactant depletion effects that manifest via lowered Nernst potentials and limiting current densities; hence, the "reactant depletion/accumulation" effect of hikes in current is substantially more influential. As illustrated in Fig. 13, the larger the initial fuel utilization, the smaller the "polarization curve" effect in comparison to the "reactant depletion/accumulation" effect. Regarding current ripple, the amplitudes and periodicities thus far tested can cause rapid oscillations along the polarization curve, without substantial realization of reactant depletion/accumulation effects. This is graphically shown in the PES studies discussed within this report.

Note that this capability to characterize SOFC response to step changes in current demand has enabled the simulation of any arbitrary load variation (e.g., fluctuation and following). This is done by using the principle of superposition, wherein any current profile can be temporally discretized as a successive number of step changes, and keeping "track", of reactants parcels (ref. above commentary) through out the entire time domain. *This feature utility has been the heart of the integrated application's ability to resolve SOFC subsystem response to PES dynamics.*

3.1.1.1.5 Planar Power Module Development

As stated the primary intention of the proof-of-concept stage was to realize a proof-of-concept systems integration tool that affords maximum validation within the scope of the Phase I award; hence, a recent commercial-scale SOFC technology was initially focused upon. This also allowed for the team's ability to accommodate a variety of SOFC designs to be exercised. *A large emphasis of the SECA program, however, is the planar design.* To this end, pilot efforts have begun regarding the transient simulation of planar cells.

Previously, a "slice technique" model had been developed that successfully simulated the polarization curve of a mature tubular SOFC design. The methodology has been bridged to simulate an anode-supported planar SOFC design. Specifically, the code analyzes unit cells, as illustrated within Fig. 14.

The unit cell includes a pair of gas flow channels bounding the P-E-N structure. Due to the numerous interior unit cells, and assuming the stack is well-insulated with well-designed manifolds, unit cells are presumed to be symmetric. The unit cells are discretized into axial slices, within which electrochemistry and heat transfer are analyzed. The electrochemical governing equation for each slice is taken from the work of Kim et al. (1999) and stated in equation (11).

$$V(i) = E_o - iR_i - a - b*\ln i + \frac{R_u T}{4F}\ln\left(1-\frac{i}{i_{cs}}\right) + \frac{R_u T}{2F}\ln\left(1-\frac{i}{i_{as}}\right) - \frac{R_u T}{2F}\ln\left(1-\frac{p_{H_2}{}^{o} i}{p_{H_2O}{}^{o} i_{as}}\right) \quad (11)$$

The model was compared against the experimental data of the stated reference, wherein an anode-supported test SOFC was operated across a range of temperatures, most pertinent of which was the 800°C operation. As illustrated in Fig. 14, the model is sufficiently accurate, based upon the button cell data available thus far.

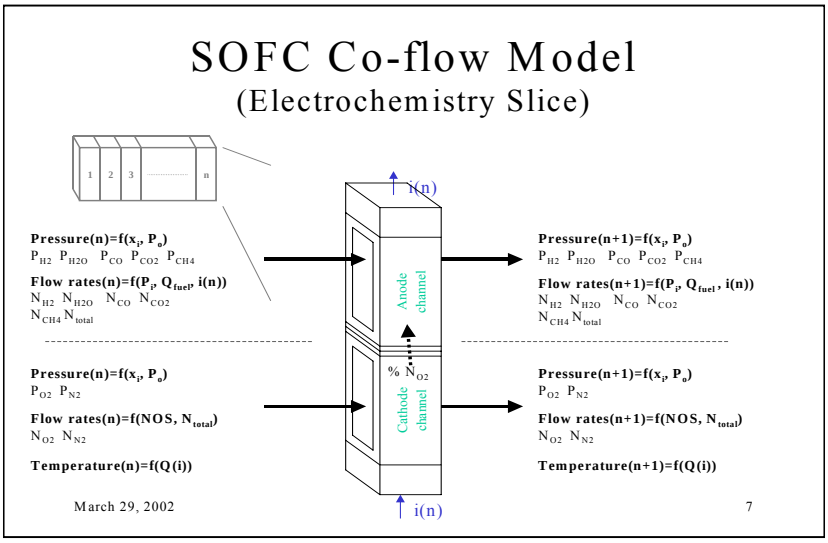

Fig. 14: Unit Cell Slice of a Planar SOFC.

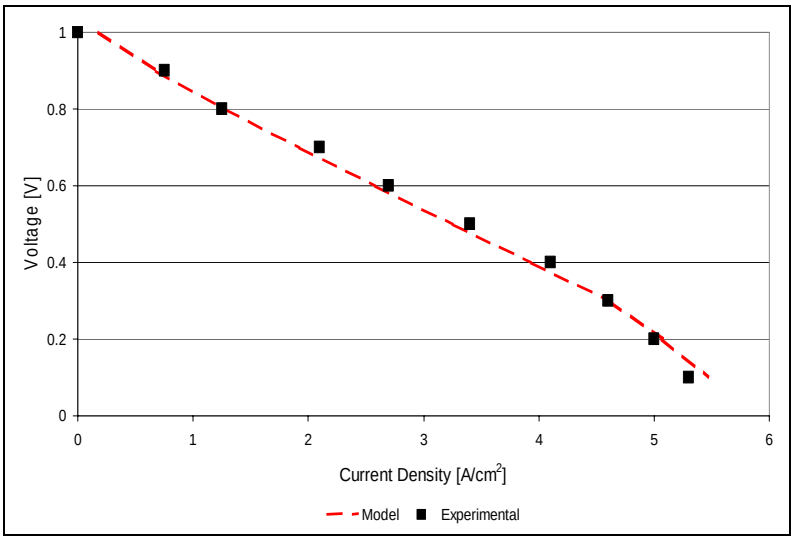

Fig. 15: (Button-cell) validation of model with published experimental data.

As with the tubular design, the progressively developing steady state model for the planar design forms a foundation for the realization of a transient model, using the same principles discussed above. This approach was extended to the planar model. A prerequisite to the transient model is a steady state model wherein the initial and final steady state points could be established and verified. This was of paramount importance to the successful steady state model of the tubular design. Preliminary data obtained from available literature has fostered a preliminary model. The model has much of the same basis as that developed for the tubular design [Haynes and Wepfer, 1999], such as the explicit axial march technique.

Table II: Preliminary Validation of Planar Model {4 3/8" Cell Pilot}

Cell Potential	Experimental C.D. [mA/cm2]	Simulated C.D. [mA/cm2]	Abs. Error
0.8	400	408	2%
0.75	500	484	3.2%
0.675	600	608	1.25%

Based upon the domain of validated data in Table II and the transient modeling approach discussed, a simulation of a step change in cell potential has begun. Preliminary results are shown in Fig. 16.

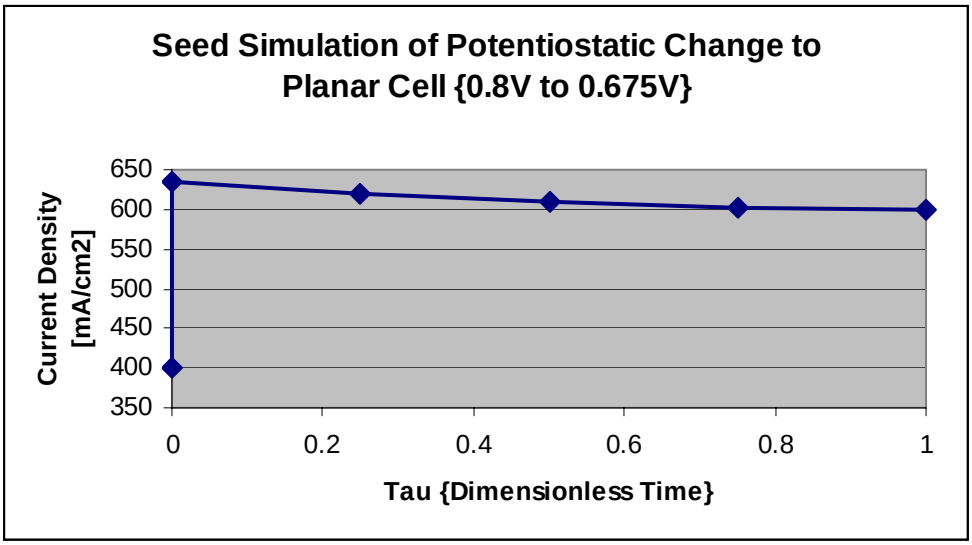

Fig. 16: Preliminary simulation of a step decrease in cell potential

The scenario involved a step decrease in cell potential from 0.8V to 0.675V. Current density spiked from 400 mA/cm2 initial steady state to 635 mA/cm^2 via the "polarization curve effect" and tapered off to the final steady state voltage of approximately 600 mA/cm^2. This latter phenomenon is due to fuel depletion effects. The reactants supply was modeled as invariant; thus, fuel utilization rose significantly and caused the ensuing current decline. Again "tau" is the time constant equal to the length of the fuel flow channel divided by the fuel velocity. The reader sees the same pattern of current (density) overshoot and subsequent decline as discussed of the tubular SOFC in Fig. 16.

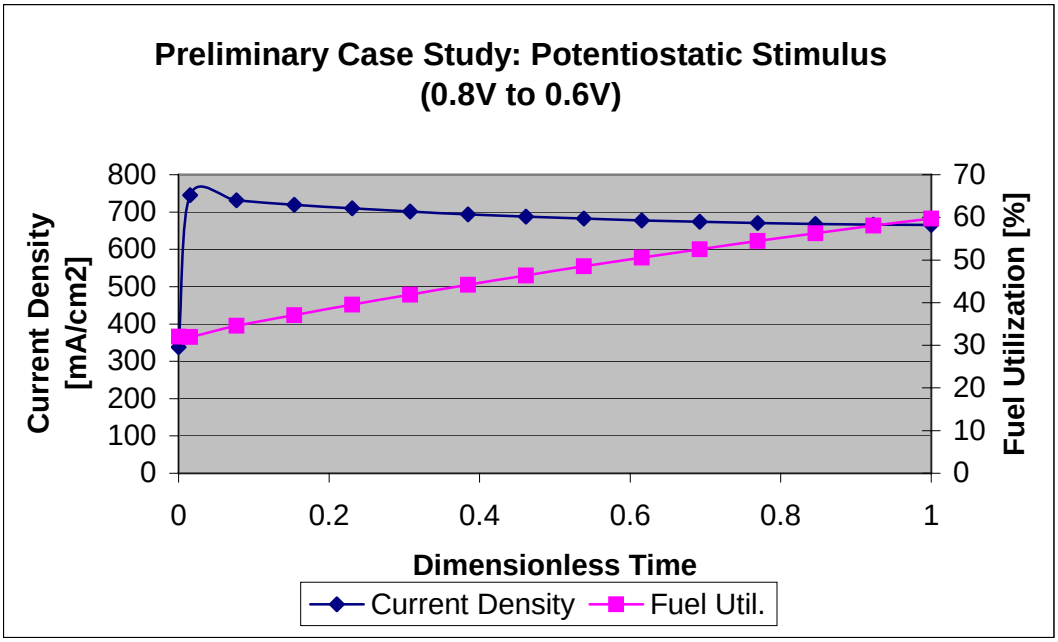

Fig. 17: Preliminary result of planar cell transient.

Fig. 17 illustrates the simulated response of a developmental planar SOFC. As a preliminary step in the transient model development, a potentiostatic step change is predicated wherein cell voltage is decreased in order to accommodate an increase in load. Initial and final steady states correspond to the data reported, and the transient trends of "current overshoot" and fuel utilization increase corroborate the same trends seen of TSOFCs.

3.1.1.1.6 SOFC Response to Bi-Modal System Transients

SOFC stack transient response may also result from reactants supply stimuli. For instance, the fuel processor may experience an anomaly or the blower/compressor may go through an off-design episode; especially during a system transition (e.g., start-up, shut-down, load variation, etc.). Such "front end" reactants supply variations to the stack may be coupled with "back end" stimuli caused by PES and/or load variational dynamics. Such bi-modal SOFC response has not been addressed at large within the literature. The stack model(s) under development are being tailored to simulate such in the last quarter of the Phase I effort. Specifically, the Lagrangian approach discussed earlier will be modified to allow for variant reactants supply. *This allowance for characterizing SOFC response to bi-modal stimuli will be pivotal to the robust controls and systems integration optimization exercises intended for Phase II.*

3.1.1.1.7 Failure Modes/ Reliability Concerns Resulting from System Transients

Pilot investigations have been performed, and will be emphasized in latter Phase I, for qualitatively and quantitatively resolving the failure modes and reliability concerns that are specifically sensitive to system transients. Load variational issues include chemical, electrochemical and thermal degradative effects; and fuel processor variational issues include anodic deactivation and thermal shock due to feedstock "slip".

A key reliability concern within the given SECA subtopic is SOFC reliability in an environment of electrical feedback such as "current ripple". *A preliminary, qualitative assessment has been arrived at that high frequency current ripple induces partial charge-discharge cycles that can lead to electrochemical and thermal cyclic fatigue effects and chemical degradation due to heightened anodic exposure to an oxidizing environment.*

Typically, so long as the magnitude is not greater than the cell's limiting current, current demand is equated to current generation at all points in time. In fact, there will always be some initial level of "charging" or "discharging" effect imposed by decreasing or increasing current demand, respectively, driven by inherent capacitive effects within the cell. Long-term current ripple may thus be viewed as a repeating series of charge-discharge cycles. Just as other galvanic cell technologies such as secondary/rechargeable batteries and supercapacitors have degradative responses associated with multiple charge-discharge cycles, SOFCs are expected to have some level of "electrochemical fatigue" and related degradation associated with periodic current ripple.

From a *performance* analysis standpoint, the current level of modeling has been appropriate; however, the fuel cell capacitive-effect model will be pertinent to Phase II, since characterizing any degradative effects of the electrode "charging" and "discharging" (that accompanies load variation) would require such. The latter attempt will be to gleam capacitive-effect principles from electrochemical storage cells (e.g., secondary batteries and/or ultracapacitors). This would further address the reliability concerns of load fluctuation such as current ripple; and should serve as a good complement to the SECA lab efforts blossoming in this area (e.g., NETL's recent initiative for physically testing electrical feedback effects).

A key concern with SOFC reliability is the number of thermal cycles that can be incurred before substantial degradation unto performance/structural failure manifests. Although the pre-eminent focus has been start-up/shut-down cycles, the electrical cycles that occur via load fluctuation also engender "mini" thermal cycles.

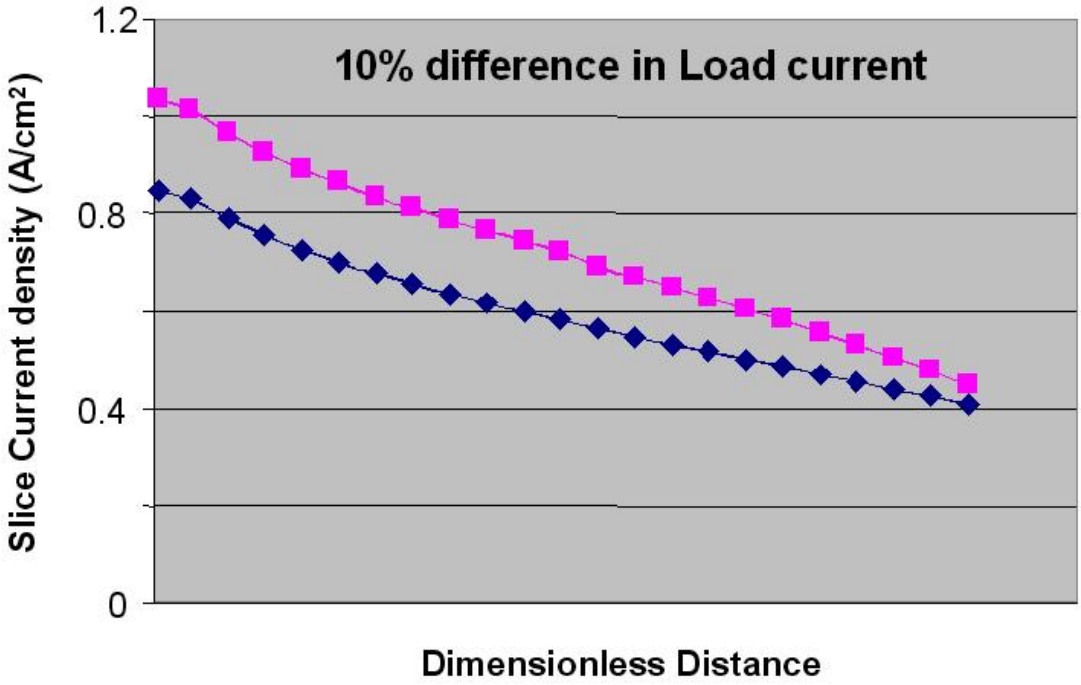

Fig. 18: Variations in current density distribution due to load variation.

Fig. 18 illustrates the variation in current density distribution that arises due to load fluctuation (the test case is the tubular SOFC discussed earlier). As the reader can see, an approximately 5% periodic current ripple about a mean current demand can result in substantially different current profiles between minimum and maximum currents realized. As a result substantial thermal gradients with respect to spatial dimensions and time are realized; these thermal gradients may induce deleterious stresses. *High frequency cycling between these two extremes can cause thus substantial thermal cycling and fatigue effects. Fortunately, the team's affiliation with Ceramatec and the SECA CTP Failure Analysis group (via mutual CTP groups member Haynes) will afford rigorous analysis as the SECA program proceeds.*

Finally, with respect to endangerment of SOFC reliability via power electronics instabilities, an aggressive attempt at nominal fuel utilization, coupled with current ripples of significant amplitude, may cause periodic episodes of effectively high fuel utilization and possibly lead to threshold exposures of the SOFC anodes to an oxidizing environment (e.g., toward the tail ends). This may invoke anode redox, causing volumetric changes in the electrode's mircrostructure by as much as 30%. *Again the proposing group's ability to quantify oxidant presence along the anode and its affiliation with the SECA CTP Failure Analysis group (via mutual CTP groups member Haynes) will afford rigorous analysis as the SECA program proceeds.*

The desire for rapid change in current may result in an aggressively timely increase in fuel supply. The related fuel-processing transient may incur a non-ideality. Specifically, there is opportunity for "slip" to occur through the fuel processor during this transition, wherein hydrocarbon fuel enters the stack. *Anode catalysis*

may be disturbed by coking and/or sulfur intolerance. Additionally, in situ (or "direct internal") reformation may occur within the stack, causing microcrack initiation via localized thermal shock. This latter possibility is highlighted.

The Georgia Tech Failure Analysis SECA CTP group, which again has Haynes as a mutual member, reported upon the threat of microcrack initiation thermal shock (Qu et al., 2003). The threshold heating value for the onset of microcracks was determined.

$$q_{th} = \frac{3\pi^2 k r_0}{2\alpha}\sqrt{\frac{G_c \pi(1-\nu)}{E_0 b(1+\nu)}} \qquad (12)$$

where

E_0 = Elastic Young's modulus of the un-cracked material

ν = Poisson's ratio of the un-cracked material

G_c = Fracture toughness of the material

b = crack size; r_0= heat source/sink length parameter

N = number of cracks per unit volume

k = Thermal conductivity

α = Coefficient of linear thermal expansion

The threshold (i.e., maximum) magnitude of the heat source/sink is proportional to the materials thermal conductivity, length parameter and square root of the medium's fracture toughness; it is inversely proportional to the coefficient of linear thermal expansion and the square roots of the Young's modulus and crack size.

The envisioned scenario is that of a point or distributed heat source/sink suddenly being introduced within a medium. The introduction of hydrocarbon fuel (i.e., methane in this case study) is known to be a vigorous, highly localized heat sink effect at the leading edges of the anodes; hence, microcracks may form accordingly. A key variable is the heat source/sink length parameter, r_o. For the given study it can be considered the effective radius of the methane reformation within the anode porous medium. Rearranging the above equation, and replacing the threshold heating value with a heat sink magnitude associated with the endothermic methane reformation:

$$r_{o,\min} = \frac{2\alpha}{3\pi^2 k}\sqrt{\frac{E_o b(1+\nu)}{G_c \pi(1-\nu)}}\, q_{\sin k} \qquad (13)$$

Equation (12) quantifies the minimum reaction radius required for a given heat sink effect associated with direct internal reformation. Based upon an allowance for crack sizes of ten microns, and the following anode property values assumed.

Table III: Thermomechanical properties of Ni/YSZ.

E(Pa)	ε	G_c (J/m^2)	k(J/(sec m K))	$\alpha(micron/(m*\mathrm{K}))$
96x10^9	0.3	9	5.84	12.22x10^{-6}

The following graphs resulted.

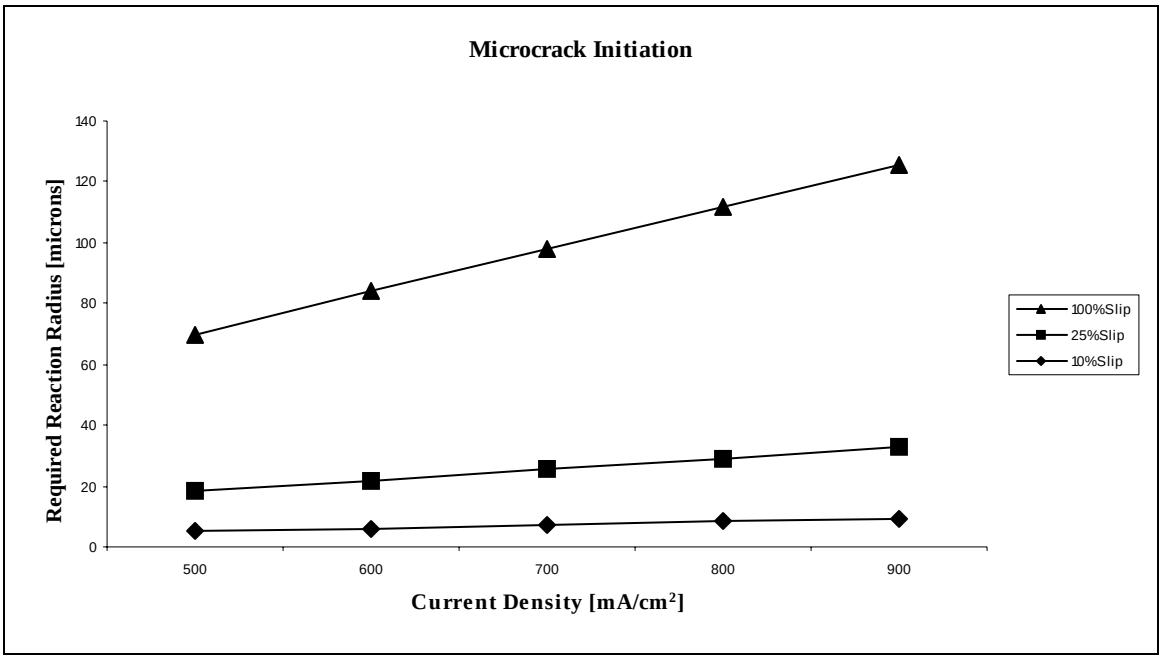

Fig. 19: Characterization of required DIR reaction radius for avoidance of microcrack initiation.

Fig.19 characterizes the minimal reaction radius required for safe direct internal reformation without inducing thermal shock via microcrack initiation. The abscissa is cell current density, based upon a standard 10 cm x 10 cm electroactive area design. Materials balances via Faraday's Law, presumed steam reformation of methane (in situ), and various methane slip values dictated the ordinate values. As a safety factor, complete methane reformation was presumed. *This is a plausible means of simulating the danger of localized thermal shock via microcrack initiation during a transient episode.* It is evident that increases in power demand (and thus current demand) can be dangerous occurrences as fuel process or yield decreases, even during short-duration transitional phases. The evaluation can also be used as an effective measure for influencing the safe and reliable microstructural design of the anode.

These seed results will have greater fidelity and impact within Phase II, wherein continued experimental validation/ correction of mechanical and thermophysical data properties, along with greater resolution of methane mass transfer and reactivity within the porous anode, will be given greater attention.

3.1.1.2 SOFC Spatial Model

Rigorous modeling of SOFCs using a finite element approach has been undertaken to predict the thermal distribution and performance of stacks in two different configurations. In contrast to the previous work in the literature, radiation heat transfer effects have been considered. The effect as been found to play a major role in determining the thermal condition of the stack and must be taken into account for accurate determination of temperature distributions. Thermal conduction effects have been coupled with electrical conduction and local electrical and chemical potentials have been rigorously computed.

3.1.1.2.1 Finite Element Modeling

The finite element method (FEM) is well suited to analysis of geometrically complex components. The principle alternative for such analysis is the finite difference method. In theory either method could achieve comparable results. In practice it is very difficult to model complex geometry's and boundary conditions with a finite difference method. This is due to the data structure of most finite difference codes, which is driven by the equation solution method and tradition. The result is that most FEA codes require a structured mesh and hand coded boundary conditions. SOFC modelers using finite differences avoid these problems by using 2-D, pseudo 3-D or homogenized models (Yentekakis et al., 1991, Erdle et al., 1991, Ferguson et al., 1991). These approaches have the merits of quick model generation and solution, but eliminate the possibility of including effects such as enclosure radiation which require a detailed geometric representation.

3.1.1.2.2 Modeling Approach

Comprehensive modeling of SOFC systems is beyond the capability of existing computational methodology due to the wide range of spatial and temporal scales, and physical phenomena which must be considered. Consequently simplified models of certain phenomena and scales must be employed. This work focuses on the detailed spatial resolution of temperature and voltage in a single cell repeat unit using simple models of fluid dynamics, electrode kinetics, and the surroundings.

3.1.1.2.3 TOPAZ

TOPAZ is a three-dimensional finite element program for heat transfer analysis from the Lawrence Livermore National Laboratory. Some of the features of TOPAZ include steady state or transient capability, orthotropic temperature dependent material properties, and interfaces to graphical pre and post processors. Boundary conditions include specified temperature, flux, convection, bulk fluid, radiation, and enclosure radiation, with parameters that may vary with time, temperature or position. A significant feature of TOPAZ is its distribution as FORTRAN source which makes it possible to add features needed for fuel cell analysis. Several extensions to the TOPAZ code were required to model SOFCs. Most of the changes are applicable to general heat transfer analysis, but a few are specific to fuel cell modeling. TOPAZ Extensions for Solid Oxide Fuel Cells Finite element spatial discretization of the nonlinear system of partial differential equations for coupled thermal and electrical conduction requires repeated solution of systems of linear equations. Solution of these linear systems generally consumes in excess of 90% of the analysis computer time. More importantly, the model resolution is usually limited by the amount of memory required to store the conductance matrix. TOPAZ uses a symmetric skyline solver which stores by column from first non-zero entry in a column to the diagonal. When coupled with a bandwidth minimization scheme, the skyline solver can be quite efficient for high aspect ratio geometry's. While, when applied to more equiaxed geometry's,

the skyline matrix has a high degree of sparsity, which equates to excessive memory demand. Several linear equation solution methods from the Sparse Linear Algebra Package (SLAP) were implemented in TOPAZ. The SLAP routines share a common pointer reference scheme in which only the non-zero array entries are stored. The algorithms and data structures needed to generate the reference pointers from finite element connectivity data were developed and implemented in TOPAZ. Application of the sparse storage technique has reduced the memory growth behavior from nodes1.7 to nodes1. A substantial improvement in solution speed also resulted. A documented but unimplemented feature of TOPAZ is the bulk fluid node. The bulk fluid node models convection from the solid to a fixed mass of fluid, as opposed to the convection boundary condition which represents an infinite amount of fluid. This capability was added to allow thermal coupling with the reactant streams. A two node advection element was also added to enable modeling of streamwise transport between bulk fluid nodes. The advection element generates a non-symmetric matrix due to the directional (upstream to downstream) nature of the transport. The original skyline equation solver and several of the SLAP solvers are for symmetric matrices only. Modifications to the pointer generation and matrix assembly routines were required to use the non-symmetric SLAP solvers. TOPAZ solves for a single degree of freedom, the temperature, at each node. In order to model fuel cell performance and the effects of localized ohmic heating an electrical potential degree of freedom was added. An iterative sequential solution method was chosen to couple the two degrees of freedom. The temperature solution is computed using the ohmic heating computed from the voltage distribution of the previous iteration. The electrical solution follows with conductivities evaluated using the temperature distribution of the previous iteration. Boundary conditions for the electrical solution include specified potential, current density, and film resistance. Analysis of problems involving coupling of radiation in an enclosure with conduction in the solid which encompasses the enclosure can be performed with TOPAZ. This type of analysis requires pre computation and storage of geometric view factors. The view factor F_{ij}, is the fraction of radiant energy emitted from surface *i* which is incident on surface *j.* View factors are stored in TOPAZ as a simple array even though most of the array entries are zero, or practically zero. Using a simple array, memory requirements grow with the square of the number of radiating surfaces. A single repeat unit cross flow SOFC model may need more than thirty thousand surfaces to provide appropriate spatial resolution. The memory required for a view factor matrix of this size is one hundred times the memory on a typical workstation. Pointer referenced sparse storage of view factors, similar to that used in SLAP, was implemented in TOPAZ resulting in linear memory growth behavior.

SOFC specific modeling needs were treated with a custom subroutine and input file. This SOFC subroutine reads a file which defines gas flow rates, and associates anode faces and corresponding cathode faces with air and fuel bulk nodes. The routine tracks gas compositions from inlet to exit. Local gas compositions and electrical potentials are used to calculate local current densities and heating rates which are used as boundary conditions in the next iteration.

3.1.1.2.4 Stack Model

Crossflow and coflow/counterflow models were developed using the modified TOPAZ program. Both configurations consist of a single cell repeat unit which includes an electrolyte with anode and cathode, and two halves of a bipolar-biflow interconnects. The parallel flow configurations allow reduction in model size by assuming that the solution has channel to channel symmetry. The symmetry assumption implies that the two sides of the stack which are parallel to the flow direction are adiabatic. This may or may not be valid depending on conditions external to the stack. Stack dimensions, representative material properties and boundary conditions are described in Khandkar et al. The temperature dependence of material properties, where known, was used in the model. Single values are reported here due to space constraints. The “effective resistance” of each component (interconnect, anode, cathode, and electrolyte) is computed by

the finite element method from actual cell geometry and temperature dependent conductivity. The convective heat transfer coefficients were derived from the laminar flow Nussult number (Nu_T) for a rectangular duct. Current density is calculated at each electrolyte element from the local electrode potential, overpotential function and local bulk gas chemical potential. Only areas directly exposed to fuel and air were electrochemically active. That is the effects of diffusion under interconnect ribs were ignored. A constant overpotential of 100mV throughout the operating range was used for the cases shown. Any function of local temperature, fuel composition and current density may be input as an overpotential function.

3.1.1.2.5 Development of the Finite Element Model

The finite element meshes of the two models are shown in Fig. 20. Khandkar et al. report information on the models, boundary conditions and computational resources required. It can be seen from the Fig. 20 that the coflow/counterflow model has benefited from the symmetry reduction by allowing a much finer mesh, while requiring much less computer time and memory. The 360 fold reduction in memory requirements for view factor storage (9432Mb to 26Mb) shows why the sparse storage scheme is essential to radiation modeling in fuel cells. The impact of sparse storage of the global conductance matrices is equally important. A schematic illustration of the equations solved in the solid and at the boundaries is shown in Figs. 21 and 22. Radiation boundaries, and enclosures used the specified inlet gas stream temperature as the temperature of the surroundings. That temperature was 1073K for the results presented here. The film resistance coefficient used as the current collection boundary was set to a value which effectively forced the surface to a uniform specified potential. Overall current and energy balances zero satisfactorily. Fuel and air stream inlet conditions are listed in Khandkar et al. for both crossflow and coflow model. These models were run on a HP 720 workstation with 64Mb of main memory and 2Gb of disk storage. The 64Mb memory is insufficient for the cross flow model as 113Mb are required when modeling with radiation and 83Mb without radiation. The virtual memory system on the machine allows such models to be run, but at a greatly reduced speed in the case of the radiation model. More memory would be required to develop a multicell model, or a single cell model with higher resolution.

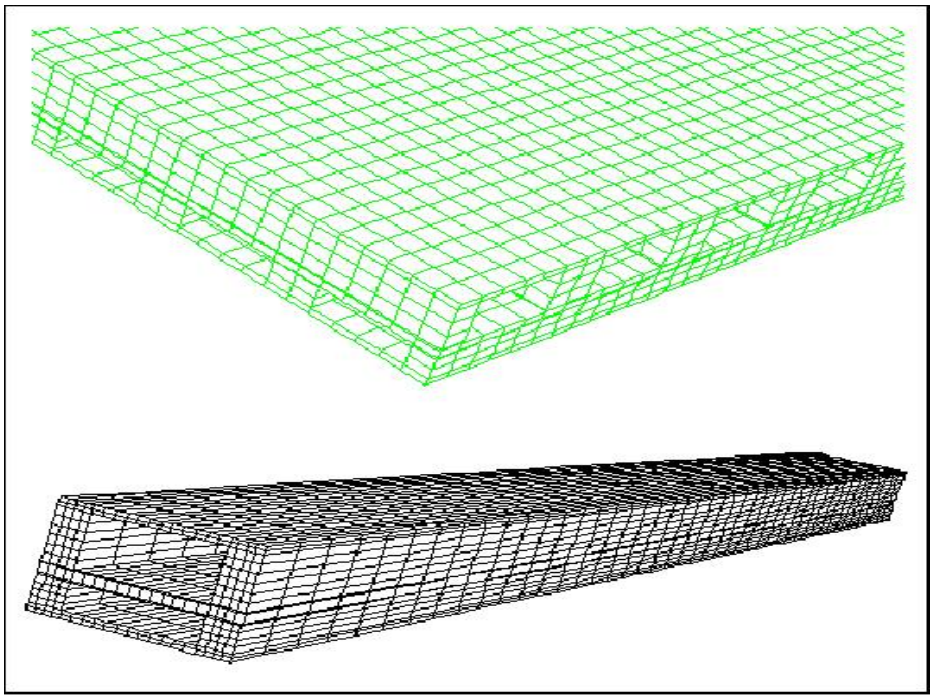

Fig. 20: Finite element meshes for cross and coflow/counterflow conditions.

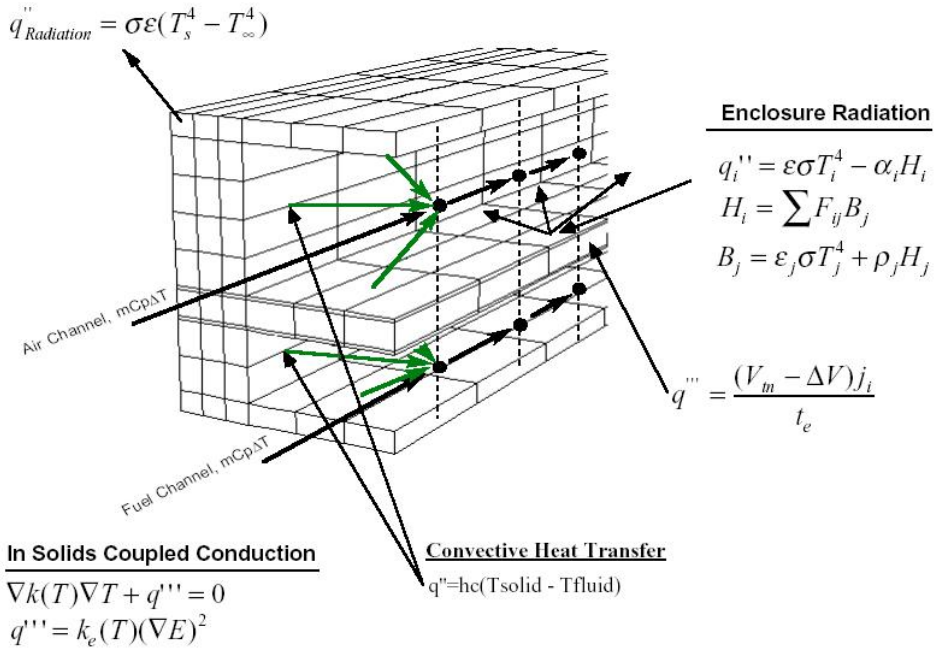

Fig. 21: Schematic of the SOFC Thermal Model.

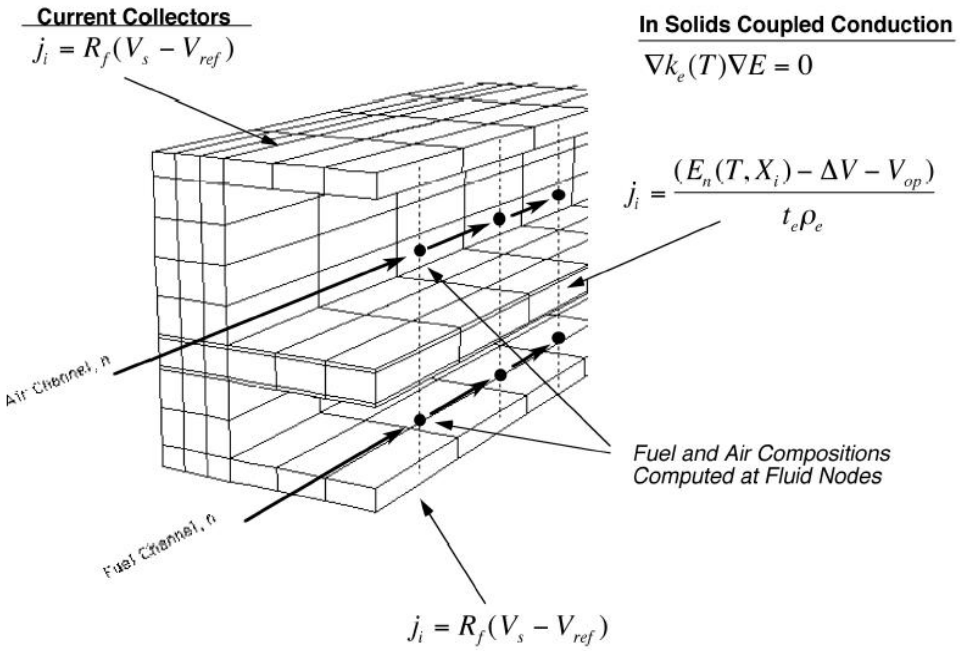

Fig. 22: Schematic of the SOFC Electrochemical Model.

3.1.2 Power-Electronics Systems (PES) Model

3.1.2.1 Motivation for developing PES models

SOFC based PESs are used to provide direct or alternating current (ac or dc) to satisfy application specific power needs. Typically, they include multiple interconnected power converters (typically a dc-dc converter followed by a dc-ac converter for stationary applications and dc-dc converter for mobile applications). The switching scheme in such power converters can be based on pulse-width modulation (PWM), resonant, quasi-resonant, soft-switched, or line-commutated. Furthermore, the topological structures of these converters can be vastly different from each other. As such, the mathematical models of the PES may include discontinuous differential equations, discrete differential equations, functional differential equations, digital automata, impulsive differential equations, non-smooth differential equations, ordinary and even partial differential equations. In addition, these models include system-level constraints.

The traditional approach to modeling such systems using averaged models (Middlebrook et al., 1977 a, b) is inadequate and in many cases, results based on them yield inaccurate results (Lee, 1990). These averaged models completely neglect the impact of switching frequency and hence can not predict the dynamics on fast scale. Instability in standalone or integrated converter can occur on a slow as well as on a fast scale (Mazumder et al., 2001a). Secondly, even the slow-scale averaged model may have more than one equilibrium solution or more than one stable orbit. A linearized small-signal analysis ignores the presence of these other solutions. Therefore, a small-signal analysis can not predict anything about the domain of attraction of the nominal solution or orbit. If two of the solutions are stable, then the system will have two operating points, one of which is the nominal solution. This possibility is completely ignored in

linearized average models. Consequently, small-signal averaged model can not predict the post-instability dynamics.

To model a PES, one needs a unified modeling framework, which can handle any type of dynamical system[8] with varying levels of detail. Such a unified framework is an indexed collection of dynamical systems along with a map for transitions among them. A transition occurs whenever the state satisfies certain conditions, given by its membership in a specified subset of the state space. Hence, the entire system can be thought of as a sequential patching together of dynamical systems with initial and final states and with the transitions performing a reset to a generally different initial state of a generally different dynamical system whenever a final state is reached. Formally, the unified model U_{model} = (P, C_{CDS}, C_{ATM}, C_{AJTM}, C_{DDC}, C_{CJS}, C_{CJDM}) is a dynamical system with the following elements: P is the set of discrete states; C_{CDS} = $\{C_{CDS_p}\}_{p\in P}$ is the collection of continuous dynamical systems, where each $C_{CDS_p} = (Y_p, S_p, T_p, U_p)$ is a dynamical system with continuous state spaces (Y_p) and dynamics (T_p) and as well as a set of continuous controls (U_p); C_{ATM} = $\{C_{ATM_p}\}_{p\in P}$, where $C_{ATM_p} \subset Y_p$ for each $p \in P$ is the collection of autonomous (state-dependent) transition maps; C_{AJTM} = $\{C_{AJTM_p}\}_{p\in P}$ is the collection of autonomous jump-transition maps; C_{DDC} = $\{C_{DDC_p}\}_{p\in P}$, is the collection of discrete dynamics and controls; C_{CJS} = $\{C_{CJS_p}\}_{p\in P}$, where $C_{CJS_p} \subset Y_p$ is the collection of controlled jump sets; C_{CJDM} = $\{C_{CJDM_p}\}_{p\in P}$ is the collection of jump destination maps (Mazumder, 2001c).

3.1.2.2 PES model development

The PES unified dynamical model is implemented in *Saber Designer* simulation platform, which has its own programming language (*MAST*) for modeling, but can accept codes written in *FORTRAN* and C. Currently, among the commercially available simulators, *Saber Designer* has the most extensive (over 30000) library of mathematical computer models in power-electronics components and systems, electromechanical-energy conversion, hydraulics, thermal, magnetic, control systems, and signal processing. The SOFC model developed in *FORTRAN* was incorporated in the PES model using dynamic link libraries (*dll*) and a *MAST* template.

For our study, we selected three PES topologies for SOFC stationary power applications. The specifications of the PES for SOFC power conditioning are,

Output voltage: ~120 V (phase voltage)
Output power: 5 kW
Input: 72 V SOFC stack.

As illustrated in Figs. 23(a)-23(c), the PES topologies essentially consist of a dc-dc boost stage to step up the voltage from 72 V to a value suitable for power conversion in the next stage. The boost converter uses

[8] A dynamical system is defined as a system $\Sigma = (Y, S, T)$, where Y is an arbitrary topological space in the state space of Σ. The transition semi-group S is a topological semi-group with identity and T is an extended transition map T. $Y \times S \rightarrow Y$ is a continuous function satisfying the identity and semi-group properties.

a PWM controller to control its switching. The PWM controller consists of a three-pole, two-zero voltage mode compensator and a PI current controller.

A dc-ac converter follows the boost converter. Fig. 23(a) shows the traditionally used thyristor-based line commutated current-source inverter (CSI) topology (El-Tamaly et al., 2000, Naik et al., 1995). The switches in the three legs switch at 60 Hz with a 120° shift between the three phases. Fig. 23(b) shows the commonly used self-commutated PWM voltage-source inverter (VSI) (Konishi et al., 1998). The switching frequency is determined by the PWM controller circuitry. Fig. 23(c) shows the high-frequency-transformer-isolated cycloconverter topology (Kawabata et al., 1990). This topology is similar to the topology in Fig. 23, except for the presence of the high-frequency transformer between the dc-ac and the ac-ac stages. The advantage of using such a topology is that the bulky line transformers, used for isolation, is replaced by a much smaller high-frequency transformer. However, such a topology uses an extra stage for ac-ac conversion. The switching losses can be minimized by using advanced switching schemes such as zero-voltage and zero-current switching.

3.1.2.3 PES electrical characteristics

PES input current depends on both the application loads as well as its switching mechanism. Filters are used to reject the high frequency harmonic components to a large extent but the low frequency ripple cannot be eliminated unless large bulky filters are used. Since the different PES topologies considered in this study have different switching schemes and high frequency rejection mechanisms, the harmonic content of input current for the three cases are vastly different. Therefore each PES will impose different stresses on the SOFC stack, and an in-depth understanding of the effect of the fast- and slow-scale ripple (Mazumder, Nayfeh, and Boroyevich, 2001a-d) is necessary to propose any reliability solution. Figs. 24 - 26 show the steady state input current and their corresponding frequency domain spectrum respectively for the topologies of Figs. 23(a)-(c). The line-commutated topology imposes a current ripple at the line-frequency and its lower order harmonics, while the topologies in (b) and (c) impose a high-frequency (switching) and a low-frequency (line) current ripple on the SOFC.

Researchers at UIC are presently investigating PES for mobile power markets. The PES consists of a step down converter, which could either be a buck or a buck-derived converter.

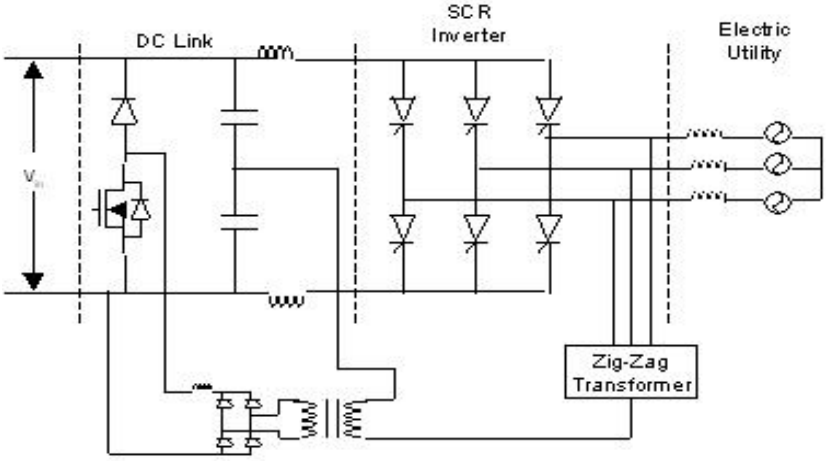

(a)

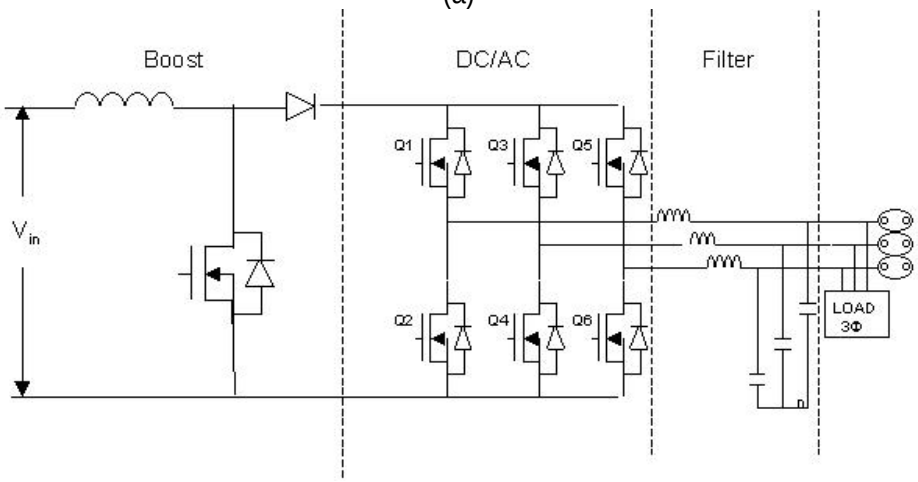

(b)

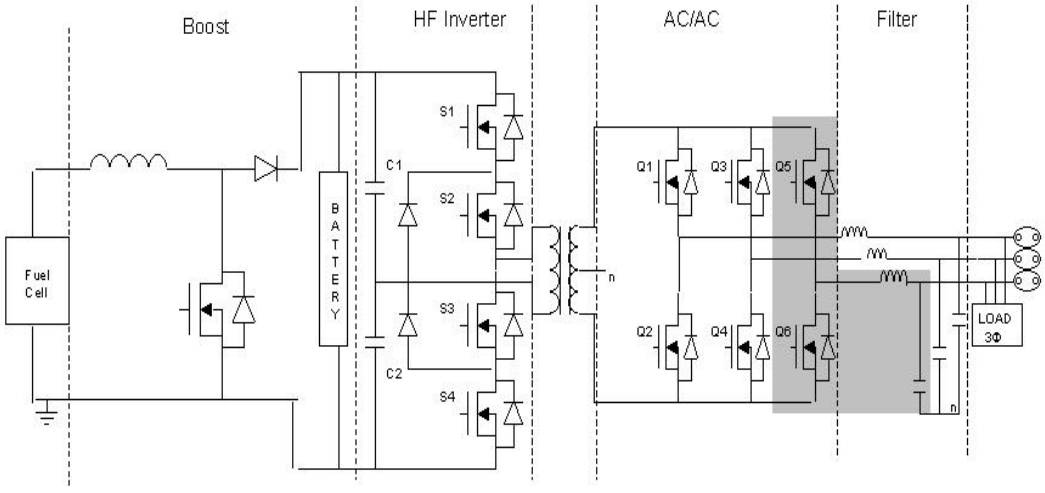

(c)

Fig. 23: The three topologies used for studying the impact of power-electronics on the SOFC stack. (a) represents line-commutated topologies while (b) and (c) represent self-commutated and transformer-assisted topologies.

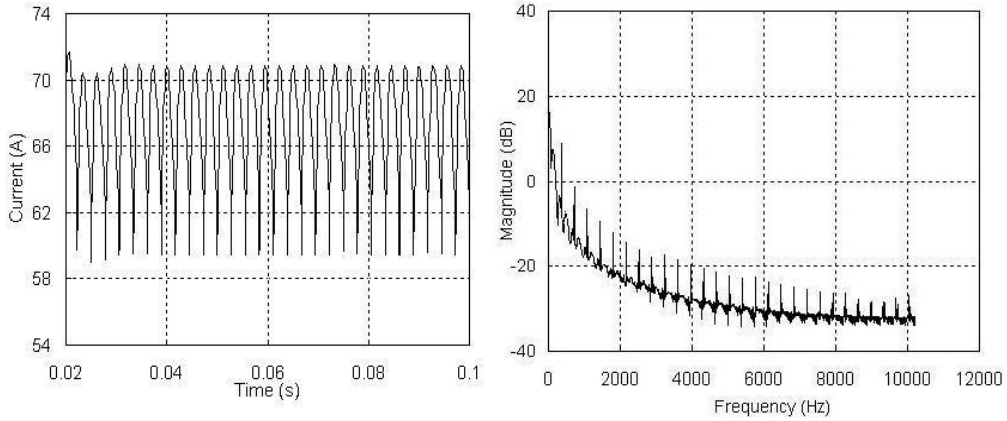

(a) (b)

Fig. 24: Steady state (a) input current characteristics and (b) frequency domain characteristics for the line-commutated CSI topology of Fig. 23(a).

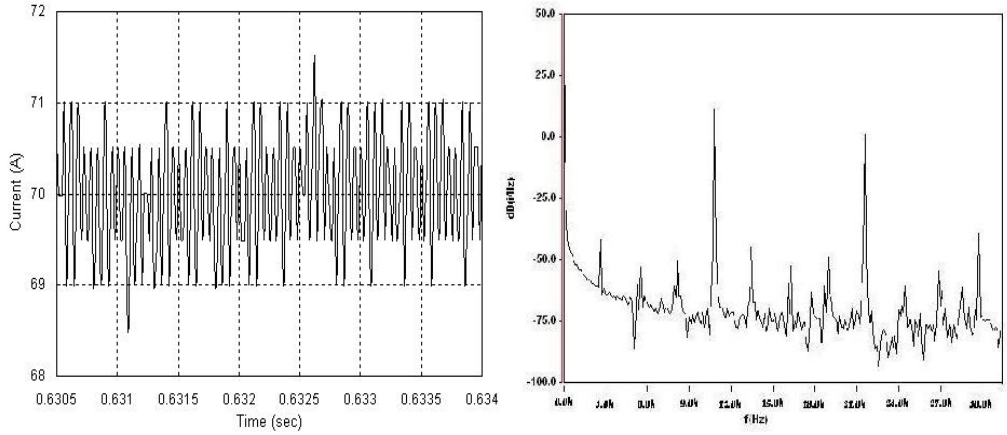

(a) (b)

Fig. 25: Steady state (a) input current characteristics and (b) frequency domain characteristics for the self-commutated PWM VSI topology of Fig. 23(b).

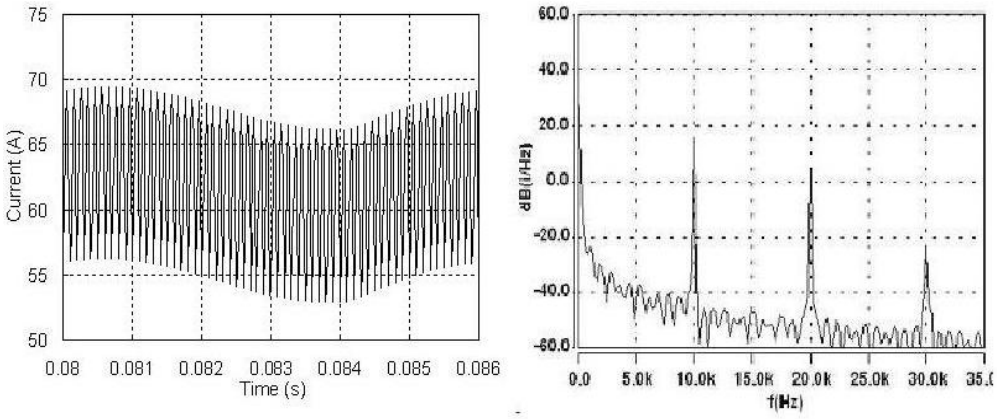

(a) (b)

Fig. 26: Steady state (a) input current characteristics and (b) frequency domain characteristics for the high-frequency transformer-isolated cycloconverter topology of Fig. 23(c).

3.1.3 Balance-of-Plant System

3.1.3.1 Fuel Processing Sub-system Description

3.1.3.1.1 Hydrogen Production by Steam Reforming of Natural Gas

Many hydrocarbons and alcohols can be considered as candidate fuels for stationary applications of fuel cells. The fuel considered in this research work is natural gas, which is a naturally occurring gas mixture, consisting mainly of methane. Table IV outlines the typical components of natural gas in the Union Gas system and the typical ranges for these values allowing for the different sources. Based on Table IV, the assumption of natural gas consisting of 100% methane was made for Phase I. Due to its low electrochemical reactivity, methane as indeed any other hydrocarbon is not used directly in fuel cells, an exception, of course, being the use of methanol in Direct Methanol Fuel Cells (DMFCs). A process such as steam reforming[9] is required to convert this fuel to a hydrogen-rich gas appropriate for the operation of the fuel cell. A simplified flow diagram of such a process is shown in Fig. 27.

Table IV: Chemical composition of natural gas (Union Gas, 2001).

Component	Typical Analysis (mole %)	Typical Range (mole %)
Methane	94.69	88.3 – 96
Ethane	2.58	2.20 – 4.32
Propane	0.20	0.16 – 0.98
iso-Butane	0.03	0.01 – 0.12
normal-Butane	0.03	0.01 – 0.18
iso-Pentane	0.01	trace – 0.06
normal-Pentane	0.01	trace – 0.03
Hexanes plus	0.01	trace – 0.03
Nitrogen	1.60	1.38 – 5.50
Carbon dioxide	0.81	0.50 – 0.92
Oxygen	0.02	0.01 – 0.05
Hydrogen	trace	trace – 0.02

[9] Steam reforming involves catalytic conversion of the hydrocarbon and steam to hydrogen and carbon oxides. The process works only with light hydrocarbons that can be vaporized completely without carbon formation (Kordesch and Simader, 1996).

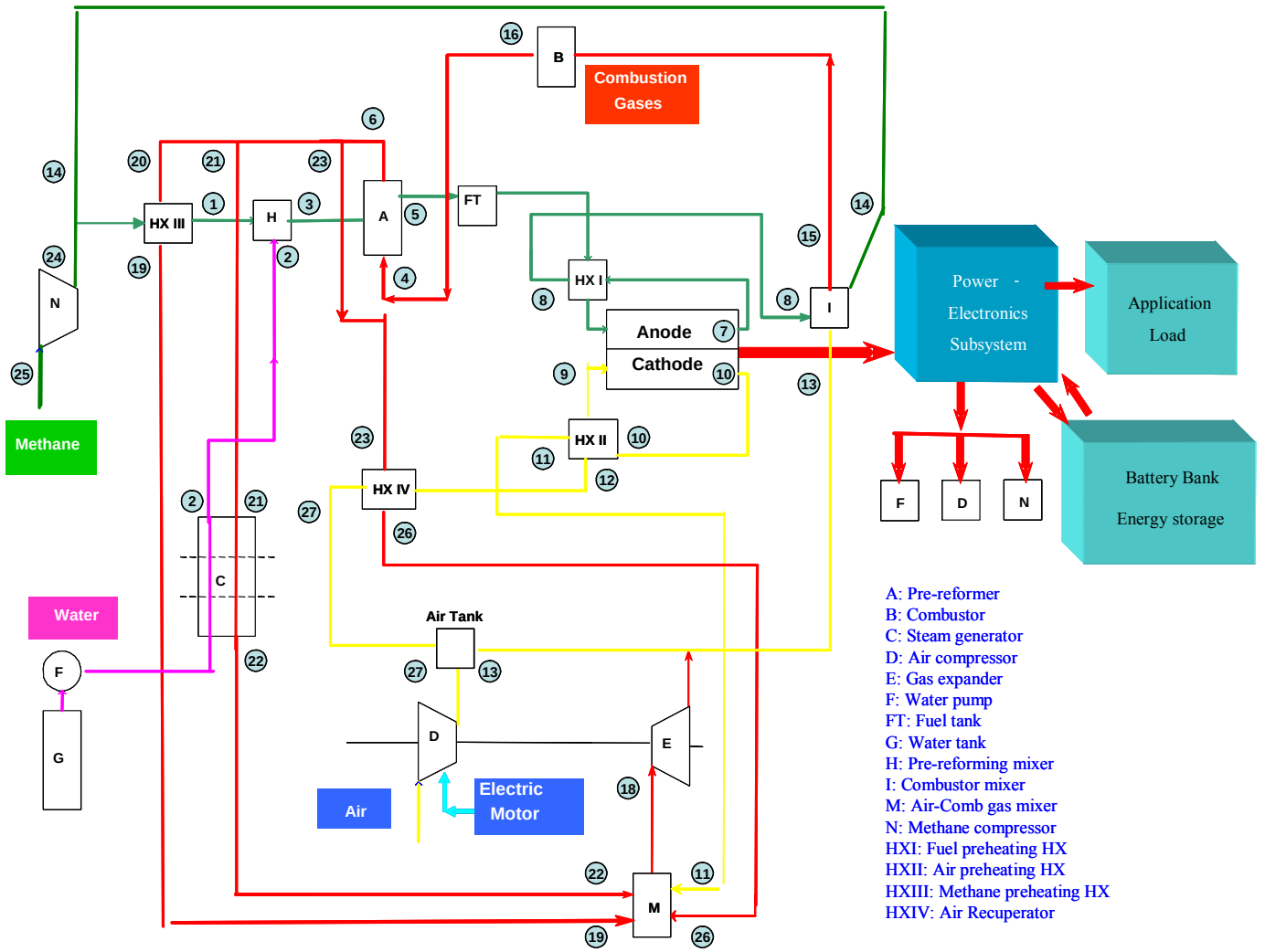

Fig. 27: System flow diagram of the proposed SOFC based power system. The thermal management sub-system is not shown here.

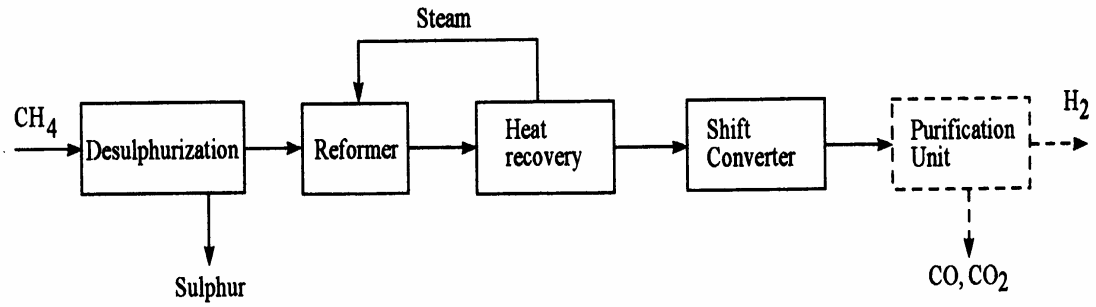

Fig. 28: Flow diagram of hydrogen production by catalytic steam reforming (Kordesch and Simader, 1996).

A schematic diagram of a steam methane reformer (SMR) reactor, similar to that developed by United Technologies Corporation for fuel cell applications, is shown in Fig. 28. The SMR consists of a pressure shell, a catalyst basket, and a combustion chamber with a burner. The pressure shell is equipped with a flanged cover to facilitate the installation of the catalyst basket. The catalyst consists of two catalyst beds in series and a number of annuli for the process mixture flow. The catalyst beds have a 4-hole cylindrical shape and normally contain nickel oxide dispersed on a calcium aluminate ceramic support promoted with alkali. Combustion takes place at the burner outside the reformer tubes.

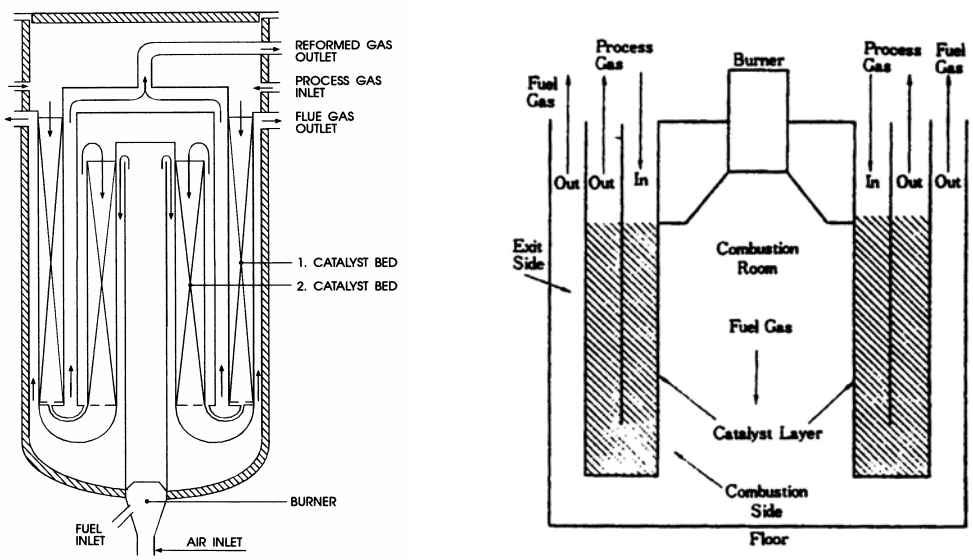

Fig. 29: Schematic diagram of a steam methane reformer reactor (Kordesch and Simader, 1996).

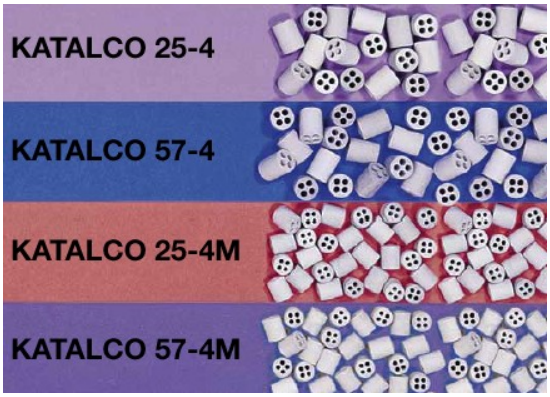

Fig. 30: Shape of the catalyst particles inside the tubes of the steam methane reformer reactor (Synetix Product Brochure, 2001).

The SMR reactor uses a combination of co-current and counter-current heat exchange between the process gas and the flue gas in order to maximize thermal efficiency and to optimize usage of construction materials. In particular, the process feed is passed downwards through the first catalyst bed receiving heat from the partly cooled combustion gas and the product gas, both in counter-current flow with the process feed. The process gas is then transferred from the first catalyst bed to the top of the second catalyst bed through a number of tubes or a channel, where it flows down through that bed receiving heat from the hot combustion gas in co-current flow with the process gas. The product gas from the second catalyst is finally passed through an annular space supplying part of its heat back to the process gas flowing in the first catalyst bed in counter-current flow.

There are up to eleven possible reactions that can take place between the constituents of the process gas[10] inside the reformer tubes (Xu and Froment, 1989). However, due to the presence of the catalysts listed in Table V, two out of the eleven are favored and therefore chosen to describe the steam reforming of methane. They are as follow:

- Demethanation reaction (endothermic):

$$CH_4 + H_2O \leftrightarrow CO + 3H_2 \qquad (\Delta H_{298} = 206 \text{ kJ/mol}) \qquad (14)$$

- Water gas shift (WGS) reaction (exothermic):

$$CO + H_2O \leftrightarrow CO_2 + H_2 \qquad (\Delta H_{298} = -40.6 \text{ kJ/mol}) \qquad (15)$$

Table V: Characteristics of the commercially available catalysts used in the steam methane reformer reactor (Synetix Product Brochure, 2001).

Catalyst	25 – 4M	57 – 4M	25 – 4	57 – 4
Form	Optimized 4-hole shape	Optimized 4-hole shape	Optimized 4-hole shape	Optimized 4-hole shape
Length (mm)	15	15	19.3	19.3
Outer diameter (mm)	11	11	14	14
Hole inner diameter (mm)	4x3	4x3	4x4	4x4
Bulk density (kg/lt)	1.0	0.9	0.9	0.85

Both of the above reactions are reversible at reforming temperatures. It is evident that at higher temperatures, less methane and more carbon monoxide (CO) is present in the reformate gas and that methane content increases with pressure and decreases with increasing steam to carbon ratio (He, 1997).

[10] From this point forward it will be referred to as reformate gas or simply reformate.

3.1.3.1.2 Fuel Processing Sub-system Configuration

The main objective of the fuel processing sub-system (FPS) is to convert the natural gas (methane), obtained from a natural gas tank, to the hydrogen-rich reformate gas that will provide the hydrogen fuel required for the operation of the SOFC stack. The FPS configuration (see Fig. 28) developed for the processing of this hydrocarbon feedstock is described in detail below. The necessary amount of fuel feed, consisting primarily of methane as shown in Table IV, is first compressed and then a part of it is supplied to the reforming line while the remaining fuel is intended for combustion. The methane flowing down the reforming line is preheated by passing through a compact plate-fin type heat exchanger and then mixed with steam produced in a steam generator before entering the SMR reactor. This preheating is a very good example of the thermal integration applied to the FPS configuration since the large amount of thermal energy contained in the combustion gases exiting the SMR reactor is used to preheat the methane and is also used in the steam generator. At this point, a synthesis or configuration variation can be proposed. The methane and steam could be mixed before the mixture is preheated and sent to the reformer or not. Which configuration is finally implemented should be the result of an optimization process of synthesis/design and operation. For the moment the two streams are preheated independently.

The reforming of the above mentioned mixture into hydrogen and carbon monoxide is carried out inside the SMR reactor. The heat needed to drive the endothermic reforming reaction is provided by the combustion gases leaving the burner. The details concerning the geometry of the steam-methane reactor as well as the chemical reactions taking place inside it and the appropriate catalysts used are given in the earlier. The reformate gases coming out of the steam reformer are stored in a tank, which acts as an energy buffer between the BOPS and the SS. This allows almost immediate supply of fuel to the stack at operational points (perturbations due to load changes) where the stack demand rate is larger than the reformer production rate. Before being delivered to the fuel cell stack, the hydrogen-rich reformate gas is brought to the desired anode inlet conditions by use of a heat exchanger.

The combustion mixture supplied to the burner consists of air taken from the air tank, the hydrogen-depleted anode exhaust gas, and the compressed methane that bypasses the reforming line. Burning the residual hydrogen in the stack tail gas translates to decreased consumption of additional methane in the burner and, therefore, to increased efficiency of the configuration. Instead of air taken from the air tank, the designer can decide to use air bleed from the stack. This may introduce additional increments in efficiency by eliminating the compression stage. However, air coming from the stack is rich in nitrogen and its amount depends on the stack requirements. Therefore, using it depends on whether or not its heat capacity is enough to meet the thermal management necessities. After providing the required thermal energy for the endothermic reforming reaction, the combustion gases are split into three streams, the first preheats the methane, and the second is passed through the steam generator where it supplies the necessary heat for producing the steam consumed in the reforming process. The third is used to preheat the air going into the stack. Finally, prior to being expanded and exhausted to the atmosphere, the combustion gas streams are mixed together.

3.1.3.2 Thermal Management and Power Recovery Sub-Systems Description

In the BOPS and SS, the temperatures of a number of critical components (particularly the SOFC stack and the pre-reformer of the FPS) have to be carefully controlled, and the flow and utilization of heat from several sources within the configuration have to be managed efficiently in order to achieve high overall efficiency. Therefore, the thermal management sub-system (TMS) plays a significant role in the operation of the SOFC power system. Its major functions include maintaining the stack operating temperature in the

appropriate range, bringing the hydrogen-rich reformate gas and compressed air to the desired anode inlet conditions before exiting the FPS and the PRS, respectively, and controlling the steam reformer operational conditions and the generation of the steam required for the FPS. A number of high performance heat exchangers are used within the configuration in order to meet these objectives. Furthermore, since the SOFC operates at a high temperature, this high-grade waste heat is of important use to precondition the streams coming into the stack. Thermal energy available from the conditioning of the reformate gas, the steam, the compressed air, and the methane are used in the WRS.

In the WRS, the combustion gases coming from the steam generator, the compressed air heat exchanger, and the methane heat exchanger are mixed together with the air coming from the stack. Thus, the mixed gases are expanded through an expander for purposes of energy recovery, i.e. to offset some of the parasitic power requirements. The work generated by the gas mixture is used to drive the air compressor, which in turn compresses the air to be used for the stack and the combustor. For most operating conditions, the work produced by the expander does not match the work required by the compressor. This additional work is supplied by an electrical motor which takes power from the SS/PES

3.1.3.3 BOPS Model Development

3.1.3.3.1 Thermodynamic, Kinetic, and Geometric FPS Models

The mathematical model of the fuel processing sub-system (FPS) consists of a set of equations that describe the mass and associated energy flows in each of the lines of the sub-system, based on the chemical reactions inside each reactor and on the laws of conservation of mass and energy for each component in the sub-system. In the case where the sub-system is in a transient state, the conservation of molar mass and energy for each component can be written as follows:

$$\sum_{in} \dot{n}_{mix} - \sum_{out} \dot{n}_{mix} = \frac{dm_{cv}}{dt} \tag{16}$$

$$\sum_{q} \dot{Q}_q - \dot{W} + \sum_{in} \dot{n}_{mix} h_{mix} - \sum_{out} \dot{n}_{mix} h_{mix} = \frac{dE_{cv}}{dt} \tag{17}$$

where the indices in and out refer to the inlet and outlet flow streams, respectively, and q to the number of heat interactions $\dot{Q}_q$ of the component with other components or sub-systems. Moreover, $\dot{W}$ represents the work done by the component, $\dot{n}_{mix}$ the inlet or outlet mixture molar flow rate, and h_{mix} the corresponding specific enthalpy. The terms m_{cv} and E_{cv} refer to the control volume mass and energy.

The mixture's molar flow rate, $\dot{n}_{mix}$, is defined as the sum of the molar flow rates of its constituents, while the corresponding specific enthalpy, h_{mix}, is given by the following relation

$$h_{mix}(T, \mathbf{y}) = \sum_{p=1}^{7} y_p h_p(T) \tag{18}$$

which is valid for a Gibbs-Dalton (ideal gas) mixture. In the above equation, y_p represents the mole fraction of the pth constituent and h_p its corresponding partial enthalpy. Since there are chemical reaction mechanisms that are active within the system, the constituent's partial enthalpy is expressed as

$$h_p(T) = \left(\Delta h_f^o\right)_p + h_p^{'}(T) - h_p^{'}(T_o) \qquad (19)$$

where $\left(\Delta h_f^o\right)_p$ is the enthalpy of formation of constituent p at standard temperature T_o and pressure P_o. The value of the enthalpy $h_p^{'}$ of the pth constituent is determined by the approximate expression

$$h_p^{'}(T) = a_p T + \frac{4}{5} b_p T^{5/4} + \frac{2}{3} c_p T^{3/2} + \frac{4}{7} d_p T^{7/4} \qquad (20)$$

which is based on a regression of data from the JANAF Thermochemical Tables (1971). The values of the constants a_p, b_p, c_p, and d_p in the above equation are tabulated in Gyftopoulos and Beretta (1991).

Table VI: Values of the constants a_p, b_p, c_p, and d_p for use in the approximate expressions in equation (20). (Gyftopoulos and Beretta, 1991).

	CH_4	H_2O	CO	CO_2	H_2	O_2	N_2
a_p	104.0	180.0	62.8	- 55.6	79.5	10.3	72.0
b_p	- 77.8	- 85.4	- 22.6	30.5	- 26.3	5.4	- 26.9
c_p	20.1	15.6	4.6	- 1.96	4.23	- 0.18	5.19
d_p	- 1.3	- 0.858	- 0.272	0.0	- 0.197	0.0	- 0.298

Chemical equilibrium calculations are necessary in the modeling of the FPS reactor in order to determine the composition of their inlet and outlet streams. The equilibrium constant of the reaction, $K(T)$, is defined as

$$K(T) = \exp\left[-\frac{\Delta g^o(T)}{RT}\right] \qquad (21)$$

where $\Delta g^o(T)$ is the Gibbs free energy of reaction at temperature T given by

$$\Delta g^o(T) = \Delta h^o(T) - T\Delta s^o(T) \qquad (22)$$

where the function $\Delta h^o(T)$ referring to the enthalpy of reaction at temperature T and pressure P_o, and $\Delta s^o(T)$ to the entropy of reaction at the same conditions. The values of these functions can be determined by using the following two relations

$$\Delta h^o(T) = \Delta h^o + \sum_{p=1}^{7} \nu_p \left[h_p^{'}(T, P_o) - h_p^{'}(T_o, P_o)\right] \qquad (23)$$

$$\Delta s^o(T) = \Delta s^o + \sum_{p=1}^{7} \nu_p \left[s_p(T, P_o) - s_p(T_o, P_o) \right] \qquad (24)$$

where

$$s_p(T, P) = a_p \ln T + 4 b_p T^{1/4} + 2 c_p T^{1/2} + \frac{4}{3} d_p T^{3/4} - R \ln P \qquad (25)$$

and ν_p is the stoichiometric coefficient of the p[th] constituent in the reaction. The term Δh^o, appearing in equation (23), is called the enthalpy of reaction at standard conditions, i.e. $T_o = 25$ °C and $P_o = 1$ atm, and is expressed as

$$\Delta h^o = \sum_{p=1}^{7} \nu_p \left(\Delta h_f^o \right)_p \qquad (26)$$

The term Δs^o, appearing in equation (24), is called the entropy of reaction at standard conditions and is given by

$$\Delta s^o = \sum_{p=1}^{7} \nu_p \left(\Delta s_f^o \right)_p \qquad (27)$$

where $\left(\Delta s_f^o \right)_p$ is the entropy of formation of constituent p at standard temperature T_o and pressure P_o. Finally, one more variable appearing in the chemical equilibrium calculations is the degree of reaction, ξ, which is defined as

$$\xi = \frac{\epsilon}{\dot{n}_{mix,i}} \qquad (28)$$

and where ϵ is the reaction coordinate and $\dot{n}_{mix,i}$ is the molar flow rate of the mixture entering the reactor.

To perform the necessary heat transfer calculations of the FPS component models, thermophysical property data is required. This is included in the simulation code as fitted correlations of data obtained directly from the Engineering Equation Solver (EES) software (1995). In particular, the EES software contains subroutines for calculating the thermophysical properties of various substances assuming either ideal or real gas behavior. Therefore, appropriate correlations for the specific heat c_p, thermal conductivity k, and dynamic viscosity μ of the seven different mixture constituents (i.e. CH_4, H_2O, CO, CO_2, H_2, O_2, and N_2) are extracted from the software based on the temperature and pressure ranges of interest. The thermophysical properties of the ideal gas mixture are then determined by using the following relation:

$$Z_{mix}(T, \mathbf{y}) = \sum_{p=1}^{7} y_p Z_p(T) \qquad (29)$$

for $Z = c_p$, k, and μ. All thermophysical properties are evaluated at the arithmetic mean of the inlet and outlet mixture temperatures unless otherwise specified.

As to the thermal analysis of the heat exchangers included in the FPS configuration, two different methods are applied, namely, the log mean temperature difference (LMTD) method and the number of transfer units (NTU) method based on the concept of a heat exchanger effectiveness. The effectiveness, ε, of a heat exchanger is the ratio of the actual heat transfer rate to the thermodynamically limited maximum possible heat transfer rate if an infinite heat transfer surface area were available in a counter-flow heat exchanger. The actual heat transfer is obtained either by the energy given off by the hot fluid or the energy received by the cold fluid. Therefore,

$$\varepsilon = \frac{\dot{Q}_{actual}}{\dot{Q}_{max}} = \frac{\dot{n}^h_{mix}\left[h^h_{mix}\left(T_{h,i}\right) - h^h_{mix}\left(T_{h,o}\right)\right]}{\dot{Q}_{max}} = \frac{\dot{n}^c_{mix}\left[h^c_{mix}\left(T_{c,o}\right) - h^c_{mix}\left(T_{c,i}\right)\right]}{\dot{Q}_{max}} \qquad (30)$$

The fluid that might undergo the maximum temperature difference is the fluid having the minimum heat capacity. Thus, in this work, the maximum possible heat transfer is expressed as

$$\dot{Q}_{max} = \dot{n}^h_{mix}\left[h^h_{mix}\left(T_{h,i}\right) - h^h_{mix}\left(T_{c,i}\right)\right] \text{ if } \left(\dot{n}C_p\right)^h_{mix} < \left(\dot{n}C_p\right)^c_{mix} \qquad (31)$$

or

$$\dot{Q}_{max} = \dot{n}^c_{mix}\left[h^c_{mix}\left(T_{h,i}\right) - h^c_{mix}\left(T_{c,i}\right)\right] \text{ if } \left(\dot{n}C_p\right)^c_{mix} < \left(\dot{n}C_p\right)^h_{mix} \qquad (32)$$

What follows is a description of the models developed for the reactor, the steam generator, and the compact heat exchangers included in the FPS configuration.

3.1.3.3.2 Modeling of the SMR Reactor

A number of simplifying assumptions are introduced to facilitate the modeling of the SMR reactor described in the previous sections. These are outlined below.

- A single reactor tube is analyzed. Thus, all the tubes in the reactor behave independently of one another.
- Reforming and combustion gases behave ideally in all sections of the reactor.
- The gas flow pattern through the channels is assumed to be plug flow.
- The demethanation reaction is considered to be the kinetically controlled and the water gas shift reaction is considered to be equilibrium controlled.
- A uniform temperature exists throughout each catalyst particle, and it is the same as the gas temperature in that section of the catalytic bed.
- No carbon deposition is allowed in the SMR reactor.
- Bed pressure drops are neglected.
- Axial dispersion and radial gradients are negligible – plug flow conditions.
- The outside shell wall is adiabatic.
- For maximum conversion of CH_4 to H_2, the mixture should be at equilibrium at the exit of the SMR

The two reactions chosen to describe the steam reforming of methane are the ones presented in the previous chapter, i.e. the endothermic demethanation reaction and the exothermic water-gas shift one. By combining these two partial chemical reaction mechanisms as shown below

$$\begin{aligned} CH_4 + \quad H_2O &\leftrightarrow \quad CO + \ 3H_2 \\ \tfrac{1}{2}CO + \tfrac{1}{2}H_2O &\leftrightarrow \ \tfrac{1}{2}CO_2 + \ \tfrac{1}{2}H_2 \end{aligned}$$

the following overall reaction mechanism is found:

$$CH_4 \quad + \tfrac{3}{2}H_2O \ \leftrightarrow \ \tfrac{1}{2}CO \ + \ \tfrac{1}{2}CO_2 + \tfrac{7}{2}H_2$$

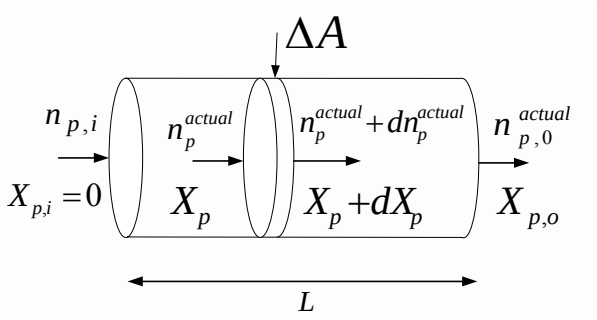

Fig. 31: Steam reformer differential discretization.

Mass balance

Fig. 31 shows the reformer differential control volume over which the mass and energy balance are performed. For plug flow conditions, dispersion is assume to be negligible, thus, the material balance that includes transport, reaction, and accumulation of the reforming gas, can be written as

$$\frac{\partial(-UC)}{\partial x} - R_a \rho_C = \frac{\partial C}{\partial t} \qquad (33)$$

where *C* is the methane molar concentration (g-mole/m^3), *U* is the superficial velocity (m/hr), R_a is the methane reaction rate per unit mass of catalyst, ρ_C is the catalyst bed density (kg catalyst / m^3 reactor), *x* is the axial direction (m), *t* is time (hr). Let Y be the mole fraction of methane and ρ the molar density of bulk gas, thus $C = \rho Y$ and the concentration balance is replaced by

$$\frac{\partial FY}{\partial x} - R_a \rho_C \frac{\pi d^2}{4} = \frac{\pi d^2}{4}\left(\rho \frac{\partial Y}{\partial t} + Y \frac{\partial \rho}{\partial t}\right) \qquad (34)$$

where F is the molar flow rate inside the reactor (g-mole/hr) and d is the inside diameter (m). Let us define

$$F = F_0 + 2X_1F_1\,;\ \rho = \frac{P}{RT}\left(\frac{F}{F_0}\right);\ Y = \frac{F_1(1-X_1)}{F_0 + 2X_1F_1}\,;\ X_1 = \frac{F_1 - F_0Y}{F_1 + 2YF_1} \qquad (35)$$

where X_1 is the conversion, F_0 is the initial total molar flow onside the reactor, and F_1 is the initial methane flow rate. Then $\frac{\partial \rho}{\partial t}$ can be defined as

$$\frac{\partial \rho}{\partial t} = \frac{\partial \rho}{\partial X_1}\frac{\partial X_1}{\partial Y}\frac{\partial Y}{\partial t} \qquad (36)$$

Energy balances

Energy balances for the tube-side of the reformer, for the tube-wall, for the combustion gases (shell–side), and for the catalyst are given next.

Reformer gas side

The reformer gas energy balance includes the gas sensible heat change, reaction enthalpies, heat transfer from the hotter tube-wall, heat transfer from the catalyst particles, and the accumulation or storage term. The energy equation is as follows:

$$-\frac{\partial\left(FC_pT\right)}{\partial x} + \sum F\left(-\Delta H\right)\frac{\partial X}{\partial x} + h_i A_i\left(T_w - T\right) + h_c A_c A_i\left(T_c - T\right) = A_i C_p \frac{\partial\left(\rho T\right)}{\partial t} \qquad (37)$$

$$\sum F\left(-\Delta H\right)\frac{\partial X}{\partial x} = F_1\left(-\Delta H_1\right)\frac{\partial X_1}{\partial x} + \left(F_3 + X_1F_1\right)\left(-\Delta H_2\right)\frac{\partial X_2}{\partial x} \qquad (38)$$

where C_p is the heat capacity of the tube-side (J/g-mole-K), A_c is the external surface area of particles per volume of catalyst bed (m^3/m^2), T_c is the catalyst temperature (^oK), h_i is the inside heat transfer coefficient (j/hr-m-K), h_c is the catalyst-fluid heat transfer coefficient(j/hr-m-K), ΔH_1 the demethanation reaction enthalpy (J/g-mole CH), ΔH_2 the water-gas shift reaction enthalpy (J/g-mole CO), X_2 the conversion of the water-gas shift reaction. The reaction enthalpies are evaluated at the reactor average temperature. Negative values indicate an exothermic reaction. The heat transfer coefficients (h) are a function of the characteristic of the fluid and the geometry of the reactor.

Shell side

The Energy balance equation for the shell-side gas includes sensible heat change, heat transfer with tube wall, and accumulation of internal energy change, it can be written as

$$\rho_0 A_0 C_{p0}\frac{\partial T_0}{\partial t} = -\rho_0 V_0 A_0 C_{p0}\frac{\partial T_0}{\partial x} - h_0 A_0\left(T_0 - T_w\right) \qquad (39)$$

where A_0 is the heat transfer area, ρ_0 is the gas density, T_0 is the gas temperature, T_W is the tube wall temperature, h_0 is the heat transfer coefficient.

Tube wall

The energy balance for the tube wall includes convective heat transfer with reformer gas and shell-side gas (combustion gases) and accumulation of internal energy change, which can be written as

$$\rho_w\left(d_0^2 - d_i^2\right)C_{p_w}\frac{\partial T_w}{\partial t} = 4h_0 d_0\left(T_0 - Tw\right) - 4h_i d_i\left(T_w - T_i\right) \qquad (40)$$

where d_0 and d_i are the external and internal diameter respectively, ρ_w is the metal density, T_0 is the reformate gas temperature, T_W is the tube wall temperature, Ti is the Combustion gases temperature, h_0 is the reformate gas side heat transfer coefficient, hi is the combustions gases side heat transfer coefficient. C_{p_w} is the wall specific heat.

Catalyst

The energy balance equation for the catalyst is

$$C_{p_C}\rho_C\frac{\partial T_C}{\partial t} = h_C A_C\left(T - T_C\right) \qquad (41)$$

where ρ_C is the catalyst density, T is the reformate gas temperature, A_c is the external surface area of particles per volume of catalyst bed (m^3/m^2), T_c is the catalyst temperature (^0K), h_c is the catalyst-fluid heat transfer coefficient(j/hr-m-K), and C_{p_c} is the catalyst specific heat.

Chemical Kinetics

Once the energy and mass balances have been solved and the corresponding flow rates of the mixture's constituents have been determined, the geometric and kinetic models presented in Tables VII and VIII, respectively, are used in order to complete the SMR modeling. Among the different rate equations found in the literature for the demethanation reaction, the one developed by Bodrov et al. (1964, 1967; Murray and Snyder (1985)) was selected to represent the demethanation reaction rate in the kinetic modeling of the SMR reactor. The values of the frequency factor K_0 and the activation energy EA, appearing in the reaction rate expression, were determined experimentally by Bodrov et al. (1964, 1967; Murray and Snyder (1985)). The methane partial pressure is written in terms of the total pressure, the steam-to-methane ratio, and the actual (kinetic) methane conversion. Finally, achieving equilibrium for the demethanation reaction at the exit of the SMR reactor is desired since it translates to maximum conversion of the methane to hydrogen. The water-gas shift reaction is equilibrium controlled.

Table VII: Geometric model of the SMR reactor.

	Variable Description	Model Equation
n_{tubes}^{SMR}	Number of tubes	Assigned value
d_i^{SMR}	Tube inner diameter	Assigned value
A_{cr}^{SMR}	Cross-sectional area (single tube)	$A_{cr}^{SMR} = \frac{\pi \left(d_i^{SMR} \right)^2}{4}$
t_w	Tube wall thickness	$d_o^{SMR} = d_i^{SMR} + 2t_w$
d_o^{SMR}	Tube outer diameter	
P_T^{SMR}	Pitch	$P_T^{SMR} = 1.2 d_o^{SMR}$
D_s^{SMR}	Shell diameter	$D_s^{SMR} = 0.661 \sqrt{\pi n_{tubes}^{SMR} \left(P_T^{SMR} \right)^2}$

Table VIII: Kinetic model of the SMR reactor.

Variable Description		Model Equation
ζ_{H_2O/CH_4}	Steam-to-methane ratio	Assigned value
$\dot{n}_{CH_4,i}$	Inlet methane molar flow rate	$X_{CH_4} = \frac{\dot{n}_{CH_4,i} - \dot{n}_{CH_4,o}}{\dot{n}_{CH_4,i}}$
$\dot{n}_{CH_4,o}$	Outlet methane molar flow rate	
X_{CH_4}	Actual (kinetic) methane conversion	
P_{CH_4}	Methane partial pressure	$P_{CH_4} = y_{CH_4} P_{SMR} = \frac{1 - X_{CH_4}}{1 + 2X_{CH_4} + \zeta_{H_2O/CH_4}} P_{SMR}$
P_{SMR}	Reformate gas mixture pressure	
T_{avg}^{SMR}	Average reformate gas temperature	$-R_a = K_0 \exp\left(-\frac{EA}{RT} \right) P_{CH4}$
Ra	Demethanation reaction rate	
L_{SMR}	SMR reactor length for the design point	$L_{SMR} = \frac{\dot{n}_{CH_4,i}}{\left(n_{tubes} A_{cr} \rho_B \right)_{SMR}} \int_0^{X_{CH_4,eq}} \frac{dX_{CH_4}}{\left(-r_{CH_4} \right)}$

3.1.3.3.3 Modeling of the Methane and Air Compressors

For the dynamic analysis of a compressor or fan, the pressure and mass flow are state variables. Assuming that the inlet temperature is also known, the performance maps can then be used to calculate the rotational speed and efficiency and then the output temperature and work input. Heat transfer from the fluid in a compressor to the impeller and casing is a complex phenomenon, particularly during star-up transients Heat flow goes from the fluid to the casing and then to the ambient; and from the fluid to the impeller and then to the casing and to the ambient through the bearings, seals, and shaft. The thermal capacitance of the casing, impeller and inlet duct can be approximated by a single thermal mode at a temperature T_0 given by

$$mC_p \frac{\partial T_0}{\partial t} = (hA)_i \left[\frac{T_1 + T_2}{2} - T_0 \right] - (hA)_0 (T_0 - T_{amb}) \quad (42)$$

where m is the mass of the thermal mode, C_p is the thermal mode specific heat, $(hA)_1$ is the inner conductance from the fluid to the thermal mode, $(hA)_0$ is the outer conductance from the mode to the ambient, and T_0 is the mode temperature. The heat transfer coefficient (h_0) is assumed as constant, the internal heat transfer coefficient (h_i) depends on the flow characteristics and the mode geometry. The heat flow from the fluid to the mode is given by

$$Q_i = (hA)_i \left[\frac{T_1 + T_2}{2} - T_0 \right] \quad (43)$$

Therefore, the temperature change of the fluid due to heat flow into the mode is

$$\Delta T_1 = \frac{(hA)_i}{\dot{m}_{2F} C_{p_F}} \left[\frac{T_1 + T_2}{2} - T_0 \right] \quad (44)$$

The temperature change from the compressor power input is expressed as

$$\Delta T_2 = \frac{T_1}{\eta_C} \left[\left(\frac{P_2}{P_1} \right)^{\frac{\gamma-1}{\gamma}} - 1 \right] \quad (45)$$

Collecting terms yields an expression for the outlet temperature given by

$$T_2 = \frac{T_1 \left[1 - \frac{(hA)_i}{2\dot{m}_{2F} C_{p_F}} + \frac{1}{\eta_C} \left(\left(\frac{P_2}{P_1} \right)^{\frac{\gamma-1}{\gamma}} - 1 \right) \right] + \frac{(hA)_i}{\dot{m}_{2F} C_{p_F}} T_0}{1 + \frac{(hA)_i}{2\dot{m}_{2F} C_{p_F}}} \quad (46)$$

Finally, the compressor work is written as

$$W_C = \frac{\dot{m}_{2C} C_p T_1}{\eta_C} \left[\left(\frac{P_2}{P_1} \right)^{\frac{\gamma-1}{\gamma}} - 1 \right] \quad (47)$$

3.1.3.3.4 Modeling of the Expander

The transient heat transfer model for an expander is similar to that for compressors. The heat transfer is calculated assuming a single thermal mode representing the casing, impeller, and duct wall temperature, and the flow and efficiency are determined from the performance maps. The outlet temperature and work output are given by

$$T_2 = \frac{T_1\left[1-\frac{(hA)_i}{2\dot{m}_{2F}C_{p_F}}+\eta_T\left(1-\left(\frac{P_2}{P_1}\right)^{\frac{\gamma-1}{\gamma}}\right)\right]+\frac{(hA)_i}{\dot{m}_{2F}C_{p_F}}T_0}{1+\frac{(hA)_i}{2\dot{m}_{2F}C_{p_F}}} \tag{48}$$

and

$$W_T = \dot{m}_{2C}C_p\eta_C T_1\left[1-\left(\frac{P_2}{P_1}\right)^{\frac{\gamma-1}{\gamma}}\right] \tag{49}$$

3.1.3.3.5 Modeling of the Shafts for the Turbomachinery

The shaft component is used to compute the turbomachinery rotational speed (*N*) based on input values of turbine power output, and compressor power input. From a power balance

$$IN\frac{\partial N}{\partial t} = \Delta W \tag{50}$$

where *I* is the moment of inertia and ΔW is the power balance given by

$$\Delta W = W_{out} - W_{in} \tag{51}$$

For a compressor coupled to a turbine

$$\Delta W = W_T - W_C - W_M \tag{52}$$

where W_M represents the mechanical loss.

At this point of the research the performance maps have been replaced by simplified analytical expression which account for the relationship between pressure, mass flow, and efficiency.

3.1.3.3.6 Modeling of the Compact Heat Exchanger

The heat exchangers used in the BOPS configuration are all plate-fin type, compact heat exchangers with a single-pass, cross-flow arrangement. Their modeling details are presented in Table IX. The heat

transfer and pressure drop models used are based on the work of Shah (1981) and Kays and London (1998). The effectiveness-NTU method is applied in order to relate the geometric models of the heat exchangers to the thermodynamic ones. The expression for the heat exchanger effectiveness is obtained from Incropera and DeWitt (1990) and is valid for single-pass, cross-flow arrangements with both fluids unmixed. It should be made clear that the equations appearing in Table IX are valid for both the hot and the cold stream sides. Therefore, they should be taken into account twice in order for the heat exchanger model to be complete. Exempt are the equations that refer to the height and number of plates of the heat exchanger, the volumes of the hot and cold sides, as well as the overall heat transfer coefficient and the heat exchanger effectiveness.

The following assumptions are made in the thermal analysis of each section of the heat exchanger:

- Fluid flow is one-dimensional
- Longitudinal conduction in the fluid or wall is negligible
- The effective conductance (hA) is known for each fluid as a function of Reynolds number
- Conduction resistances through the wall are negligible
- The wall temperature in each section is a function of time (spatially constant)
- The heat exchanger is adiabatic overall.
- Since the fluid is a gas, its thermal capacitance is assumed to be small compared to the wall.

Table IX: Geometric and heat transfer models of a plate-fin heat exchanger.

	Variable Description	Model Equation
L_h	Hot-side length	Assigned value
L_c	Cold-side length	Assigned value
H	Height	$H = b_h + 2a + n_{plates}\left(b_h + b_c + 2a\right)$
n_{plates}	Number of plates	
l_f	Fin length	$l_f = \frac{b}{2} - t_f$
V_p^h	Hot-side volume	$V_p^h = L_c L_h b_h \left(n_{plates} + 1\right)$
V_p^c	Cold-side volume	$V_p^c = L_c L_h b_c n_{plates}$
A	Heat transfer area	$A = \beta V_p$, $A_o = \frac{D_h A}{4L}$
A_o	Minimum free flow area	
A_f	Finned area	$A_{fr} = LH$, $m = \sqrt{\frac{2h}{k_f t_f}}$
A_{fr}	Frontal area	
η_f	Fin efficiency	$\eta_f = \frac{\tanh\left(ml_f\right)}{ml_f}$, $\eta_o = 1 - \left(1 - \eta_f\right)\frac{A_f}{A}$
η_o	Outside overall surface efficiency	
$\dot{n}$	Mixture molar flow rate	$G = \frac{\dot{n}}{A_o}$
j	Colburn factor	$Pr = \frac{\mu C_p}{k}$
G	Maximum mass velocity	$h = jGC_p Pr^{-2/3}$
Pr	Prandtl number	

h	Heat transfer coefficient	
U	Overall heat transfer coefficient	$C_{min} = \min\left(\dot{n}_c C_p^c,\ \dot{n}_h C_p^h\right),\ C_{max} = \max\left(\dot{n}_c C_p^c,\ \dot{n}_h C_p^h\right)$
C_{min}	Minimum heat capacity	
C_{max}	Maximum heat capacity	$UA = \dfrac{1}{\dfrac{1}{(\eta_o Ah)_h} + \dfrac{1}{(\eta_o Ah)_c}},\ C_r = \dfrac{C_{min}}{C_{max}},\ NTU = \dfrac{UA}{C_{min}}$
C_r	Heat capacity ratio	
NTU	Number of transfer units	
ε	Effectiveness	$\varepsilon = 1 - \exp\left[\left(\dfrac{1}{C_r}\right)(NTU)^{0.22}\left\{\exp\left[-C_r\,(NTU)^{0.78}\right] - 1\right\}\right]$

The governing partial differential equations for the cross-flow section shown in Fig. 32 are

Hot side

$$\left(MC_p\right)_h \frac{\partial T_h}{\partial t} + \left(\dot{m}C_p\right)_h L_x \frac{\partial T_h}{\partial x} + \left(hA\right)_h \left(T_h - T_w\right) \tag{53}$$

Cold side

$$\left(MC_p\right)_C \frac{\partial T_C}{\partial t} + \left(\dot{m}C_p\right)_C L_y \frac{\partial T_C}{\partial y} + \left(hA\right)_C \left(T_C - T_w\right) \tag{54}$$

Wall

$$\left(MC_p\right)_w \frac{\partial T_w}{\partial t} = \left(hA\right)_C \left(\overline{T}_C - T_w\right) + \left(hA\right)_h \left(\overline{T}_h - T_w\right) \tag{55}$$

where M is the mass in the control volume, subscript h indicates the hot side, subscript c indicates the cold side, subscript w indicates the wall, x and y are the longitudinal and transverse directions, respectively. A refers to the heat transfer area, h is the heat transfer coefficients.

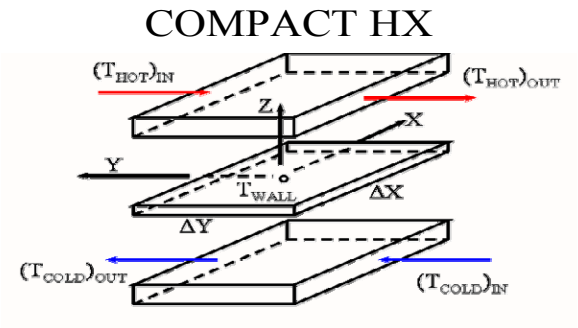

Fig. 32: Compact heat exchanger section.

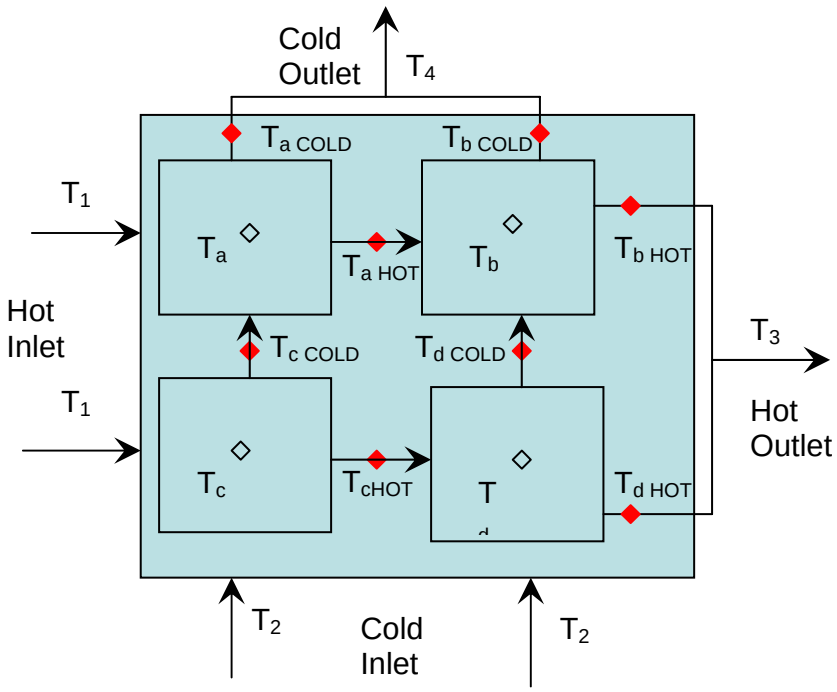

Fig. 33: Compact heat exchanger spatial discretization.

In this research, a numerical approach was applied to solve the transient thermal response of the compact heat exchangers. This is due to the fact that the partial differential equations describing the wall and fluid temperature responses are complex and non-linear, and there are no general solutions. In order to guarantee adequate accuracy, spatial discretization as depicted in Fig. 33 was applied to the heat exchanger.

3.1.3.3.7 Modeling of the Steam Generator

The steam generator (SG) considered in this research consists of an economizer, an evaporator, and a superheater. These three integrated component parts have been modeled as a cross-flow, shell-and-tube heat exchanger with a single-pass shell and one tube pass. Since the same type of shell-and-tube heat exchanger is taken into account to describe the economizer, evaporator, and superheater geometries, the geometric models developed are identical. The necessary equations are obtained from Kakaç and Liu (1998) and are the appropriate ones for this particular shell-and-tube configuration. The geometric model of the steam generator is presented in Table X.

The economizer, evaporator, and superheater dynamic models are formulated similarly. In general the steam generator is discretized spatially in *n* sections. For each section (index *i*), a dynamic energy balance for the pipe is formulated as follow:

$$\frac{1}{n}\left(mC_p\right)_w \frac{\partial T_{wi}}{\partial t} = \dot{Q}_{gas-steel\,i} - \dot{Q}_{steel-steam\,i} \qquad (56)$$

where the heat flows are calculate by

$$\dot{Q}_{gas-steel\,i} = \frac{1}{n} U_{gas_i} A\left(T_{gas_i} - T_{steel\,i}\right) \qquad (57)$$

$$\dot{Q}_{steel-steam\,i} = \frac{1}{n} U_{steam\,i} A\left(T_{steel\,i} - T_{steam\,i}\right) \quad (58)$$

The temperatures of the gas and steam for each section of the counter flow heat exchanger are calculated implicitly as follow:

$$\dot{Q}_{gas-steel\,i} = \left(\dot{m}C_p\right)_{gas}\left(T_{gas_{i-1}} - T_{gas_i}\right) \quad (59)$$

$$\dot{Q}_{steel-steam\,i} = \left(\dot{m}C_p\right)_{steam}\left(T_{steam\,i} - T_{steam\,i+1}\right) \quad (60)$$

For the evaporator the last equation is replaced by

$$\dot{Q}_{steel-steam\,i} = \left(\dot{m}\right)_{steam}\left(h_{steam\,i} - h_{steam\,i+1}\right) \quad (61)$$

Table X: Geometric model of the steam generator.

Fixed Parameter Description		Value	Fixed Parameter Description		Value
t_w	Tube wall thickness (mm)	1.5	CTP	Tube count calculation constant	0.93
n_{passes}^{SG}	Number of passes	2	CL	Tube layout constant	1
Variable Description			Model Equation		
d_i^{SG}	Tube inner diameter		Assigned value		
n_{tubes}^{SG}	Number of tubes		Assigned value		
L_{SG}	Length		Assigned value		
d_o^{SG}	Tube outer diameter		$d_o^{SG} = d_i^{SG} + 2t_w$		
P_T^{SG}	Pitch		$P_T^{SG} = 1.25 d_o^{SG}$		
D_s^{SG}	Shell diameter		$D_s^{SG} = 0.637\sqrt{\frac{CL}{CTP}}\sqrt{\pi n_{tubes}^{SG}\left(P_T^{SG}\right)^2}$		
B	Baffle spacing		$B = 0.6 D_s^{SG}$		

As far as the heat transfer analysis of the steam generator is concerned, three different heat transfer models are developed and presented in the following pages due to the fact that different convection heat transfer coefficients as well as methods are considered in the design/analysis of its three parts.

The LMTD method is applied to the thermal analysis of the economizer. Two different expressions for the tube-side heat transfer coefficient are given depending on whether the water flow inside the tubes is fully developed laminar or turbulent. The correlation used for the shell-side heat transfer coefficient is the one suggested by Kern (1950). The details of the economizer's heat transfer model are given in Table XI.

For saturated convective boiling prior to dry-out, relations to predict the heat transfer coefficient have typically been formulated to impose a gradual suppression of nucleate boiling and a gradual increase in liquid film evaporation heat transfer as the quality increases. A number of correlations based on this approach have been developed. The one recently developed by Kandlikar (1990), which has been fit to a broad spectrum of data for both horizontal and vertical tubes, is used to calculate the tube-side heat transfer coefficient for the evaporator. The equations of the evaporator's heat transfer model are presented in detail in Table XII.

As to the heat transfer model of the superheater, this is presented in Table XIII. The correlations used to calculate the tube-side and shell-side heat transfer coefficients are the same as those appearing in the model for the economizer. The main difference, however, is that the thermal analysis of the superheater is based on the effectiveness-NTU method and not on the LMTD one. The reason why the latter is used to relate the geometric variables of the economizer to its thermodynamic ones is explained as follows. Let us assume that the effectiveness-NTU method is applied to the modeling of the economizer and that the cold fluid (i.e. the water) is found to have the minimum heat capacity. According to the expression for the maximum possible heat transfer, the water stream would then exit the economizer at the inlet temperature of the combustion gases. It is highly likely though that the resulting inlet pressure and temperature of the combustion gases would correspond to a water state at the exit of the economizer different from that for a saturated liquid (e.g., a superheated vapor). Such an inconsistency is not desired in the design of the economizer. For that reason, the LMTD method, which does not introduce a discrepancy of this kind, is used.

Table XI: Heat transfer model of the economizer.

Variable Description		Model Equation
Re_{eco}	Tube-side Reynolds number	$Re_{eco} = \left(\frac{4\dot{n}_{H_2O}}{\pi d_i \mu_{H_2O} n_{tubes}} \right)_{eco}$, $Pr_{eco} = \left(\frac{\mu_{H_2O} C_{p_{H_2O}}}{k_{H_2O}} \right)_{eco}$
Pr_{eco}	Tube-side Prandtl number	
$h_{H_2O}^{eco}$	Tube-side heat transfer coefficient	If $Re_{eco} \le 2300$ $\quad h_{H_2O}^{eco} = 4.36 \left(\frac{k_{H_2O}}{d_i} \right)_{eco}$ otherwise $h_{H_2O}^{eco} = 0.023 \left(\frac{k_{H_2O}}{d_i} \right)_{eco} \left(Re_{eco} \right)^{0.8} \left(Pr_{eco} \right)^{0.4}$
D_{eq}^{eco}	Shell-side equivalent diameter	$D_{eq}^{eco} = \frac{4\left(P_T^{eco} \right)^2 - \pi \left(d_o^{eco} \right)^2}{\pi d_o^{eco}}$
A_s^{eco}	Bundle cross-flow area	$A_s^{eco} = \frac{D_s^{eco} \left(P_T^{eco} - d_o^{eco} \right) B_{eco}}{P_T^{eco}}$, $G_s^{eco} = \frac{\dot{n}_{gas}}{A_s^{eco}}$
G_s^{eco}	Shell-side mass velocity	
h_{gas}^{eco}	Shell-side heat transfer coefficient	$h_{gas}^{eco} = 0.36 \left(\frac{k_{gas}}{D_{eq}} \right)_{eco} \left(\frac{D_{eq} G_s}{\mu_{gas}} \right)_{eco}^{0.55} \left(\frac{C_{p_{gas}} \mu_{gas}}{k_{gas}} \right)_{eco}^{1/3} \left(\frac{\mu_{gas}}{\mu_{wall}} \right)_{eco}^{0.14}$
U_{eco}	Overall heat transfer coefficient	$U_{eco} = \frac{1}{\frac{1}{h_{H_2O}^{eco}} + \frac{1}{h_{gas}^{eco}}}$, $A_{eco} = \left(\pi d_o L n_{tubes} n_{passes} \right)_{eco}$
A_{eco}	Heat transfer area	
ΔT_{lm}^{eco}	Log mean temperature difference	$\Delta T_{lm}^{eco} = \frac{\left(T_{gas,i} - T_{H_2O,o} \right)_{eco} - \left(T_{gas,o} - T_{H_2O,i} \right)_{eco}}{\ln \left[\frac{\left(T_{gas,i} - T_{H_2O,o} \right)_{eco}}{\left(T_{gas,o} - T_{H_2O,i} \right)_{eco}} \right]}$
$\dot{Q}_{eco}$	Heat transfer rate	$\dot{Q}_{eco} = \dot{n}_{gas} C_{p_{gas}}^{eco} \left(T_{gas,i}^{eco} - T_{gas,o}^{eco} \right) = U_{eco} A_{eco} \Delta T_{lm}^{eco}$

Table XII: Heat transfer model of the evaporator.

Variable Description		Model Equation
A_{cr}^{evap}	Cross-sectional area	$A_{cr}^{evap} = \frac{\pi \left(d_i^{evap} \right)^2}{4}$, $G_{tube}^{evap} = \frac{\dot{n}_{H_2O}}{n_{tubes}^{evap} A_{cr}^{evap}}$
G_{tube}^{evap}	Tube-side mass velocity	
Co	Convection number	$Co = \left(\frac{1-\chi}{\chi} \right)^{0.8} \left(\frac{\rho_{H_2O}^{vap}}{\rho_{H_2O}^{liq}} \right)^{0.5}$
Fr_{le}	Froude number	$Fr_{le} = \frac{\left(G_{tube}^{evap} \right)^2}{\left(\rho_{H_2O}^{liq} \right)^2 g d_i^{evap}}$
Bo	Boiling number	$Bo = \frac{q''_{evap}}{G_{tube}^{evap} h_{fg}}$
h_{liq}	Heat transfer coefficient for the liquid phase	$h_{liq} = 0.023 \frac{k_{H_2O}^{liq}}{d_i^{evap}} \left(\frac{G_{tube}^{evap} (1-\chi) d_i^{evap}}{\mu_{H_2O}^{liq}} \right)^{0.8} \left(\frac{\mu_{H_2O} C_{p_{H_2O}}}{k_{H_2O}} \right)_{liq}^{0.4}$
$h_{H_2O}^{evap}$	Tube-side heat transfer coefficient	$h_{H_2O}^{evap} = h_{liq} \left[C_1 Co^{C_2} \left(25 Fr_{le} \right)^{C_5} + C_3 Bo^{C_4} \right]$
D_{eq}^{evap}	Shell-side equivalent diameter	$D_{eq}^{evap} = \frac{4\left(P_T^{evap} \right)^2 - \pi \left(d_o^{evap} \right)^2}{\pi d_o^{evap}}$
A_s^{evap}	Bundle cross-flow area	$A_s^{evap} = \frac{D_s^{evap} \left(P_T^{evap} - d_o^{evap} \right) B_{evap}}{P_T^{evap}}$, $G_s^{evap} = \frac{\dot{n}_{gas}}{A_s^{evap}}$
G_s^{evap}	Shell-side mass velocity	
h_{gas}^{evap}	Shell-side heat transfer coefficient	$h_{gas}^{evap} = 0.36 \left(\frac{k_{gas}}{D_{eq}} \right)_{evap} \left(\frac{D_{eq} G_s}{\mu_{gas}} \right)_{evap}^{0.55} \left(\frac{C_{p_{gas}} \mu_{gas}}{k_{gas}} \right)_{evap}^{1/3} \left(\frac{\mu_{gas}}{\mu_{wall}} \right)_{evap}^{0.14}$
U_{evap}	Overall heat transfer coefficient	$U_{evap} = \frac{1}{\frac{1}{h_{H_2O}^{evap}} + \frac{1}{h_{gas}^{evap}}}$
A_{evap}	Heat transfer area	$A_{evap} = \left(\pi d_o L n_{tubes} n_{passes} \right)_{evap}$
ΔT_{lm}^{evap}	Log mean temperature difference	$\Delta T_{lm}^{evap} = \frac{\left(T_{gas,i} - T_{gas,o} \right)_{evap}}{\ln \left[\frac{\left(T_{gas,i} - T_{H_2O} \right)_{evap}}{\left(T_{gas,o} - T_{H_2O} \right)_{evap}} \right]}$
q''_{evap}	Surface heat flux (single tube)	$q''_{evap} = \frac{\dot{n}_{gas} C_{p_{gas}}^{evap} \left(T_{gas,i}^{evap} - T_{gas,o}^{evap} \right)}{n_{tubes}^{evap} A_{evap}} = \frac{U_{evap} \Delta T_{lm}^{evap}}{n_{tubes}^{evap}}$

Table XIII: Heat transfer model of the superheater.

Variable Description		Model Equation
Re_{super}	Tube-side Reynolds number	$Re_{super} = \left(\frac{4\dot{n}_{H_2O}}{\pi d_i \mu_{H_2O} n_{tubes}} \right)_{super}$, $Pr_{super} = \left(\frac{\mu_{H_2O} C_{p_{H_2O}}}{k_{H_2O}} \right)_{super}$
Pr_{super}	Tube-side Prandtl number	
$h_{H_2O}^{super}$	Tube-side heat transfer coefficient	$h_{H_2O}^{super} = 0.023 \left(\frac{k_{H_2O}}{d_i} \right)_{super} \left(Re_{super} \right)^{0.8} \left(Pr_{super} \right)^{0.4}$
D_{eq}^{super}	Shell-side equivalent diameter	$D_{eq}^{super} = \frac{4\left(P_T^{super} \right)^2 - \pi \left(d_o^{super} \right)^2}{\pi d_o^{super}}$
A_s^{super}	Bundle cross-flow area	$A_s^{super} = \frac{D_s^{super} \left(P_T^{super} - d_o^{super} \right) B_{super}}{P_T^{super}}$, $G_s^{super} = \frac{\dot{n}_{gas}}{A_s^{super}}$
G_s^{super}	Shell-side mass velocity	
h_{gas}^{super}	Shell-side heat transfer coefficient	$h_{gas}^{super} = 0.36 \left(\frac{k_{gas}}{D_{eq}} \right)_{super} \left(\frac{D_{eq} G_s}{\mu_{gas}} \right)_{super}^{0.55} \left(\frac{C_{p_{gas}} \mu_{gas}}{k_{gas}} \right)_{super}^{1/3} \left(\frac{\mu_{gas}}{\mu_{wall}} \right)_{super}^{0.14}$
U_{super}	Overall heat transfer coefficient	$U_{super} = \frac{1}{\frac{1}{h_{H_2O}^{super}} + \frac{1}{h_{gas}^{super}}}$, $A_{super} = \left(\pi d_o L n_{tubes} n_{passes} \right)_{super}$
A_{super}	Heat transfer area	
C_{min}	Minimum heat capacity	$C_{min} = \min \left(\dot{n}_{H_2O} C_{p_{H_2O}}^{super} , \dot{n}_{gas} C_{p_{gas}}^{super} \right)$
C_{max}	Maximum heat capacity	$C_{max} = \max \left(\dot{n}_{H_2O} C_{p_{H_2O}}^{super} , \dot{n}_{gas} C_{p_{gas}}^{super} \right)$
C_r	Heat capacity ratio	$C_r = \frac{C_{min}}{C_{max}}$, $NTU = \frac{U_{super} A_{super}}{C_{min}}$
NTU	Number of transfer units	
ε_{super}	Superheater effectiveness	$\varepsilon_{super} = \frac{2}{1 + C_r + \sqrt{1 + C_r^2} \frac{1 + \exp\left(-NTU \sqrt{1 + C_r^2} \right)}{1 - \exp\left(-NTU \sqrt{1 + C_r^2} \right)}}$

3.1.3.4 gPROMS® BOPS Environment

Process modeling is now a recognized essential technology for successful design and operation of process plants. Steady-state models are used in almost all process design; dynamic simulation analyses are performed as a routine part of control verification and tuning and the design of start-up, shut-down and emergency procedures, and process models can form the basis for a number of process control and related operations. Many other activities rely on the availability of a detailed, predictive model of the process. PSE's (Process Systems Enterprise's) gPROMS is a powerful general-purpose process modeling and optimization environment used to enhance design and operation of continuous and batch processes. It provides unrivalled modeling and solution capabilities which allow one to build high-accuracy models of production facilities.

gPROMS® stands for general Process Modeling System. It is the most advanced general purpose process modeling, simulation and optimization software available today. gPROMS is actually a family of products that takes process modeling across the traditional boundaries within the typical organization - from R&D specialists and engineers to CFD practitioners, control engineers and operations personnel. gPROMS models can be used for steady-state and dynamic simulation, estimation and optimization within the gPROMS user interface, or within an embedded gPROMS modeling and solution engine in packages such as FLUENT, Aspen Plus, Hysys, Matlab, Simulink or various automation systems. The gPROMS integrated capabilities are shown in Fig. 34.

3.1.3.4.1 gPROMS' Underlying Technology

At its core gPROMS is an equation-based system, meaning that processes are described by their underlying physical and chemical relationships and the operational task sequences superimposed on them. gPROMS analyses the relationships governing the process and then performs your solution of choice - dynamic or steady-state simulation, optimization or parameter estimation. This enables process designers and operations personnel to quantify process design and operation,. Some characteristics of gPROMS are: a powerful modeling language, robust and fast solution technology, and a modular, well-designed underlying software structure.

gPROMS is widely recognized as a 'best-in-class' simulation environment. It is designed to be both a fully-fledged simulation environment in its own right, and a simulation engine which can be embedded in applications or combined with other 'best-in-class' applications to provide a comprehensive design and operations tool. Similarly, gPROMS allows models to link to external components, for example, physical properties packages or control system software with ease. Advanced features such as dynamic optimization allow simultaneous optimization of equipment sizes and operating procedures.

3.1.3.4.2 Application Across the Process and System Lifecycle

With a gPROMS model of your process, you can perform many activities using a single evolving model basis:

- Optimize equipment design - determine the optimum equipment sizes for the required operation.
- Optimize operating procedures - determine the optimum procedures for operations such as startup (for example, to minimize startup time subject to operating constraints), shutdown, and emergency handling.
- Optimize control system performance by determining the optimum controller settings for anticipated disturbances.
- Provide automation applications such as data reconciliation, model-based predictive control and inferential measurement.
- Provide on-site decision support tools, for example, a dynamic simulation or optimization of a process embedded in an Excel or web browser front end, for use by operators in the control room.

All of these help ensure that the system at hand is designed for optimum performance, and operations are as close to the optimum for the given plant configuration as possible.

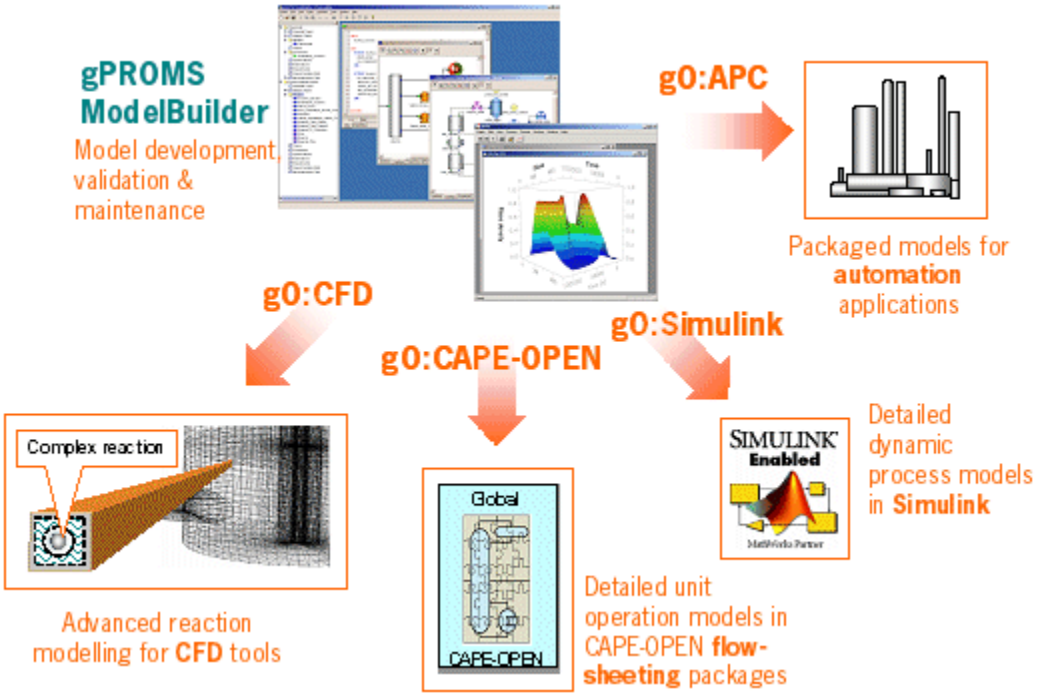

Fig. 34: The gPROMS integrated capabilities (gPROMS introductory manual).

3.1.3.4.3 gPROMS® for Fuel Cell System Modeling

Fuel cell technology is one of today's key areas of process development and design. Process Systems Enterprise's gPROMS process modeling environment is the modeling tool of choice for many of the companies and research organizations leading the field in this development. gPROMS' unique features bring significant benefits to researchers and engineers modeling fuel pre-treatment systems and the cell process itself, making it feasible to set up detailed system models capable of highly accurate predictions. Once a model is available, it can be used to optimize synthesis design of equipment and operations, thereby improving synthesis/design solutions and reducing development times at every stage.

A detailed process model of systems such as the one shown in Fig. 34 above can be used to provide quantitative information for decisions on many critical aspects of synthesis/design, to establish the operating envelope, and to test the whole range of operations exhaustively. In particular, the key technology of dynamic optimization can be used to optimize simultaneously both the static design parameters and the dynamic performance of the system. gPROMS is suitable with the tools required to characterize the reactions in complex reaction systems, to investigate catalyst performance, and to design reactor control systems. These facilities are all available to developer of fuel pre-treatment systems for fuel cells.

3.1.3.4.4 gPROMS® for Control Engineers

gPROMS provides numerous facilities for design of control systems and their implementation. This section describes three areas: the general facilities gPROMS offers, the Simulink block object, and the model linearization capability.

Control System Design and Optimization

Controllers built in gPROMS can be optimally tuned for a range of disturbances with a single optimization run. gPROMS can be used to design and optimize equipment and control system simultaneously, for example, to determine the best reactor diameter and controller tunings in a single run. gPROMS is used extensively for determining optimum operating procedures for start-up, shutdown, and general batch operations.

The Simulink Block Object

The gPROMS Block Object for Simulink allows complex non-linear gPROMS process models to be incorporated directly in your MATLAB® Simulink applications. This enables Control Engineers to design controllers in Simulink using detailed process models created by process engineers for process design. The solution of gPROMS models within Simulink is rapid and robust. gPROMS takes care of all the mathematics required to reduce the problems to the form expected by Simulink, however complex the set of partial and ordinary differential and algebraic equations within the gPROMS model.

The Model Linearization Capability

Using the gPROMS LINEARISE command, you can generate a linearized model at any point during the execution of a gPROMS simulation for use in linear control system design techniques or in model predictive control. Using gPROMS to generate linearised models means that you can:

- generate state-space matrices for use in control system design within MATLAB
- generate linear models for use in Model-Predictive Controllers (MPC) from a detailed dynamic model, without perturbing plant operation
- generate linear models at any operational state you require. For example, you can generate separate linear models for high throughput and low throughput cases, in order to provide the MPC with the most appropriate operating model
- take advantage of the wide variety of existing gPROMS models in all walks of industry and academia to streamline control system design.

3.1.4 SOFC Power-Conditioning-System Model

The problem of integrated-system design/operational optimization for variable loads and/or environmental conditions is complex and difficult to solve. It represents a mixed integer and non-linear programming (MINLP) problem for which no general solution has been found. This is further complicated by the need to examine a large number of alternate syntheses, designs, and operational-control strategies at each level of the problem. SOFC stacks respond quickly to changes in load, because of their rapid electrochemistry. The PES also responds quickly to changes in application load or other variations. This is however not true for the thermal, mechanical, and chemical BOPS components and particularly for the fuel-processing sub-system, where load-following time constants are typically several orders of magnitude higher. Differences in response times between the electrochemical/electrical and thermal/mechanical/chemical sub-systems of the overall SOFC system significantly increase the computational complexity. For example, the load following time constants of the BOPS are typically of the

order of seconds, while that of the SOFC and the PES is in microseconds. Hence the number of iterations of the PES/SOFC model has to be of the order of millions for us to get any meaningful results. Such complex simulations are extremely cumbersome on commercially available computational facilities (as specified by DOE). Hence there is a need to develop efficient simulation techniques to model such systems. This section first describes the comprehensive system model and then goes on to describe the reduced order models that are developed for efficient and less cumbersome calculations.

3.1.4.1 Comprehensive Integrated Model and Methodology on Multi-Software Platform

Such a methodology enables the use of software/package that is most suited to model any given sub-systemTo study the electrical interaction of SOFC, PES, BOPS, and the application loads as a whole, a multi-software platform as shown in Fig. 35 were implemented using *iSIGHT*[11]. While the *Visual-Fortran* code (SOFC) is embedded in the *Saber Designer* (PES and application load) using *dynamic link library (dlls)*, modules developed in the *gPROMS*[12] (BOPS) environment was integrated with *Saber Designer* using *iSIGHT* software (Mazumder et al., 2003). The PES model supplies input power data to the BOPS model through the *iSIGHT* interface. The BOPS model then calculates the SOFC stack parameters (like fuel-flow rate and temperatures) and supplies this data to the SOFC model, using *iSIGHT* and *dlls*. This integration of multiple software platforms enable us to use the most powerful software tools used to model each of the SOFC sub-systems.

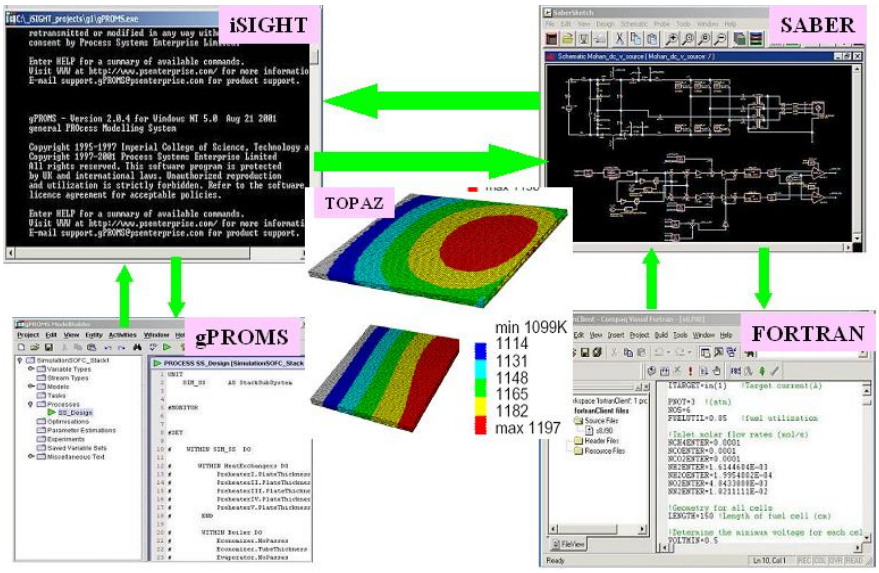

Fig. 35: Implementation of a unified model for a SOFC power-conditioning system using multi-software platform.

[11] iSight is a software developed and distributed by Engineous Software Inc. iSIGHT integrates simulation codes and provides engineering intelligence to drive the investigation of design alternatives. iSIGHT frees engineers from doing countless iterative routines at the keyboard, leaving more time to create innovative ideas and gain competitive position.

[12] gPROMS is an equation-based system (i.e. based on *first principles*) which analyzes the relationships governing a process (chemical, thermal, mechanical, electrochemical, and electrical) and then performs a dynamic or steady-state simulation, optimization or parameter estimation. The powerful modeling language and a robust and fast-solution technology provides a framework, which has a high degree of success in both synthesis/design and operational modeling, simulation, and optimization of complex and dynamic fuel-cell based total-energy systems. Thus, a general model for the balance-of-plant in the gPROMS environment requires modifying or adding to the existing thermodynamic, kinetic, geometric, and cost models, which have been integrated with the PES and SOFCSS modules.

For SOFC cell-level analysis, an additional finite-element (FE) simulating package *TOPAZ/FEMLAB*[13] was used in addition to the above multi-software platform. Initially a long-term simulation is conducted using the analytical models of SOFC, BOPS, PES, and application load. Once a steady-state is reached, the equilibrium values of the SOFC current and voltages are fed to the FE model of the SOFC (the parameters of this model is the same as that of the analytical SOFC model) along with boundary conditions to obtain the spatial resolution of cell current-density and temperature distributions.

With such tools for dynamic simulation and modeling, it is possible to conduct parametric studies and optimizations to determine control strategies (for stationary and/or transportation auxiliary power load profiles) and their effects on the efficiency, power density, fuel utilization and conversion, system response and configuration, and component design of SOFC systems.

3.1.4.2 Reduced-Order Models to Resolve Effect of Multiple Time Scales

Differences in response times between the electrochemical/electrical and thermal/mechanical/chemical sub-systems of the overall SOFC system imply that real-time simulations have to be performed in order to obtain meaningful results. However real-time simulations using the comprehensive model are extremely cumbersome and time consuming. Hence more efficient simulation techniques are needed for studying the system interactions.

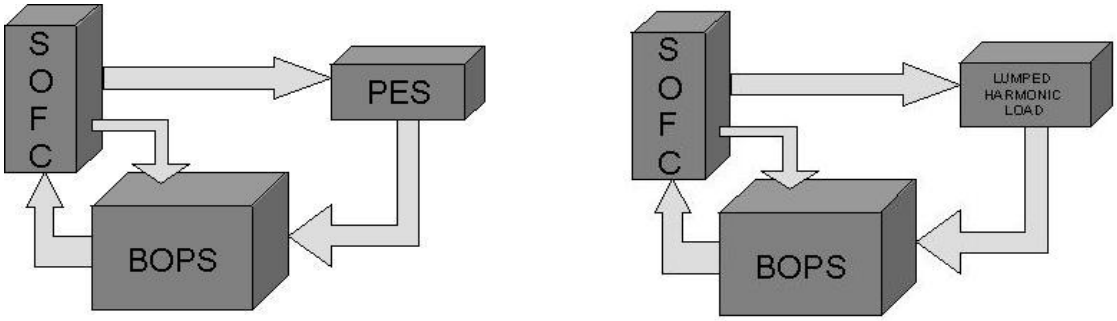

(a) (b)

Fig. 36: (a) Comprehensive model block diagram; (b) reduced order model with lumped harmonic load replacing the PES.

Since the PES model comprises of a number of switching functions[14], their real-time simulation using the comprehensive model (as discussed in Section 3.1.4.1) is extremely tedious. In order to reduce the complexity of the simulation, a two-step approach was taken. In the first step simulations on different PES topologies were performed using *Saber Designer* with an ideal voltage source as the input. The harmonic content (obtained using Fourier transforms) and the profile of the PES input current was estimated. In the second step, the PES is replaced by a lumped load (with similar harmonic content and profile as estimated

[13] FEMLAB supplies highly sought-after new technology for the modeling and simulation of physics in all science and engineering fields. Its main attribute is the ease with which modeling can be performed and its unlimited multiphysics capabilities, in 1D, 2D and 3D — the perfect way to apply state-of-the-art numerical analysis to your expertise in modeling.

[14] The switching functions are determined by the state-variables of the system at each time instant. A transition in the switching function occurs whenever the state-variables satisfy certain conditions.

in the first step) in the comprehensive simulation platform as shown in Figs. 36(a) and (b). While developing the lumped load, it was ensured that all the harmonics were present and the magnitudes matched, so that the stresses imposed by the lumped load on the SOFC is similar to that imposed by the PES. The process of the lumped load development was purely iterative. The reduced order model was then used to investigate the effect of the PES dynamics on the SOFC stack life and performance. This model substantially reduces the simulation times and at the same time can model the power electronic system to a good degree of accuracy. This reduced order model enables us to perform real-time simulations on the SOFC based system.

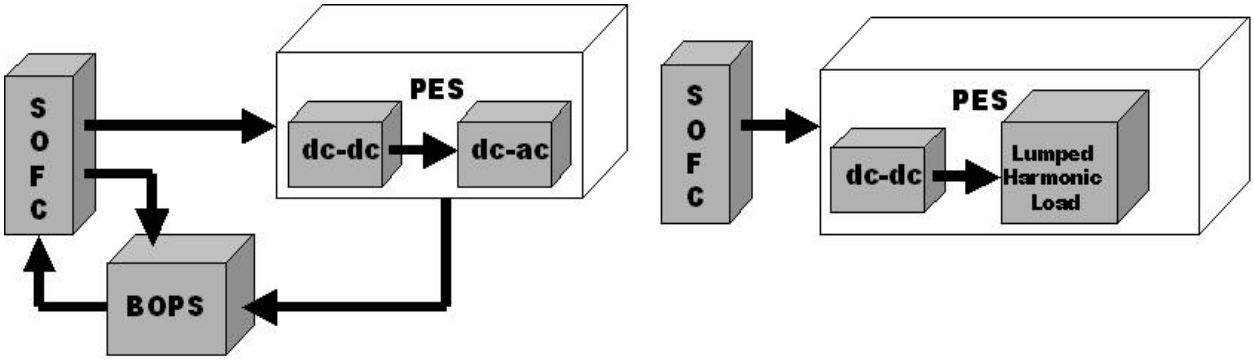

(a) (b)

Fig. 37: (a) Comprehensive model block diagram; (b) reduced order model with lumped harmonic load replacing the PES.

In order to study the effect of SOFC variations on PES network transients and dynamics, a second reduced order model as shown in Fig. 37 is implemented. Here the SOFC is assumed to be a time varying voltage source, where the output voltage varies with the PES input current. Since the time scales for the PES dynamics are comparatively much smaller, the BOPS model was neglected for this reduced order study. For obtaining seed results, the investigation was limited to the dc-dc boost converter, with the dc-ac stage replaced by a lumped harmonic load, which is obtained following a similar procedure as outlined earlier in this section.

3.1.5 Application Load Model

An application load model was developed using the load profile reported by NAHB Research Center, Inc. Figs. 38-41 shows the hourly distribution residential utility load for five different locations in the country. The hourly change in electrical demand provides a snapshot of what may be expected of the distributed generation equipment through a diurnal period. Using the previously considered utility residential load profile data, the data are analyzed for each hour of the day across all days in the year.

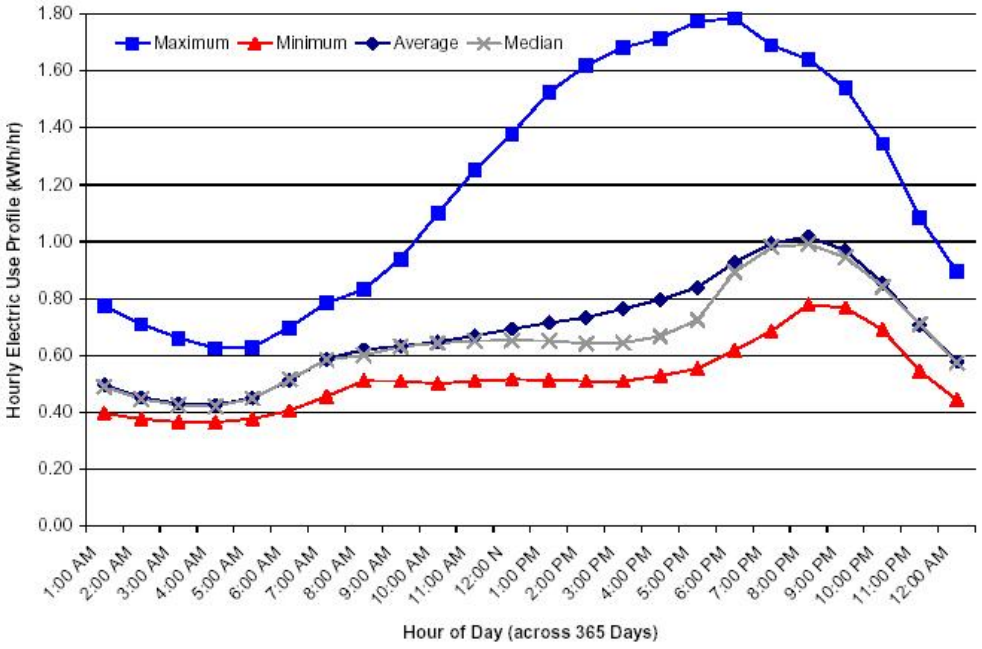

Fig. 38: Hourly Average Residential Load Profile (Southern California Edison Territory).

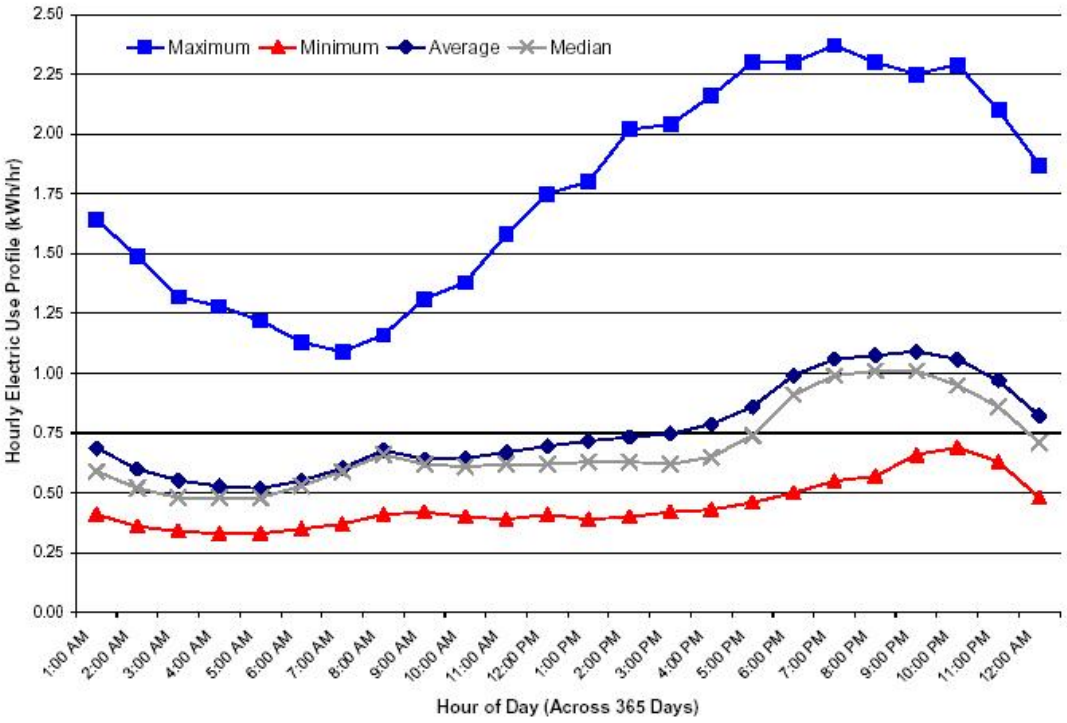

Fig. 39: Hourly Residential Load Profile (Public Service Electric & Gas Territory, Non-Electric Space Heating).

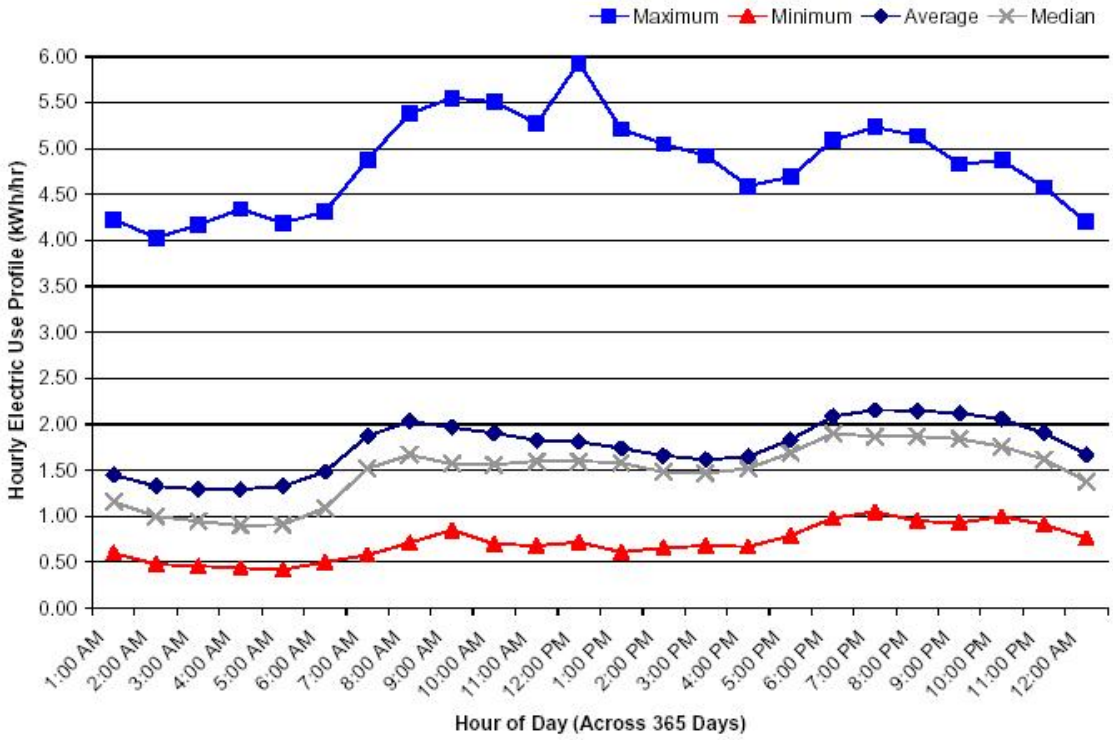

Fig. 40: Hourly Residential Load Profile (Public Service Electric & Gas Territory, Electric Space Heating).

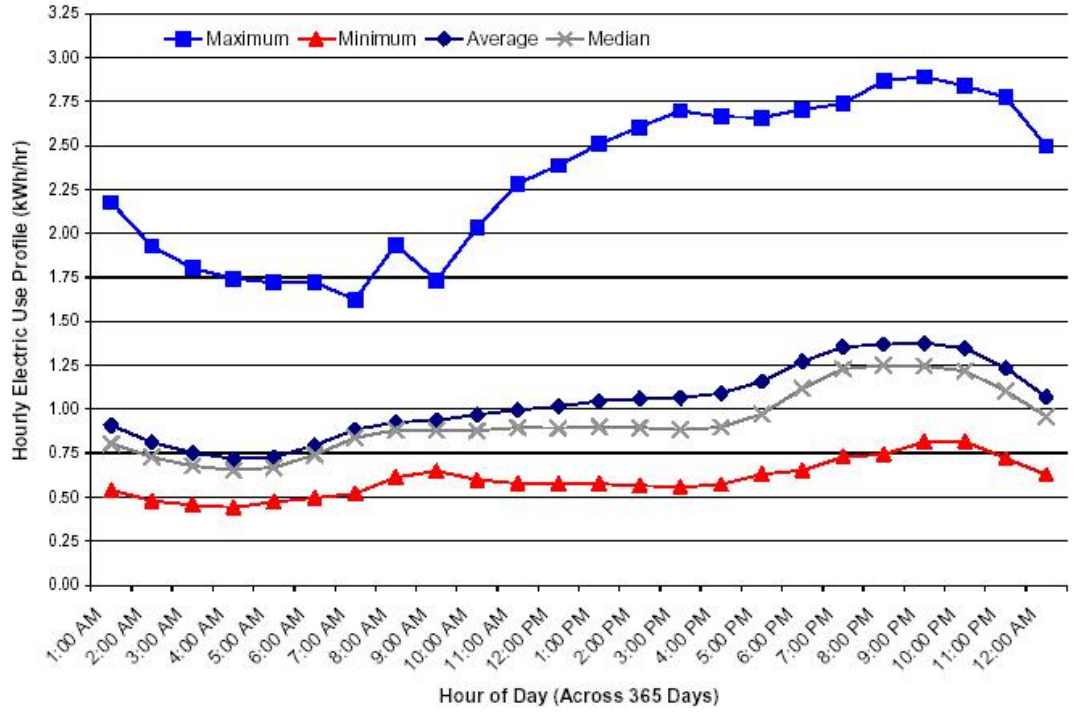

Fig. 41: Hourly Residential Load Profile (Baltimore Gas and Electric Territory, Non-Electric Space Heating).

Fig. 38 shows the average hourly use from SCE's residential load profile data, and including the median, maximum and minimum for each hour. For the PSE&G residential load profile data, Fig. 39 and Fig. 40 show the hourly load profile for homes without electric space heating and homes with electric space heating, respectively. Hourly average, median, maximum and minimum loads are included. Similar hourly data for the BGE residential electric load profile is shown in Fig. 41. The data is also divided according to homes that do not use electricity for heating and those that do.

The hourly data, which spans all hours of the year, represents the range of change in electrical use for each hour of the day throughout the year. The average, median maximum and minimum are shown for each hour across the year. Most notable from the data is the difference from the minimum to the average relative to the difference between the average and the maximum for each hour. The difference between the maximum and the average is about three times more than the difference between the average and the minimum. This implies that the data is skewed towards the minimum level of consumption for each hour of the day and throughout the year. This appears to be consistent for all locations analyzed.

3.2 SYSTEM-INTERACTION ANALYSIS

3.2.1 Effect of PES on SOFC

The factors that effect the stack lifetime and durability include operating temperature, thermal cycling of SOFC stack material, mechanical pressure fluctuations. Effect of these factors on the material properties of SOFC has been reported earlier (Virkar et al., Huang et al., Hsiao et al. and Travis et al.). These studies on SOFC stack reliability have primarily focused on investigating the effect of material properties and electro-kinetics of the chemical reactions on the operating life and performance. However the effect of the PES dynamics on the performance of SOFC stack has not been investigated in great detail. Recently, Gemmen et al. attempted to estimate the effects of electrical loads and inverter ripple on the durability and performance of PEM fuel cells using a simple first order model for the PES. An understanding of the effect of inverter loads on conditions near the electrolyte surface was achieved. As part of our project, we study the effect of PES dynamics (the models have been described in Section 3.1.2.2) on the SOFC stack performance. Our focus in this study has been to investigate the system level interactions between the various sub-systems of the SOFC based system, specifically to study the effect of load transients and steady-state ripple and harmonics on SOFC properties. We investigate the effect of the PES dynamics on hydrogen utilization and operating temperature of the SOFC. We then use the results of (Virkar et al., Huang et al., 2001, Hsiao et al., and Travis et al., 2003) to relate the PES dynamics to the performance and operating lifetime of the SOFC.

3.2.1.1 Impact of Load Variations and Ripple Characteristics on SOFC Performance

SOFC hydrogen utilization is directly proportional to the current drawn by the PES (Khandkar et al., 1998) and can be defined as

$$U = \frac{I}{\dot{n}_n nF} \qquad (62)$$

where $\dot{n}$ is the hydrogen flow rate, which is determined by the BOPS and nF is the charge flow between the anode and the cathode. Figs. 42(a) and (b) illustrate the hydrogen utilization for the converter topologies shown in Figs. 23(a) and (c), respectively. Clearly, from Figs. 24-26 and 42 we see that the hydrogen utilization closely follows the PES input current. SOFC temperature can be obtained by using basic thermodynamic equations and has been studied in literature (Haynes et al. a). These results can be used to relate the SOFC current to its temperature.

Figs. 43(a) and (b) illustrate the hydrogen utilization and air supply pipe temperature with variation in the current amplitude and ripple-factor. It is clear that to meet higher load demands the hydrogen utilization has to increase significantly. Magnitude of current ripple has minimal impact for low loads. However at higher loads, as the ripple is increased, the hydrogen utilization was found to increase. However, the variation of temperature with current ripple is insignificant. Figs. 44(a) and (b) illustrate the hydrogen utilization and air supply pipe temperature with variation in the current amplitude and frequency. Fig. 44(a) shows that the hydrogen utilization significantly decreases at a low frequency. Also temperature is shown to rise significantly at lower frequencies. We can conclude from Fig. 45 that low frequency current ripple would lead to depletion of hydrogen, which has a detrimental effect on the SOFC stack operating life. Also, for a low-frequency current ripple, temperatures were found to rise beyond their nominal operating points. Theoretical studies indicate interaction between the standard cathode, $(La_{0.85}Sr_{0.15})_{0.95}MnO_3$ (LSM) and the standard electrolyte, Yttrium Stabilized Zirconia (YSZ) above temperatures of 1000°C (Hsiao et al.). In long-term operation, an interlayer of $LaZr_2O_7$ forms, whose conductivity is much less than that of LSM and hence has an impact on the output voltage and current supplied by the SOFC. Thus low-frequency current ripple has a degrading effect on the performance of the fuel cell.

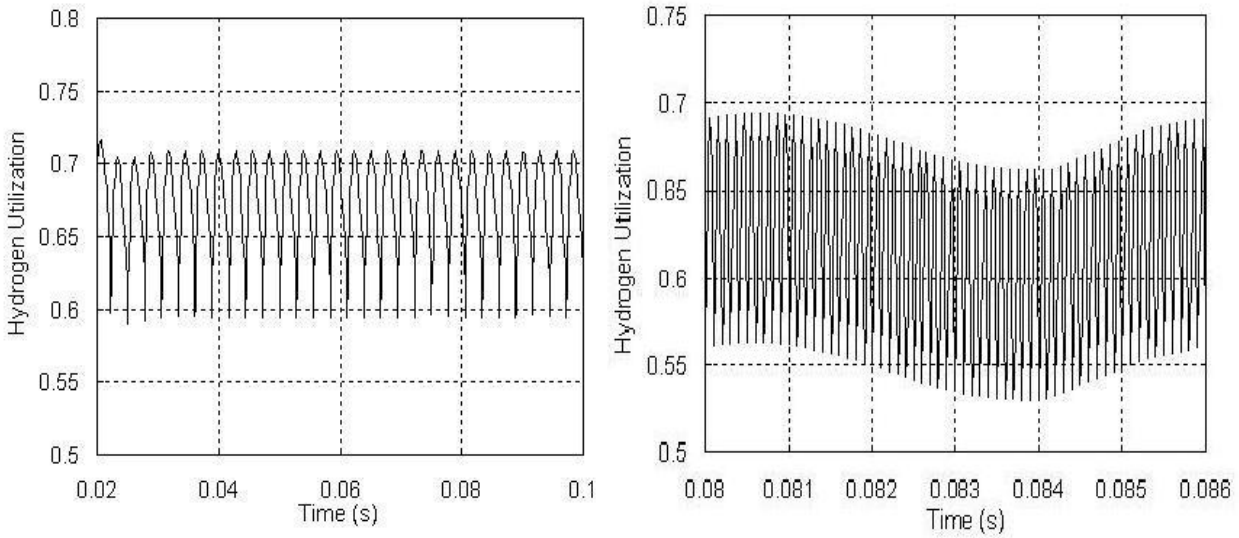

Fig. 42: SOFC hydrogen utilization for (a) line-commutated topology of Fig. 23(a), and (b) high-frequency transformer-isolated cycloconverter topology of Fig. 23(c).

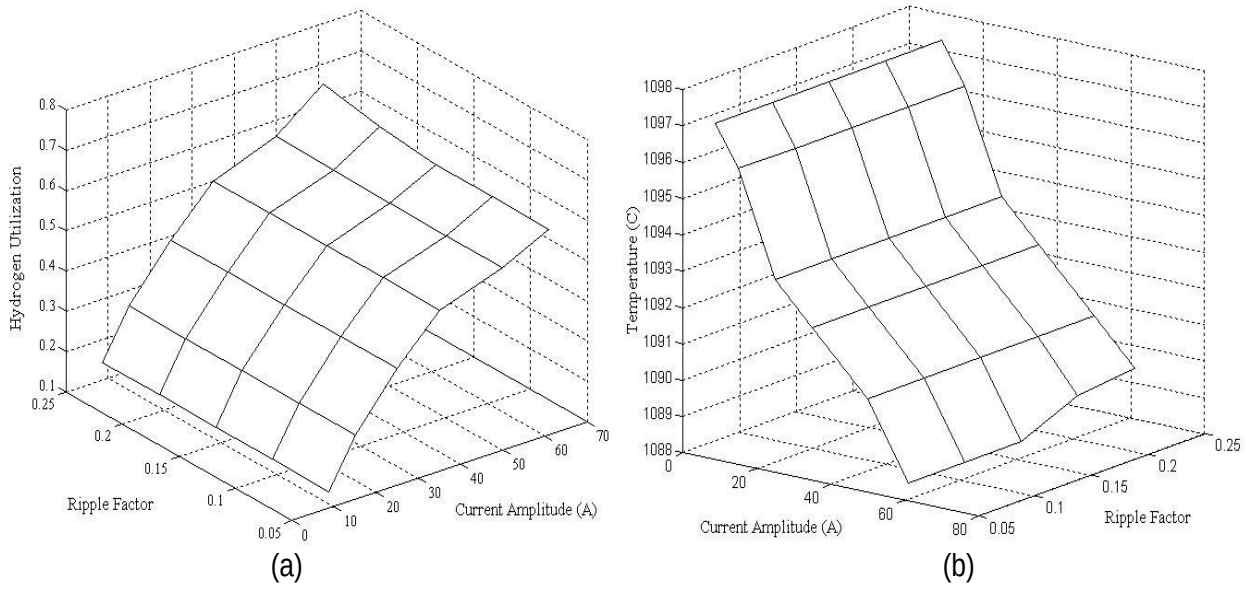

Fig. 43: (a) Hydrogen utilization and (b) air supply pipe temperature as a function of current amplitude and ripple factor.

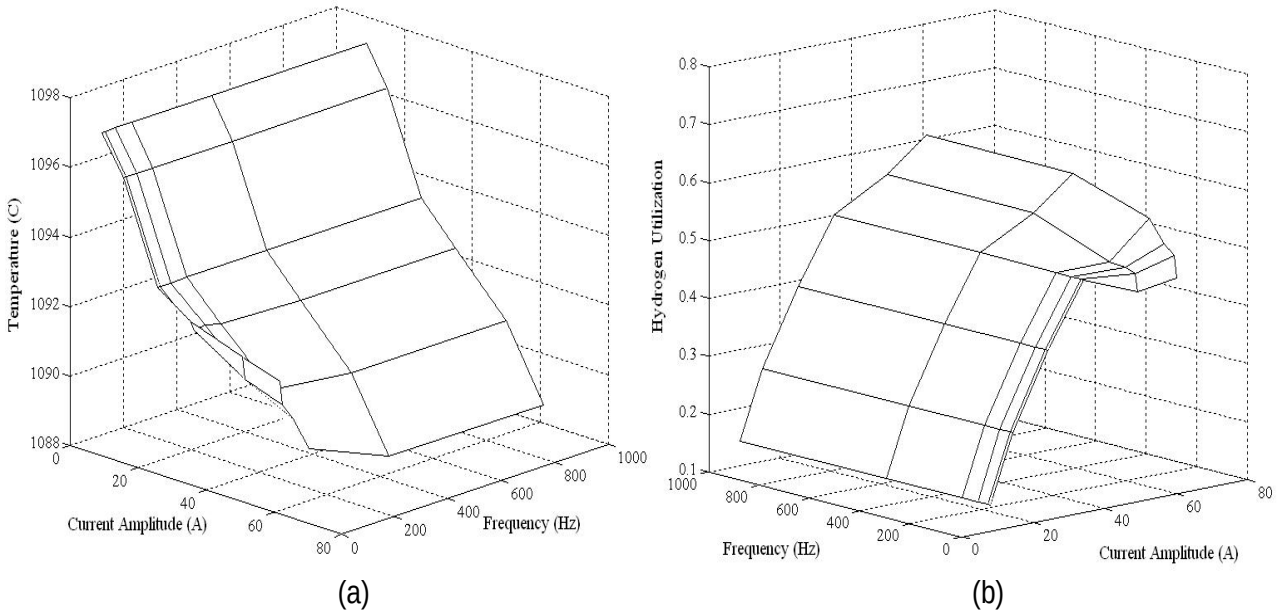

Fig. 44: (a) Hydrogen utilization and (b) air supply pipe temperature as a function of current amplitude and switching frequency.

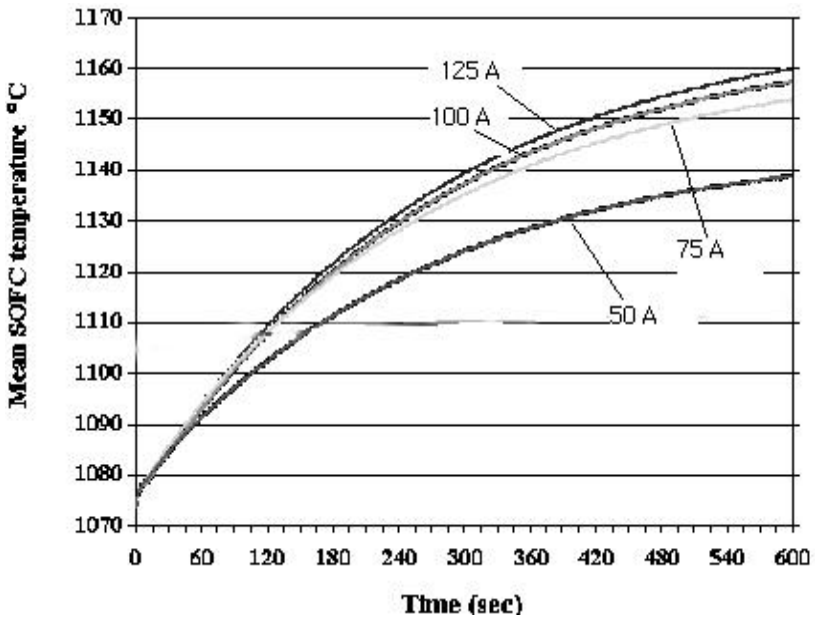

Fig. 45: SOFC mean temperature for step load transients (at Time = 0 s) from no-load to 125 A, 100A, 75A and 50 A.

3.2.1.2 Impact of Load Current Amplitude on SOFC Material Properties

Load transients also affect the operating conditions of the SOFC stack. Since the BOPS cannot respond to such changes instantaneously, a detrimental effect on the performance of the SOFC stack is expected. The details of this study will be presented in section 3.3.2, where we study the behavior of various modulation strategies on the transient behavior of the fuel cell. Fig. 45 shows the variation of SOFC mean temperature with time for a step load transient at time t = 0. Clearly with increase in current, the SOFC temperature increases and the heat generated has a degrading effect on the material properties. The heat dissipation in the SOFC is due to (a) dissipation in the area specific resistance of the fuel cell, and (b) dissipation due to the chemical reaction ($T\Delta S$). It has been reported that heat dissipated by the fuel cell, if not managed properly can have a significant impact on the microcrack density of the fuel cell electrolyte (Qu et al. 2003). For a given material and spatial heat source, the microcrack density is directly proportional to the heat rate. It has been shown that microcrack density increases beyond a certain threshold heating rate given by

$$q'_{th} = \frac{3\pi^2 k r_o}{2\alpha}\sqrt{\frac{G_c \pi(1-\nu)}{E_o b(1+\nu)}} \qquad (63)$$

where r_o is the length parameter that characterizes spatial non-uniformity of heat source, k is the thermal diffusivity, α is the coefficient of linear thermal expansion, G_c is the fracture toughness of the

material, E_o is the Young's elastic modulus of uncracked material, b is the crack size, and ν is Poisson's ratio of the uncracked material.

The threshold current beyond which the microcrack density increases can then be expressed as

$$I_{th} = \sqrt{\frac{q'_{th} - q_{chemical}}{R_{SOFC}}} \qquad (64)$$

where R_{SOFC} is the area specific resistance of the SOFC, and $q_{chemical}$ is the heating rate due to the chemical reaction. Fig. 46 shows the variation of the maximum allocable heat and the maximum current that a fuel cell can handle for a 30% microcrack density calculated from equations (63) and (64). Beyond these threshold values higher microcrack densities are expected, which would significantly degrade the reliability of the SOFC. Clearly the currents encountered by the SOFC (as discussed in Section 3.1.2) are much higher than the threshold values indicated in Fig. 46 hence for the application considered in this study, a sufficient microcrack density is expected, which would degrade the long-term performance of the SOFC stack.

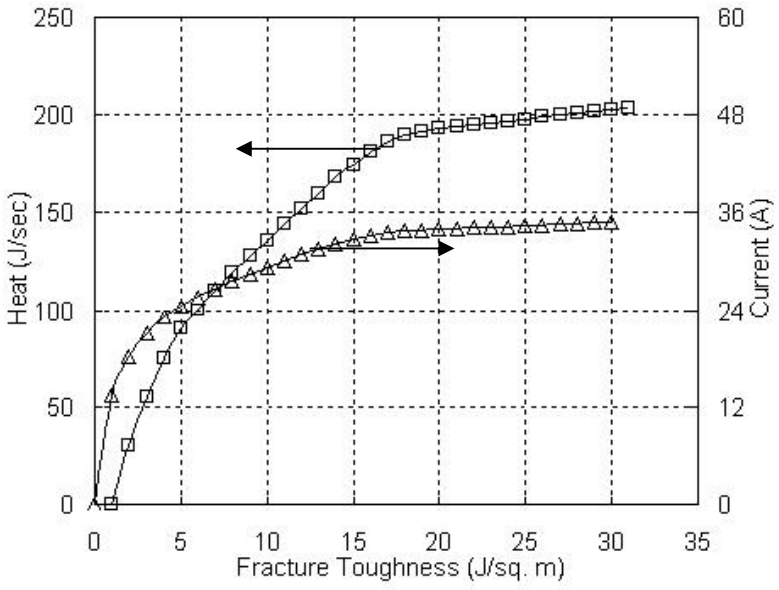

Fig. 46: Maximum allocable heat and current for a microcrack density of 30% as a function of fracture toughness.

3.2.2 Effect of SOFC Variations on PES Network Transients and Dynamics

3.2.2.1 Motivation for studying the effect of SOFC variation on PES dynamics

SOFC stacks provide non-uniform input voltage to the PES. The output voltage of the SOFC depends on the current drawn by the PES and is given by

$$V_{SOFC} = V^{\circ} - I_{SOFC}Z - I_{SOFC}\eta_a - I_{SOFC}\eta_c \qquad (65)$$

where V° is the Nernst potential of the SOFC, Z is the electrical resistance within the cell, η_a is the activation polarization that result from the electrochemical barriers that oppose current and ion flow, and η_c is the concentration polarization that result from local depletion of reactants on the electrodes. As discussed in the previous sections, there is a delay before the system stabilizes back to its steady state in case of load transients, since the BOPS cannot immediately respond to the higher fuel demand. As a result, the SOFC voltage drops when there is a transition from low to high load; where the voltage follows the expression in equation (65). For the SOFC system considered in this study, the voltage drops from a nominal operating point of 72V at no load to 48V at full load (5 kW).

Because the PES is a nonlinear discontinuous system, conventional averaged small-signal analysis is not sufficient (Mazumder et al., 2001a-d) and hence, nonlinear methodologies such as bifurcation algorithms have been developed. It has been observed that the drop in the input voltage of the PES could cause unwanted dynamics (Banerjee et al., 1998). Occurrence of nonlinear phenomena like sub-harmonics and chaos in power electronic circuits has been reported (Wood et al. 1989, Deane et al. 1990, Hamill et al. 1995). In recent times it has been observed that some PES exhibit deterministic chaos, and it has been suspected that such phenomena may be responsible for the unusually high noise in some PES. It has been demonstrated that current-mode-controlled buck converter and boost converter are prone to sub-harmonic behavior and chaos (Deane et al. 1991, Deane et al. 1992, Tse et al. 1994). In this study, we have investigated the effect of the input voltage variation on the sub-harmonic behavior of the boost converter used in SOFC based system[15]. Bifurcation analysis can reveal three things: when and why does instability occur and post-instability dynamics. Advanced bifurcation algorithms can predict the global dynamics, which is important in analyzing the effectiveness of control design, effect of parametric variations, and disturbance-rejection capability of a PES. Incorporation of such advanced analytical methodologies and computation techniques will provide design loopholes even before building an expensive SOFC power system.

We chose the boost converter to perform the codimension-one bifurcation analysis, primarily because it is directly connected to the SOFC and any change in the SOFC dynamics is primarily going to affect its performance. The effect of the input voltage and load variation on the PES dynamics is investigated. Such an analysis gives an estimate of the "safe operating region" of the SOFC based system.

[15] SOFC based system for utility applications essentially comprises of a boost stage and a dc-ac converter as described in detail in Section 3.1.2. For the purpose of this analysis a harmonic load emulates the dc-ac converter. The load profile was obtained from comprehensive simulations in a manner similar to that described in 3.1.4.2.

3.2.2.2 Bifurcation analysis methodology

A nonlinear switching model of the boost converter is developed. The system is governed by two sets of linear differential equations pertaining to the *on* and *off* states of the controlled switch. The output voltage and the inductor current are the state variables. When the switch is *on*, the state variables are defined as

$$\frac{di_L}{dt} = \frac{\left(V_{in} - r_L i_L\right)}{L} \tag{66}$$

$$\frac{dv_C}{dt} = \frac{-v_C}{C\left(R + r_C\right)} \tag{67}$$

When the switch is off, the state variables are defined as

$$\frac{di_L}{dt} = \frac{1}{L}\left(V_{in} - i_L\left(r_L + \frac{Rr_C}{R + r_C}\right) - v_C \frac{R}{R + r_C}\right) \tag{68}$$

$$\frac{dv_C}{dt} = \frac{1}{C\left(R + r_C\right)}\left(Ri_L - v_C\right) \tag{69}$$

where i_L and v_C are the state variables of the boost converter and r_L and r_C are the parasitic resistances of the inductor and the capacitor. The feedback controller shown in Fig. 47 governs the switching between the two states.

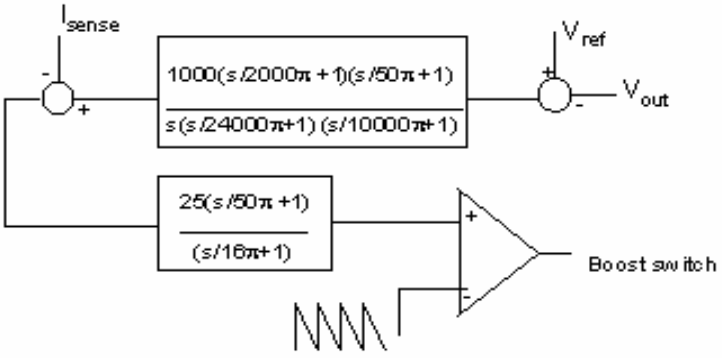

Fig. 47: Implemented control structure with transfer functions for the voltage and current loops of the boost converter.

To study the effect of input voltage variation on the converter performance, initially we perform a long-term simulation to obtain the steady-state operating condition of the converter. Next, we gradually vary the bifurcation parameter in order to obtain solutions to the state equations. The last several steady state solutions are noted and plotted to give the bifurcation diagram of the converter. Next we calculate the maximal Lyapunov exponents of the system in order to obtain an idea about the divergence of the nearby

trajectories. The Lyapunov exponents can be used to predict the dynamics of the system. A negative Lyapunov exponent implies a period-one solution, a value equal to zero indicates quasi-periodic solution, while a positive Lyapunov exponent implies chaotic solutions.

3.2.2.3 Bifurcation Results

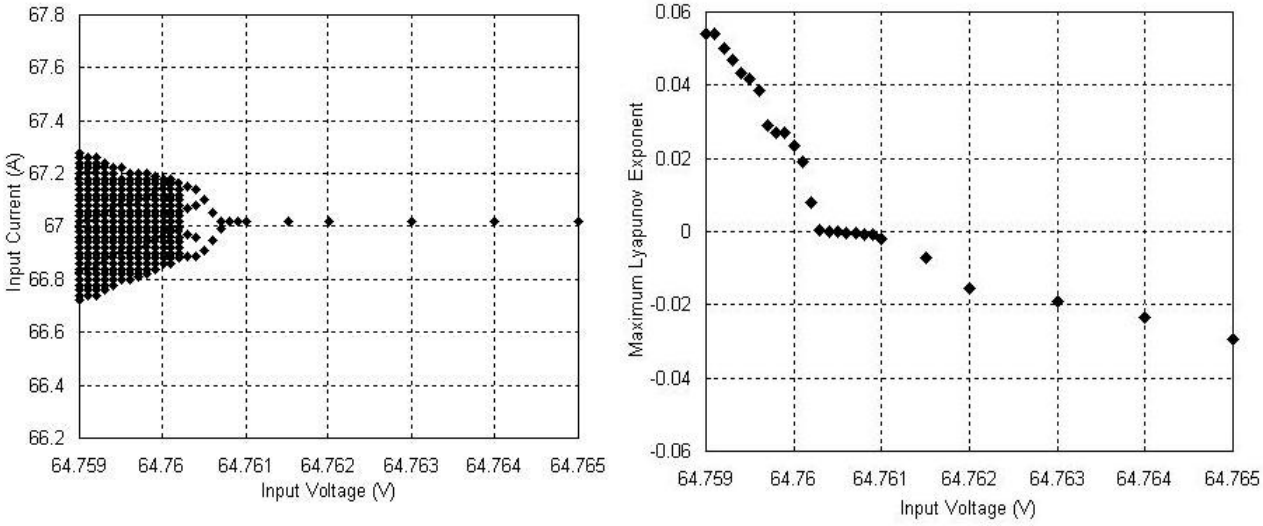

(a) (b)

Fig. 48: (a) Bifurcation diagram of boost converter with input voltage as bifurcation parameter (b) spectrum of maximal Lyapunov exponents.

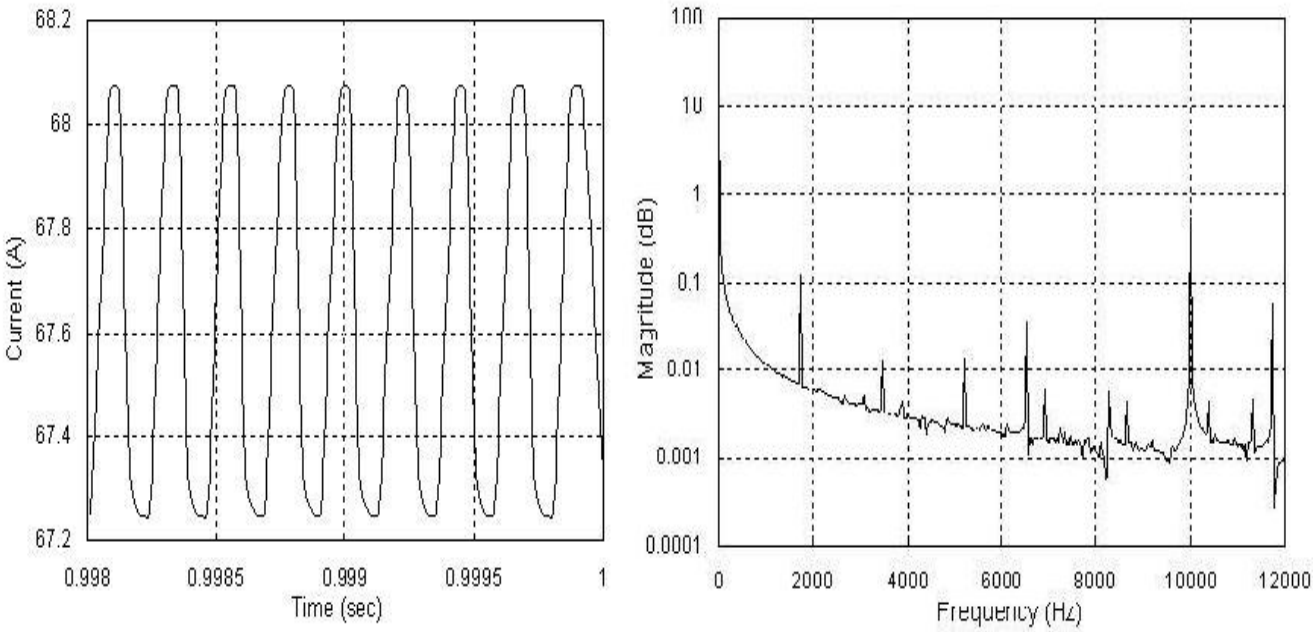

(a) (b)

Fig. 49: (a) Time domain input current waveforms and (b) corresponding frequency domain analysis for period-1 solution.

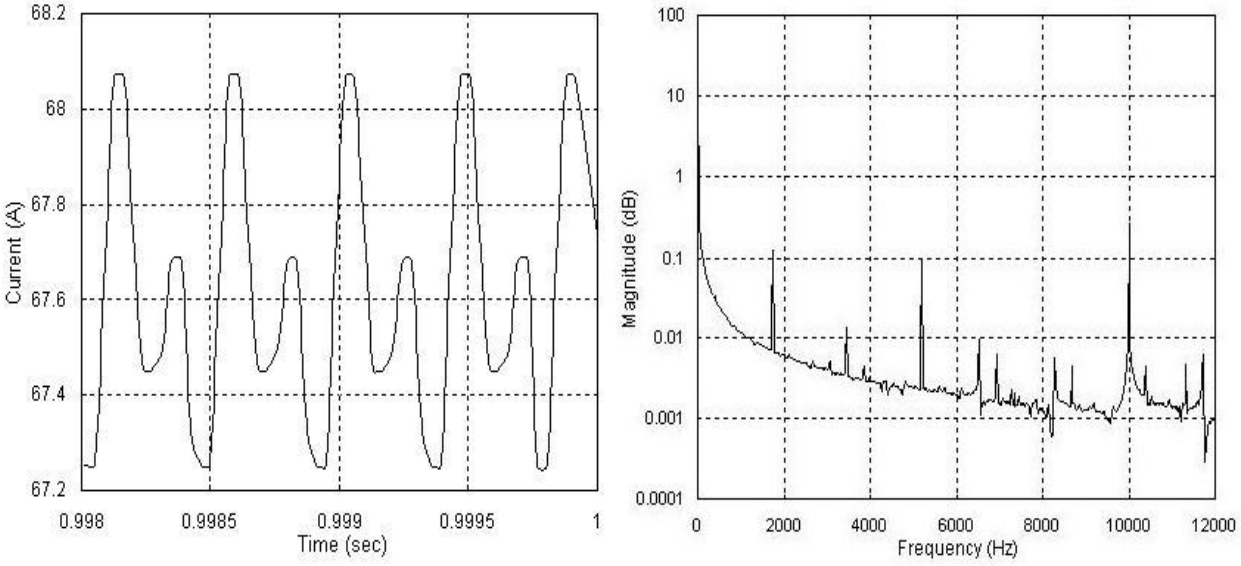

(a) (b)

Fig. 50: (a) Time domain input current waveforms and (b) corresponding frequency domain analysis for period-2 solution.

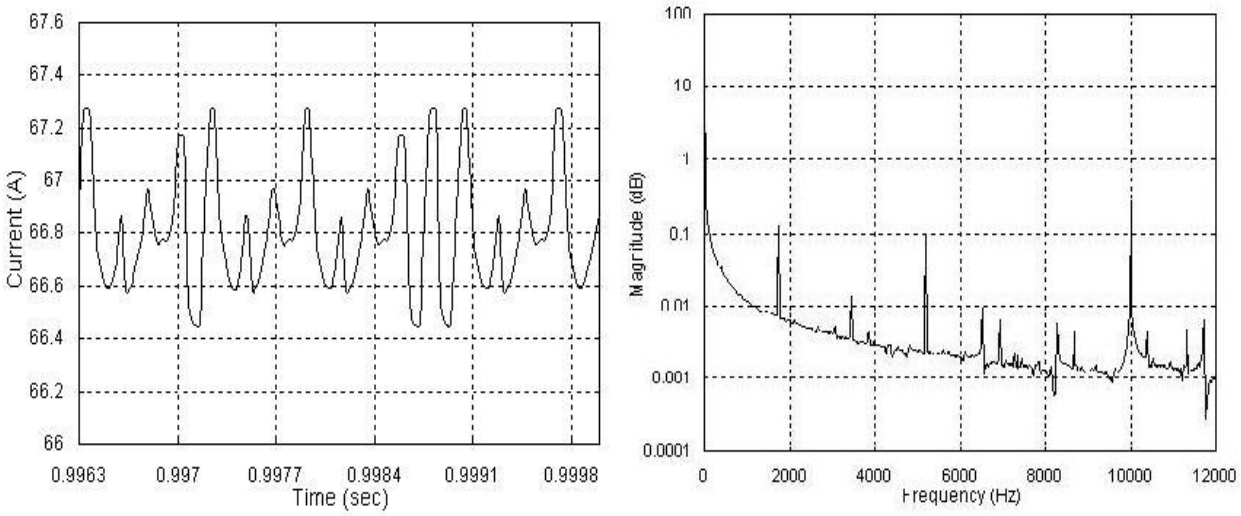

(a) (b)

Fig. 51: (a) Time domain input current waveforms and (b) corresponding frequency domain analysis for chaotic solution.

We obtain the bifurcation diagram with input voltage as the bifurcation parameter as shown in Fig. 48(a). The boost converter was seen to enter into the chaotic state as input voltage is varied from 72V to 63V. Fig. 48(b) shows the corresponding spectrum of the maximal Lyapunov exponents[16]. From Fig. 48, it can be seen that the first bifurcation takes place at 64.7605V where period-1 bifurcates to period-2. As V_{in} is reduced below 64.76 V, the system enters the chaotic region. Figs. 49 - 51 show the time domain and frequency domain plots for the period-1, period-2 and the chaotic regions. Since the PES for fuel cell applications is expected to be robust for all operating conditions, the bifurcation analysis shows that there is a necessity of operating the converter away from the boundaries marking different asymptotic behaviors. This study can be used to define the operating conditions of the fuel cell.

Similar bifurcation analysis was performed to see the effect of load resistance variation on the asymptotic behavior of the dc-dc converter. Figs. 52 shows the bifurcation results for load as the bifurcation parameter. It is clear from Fig. 52 that the first bifurcation occurs at a load resistance of 27.5 Ω, where the period-1 solution bifurcates to period-2. As load resistance is reduced below 37.76 Ω, the system enters the chaotic region.

[16] If two nearby trajectories on a chaotic attractor start off with a separation d_0 at time, $t = 0$, then the Lyapunov exponents of the system can be obtained from the expression

$$d(t) = d_0 e^{\lambda t}$$

where is the Lyapunov exponent of the system, and $d(t)$ is the separation of the solution with the steady state solution at time, t.

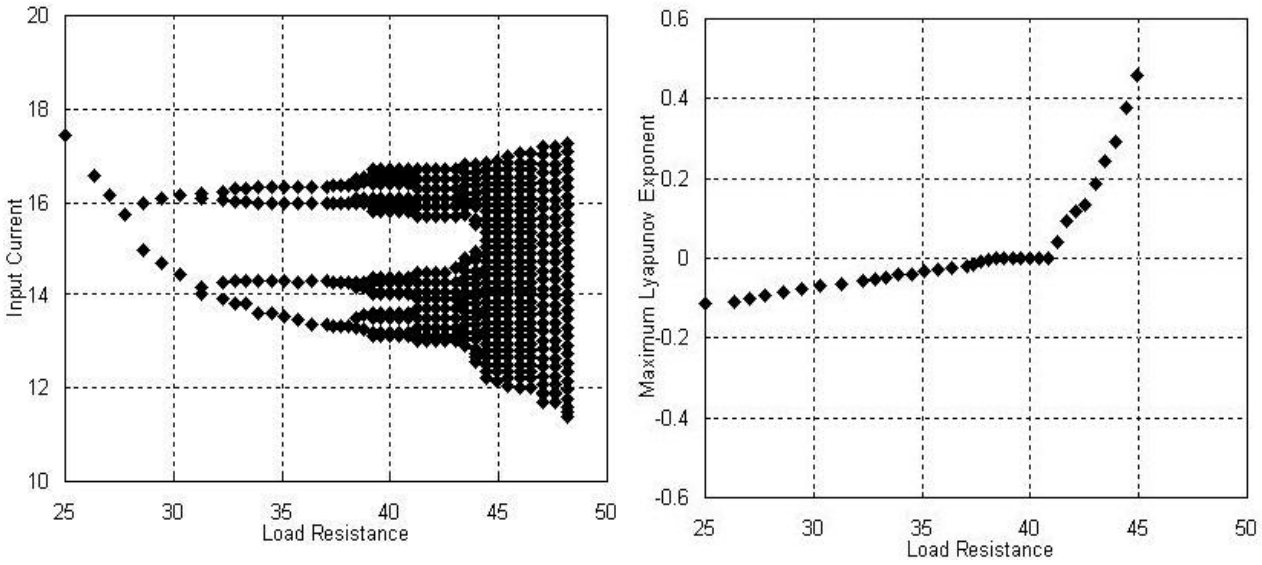

(a) (b)

Fig. 52: (a) Bifurcation diagram of boost converter with load variation as bifurcation parameter (b) spectrum of maximal Lyapunov exponents.

3.2.3 BOPS Results

In order to evaluate the performance of the selected SOFC power system configuration and develop robust control strategies, which minimize time response while optimizing fuel consumption, a set of Phase I parametric studies were performed (1. and 2. below) or are currently being performed (3. to 6.). The proposed parametric studies are:

1. Power demand perturbation: Large perturbations in power demand are modeled while keeping constant the system-level control parameters. The same perturbations are modeled for different combinations of the system-level parameters. The time response for the temperature and mass flow transients are computed for each component of the BOPS. The time response is defined as the time required for the component to reach steady state after a given perturbation. The system-level parameters being analyzed are the fuel utilization (FU), the steam to methane ration (SMR), and the fuel reformate ratio (FRR). Additional system level parameters will be studied. The results from this analysis allow the designer to understand how the system and its components behave at low, intermediate, and high levels of power demand for various combinations of these parameters. At this stage, the system thermal and energy efficiencies are monitored.
2. Power demand and system-level parameter perturbations: Perturbations in the system-level parameters are introduced at the same time as the perturbation in power demand. For instance, if the system is operating at steady state producing 1 kW with fixed values of FU, SMR and FRR. At some time (t), the power demand increases from 1 to 2 kW, while at the same time a perturbation in the SMR parameter is introduced (e.g., change of the SMR from 3.4 to 3.8). The time response is then computed. This kind of analysis gives insight into how the system-level parameters change with respect to each other when large, intermediate, and small perturbations in power demand take place at various power levels. This is done in order to understand how, for example, system efficiency and time response can be controlled. In the same manner, the best range of operating temperatures for each component can be selected.

3. Small changes in power demand with floating fuel utilization: Small perturbations in power demand are simulated while keeping constant the SMR, the FRR, and the fuel flow. For small increments, this means that the fuel utilization increases, while the opposite is true when small reductions in demand are simulated. The objective is to replicate the ripples produced by the switching of the PES and study how small-high-frequency perturbations affect the stack and the BOPS at different load levels for various values of the system-level parameters. For a given demand, the best BOPS operational condition may be defined.
4. Power demand perturbation with temperature control: The objective is to control the operational temperature, fixing them for the most important components (e.g., the steam-methane reformer, fuel cell stack, etc.) while large power demand perturbations are simulated. This means that the system-level parameters must be allowed to float within appropriate ranges. This study will lead toward more complex, although more effective control strategies.
5. Total system efficiency analysis: The total system efficiency is evaluated at both steady and transient states for different sets of systems-level control parameters.
6. Start-up and shut-down: System start-up and shut-down simulations are performed for different sets of system-level control parameters. The objective is to develop appropriate control strategies for these two critical operational points. Fuel consumption and time response are the parameters to be improved.

3.2.3.1 Power Demand Perturbation

In this section, results of the first parametric study are presented for the steam-methane reformer, compact heat exchanger IV, and the methane compressor. These three components are representative of the BOPS system. Results for all components are presented in Appendix C. Fig. 52 shows the thermal transient response of the steam-methane reformer. Large perturbations in power demand are modeled while keeping constant the SMR and the FRR. Three simulations are shown for three different values of FU. Fig. 53 shows how for increments in power from 1 kW up to 5 kW the time responses for all three values of FU are comparable. However, different levels of fuel utilization factor may affect the stack differently, and, thus, the designer should assess how running the system at these different levels for short periods or longer periods of time (between 10 and 23 secs) may affect, for example, stack lifetime or system efficiency. For incremental changes in power, the second best thermal time response happens for a FU factor of 0.7. This same fuel utilization factor provides the fastest thermal response for reductions in power demand. However, system operation at such low values of fuel utilization generates a decrease in system efficiency. In general a fuel utilization of 85% seems to yield the slowest thermal response. However, these conclusions must be prefaced with a caution since at this point it is unclear whether or not the differences depicted here are a result of the phenomena present or simply within the numerical uncertainties related to determining the onset of steady state. We should know which it is by the end of Phase I by looking at the uncertainties involved. What is for certain is that this figure depicts the relative time responses for different load changes for the BOPS pre-reformer under the conditions posed.

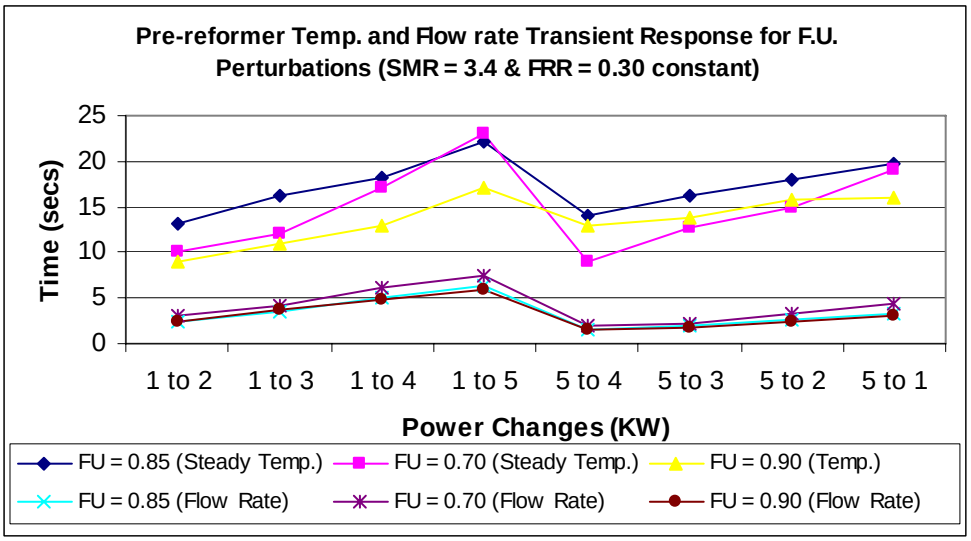

Fig. 53: Pre-reformer transient response for various values of fuel utilization (SMR = 3.4 and FRR = 0.3).

Fig. 54 shows the thermal transient response of the steam-methane reformer for different values of the SMR. Large perturbations in power demand are modeled while keeping constant the FU and the FRR. From this figure it appears that the time response is almost independent of the values of SMR. For reductions in load demand a similar conclusion is reached which potentially could greatly simplify any control strategy determined. For example, this insensitivity to the SMR may dictate how to control the water pump and the methane compressor for a given perturbation based on the initial operating point in force at the start of the perturbation.

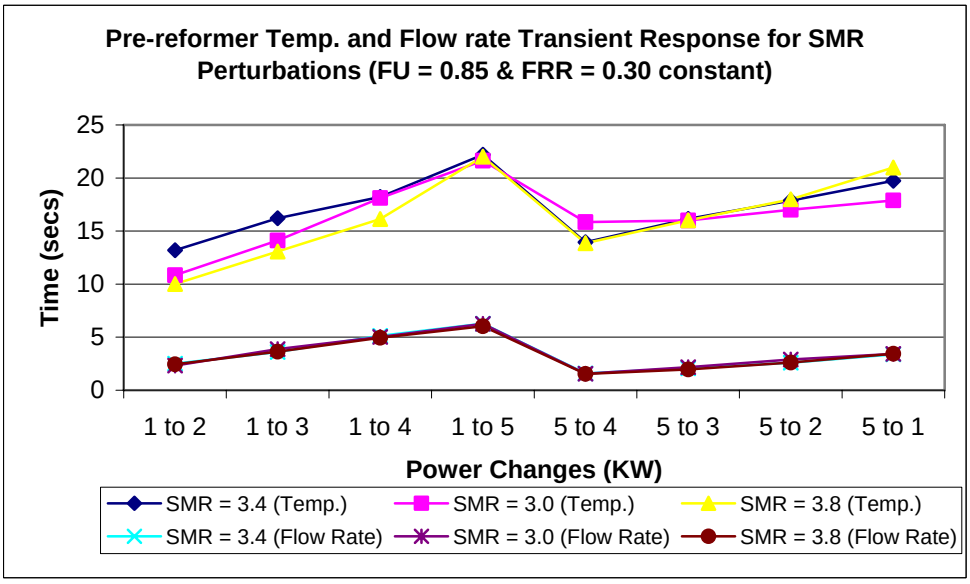

Fig. 54: Pre-reformer transient response for various values of SMR (FU =0.85 and FRR=0.3).

Fig. 55 shows the thermal transient response of the steam-methane reformer for different values of the FRR. Large perturbations in power demand are modeled while keeping constant the FU and the SMR.

Again, it appears that the time response is almost independent of the values of FRR. For reductions in load demand a similar conclusion is reached. On the other hand, a low FRR factor is positive in terms of efficiency, meaning that the thermal management system requires less energy input in order to generate the right system conditions. Of course, as expected, the bigger the power demand perturbation (up or down) is, the longer the time response, noting, of course, that the thermal response is significantly greater than the mechanical.

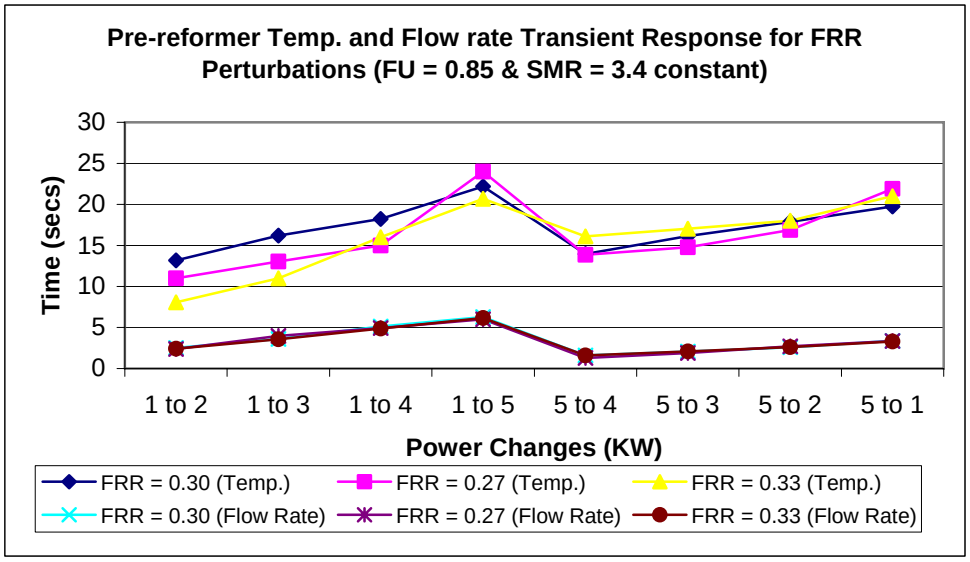

Fig. 55: Pre-reformer transient response for various values of FRR (FU =0.85 and SMR=3.8).

Now, compact heat exchanger IV is analyzed on the same basis as for the steam-methane reformer. This component is extremely important in terms of integration with the stack due to its location in the layout just prior to the final stage of conditioning of the fuel and the air before entering the SOFC stack. Figs. 53-55 show how in general the transient response of heat exchanger is shorter then that for the steam-methane reformer. This fact is also illustrated in Table XIV further down in this section which shows that the last component to reach steady state for almost all of the perturbations is the steam-methane reformer. A comparison between Figs. 56 and 57 shows how the slowest response for the compact heat exchanger IV is faster that the fastest response for the steam-methane reformer. This is not only true for the case in which the fuel utilization is modified but also for the cases in which the FRR and SMR are modified. Furthermore, Fig. 56 shows how for fixed values of the SMR and the FRR the shortest response occurs with a fuel utilization of 85% (with the proviso that an uncertainty analysis is still indicated).

Fig. 58 shows how for power perturbations that the fastest response occurs with a SMR of 3, which, however, is less beneficial in terms of system efficiency. In addition, as was the case for changes in FU, in general the slowest response for compact heat exchanger IV is faster than the slowest response of the steam-methane reformer. Therefore, it is not necessary to pay a penalty in efficiency by operating at low SMR. Furthermore, Fig. 59 is quite interesting; in that it shows how for large perturbations from low to high demand operating at low FRR increases considerably the thermal time response. Therefore, for FRR a compromise between system efficiency and time response may have to be considered.

Table XIV: Slowest components for parametric study #1

FU : Fuel Utilization; SMR : Steam to Methane Ratio; FRR : Fuel Reformate Ratio
The Table shows the system components (with their streams in green) contributing to the prolonged stability time (time given in blue), as regards to Stable Temperature, for changes in power requirements and changes in Fuel Utilization, Steam to Methane Ratio and Fuel Reformate Ratio.

S No.	Power Change	Components contributing to increased time for the stability of the system						
		FU 0.85 SMR 3.40 FRR 0.30	FU 0.70 SMR 3.40 FRR 0.30	FU 0.90 SMR 3.40 FRR 0.30	FU 0.85 SMR 3.00 FRR 0.30	FU 0.85 SMR 3.80 FRR 0.30	FU 0.85 SMR 3.40 FRR 0.27	FU 0.85 SMR 3.40 FRR 0.33
1	1000 W to 2000 W	Pre-reformer (5) (13.1880)	Pre-reformer (5) HXI (8) (10)	Pre-reformer (5) HXI (8) (8.997)	HXI (8) (10.9970)	Pre-reformer (5) HXI (8) (10.119)	HXI (8) (15.997)	Pre-reformer (5) (8.0620)
2	1000 W to 3000 W	Pre-reformer (5) (16.2010)	Pre-reformer (5) HXI (8) (12.033)	Pre-reformer (5) HXI (8) (10.997)	Pre-reformer (5) (14.1160)	Pre-reformer (5) (12.1990)	Pre-reformer (5) HXI (8) (18.869)	Pre-reformer (5) HXI (8) (11)
3	1000 W to 4000 W	Pre-reformer (5) (18.2160)	Pre-reformer (5) HXI (8) (17.023)	Pre-reformer (5) HXI (8) (12.997)	HXI (8) (18.116)	Pre-reformer (5) (21.1990)	Pre-reformer (5) (20.967)	Pre-reformer (5) HXI (8) (16)
4	1000 W to 5000 W	Pre-reformer (5) (22.2030)	Pre-reformer (5) (22.9970)	Pre-reformer (5) (16.9970)	Pre-reformer (5) HXI (8), Steam Generator (2) (21.64)	Pre-reformer (5) (20.003)	Pre-reformer (5) HXI (8) (24.692)	Pre-reformer (5) (20.6780)
5	5000 W to 4000 W	Pre-reformer (5) HXI (8), Steam Generator (2) (13.9530)	Pre-reformer (5) HXI (8) (8.9690)	Pre-reformer (5) HXI (8) (13)	Pre-reformer (5) HXI (8) (15.850)	Pre-reformer (5) HXI (8) (13.852)	Pre-reformer (5) HXI (8) (26.8570)	Pre-reformer (5) HXI (8) (16.091)
6	5000 W to 3000 W	Pre-reformer (5) HXI (8), Steam Generator (2) (16.1430)	Pre-reformer (5) HXI (8) (12.8060)	Pre-reformer (5) HXI (8) (13.844)	Pre-reformer (5) (16)	HXI (8) (15.077)	Pre-reformer (5) HXI (8), Steam Generator (2) (19)	Pre-reformer (5) HXI (8) (17.030)
7	5000 W to 2000 W	Pre-reformer (5) HXI (8), Steam Generator (2) (17.8760)	Pre-reformer (5) HXI (8) (15)	Pre-reformer (5) HXI (8) (15.8810)	Pre-reformer (5) HXI (8) (16.9970)	HXI (8) (19.006)	Steam Generator (2) (20.8810)	Pre-reformer (5) HXI (8) (18)
8	5000 W to 1000 W	Steam Generator (2) (22.8080)	Pre-reformer (5) HXI (8) (19)	Pre-reformer (5) (16.0920)	Steam Generator (2) (18.840)	Pre-reformer (5) (20.1010)	Steam Generator (2) (20.9020)	Pre-reformer (5) (21)

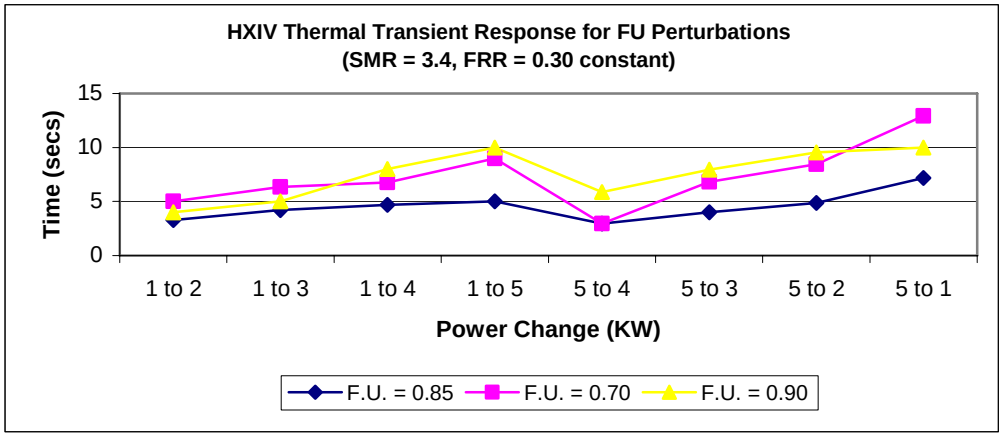

Fig. 56: Compact heat exchanger IV thermal transient response for various values of FU (FRR=0.3 and SMR=3.4).

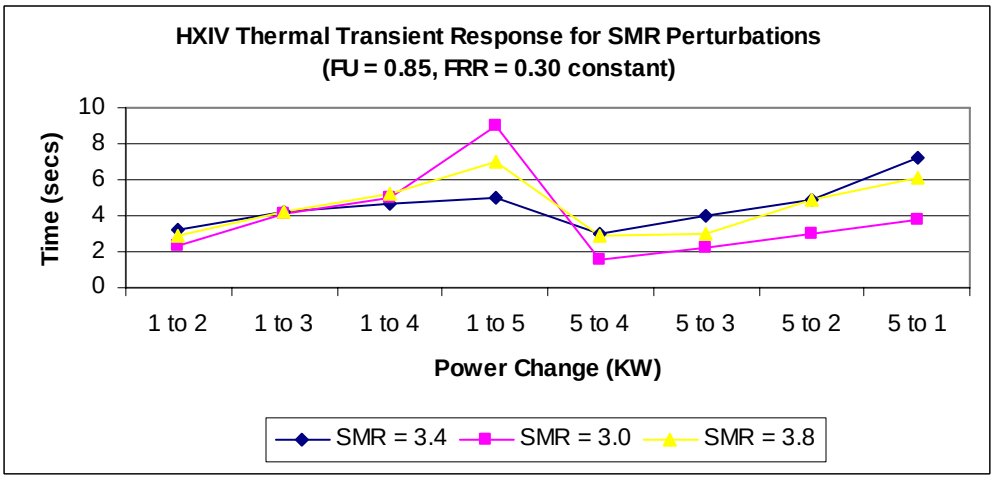

Fig. 57: Compact heat exchanger IV thermal transient response for various values of SMR (FRR=0.3 and FU=0.85).

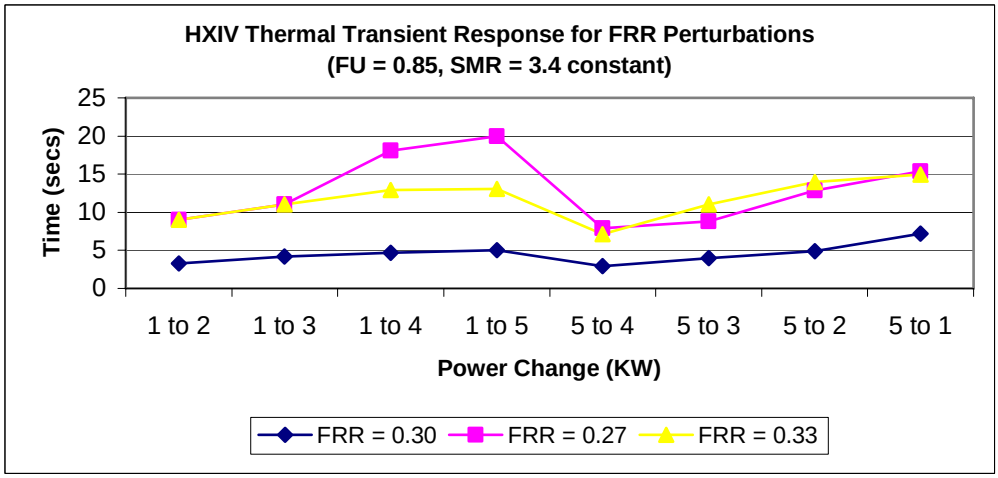

Fig. 58: Compact heat exchanger IV thermal transient response for various values of FRR (FU=0.85 and SMR=3.4).

Now the methane compressor is analyzed on the same basis as for the steam-methane reformer and the compact heat exchanger. This analysis illustrates typical behavior for the turbomachinery present in the SOFC system. Figs. 59-61 show the methane compressor thermal response to perturbation in power demand for various values of FU, SMR, and FRR. In general the thermal response has the same shape. Hence, the larger the perturbation the longer the response for both increments and reductions in load demand. Additionally, notice that different from what happens in the steam-methane reformer, for perturbations of the same magnitude at low power demand level the time response is longer than the response at high power demand. In particular, Fig. 62 shows how the fastest response results from operating with a FU factor of 0.9. However, as mentioned before such a high FU may affect the stack. On the other hand, the response with a FU factor of 0.85 shows almost identical behavior. The most important result from Figs. 60 and 61 is the fact that changes in steam methane ratio and fuel reformate ratio do no affect the transient response of the component (methane compressor). Thus, one can see how the curves almost overlap each other perfectly. This lack of sensitivity for the methane compressor due to changes in the system-level parameters may be due to several reasons. First, there is only one stream coming in and out of the compressor which my affect the component. Secondly, the size (mass) of the component is relatively small when compared to those of the air compressor, expander or steam-methane reformer. Finally, the location of the component in the system configuration may also be a reason since it takes fuel from a tank whose conditions (temperature and pressure) are assumed constants.

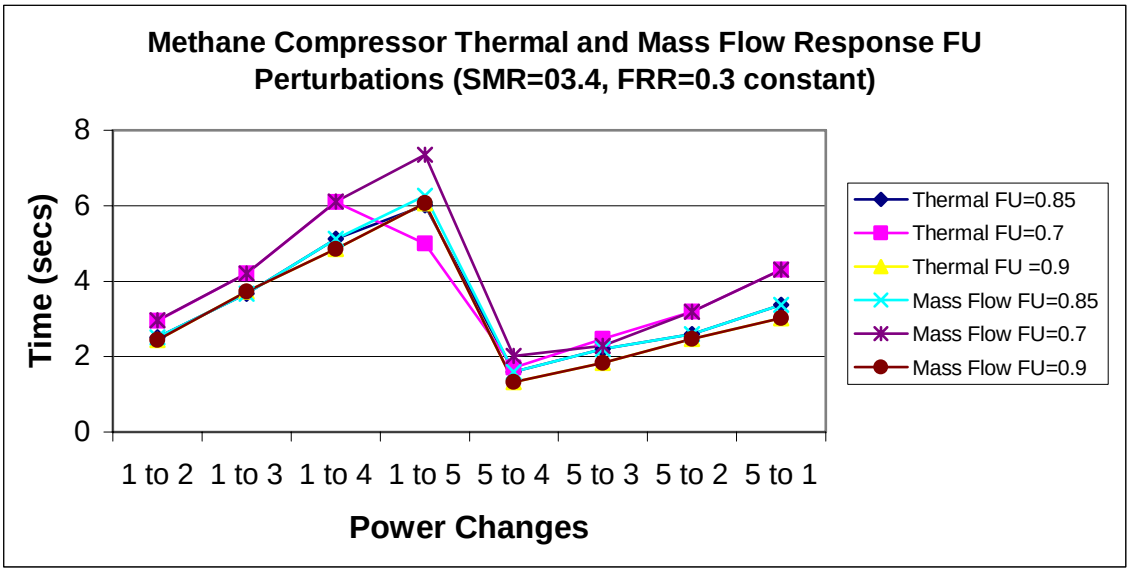

Fig. 59: Methane compressor thermal transient response for various values of FU (FRR=0.3 and SMR=3.4).

As shown above, the time response for compact heat exchanger IV and the methane compressor is much shorter than that for the steam-methane reactor. Further analysis shows that the determinant factors are the size of the perturbation, the characteristics and initial condition of the streams involved (heat capacity, temperature and mass flow), initial conditions of the component (metal temperature), and the mass and geometry of the component. The steam-methane reformer is, in fact, the component with the largest mass and its geometry (flow path) is complex. There are two streams coming in and out, the combustion gases and the steam-methane mixture. Before approaching the reformer, both streams go through other transient processes, i.e. the heat transfer process in heat exchanger III, the steam generator

and the combustion process. Inside the reactor there are several processes taking place: chemical reactions, heat transfer from the catalyst to the reformate gas, heat transfer from the combustion gases to the wall, and heat transfer from the wall to the reformate gas.

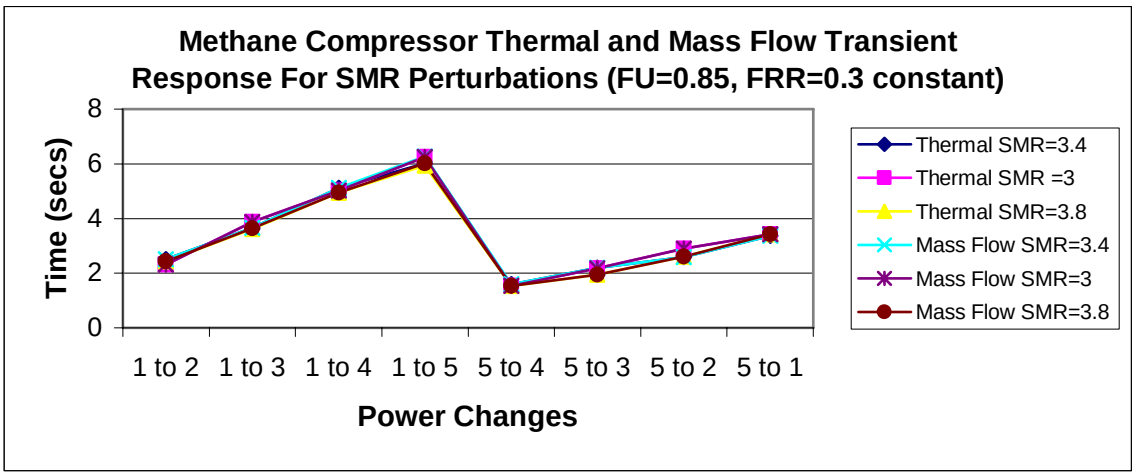

Fig. 60: Methane compressor thermal transient response for various values of SMR (FRR=0.3 and FU=0.85).

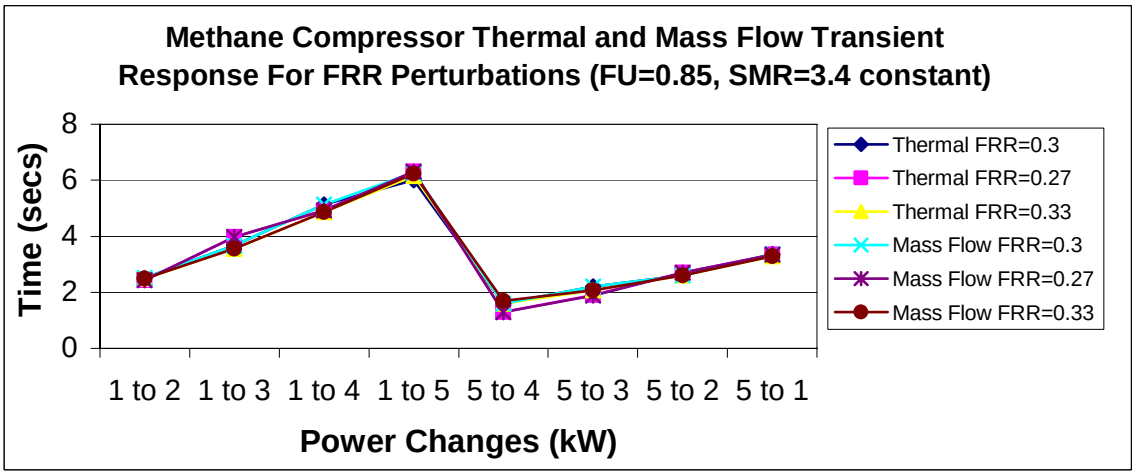

Fig. 61: Methane compressor thermal transient response for various values of FRR (FU=0.85 and SMR=3.4).

3.2.3.2 Power Demand and System-level Parameter Perturbations

In this section results of the second parametric study are presented for the steam-methane reformer. Results for the other system components are shown in Appendix C2. Perturbations in system-level parameters are introduced at the same time as perturbations in power demand. For instance, the system is operating at steady state producing 1 kWe with fixed values of FU, SMR and FRR. At some time (t) the power demand increases from 1 to 2 kWe, while at the same time a perturbation in the FU parameter is introduced (e.g., change of FU from 0.85 to 0.9). The time response is then computed. Analysis of Figs. 62 and 63 is very similar to the previous analysis of Figs. 63 to 65 For instance, Fig. 61 shows the thermal transient response of the steam-methane reformer. Large perturbations in power demand and perturbation in fuel utilization are modeled while keeping constant the SMR and FRR. Again, the question of uncertainty in the determination of the point at which steady state is reached must be resolved before conclusions as presented with the previous figures can be proven or disproved. This awaits the end of Phase I.

The most remarkable conclusion from this parametric study results from comparing Figs. 62 and 63 with Figs. 53 to 55, respectively. It can be observed how the transient thermal responses are almost identical for each case. This seems to imply that the time response is independent of the system-level parameter conditions before the power demand occurs. Instead, it is a function of the system-level parameters conditions through the transient. This fact makes necessary the design of a new parametric study. For instance, an analysis is needed on what the time response is when the system-level parameters are changed not only at the beginning of the power demand perturbation (i.e. in a step-change) but also throughout the entire transient (i.e. as a gradual change). This in fact is the first approach to optimal control and synthesis/design. This new parametric study will be performed in the next couple of months and will be presented subsequently.

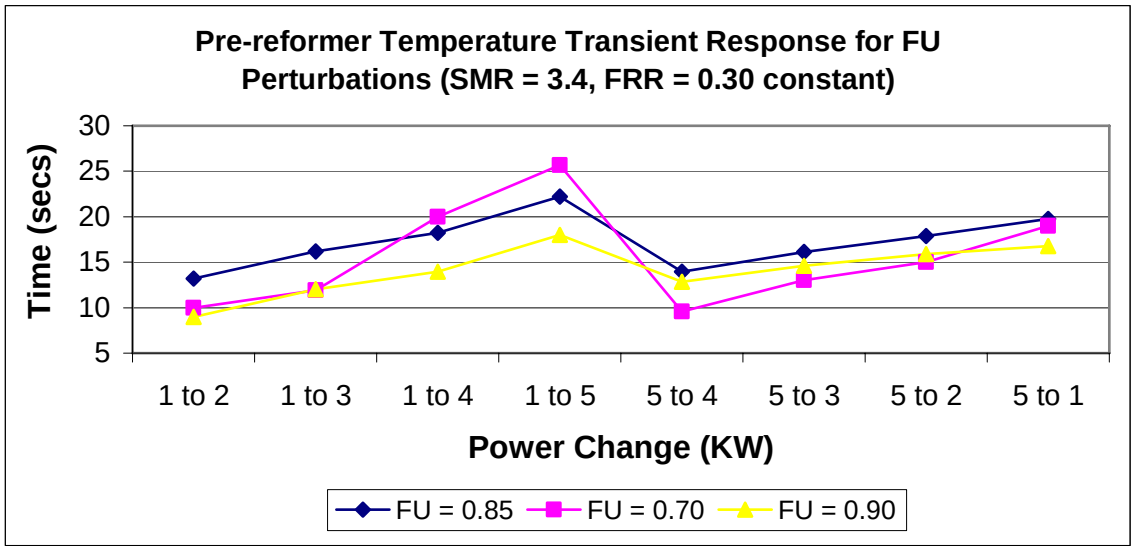

Fig. 62: Steam-methane reactor thermal transient response for power and FU perturbations (FRR = 0.3 and SMR = 3.4).

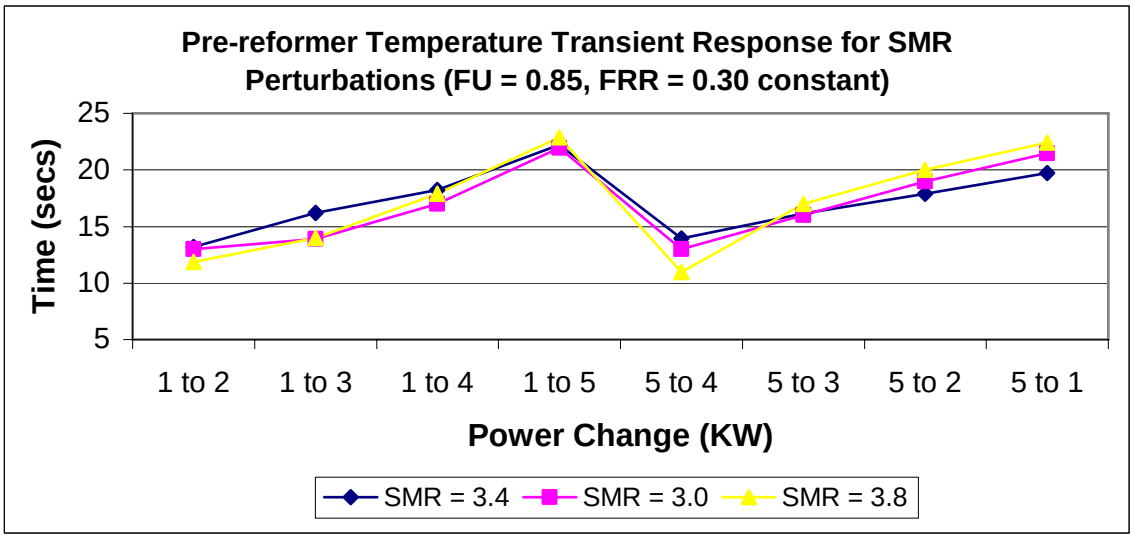

Fig. 63: Methane reactor thermal transient response for power and SMR perturbations FRR=0.3 and FU=0.85).

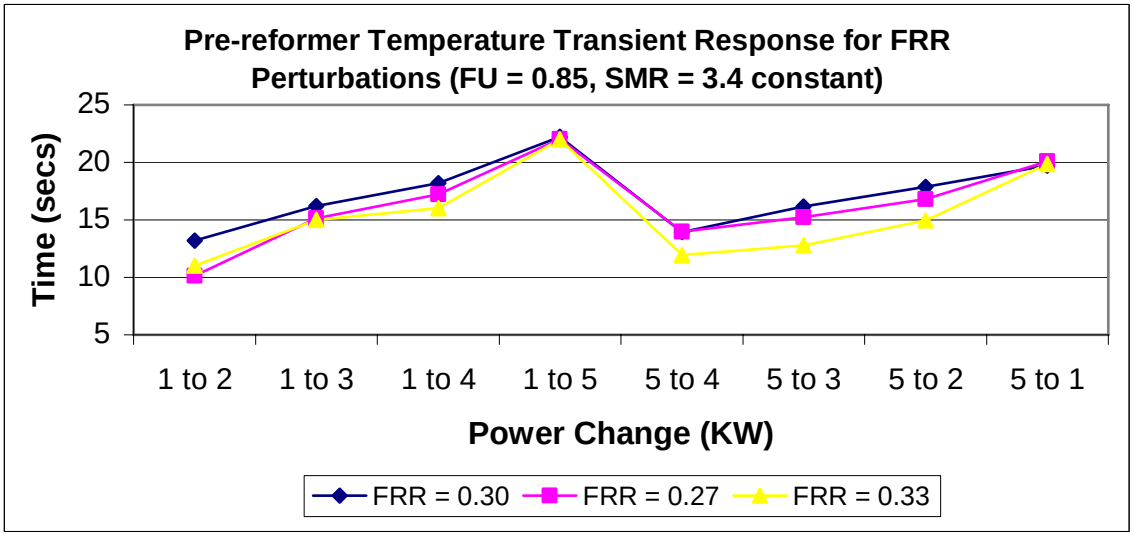

Fig. 64: Methane reactor thermal transient response for power and FRR perturbations (FU=0.85 and SMR=3.4).

3.2.3.3 Small Changes in Power Demand with Flowting Fuel Utilization

For this third parametric study, the value of the system-level fuel utilization (FU) parameter is allowed to vary for small load variations in the load (e.g., to simulate load variations due to such things as current/voltage ripples) while holding the total flow rate of hydrogen entering the SOFC stack subsystem constant. Other system-level parameters such as the steam to methane ratio (SMR), fuel reformate ratio (FRR), and air to fuel ratio (AFR) are held constant at 3.4, 0.3, and 20, respectively. Net power values are increased and decreased in steps of 100 watts from some initial net power (IP) or load (i.e. from IPs of 1000 W to 5000 W in increments of 1000W). The values of the hydrogen flow rates corresponding to the IPs are shown in Table XV. These values are the total hydrogen flow rate values required by the SOFC stack to produce its corresponding IP. In addition, the value of fuel utilization is initially set at 0.85 but then allowed to vary in order to meet the new load imposed on the stack. Of interest here are both the maximum and minimum power levels that a fixed hydrogen flow rate can sustain as well as system efficiency and the thermal and flow transient response times of the components of the SOFC based APU.

Table XV: Fixed H_2 molar flow rates used.

IP	H_2 molar flow rate
1000 W	1.00030e-005 kmol/sec
2000 W	1.77030e-005 kmol/sec
3000 W	2.46790e-005 kmol/sec
4000 W	3.10605e-005 kmol/sec
5000 W	3.67564e-005 kmol/sec

An analysis of the results for this third parametric study leads to some general conclusions about the behavior of the system both in terms of fuel utilization, system efficiency, and transient response. They are as follow (more results are given in Appendix C3):

- Fuel utilization follows increases and decreases in load up or down, respectively.
- For lower values of IP, the change in the fuel utilization is greater, i.e. at an IP of 1000 W it is greater than at 5000 W.
- The maximum fuel utilization observed is 0.94 at an IP of 5000 W while the minimum fuel utilization observed is 0.78 at an IP of 1000 W.
- A maximum thermal efficiency value of 50% (energy efficiency of 49%) was observed for a maximum load of 5700 W achieved starting from an initial net power of 5000 W. Also the maximum value of fuel utilization (0.94) was obtained at this load. A minimum thermal efficiency value of 24% (energy efficiency of 23%) was observed for a minimum load of 900 W that was achieved starting from an initial net power of 1000 W.
- Of all the components analyzed, Heat Exchanger II (streams 9); Heat Exchanger III (streams 1) and Heat Exchanger IV (streams 12) showed no thermal transients due to the small load variations from the IP level applied in this parametric study. This was because.the flow of hydrogen did not affect these components.
- The thermal transient for outlet air and combustion gas streams (streams 27, 13, 18) increases steadily with decreasing IP (except between IPs of 2000 W and 3000 W). This can, for example, be seen in Fig. 65 for stream 27 (air compressor). Figures 66 to 68 show that for a given IP, the thermal response times for streams 5 (pre-reformer), 2 (steam generator), and 8 (heat exchanger I) do not change with small perturbations in load. This is also true for streams 6, 16, 22, 19 and 26.

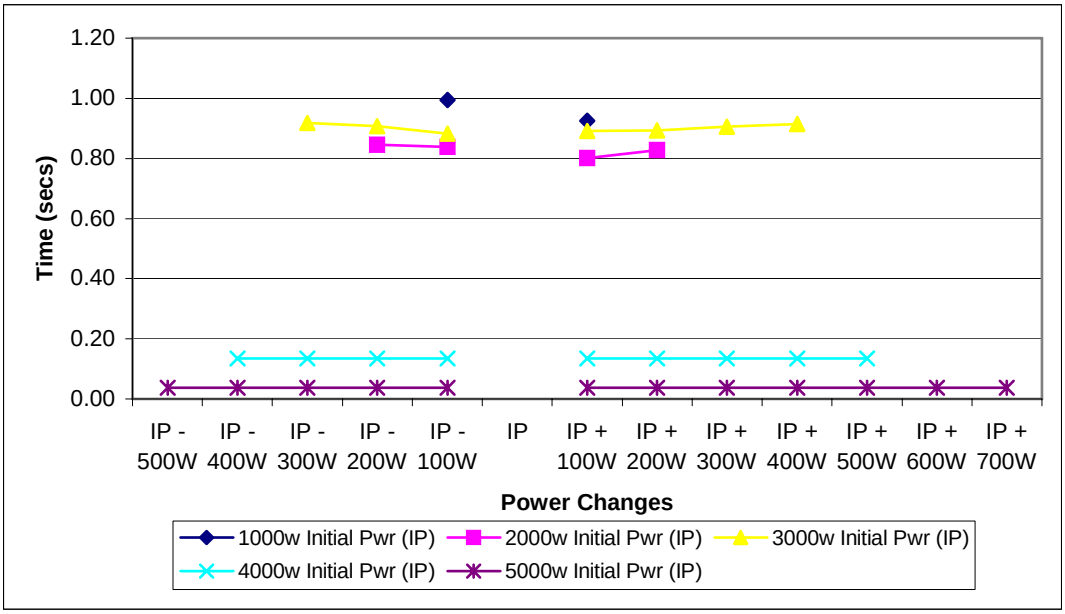

Fig. 65: Air compressor thermal transient response for small power changes holding the flow rate of H2 constant at a value corresponding to the initial load condition (IP) for the system (stream 27).

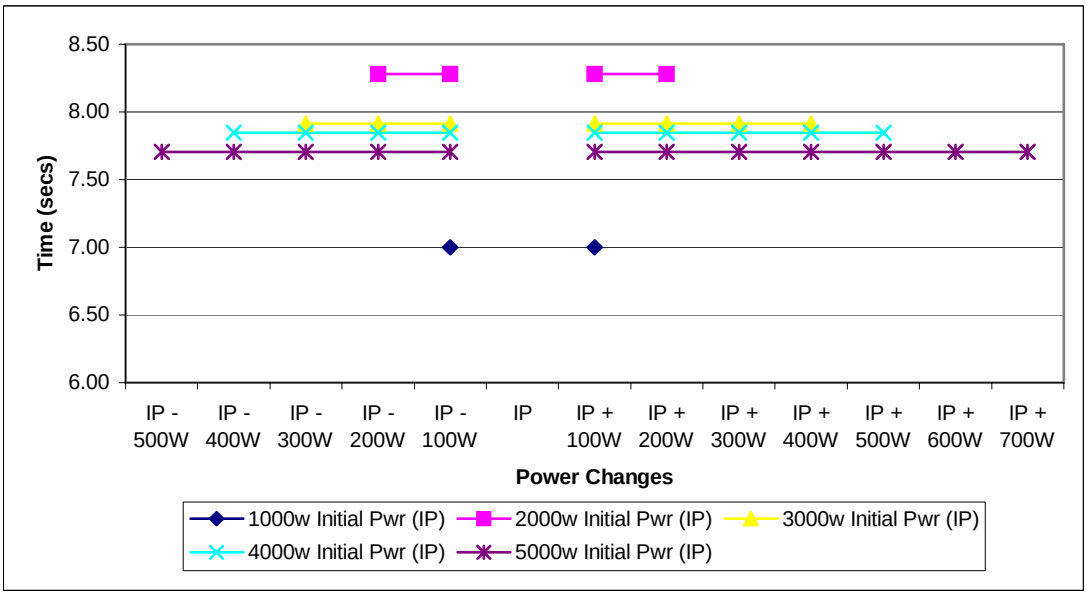

Fig. 66: Pre-reformer thermal transient response for small power changes holding the flow rate of H2 constant at a value corresponding to the initial load condition (IP) for the system (stream 5).

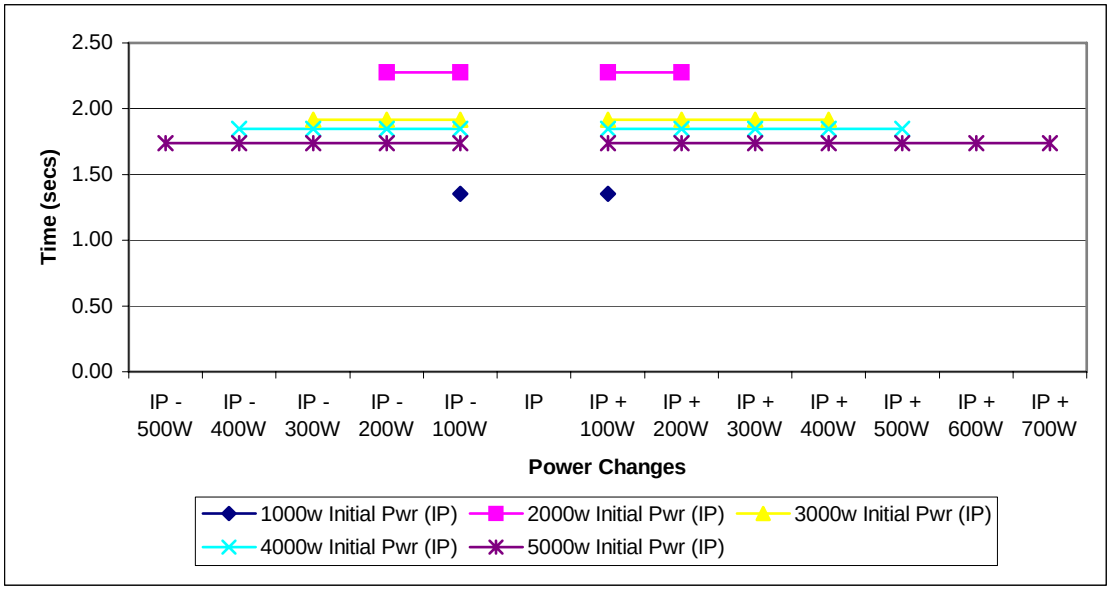

Fig. 67: Steam generator thermal transient response for small power changes holding the flow rate of H2 constant at a value corresponding to the initial load condition (IP) for the system (stream 2).

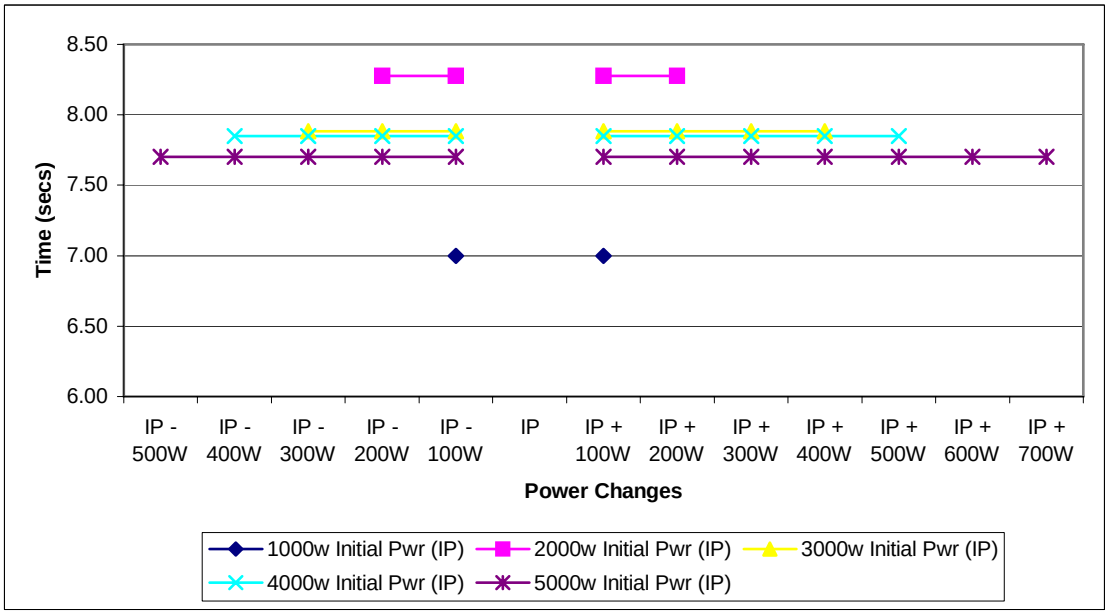

Fig. 68: Heat exchanger I thermal transient response for small power changes holding the flow rate of H2 constant at a value corresponding to the initial load condition (IP) for the system (stream 8).

- Of all the components, the pre-reformer (stream 5) is the one that takes the longest time to come to steady state while the turbo-machinery subsystem components require the least amount of time and significantly so.
- The turbo-machinery components (the air compressor and gas expander) and stream 26 of heat exchanger IV show changes in their flow rates due to small load perturbations (for example, see Fig. 69) while the air-combustion gas mixer and heat exchangers II and IV (stream 12 only) display no such changes (see Figs. 70 and 71).

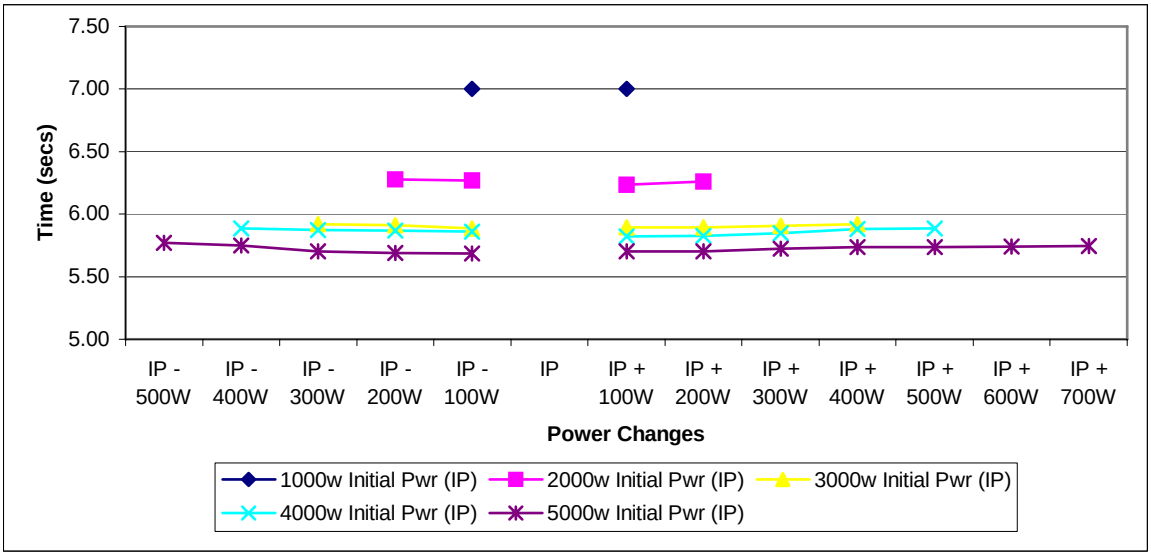

Fig. 69: Gas expander flow rate transient response for small power changes holding the flow rate of H2 constant at a value corresponding to the initial load condition (IP) for the system (stream 13).

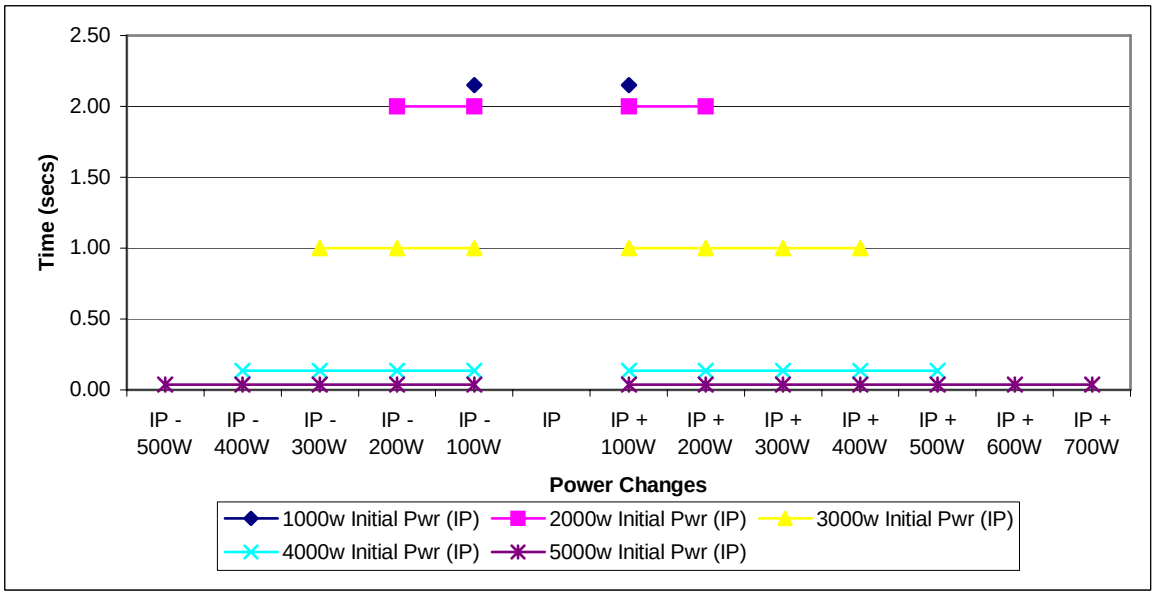

Fig. 70: Heat exchanger II flow rate transient response for small power changes holding the flow rate of H2 constant at a value corresponding to the initial load condition (IP) for the system (stream 9).

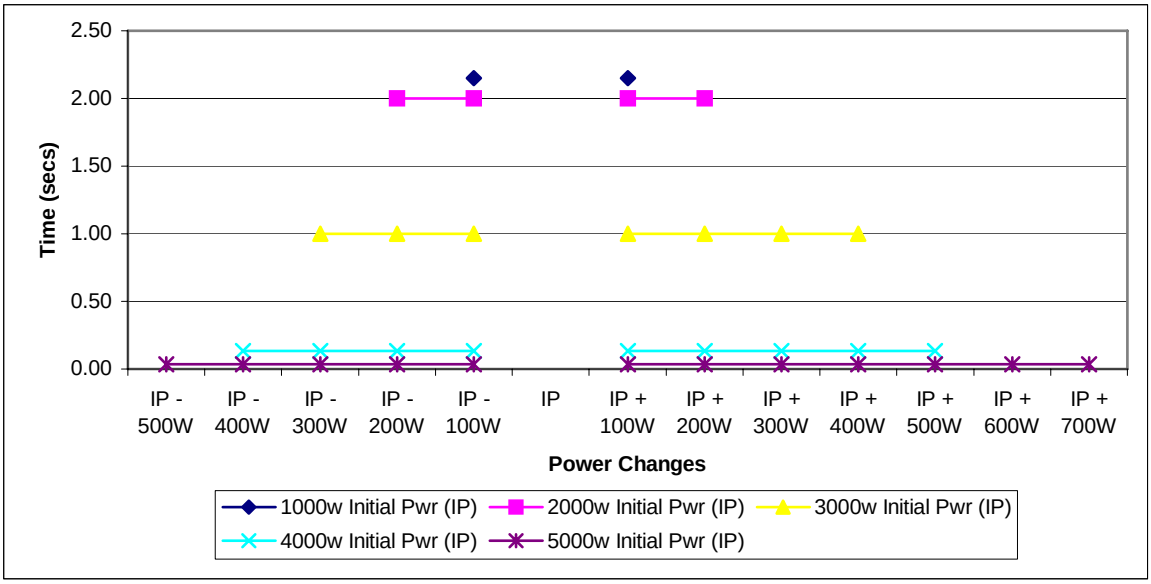

Fig. 71: Heat exchanger IV flow rate transient response for small power changes holding the flow rate of H_2 constant at a value corresponding to the initial load condition (IP) for the system (stream 12).

- The flow rate transient response times for streams and components exhibiting them are larger for small values of IP.
- The gas expander (stream 13) and stream 26 of heat exchanger IV have the longest flow rate transient response times.

1. The maximum and minimum values of power that can be obtained for each IP are shown in Table XVI.

Table XVI: Maximum and minimum power levels attainable for a fixed H2 flow rate beginning at a given IP.

IP	Maximum Power	Minimum Power
1000 W	5700 W	4500 W
2000 W	4500 W	3600 W
3000 W	3400 W	2700 W
4000 W	2200 W	1800 W
5000 W	1100 W	900 W

2. For perturbation increases in IP, the value of fuel utilization is greater for higher IP values than for lower ones while this trend reverses when the perturbations are decreasing (see Fig. 72). Further more, as seen from Fig. 72, the value of fuel utilization that can be obtained at the maximum and minimum loads associated with an IP of 1000 W (see Table XVI) and a constant H_2 flow rate are 0.9104 and 0.7877, respectively. Those at the maximum and minimum loads associated with an IP of 5000 W (see Table XV) are 0.9387 and 0.7849, respectively.

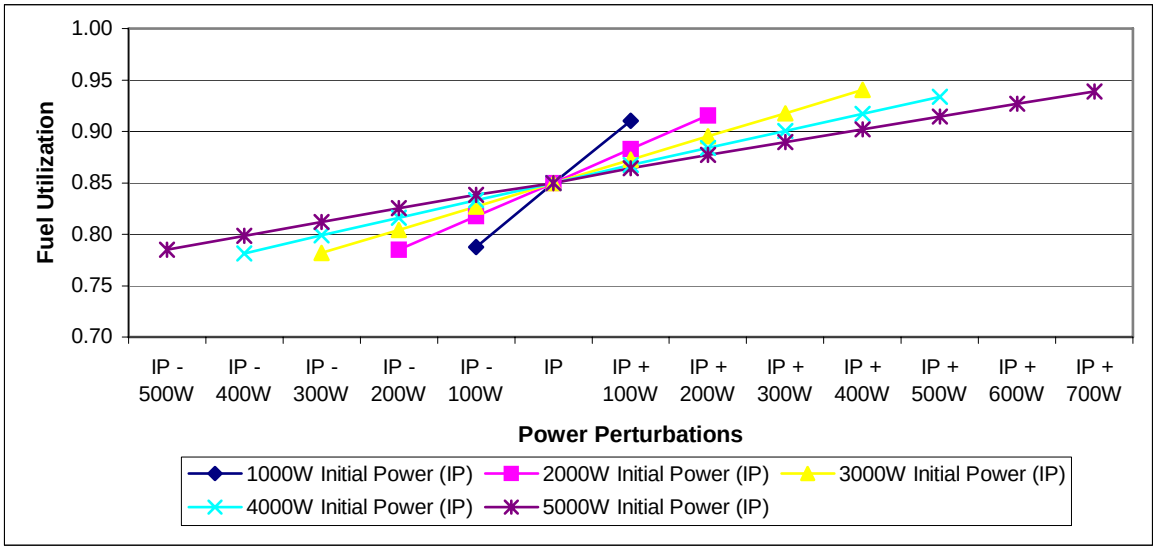

Fig. 72: Variations in fuel utilization for small power changes holding the flow rate of H2 constant at a value corresponding to the initial load condition (IP) for the system.

3. Power perturbations for the highest IP exhibit the highest system thermal andenergy efficiency values (see Figs. 73 and 74). Note that the downward trend of these curves is consistent with the synthesis/design point (5 kW) chosen for the SOFC based APU modeled during Phase I. Phase two will explore whether or not that or some other synthesis/design point (e.g., at a lower power rating) would indeed be a better choice.

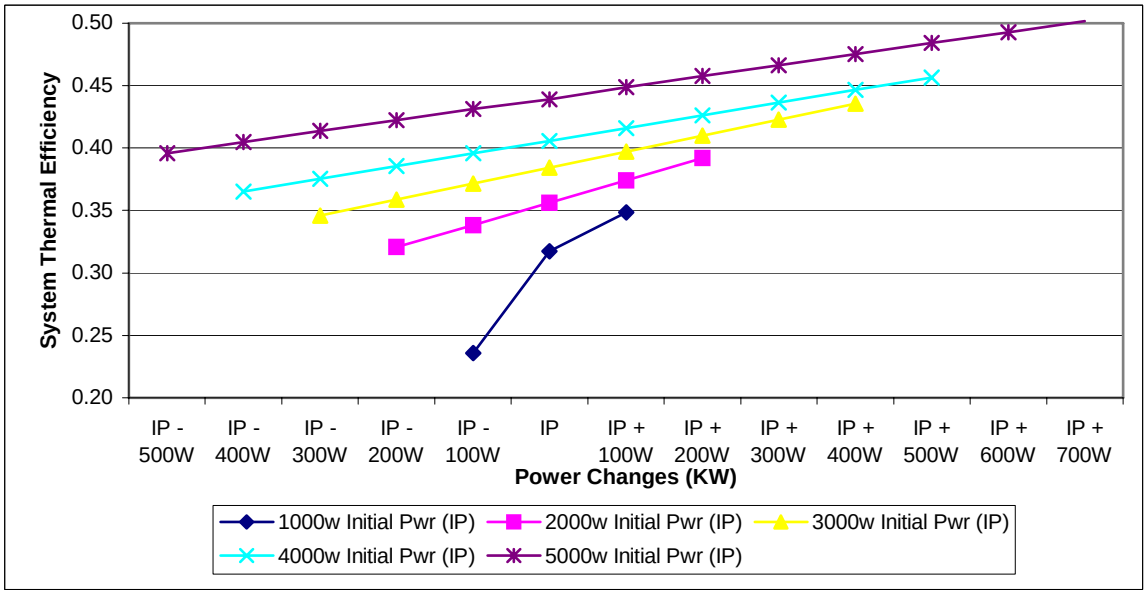

Fig. 73: System thermal efficiencies for small power changes holding the flow rate of H_2 constant at a value corresponding to the initial load condition (IP) for the system.

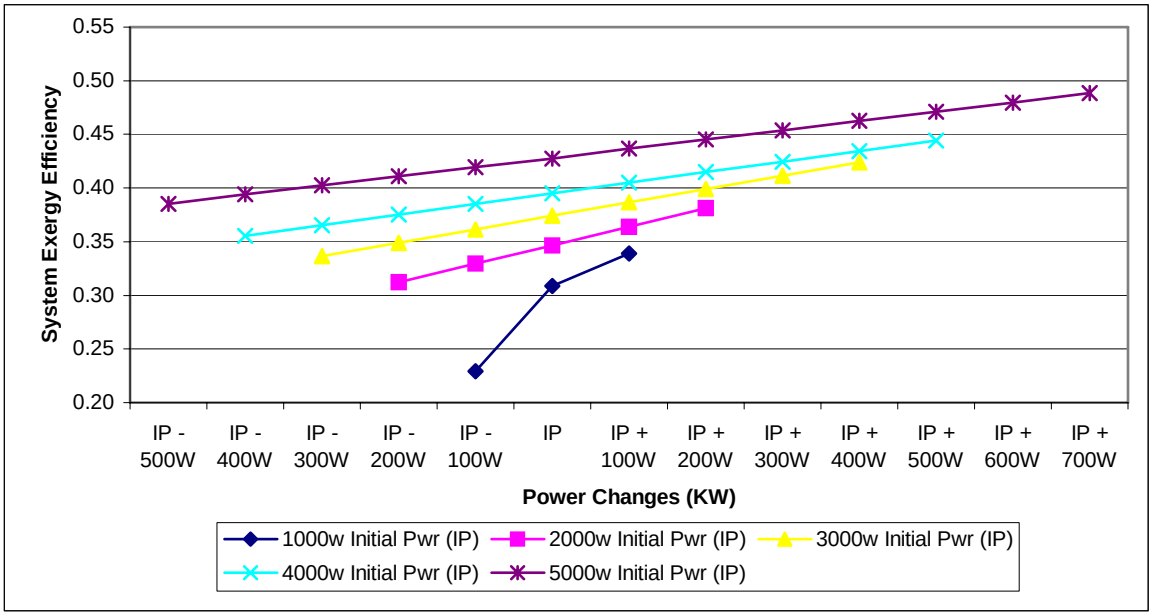

Fig. 74: System energy efficiencies for small power changes holding the flow rate of H_2 constant at a value corresponding to the initial load condition (IP) for the system.

3.2.3.4 Power Demand Perturbation with Temperature Control

This fourth parametric study is primarily focused on the pre-reformer component since the previous three studies had shown the pre-reformer to be the component with the longest transient response times. Thus, the effects of pre-reformer temperature and molar flow rate control on transient responses and system thermal andenergy efficiencies were studied and are presented here.

The Pre-reformer component has four mass streams: an inlet steam-methane stream (3), an outlet steam-methane stream (5), an inlet combustion gas stream (4) and an outlet combustion gas stream (6). The inlet combustion gas stream is used to heat up the inlet steam-methane stream entering the pre-reformer. The outlet combustion gas stream is in turn used to pre-heat the inlet methane stream of heat exchanger III, generate steam in the steam generator and preheat the air in heat exchanger IV. The effects of temperature and molar flow rate control are then analyzed in the following sequence of studies:

a. Study 4a: Inlet combustion gas stream temperature (T_4) control.
b. Study 4b: Inlet steam-methane temperature (T_3) control.
c. Study 4c: Control of the inlet water temperature to the steam generator.
d. Study 4d: Control of the molar flow rate of the steam generator inlet combustion gas stream.

Study 4a: In this study, the inlet combustion gas stream temperature T_4 is varied for increases and decreases in load ranging from 1 kW to 4 kW. Values of T_4 considered are 1120 ^oK, 1150 ^oK, 1200 ^oK, 1300 ^oK, 1400 ^oK, 1500 ^oK, 1550 ^oK, and 1570 ^oK. The thermal transient responses of streams 3, 5 and 6 were then observed with the objective of determining the inlet combustion gas temperature (T_4) which minimizes the transient response time of the pre-reformer. Figure 75 shows the thermal response time of pre-reformer stream 5 for power decreases while Fig. 76 shows it for power increases. Appendix C4 provides figures showing variations in response times for streams 3 and 6.

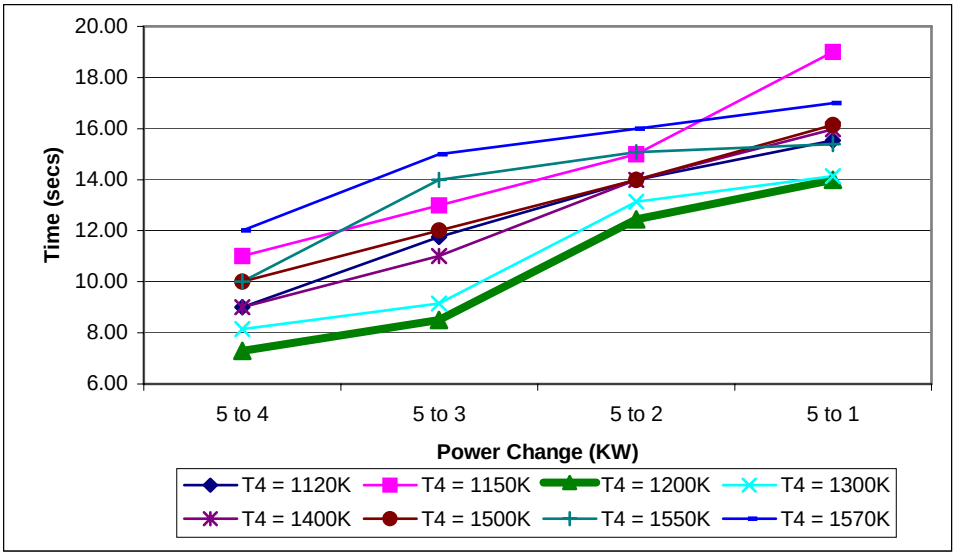

Fig. 75: Thermal transient response times of pre-reformer stream 5 (outlet steam-methane stream) for decreases in load and a range of values for T4 (inlet gas stream temperature).

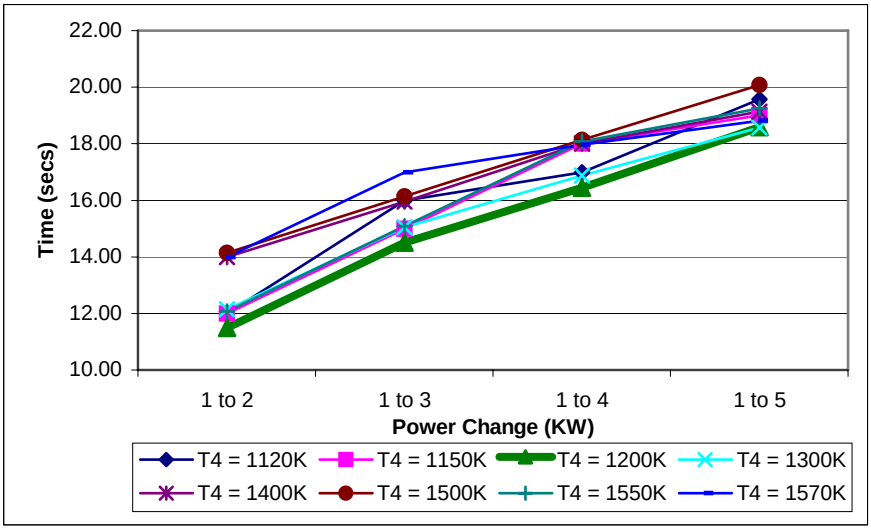

Fig. 76: Thermal transient response times of pre-reformer stream 5 (outlet steam-methane stream) for increases in load and a range of values for T4 (inlet gas stream temperature).

Clearly from these two figures, the value of T_4 which minimizes the thermal transient response of the pre-reformer is 1200K. Both for power increases and decreases, the outlet steam-methane stream (5) temperature shows increased thermal response times for values of T_4 different from T_4 = 1200 ^{o}K.

System thermal and energy efficiencies as a function of load and temperature T4 are given in Figs. 77 and 78 and in Appendix C4. The trends are similar for both power increases and decreases. The lower T_4 is, the higher the efficiency. Once again note, however, that the downward trend of these curves is consistent with the synthesis/design point (5 kW) chosen for the SOFC based APU modeled during Phase I. Phase two will explore whether or not that or some other synthesis/design point (e.g., at a lower power rating) would indeed be a better choice.

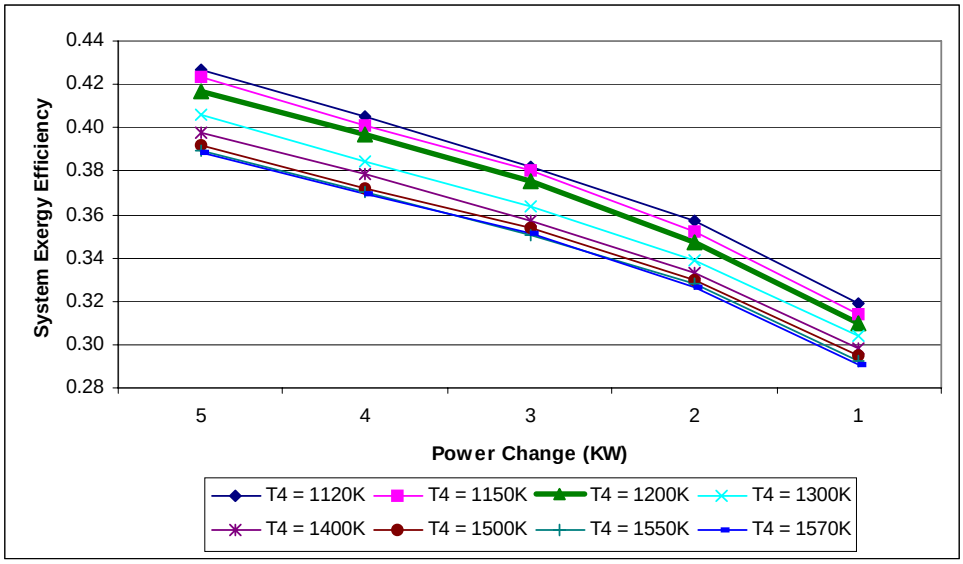

Fig. 77: System energy efficiency as a function of load and pre-reformer inlet gas temperature T4.

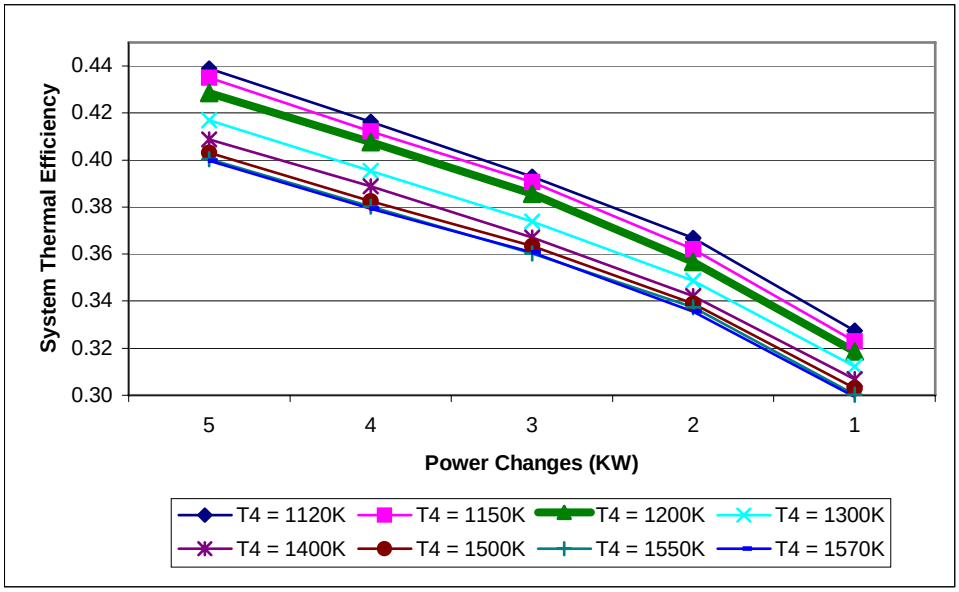

Fig. 78: System thermal efficiency as a function of load and pre-reformer inlet gas temperature T4.

Study 4b: In this study, the inlet steam-methane stream temperature T_3 is varied for increases and decreases in load ranging from 1 kW to 4 kW. Keeping T_4 constant at 1200 ^{0}K, values of T_3 are either fixed at 800 ^{0}K or 870 ^{0}K or allowed to vary as in study 4a (IS - initial system). The thermal transient response times for stream 5 are given in Figs. 79 and 80 while those for stream 6 appear in Appendix C4. As is obvious from these figures, fixing T_3 at 800 ^{0}K or 870 ^{0}K, as opposed to allowing it to vary, results in longer thermal transients for stream 5. The same is seen in the figures given in Appendix C4 for stream 6.

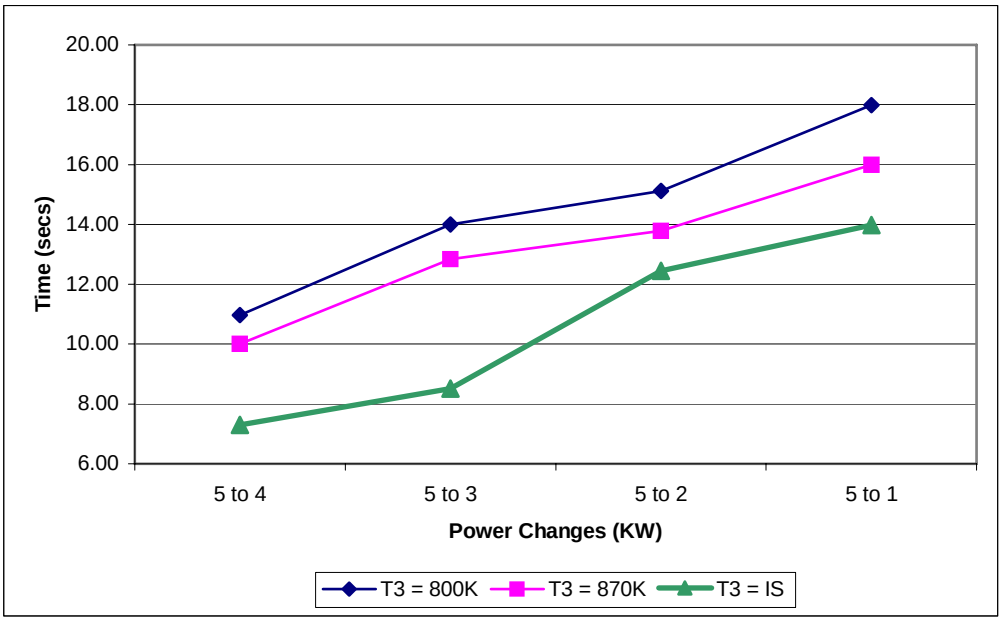

Fig. 79: Thermal transient response times of pre-reformer stream 5 (outlet steam-methane stream) for decreases in load, T4 fixed at 1200 ^{0}K, and a range of values for T3 (inlet steam-methane stream temperature).

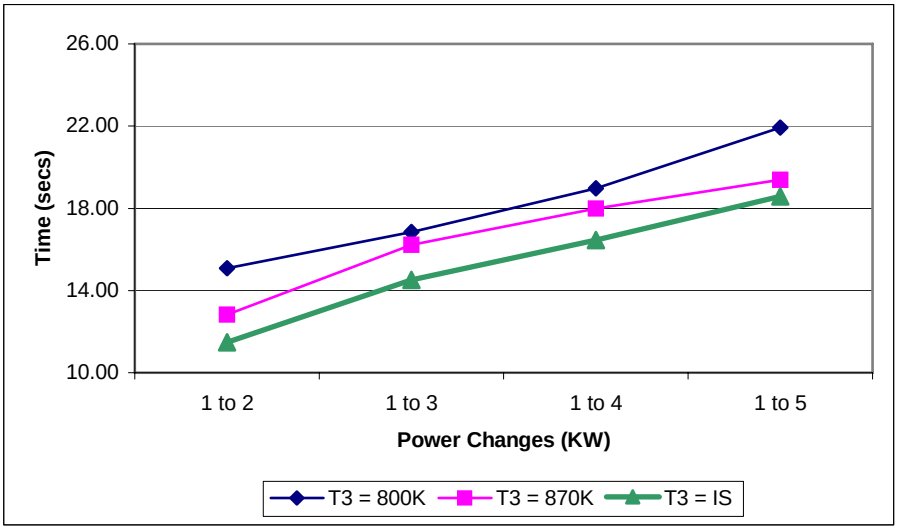

Fig. 80: Thermal transient response times of pre-reformer stream 5 (outlet steam-methane stream) for increases in load, T4 fixed at 1200 ^{o}K, and a range of values for T3 (inlet steam-methane stream temperature).

System thermal andenergy efficiencies as a function of load and temperature T_3 are given in Figs. 81 and 82 and in Appendix C4. The trends are similar for both power increases and decreases. The lower T_3 is, the lower the efficiency although the effect of T_3 is minimal.

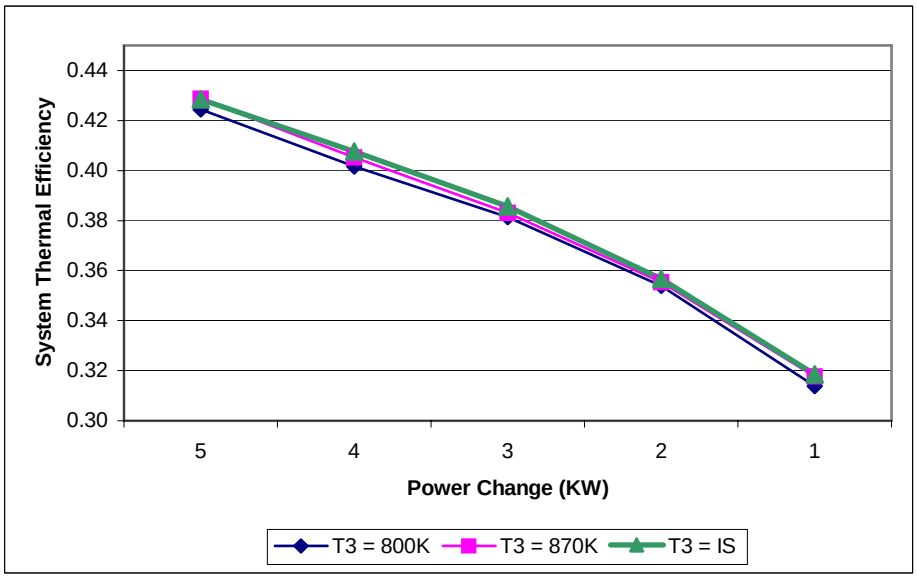

Fig. 81: System thermal efficiency as a function of load and pre-reformer inlet steam-methane temperature T3 (T4 is fixed at 1200 ^{o}K).

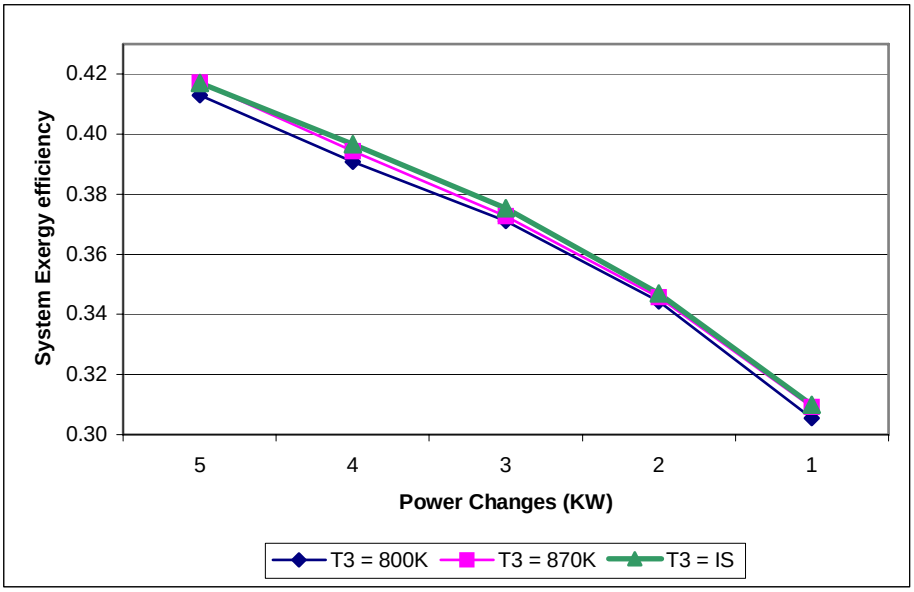

Fig. 82: System energy efficiency as a function of load and pre-reformer inlet steam-methane temperature T3 (T4 is fixed at 1200 ^{o}K)

Study 4c: In this study, the inlet water temperature to the steam generator is varied for increases and decreases in load ranging from 1 kW to 4 kW. Changes in this temperature, which include 150 ^{o}K, 200 ^{o}K, 293 ^{o}K, 350 ^{o}K and 450 ^{o}K, affect the thermal and molar flow rate transients of the pre-reformer, i.e. streams 3, 5, and 6. Altering the inlet water temperature alters the outlet steam temperature of the steam generator, which feeds into the pre-reforming mixer. This in-turn induces thermal transient responses in the pre-reformer streams: In this particular study, the inlet combustion gas stream temperature (stream 4) of the pre-reformer is kept constant at 1200 ^{o}K.

The thermal transient response times of pre-reformer streams 3 and 5 for increasing and decreasing power values are shown in Figs. 83 and 84 below while those for pre-reformer stream 6 are given in Appendix C4. From these figures, it is apparent that values of the inlet water temperature at or above 293 ^{o}K result in higher thermal transient response times for both increasing and decreasing load values. Furthermore, both temperatures significantly below and above 293 ^{o}K require energy in either a cooling or heating effect with a consequent negative impact on system efficiency unless offset by some other significant gain in efficiency in the system due to a lower or higher inlet water temperature. As will be seen in Figs. 85 and 86 below, there is no such significant gain.

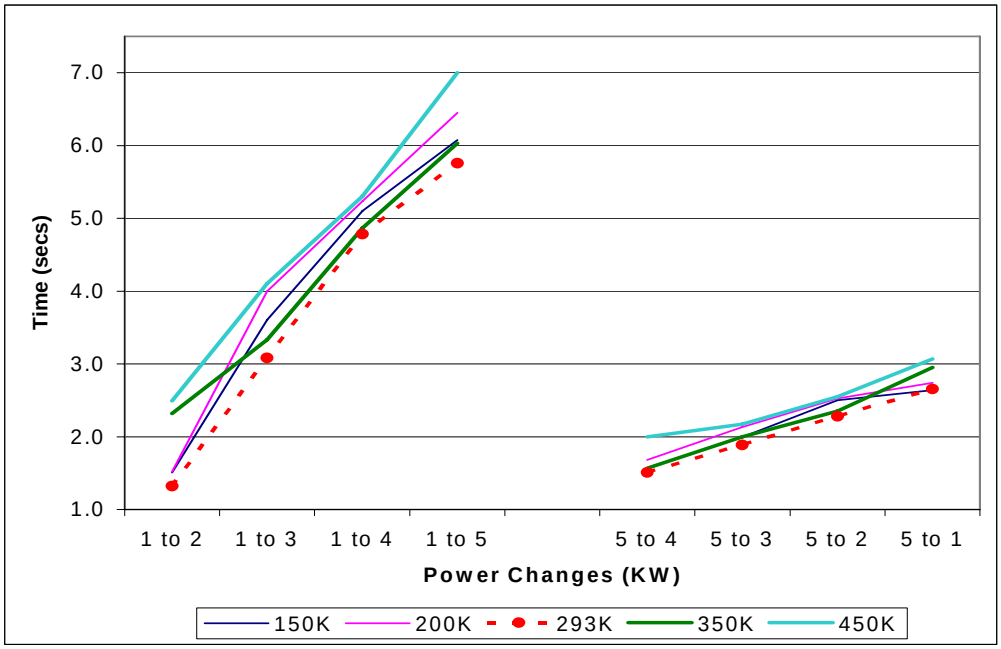

Fig. 83: System thermal transient response times of pre-reformer stream 3 (inlet steam-methane stream) for increases and decreases in load, T4 fixed at 1200 ^{0}K, and a range of values for the inlet water temperature to the steam generator.

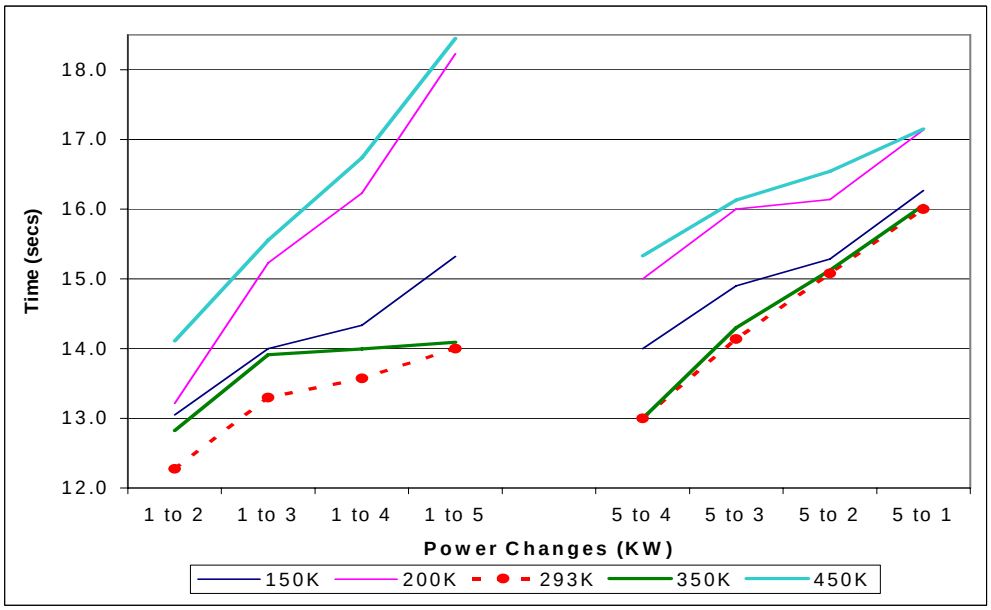

Fig. 84: System thermal transient response times of pre-reformer stream 5 (outlet steam-methane stream) for increases and decreases in load, T4 fixed at 1200 ^{0}K, and a range of values for the inlet water temperature to the steam generator.

System thermal andenergy efficiencies as a function of load and the inlet water temperature of the steam generator are given in Figs. 85 and 86 and in Appendix C4. The trends are similar for both power increases and decreases. As already noted above, maximum system efficiencies are obtained when the inlet steam temperature is at 293 ^{0}K. The reasons for this are as outlined in the discussions surrounding Figs. 83 and 84.

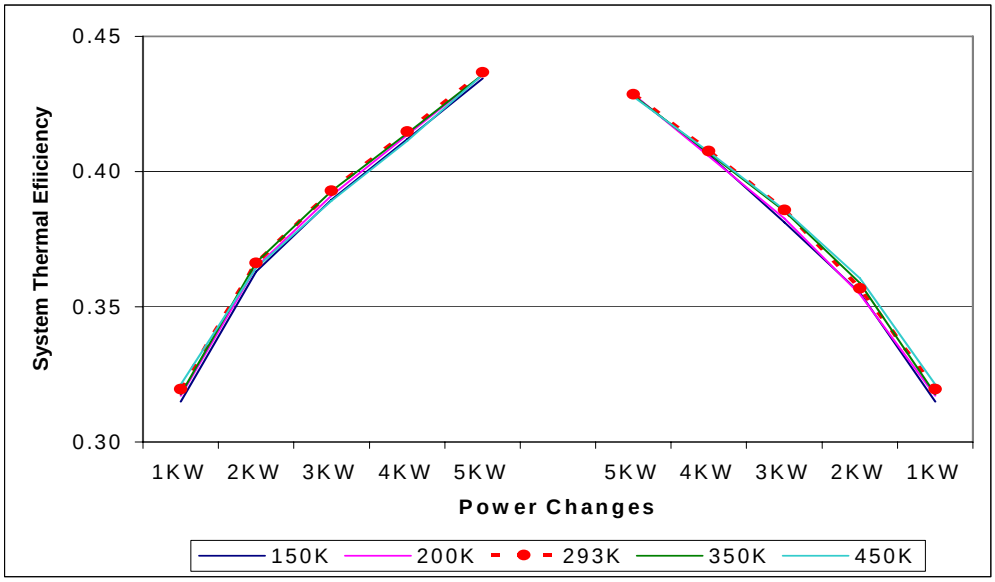

Fig. 85: System thermal efficiency as a function of load and the inlet water temperature of the steam generator (T4 is fixed at 1200 ^{o}K).

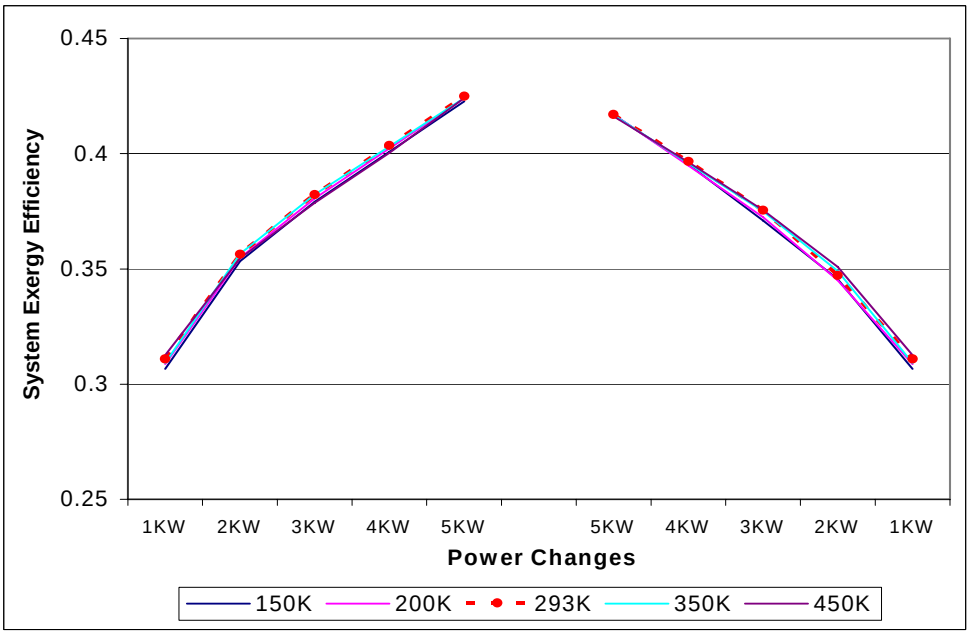

Fig. 86: Systemenergy efficiency as a function of load and the inlet water temperature of the steam generator (T4 is fixed at 1200 ^{o}K).

Study 4d: In this final study, the steam generator inlet combustion gas flow rate is varied for increases and decreases in load ranging from 1 kW to 4 kW. Changes in this molar flow rate, which varies in multiples of the flow rate of the combustion gas stream exiting the pre-reformer (stream 6), affect the thermal and molar flow rate transients of said component, i.e. streams 3, 5, and 6. The multiples of stream 6 used are 0.30, 0.35, 0.427, 0.50, and 0.55. As in the previous three studies, the inlet combustion gas stream temperature (stream 4) of the pre-reformer is again held fixed at 1200 ^{o}K.

The transient effects on the pre-reformer inlet steam-methane stream (stream 3) appear in Fig. 87 both for decreasing and increasing loads while those for pre-reformer stream 6 are given in Appendix C4. From this figure, it is apparent that values of the multiple of stream 6 above or below 0.427 (our nominal value) result in higher thermal transient response times for both increasing and decreasing load values. This is even more pronounced for the pre-reformer outlet steam-methane stream (stream 5) in which the thermal transient response times of the stream (see Fig. 88) deviate more significantly from the stream's nominal value than was the case for stream 3.

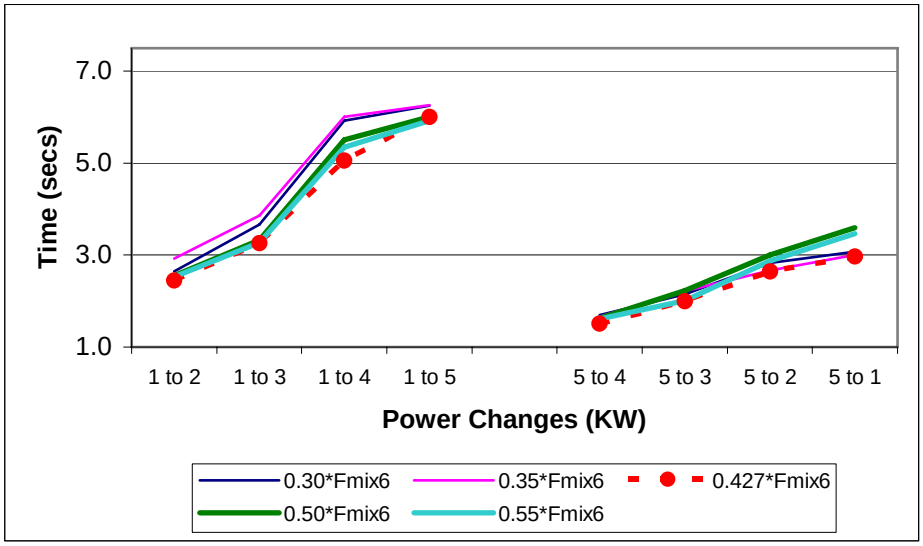

Fig. 87: System thermal transient response times of pre-reformer stream 3 (inlet steam-methane stream) for increases and decreases in load, T4 fixed at 1200 ^{o}K, and a range of values for the steam generator inlet combustion gas flow rate.

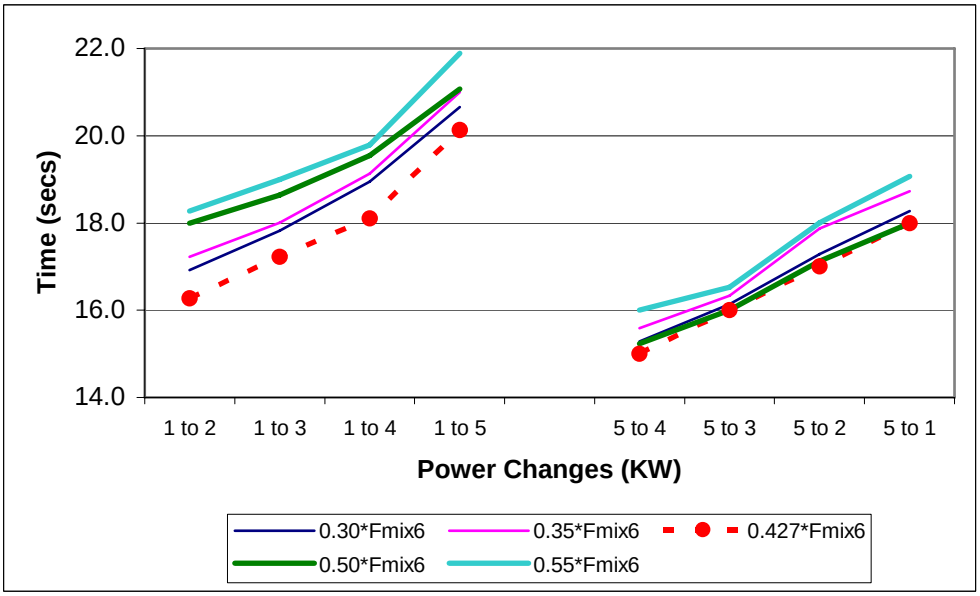

Fig. 88: System thermal transient response times of pre-reformer stream 5 (outlet steam-methane stream) for increases and decreases in load, T4 fixed at 1200 ^{o}K, and a range of values for the steam generator inlet combustion gas flow rate.

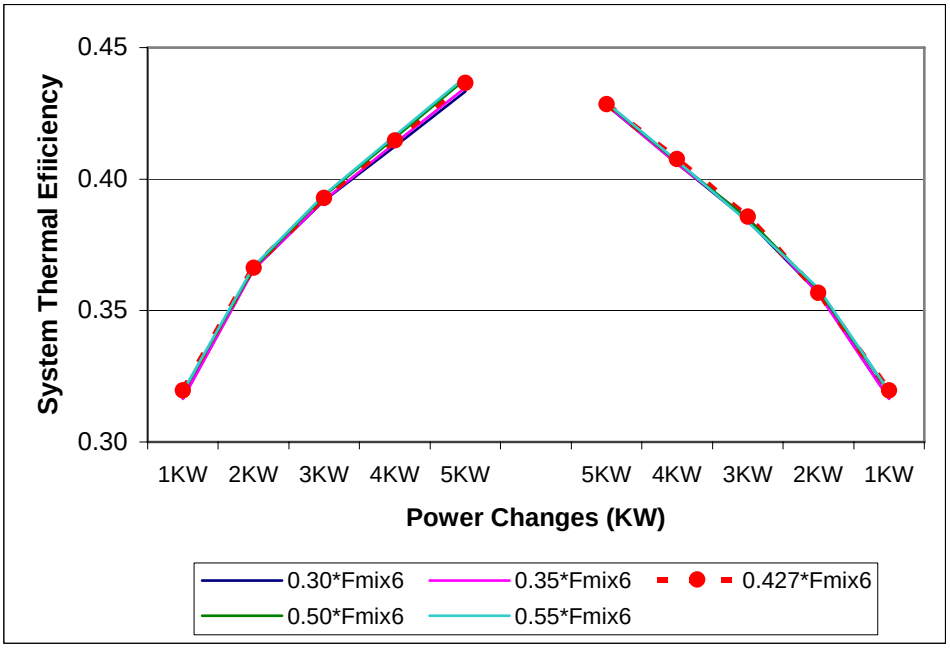

Fig. 89: System thermal efficiency as a function of load and the steam generator inlet combustion gas flow rate (T4 is fixed at 1200 ^{o}K).

System thermal and energy efficiencies as a function of load and the steam generator inlet combustion gas flow rate are given in Figs. 89 and 90 and in Appendix C4. The trends are similar for both power increases and decreases. As is seen in these two figures, system efficiencies are little affected by the different multiples of pre-reformer stream 6, thus, leading to the conclusion that the range of steam generator inlet combustion gas flow rates investigated can only marginally improve or degrade overall system efficiency.

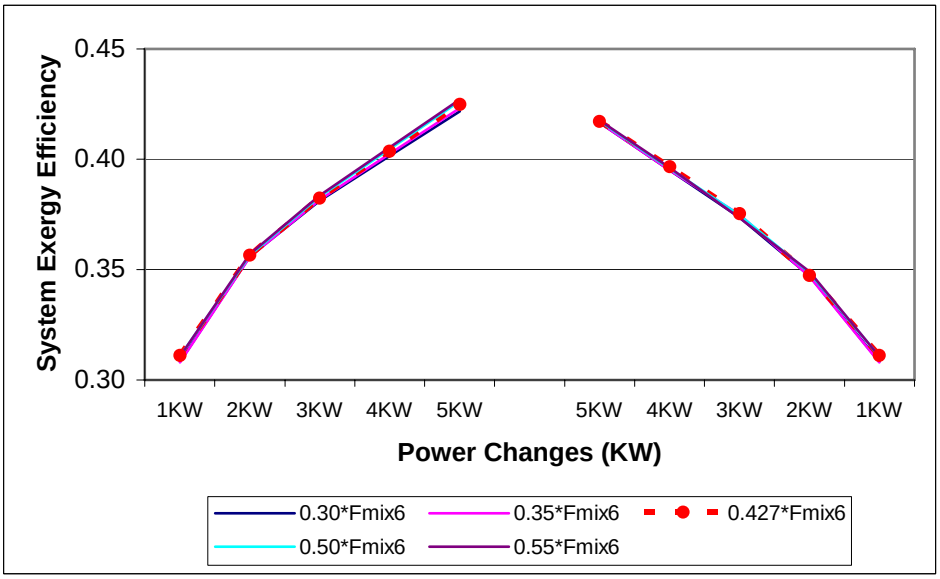

Fig. 90: System energy efficiency as a function of load and the steam generator inlet combustion gas flow rate (T4 is fixed at 1200 ^{o}K).

3.2.3.5 Start-up Transient Response

A typical approach to the synthesis/design optimization of energy systems is to *only* use steady state operation and high efficiency (or low total life cycle cost) at full load as the basis of the synthesis/design. Transient operation as reflected by changes in power demand, shut-down, and start-up are left as secondary tasks to be solved by system and control engineers once the synthesis/design is fixed. However, start-up and shut-down may be events that happen quite often and, thus, may be quite important in the creative process of developing the system. This is especially true for small power units used in transportation applications or for domestic energy supplies, where the load demand changes frequently and peaks in load of short duration are common. The duration of start-up is, of course, a major factor which must be considered and, in fact, controlling the start-up process is very important for the application at hand because rapid system response is a major factor in determining the feasibility of SOFC based auxiliary power units (APUs). Start-up and shut-down may also significantly affect the life span of the system due to thermal stresses on all system components since each experiences relatively large temperature differences. Therefore, a proper balance between a slow transient ,and a fast one must be struck so that start-up or any other transient process can be accomplished in as short a time as possible and with, of course, a minimum in fuel consumption.

Thus, the transient process occurring, for example, in a SOFC based APU should be systematically treated during the entire creative process of synthesis, design, and operational control, leading in its most general sense to a dynamic optimization problem. This entails finding an optimal system/component synthesis/design taking into account on- and off-design operation which in turn entails finding an optimal control strategy and control profile for each sub-system/component and control variable, respectively. Such an optimization minimizes an appropriated objective function, e.g., time and/or fuel consumption or total cost of the system for a period of time (capital and operational), while satisfying all system constraints. The application of such a comprehensive approach to the synthesis/design and control of a SOFC based APU is one of the goals of the second phase of this project. Phase I achievements include developing a feasible energy integrated system synthesis/design as well as a novel control strategy for system start-up and shut-down.

At the end of Phase I, start-up models and simulations have been developed and implemented for all system components. The results of simulations of two of these components which are considered representative of system component behavior are presented below. These start-up simulations are performed for fixed values of the system-level parameters (i.e. fuel utilization (FU), steam to methane ratio (SMR), and fuel reformate ratio (FRR)). The objective is to gather high fidelity information which will allow the development of appropriate control strategies for this critical operating point. Fuel consumption and time response are the parameters to be improved.

Figure 91 shows the thermal and mechanical transient response for the steam-methane reformer. Initial conditions are given by the initial temperature of the reformer wall (295 ^{o}K), and the initial and final conditions of the steam-methane mixture coming into the reformer (500 ^{o}K and 890 ^{o}K, respectively). The combustion gases inlet temperature is held constant at 1200 ^{o}K. The yellow curve indicates the mass flow transient response, which can be read from the upper and right axes. With respect to mass flow, it took 8 sec for the system to reach steady state, which is a considerably shorter period of time when compared to the thermal transient response. The pink and blue curves indicate the average reformer wall temperature and the reformate exit temperature, respectively. They can be read from the lower and left axes. For the given conditions, it takes the reformer walls 1980 sec to reach a steady state temperature of 1005 ^{o}K. Most importantly, it takes 1750 sec for the exit reformate gases to reach steady state at 870 ^{o}K although they do

reach operational temperatures (higher than 800 ^{o}K) in about 500 sec. The initial reformate gases exit temperature is 510 ^{o}K. Despite the long period of time that it takes the reformate gases to reach steady state; they do reach operational temperatures (higher than 800 K) in about 500 secs.

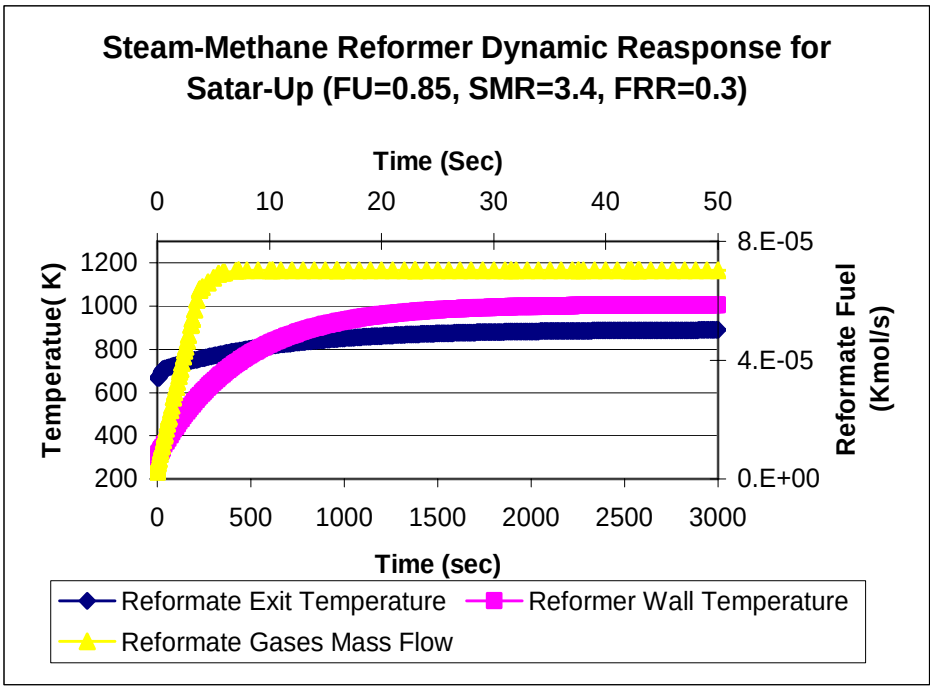

Fig. 91: Steam-methane reformer's start-up transient response for a final power demand of 5kW (FU=0.85, SMR=3.4, and FRR=03).

As indicated earlier, the mass of the steam reformer and its inner characteristics (i.e. specific heat, thermal capacitance, and density) are determinant in the length of the time response. The smaller the reformer mass is, the shorter the time response for any given set of conditions and perturbations. Since start-up time response is a current constraint for SOFC applications, future developments have to adequately address component weight and geometry. In the same vein, research on component materials is needed. This is also true for the other components. Optimizing component weight and geometry must, of course, be done as a system problem, which due to its complexity and nature, i.e. it is a mixed integer non-linear programming problem, may require a decomposition technique such as ILGO (Rancruel D, 2003; Rancruel D, and von Spakovsky 2003).

Figure 92 shows the thermal transient response for heat exchanger IV. Initial conditions are given by the initial temperature of the heat exchanger walls (295 ^{o}K), and the conditions of the hot and cold streams coming into the heat exchanger (870 ^{o}K and 340 ^{o}K, respectively). The yellow, light blue, and maroon curves indicate the thermal transient response of the walls at the hot side inlet, mid-point, and exit, respectively. Since this is a cross-flow, one-pass compact heat exchanger, the hot-side inlet corresponds to the cold-side exit and the hot-side exit to the cold-side inlet. In this analysis, attention is focused on the cold-side, since the exit air is going to be used directly in the SOFC stack. For the wall cold-side inlet, mid-point, and exit it takes 650, 1050 and 600 sec, respectively, to reach steady state. The air (cold-side) exit temperature (dark blue curve) reaches steady state in 800 sec. However, more important is the fact that operational temperatures (higher than 800 ^{o}K) are reached within 250 sec. The air final exit temperature is

860 ^{o}K. The hot-side (combustion gases) exit temperature (pink curve) reaches steady state in 850 sec. The combustion gases final temperature is 452 ^{o}K.

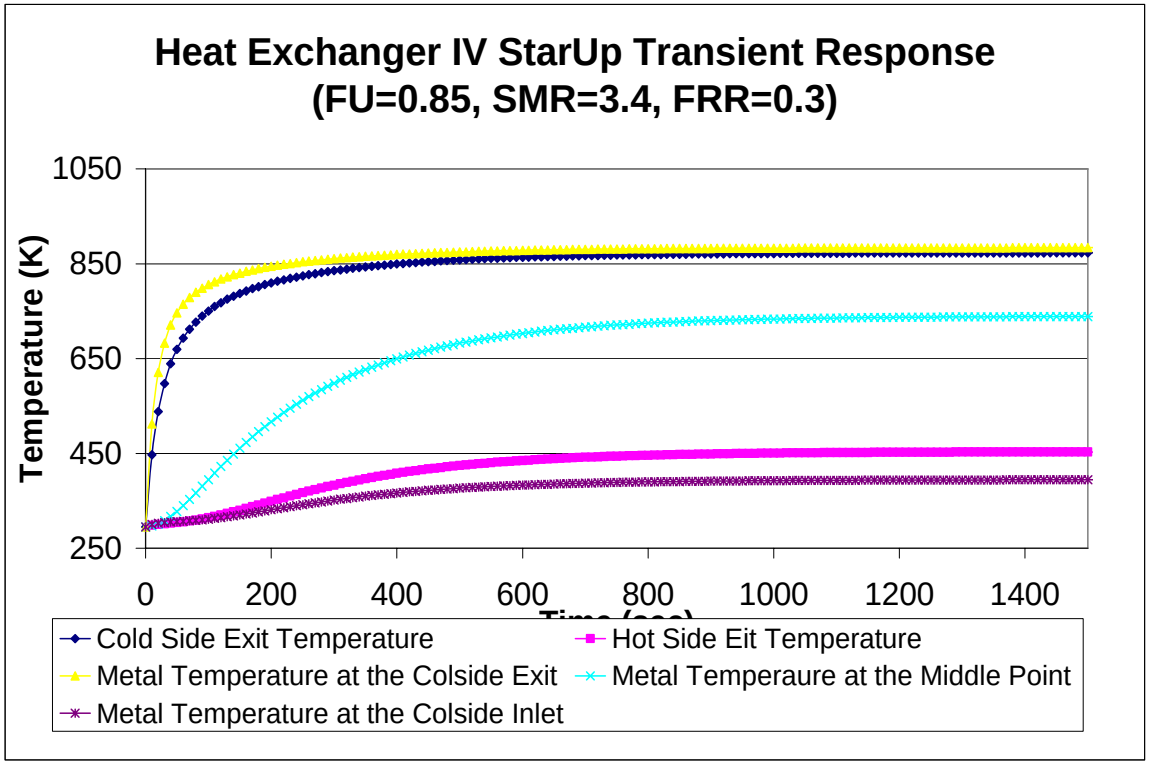

Fig. 92: Heat Exchanger IV Startup Thermal Transient Response Final power demand is 5kW (FU=0.85, SMR=3.4, and FRR=03 are constant).

Additional hardware added to the initial system configuration includes a hydrogen storage tank for fuel buffering, which minimizes the effect of transients on fuel cell stack performance and life time by supplying, almost immediately, the required fuel to the stack for any given load. An air tank is used in a similar way to provide reactant air to the stack. A control strategy was developed to guarantee that the fuel in the tank is never depleted. Part of this strategy includes ensuring that no shut-down process is complete before proper levels of fuel in the tank are reached. Furthermore, the processing of fuel in the fuel pre-reformer is primarily determined by the fuel tank level and secondarily by the load demand. Since the fuel and air tanks are pressurized, their contents can be immediately used for start-up. However, this depends on the minimum admissible temperature of the fuel at the inlet to the stack. If the fuel is too cold, it has to be pre-heated before being feed into the SOFC stack. The load requirement in the mean while is met by a battery bank. Simulation has shown how this approach improves the time response by minimizing the effects of the time delay due to the fuel reforming sub-system. A more detailed discussion on fuel buffering is given in section 3.3.4.

Two general start-up scenarios can be envisioned: one with fuel and energy buffering and the second without any. In Phase I, the scenario without buffering was considered. It is the most general and includes the worst possible conditions yet has a number of start-up procedures in common with the scenario with buffering. Both scenarios will be considered in Phase II. For the case without buffering, each component is initially assumed to be at ambient temperature (e.g., after being shut-off for a long time),

which in turn is the worst possible situation. Since no fuel buffering is available, the first task is to generate fuel. Thus, initially vapor has to be produced for the fuel reforming process. To do this, the methane compressor is started at the same time as the water pump and the air compressor. Fuel is burned to generated hot combustion gases in order to produce vapor at the steam generator. The water is re-circulated in the steam generator up to the point that steam at the appropriate temperature is coming out of the steam generator. At that point, re-circulation is stopped and continuous operation follows. Some preliminary results for this scenario are given below. More detailed results and a complete system control strategy for start-up and shut-down as well as a system start-up model linking all the current component start-up models will be developed in Phase II.

Fig. 93 shows how the steam temperature changes with time. Different re-circulation interruption temperatures were evaluated to determine the fastest transient response to reach steady state at a predefined operational temperature of 750 ^{o}K. This is achieved when the recirculation is stopped at 700 ^{o}K. In order to ensure that a maximum heat flux which could lead to burnout is never reached throughout this star-up process, the heat fluxes occurring throughout the steam generator during this start-up process were determined. Fig. 94 shows these heat fluxes for the steam generator. The maximum (340 kW/m^2) heat flux to avoid burnout is never reached. As a matter of fact the maximum heat flux is about 150 kW/m^2, which allows for a big margin of safety for this component.

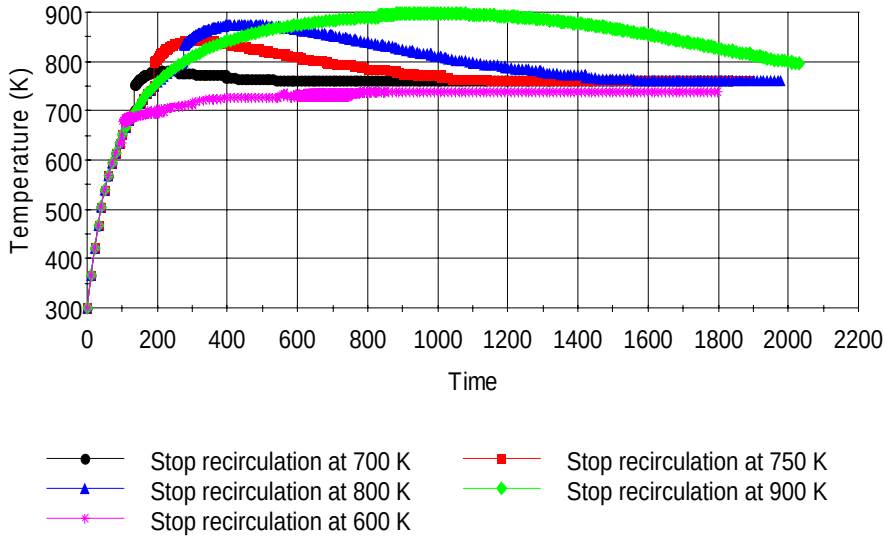

Fig. 93: Steam Generator start-up simulation

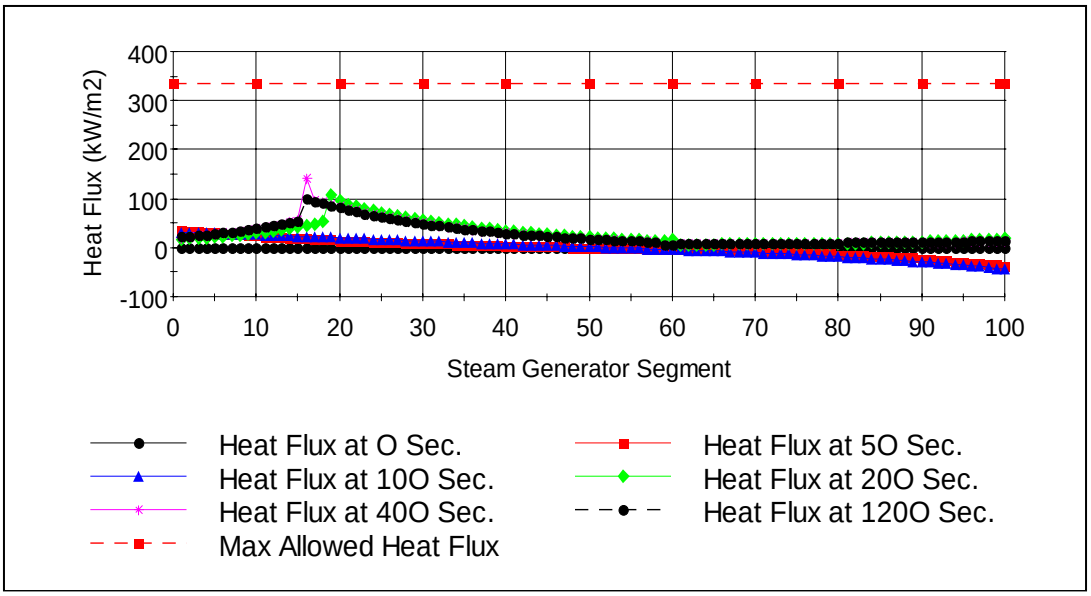

Fig. 94: Steam Generator Heat Flux

While vapor at the required temperature is generated, additional fuel is burned and the combustion gases generated are used to preheat all other system components. Fig. 95 shows the thermal response of heat exchanger III without cold-side flow. This figure shows how the response of this heat exchanger is much faster than that of for heat exchange IV seen in Fig. 92. Finally, using the start-up strategy just outlined and illustrated with Figs. 93 to 94 will reduce by a significant amount the time required in getting the system to continuous operation. A more detailed set of results and analyses will be presented in Phase II once the system start-up and shut-down models have been completed.

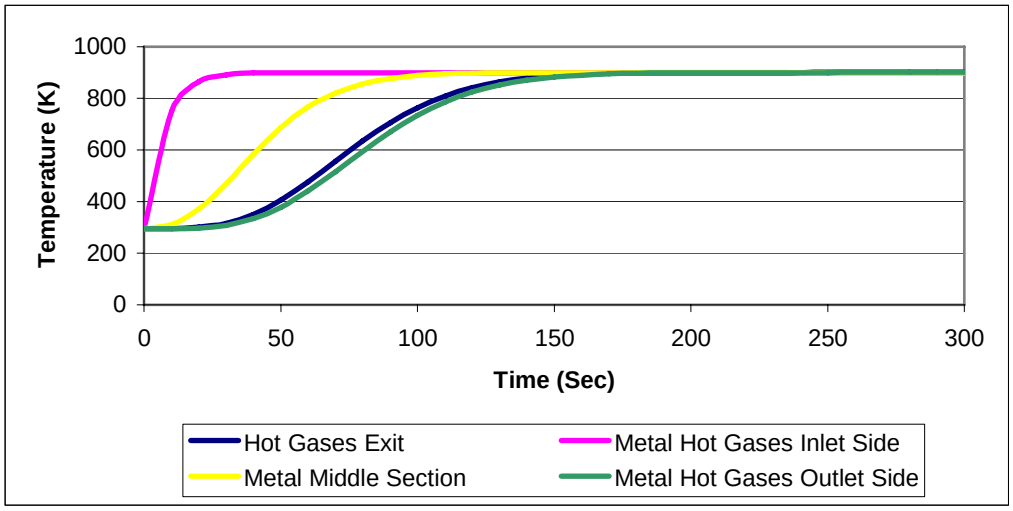

Fig. 95: Heat exchanger start-up without flow at the cold side

Figs. 96-98 show the system thermal efficiency versus power demand for a range of the system parameters values. Fig. 70 shows the efficiency curves for different values of FU, the highest efficiency is reach by using a FU of 0.9. However, operating the system under these conditions put in risk the fuel cell stack. In general, the higher the FU, the higher the efficiency, when all others parameters are kept constant.

Fig. 97 shows that increments in efficiency result from operating under high SMR factors. This is true for all load conditions. Fig. 98 shows how FRR should be kept as lows as possible in order reach higher system efficiency.

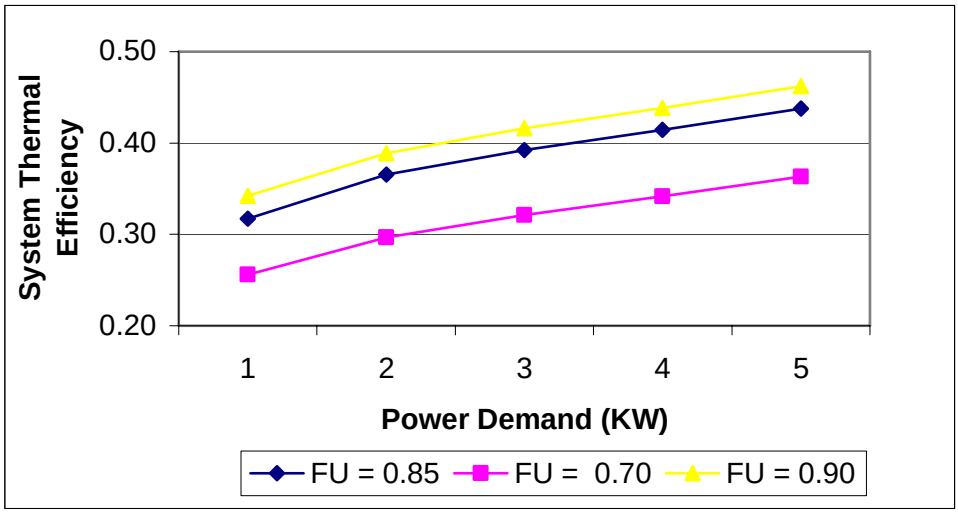

Fig. 96: System Thermal Efficiency for Various Values of Fuel Utilization (SMR=3.4, FRR=0.3).

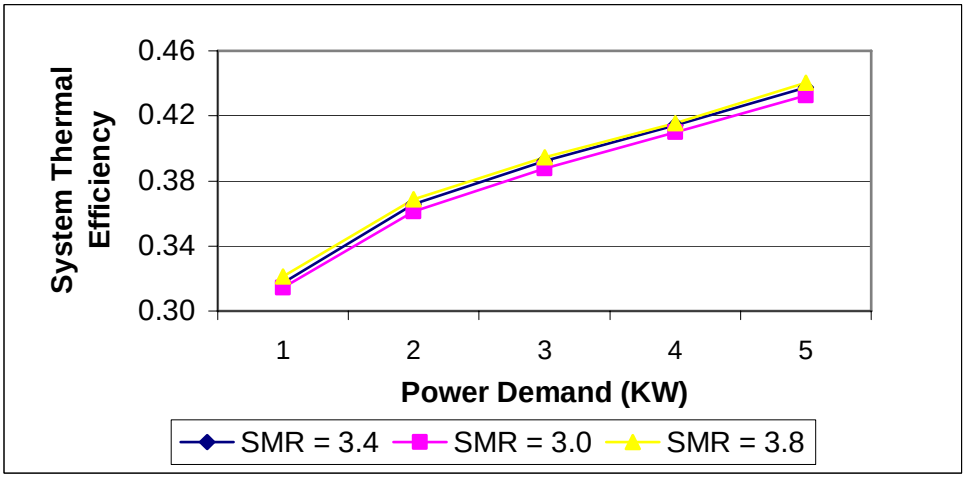

Fig. 97: System Thermal Efficiency for Various Values of SMR (FU=0.85, FRR=0.3).

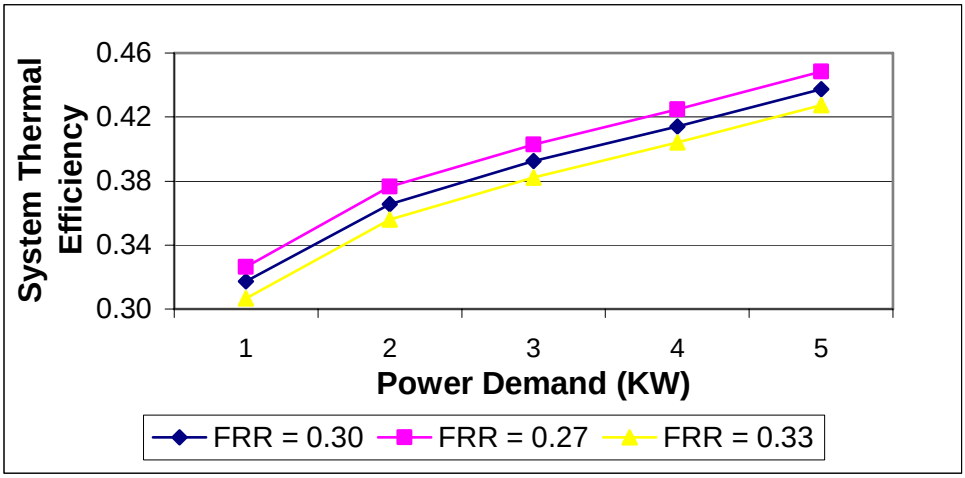

Fig. 98: System Thermal Efficiency For Various Values of FRR (SMR=3.4, FU=0.85).

3.3 CONTROL DESIGN

3.3.1 Novel PES Hybrid Nonlinear Controller for DC-DC Converter

If the PES is locally unstable (PES with global instability is inoperable), then the dynamics of the current ripple may be completely different from the nominal ripple in magnitude and frequency and this may have a direct impact on the durability of the SOFC. Additionally, a poor transient response of the controller may result lead to current-overshoot during load-transients that may lead to electrically induced thermal effects in the SOFC stack due to high fuel utilization. On the same note, SOFC output voltage variations (due to change in load demand or due to low bandwidth of BOPS) act as a feedforward disturbance on the PES, which can destabilize the electronic subsystem.

To address these issues properly, we have developed a novel nonlinear[17] hybrid[18] controller (Mazumder et al., 2002) for a single/parallel DC-DC boost (or a buck/boost-derived/buck-derived) converter as well as single/three phase DC-AC converters by combining integral-variable-structure control (IVSC) scheme and multiple-sliding-surface control (MSSC)[19]. Currently, the hybrid-control concept is being extended to the DC-AC converters by combining MSSC and IVSC as well as space-vector modulation (SVM), and the work is scheduled for completion in phase II.

---

[17] The closed-loop PES (which may comprise a DC-DC and a DC-AC converter) is a nonlinear hybrid system. It may have more than one equilibrium solution. How close to the nominal solution the PES operates (i.e., how stable the system is) depends on the controller performance and disturbance-rejection capability. Hence, conventional small-signal (linearized) PES controllers are not always equipped to handle large-scale disturbances because they are designed to operate in the vicinity of the nominal solution.

[18] The hybrid controller has an outer controller and an inner controller and switches between the two depending on whether the error trajectory is outside or inside the assumed boundary layer. The boundary layer is formed by a ramp signal of frequency f_s (= $1/T$) with the limits corresponding to the maximum and minimum values of the ramp.

[19] The IVSC is simple, robust and has a good dynamic response. It eliminates the bus voltage error and the error between the load currents of the individual converter modules under steady-state conditions. By using the concepts of multiple-sliding-surface control (MSSC), any mismatched disturbances are rejected and the switching frequency is maintained constant at steady state.

The hybrid control scheme for the PES has several advantages over conventional controller and will be of significant benefit to the industry. First, it is easy to design because sliding surface(s) (Utkin et al.) is (are) independently controlled. Second, the controller yields excellent steady-state and transient responses even under parametric variations and under perturbations of SOFC stack voltage and load. Third, the controller eliminates the bus-voltage error with a reduced control effort. Fourth, the integrators in the control scheme can reduce the impact of very high-frequency dynamics due to parasitics on an experimental closed-loop system. Fifth, the control scheme within the boundary layer enables operation of the converter with a finite switching frequency. Sixth, the converter modules can be operated in interleaving or synchronicity modes.

3.3.1.1 Hybrid controller description

The hybrid controller comprises a combination of integral-variable-structure control (IVSC) scheme and multiple-sliding-surface control (MSSC). The IVSC is simple, robust and has a good dynamic response. It eliminates the bus voltage error and the error between the load currents of the individual converter modules under steady-state conditions. By using the concepts of multiple-sliding-surface control (MSSC), any mismatched disturbances are rejected and the switching frequency is maintained constant at steady state.

The hybrid controller has an outer controller and an inner controller and switches between the two depending on whether the error trajectory σ is outside or inside the assumed boundary layer. The boundary layer is formed by a ramp signal of frequency f_s (= 1/T) with the limits corresponding to the maximum and minimum values of the ramp.

Mode 1: Outside the Boundary Layer

In this mode of operation the error trajectory σ is computed as shown in Fig. 99. The constants G_1, G_2, and G_3 are the controller gains and f_v (≤1) and f_i (≤1) are the feedback sensor gains for the output voltage and inductor currents, respectively. V_{Ref} are the references of the bus voltage. If σ is greater than the boundary the control signal to the high-side switch of the buck converter is a constant high and if it is less than the boundary the switch is turned off till the error trajectory falls within the boundary layer In the latter case, the high side switch is turned off till the error trajectory reaches the minimum value of the boundary layer.

$$\sigma_k = G_1(V_{ref} - f_v v_C) + G_2 \int (V_{ref} - f_v v_C) d\tau - f_i i_L \qquad (70)$$

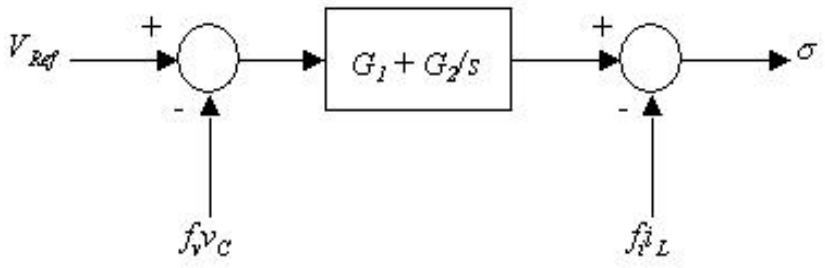

Fig. 99: Block diagram for the generation of σ

Mode 2: inside the boundary layer

Since the switching frequency is finite, the boundary layers have a finite width. Therefore the control laws assumed in the preceding section will only guarantee that the error trajectories will reach the boundary layer. The inner control ensures that the error trajectories stay within the boundary layer under steady-state conditions. The sliding surfaces/error trajectories inside the boundary layer (11) and the PWM signal is obtained as shown in Figs. 99 and 100. In Fig. 100(a), $\overline{\sigma_1}$ is determined from the filtered values of the inductor currents, $f_i \overline{i_L}$ and output voltage $f_v \overline{v_C}$. In Fig. 100(b) $\beta_1, \beta_2, \beta_3$ are constants chosen such that the dynamics on $\overline{\sigma_1} = 0$ are convergent (for $\overline{\sigma_1}$ > 0 or $\overline{\sigma_1}$ < 0). The duty ratio is derived using *Lyapunov's* theorem and converted to error signal by multiplying it with *1/V*$_m$. The PWM signal is obtained by comparing it with a ramp of frequency f_s (= 1/*T*). In this mode of operation, the controller behaves as a duty ratio controlled *Lyapunov* controller.

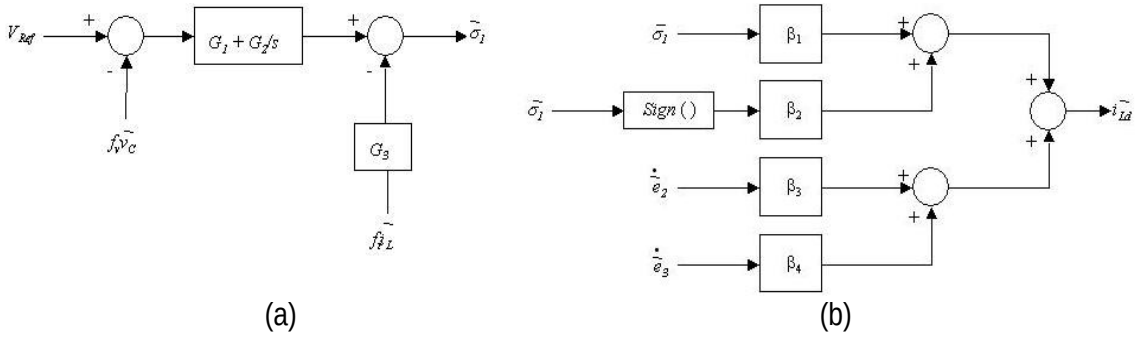

Fig. 100: Generation of PWM signal inside the boundary layer.

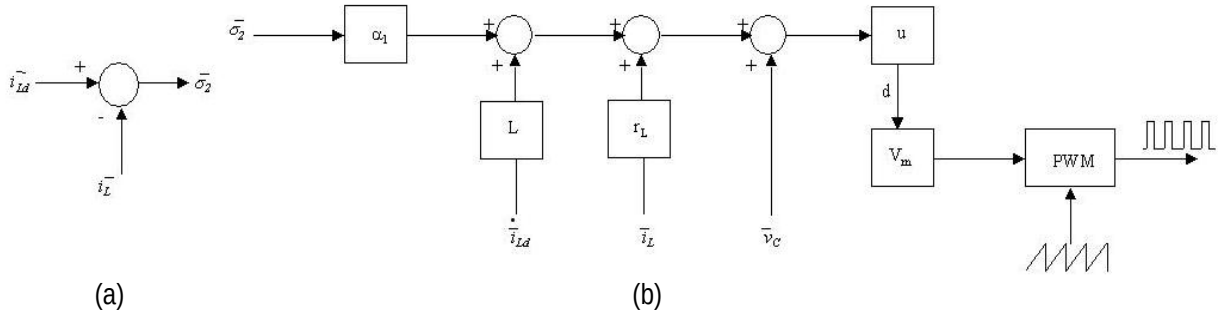

Fig. 101: Generation of PWM signal inside the boundary layer.

Switching between the two controls:

The mode of operation is determined at the beginning of each switching cycle and cannot change within a cycle. The error trajectory σ_k is sampled at the switching frequency and compared with the limits of the boundary layers.

The block diagram of the control scheme, implemented for one module of a four phase synchronous buck converter, can be extended to any number of modules. The inductor currents are detected through

sensing resistors and average current sharing technique is used to ensure equal distribution of current between the different modules. The control signal for each module is derived as discussed in the above sections.

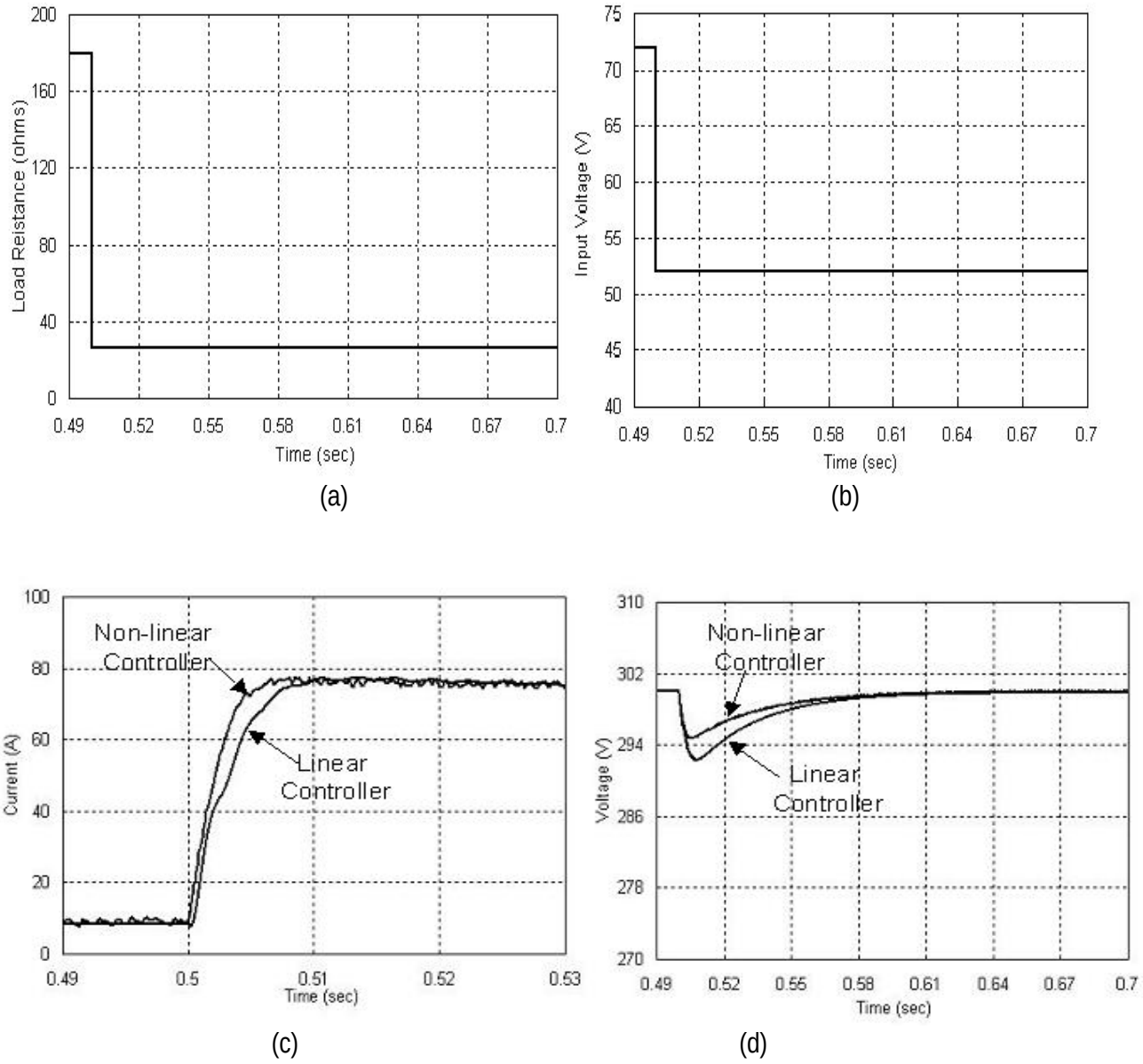

Fig. 102: Low- to full-load transient at 0.5sec: (a) Load resistance variation, (b) SOFC voltage; (c) inductor current and (d) capacitor voltage response to load transient for the boost converter using non-linear controller and linear controller.

3.3.1.2 Results

Fig. 102 shows the comparison between the linear and the non-linear controller for a step change in the load (light to full-load conditions). Figs. 102 (c) and (d) show the inductor current and the capacitor voltage response respectively to the step load change. SOFC stack voltage depends on the current drawn (as expressed in (4)). Both the controllers are adjusted so as to ensure critically damped response to the load transients. We observe that the non-linear controller is more robust to changes in the load, i.e. the response to load transients is faster in case of the non-linear controller. Both stationary and mobile SOFC based systems are subjected to load transients at regular time intervals. Hence, a marked improvement in the dynamic response of the system is expected in case of the non-linear controller. However (as will be shown in the next section for PWM VSI) the heating rate in case of non-linear controller is expected to be higher than that of the linear controller; hence higher microcrack density can be expected. Thus the enhanced performance of the non-linear controller is expected to come at the cost of higher localized current densities and fuel-flow rates, both of which may be detrimental to the SOFC stack.

3.3.2 Comparison of Inverter Control/Modulation Methodologies for Load Alleviation

Finally, sinusoidal PWM (SPWM) (Konishi et al., 1998) and space-vector modulation (SVM) (Holtz et al., 1993, Stefanovic and Vukosavic, 1992) strategies were considered to study the effect of load transients on SOFC fuel flow rates and current densities across the SOFC cross-section, using finite-element analysis described in (Khandkar et al., 1998). Spatial finite element analysis was also performed to observe the effect of load transient on SOFC temperature. The load transient analysis was performed on the self-commutated PWM VSI of Fig. 23(b). Fig. 103 illustrates the SOFC current for the SPWM and the SVM modulation schemes. SVM technique offers improved dc-bus utilization and hence improved the input current response. However the heating rate in case of SVM is higher than that of SPWM; hence higher microcrack density can be expected. Fig. 104(a) illustrates the hydrogen molar flow rate across the cross-section of the SOFC during the load transient. Non-uniform flow rates and non-uniform current density across the SOFC cross-section, as shown in Fig. 104(b) were observed for both the modulation schemes. This may cause unequal heating across the SOFC cross-section and hence could damage the SOFC materials.

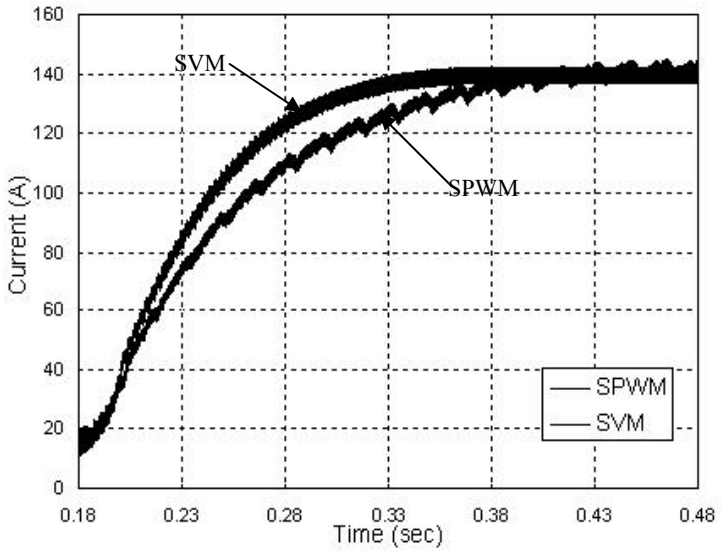

Fig. 103: SOFC input current during load transient showing difference between sinusoidal PWM (SPWM) and space vector modulation (SVM).

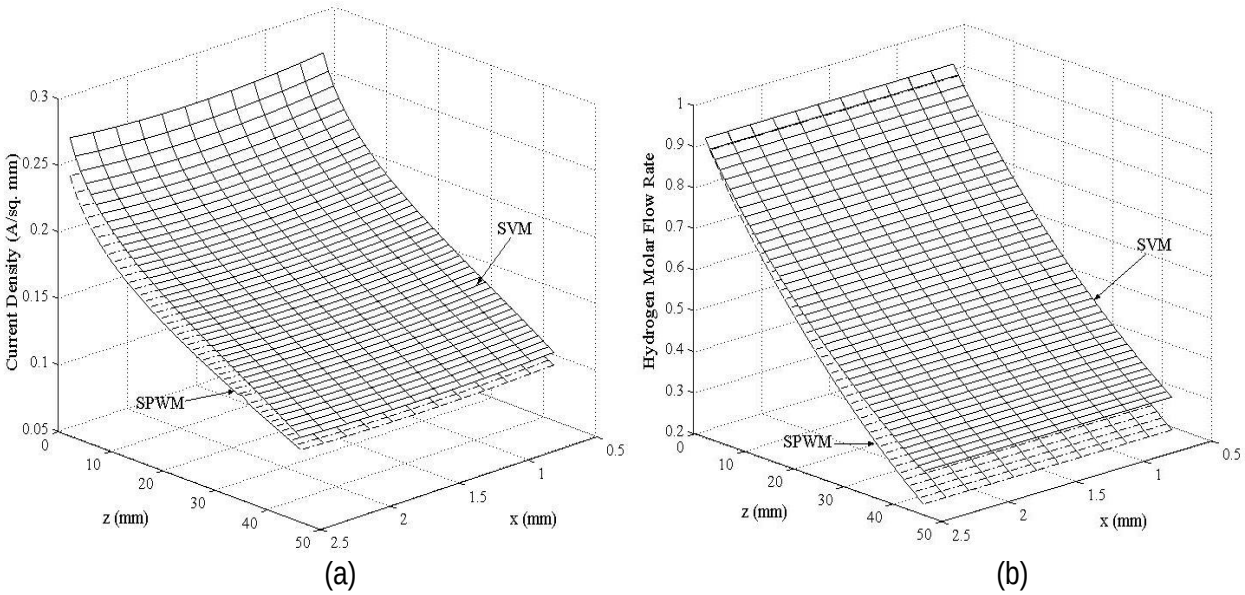

(a) (b)

Fig. 104: (a) Hydrogen molar flow rate, and (b) current density across the cross-section of the SOFC during the load transient.

Thus, for the self-commutated PES topology, while the superior dynamic-performance capability of SVM for three-phase inverters is well known, what is often overlooked in such analysis is the need for a stiff DC voltage source. As such, for SOFC, which is not a stiff DC voltage source, the enhanced performance of SVM comes at the cost of higher localized current densities and fuel-flow rates, both of which may be detrimental to the SOFC stack.

3.3.3 BOPS Control

3.3.3.1 Control Parameter and Control Variable Set Definitions

A set of system level control parameters have been defined, whose purpose is to keep the component level dependant variables within acceptable ranges, which in turn can be initially defined as component control limits (e.g., design limitations such as maximum stack inlet temperature) or as the output of a trade-off or optimization process (e.g., steam reformer optimum operational temperature).

The system-level control parameters for the BOPS are the steam to methane ratio (SMR), the fuel utilization (FU), the air to fuel ratio (AFR), and the fuel reformate ratio (FRR). The steam to methane ratio allows control of the chemical reaction inside the steam reformer and the reactants inlet temperature. The fuel utilization defines the heat and work recovery and is important for characterizing the reaction in the stack. The air to fuel ratio defines the parasitic power requirements. Finally, the fuel reformate ratio allows control of the inlet temperature in the stack and the outlet temperature of the steam reformer. In addition, the stream of combustion gases leaving the steam reformer is divided into three streams which go to two heat exchangers and the steam generator. The proportions into which this stream is divided can be used as a control parameter.

These system level control parameters, in the early stages of the design process, are considered as design choices, which are a valid subject for system optimization. The optimization process then determines an optimal system synthesis and a set of optimal component designs consistent with an optimal choice of values for these control parameters both at design and off-design. Thus, transient phenomena (e.g. change in power demand, start-up, etc.) are taken into account in the optimal synthesis/design process by, for example, minimizing the time response or fuel consumption of these parameters at off-design so that the optimal control of the system's operation affects (compromises) what would otherwise simply be a single-point synthesis-design. A methodology, of course, to do this is required and has, in fact, already been developed in previous work by members of our team (i.e. Iterative Local-Global Optimization, a decomposition approach for the large-scale optimization of highly complex and dynamic systems). In addition, such a methodology requires a platform, which allows one to approach the software integration and significant time-scale problems for the different sub-systems.

3.3.4 Fuel and Energy Buffering

SOFC stacks respond quickly to changes in load while the BOPS responds in times several orders of magnitude higher. This dichotomy diminishes the reliability and performance of SOFC electrodes with increasing load as do current and voltage ripples which result from particular PES topologies and operation. These ripples, load changes, and the difference in transient response between the electrical-electrochemical components for the PES and SS and those for the chemical-thermal-mechanical components of the BOPS must be approached in a way which makes operation of the entire system not

only feasible but ensures that efficiency and power density, fuel utilization, fuel conversion, and system response is optimal at all load conditions. The undesirable effects of these orders of magnitude differences in transients can be approached by introducing fuel and electrical energy buffering into the system layout. Fuel and air buffering have been shown to be a practical and efficient way of reducing the time delay due to the fuel processing sub-system. In the same way electrical energy buffering compensates the PES imbalance due to load perturbations, especially during start-up.

3.3.4.1 Advantages of Developing the BOPS Configuration with Electrical Energy and Fuel and Air Buffering

As already mentioned above, a significant increase in the load demand can cause anode degradation (i.e., oxidation) due to "fuel starvation" along the electrode. Fuel buffering minimizes this effect by supplying, almost immediately, the required fuel to the stack for any given load. Control strategies should be developed to guarantee that the fuel in the tank is never depleted. Furthermore, since the fuel and air tanks are pressurized, their contents can be immediately used for start-up. This improves the time response by minimizing the effects of the time delay due to the fuel reforming sub-system.

As to the electric energy buffering, because the SOFC is not a stiff voltage source, it is connected to a PES, which serves as an interface between the SOFC and the application load. The behaviors of the PES (for example, the magnitude and frequency of the current and voltage ripples) and that of the time-varying load have a direct impact on the stack performance and the durability (lifetime) of the fuel cell. If the peak-current levels from these loads are high, it can lead to a low-reactant condition within the SOFC. Similarly, variations in the output voltage (of the SOFC) can directly affect the operation of the integrated PES and the application load. Thus, having a supply of electrical energy during operation at peak-current levels lessens undesirable effects on the SOFC stack.

3.3.4.2 Fuel and Air Buffering Capacity Determination

Thermodynamic models are developed by applying dynamic mass and energy balances to the fuel and air tanks in order to determine the required inlet and exit mass flows. Creation of robust and detailed thermodynamic models of these components is complemented by geometric models, which are widely applicable and can be used to simulate the buffering requirements at both full and part loads. The final dimensions of the tanks are found by simulating the biggest possible disturbance under the most demanding condition, taking into account the power demand profile and final operating conditions, and finally applying a special algorithm to compute the fuel demand during the transient.

3.3.4.3 Energy-Storage Devices for Load-Transient Mitigation

To alleviate the degrading effects of low-reactant conditions near the TSOFC electrodes during load transients, fuel- and energy-buffering techniques are used. During load transients, these techniques are used to provide the additional energy requirements (until the BOPS supplies fuel at the required rates), thereby protecting the TSOFCS from the undesirable effects of load transients and enhancing its reliability.

We analyze the impacts of battery[20] and pressurized-hydrogen-fuel tank[21] in mitigating the degrading effects of load transients.

Figure 105(a) shows a typical TSOFC PCS to supply stationary power to an electric grid. For mitigating the effects of load transients, a battery is connected between the DC-DC and DC-AC stage, while a pressurized-hydrogen tank supplies the instantaneous requirements of hydrogen to the TSOFCS. During steady-state operation, the TSOFCS provides power to meet the load demands, as well as to recharge the battery. Figure 105(b) shows the circuit used for simulations. In this circuit, we replace the DC-AC converter and AL with a lumped harmonic load.

For durable TSOFCS PCS, the energy-storage devices have to be large enough to mitigate the effects of load transients. Figure 106 shows the variation of the response time[22] of the TSOFCS with the size of the battery and hydrogen molar-flow rates of the pressurized-hydrogen-fuel tank. From Figure 106, we observe that the smallest response time can be achieved using large size of the battery and high hydrogen molar-flow rates. However, this comes at the cost of low-power-density and high cost. For the purpose of this study, we assume that response times in the range of 0.2 seconds-0.35 seconds are acceptable for reliable TSOFCS operation. To find the optimum size of the battery and the pressurized-hydrogen-fuel tank that result in response times within the acceptable range, we conduct an initial optimization study. This is however, an unconstrained optimization study, because of the lack of information regarding size and weight constraints for the TSOFC PCS. Figures 107(a)-107(c) show that the variation of the size and weight of the energy-storage devices with their costs[23] for the different response times within the acceptable reliability range. These figures illustrate that optimal values of battery size and pressurized-hydrogen-tank are about 0.12 Ah and 1.00 x 10^{-4} moles/sec, 0.1 Ah and 5 x 10^{-5} moles/sec, and 0.08 Ah and 5 x 10^{-5} moles/sec for response times of 0.2 seconds, 0.3 seconds, and 0.35 seconds respectively. As expected, the optimal size of battery size and pressurized hydrogen tank reduces with increase in the response times.

[20] High-energy-density batteries are used to supply the instantaneous energy requirements during load transients. However, because the batteries (depending on their size), discharge at rapid rates, their operating life is very small.

[21] Fuel-buffering using pressurized-hydrogen-fuel tank mitigates the effects of load transients by supplying, almost immediately, fuel at the required rates to the stack for any load condition. Suitable control strategies guarantee that the fuel in the tank is never depleted. Furthermore, since the fuel- and air-supply-tanks are pressurized, their contents can be also be used during start-up.

[22] TSOFC PCS response times are a measure of its reliability. TSOFCS reliability increases with decrease in the response times.

[23] Typically, the cost of commercially available pressurized hydrogen tank is three times that of the battery, while its weight is around one and a half times the size of battery for comparable power handling capacities.

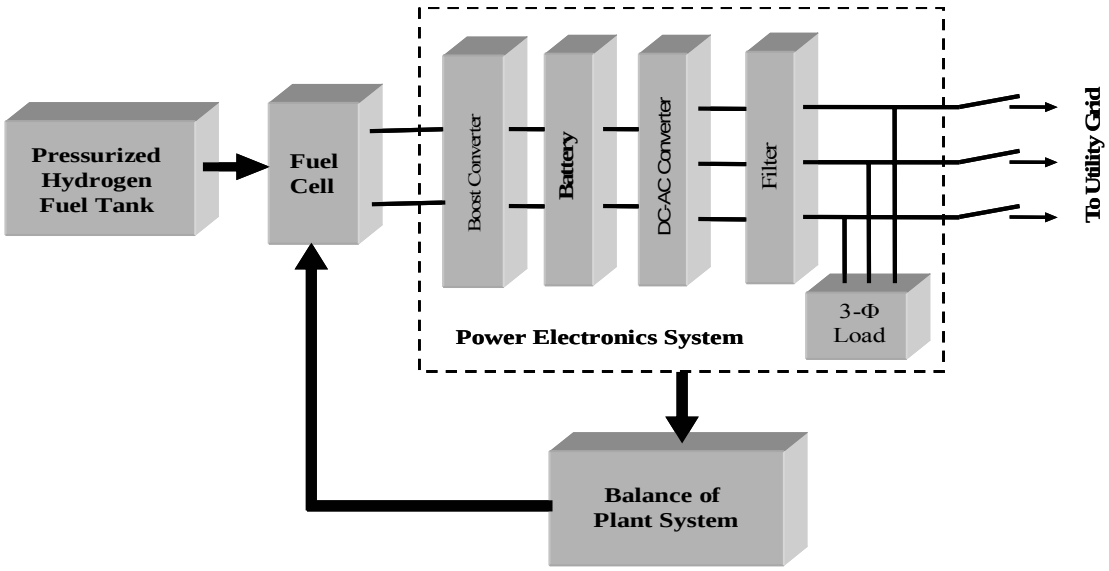

(a)

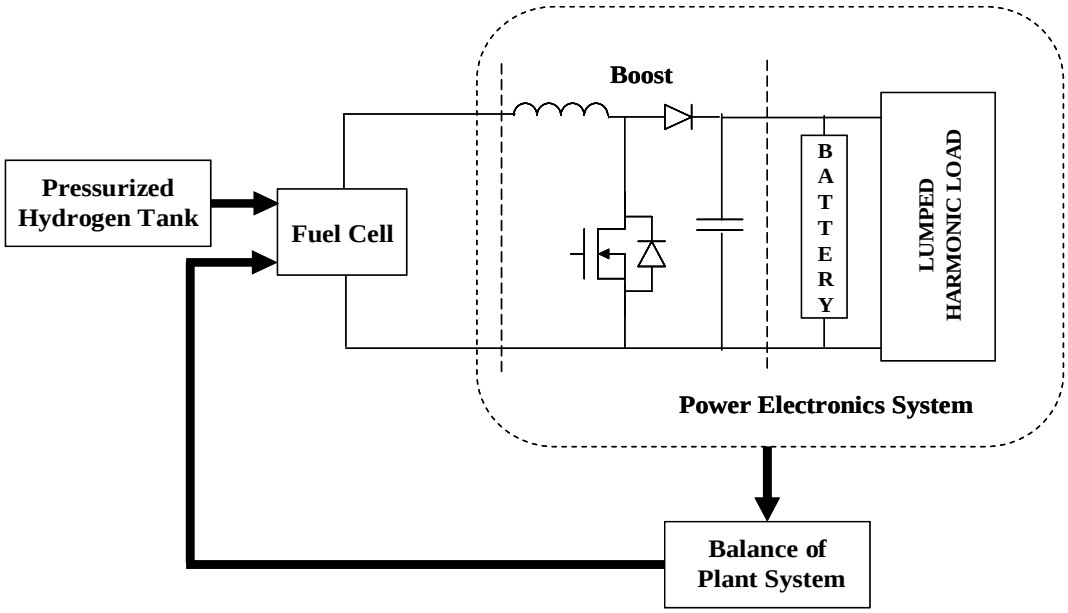

(b)

Fig. 105: (a) TSOFC PCS topology containing pressurized hydrogen fuel tank and battery for load-transient mitigation (d) Simulation model for obtaining optimum size of the energy-storage devices for load-transient mitigation.

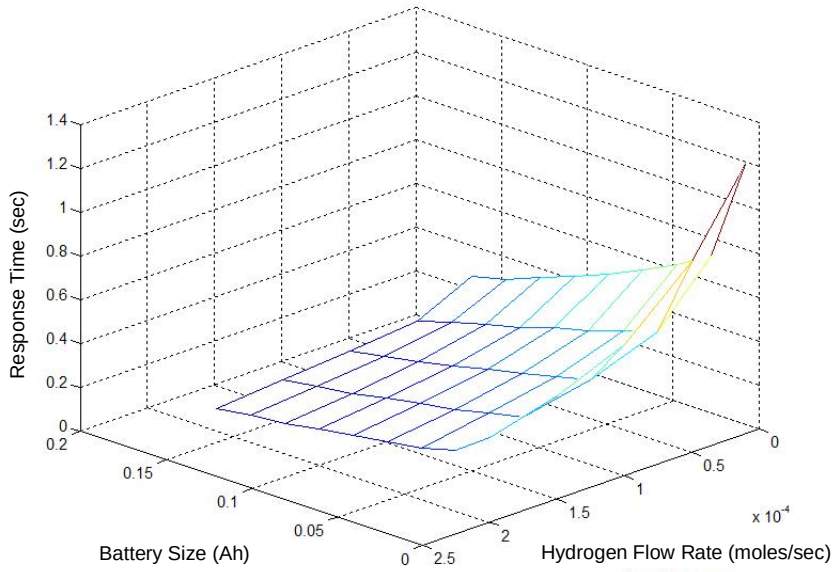

Fig. 106: Variation of TSOFC response time with Battery Size and Hydrogen Flow Rate.

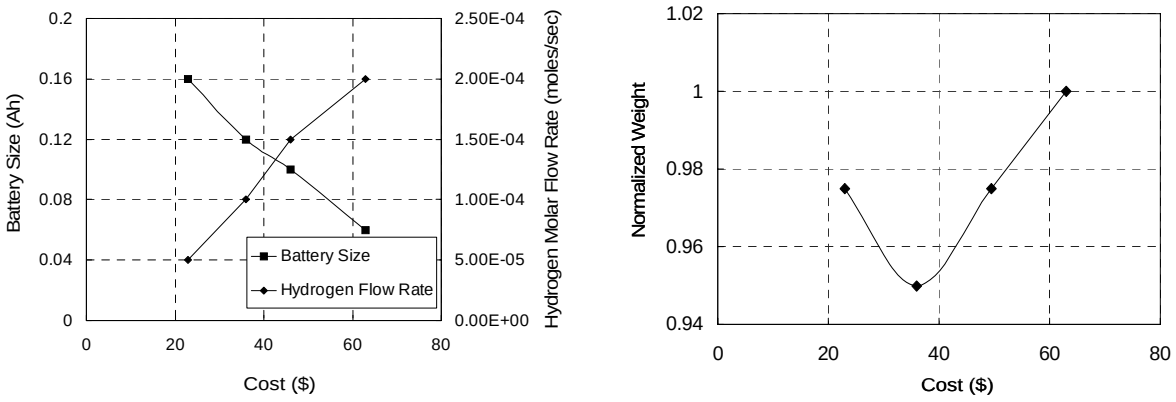

(a)

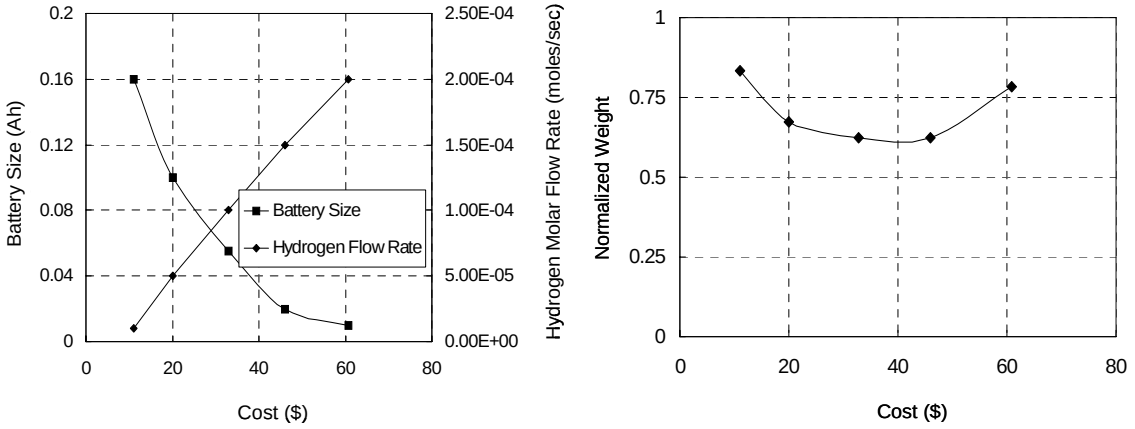

(b)

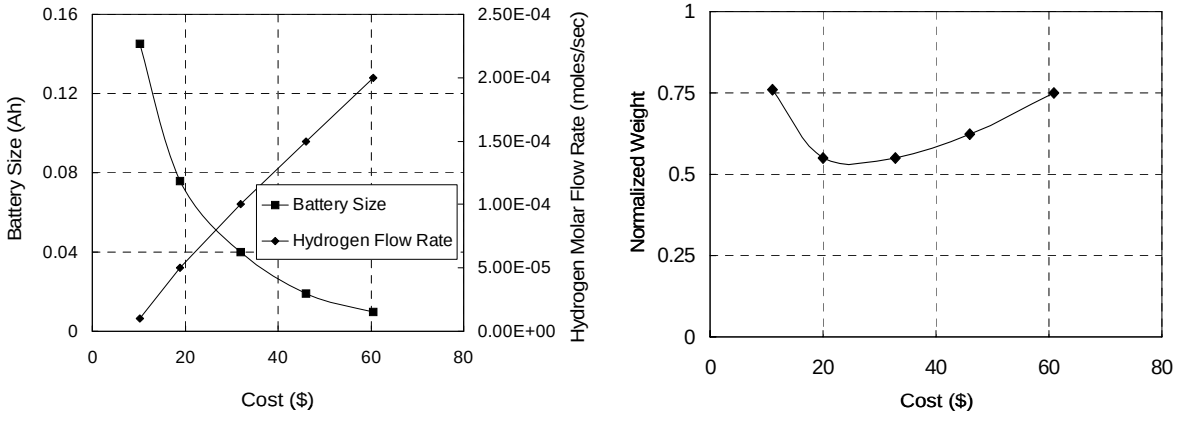

(c)

Fig. 107: Comparison of battery size and hydrogen flow rate with the normalized system cost for a response time of (a) 0.2, (b) 0.3, and (c) 0.35 seconds respectively.

3.4 NOVEL/OPTIMAL PES DESIGN FOR DURABLE SOFC

3.4.1 Components of the Novel PES Topology

The proposed power-electronics system (PES) shown in Fig. 108 has the following power-stage sub-systems: (A) zero-ripple boost converter, (B) high-frequency (HF) inverter, and (C) an AC/AC converter.

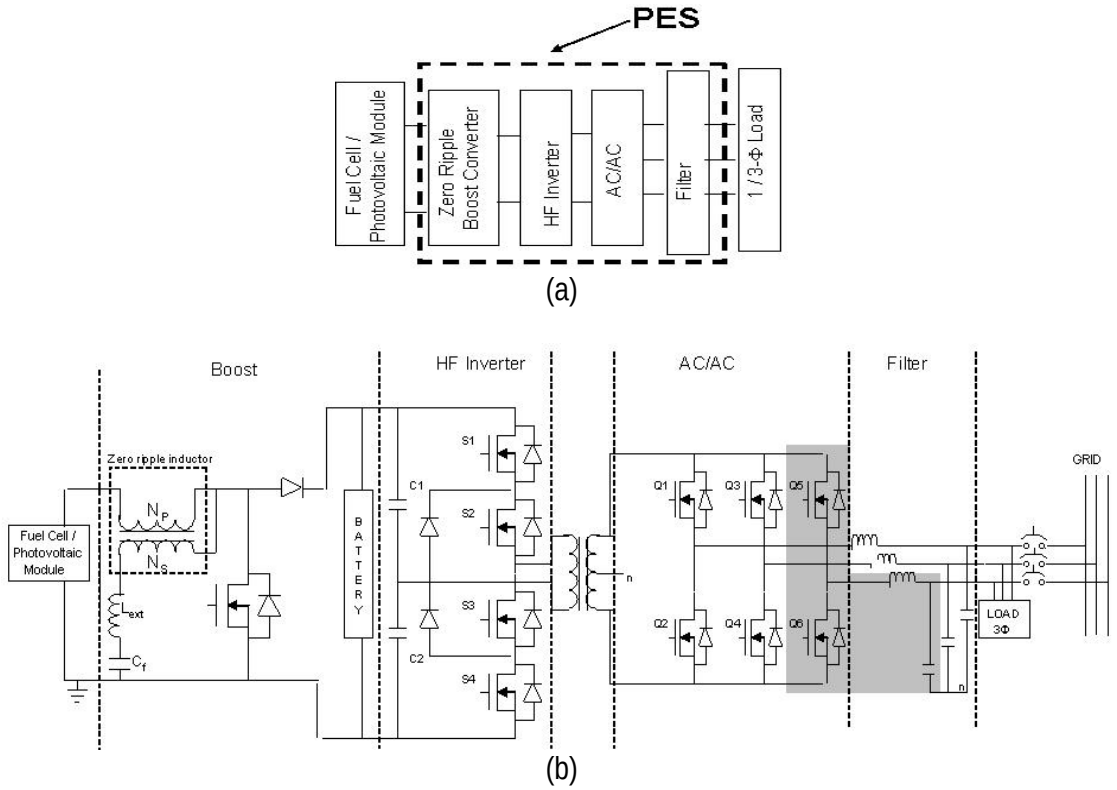

Fig. 108: (a) Block diagram and (b) schematic of the proposed PES[24]. The shaded block in (b) illustrates the extension of the proposed PES to a three-phase output system[25]. *The energy conversion is direct and does not require any bulky capacitors.*

3.4.1.1 Zero-Ripple Boost Converter (ZRBC)

Fig. 109(a) shows the schematic of the proposed ZRBC, which steps up the voltage of a fuel-cell stack or a photovoltaic module (comprising solar cells). *Unlike a conventional boost converter, because the ZRBC*

[24] The actual prototype will have 2 dc-dc converter modules in parallel to get 98% efficiency (Table IV), with each component rated for "half" the output power and all the magnetics for the 2 modules "integrated" on the same core. The cost of fabrication of the PES meets $40/kW.

[25] The proposed PES can be easily extended to applications with power rating higher than 5-10 kW by paralleling the output power modules.

eliminates the switching ripple of the source current, it enhances the durability and life of the fuel cell or photovoltaic module.

The main feature of the ZRBC is the zero-ripple inductor, which is a very tightly coupled (k = 1) ideal transformer. The transformer the primary winding comprises N_1 turns and has a self- inductance L_1 and secondary winding comprises N_2 turns and has a self- inductance L_2. Fig. 109 explains the concept of the zero ripple inductor starting with a non-ideal transformer (k < 1) (Fig. 105(b)). The currents I_{in} and I_{out} are AC currents and voltages V_{in} and V_o are input and output voltages, respectively. In practice k < 1 and the secondary winding will have fewer turns than the primary winding. The ripple gain is zero for an ideal zero ripple inductor, but in practice a very small ripple is there. Typically the voltage across the capacitor C_f is same as the input voltage with a small voltage ripple because of ripple current. The secondary winding carries the ripple current and the primary winding carries the dc current. For a tightly coupled transformer (k = 1) L_{ext} is adjusted to vary the current ripple.

3.4.1.2 High-Frequency (HF) Inverter

The proposed high-frequency inverter (Fig. 110(a)) has 4 switches (S1-S4) just like the conventional high-frequency inverter (as shown in Fig. 81b)). *However, unlike the conventional HF inverter, the switches are arranged in a multilevel topology leading to a 50% lower voltage stress on the power devices and reduced switching losses*. The proposed inverter has a high-frequency transformer (N = 1) with a center-tapped secondary (Fig. 107(b)). Turn-on and turn-off of switches S1 and S2 and S3 and S4 are complementary. During first half of the switching cycle, S1 and S2 are turned on (while S3 and S4 are turned off) allowing the current to ramp up in the primary of the transformer and flow through capacitor C1. In the second half, current flows through capacitor C2, transformer primary, S3 and S4 and hence, the current is negative. *During the off state, the voltage across the switch is equal to half the input voltage and hence, switches with a voltage rating of $V_{in}/2$ could be used. This also leads to lower switching losses.* The zero-current in the transformer primary is due to the freewheeling current in the ac/ac converter switches and the load, as explained in the next section.

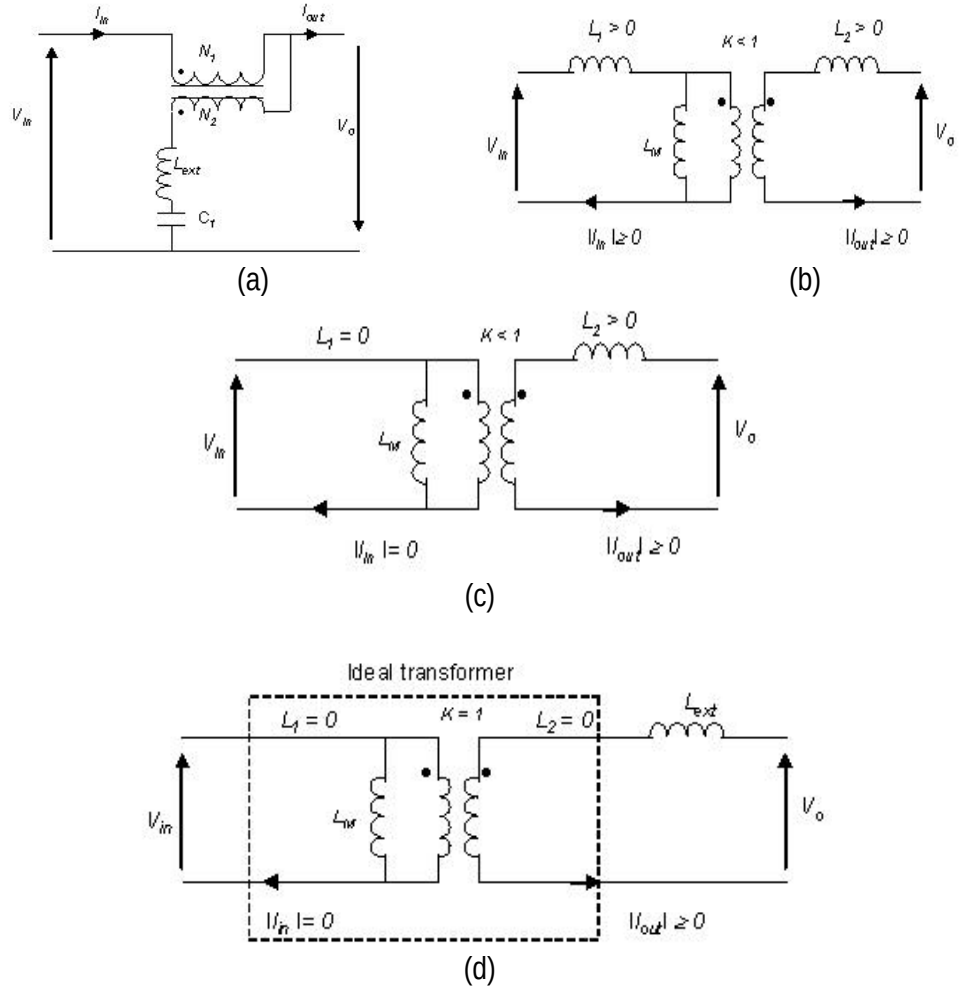

Fig. 109: (a) Zero ripple inductor (an ideal transformer) with an external inductor and a filter capacitor; (b) transformer model showing the leakage inductances (L_1, L_2), magnetizing inductance (L_M); (c) transformer model with zero primary leakage inductance; and (d) ideal transformer model with an external trimming inductor connected to the secondary.

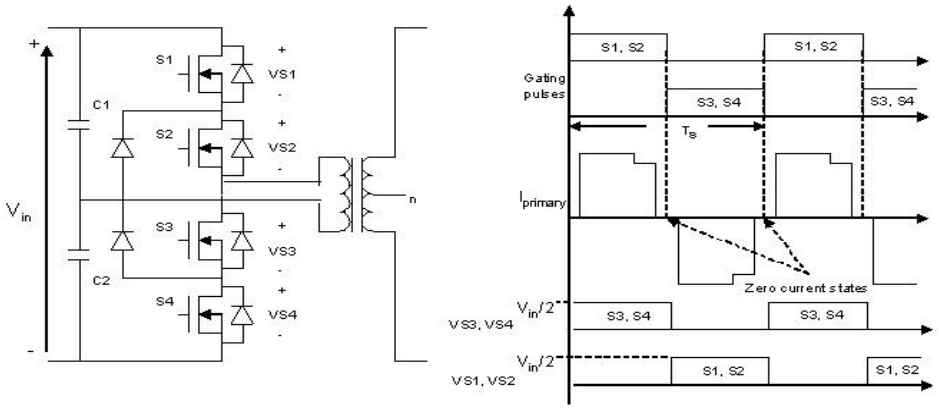

(a)

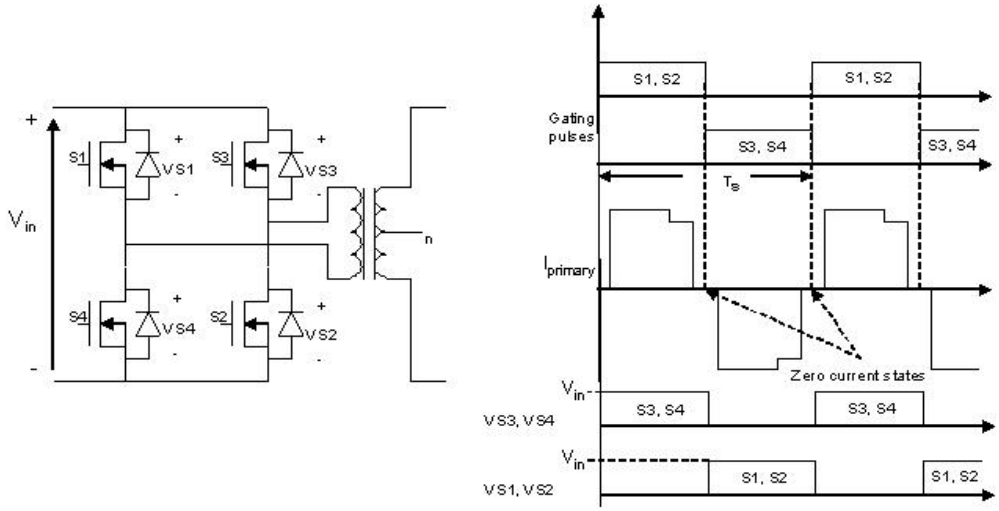

(b)

Fig. 110: (a) Proposed and (b) conventional high-frequency inverters. The proposed HF inverter reduces voltage stress of the power devices by 50%, which also leads to lower switching losses.

3.4.1.3 AC-AC Converter

The AC-AC converter has 4 or 6 bidirectional switches (Q1-Q4 or Q1-Q6 for single or three phase output), with two switches on each leg as shown in Fig. 111(a). Switches on each leg are switched complimentary to each other, so that two switches on the same leg are never turned on at the same time. A simple sine-wave-modulated PWM control is implemented to provide gating pulses for the switches. The scaled output voltages V_a, V_b, and V_c are compared with sinusoidal references, and the resulting control[26] signals V_a*, V_b* and V_c* are fed to the PWM comparator (Figs. 111(b) and 111(c)). The so obtained PWM signal is *XNOR*-ed with the gate signal of switch S1 of the high-frequency inverter. The high-frequency inverter feeds the input of the AC-AC converter.

[26] For a grid-connected system, this voltage-mode controls work as long as the grid is available. However, when the grid fails, the control system changes mode from voltage-mode control to current-mode control, as described in (9).

Zero-Current Switching:

When the AC-AC converter outputs a nonzero voltage, the load current is supplied from the inverter through the high-frequency transformer. When the output voltage of the AC-AC converter is zero, the load current freewheels in the converter. This results in a zero-current condition in the secondary of the transformer, and consequently, a zero-current condition in the primary winding of the transformer. Thus, inverter switches S1 and S2 and S3 and S3 and S4 can, respectively, be turned off/on and on/off under zero-current-switching conditions, leading to reduction in switching losses and increase in efficiency.

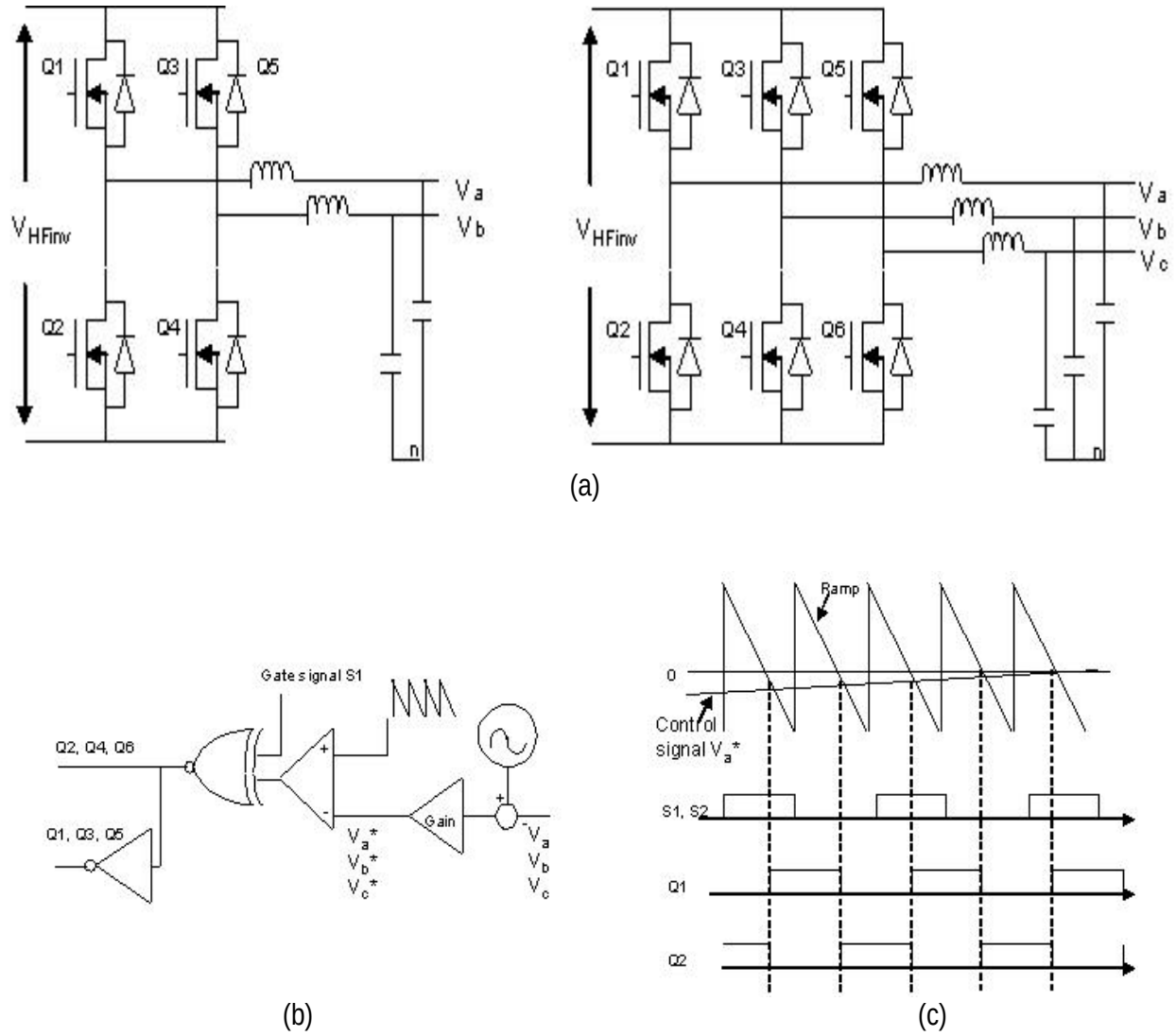

Fig. 111: (a) Schematic of the AC-AC converter topology for single- and three-phase applications; (b) sine-wave-modulated PWM control of phase a of the AC-AC converter; and (c) timing chart showing the scheme for the gating pulses for switches Q1 and Q2.

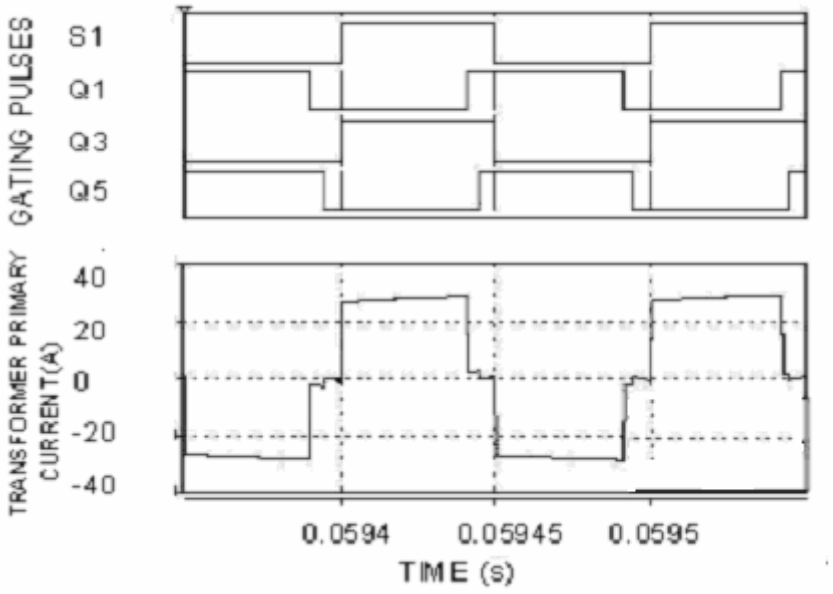

Fig. 112: Current is reduced to zero from a positive value when the load current freewheels (Q1, Q3 and Q5 are simultaneously turned on).

3.4.2 Comparisons of the Proposed PES with the State-of-the-Art

The cost target of $40/kW has been recently recommended for the power electronics by Department of Energy in 2002 for market competitiveness. As such, to this date, no converter has been commercially designed which meets the challenging cost requirement of $40/kW for the proposed converter.

The proposed converter for fuel cell/photovoltaic cell power conditioning system can be divided into three stages for analysis. A dc-dc boost converter is used to step up the input voltage, while a multilevel converter and an ac-ac converter comprise the dc-ac stage. Fig. 113 shows the variation of the efficiency of the various stages of the proposed three-stage converter. The conduction loss of the parallel boost converter decreases with increase in the number of modules, hence the efficiency increases with increase in the number of modules as shown in Fig. 84(a). Peak efficiencies of 96% (for 1 module and 98% for 2 multiphase modules) for the dc-dc boost stage, > 98% for the high-frequency multilevel stage, and > 94.5% (> 93.15%) for the complete dc-ac-ac converter (single- and three-phase output, respectively) is achieved using the proposed PES. Table XVII shows a comparison of the efficiencies of the proposed converter with the state-of-the-art topologies for fuel cell/photovoltaic power conditioning.

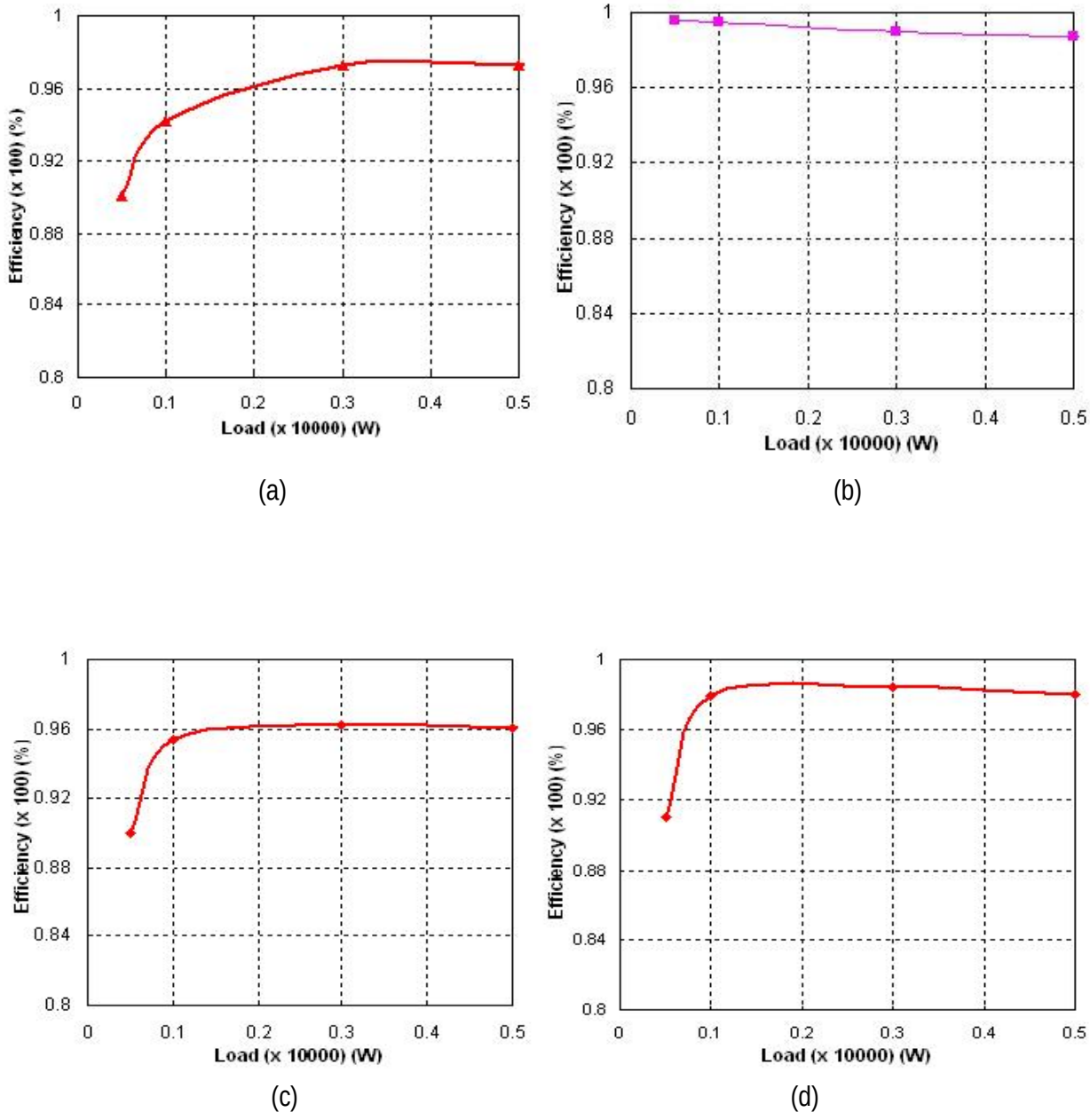

Fig. 113: Calculated efficiencies of the proposed PES: (a) boost converter, (b) multilevel HF inverter, (c) three-phase DC-AC converter, and (d) single-phase dc-ac converter. The overall efficiencies for single- and three-phase PES are shown in Table XVII.

Table XVII: Efficiency comparisons of the proposed PES (and its sub-systems) with the state-of-the-art fuel-cell and photovoltaic power electronics based on data in published literature. Unless specified otherwise, the efficiencies are measured at 5 kW.

System #	No. of output phases	*Efficiency of PES and its sub-systems*			
		DC-DC Boost	*Multilevel DC-DC*	*DC-AC*	*Overall PES*
1 (Lai, 2003)	NA	96% (PC)	NA	NA	NA
2 (Lai, 2003)	NA	94% (PC)	NA	NA	NA
3 (Pinhiero et al., 1993)	NA	NA	92% @1.5 kW (measured)	NA	NA
4 (Anderson et al.)	1	92% @1 kW (measured)	NA	87% @1 kW (measured)	80% @1 kW (measured)
5 (Soter et al., 2002)	1	NP	NA	NP	92% (measured)[27]
6 (Tuckey et al., 2002)	1	NP	NA	NP	90% (calculated)
7 (Ertl et al., 2002)	1	NP	NA	NP	92% (measured)[28]
9 (Kawabata et al., 1990)	3	NP	NA	NP	89% @ 1 kW (measured)
Proposed PES	1	98% (PC)	98.5% (PC)	98% (PC)	94.5 % (PC)
	3	98% (PC)	98.5% (PC)	96.5% (PC)	93.15% (PC)

NA -- Not Applicable NP -- Not Published PC -- Preliminary Calculation

Table XVII indicates that, while the efficiency of the boost stage is comparable to that of the other boost topologies proposed in the literature, a significant improvement in the efficiencies of the dc-ac stage has been achieved. The dc-ac converter discussed in (Kawabata et al., 1990) uses inefficient switching mechanism as shown in Fig. 114. Conduction losses would be significantly higher in these switches than the conventional power MOSFET used in the proposed topology. The multilevel converter in (Pinhiero et al., 1993) operates at a switching frequency of 100 kHz, hence its switching losses is much higher than the proposed converter (which operates at 10 kHz); hence significant improvement in efficiency is obtained.

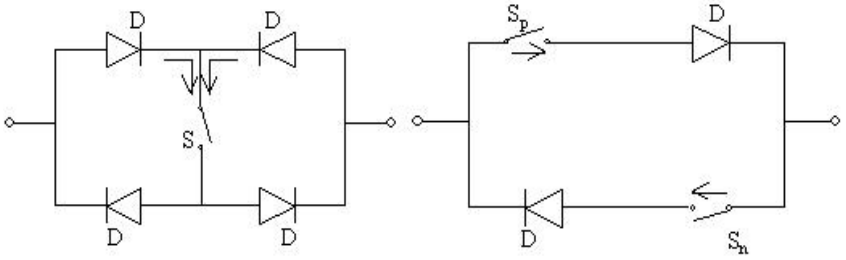

(a) (b)

Fig. 114: Bidirectional switch configuration (a) bridge-type, (b) anti-parallel type, used in the converter topology proposed in (Kawabata et al., 1990).

Exhaustive literature search indicates lack of efficiency data for fuel cell power conditioning system feeding three phase ac loads. Converters discussed in (4-7) are single-phase dc-ac converters for fuel

[27] The converter efficiency does not include the conduction losses owing to the isolation transformers.The converter uses "expensive" silicon carbide diodes and CoolMOS devices. The proposed converter achieves an efficiency of 94% without using such expensive devices.

[28] This converter uses 24 switches (4 modules connected in parallel) instead of 9 for the proposed PES to achieve an output power of 2 kW. As such, it has major reliability issue. Notably, if the proposed PES uses 4 modules in parallel, the overall efficiency will exceed 98%.

cell/photovoltaic cell power conditioning. The converters discussed in (4) and (5) use a voltage source inverter for dc-ac conversion, while the topologies of (5) and (7) use high frequency transformers, similar to the proposed topology. Efficiency >92% were obtained for the single-phase converter discussed in (Soter et al., 2002) using CoolMOS power switches (low on-resistance) for the dc-ac converter and SiC Schottky diodes (low switching losses) for the dc-dc converter. *The proposed three-phase converter has efficiencies comparable to that of the converter in* (Soter et al., 2002) *without using CoolMOS power switches and SiC Schottky diodes, which are more expensive and have reliability problems*.

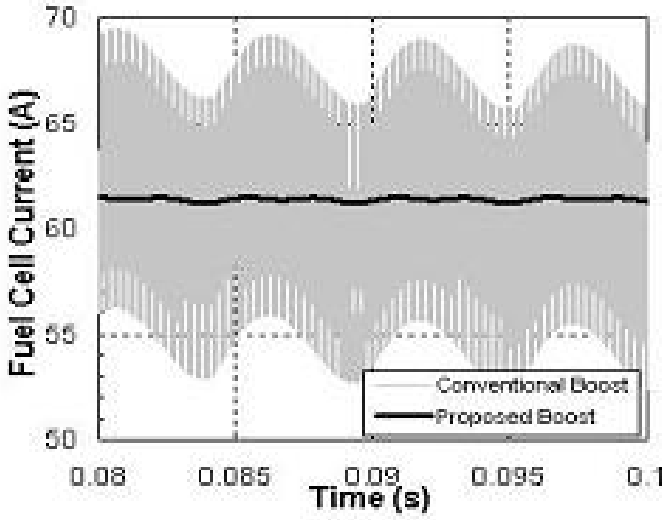

Fig. 115: Comparison of the input current ripple for conventional boost converter and the proposed boost converter

Durability and Reliability:

As shown in Fig. 112(a), the voltage stress on the devices is reduced by a factor of two in the proposed converter, resulting in significant improvement in the reliability of the proposed converter. Currently, there is no commercial fuel- cell or photovoltaic PES that has a multilevel structure.

Reduction in the current ripple is known to have a significant impact on the durability of the renewable power sources (fuel cell / photovoltaic). The conventional approach to minimizing the ripple is to use a large input filter. This adds to the cost, size, and weight of the overall PES. Using a zero-ripple-elimination scheme, the proposed converter significantly reduces the input current switching ripple without using “any bulky input filter”, as shown in Fig. 115. Hence, (as compared to a conventional PES), the proposed converter proposes an improved solution to improve the reliability of the power source.

4. CONCLUSION

Phase I of this project directly addresses several key technical problem areas. To achieve the projected SECA target for SOFC power-conditioning electronics, *following key issues were addressed: (a) cost, (b) durability and reliability of SOFC stack, and (c) energy efficiency and power density*. To come up with durable and reliable solutions for SOFC stack, the industry as well as national labs such as PNNL and NETL are looking for modeling and simulation solutions and software codes/tools, which enable rapid syntheses/designs of a wide range of SOFC based power systems and APUs in a virtual environment to minimize the actual costs and times for development. Towards that end, we have developed a *virtual prototype, based on comprehensive and accurate models of the SOFC stack (SS), BOPS, PES, and application loads to determine potential component and system synthesis/design problems; analyze interactions among the various subsystems and application loads on a system as well as a detailed-component level (e.g., component geometries in general and the internal dynamics and properties of SOFC stacks in particular) during steady-state, transient, and rapid start-up conditions; predict stack lifetimes and component electrical and thermal behavior; investigate control system design; and conduct analyses, investigations, and predictions using mathematical optimization and/or trade-off studies*. The SOFC stack model has already been experimentally validated within an impressive 3-5% of accuracy. The model validation for this novel topology is targeted for Phase II of this project. The BOPS model consists of a set of temporal and spatial thermal, physical, and kinetic component models which include those for steam reformers, compact heat exchangers, methane and air compressors, air expanders, fuel and air storage tanks, steam generators, combustors, mixers, and water pumps. These Phase-I BOPS models based on first principles have been validated with a mix of analytical and experimental results published in the literature. Phase II will see these models updated and/or enhanced and additional component models such as for auto-thermal reforming developed with validation consisting of a mix of results published in the literature, manufacturers' data (e.g., compressor and expander maps), and experimental data from one of our industrial partners (i.e. Ceramatec) and national labs (e.g., PNNL and NETL) and/or industry. However, since there is a significant difference in the time-scales of the subsystems, the simulations using the comprehensive model are time consuming and cumbersome, especially without using powerful and expensive computational tools, a condition which the industry do not want to impose. In order to reduce the computational burden and time, a novel reduced-order hybrid modeling technique has been developed. Its advantages include: (a) resolving significant time-scale variations between the SOFC and BOPS and PES without losing resolution; (b) accomplishing system-level analysis in minutes rather than in days; (c) enabling long-term performance and reliability modeling without losing resolution and without requiring a large computational facility and amount of time; and (d) eliminating the need for calculating difficult analytical equilibrium solutions. Thus, the hybrid modeling technique solves one of the biggest problems in SOFC system simulation and will be of considerable interest to industry and national labs such as PNNL/NETL/ORNL.

We have characterized the electrical feedback effects resulting from PES topology variations and non-ideal, yet affordable control of load fluctuations to the stack. The team has developed pilot dependencies of stack response to load variations. Specific to load-following, pertinent time constants have been established which are functions of stack geometry and flow field characteristics. These cell- and stack-level spatial dependencies also supplement the analytical work of the SECA national labs with regard to load-fluctuation (e.g., Gemmen et al., 2003); in that it superimposes flow field spatial effects upon the P-E-N geometrical sensitivity of SOFC feedback response. Another benefit that is being realized is the response of the stack to bi-modal stimuli. Typically the small number of published results that have highlighted dynamic SOFC response have done so with the control extremes of either invariant (initial conditions) or completely

responsive (i.e., continual design point setting) reactant supply throughout the entire transient episode. The latter part of Phase I will have the realization of a SOFC transient model that does not prescribe possibly unrealistic fuel process conditions, but takes actual fuel process conditions (as simulated within the BOPS model) as an additional transient input to the load demand variance.

We demonstrate that on a short time frame, fast- (switching) scale current ripple imposed by the power-electronics subsystem (PES) has negligible impact on the SOFC. However, the impact of the switching ripple in a longer time frame (> 40000 hours for stationary applications and > 5000 hours for transportation applications) needs further analysis. Low-frequency current ripple with large magnitudes result in electrically induced thermal variations and variations in hydrogen utilizations, both of which have a direct impact on the performance and efficiency and life of a SOFC stack. Again, long-term studies are needed for life predictions. We also demonstrate the effect of PES control strategies on the performance of the SOFC stack. For the self-commutated PES topology, space-vector modulation (SVM), as compared to sine-wave pulse width modulation (SPWM), of the inverter, yields faster dynamic response under load-transients. While the superior dynamic-performance capability of SVM for three-phase inverters is well known, what is often overlooked in such analysis is the need for a stiff DC voltage source. As such, for SOFC, which is not a stiff DC voltage source, the enhanced performance of SVM comes at the cost of higher localized current densities and fuel-flow rates, both of which may be detrimental to the SOFC stack. Non-uniformities during load transients will result in localized oxidization of SOFC electrolyte material, which could result in reduced conductivity because of the formation of $LaZr_2O_7$. For the boost stage, we compare two different control strategies, one based on a simple linear controller and the other a novel nonlinear hybrid controller for a single/parallel DC-DC boost (or a buck/boost-derived/buck-derived) converter as well as single/three phase DC-AC converters by combining integral-variable-structure control (IVSC) scheme and multiple-sliding-surface control (MSSC). *The hybrid control scheme for the PES has several advantages over conventional controller and will be of significant benefit to the industry. First, it is easy to design because sliding surface(s) is (are) independently controlled. Second, the controller yields excellent steady-state and transient responses even under parametric variations and under perturbations of SOFC stack voltage and load. Third, the controller eliminates the bus-voltage error with a reduced control effort. Fourth, the integrators in the control scheme can reduce the impact of very high-frequency dynamics due to parasitics on an experimental closed-loop system. Fifth, the control scheme within the boundary layer enables operation of the converter with a finite switching frequency. Sixth, the converter modules can be operated in interleaving or synchronicity modes*. SOFC power conditioning system load transients were also shown to lead to nonuniform thermal distribution. Depending on how high the temperature is at any spatial location within the stack/cell, it can have a negative impact on the material properties and microcrack densities of the SOFC and hence, on the durability of the SOFC. Currently, we are investigating the long-term effects of electrical feedbacks on the SOFC durability and performance, to enable low-cost power-electronics design and SOFC power-system optimization, both of which are of importance to the SOFC manufacturers and PES designers.

We also investigate the effects of variations in the SOFC output voltage on the PES transients and stability by using the hybrid-analysis methodology outlined in Section 3.1.2.2.1. Initially, we emulate the SOFC output voltage (by incorporating the effect of the BOPS) as a current-dependent harmonic voltage source and then, using this source conduct dynamics and stability analyses. Because the PES is a nonlinear discontinuous system, nonlinear methodologies such as bifurcation algorithms have been developed. Advanced bifurcation algorithms are used to predict the global dynamics, which is important analyzing the effectiveness of control design, effects of parametric variations, and disturbance-rejection capability of a PES. *Incorporation of such advanced analytical methodologies and computation techniques will provide design loopholes to the industry even before building an expensive SOFC power system*. Our study indicates that the drop in the PES input voltage under high-load conditions (since the BOPS cannot

respond quickly to changes in load, the SOFC voltage depends on the current drawn) could lead to unwanted dynamics in the PES. Occurrence of nonlinear phenomena like subharmonics and chaos in the boost stage is observed. Since the PES for fuel cell applications is expected to be robust for all operating conditions, the bifurcation analysis shows that there is a necessity of operating the converter away from the boundaries marking different asymptotic behaviors. This study can be used to define the operating conditions of the fuel cell for a particular application.

Finally, a novel, efficient, reliable fuel cell PES topology is realized in order to address the issues of SOFC stack reliability keeping in mind the cost constraints[29]. The issue of durability of the SOFC stack is of key importance. Recent preliminary studies by National Energy Technology Laboratory (NETL) have shown that power-electronics, which interfaces directly to the cell array and stacks, has a significant impact on the long-term durability (life) and reliable energy efficiency of the SOFC. Energy-conversion efficiency (of the power-conditioning system) for SOFC is of significant importance primarily in light of the lower kW/dollar of some of the conventional energy systems, a selective few of which (e.g., combined cycle), incidentally, have achieved near-comparable efficiencies in recent years. Today, the efficiencies of power–electronics conversion technology have exceeded 90%; however, under severe cost constraints, most of these technologies are not economically viable. As such, *achieving high power-conversion efficiency at significantly low cost for the viability of SOFC based APUs and is a daunting challenge*. *Our Phase-I effort has led to the design of a novel cost-effective, zero-ripple, high efficiency, and high-power-density PES, which can meet $40/kW price target in volume production and which can enhance the durability of SOFC stack.* The proposed novel PES achieves (a) 98% efficiency for dc-dc boost converter (using multiphasing) at 5 kW (full load), (b) over 94% (> 93%) efficiency at full load for single-phase (three-phase) output, (c) elimination of the ripple current drawn from the SOFC stack without using any bulky input filter, thereby significantly enhancing the life and energy efficiency of the SOFC stack (d) 50% reduction in voltage stresses for the intermediate inverter, which leads to higher reliability, (e) direct power conversion, i.e., does not require any intermediate energy-storage bulk capacitors, thereby significantly reducing the size of the power-electronics package. A comparison of the performance of the proposed converter with the state-of-the art (as detailed in Section 3.4 of this report) clearly shows the improved performance of the proposed topology.

[29] Currently, the higher costs for SOFC energy systems (as compared to conventional energy systems) are primarily due to the energy sources (fuel cells) and the power systems. *A big part of the power-systems cost is due to the power-electronics technology*. DOE-sponsored study has shown that unless the cost of power-electronics for fuel-cell power system reduces to $400/kW ($40/kW for PES), such an energy system may not be economically viable.

REFERENCES

1. Acharya, K., Mazumder, S.K., Burra, R., Williams, R., Haynes, C., 2003, "System-interaction analyses of solid-oxide fuel cell (SOFC) power-conditioning system", in press, *Proceedings of IEEE IAS Conference.*
2. Achenbach, E., 1995, "Response of a solid oxide fuel cell to load change," *Journal of Power Sources*, vol. 57, pp. 105-109.
3. Adelman, S. T., Hoffman, M. A., and Baughn, J. W., 1995, "A methane-steam reformer for a basic chemically recuperated gas turbine", *Journal of Engineering for Gas Turbines and Power*, vol. 117, pp. 16-23, January.
4. Air Products and Chemicals, Inc., 2001, "Hydrocarbon separation and purification", http://www.airproducts.com/hydrocarbon.
5. Alatiqi, I. M., Meziou, A. M., and Gasmelseed, G. A., 1989, "Modeling, simulation, and sensitivity analysis of steam-methane reformers", *International Journal of Hydrogen Energy*, vol. 14, No. 4, pp. 241-256.
6. Andersen G.K., Klumpner C., Kjaer S.B., and Blaabjerg F., "A new green power inverter for fuel cells".
7. Arthur D. Little, 1994, *Multi-Fuel Reformers for Fuel Cells Used in Transportation*, Final Report for the U.S. Department of Energy, Report No. DOE/CE/50343-2, Cambridge, Massachusetts.
8. Azevedo, J. L. T. and Cunha, J., 2000, "Modeling the integration of a compact plate steam reformer in a fuel cell system", *Journal of Power Sources*, vol. 86, pp. 515-522.
9. Bagotsky, V.S., 1993, *Fundamentals of Electrochemistry*, Plenum, New York.
10. Banerjee, S. and Chakrabarty, K., 1998, "Nonlinear modeling and bifurcations in the boost converter", *IEEE Transactions on Power Electronics*, vol. 13, no. 2, pp. 252-260.
11. Bessette, N., 1994, *Modeling and Simulation for Solid Oxide Fuel Cell Power Systems*, Ph.D. Thesis, Georgia Institute of Technology, Atlanta, Georgia.
12. Bodrov, N.M., Apel'baum, L.O.,Temkin, M.I., 1964, Kinet. Katal. 5(4), pp. 696.
13. Bodrov, N.M., Apel'baum, L.O.,Temkin, M.I., 1967, Kinet. Katal. 8(4), pp. 821.
14. Boehm, R. F., 1987, *Design Analysis of Thermal Systems*, John Wiley and Sons, Inc., New York.
15. Deane, J.H.B. and Hamill, D.C., 1990, "Instability, subharmonics, and chaos in power electronic circuits," *IEEE Trans. Power Electronics,* vol. 5, pp. 260–268.
16. Deane, J.H.B. and Hamill, D.C., 1991, "Chaotic behavior in current mode controlled dc–dc converter," *Electron. Lett.,* vol. 27, no. 13, pp. 1172–1173.
17. Deane, J.H.B., 1992, "Chaos in a current-mode controlled boost dc–dc converter," *IEEE Trans. Circuits Syst. 1,* vol. 39, pp. 680–683.
18. DeWitt, D. P. and Incropera, F. P., 1990, Fundamentals of Heat and Mass Transfer, 3rd edition, John Wiley and Sons, Inc., New York.
19. Drakunov, S. V., Izosimov, D. B., Lukajanov, A. G., Utkin, V. and Utkin, V. I., 1990, "Block control principle: Part I," *Automat. Remote Contol.*, vol. 51, no. 5, pp. 38–46.
20. Eaton, B., von Spakovsky, M. R., Ellis, M. W., Nelson, D. J., Olsommer, B., Siegel, N., 2001, "One-dimensional, transient model of heat, mass, and charge transfer in a proton exchange membrane", *International Mechanical Engineering Congress and Exposition – IMECE'2001, ASME*, N.Y., N.Y.
21. Ellis, M.W., von Spakovsky, M.R., and Nelson, D.J., 2001, "Fuel cell systems: efficient, flexible energy conversion for the 21st century", *Proceedings of the IEEE*, vol. 89, no. 12, pp. 1808-1818.
22. El-Tamaly, A.M., Enjeti, P.N., and El -Tamaly, H.H., 2000, "An improved approach to reduce harmonics in the utility interface of wind, photovoltaic and fuel cell power systems", *IEEE Applied Power Electronics Conference*, pp. 1059-1065.

23. Erdle, E., Gross, J., Müller, H.G., Müller, W.J.C., Reusch, H.-J., and Sonnenschein, R., 1991. *Proc. 2nd. Intl. Symp. on SOFCs*, Singhal et. al. eds., Athens, Greece, pp. 265.
24. Ertl H., Kolar J.W., and Zach F.C., 2002, "A novel multicell dc-ac converter for applications in renewable energy systems", *IEEE Trans. Industrial Electronics*, vol. 49 pp. 1048-1057.
25. Escombe, F. M., 1995, *Fuel Cells: Applications and Opportunities - Executive Summary*, ESCOVALE Consultancy Services, Report No. 5020, Surrey, United Kingdom, January.
26. Ferguson, J.R., 1991. *Proc. 2nd. Intl. Symp. on SOFCs*, Singhal et. al. eds., Athens, Greece, pp. 305.
27. *Fuel Cell Handbook*, 2000, 5th edition, Office of Fossil Energy, National Energy Technology Laboratory, Morgantown, West Virginia, October.
28. Gemmen, R., 2001 "Analysis for the effect of inverter ripple current on fuel cell operating condition", *Proceedings of IMECE: ASME International Mechanical Engineering Congress and Exposition*.
29. George, R.A. and Bessette, N.F., 1998, "Reducing the Manufacturing Cost of Tubular SOFC Technology," *Journal of Power Sources*, vol. 71, pp. 131-137.
30. Georgopoulos, N., von Spakovsky, M. R., and Muñoz, J. R., 2002, "Application of a decomposition strategy to the optimal synthesis/design and operation of a fuel cell based total energy system for residential applications", *International Mechanical Engineering Congress and Exposition – IMECE'2002*, ASME, N.Y., N.Y., November.
31. Godat, J., 2002, *Thermodynamic Modeling and Analysis of a Stationary Solid Oxide Fuel Cell (SOFC) System*, diplôme thesis, advisor: M.R. von Spakovsky, Energy Management Institute, M. E. Dept., Virginia Polytechnic Institute and State University, Blacksburg, VA.
32. *gPROMS*, 2000, User Guide, version 2.2, Process Systems Enterprise Ltd., London, United Kingdom.
33. Gunes, M. B., 2001, *Investigation of a Fuel Cell Based Total Energy System for Residential Applications*, M.S. Thesis, Department of Mechanical Engineering, Virginia Polytechnic Institute and State University, Blacksburg, Virginia.
34. Gyftopoulos, E. P. and Beretta, G. P., 1991, Thermodynamics: Foundations and Applications, Macmillan Publishing Company, New York.
35. Hamill, D.C., 1995, "Power electronics: A field rich in nonlinear dynamics", *Nonlinear Dynamics of Electronic Systems,* Dublin, Ireland.
36. Hartvigsen, J., 2002, "A transient model of solid-oxide fuel cell operation in a high cycle regime of inverter induced current variation", *Fatigue*.
37. Haynes, C., 1999, *Simulation of Tubular Solid Oxide Fuel Cell Behavior for Integration Into Gas Turbine Cycles*, Ph.D. Thesis, Georgia Institute of Technology, Atlanta.
38. Haynes, C.L. and Wepfer, W.J., 2000 "Design for power of a commercial-grade tubular solid oxide fuel cell," *Energy Conversion and Management, v*ol. 41, pp. 1123-1139 (*Erratum* 2063-2067).
39. Haynes, C. and Wepfer, W.J., "Characterizing heat transfer within a commercial-grade tubular solid oxide fuel cell for enhanced thermal management" *International Journal of Hydrogen Energy*, vol. 26, pp. 369-379.
40. Hirschenhofer, J.H., Stauffer, D.B., and Engelman, R.R., 1994, *Fuel Cells: A Handbook* (rev. 3), US DOE Office of Fossil Energy, Morgantown.
41. Holtz, J., Lotzkat, W. and Khambadkone, A.M., 1993, "On continuous control of PWM inverters in the overmodulation range including the six-step mode", *IEEE Transactions on Power Electronics*, vol. 8, 546-553.
42. Hsiao, Y.C. and Selman, J.R., "The degradation of SOFC electrodes", *Proceedings of Solid State Ionics*, vol. 98, pp. 33-38.
43. Huang, X. and Reifsnider, K., 2001, "Modeling long-term performance of solid oxide fuel cells: A phenomenological approach".

44. JANAF Thermochemical Tables, 1971, 2nd edition, Stull, D. R. and Prophet, H. (Project Directors), NSRDS-NBS37.
45. Kakaç, S. and Liu, H., 1998, *Heat exchangers: Selection, Rating, and Thermal Design*, CRC Press, Boca Raton, Florida.
46. Kanamura,K., Shoji,Y., and Zen-ichiro, T., 1989, "Temperature Distribution in Tubular Solid Oxide Fuel Cell," *Proceedings of the First International Symposium on Solid Oxide Fuel Cells*, S.C. Singhal, ed., Electrochemical Society, Pennington, pp. 293-303.
47. Kandlikar, S.G., 1990, "A General Correlation for Saturated Two-Phase Flow Boiling Heat Transfer Inside Horizontal and Vertical Tubes", J. Heat Transfer, Vol. 112, pp.219 – 228.
48. He, W., 1997, "Dynamic Performance of a Reformer for Molten Carbonate Fuel Cell Power Generation Systems", *Fuel Processing Technology*, Vol. 53, pp. 99-113, July.
49. Synetix Product Brochure, 2001, "Refineries: Product Brochures and Operating Manuals", http://www.syntix.com/refineries
50. Kawabata, T., Honjo, K., Sashida, N., Sanada, K., and Koyama, M., 1990, "High frequency link dc/ac converter with PWM cycloconverter", *IEEE Industry Applications Society Conference*, pp. 1119-1124.
51. Kays, W. M. and London, A. L., 1998, *Compact Heat Exchangers*, Krieger Publishing Company, Malabar, Florida.
52. Keiski, R. L., Desponds, O., Chang, Y. –F., and Somorjai, G. A., 1993, "Kinetics of the Water-Gas Shift Reaction over Several Alkane Activation and Water-Gas Shift Catalysts", *Applied Catalysis A*, Vol. 101, No. 2, pp. 317-338, August.
53. Kern, D. Q., 1950, *Process Heat Transfer*, McGraw-Hill, New York.
54. *Key Issues in Developing Renewables*, 1997, International Energy Agency Report.
55. Khandkar, A., Hartvigsen, J., and Elangovan, S., 1998,"Selection of SOFC stack operating point for optimal balance of efficiency and power" *Proceedings of the Third European Solid-oxide Fuel Cell Forum*.
56. Kim, J.W., Virkar, A.V., Fung, K.Z., Mehta, K., and Singhal, S.C., 1999, "Polarization Effects in Intermediate Temperature, Anode-Supported Solid Oxide Fuel Cells," *Journal of the Electrochemical Society*, vol. 146, no. 1, pp. 69-78.
57. Konishi, Y., Feng, Y.L., and Nakaoka, M, 1998, "Three-phase voltage-fed inverter with new conceptual optimum PWM strategy for high-power applications", *Power Electronics and Variable Speed Drives Conference*, pp. 600-605.
58. Kordesch, K. and Simader, G., 1996, *Fuel Cells and Their Applications*, VCH Publishers, Inc., New York.
59. Lai J., 2003, "A high-efficiency low-cost dc-dc converter for SOFC", *SECA Core Technology Program Review Meeting.*
60. Lane, R. M., Fry M. R., and Baker J. N., 1995, *Initial Assessment of Fuel Cells*, IEA Greenhouse Gas R&D Programme, EA Technology, Report No. PH2/1, Gloucestershire, United Kingdom.
61. Lee, F. C., 1990, *Modeling, Analysis, and Design of PWM Converter*, Virginia Power Electronic Center Publications Series, vol. 2, Blacksburg, Virginia.
62. Maskalick, N.J., 1989, "Design and performance of tubular solid oxide fuel cells," *Proceedings of the First International Symposium on Solid Oxide Fuel Cells*, Hollywood, FL.
63. Mazumder, S.K., Burra, R., Acharya, K., Von Spakovsky, M.R., Nelson, D.J., Rancruel, D., Haynes, C., Williams, R., 2003, "Development of a comprehensive simulation platform to investigate system interactions among solid-oxide fuel cell, power-conditioning systems, and application loads", *Proceedings of ASME First International Conference on Fuel Cell Science, Engineering and Technology.*

64. Mazumder, S. K., Nayfeh, A. H., and Boroyevich, D., 2001a, “Theoretical and experimental investigation of the fast- and slow-scale instabilities of a dc-dc converter”, *IEEE Transactions on Power Electronics*, vol. 16, no. 2, pp. 201-216.
65. Mazumder, S. K., Nayfeh, A. H., and Boroyevich, D., 2001b, “Nonlinear analysis of power-electronic converters: towards stable distributed power systems”, Invited Paper, *International Conference on Energy, Automation, and Information Technology*.
66. Mazumder, S. K., Nayfeh, A. H., and Boroyevich, D., 2001c, “Nonlinear dynamics and stability analysis of parallel dc-dc converters including the effect of saturation”, *JVC: Special Issue on Nonlinear Dynamics and Control*, in press.
67. Mazumder, S. K., Nayfeh, A. H., and Boroyevich, D., 2001d, “Robust control of parallel dc-dc buck converters by combing the concepts of integral-variable-structure- and multiple-sliding-surface control schemes”, *IEEE Transactions on Power Electronics*, to be published in March 2002.
68. Middlebrook, R. D. and Cuk, S., 1977a, “A general unified approach to modeling switching-converter power stages”, *IEEE Power Electronics Specialists Conference*, pp. 521-550.
69. Middlebrook, R. D. and Cuk, S., 1977b, “A general unified approach to modeling switching dc to dc converters in discontinuous conduction mode”, *IEEE Power Electronic Specialists Conference*, pp. 36-57.
70. Minh, T.Q. and Takahashi, T., 1995, *Science and Technology of Ceramic Fuel Cells*, Elsevier, Amsterdam.
71. Muñoz, J. R. and von Spakovsky, M. R., 2000a, “An integrated thermoeconomic modeling and optimization strategy for aircraft/aerospace energy system sesign”, *Efficiency, Costs, Optimization, Simulation and Environmental Aspects of Energy Systems (ECOS ‘00)*, ASME, Twente University, Netherlands, July 5-7.
72. Murray, A. P. and Snyder, T. S., 1985, “Steam-methane reformer kinetic computer model with heat transfer and geometry options”, Industrial Engineering Chemical Process Design and Development, vol. 24, no. 2, pp. 289.
73. NAHB Research Center, Inc. report for PATH Inc., *Review of Residential Electrical Energy Use Data.*
74. Naik, R., Mohan, N., Rogers, M., and Bulawka, A., 1995, “A novel grid interface, optimized for utility-scale applications of photovoltaic, wind-electric, and fuel-cell systems”, *IEEE Transactions on Power Delivery*, vol. 10, no. 4, pp. 1920-1926.
75. Nisancogliu, K., 1989, "Ohmic losses in natural gas fuelled solid oxide fuel cells and systems", *Proceedings of the IEA Workshop on Mathematical Modelling, Charmey*, Switzerland, pp. 87-98.
76. Padulles, J., Ault, G. W., and McDonald, J. R., 2000, “An integrated SOFC plant dynamic model for power systems simulation”, *Journal of Power Sources*, pp. 495-500.
77. Pinhiero J.R. and Barbi I., 1993, “The three-level ZVS-PWM dc-to-dc converter”, *IEEE Trans. Power Electronics*, vol. 8, pp 486-492.
78. Prentice, G., 1991, *Electrochemical Engineering Principles*, Prentice-Hall, Englewood Cliffs.
79. Qu, J., Fedorov, A., Haynes, C., 2003, “An Integrated approach to modeling and mitigating SOFC failure”, *Monthly Project Highlight Reported submitted to National Energy Technology Laboratory*.
80. Raissi, A.T., 1997, “Current technology of fuel cell systems”, *Proceedings of the 32nd Intersociety Energy Conversion Engineering Conference*, vol. 3, pp. 1953-1957.
81. Rase, H. F., 1977, *Chemical Reactor Design for Process Plants*, John Wiley and Sons, Inc., New York.
82. Shah, R.S., 1981, Compact Heat Exchanger Design Procedure, in Heat Exchangers, Thermal-Hydraulic Fundamentals and Design, S. Kakac, A.E. Bergles and F. Matinger editors, Hemisphere Publishing Corporation, pp 495-536.
83. Soter S. and Buchhold S., 2002, “Adaptable inverter for injection of fuel cell and photovoltaic power”, *Power Conversion Conference*, vol. 3, pp: 1453 -1455.

84. Stefanovic, V.R. and Vukosavic, S.N., 1992, “Space-vector PWM voltage control with optimized switching strategy”, *IEEE IAS Annual Meeting*, pp. 1025-1033.
85. Travis, R.P., 2003, “Issues affecting the mechanical integrity of fuel cells”, *Proceedings of ASME First International Conference on Fuel Cell*.
86. Tse, C.K., 1994, “Flip bifurcation and chaos in three-state boost switching regulators,” *IEEE Trans. Circuits Syst. I,* vol. 41, pp. 16–23.
87. Tuckey A.M. and Krase J.N., 2002 “A low-cost inverter for domestic fuel cell applications”, *Proceedings of IEEE PESC Conference*, vol. 1, pp. 339-346.
88. Virkar, A.V., Kim, J.W., Mehta, K., and Fung, K.Z., “Low temperature, high performance, planar solid oxide fuel cells and stacks”, *www.netl.doe.gov/publications/proceedings/97/97fc/FC6-5.PDF*.
89. Wood, J.R., 1989 “Chaos: A real phenomenon in power electronics,” *IEEE Applied Power Electronics Conference.,* Baltimore, MD.
90. Xu, J. and Froment, G. F., 1989, “Methane Steam Reforming, Methanation and Water-Gas Shift: I. Intrinsic Kinetics”, *AIChE Journal*, Vol. 35, No. 1, pp. 88-96, January.
91. Xu, J. and Froment, G. F., 1989, “Methane Steam Reforming: II. Diffusional Limitations and Reactor Simulation”, *AIChE Journal*, vol. 35, No. 1, pp. 97-103, January.
92. Yentekakis, I.V., Neophytides, S., Seimanides, S., and Vayenas, C.G., 1991. *Proc. 2nd. Intl. Symp. on SOFCs*, Singhal et. al. eds., Athens, Greece.
93. Rancruel, D. F. 2003 “A Decomposition Strategy Based on Thermoeconomic Isolation Applied to the Optimal Synthesis/Design and Operation of an Advanced Fighter Aircraft System”, Master thesis, Virginia Polytechnic Institute and State University, Blacksburg,VA.
94. Rancruel, D. F., von Spakovsky, MR, 2003, “A Decomposition Strategy Applied to the Optimal Synthesis/Design and Operation of an Advanced Fighter Aircraft System: A Comparison with and Without Airframe Degrees of Freedom”, Proceedings of the IMECE, Washington, D.C., November 16-21, 2003.
95. Rancruel, D. F., von Spakovsky, MR, 2003, “Decomposition With Thermoeconomic Isolation Applied To The Optimal Synthesis/Design Of An Advanced Fighter Aircraft System”. The International Journal of Thermodynamics, October 2003.

APENDICES

Appendix A. SOFC Fortran Code

```
!  sofctrans_ver5.f90
!
!  FUNCTIONS:
! sofctrans_ver5      - Entry point of console application.
!

!*****************************************************************************
!
!  PROGRAM: sofctrans_ver5
!
!  PURPOSE:  To characterize the SOFC stack
!       based upon current profile change events.
!       External reformation is presumed.
!*****************************************************************************

program sofctrans_ver5

  implicit none

  ! Variables from input files
  ! Fuel stream mole fractions
  Real xh2in,xh2oin,xcoin,xco2in,xn2fsin
  Real fuelutil,nos,pnot,current,milliseconds
  ! NOS: Number of stoichs or inverse equivalence ratio. Based upon ratio of air-to-fuel. >1.3
  ! Pnot: Pressurization of the cell (atm) >2atm
  ! FuelUtil: Nominal fuel utilization percentage <85%
  ! Current: Initial stead-state current (amps).  Ranges from 750-1500A for TSOFC in triad
parallel

  ! Temp variable to test if any mole fraction parameters equal zero
  Integer test

  test=0

  !Get operating parameters
  Open(1,file='c:\fctest\data1.txt',status='old')
```

```
  Read(1,*) xh2in,xcoin,xh2oin,xco2in,xn2fsin,nos,pnot,fuelutil,current
  Close(1)

  if ((xH2in.eq.0).or.(xCOin.eq.0)) test=1
  if ((xCO2in.eq.0).or.(xH2Oin.eq.0)) test=1
  if (xN2FSin.eq.0) test=1

  if (test.eq.1) then
    Print *,'Mole fractions for fuel stream must be greater than zero for stablility.'
    Print *,'Press ENTER key to end.'
    Read (*,*)
    Stop
  end if   ! If statement to test for mole fractions equal to zero

  ! Read in the total number of timesteps to use
  Open(1,file='c:\fctest\data2.txt',status='old')
  Read(1,*) milliseconds

  !Call the processing module
  !Only the inputs are sent.  The subprogram outputs will go to files.
  Call Openfiles()
  Call Processor(xh2in,xcoin,xh2oin,xco2in,xn2fsin,nos,pnot,fuelutil,current,milliseconds)
  Call Closefiles()

  Print *,'Simulation completed.'
  Print *,'Press enter key to end.'
  Read (*,*)

end program sofctrans_ver5

!***********************************************************************
!***********************************************************************
Subroutine Processor(xh2in,xcoin,xh2oin,xco2in,xn2fsin,nos,pnot,fuelutil,current,milliseconds)

  !Declare dummy variables
  Real xh2in,xh2oin,xcoin,xco2in,xn2fsin
  Real fuelutil,nos,pnot,current,milliseconds

  !Declare variables for other subroutine
  Integer number,event
  Real deltax,deltaxlastslice,tbulk,timeincrement,volt,time,fueluse

  !Dimension is the axial position; the elements are slices
  Real,Dimension (1:5000)::emfstart,nn2fs,nco,nco2,nh2,nh2o,nn2,no2,ntot
  Real,Dimension (1:milliseconds)::currentprofile
```

```
  !Read in current profile with numberevents total number of items
  Do event=1,milliseconds
    Read(1,*) currentprofile(event)
  End Do
  Close(1)

  !Find the steady-state environment of the system at the current currentprofile(1)
  Print *,'Target steady-state current: ',current

  Call
Electrochemistry(deltax,deltaxlastslice,number,current,pnot,fuelutil,nos,tbulk,volt,timeincrement,
emfstart,xh2in,xcoin,xh2oin,xco2in,xn2fsin,nh2,nco,nh2o,nco2,nn2fs,no2,nn2,ntot)

  Print *,'Steady-state bundle voltage: ',volt*8
  print *,'NH2 initial SS: ',nh2(1),' NH2 final SS: ',nh2(number+1)
  Print *,'Total slices: ',number
  print *,'_____'

  !Set inital time to zero
  time=0

  ! Find the transient state of the cell
  Call
Electrotransient(deltax,deltaxlastslice,number,emfstart,pnot,volt,time,timeincrement,milliseconds
,currentprofile,nn2fs,nco,nco2,nh2,nh2o,nn2,no2)

End Subroutine Processor


!#############################################################################
#
!#############################################################################
#
Subroutine
Electrochemistry(deltax,deltaxlastslice,number,itarget,pnot,fuelutil,nos,tbulk,volt,timeincrement,
emfstart,xh2in,xcoin,xh2oin,xco2in,xn2fsin,nh2,nco,nh2o,nco2,nn2fs,no2,nn2,ntot)

  ! Subroutine to calculate to the steady-state of the fuel cell stack
  Implicit None

  ! Declare dummy variables
  Real deltax,deltaxlastslice,itarget,pnot,fuelutil
  Real nos,tbulk,volt,timeincrement
  Real xCOin,xCO2in,xH2in,xH2Oin,xN2FSin,xN2in,xO2in

  Integer number
```

```
  Real,Dimension (1:5000)::emfstart,nn2fs,nco,nco2,nh2,nh2o,no2,nn2
  Real,Dimension (1:5000)::islice,emf

  !Functions
  Real Rtflsp4

  !Spacial and counter variables
  Integer slice,N,maxiter,maxitercounter
  Parameter(maxiter=75)

  !Fuel cell dimensions
  Real hydrdiam,innfcdiam,fuelflowareA,length,thkae,thke,thkfe,thkic,thknf
  Parameter(hydrdiam=7.44e-3)    ! units of meters
  Parameter(fuelflowarea=1.04)  ! Cross-sectional area based upon subtracting TSOFC cross-
sectional area from TSOFC outer diameter squared

  !Process parameters
  Integer farad
  Real deltag,fctemp,mfambn2,mfambo2,R,reftemp,tamb,Q,deltaxcalc
  Parameter (farad=96487)
  Parameter (deltag=177300)    !based on 1000 C fuel cell temp, in units J/rxn
  Parameter (mfambn2=0.79)
  Parameter (mfambo2=0.21)
  Parameter (R=8.314)         !units of J/mol*K
  Parameter (tamb=300)
  Parameter (fctemp=1273)

  !Parameters to calculate required oxidant flow based upon NOS and fuel flow
  Real n1,m1,s1

  !Reactant limiting currents along cell
  Real ilimith2,ilimito2      !units of amps

  !Current convergence parameters
  Real x1,x2,xacc,vtotpol,tmpxh2o,vmax,v1,v2
  Real itotal,emftot,idiff
  Real nh2consumed,no2consumed,nh2oproduced,fh,fl
  Real nh2exit,nh2oexit,no2exit,no2start,fueluse
  Real xh2exit,xh2oexit,xo2exit,z1,z2,zacc,voltmin
  Parameter(voltmin=0.5)

  !Mole balancing parameters
  Real ncostart,nco2start,nh2start,nh2ostart

  !Time increment determination parameters
```

```
  Real densityairann,velocityann,airflow,annarea
  Parameter (annarea=1.622e-4)

  !Shift equilibrium factors
  Real A,B,C,kshift,x


  Parameter (kshift=0.7296)

  ! Convected heat
  Real Qconvect,A1,B1,C1,D1,envloss,heatgen
  Parameter (A1=3.64)
  Parameter (B1=-1.101E-3)
  Parameter (C1=2.466E-6)
  Parameter (D1=-.942E-9)
  Parameter (envloss=0.02)
  Real tair, tempavg1,cpavg,tempavg2

  !Mole balancing arrays
  Real,Dimension(1:5000)::ntot,xn2fs,xco,xco2,xh2,xh2o,xo2,xn2
  Real,Dimension(1:5000)::pn2fs,pco,pco2,ph2,ph2o,po2,pn2

  ! Output variables
  Real fuelsupply,airsupply,taircentigrade,bundlevolt,bundlepower

  !Begin active section of subroutine
  reftemp=1200
  length=150        !Fuel cell length, units of cm.
  thkae=0.22        !Air electrode (cathode) thickness (cm)
  thke=0.004        !Electrolyte thickness (cm)
  thkfe=0.01        !Fuel electrode (anode) thickness (cm)
  thkic=0.01        !Interconnect thickness (cm)
  thknf=0.3        !Nickel felt thickness (cm)
  innfcdiam=1.76       !inner diameter of fuel cell (cm)

  !Set voltage initially to minimum amount
  volt=voltmin
  itarget=itarget/3
  maxitercounter=0

  !Clear accumulation parameters
5 itotal=0
  emftot=0          !Used to find the average emf along the cell.

  !Inlet mole fractions
  xn2fs(1)=xn2fsin
```

```
  xco(1)=xcoin
  xco2(1)=xco2in
  xh2(1)=xh2in
  xh2o(1)=xh2oin
  xn2(1)=mfambn2
  xo2(1)=mfambo2

  !Calculate initial fuel flow rate Q
  Q=itarget/2/farad/fuelutil/(xcoin+xh2in)

6 pn2fs(1)=xn2fs(1)*pnot
  pco(1)=xco(1)*pnot
  pco2(1)=xco2(1)*pnot
  ph2(1)=xh2(1)*pnot
  ph2o(1)=xh2o(1)*pnot
  po2(1)=xo2(1)*pnot
  pn2(1)=xn2(1)*pnot

  !Fuel stream flow rates mol/s
  ntot(1)=Q
  nh2(1)=xh2(1)*ntot(1)
  nn2fs(1)=xn2fs(1)*ntot(1)
  nco(1)=xco(1)*ntot(1)
  nco2(1)=xco2(1)*ntot(1)
  nh2o(1)=xh2o(1)*ntot(1)

  !Calculation of n,m,s parameters for equivalent fuel CnHmOs at fuel cell inlet
  n1=xco(1)*1 + xco2(1)*1
  m1=xh2(1)*2 + xh2o(1)*1
  s1=xco(1)*1 + xco2(1)*2 + xh2o(1)*1

  !Oxidant molar flow rates
  no2(1)=ntot(1)*nos*(n1 + m1/4. - s1/2)
  nn2(1)=xn2(1)/xo2(1)*no2(1)

  !Axial length of fuel cell slices (cm)
  deltax=0.01*ntot(1)*R*fctemp/pnot/fuelflowarea     ! Slice length (cm) based upon 1 ms
  number=int(length/deltax) + 1
  deltaxlastslice=length - (number-1)*deltax

  !Calculate the time increment
  timeincrement=0.001

  deltaxcalc=deltax

  !Begin expressions to calculate the maximum allowable voltage (No account for shift!!!)
```

```
  nh2consumed=itarget/2/farad
  no2consumed=itarget/4/farad
  nh2oproduced=itarget/2/farad

  !Calculate the exit molar flow rates for H2, O2, and H2O
  nh2exit=nh2(1)-nh2consumed+nco(1)
  no2exit=no2(1)-no2consumed
  nh2oexit=nh2o(1)+nh2oproduced

  !Calculate the exit mole fractions for H2, O2, H2O
  xh2exit=nh2exit/ntot(1)
  xo2exit=no2exit/(no2exit + nn2(1))
  xh2oexit=nh2oexit/ntot(1)

  !Calculate the maximum voltage allowed based on lowest Nernst potential (i.e. cell exit).
  vmax=deltag/2/farad +
R*fctemp/2/farad*log((xh2exit*pnot)*(xo2exit*pnot)**0.5/(xh2oexit*pnot))
  vmax=0.99*vmax
  zacc=0.00015
  !Begin cycling through all the slices
  Do N=1,number

    !Check for last slice
    if (N.eq.number) deltaxcalc=deltaxlastslice

    !Nernst potential estimation
    emfstart(N)=deltag/(2.*farad) +
R*fctemp/(2.*farad)*log((xh2(N)*pnot)*(xo2(N)*pnot)**0.5/(xh2o(N)*pnot))

10   vtotpol=emfstart(N)-volt

    !Protect against too high an operating voltage
    if (vtotpol.le.0) then
      print *,N,volt,'Positive polarization required! --Electrochemistry'
      Print *,'Press ENTER key to end.'
      Read (*,*)
      stop
    end if

    !Lower bound of current value for the slice.
    x1=0

    !Establish limiting currents for slice, from experimentally based constants
    ilimith2=37.5*xh2(N)
    ilimito2=250.71*xo2(N)
```

```
    !For stability, set the upper bound of the guess just below the overall limiting current
    x2=0.99*min(ilimith2,ilimito2)

    !Designate the required converence accuracy
    xacc=0.000001*(x1+x2)/2

    !Calculate the current for the slice

  islice(N)=rtflsp4(deltaxcalc,innfcdiam,thkae,thke,thkfe,thkic,thknf,vtotpol,x1,x2,xacc,xh2(N),x
o2(N))

    !Recalculate EMF based on actual product constituency after reaction
    tmpxh2o=(nh2o(N) + islice(N)/2/farad)/ntot(N)

    emf(N)=deltag/2/farad +
R*fctemp/2/farad*log((xh2(N)*pnot)*(xo2(N)*pnot)**0.5/(tmpxh2o*pnot))

    !Incorporation of convergence criteria on EMF
    if (abs(emfstart(N)-emf(N))*100/emfstart(N) > 0.005) then
      emfstart(N)=(emfstart(N) + emf(N))/2
      islice(N)=0
      goto 10
    end if

    !Accumulation parameters
    itotal=itotal + islice(N)

    !Mole balancing
    nn2fs(N+1)=nn2fs(N)
    ncostart=nco(N)
    nco2start=nco2(N)
    nh2start=nh2(N) - islice(N)/2/farad
    nh2ostart=nh2o(N) + islice(N)/2/farad
    ntot(N+1)=ntot(N)
    no2(N+1)=no2(N) - 0.5*islice(N)/2/farad
    nn2(N+1)=nn2(N)

    !Now take into account the shift equilibrium; kshift and A are constants
    a=1
    b=(kshift*(nh2ostart-ncostart) + nco2start + 2*ncostart + nh2start)/(kshift-1)
    c=-1*(nco2start + ncostart)*(nh2start + ncostart)/(kshift-1)
    !For the typical reformer temperatures, the denominator, and hence
    !B, will be a negative; use the difference arithmetic in
    !the numerator of the quadratic expression for X for accurate
    !equilibrium mole counts
    x=(-1*b-(b*b - 4*a*c)**0.5)/2/a
```

```
  !Results of shift
  nco(N+1)=x
  nco2(N+1)=nco2start + ncostart - x
  nh2(N+1)=nh2start + ncostart - x
  nh2o(N+1)=nh2ostart - ncostart + x

  !Calculate new mole fractions
  xn2fs(N+1)=nn2fs(n+1)/ntot(N+1)
  xco(N+1)=nco(N+1)/ntot(N+1)
  xco2(N+1)=nco2(N+1)/ntot(N+1)
  xh2(N+1)=nh2(N+1)/ntot(N+1)
  xh2o(N+1)=nh2o(N+1)/ntot(N+1)
  xo2(N+1)=no2(N+1)/(no2(N+1) + nn2(N+1))
  xn2(N+1)=nn2(N+1)/(no2(N+1) + nn2(N+1))

  !Calculate downstream partial pressures
  pn2fs(N+1)=xn2fs(N+1)*pnot
  pco(N+1)=xco(N+1)*pnot
  pco2(N+1)=xco2(N+1)*pnot
  ph2(N+1)=xh2(N+1)*pnot
  ph2o(N+1)=xh2o(N+1)*pnot
  po2(N+1)=xo2(N+1)*pnot
  pn2(N+1)=xn2(N+1)*pnot
End Do

!Calculate fuel usage
fueluse=((nh2(1)-nh2(number+1))+(nco(1)-nco(number+1)))/(nh2(1)+nco(1))

!Begin loop to converge on correct current
idiff=itarget-itotal
if (volt.eq.voltmin) then
  fl=idiff
  v1=voltmin
end if
if (volt.eq.vmax) then
  fh=idiff
  v2=vmax
end if
!Check to see how close previous voltage guess was on current output
if (abs(idiff).le.zacc) goto 45

if (volt.eq.voltmin) then
  volt=vmax
else if (volt.eq.vmax) then
  volt=v1 + (v2-v1)*fl/(fl-fh)
```

```
  else if ((volt.ne.voltmin).and.(volt.ne.vmax)) then
    if (fh*fl>0) then
      print *,'Root must be bounded.  -Electrochemistry'
      Print *,'Press ENTER key to end.'
      Read (*,*)
      stop
    end if
    if (idiff>0) then
      v2=volt
      fh=idiff
      volt=v1+(v2-v1)*fl/(fl-fh)
    else
      v1=volt
      fl=idiff
      volt=v1+(v2-v1)*fl/(fl-fh)
    end if
  end if
    maxitercounter=maxitercounter+1
    !Check for too many iterations
    if (maxitercounter.ge.maxiter) then
      print *,'Maximum number of iterations exceeded -Electrotransients'
      print *,'Voltage: ',volt,' Current: ',itotal,' Idiff: ',idiff
      print *,'Target current is: ',itarget,' Fuel usage: ',fueluse
      print *,'Maximum voltage allowed: ',vmax
      print *,'V1 voltage: ',v1,' V2 voltage: ',v2
      Print *,'Press ENTER key to end.'
      Read (*,*)
      stop
    end if
    goto 5

  !Converge on specified fuel utilization
45 if ((abs(fueluse-fuelutil)>0.001)) then
    Q=Q*fueluse/fuelutil
    volt=voltmin
    itotal=0
    emftot=0

    !Start new iteration with revised fuel flow rate
    goto 6
  end if
  print *,'Steady-state current: ',itotal*3
  print *,'Fuel utilization: ',fueluse

  ! Measure of heat generated {LHV of hydrogen oxidation per rxn. at 1000 deg. C is 249415 J}
  ! Small effect of shift is included {heat (out) of rxn. at a prescribed fuel
```

```
  ! stream temperature of 1200K (927 C) is the factor for shift}
  heatgen=itotal*(1/2/farad*249415 - volt) + (nco(1)-nco(number+1))*32800
  airflow=no2(1)*0.032 + nn2(1)*0.028

  ! (Thermally) Steady state requirement of air inlet temp.,
  ! taking into account the envelope losses
  Qconvect=(1-envloss)*heatgen

  ! Initial guess
  tempavg1=800

  ! Estimate the average specific heat of the air through the cell stack
46 cpavg=287*(A1 + B1*tempavg2 + C1*tempavg1**2 + D1*tempavg1**3)

  ! Base inlet air temperature requirement on the fact that air
  ! will come into thermal equilibrium with the cell.
  tair=fctemp - Qconvect/airflow/cpavg
  tempavg2=(fctemp + tair)/2

  if ((abs(tempavg1-tempavg2)/tempavg1).gt.0.005) then
    tempavg1=(tempavg1 + tempavg2)/2
    goto 46
  end if

  !Store the pertinent output
  fuelsupply=24*ntot(1)
  airsupply=24*(nn2(1)+no2(1))
  taircentigrade=tair-273
  bundlevolt=8*volt
  bundlepower=bundlevolt*itotal*3/1000

  write (2,*) 'Fuel supply (mmol/sec)   : ',fuelsupply
  write (2,*) 'Air supply (mmol/sec)    : ',airsupply
  write (2,*) 'Air inlet Temperature (C): ',taircentigrade
  write (2,*) 'Bundle voltage (V)       : ',bundlevolt
  write (2,*) 'Bundle power (kW)        : ',bundlepower
  write (2,*) 'Fuel utilization         : ',((nh2(1)-nh2(number+1))+(nco(1)-
nco(number+1)))/(nh2(1)+nco(1))

  write (8,*) 'Slice:',1,' Current:',islice(1)
  do N=1,number
    if ((N/100.).eq.(int(N/100))) write (4,*)'Slice:',N,' Current:',islice(N)
  end do

  write (3,*) '(Time (ms)) (Current (A)) (Bundle V (V)) (Bundle P (kW)) (Fuel Utilization)'
  write (3,*) 0,itotal*3,bundlevolt,bundlepower,fuelutil
```

```
  write (4,*) 'Time Increment = ',timeincrement
  write (4,*) '0'

  write (5,*) 'Time Increment = ',timeincrement
  write (5,*) '0'
  Do slice = 10, number, 10
    write (5,*) slice, xh2(slice)
  end do
  write (5,*) ' '

  write (6,*) 'Time Increment = ',timeincrement
  write (6,*) '0'
  Do slice = 10, number, 10
    write (6,*) slice, xo2(slice)
  end do
  write (6,*) ' '

  write (7,*) 'Time Increment = ',timeincrement
  write (7,*) '0'
  Do slice = 10, number, 10
    write (7,*) slice, xh2o(slice)
  end do
  write (7,*) ' '

  write (8,*) 1,islice(1)
  do slice = 10, number, 10
    write (8,*) slice, islice(slice)
  end do
  write (8,*) ' '

  write (9,*) 'Time Increment = ',timeincrement
  write (9,*) '0    Voltage    Current     Fuel Usage'
  write (9,*) '0    ',volt,itotal,fueluse

end subroutine Electrochemistry

!#########################################################################################
#
!#########################################################################################
#
Subroutine
Electrotransient(deltax,deltaxlastslice,number,emfstart,pnot,volt,time,timeincrement,milliseconds
,currentprofile,nn2fs,nco,nco2,nh2,nh2o,nn2,no2)

Implicit None
```

```
!Axial divisions
Integer number

!Declare dummy variables and arrays
Real deltax,deltaxlastslice,pnot,volt,itarget,time,timeincrement,milliseconds
Real,Dimension(1:5000)::emfstart,nn2fs,nco,nco2,nh2,nh2o,nn2,no2,ntot
Real,Dimension(1:milliseconds)::currentprofile

!Declare functions used
Real rtflsp4

!Time counter and slice parameters
Integer time2,N

!Fuel cell dimensions
Real length,thkae,thke,thkfe,thkic,thknf,innfcdiam

!Faraday's Law consideration along the fuel cell
Real ncostart,nco2start,nh2start,nh2ostart

!Shift equilibrium factors
Real a,b,c,kshift,x
Parameter (kshift=0.7296)

!Process parameters
Real fctemp,mfambn2,mfambo2,R
Integer farad
Parameter (fctemp=1273)
Parameter (mfambo2=0.21)
Parameter (mfambn2=0.79)
Parameter (farad=96487)
Parameter (R=8.314)

!Reactant limiting currents along cell
Real ilimith2,ilimito2

!Current convergence parameters
Real deltag,vtotpol,x1,x2,xacc,tmpxh2o,maxiter,maxitercounter
Real idiff,fh,fl,v1,v2,vmin,vmax,vacc,futiltesth,deltaxcalc
Parameter(deltag=177300)
Parameter(vacc=5e-2)
Parameter(vmin=0.3)
Parameter(maxiter=100)

! Output variables
```

```
  Real,Dimension(1:milliseconds)::bundlevolt,bundlepower,fueluse

  !Accumulation parameters
  Real itotal

  !Process transient variables
  Real,Dimension(1:number+2)::emfstarttrans,ntottrans
  Real,Dimension(1:number+2)::nn2fstrans,ncotrans,nco2trans,nh2trans,nh2otrans,no2trans,nn2tr
ans
  Real,Dimension(1:number+2)::xn2fstrans,xcotrans,xco2trans,xh2trans,xh2otrans,xo2trans,xn2tr
ans

  !Convergence parameters
  Real,Dimension(1:number+2)::islice,emf

  !fuel cell dimensions
  length=150          !Fuel cell length, units of cm.
  thkae=0.22          !Air electrode (cathode) thickness (cm)
  thke=0.004          !Electrolyte thickness (cm)
  thkfe=0.01          !Fuel electrode (anode) thickness (cm)
  thkic=0.01          !Interconnect thickness (cm)
  thknf=0.3          !Nickel felt thickness (cm)
  innfcdiam=1.76        !inner diameter of fuel cell (cm)

  !Set inital transient conditions to the steady state values or previous step values
  do N=1,number+1
    emfstarttrans(N)=emfstart(N)
    nn2fstrans(N)=nn2fs(N)
    ncotrans(N)=nco(N)
    nco2trans(N)=nco2(N)
    nh2trans(N)=nh2(N)
    nh2otrans(N)=nh2o(N)
    no2trans(N)=no2(N)
    nn2trans(N)=nn2(N)
    ntottrans(N)=nn2fs(N)+nco(N)+nco2(N)+nh2(N)+nh2o(N)
    xn2fstrans(N)=nn2fs(N)/ntottrans(N)
    xcotrans(N)=nco(N)/ntottrans(N)
    xco2trans(N)=nco2(N)/ntottrans(N)
    xh2trans(N)=nh2(N)/ntottrans(N)
    xh2otrans(N)=nh2o(N)/ntottrans(N)
    xo2trans(N)=0.21
    xn2trans(N)=0.79
  end do
```

```
  DO time2=1,(milliseconds) !Reactant stream transients end when the fluid element at the
annulus inlet,
              !at the beginning of the transient, reaches the end of the fuel cell.
             !This occurs when "NUMBER" time steps have occured (STEMMING FROM
             !LAGRANGIAN METHODOLOGY). "NUMBER+1" is used as a safety factor, of
sorts,
             !to assure that the reactant stream flows has reached a steady state.

    ! Show status of simulation
    Print *,'Time(ms): ',time2
    !check for proper fuel utilization parameters
    futiltesth=(nh2trans(1)+ncotrans(1))*2*farad*0.95
    if (currentprofile(time2)/3>futiltesth) then
      Print *,'Warning! Current step requires greater than 85 percent fuel utilization'
      Print *,'Maximum allowable current is: ',futiltesth
      Print *,'Total fuel utilization will be:
',currentprofile(time2)/3/(nh2trans(1)+ncotrans(1))/2/farad
      Print *,'Press ENTER key to end.'
      Read (*,*)
      stop
    end if

    ! Calculate maximum allowable voltage
    vmax=deltag/2/farad +
R*fctemp/2/farad*log((xh2trans(number+1)*pnot)*(xo2trans(number+1)*pnot)**0.5/(xh2otrans(
number+1)*pnot))
    vmax=0.95*vmax

    volt=vmin
    maxitercounter=0
50   itotal=0

    !Set molar flow rates and mole fractions of the entering fuel stream at any instant (mol/s)
    nn2fstrans(1)=nn2fs(1)
    ncotrans(1)=nco(1)
    nco2trans(1)=nco2(1)
    nh2trans(1)=nh2(1)
    nh2otrans(1)=nh2o(1)
    ntottrans(1)=nn2fs(1)+nco(1)+nco2(1)+nh2(1)+nh2o(1)
    xn2fstrans(1)=nn2fs(1)/ntottrans(1)
    xcotrans(1)=nco(1)/ntottrans(1)
    xco2trans(1)=nco2(1)/ntottrans(1)
    xh2trans(1)=nh2(1)/ntottrans(1)
    xh2otrans(1)=nh2o(1)/ntottrans(1)

    !Establish oxidant molar flow rates and mole fractions at any instant
```

```
    no2trans(1)=no2(1)
    nn2trans(1)=nn2(1)
    xo2trans(1)=mfambo2
    xn2trans(1)=mfambn2

    do N=1,number
      emfstarttrans(N)=deltag/2/farad +
R*fctemp/2/farad*log((xh2trans(N)*pnot)*(xo2trans(N)*pnot)**0.5/(xh2otrans(N)*pnot))
    end do

    !Begin cycling through the slices
    Do N=1,number
60      vtotpol=emfstarttrans(N)-volt

      !Protect against too high an operating voltage
      if (vtotpol.le.0) then
        Print *,'Positive polarization required -Electrotransients'
        Print *,'Slice: ',N,' Polarization: ',vtotpol,' Voltage: ',volt
        Print *,'Press ENTER key to end.'
        Read (*,*)
        stop
      end if

      !Upper/lower bound for current value of slice and limiting currents
      x1=0
      ilimith2=37.5*xh2trans(N)
      ilimito2=250.71*xo2trans(N)
      x2=0.99*min(ilimith2,ilimito2)
      xacc=0.000001*(x1 + x2)/2

      ! Set the correct slice length
      if (N.eq.number) then
        deltaxcalc=deltaxlastslice
      else
        deltaxcalc=deltax
      end if

      !Determine current of the slice

  islice(N)=rtflsp4(deltaxcalc,innfcdiam,thkae,thke,thkfe,thkic,thknf,vtotpol,x1,x2,xacc,xh2trans(
N),xo2trans(N))

      if ((time2.eq.(4*number+1)).and.(N.eq.1)) then
        write (5,*) N,islice(N)
      end if
      if ((time2.eq.(4*number+1)).and.((N/10.).eq.int(N/10.))) then
```

```
        write (5,*) N,islice(N)
      end if

      !Recalculation of emf based upon actual product constituency
      tmpxh2o=(nh2otrans(N) + islice(N)/2/farad)/ntottrans(N)

      emf(N)=deltag/2/farad +
R*fctemp/2/farad*log((xh2trans(N)*pnot)*(xo2trans(N)*pnot)**0.5/(tmpxh2o*pnot))

      !Incorporate convergence critia on emf
      if (abs(emfstarttrans(N) - emf(N))/emfstarttrans(N) > 0.005) then
        emfstarttrans(N)=(emfstarttrans(N)+emf(N))/2
        islice=0
        goto 60
      end if

      !Accumulation parameters
      itotal=itotal+islice(N)

    end do !end counter for slices

    !Begin loop to converge on correct current
    idiff=currentprofile(time2)/3-itotal
    if (volt.eq.vmin) then
      fl=idiff
      v1=vmin
    end if
    if (volt.eq.vmax) then
      fh=idiff
      v2=vmax
    end if

    !Check to see how close previous voltage guess was on current output
    if (abs(idiff).le.vacc) goto 95
    if (volt.eq.vmin) then
      volt=vmax
    else if (volt.eq.vmax) then
      volt=v1 + (v2-v1)*fl/(fl-fh)
    else
      if (fh*fl>0) then
        print *,'Root must be bounded.  -Electrotransient'
        Print *,'Press ENTER key to end.'
        Read (*,*)
        stop
      end if
      if (idiff>0) then
```

```
        v2=volt
        fh=idiff
        volt=v1+(v2-v1)*fl/(fl-fh)
      else
        v1=volt
        fl=idiff
        volt=v1+(v2-v1)*fl/(fl-fh)
      end if
    end if
    maxitercounter=maxitercounter+1
    !Check for too many iterations
    if (maxitercounter.ge.maxiter) then
      print *,'Maximum number of iterations exceeded -Electrotransients'
      print *,'Voltage: ',volt,' Current: ',itotal,' Time: ',time
      print *,'Target current is: ',currentprofile(time2)/3
      print *,'Maximum voltage allowed: ',vmax
      print *,'V1 voltage: ',v1,' V2 voltage: ',v2
      Print *,'Press ENTER key to end.'
      Read (*,*)
      stop
    end if
    goto 50

    !Advance the overall time counter
95   time=time+timeincrement

    do N=1,number+1
      emfstart(N)=emfstarttrans(N)
      nn2fs(N)=nn2fstrans(N)
      nco(n)=ncotrans(N)
      nco2(n)=nco2trans(N)
      nh2(n)=nh2trans(N)
      nh2o(n)=nh2otrans(N)
      no2(n)=no2trans(N)
      nn2(n)=nn2trans(N)
      ntot(n)=ntottrans(n)
    end do

    do N=1,number
      !Mole balances, considering effects of oxidation
      nn2fstrans(N+1)=nn2fs(N)
      ncostart=nco(N)
      nco2start=nco2(N)
      nh2start=nh2(N)-islice(N)/2/farad
      nh2ostart=nh2o(N)+islice(N)/2/farad
      ntottrans(N+1)=ntot(N)
```

```
      no2trans(N+1)=no2(N)-islice(N)/4/farad
      nn2trans(N+1)=nn2(N)

      !Calculate shift parameters
      a=1
      b=(kshift*(nh2ostart-ncostart) + nco2start + 2*ncostart + nh2start)/(kshift - 1)
      c=-1*(nco2start + ncostart)*(nh2start + ncostart)/(kshift - 1)
      x=(-1*b-(b*b - 4*a*c)**0.5)/2/a

      !Shift results
      ncotrans(N+1)=x
      nco2trans(N+1)=nco2start+ncostart-x
      nh2trans(N+1)=nh2start+ncostart-x
      nh2otrans(N+1)=nh2ostart-ncostart+x
    end do

    do N=1,number

      !Calculation of new mole fractions
      xn2fstrans(N+1)=nn2fstrans(N+1)/ntottrans(N+1)
      xh2trans(N+1)=nh2trans(N+1)/ntottrans(N+1)
      xcotrans(N+1)=ncotrans(N+1)/ntottrans(N+1)
      xco2trans(N+1)=nco2trans(N+1)/ntottrans(N+1)
      xh2otrans(N+1)=nh2otrans(N+1)/ntottrans(N+1)
      xo2trans(N+1)=no2trans(N+1)/(no2trans(N+1)+nn2trans(N+1))
      xn2trans(N+1)=nn2trans(N+1)/(no2trans(N+1)+nn2trans(N+1))
    end do

    !Calculation of fuel utilization
    fueluse(time2+1)=((nh2trans(1)-nh2trans(number+1))+(ncotrans(1)-
ncotrans(number+1)))/(nh2trans(1)+ncotrans(1))

    !Begin writing output of pertinent data
    if ((time2/2.).eq.int(time2/2.)) then
      write(1,*) time,fueluse(time2+1)
      write(5,*) time
      write(6,*) time
      write(7,*) time
      write(9,*) time,volt,itotal,fueluse(time2+1)

      do N=1,number
        if((N/10.).eq.int(N/10.)) then
          write(5,*) N,xh2trans(N)
          write(6,*) N,xo2trans(N)
          write(7,*) N,xh2otrans(N)
        end if
```

```
      end do !Oputting transient mole fractions loop
      write(5,*) ' '
      write(6,*) ' '
      write(7,*) ' '
    end if


    do N=1,number+1
      emfstart(N)=emfstarttrans(N)
      nn2fs(N)=nn2fstrans(N)
      nco(n)=ncotrans(N)
      nco2(n)=nco2trans(N)
      nh2(n)=nh2trans(N)
      nh2o(n)=nh2otrans(N)
      no2(n)=no2trans(N)
      nn2(n)=nn2trans(N)
    end do

    ! Calculation of transient results
    fueluse(time2+1)=((nh2trans(1)-nh2trans(number+1))+(ncotrans(1)-
ncotrans(number+1)))/(nh2trans(1)+ncotrans(1))
    bundlevolt(time2+1)=volt*8
    bundlepower(time2+1)=bundlevolt(time2+1)*itotal*3/1000

    !Begin writing output of pertinent data
    write (3,*) time,itotal*3,bundlevolt(time2+1),bundlepower(time2+1),fueluse(time2+1)


    !Check to see if time has been exceeded for current step
    if (time2.ge.(milliseconds-1)) exit
  end do !Time loop

  write(1,*) '_____'
  write(5,*) '_____'
  write(6,*) '_____'
  write(7,*) '_____'
  write(9,*) '_____'

end subroutine Electrotransient


!*************************************************************************
*
!*************************************************************************
*
```

```
REAL FUNCTION
RTFLSP4(DELTAX,INNFCDIAM,THKAE,THKE,THKFE,THKIC,THKNF,VTOTPOL,X1,
X2, XACC,XH2,XO2)
! This function uses the false root position method to
! converge on slice current

IMPLICIT NONE

INTEGER MAXIT,J
REAL FL,FH,XL,XH,DX,TRTFLSP,DEL,TMP,F,FUNC

! Dummy variables
REAL DELTAX,INNFCDIAM,THKAE,THKE,THKFE,THKIC,THKNF,VTOTPOL,X1, X2,
XACC,XH2,XO2,A

PARAMETER (MAXIT=50)

! Confirming that the current root is bound
FL=FUNC(DELTAX,INNFCDIAM,THKAE,THKE,THKFE,THKIC,THKNF,VTOTPOL,X1,X
H2,XO2)
FH=FUNC(DELTAX,INNFCDIAM,THKAE,THKE,THKFE,THKIC,THKNF,VTOTPOL,X2,X
H2,XO2)
IF ((FL*FH)>0) THEN
  PRINT *,FL,FH
  STOP 'Current root must be bracketed for false position method.'
  Print *,'Press ENTER key to end.'
  Read (*,*)
END IF

! Heart of the algorithm
IF (FL<0) THEN
  XL=X1
  XH=X2
ELSE
  XL=X2
  XH=X1
  TMP=FH
  FH=FL
  FL=TMP
END IF
DX=XH-XL
  DO J=1,MAXIT
    TRTFLSP=XL+DX*FL/(FL-FH)
  F=FUNC(DELTAX,INNFCDIAM,THKAE,THKE,THKFE,THKIC,THKNF,VTOTPOL,TRTF
LSP,XH2,XO2)
  IF (F<0) THEN
```

```
    DEL=XL-TRTFLSP
    XL=TRTFLSP
     FL=F
   ELSE
    DEL=XH-TRTFLSP
    XH=TRTFLSP
     FH=F
   END IF
   DX=XH-XL
    RTFLSP4=TRTFLSP
   IF ((ABS(DEL)<XACC).OR.(F==0)) GOTO 40
   END DO
PRINT *, 'RTFLSP4 exceeded maximum iterations.'
40 A=1
END FUNCTION

!***********************************************************************
!***********************************************************************
!***********************************************************************
REAL FUNCTION
FUNC(DELTAX,INNFCDIAM,THKAE,THKE,THKFE,THKIC,THKNF,VTOTPOL,X,XH2,X
O2)
! Function establishing the error of the current guess, based on the
! required polarization

IMPLICIT NONE

!Dummy variables passed (X is slice current)
REAL
DELTAX,INNFCDIAM,THKAE,THKE,THKFE,THKIC,THKNF,VTOTPOL,X,XH2,XO2

! Polarization parameters
REAL LE,LICM,NFWIDTH,JE,NEGJE,JICM,NEGJICM
PARAMETER (NFWIDTH=.6)
!LE is length if electrolyte material that has current cross it (cm)
!LICM is length of electrolyte material (cm)
!THKIC is thickness of interconnect material (cm)
!NFWIDTH is width of nickel felt pads (cm)
!THKNF is thickness of nickel felt pads (cm)

!Fuel cell inner radius
REAL RINNER,RADAE,RADE,RADFE

! Material resistivities (at operating temperature)
REAL RHOAE, RHOE, RHOFE, RHOIC, RHONF
PARAMETER (RHOAE=.013, RHOE=10, RHOFE=.001,RHOIC=.1, RHONF=.01)
```

```
!Parameters for equation for which roots need to be found
REAL COMP1,COMP2,COMP3,COMP4,COMP5,COMP6,COMP7,COMP8,COMP9,COMP10
REAL ADD1,ADD2,ADD3,ADD4,ADD5

! Cell layer radii
RINNER=INNFCDIAM/2.
RADAE=RINNER+THKAE
RADE=RADAE+THKE
RADFE=RADE+THKFE

! Necessary computations for ohmic loss
LE=2*3.1416*290./360.*(RINNER+THKAE+THKE/2)
LICM=2*3.1416*70./360.*(RINNER+THKAE+THKIC/2)
JE=LE/2*((RHOE*THKE)**(-1)*(RHOAE/THKAE+RHOFE/THKFE))**(.5)
NEGJE=-1*JE

JICM=LICM/2*(RHOAE/THKAE*(RHOIC*THKIC)**(-1))**(.5)
NEGJICM=-1*JICM

COMP1=((RHOFE/THKFE)**2+(RHOAE/THKAE)**2)
COMP2=.5*(EXP(JE)+EXP(NEGJE))
COMP3=(RHOFE/THKFE)*(RHOAE/THKAE)
COMP4=(2+JE*.5*(EXP(JE)-EXP(NEGJE)))

COMP5=2*(RHOE*THKE)**(-.5)
COMP6=(RHOFE/THKFE+RHOAE/THKAE)**(1.5)
COMP7=.5*(EXP(JE)-EXP(NEGJE))
COMP8=.268*RHOAE/THKAE
COMP9=.5*(RHOIC*THKIC*RHOAE/THKAE)**(.5)
COMP10=((EXP(JICM)-EXP(NEGJICM))/(EXP(JICM)+EXP(NEGJICM)))

ADD1=X*1/DELTAX*(COMP1*COMP2+COMP3*COMP4)/(COMP5*COMP6*COMP7)
ADD2=X*1/DELTAX*(COMP8+COMP9/COMP10)
ADD3=X*1/DELTAX*(RHONF*THKNF/NFWIDTH)

! O2 conc. polarization
ADD4=-.027*LOG(1-X/(250.71*XO2))

! H2 conc. polarization
ADD5=-.054*LOG(1-X/(37.5*XH2))

FUNC=ADD1+ADD2+ADD3+ADD4+ADD5-VTOTPOL
END FUNCTION FUNC

!#########################################################################
```

```
!#########################################################################
SUBROUTINE Openfiles()

!OPENS ALL NEEDED FILES FOR DATA WRITING
IMPLICIT NONE

  OPEN (2,FILE='C:\FCTEST\DATA3.TXT',STATUS='NEW')
  OPEN (3,FILE='C:\FCTEST\DATA4.TXT',STATUS='NEW')
  OPEN (4,FILE='C:\FCTEST\ELECTROTRANS.TXT',STATUS='NEW')
  OPEN (5,FILE='C:\FCTEST\ELECTROTRANSH2.TXT',STATUS='NEW')
  OPEN (6,FILE='C:\FCTEST\ELECTROTRANSO2.TXT',STATUS='NEW')
  OPEN (7,FILE='C:\FCTEST\ELECTROTRANSH2O.TXT',STATUS='NEW')
  OPEN (8,FILE='C:\FCTEST\slicecurrents.txt',STATUS='NEW')
  OPEN (9,FILE='C:\FCTEST\VOLTTRANS.TXT',STATUS='NEW')

END SUBROUTINE Openfiles

!#########################################################################
!#########################################################################
SUBROUTINE Closefiles()

!CLOSES ALL OPENED FILES
IMPLICIT NONE

  CLOSE (2)
  CLOSE (3)
  CLOSE (4)
  CLOSE (5)
  CLOSE (6)
  CLOSE (7)
  CLOSE (8)
  CLOSE (9)

END SUBROUTINE Closefiles
```

Appendix B.1 Saber Designer Netlists and MAST Templates

Line-commutated current-source Inverter:

```
##########################################################################################
##

clock_l4.clock_l4_1 clock:gate4_a_h = td=3/360, freq=60, duty=1/3
sw1_l4.sym1 p:__bridge_a m:__d c:gate4_a_h
sw1_l4.sym2 p:__f m:__bridge_a c:gate1_a_l
clock_l4.clock_l4_3 clock:gate1_a_l = td=0, freq=60, duty=1/3
sw1_l4.sym3 p:bridge_b m:__d c:gate6_b_a
clock_l4.clock_l4_4 clock:gate6_b_a = td=5/360, freq=60, duty=1/3
sw1_l4.sym4 p:__f m:bridge_b c:gate3_b_l
clock_l4.clock_l4_5 clock:gate3_b_l = td=2/360, freq=60, duty=1/3
sw1_l4.sym5 p:_n2612 m:__d c:gate2_c_h
clock_l4.clock_l4_6 clock:gate2_c_h = td=1/360, freq=60, duty=1/3
sw1_l4.sym6 p:__f m:_n2612 c:gate5_c_l
clock_l4.clock_l4_7 clock:gate5_c_l = td=4/360, freq=60, duty=1/3
v3p.v3p1 a:__Uan_utility b:_n1905 c:_n1902 n:0 = delay=19.5/2160, ampl=120
r.r8 p:@"__id+i3_plus" m:@"__id+i3_minus" = rnom=0.001
short.@"id-i3" p:_n2002 m:@"__id+i3_plus"
l.l2 p:__f m:@"__id-i3_plus" = l=1m
l.l3 p:__d m:@"__id+i3_minus" = l=1m
short.Isa p:_n3440 m:__Uan_utility
x2.x2_5 pp:_n2377 pm:0 sp:_n177 sm:_n176 = n2=1732, n1=1000
x2.x2_8 pp:_n2611 pm:0 sp:_n176 sm:_n175 = n2=1732, n1=1000
x2.x2_9 pp:_n1514 pm:0 sp:_n175 sm:_n177 = n2=1732, n1=1000
c.c1 p:c_t_plus m:c_t_minus = esr=100m, c=250u
c.c2 p:c_b_plus m:c_b_minus = esr=100m, c=250u
pwld.pwld1 p:_n2620 m:_n2002
pwld.pwld2 p:_n1150 m:_n2620
sw1_l4.sw1_l4_7 p:_n1150 m:_n2721 c:__bottom_trig
```

```
lpf1.lpf1_1 in:_n2148 out:_n2151 = wn=50
v2var.v2var1 p:__d m:__f out:_n2148
pv2i.pv2i2 m:@"_Id,ref" q:_n2151
dly.dly1 out:_n2167 in:_n2165 = td=1/240-1/(8*180)+19.5/2160, k=1
c_sin.c_sin1 out:_n2165 = ac_phase=0, frequency=180, amplitude=1, ac_mag=1
gain.gain1 out:_n2166 in:@"_Id,ref" = k=0.52
mult.mult2 out:@"_I3,ref" in1:_n2166 in2:_n2167
r.r7 p:@"__id-i3_minus" m:@"__id-i3_plus" = rnom=0.001
short.@"id+i3" p:@"__id-i3_minus" m:_n1150
diff.diff2 out:_n2949 in1:__top_Iref in2:__top_i
diff.diff3 out:_n2951 in1:__btm_iref in2:__btm_i
v2var.v2var2 p:@"__id-i3_plus" m:@"__id-i3_minus" out:__btm_i
v2var.v2var3 p:@"__id+i3_plus" m:@"__id+i3_minus" out:__top_i
clock_l4.clock_l4_10 clock:_n2254 = td=1/60, freq=60, duty=1
var2v.var2v1 in:_n2777 p:__top_err m:0
comp_l4.comp_l4_1 p:__top_err enbl:_n2254 out:__upper_trig m:__ramp = hys=0.1
clock_l4.clock_l4_11 clock:_n2257 = td=1/60, freq=60, duty=1
var2v.var2v2 in:_n2779 p:__btm_err m:0
comp_l4.comp_l4_2 p:__btm_err enbl:_n2257 out:__bottom_trig m:__ramp = hys=0.1
vtri.vtri1 p:__ramp m:0 = period=1/10e3, offset=0, delay=0.1, ampl=0.1, \
      rtime=0.99/10e3
gain.gain7 out:__btm_iref in:_n2969 = k=0.001
short.Iar p:__bridge_a m:_n2377
diff.diff4 out:_n2970 in1:@"_Id,ref" in2:@"_I3,ref"
sum.sum2 out:_n2968 in1:@"_Id,ref" in2:@"_I3,ref"
short.Ibr p:bridge_b m:_n2611
short.Icr p:_n2612 m:_n1514
short.short9 p:_n3441 m:_n1905
short.short10 p:_n3442 m:_n1902
sw1_l4.sw1_l4_9 p:_n2722 m:_n2002 c:__upper_trig
short.@"2*I3" p:_n2620 m:0
short.c_top p:c_t_minus m:_n2620
short.c_btm p:c_b_plus m:_n2620
```

pwld.pwld3 p:_n2721 m:c_b_minus
pwld.pwld4 p:c_t_plus m:_n2722
prop_int.prop_int1 out:_n2777 in:_n2910 = init=0, ki=100, kp=100
prop_int.prop_int2 out:_n2779 in:_n2912 = init=0, ki=100, kp=100
v2var.v2var4 p:c_t_plus m:c_t_minus out:_n2834
v2var.v2var5 p:c_b_plus m:c_b_minus out:_n2835
diff.diff5 out:__Real_V_Diff in1:_n2834 in2:_n2835
gain.gain5 out:_n2845 in:__Real_V_Diff = k=0.001
sum.sum3 out:_n2910 in1:_n2950 in2:_n2845
diff.diff6 out:_n2912 in1:_n2952 in2:_n2845
gain.gain8 out:__top_Iref in:_n2971 = k=0.001
gain.gain6 out:_n2950 in:_n2949 = k=2
gain.gain9 out:_n2952 in:_n2951 = k=2
gain.gain10 out:_n2964 in:@"_Id,ref" = k=0.035
c_sin.c_sin2 out:_n2965 = ac_phase=0, frequency=360, amplitude=1, ac_mag=1
mult.mult3 out:_n2967 in1:_n2964 in2:_n2963
dly.dly2 out:_n2963 in:_n2965 = td=1/240-1/(2*360)+19.5/2160, k=1
sum.sum4 out:_n2969 in1:_n2968 in2:_n2967
sum.sum5 out:_n2971 in1:_n2970 in2:_n2967
l.l4 p:c_t_plus m:_n3053 = l=0.5m, r=100m
l.l6 p:c_b_minus m:_n3242 = l=0.5m, r=100m
short.short14 p:_n3241 m:_n3053
r.r9 p:_n177 m:_n3440 = rnom=0.5
r.r10 p:_n176 m:_n3441 = rnom=0.5
r.r11 p:_n175 m:_n3442 = rnom=0.5
v_dc.v_dc1 p:_n3241 m:_n3242 = dc_value=450

Self-commutated voltage-source Inverter:

```
##############################################################################
##

sw1_l4.sw1_l4_1 p:_n1156 m:_n6 c:S1 = ron=0.01, ton=0.1n, toff=0.1n
sw1_l4.sw1_l4_2 p:vminus m:_n1156 c:S4 = ron=0.01, ton=0.1n, toff=0.1n
sw1_l4.sw1_l4_3 p:_n194 m:_n6 c:S2 = ron=0.01, ton=0.1n, toff=0.1n
sw1_l4.sw1_l4_4 p:vminus m:_n194 c:S5 = ron=0.01, ton=0.1n, toff=0.1n
sw1_l4.sw1_l4_8 p:_n195 m:_n6 c:S3 = ron=0.01, ton=0.1n, toff=0.1n
sw1_l4.sw1_l4_9 p:vminus m:_n195 c:S6 = ron=0.01, ton=0.1n, toff=0.1n
short.short1 p:_n1156 m:_n3407
short.short2 p:_n194 m:_n3408
short.short3 p:_n195 m:_n3409
l.l4 p:_n3407 m:Abar = l=1m/4, r=100m
l.l5 p:_n3408 m:Bbar = l=1m/4, r=100m
l.l6 p:_n3409 m:Cbar = l=1m/4, r=100m
c.c1 p:Abar m:0 = ic=undef, esr=100m, c=1m/2
c.c5 p:Bbar m:0 = ic=undef, esr=100m, c=1m/2
c.c6 p:Cbar m:0 = ic=undef, esr=100m, c=1m/2
short.short8 p:boost_out m:_n6
inv_l4.inv_l4_4 out:S4 in:S1
inv_l4.inv_l4_5 out:S5 in:S2
inv_l4.inv_l4_6 out:S6 in:S3
sum.sum11 out:alpha_ref in1:_n3793 in2:_n3805
sum.sum12 out:_n3793 in1:_n3802 in2:_n3804
gain.gain17 out:_n3802 in:A1 = k=2/3
gain.gain18 out:_n3804 in:B1 = k=-1/3
gain.gain19 out:_n3805 in:C1 = k=-1/3
gain.gain20 out:_n3816 in:C1 = k=-0.57735
sum.sum13 out:beta_ref in1:_n3811 in2:_n3816
gain.gain22 out:_n3811 in:B1 = k=0.57735
gain.gain23 out:_n3835 in:Cbar1 = k=-1/3
```

```
sum.sum15 out:alpha_sig in1:_n3832 in2:_n3835
gain.gain24 out:_n3823 in:Bbar1 = k=-1/3
gain.gain25 out:_n3824 in:Abar1 = k=2/3
sum.sum16 out:beta_sig in1:_n3831 in2:_n3821
v2var.v2var10 p:Bbar m:0 out:Bbar1 = k=1/120
gain.gain26 out:_n3821 in:Cbar1 = k=-0.57735
sum.sum17 out:_n3832 in1:_n3824 in2:_n3823
gain.gain27 out:_n3831 in:Bbar1 = k=0.57735
v2var.v2var11 p:Abar m:0 out:Abar1 = k=1/120
v2var.v2var12 p:Cbar m:0 out:Cbar1 = k=1/120
diff.diff3 out:_n3841 in1:alpha_ref in2:alpha_sig
gain.gain28 out:alpha1 in:_n3841 = k=20
var2v.var2v3 in:alpha1 p:_n4610 m:0
diff.diff4 out:_n3845 in1:beta_ref in2:beta_sig
var2v.var2v4 in:error2 p:_n4611 m:0
gain.gain13 out:beta1 in:_n3845 = k=20
gain.gain14 out:_n4495 in:beta1 = k=0.866
gain.gain16 out:_n4489 in:alpha1 = k=1/2
diff.diff5 out:error2 in1:_n4495 in2:_n4489
gain.gain21 out:_n4497 in:beta1 = k=-0.866
gain.gain29 out:_n4498 in:alpha1 = k=-1/2
sum.sum9 out:error3 in1:_n4498 in2:_n4497
var2v.var2v5 in:error3 p:_n4612 m:0
comp_l4.comp_l4_1 p:_n4610 enbl:freeNet1 out:S1 m:_n4563 = enable_init=_1
comp_l4.comp_l4_2 p:_n4611 enbl:freeNet2 out:S2 m:_n4565 = enable_init=_1
comp_l4.comp_l4_3 p:_n4612 enbl:freeNet3 out:S3 m:_n4567 = enable_init=_1
vtri.vtri1 p:_n4563 m:0 = period=1/18e3, ampl=1
vtri.vtri2 p:_n4565 m:0 = period=1/18e3, ampl=1
vtri.vtri3 p:_n4567 m:0 = period=1/18e3, ampl=1
c_sin.c_sin1 out:A1 = ac_phase=0, frequency=60, amplitude=1, ac_mag=1
c_sin.c_sin2 out:B1 = ac_phase=0, frequency=60, amplitude=1, phase=-120, ac_mag=1
c_sin.c_sin3 out:C1 = ac_phase=0, frequency=60, amplitude=1, phase=-240, ac_mag=1
lead_lag.lead_lag1 out:_n4810 in:_n4804 = k=100, w2=2*3.1415*8000, \
```

```
      w1=2*3.1415*1500
diff.diff6 out:_n4811 in1:_n4805 in2:_n4795 = k2=0.1, k1=0.1
v_ppwl.v_ppwl1 p:_n4798 m:0 = ppwl=(0,0,0.99/18e3,2.2,1/18e3,0)
integ.integ1 out:_n4803 in:_n4811 = k=1, init=0
v_pwl.v_pwl1 p:_n4802 m:0 = pwl=(0,0,10e-3,1)
v2var.v2var4 p:boost_out m:vminus out:_n4795 = k=1/200
vsum.vsum1 vin1:sense2 vin2:sense1 vout:_n4800 = k2=-1
var2v.var2v6 in:_n4810 p:_n4807 m:0 = k=1
comp_l4.comp_l4_4 p:_n4801 enbl:freeNet4 out:boost_sw1 m:_n4798 = enable_init=_1
vsum.vsum2 vin1:_n4807 vin2:_n4800 vout:_n4790 = k2=-1
v2var.v2var5 p:_n4790 m:0 out:_n4797 = k=1/200
v2var.v2var6 p:_n4802 m:0 out:_n4805 = k=1
lead_lag.lead_lag2 out:_n4804 in:_n4803 = k=7.5, w2=2*3.1415*5000, \
      w1=2*3.1415*100
var2v.var2v7 in:_n4806 p:_n4801 m:0 = k=1
short.short5 p:_n4823 m:sense2
short.short6 p:_n4816 m:_n4819
l.l7 p:sense1 m:_n4816 = l=300u, ic=0, r=1m
short.short7 p:_n4819 m:_n4815
dp.dp1 n:boost_out p:_n4819 = model=model(dp.dp1)<-(bv=1000)
c.c4 p:boost_out m:vminus = ic=undef, esr=50m, c=500u
r.r1 p:sense2 m:sense1 = rnom=0.01
sw1_l4.sw1_l4_7 p:vminus m:_n4815 c:boost_sw1 = ton=1n, toff=1n
lead_lag.lead_lag3 out:_n4806 in:_n4797 = k=1e6, w2=2*3.1415*0.01, w1=2*3.1415*10
fuelcell450.fuelcell450_1 p:_n4823 m:vminus
load.load1 p:Abar m:0
load.load4 p:Bbar m:0
load.load5 p:Cbar m:0
```

Space-Vector Modulation Implementation using MAST:

```
template svm1 f dalph dbet sa sb sc =fr
electrical dalph,dbet
state logic_4 sa,sb,sc,f
number fr = undef
{
state nu d1,d2,d3,sec,i,va,vb,d0,t1,t2,t3,mag
number T,norm
parameters {
norm = sqrt(3)/2
T = 1/fr
}

when (dc_init) {
schedule_event(time,sa,l4_1)
schedule_event(time,sb,l4_0)
schedule_event(time,sc,l4_0)
}

when (event_on(f)){
  va = v(dalph)
  vb = v(dbet)
  if(va*vb > 0){
    if(sqrt(3)*abs(va)>abs(vb)){
      d1 = abs(va) - abs(vb)/sqrt(3)
      d2 = 2*abs(vb)/sqrt(3)
      t1 = d1*T
      t2 = d2*T
      t3 = T-t1-t2
    if(vb>0){
      i = 1
```

```
  sec=2

  schedule_event(time,sa,l4_1)
  schedule_event(time+t1/2,sa,l4_1)
  schedule_event(time+t2/2+t1/2,sa,l4_1)
  schedule_event(time+t3/2+t1/2+t2/2,sa,l4_1)
  schedule_event(time+t3/2+t1/2+t2,sa,l4_1)
  schedule_event(time+t3/2+t1+t2,sa,l4_0)

  schedule_event(time,sb,l4_0)
  schedule_event(time+t1/2,sb,l4_1)
  schedule_event(time+t2/2+t1/2,sb,l4_1)
  schedule_event(time+t3/2+t1/2+t2/2,sb,l4_1)
  schedule_event(time+t3/2+t1/2+t2,sb,l4_0)
  schedule_event(time+t3/2+t1+t2,sb,l4_0)

  schedule_event(time,sc,l4_0)
  schedule_event(time+t1/2,sc,l4_0)
  schedule_event(time+t2/2+t1/2,sc,l4_1)
  schedule_event(time+t3/2+t1/2+t2/2,sc,l4_0)
  schedule_event(time+t3/2+t1/2+t2,sc,l4_0)
  schedule_event(time+t3/2+t1+t2,sc,l4_0)


  }
else{
  i = 4
  sec = 5

  schedule_event(time,sa,l4_0)
  schedule_event(time+t2/2,sa,l4_0)
  schedule_event(time+t2/2+t1/2,sa,l4_1)
  schedule_event(time+t3/2+t1/2+t2/2,sa,l4_0)
```

```
  schedule_event(time+t3/2+t1+t2/2,sa,l4_0)
  schedule_event(time+t3/2+t1+t2,sa,l4_0)

  schedule_event(time,sb,l4_0)
  schedule_event(time+t2/2,sb,l4_1)
  schedule_event(time+t2/2+t1/2,sb,l4_1)
  schedule_event(time+t3/2+t1/2+t2/2,sb,l4_1)
  schedule_event(time+t3/2+t1+t2/2,sb,l4_0)
  schedule_event(time+t3/2+t1+t2,sb,l4_0)

  schedule_event(time,sc,l4_1)
  schedule_event(time+t2/2,sc,l4_1)
  schedule_event(time+t2/2+t1/2,sc,l4_1)
  schedule_event(time+t3/2+t1/2+t2/2,sc,l4_1)
  schedule_event(time+t3/2+t1+t2/2,sc,l4_1)
  schedule_event(time+t3/2+t1+t2,sc,l4_0)


  }
}

else{
  d1 = abs(va) + abs(vb)/sqrt(3)
  d2 = abs(vb)/sqrt(3) - abs(va)
  t1 = d1*T
  t2 = d2*T
  t3 = T-t1-t2

if(vb>0){
  i = 2
  sec=3

  schedule_event(time,sa,l4_0)
```

```
  schedule_event(time+t2/2,sa,l4_1)
  schedule_event(time+t2/2+t1/2,sa,l4_1)
  schedule_event(time+t3/2+t1/2+t2/2,sa,l4_1)
  schedule_event(time+t3/2+t2/2+t1,sa,l4_0)
  schedule_event(time+t3/2+t1+t2,sa,l4_0)

  schedule_event(time,sb,l4_1)
  schedule_event(time+t2/2,sb,l4_1)
  schedule_event(time+t2/2+t1/2,sb,l4_1)
  schedule_event(time+t3/2+t1/2+t2/2,sb,l4_1)
  schedule_event(time+t3/2+t2/2+t1,sb,l4_1)
  schedule_event(time+t3/2+t1+t2,sb,l4_0)

  schedule_event(time,sc,l4_0)
  schedule_event(time+t2/2,sc,l4_0)
  schedule_event(time+t2/2+t1/2,sc,l4_1)
  schedule_event(time+t3/2+t1/2+t2/2,sc,l4_0)
  schedule_event(time+t3/2+t2/2+t1,sc,l4_0)
  schedule_event(time+t3/2+t1+t2,sc,l4_0)


  }
else{
  i = 5
  sec=6

  schedule_event(time,sa,l4_0)
  schedule_event(time+t1/2,sa,l4_1)
  schedule_event(time+t2/2+t1/2,sa,l4_1)
  schedule_event(time+t3/2+t1/2+t2/2,sa,l4_1)
  schedule_event(time+t3/2+t1+t2/2,sa,l4_0)
  schedule_event(time+t3/2+t1+t2,sa,l4_0)
```

```
  schedule_event(time,sb,l4_0)
  schedule_event(time+t1/2,sb,l4_0)
  schedule_event(time+t2/2+t1/2,sb,l4_1)
  schedule_event(time+t3/2+t1/2+t2/2,sb,l4_0)
  schedule_event(time+t3/2+t1+t2/2,sb,l4_0)
  schedule_event(time+t3/2+t1+t2,sb,l4_0)

  schedule_event(time,sc,l4_1)
  schedule_event(time+t1/2,sc,l4_1)
  schedule_event(time+t2/2+t1/2,sc,l4_1)
  schedule_event(time+t3/2+t1/2+t2/2,sc,l4_1)
  schedule_event(time+t3/2+t1+t2/2,sc,l4_1)
  schedule_event(time+t3/2+t1+t2,sc,l4_0)

  }
}
}
else{
if(sqrt(3)*abs(va)>abs(vb)){
  d2 = abs(va) - abs(vb)/sqrt(3)
  d1 = 2*abs(vb)/sqrt(3)
  t1 = d1*T
  t2 = d2*T
  t3 = T-t1-t2
if(vb>0){
  i = 3
  sec=4

  schedule_event(time,sa,l4_0)
  schedule_event(time+t1/2,sa,l4_0)
  schedule_event(time+t2/2+t1/2,sa,l4_1)
  schedule_event(time+t3/2+t1/2+t2/2,sa,l4_0)
  schedule_event(time+t3/2+t1/2+t2,sa,l4_0)
```

```
  schedule_event(time+t3/2+t1+t2,sa,l4_0)

  schedule_event(time,sb,l4_1)
  schedule_event(time+t1/2,sb,l4_1)
  schedule_event(time+t2/2+t1/2,sb,l4_1)
  schedule_event(time+t3/2+t1/2+t2/2,sb,l4_1)
  schedule_event(time+t3/2+t1/2+t2,sb,l4_1)
  schedule_event(time+t3/2+t1+t2,sb,l4_0)

  schedule_event(time,sc,l4_0)
  schedule_event(time+t1/2,sc,l4_1)
  schedule_event(time+t2/2+t1/2,sc,l4_1)
  schedule_event(time+t3/2+t1/2+t2/2,sc,l4_1)
  schedule_event(time+t3/2+t1/2+t2,sc,l4_0)
  schedule_event(time+t3/2+t1+t2,sc,l4_0)


  }
else{
  i = 6
  sec=1

  schedule_event(time,sa,l4_1)
  schedule_event(time+t2/2,sa,l4_1)
  schedule_event(time+t2/2+t1/2,sa,l4_1)
  schedule_event(time+t3/2+t1/2+t2/2,sa,l4_1)
  schedule_event(time+t3/2+t1/2+t2,sa,l4_1)
  schedule_event(time+t3/2+t1+t2,sa,l4_0)

  schedule_event(time,sb,l4_0)
  schedule_event(time+t2/2,sb,l4_0)
  schedule_event(time+t2/2+t1/2,sb,l4_1)
  schedule_event(time+t3/2+t1/2+t2/2,sb,l4_0)
```

```
  schedule_event(time+t3/2+t1/2+t2,sb,l4_0)
  schedule_event(time+t3/2+t1+t2,sb,l4_0)

  schedule_event(time,sc,l4_0)
  schedule_event(time+t2/2,sc,l4_1)
  schedule_event(time+t2/2+t1/2,sc,l4_1)
  schedule_event(time+t3/2+t1/2+t2/2,sc,l4_1)
  schedule_event(time+t3/2+t1/2+t2,sc,l4_0)
  schedule_event(time+t3/2+t1+t2,sc,l4_0)

  }
}
else{
  d2 = abs(va) + abs(vb)/sqrt(3)
  d1 = abs(vb)/sqrt(3) - abs(va)
  t1 = d1*T
  t2 = d2*T
  t3 = T-t1-t2
if(vb>0){
  i = 2
  sec=3

  schedule_event(time,sa,l4_0)
  schedule_event(time+t2/2,sa,l4_1)
  schedule_event(time+t2/2+t1/2,sa,l4_1)
  schedule_event(time+t3/2+t1/2+t2/2,sa,l4_1)
  schedule_event(time+t3/2+t2/2+t1,sa,l4_0)
  schedule_event(time+t3/2+t1+t2,sa,l4_0)

  schedule_event(time,sb,l4_1)
  schedule_event(time+t2/2,sb,l4_1)
  schedule_event(time+t2/2+t1/2,sb,l4_1)
  schedule_event(time+t3/2+t1/2+t2/2,sb,l4_1)
```

```
  schedule_event(time+t3/2+t2/2+t1,sb,l4_1)
  schedule_event(time+t3/2+t1+t2,sb,l4_0)

  schedule_event(time,sc,l4_0)
  schedule_event(time+t2/2,sc,l4_0)
  schedule_event(time+t2/2+t1/2,sc,l4_1)
  schedule_event(time+t3/2+t1/2+t2/2,sc,l4_0)
  schedule_event(time+t3/2+t2/2+t1,sc,l4_0)
  schedule_event(time+t3/2+t1+t2,sc,l4_0)

  }
else{
  i = 5
  sec=6

  schedule_event(time,sa,l4_0)
  schedule_event(time+t1/2,sa,l4_1)
  schedule_event(time+t2/2+t1/2,sa,l4_1)
  schedule_event(time+t3/2+t1/2+t2/2,sa,l4_1)
  schedule_event(time+t3/2+t1+t2/2,sa,l4_0)
  schedule_event(time+t3/2+t1+t2,sa,l4_0)

  schedule_event(time,sb,l4_0)
  schedule_event(time+t1/2,sb,l4_0)
  schedule_event(time+t2/2+t1/2,sb,l4_1)
  schedule_event(time+t3/2+t1/2+t2/2,sb,l4_0)
  schedule_event(time+t3/2+t1+t2/2,sb,l4_0)
  schedule_event(time+t3/2+t1+t2,sb,l4_0)

  schedule_event(time,sc,l4_1)
  schedule_event(time+t1/2,sc,l4_1)
  schedule_event(time+t2/2+t1/2,sc,l4_1)
  schedule_event(time+t3/2+t1/2+t2/2,sc,l4_1)
```

```
      schedule_event(time+t3/2+t1+t2/2,sc,l4_1)
      schedule_event(time+t3/2+t1+t2,sc,l4_0)


#     schedule_event(time+t3/2+t1+t2,f,l4_1)
      }
    }
  }
  }
}
```

High-frequency transformer isolated cycloconverter topology:

```
##############################################################################
##
#                                                                            #
#  Saber netlist for design kawabata2withboost                               #
#  Created by the Saber Integration Toolkit 2001.4-3.4 of Analogy, Inc.      #
#  Created on Sun Jun 08 15:17:30 2003.                                      #
#                                                                            #
##############################################################################
##



##############################################################################
##
#                                                                            #
#  Instances found in the top level of design kawabata2withboost             #
#                                                                            #
##############################################################################
##

short.IP p:_n1318 m:_n5677
sw1_l4.sw1_l4_1 p:_n1318 m:_n5948 c:s1
sw1_l4.sw1_l4_2 p:@"HFin-" m:_n5948 c:s2
sw1_l4.sw1_l4_3 p:0 m:_n1318 c:s2
sw1_l4.sw1_l4_4 p:0 m:@"HFin-" c:s1
diff.diff1 out:_n5213 in1:_n5169 in2:_n5156
v2var.v2var1 p:la m:0 out:_n5156 = k=1/120
inv_l4.inv_l4_12 out:q7 in:q8
comp_l4.comp_l4_4 p:_n5149 enbl:freeNet1 out:_n5210 m:_n5241 = enable_init=_1
short.short6 p:_n5143 m:_n5233
var2v.var2v4 in:_n5213 p:_n5147 m:0 = k=5
l.l5 p:_n5155 m:la = l=1m, r=10m
var2v.var2v5 in:_n5188 p:_n5241 m:0 = k=5
```

```
x3.x3_2 p1:_n5676 m1:@"HFin-" p2:_n5181 m2:_n5167 p3:_n5167 m3:_n5183 = n3=50, \
      n2=50, n1=100
short.short7 p:_n5152 m:_n5160
v_ppwl.v_ppwl6 p:_n5187 m:0 = ppwl=(0,0,0.001u,4,50u,0)
diff.diff2 out:_n5206 in1:_n5226 in2:_n5153
v_dc.v_dc8 p:_n5235 m:_n5242 = dc_value=-2
v2var.v2var2 p:lb m:0 out:_n5203 = k=1/120
sw1_l4.sw1_l4_17 p:_n5143 m:_n5146 c:q5 = ton=0.3u, toff=0.3u
inv_l4.inv_l4_13 out:q5 in:q6
nxor2_l4.nxor2_l4_7 in1:s1 out:q8 in2:_n5210
v2var.v2var3 p:lc m:0 out:_n5153 = k=1/120
short.short8 p:_n5152 m:_n5146
sw1_l4.sw1_l4_18 p:_n5175 m:_n5198 c:q8 = ton=0.3u, toff=0.3u
c_sin.c_sin4 out:_n5169 = ac_phase=0, frequency=60, amplitude=1, ac_mag=1
c.c6 p:lb m:0 = esr=10m, c=1m
short.short9 p:_n6235 m:_n5167
inv_l4.inv_l4_14 out:q9 in:q10
v_ppwl.v_ppwl7 p:_n5184 m:0 = ppwl=(0,0,0.001u,4,50u,0)
short.short10 p:_n5181 m:_n5152
nxor2_l4.nxor2_l4_8 in1:s1 out:q6 in2:_n5194
v_dc.v_dc9 p:_n5145 m:_n5184 = dc_value=-2
sw1_l4.sw1_l4_19 p:_n5209 m:_n5160 c:q9 = ton=0.3u, toff=0.3u
diff.diff3 out:_n5188 in1:_n5200 in2:_n5203
comp_l4.comp_l4_5 p:_n5235 enbl:freeNet2 out:_n5194 m:_n5147 = enable_init=_1
l.l6 p:_n5223 m:lb = l=1m, r=10m
short.short11 p:_n5143 m:_n5155
comp_l4.comp_l4_6 p:_n5145 enbl:freeNet3 out:_n5202 m:_n5166 = enable_init=_1
nxor2_l4.nxor2_l4_9 in1:s1 out:q10 in2:_n5202
c.c7 p:lc m:0 = esr=10m, c=1m
v_ppwl.v_ppwl8 p:_n5242 m:0 = ppwl=(0,0,0.001u,4,50u,0)
c_sin.c_sin5 out:_n5200 = ac_phase=0, frequency=60, amplitude=1, phase=-120, \
      ac_mag=1
short.short15 p:_n5183 m:_n5175
```

```
l.l8 p:_n5161 m:lc = l=1m, r=10m
sw1_l4.sw1_l4_20 p:_n5175 m:_n5233 c:q6 = ton=0.3u, toff=0.3u
short.short16 p:_n5209 m:_n5161
v_dc.v_dc10 p:_n5149 m:_n5187 = dc_value=-2
sw1_l4.sw1_l4_21 p:_n5175 m:_n5209 c:q10 = ton=0.3u, toff=0.3u
c_sin.c_sin6 out:_n5226 = ac_phase=0, frequency=60, amplitude=1, phase=-240, \
       ac_mag=1
sw1_l4.sw1_l4_22 p:_n5198 m:_n5151 c:q7 = ton=0.3u, toff=0.3u
short.short17 p:_n5198 m:_n5223
var2v.var2v6 in:_n5206 p:_n5166 m:0 = k=5
c.c8 p:la m:0 = esr=10m, c=1m
short.short18 p:_n5152 m:_n5151
clock_l4.clock_l4_7 clock:s1 = freq=10k, duty=0.5
inv_l4.inv_l4_15 out:s2 in:s1
l.l10 p:_n5677 m:_n5676 = l=5u, ic=0
v2var.v2var6 p:_n5914 m:0 out:_n5917 = k=1/200
sw1_l4.sw1_l4_14 p:0 m:_n5902 c:boost_sw = ton=1n, toff=1n
var2v.var2v7 in:_n5934 p:_n5939 m:0 = k=1
short.short19 p:_n5942 m:_n5904
vsum.vsum1 vin1:_n5932 vin2:_n5923 vout:_n5914 = k2=-1
c.c9 p:VIN m:0 = ic=0, esr=50m, c=1m
comp_l4.comp_l4_7 p:_n5939 enbl:freeNet4 out:boost_sw m:_n5929 = enable_init=_1
v_ppwl.v_ppwl5 p:_n5929 m:0 = ppwl=(0,0,0.99/10e3,2.2,1/10e3,0)
diff.diff5 out:_n5935 in1:_n5913 in2:_n5903 = k2=0.1, k1=0.1
v2var.v2var7 p:_n5910 m:0 out:_n5913 = k=1
integ.integ1 out:_n5905 in:_n5935 = k=1, init=0
v2var.v2var8 p:VIN m:0 out:_n5903 = k=1/200
lead_lag.lead_lag1 out:_n5934 in:_n5917 = k=2e5, w2=2*3.1415*0.01, w1=2*3.1415*5
r.r6 p:_n5925 m:_n5901 = rnom=0.01
v_dc.v_dc6 p:_n6263 m:0 = dc_value=70
short.short20 p:_n5904 m:_n5902
vsum.vsum2 vin1:_n5925 vin2:_n5901 vout:_n5923 = k2=-1
var2v.var2v8 in:_n5941 p:_n5932 m:0 = k=1
```

```
v_pwl.v_pwl1 p:_n5910 m:0 = pwl=(0,0,15e-3,1)
dp.dp2 n:VIN p:_n5904 = model=model(dp.dp2)<-(bv=1000)
l.l7 p:_n5901 m:_n5942 = l=0.3m, ic=0, r=10m
short.short21 p:_n6263 m:_n5925
short.short22 p:VIN m:_n5948
lead_lag.lead_lag3 out:_n5941 in:_n5920 = k=100, w2=2*3.1415*8000, \
      w1=2*3.1415*1200
lead_lag.lead_lag2 out:_n5920 in:_n5905 = k=10, w2=2*3.1415*5000, w1=2*3.1415*10
c.c10 p:_n6235 m:0 = ic=0, c=100u
kawaload.kawaload1 p:la m:0
kawaload.kawaload2 p:lb m:0
kawaload.kawaload3 p:lc m:0
```

Appendix B.2 PES Loss Estimation

List of symbols:

D duty ratio
f_{sw} switching frequency
C_{oss} MOSFET/IGBT effective output capacitance
V_{off} MOSFET/IGBT off state voltage
I_{on} MOSFET/IGBT on state current
R_g MOSFET/IGBT gate resistance
C_{iss} MOSFET/IGBT effective input capacitance
V_{gon} minimum gate voltage required to support the on state current (I_{on})
V_{tn} n-channel MOSFET/IGBT threshold voltage
I_L average inductor current
R_L inductor winding resistance
V_{th} diode threshold voltage
I_d average diode current
k_L inductor coefficient
k_{tr} transformer coefficient
I_{pri} transformer primary current
I_{sec} transformer secondary current
R_{pri} transformer primary winding resistance
R_{sec} transformer secondary winding resistance
R_{esr} capacitor series resistance
I_{in} average input current
$R_{para\text{-}lumped}$ lumped parasitic resistance

1) MOSFET Losses:

Switching losses

$$L_{sw} = Df_{sw}\left(\frac{2C_{oss}V_{off}^2}{3} + \frac{V_{off}I_{on}R_gC_{iss}}{2}\ln\left[\frac{V_{gon}}{V_{tn}}\right]\right)$$

for hard switching

$$L_{sw} = Df_{sw}\left(\frac{2C_{oss}V_{off}^2}{3}\right)$$ for ZCS

Conduction losses

$$L_{cond} = DI_{on}R_{on}$$

2) Diode Losses:

Switching losses

$$L_{sw} = (1-D) f_{sw} (\frac{2C_{out} V_{off}^2}{3})$$

Conduction losses

$$L_{cond} = (1-D)(V_{th} I_d + I_d^2 R_d)$$

3) Inductor Losses:

Winding loss (copper loss)

$$L_{L-cu} = I_L^2 R_L$$

Core loss

$$L_{L-core} = k_L (\Delta i_L)^2 f_{sw}$$

4) Capacitor Losses:

$$L_{cap} = (\Delta i_{cap})^2 R_{esr}$$

5) Transformer Losses:

Winding loss (copper loss)

$$L_{tr-cu} = D(I_{pri}^2 R_{pri} + I_{\sec}^2 R_{\sec})$$

Core loss

$$L_{L-core} = k_{tr} B^2 f_{sw}$$

6) Parasitic Losses:

$$L_{para} = I_{in}^2 R_{para-lumped}$$

Appendix C.1 Parametric Analysis #1 of the SOFC based APU

Perturbations to be performed:

a. As regards to Power

1. Increase the Net Power required steadily – Starting from 1000 W, we proceed to 2000 W, 3000 W, 4000 W, 5000 W in steps of 1000 W.
2. Decrease the Net Power required steadily – Starting from 5000 W, we proceed to 4000 W, 3000 W, 2000 W, 1000 W in steps of 1000 W.

b. As regards to process parameters

1. Simulate the process with initial conditions such as Fuel Utilization: 0.85; Steam to Methane ratio: 3.4, Fuel Reformate ratio: 0.3, Air to Fuel ratio: 20.

2. Simulate the process keeping all the parameters constant and only changing the Fuel Utilization from:
   0.85 to 0.70
   0.85 to 0.90

3. Simulate the process this time changing the Steam to Fuel ratio only and keeping the other parameters constant. The changes in the Steam to Methane ratios are:
   3.4 to 3.0
   3.4 to 3.8

4. Simulate by changing the Fuel Reformate ratio alone and keeping the other parameters constants. The changes to the Fuel Reformate ratio were:
   0.3 to 0.27
   0.3 to 0.33

As regards to parameters, we can also vary the Air to Fuel ratios at the Stack and the Burner.

Parametric Study Analysis:

The variation of the process variables due to the above said perturbations are analyzed at the following components of the SOFC APU system. The components are:

1. A: Pre-reformer …… @ Stream 5
2. B: Combustor ……@ Stream 16
3. C: Steam Generator ……@ Stream 2
4. D: Air Compressor ……@ Stream 27
5. E: Gas Expander ……@ Stream 13
6. M: Air-Combustion Gas Mixer ……@ Stream 18
7. N: Methane Compressor ……@ Stream 24
8. HXI: Fuel Preheating HX ……@ Stream 8

9. HXII: Air Preheating HX ……@ Stream 9
10. HXIII: Methane Preheating HX ……@ Stream 1
11. HIV: Air Recuperator ……@ Stream 26

The effects of the perturbations on the temperatures and the Mixture Flow rates at these above components are tabulated and analyzed. Based on the time for steady state of the temperatures and the Mixture Flow rates, the time for the system to stabilize is deduced. Also the System Thermal and System Energy efficiencies for the perturbations are also tabulated.

Table showing the components contributing to the attainment of the stability (Temperature) of the System

FU : Fuel Utilization; SMR : Steam to Methane Ratio; FRR : Fuel Reformate Ratio

The Table shows the system components (with their streams in green) contributing to the prolonged stability time (time given in blue), as regards to Stable Temperature, for changes in power requirements and changes in Fuel Utilization, Steam to Methane Ratio and Fuel Reformate Ratio.

S No.	Power Change	Components contributing to increased time for the stability of the system						
		FU 0.85 SMR 3.40 FRR 0.30	FU 0.70 SMR 3.40 FRR 0.30	FU 0.90 SMR 3.40 FRR 0.30	FU 0.85 SMR 3.00 FRR 0.30	FU 0.85 SMR 3.80 FRR 0.30	FU 0.85 SMR 3.40 FRR 0.27	FU 0.85 SMR 3.40 FRR 0.33
1	1000 W to 2000 W	Pre-reformer (5) (13.1880)	Pre-reformer (5) HXI (8) (10)	Pre-reformer (5) HXI (8) (8.997)	HXI (8) (10.9970)	Pre-reformer (5) HXI (8) (10.119)	HXI (8) (15.997)	Pre-reformer (5) (8.0620)
2	1000 W to 3000 W	Pre-reformer (5) (16.2010)	Pre-reformer (5) HXI (8) (12.033)	Pre-reformer (5) HXI (8) (10.997)	Pre-reformer (5) (14.1160)	Pre-reformer (5) (12.1990)	Pre-reformer (5) HXI (8) (18.869)	Pre-reformer (5) HXI (8) (11)
3	1000 W to 4000 W	Pre-reformer (5) (18.2160)	Pre-reformer (5) HXI (8) (17.023)	Pre-reformer (5) HXI (8) (12.997)	HXI (8) (18.116)	Pre-reformer (5) (21.1990)	Pre-reformer (5) (20.967)	Pre-reformer (5) HXI (8) (16)
4	1000 W to 5000 W	Pre-reformer (5) (22.2030)	Pre-reformer (5) (22.9970)	Pre-reformer (5) (16.9970)	Pre-reformer (5) HXI (8), Steam Generator (2) (21.64)	Pre-reformer (5) (20.003)	Pre-reformer (5) HXI (8) (24.692)	Pre-reformer (5) (20.6780)
5	5000 W to 4000 W	Pre-reformer (5) HXI (8), Steam Generator (2) (13.9530)	Pre-reformer (5) HXI (8) (8.9690)	Pre-reformer (5) HXI (8) (13)	Pre-reformer (5) HXI (8) (15.850)	Pre-reformer (5) HXI (8) (13.852)	Pre-reformer (5) HXI (8) (26.8570)	Pre-reformer (5) HXI (8) (16.091)
6	5000 W to 3000 W	Pre-reformer (5) HXI (8), Steam Generator (2) (16.1430)	Pre-reformer (5) HXI (8) (12.8060)	Pre-reformer (5) HXI (8) (13.844)	Pre-reformer (5) (16)	HXI (8) (15.077)	Pre-reformer (5) HXI (8), Steam Generator (2) (19)	Pre-reformer (5) HXI (8) (17.030)
7	5000 W to 2000 W	Pre-reformer (5) HXI (8), Steam Generator (2) (17.8760)	Pre-reformer (5) HXI (8) (15)	Pre-reformer (5) HXI (8) (15.8810)	Pre-reformer (5) HXI (8) (16.9970)	HXI (8) (19.006)	Steam Generator (2) (20.8810)	Pre-reformer (5) HXI (8) (18)
8	5000 W to 1000 W	Steam Generator (2) (22.8080)	Pre-reformer (5) HXI (8) (19)	Pre-reformer (5) (16.0920)	Steam Generator (2) (18.840)	Pre-reformer (5) (20.1010)	Steam Generator (2) (20.9020)	Pre-reformer (5) (21)

Table showing the components contributing to the attainment of the stability (Flow rate) of the System

FU : Fuel Utilization; SMR : Steam to Methane Ratio; FRR : Fuel Reformate Ratio

The Table shows the system components (with their streams in green) contributing to the prolonged stability time (time given in blue), as regards to Stable Flow rate, for changes in power requirements and changes in Fuel Utilization, Steam to Methane Ratio and Fuel Reformate Ratio.

S No.	Power Change	Components contributing to increased time for the stability of the system						
		FU 0.85 SMR 3.40 FRR 0.30	FU 0.70 SMR 3.40 FRR 0.30	FU 0.90 SMR 3.40 FRR 0.30	FU 0.85 SMR 3.00 FRR 0.30	FU 0.85 SMR 3.80 FRR 0.30	FU 0.85 SMR 3.40 FRR 0.27	FU 0.85 SMR 3.40 FRR 0.33
1	1000 W to 2000 W	Air Comb. Gas Mixer (18) (5.28)	Combustor (16) (3.211)	Air Comp. (27) HXI (8), Air CombMixer (18) (2.445)	Air Comp. (27) HXI (8) HXII (9) (2.32)	Air Comp. (27) Air CombMixer (18) (2.442)	HXI (8), HXII (9) (2.444)	HXI (8) (3.131)
2	1000 W to 3000 W	Air Comp. (27) HXII (9) (3.666)	HXIV (26) (5.100)	HXI (8) (4.902)	Air Comp. (27) HXI (8), HXII (9) (3.881)	CH4 Comp. (24) HXI (8), Air CombMixer (18) (3.632)	HXI (8) (4.055)	HXI (8) (6.131)
3	1000 W to 4000 W	Air Comp. (27) HXII (9) (5.128)	HXI (8) (8.104)	HXI (8) (5.00)	Air Comp. (27) HXI (8), HXII (9) (5.025)	Air Comp. (27) HXI (8) (4.947)	HXI (8) (6.005)	HXI (8) (7.131)
4	1000 W to 5000 W	Air Comp. (27) HXII (9) (6.266)	HXI (8) (8.104)	Steam Gen. (2) HXIII (1) (6.066)	HXIV (26) (6.997)	Air Comp. (27) Air CombMixer (18) (6.022)	Air Comp. (27) Air CombMixer (18) (6.303)	HXI (8) (11.131)
5	5000 W to 4000 W	HXII (9) (2.080)	HXI (8) (4.00)	Pre-reformer (5) HXII (9) (1.471)	HXI (8) (3.00)	HXI (8) (3.00)	Air Comp. (27) HXII (9) (2.00)	HXI (8) (6.0941)
6	5000 W to 3000 W	Air Comp. (27) (2.143)	HXI (8) (5.00)	Air Comp. (27) HXI (8) (3.00)	HXI (8) (4.00)	HXI (8) (3.103)	HXI (8) (4.00)	HXI (8) (9.131)
7	5000 W to 2000 W	Air Comp. (27) HXII (9), Air CombMixer (18) (2.720)	HXI (8) (6.82)	Air Comp. (27) HXI (8) (4.00)	HXI (8) (5.943)	HXI (8) (4.922)	HXI (8) (4.00)	HXI (8) (9.094)
8	5000 W to 1000 W	Combustor (16) (4.179)	HXIV (26) (8)	Air Comp. (27) HXI (8) (6.00)	HXI (8) (8.00)	HXI (8) (6.202)	HXI (8) (4.00)	HXI (8) (12.131)

Parametric Analysis #1

FU: Fuel Utilization SMR: Steam to Methane Ratio FRR: Fuel Reformate Ratio

Components and the time taken for steady temperature:

Pre-reformer

	Initial	F.U 0.70	F.U 0.90	SMR 3.0	SMR 3.8	FRR 0.27	FRR 0.33
1 to 2	13.1880	10.0000	8.9970	10.8380	10.0100	10.9970	8.0620
1 to 3	16.2010	12.0330	10.9970	14.1160	13.0750	13.0520	11.0000
1 to 4	18.2160	17.0230	12.9970	18.1130	16.1360	15.0000	16.0000
1 to 5	22.2030	22.9970	16.9970	21.6400	22.0230	23.9970	20.6780
5 to 4	13.9530	8.9690	13.0000	15.8500	13.8520	13.8570	16.0910
5 to 3	16.1430	12.8060	13.8440	16.0000	16.0060	14.7820	17.0300
5 to 2	17.8760	15.0000	15.8810	16.9970	18.0000	16.8810	18.0000
5 to 1	19.7380	19.0000	16.0920	17.8970	21.0000	21.9020	21.0000

Combustor

	Initial	F.U 0.70	F.U 0.90	SMR 3.0	SMR 3.8	FRR 0.27	FRR 0.33
1 to 2	12.2770	8.0170	7.9970	9.9970	9.1190	13.9970	7.1620
1 to 3	15.2770	9.7130	8.9970	13.1130	12.1990	14.0520	7.3200
1 to 4	17.2770	10.1000	10.9970	15.1130	20.1990	15.0520	11.1280
1 to 5	21.2770	12.0000	13.9970	20.9970	20.0030	17.9970	18.1280
5 to 4	13.9530	5.9690	7.8580	11.8500	12.8520	11.8570	13.0941
5 to 3	16.1430	8.8060	9.8440	12.0000	14.0060	15.7820	14.0300
5 to 2	17.8760	12.9700	11.8810	14.9970	17.0770	17.8810	16.0000
5 to 1	21.2800	17.9750	14.7400	16.8970	20.1010	19.4020	18.0260

Steam Generator

	Initial	F.U 0.70	F.U 0.90	SMR 3.0	SMR 3.8	FRR 0.27	FRR 0.33
1 to 2	12.2770	6.0170	5.9970	6.9970	9.1350	10.9970	6.0620
1 to 3	14.2190	10.0330	8.9970	8.1130	12.0730	12.0520	8.0680
1 to 4	18.0910	16.0000	10.1230	14.1130	17.1990	18.0520	13.0000
1 to 5	21.0090	17.9970	11.9970	21.6400	19.1030	22.9970	19.0480
5 to 4	13.9530	7.6610	6.8580	10.8500	6.8520	16.8570	6.0300
5 to 3	16.1430	10.8060	7.8440	12.9800	12.0060	19.0000	9.1320
5 to 2	17.8760	11.7620	8.8810	14.9970	12.0770	20.8810	13.0941
5 to 1	22.8080	14.0000	10.7400	18.8400	18.1010	21.9020	19.0260

Air Compressor

	Initial	F.U 0.70	F.U 0.90	SMR 3.0	SMR 3.8	FRR 0.27	FRR 0.33
1 to 2	2.5090	3.2140	2.4450	2.3200	2.4420	2.4440	2.4920
1 to 3	3.6660	4.1040	3.0000	3.8810	3.2020	3.9690	3.5580
1 to 4	5.1280	4.6720	4.8520	5.0250	4.9470	6.0550	4.8760
1 to 5	6.2660	6.1160	2.5980	6.2560	6.0220	6.3030	6.2350
5 to 4	1.6350	1.5880	2.0000	1.6960	1.6900	1.4370	1.6881
5 to 3	4.0000	4.0000	1.9860	2.1930	2.0480	2.1060	2.1170
5 to 2	4.1430	4.3300	2.5840	2.8950	2.5840	2.8220	2.7010
5 to 1	6.0390	6.8200	2.9630	3.5260	3.0640	3.4370	3.3990

Gas Expander

	Initial	F.U 0.70	F.U 0.90	SMR 3.0	SMR 3.8	FRR 0.27	FRR 0.33
1 to 2	2.5090	3.2140	2.4450	2.3200	2.4420	2.4440	2.4920
1 to 3	3.6660	4.1040	3.7230	3.8810	3.2020	3.9690	3.5580
1 to 4	5.1280	4.6720	4.8520	5.0250	4.9470	6.0550	4.8760
1 to 5	6.2660	6.1160	6.2630	6.2560	6.0220	6.3030	6.2320
5 to 4	1.6350	1.5880	2.0000	1.6960	1.6900	1.4370	1.6881
5 to 3	4.0000	4.0000	1.9860	2.1930	2.0480	2.1060	2.1170
5 to 2	4.1430	4.3300	2.5840	2.8950	2.5840	2.8220	2.7010
5 to 1	6.0390	6.8200	2.9630	3.5260	3.0640	5.0000	3.3990

Methane Compressor

	Initial	F.U 0.70	F.U 0.90	SMR 3.0	SMR 3.8	FRR 0.27	FRR 0.33
1 to 2	2.5060	2.9490	2.4420	2.3170	2.4390	2.4410	2.4890
1 to 3	3.6630	4.2080	3.7200	3.8780	3.6290	3.9660	3.5550
1 to 4	5.1250	4.9970	4.8490	5.0220	4.9440	4.9210	4.8730
1 to 5	6.2630	6.1000	6.0660	6.2560	5.9420	6.3000	6.1520
5 to 4	1.5880	1.7030	1.3290	1.5460	1.5420	1.2940	1.5940
5 to 3	2.0660	2.4740	1.8300	2.1730	1.9510	1.8940	2.0760
5 to 2	2.5960	3.1820	2.4650	2.8920	2.6120	2.7030	2.6070
5 to 1	3.3660	4.3050	3.0260	3.4230	3.4290	3.3390	3.2940

HXI

	Initial	F.U 0.70	F.U 0.90	SMR 3.0	SMR 3.8	FRR 0.27	FRR 0.33
1 to 2	13.0880	10.0000	8.9970	10.9970	10.1190	15.9970	6.0000
1 to 3	15.0530	12.0330	10.9970	14.1130	12.1190	18.8690	11.0000
1 to 4	17.0880	17.0230	12.9970	18.1160	20.1990	20.7300	16.0000
1 to 5	22.1570	20.9970	15.8320	21.6400	19.1000	24.6920	18.0480
5 to 4	13.9530	8.9690	13.0000	15.8500	13.8200	26.8570	16.0910
5 to 3	16.1430	12.8060	13.8440	15.9800	15.0770	19.0000	17.0300
5 to 2	17.8760	15.0000	15.8810	16.9970	19.0060	17.8810	18.0000
5 to 1	22.2800	19.0000	15.7400	17.8970	20.1010	19.9020	20.1310

HXIII

	Initial	F.U 0.70	F.U 0.90	SMR 3.0	SMR 3.8	FRR 0.27	FRR 0.33
1 to 2	2.5060	2.9660	2.4420	2.3170	2.4390	2.4410	2.4890
1 to 3	3.6630	4.2080	3.7200	4.1130	3.6290	3.9660	3.5550
1 to 4	5.1250	6.1000	4.8490	5.0220	4.9440	4.9210	4.8730
1 to 5	6.2630	6.9970	5.9970	6.2530	6.0190	6.3000	6.2320
5 to 4	1.9530	1.9690	1.0590	1.8500	1.5420	1.2940	2.0910
5 to 3	2.5960	2.2800	1.8440	2.1730	1.9510	2.7820	2.0760
5 to 2	3.1400	3.9700	2.4650	2.8920	2.6120	2.7030	2.6800
5 to 1	3.3660	4.3050	3.0260	3.4320	3.4290	3.3390	3.2940

HXIV

	Initial	F.U 0.70	F.U 0.90	SMR 3.0	SMR 3.8	FRR 0.27	FRR 0.33
1 to 2	3.2770	5.0200	3.9970	2.3170	2.8670	8.9970	9.0000
1 to 3	4.2010	6.3480	4.9970	4.1130	4.1990	11.0520	11.0510
1 to 4	4.6750	6.7700	7.9970	5.0220	5.1990	18.0520	12.9530
1 to 5	5.0090	8.9970	9.9970	8.9970	7.0230	19.9970	13.0480
5 to 4	2.9530	2.9690	5.8580	1.5460	2.8520	7.8570	7.0910
5 to 3	4.0000	6.8060	7.9320	2.1930	3.0060	8.7820	11.0300
5 to 2	4.8760	8.4480	9.5450	3.0320	4.8960	12.8810	14.0000
5 to 1	7.1790	12.9250	10.0000	3.8060	6.1010	15.3850	14.9150

Components and the time taken for steady mass flow rate:

Pre-reformer

	Initial	F.U 0.70	F.U 0.90	SMR 3.0	SMR 3.8	FRR 0.27	FRR 0.33
1 to 2	2.5060	2.9660	2.4420	2.3170	2.4390	2.3760	2.4230
1 to 3	3.6050	4.2080	3.7200	3.8780	3.6290	3.9660	3.5550
1 to 4	5.1250	6.1120	4.8490	5.0220	4.9440	4.9210	4.8760
1 to 5	6.2630	7.3490	5.9770	6.2560	6.0190	6.0000	6.1520
5 to 4	1.5880	2.0110	1.4710	1.5460	1.5420	1.2940	1.5940
5 to 3	2.0660	2.2800	1.8300	2.1730	1.9510	1.8880	2.0760
5 to 2	2.5960	3.1820	2.4650	2.8920	2.6120	2.7030	2.6070
5 to 1	3.3660	4.3050	3.0260	3.4230	3.4290	3.3390	3.2940

Combustor

	Initial	F.U 0.70	F.U 0.90	SMR 3.0	SMR 3.8	FRR 0.27	FRR 0.33
1 to 2	2.2770	3.2110	2.4420	2.3170	2.4390	2.4410	2.4920
1 to 3	3.6630	4.1000	3.7200	3.8780	3.6290	3.9690	3.4950
1 to 4	4.8610	4.1000	4.8490	5.0220	4.9440	4.9210	4.8730
1 to 5	6.2630	7.3490	5.9970	6.2560	6.0190	6.3000	6.1310
5 to 4	1.6350	1.9690	1.4710	1.5460	1.5420	1.2940	1.5940
5 to 3	2.0660	2.2800	1.8300	2.1730	1.9510	1.8880	2.0300
5 to 2	2.5960	3.2120	2.5840	2.8920	2.6120	2.7030	2.6070
5 to 1	4.1790	4.3050	3.0260	3.4230	3.4290	3.3390	3.2940

Steam Generator

	Initial	F.U 0.70	F.U 0.90	SMR 3.0	SMR 3.8	FRR 0.27	FRR 0.33
1 to 2	2.2120	2.9660	2.4420	2.3170	2.4390	2.4410	2.4890
1 to 3	3.6050	4.2080	3.7200	3.8780	3.6290	3.9660	3.5550
1 to 4	5.1250	6.1120	4.8510	5.0220	4.9440	4.9210	4.8660
1 to 5	6.1890	7.3490	6.0660	6.2530	6.0190	6.3000	6.2320
5 to 4	1.5880	2.0110	1.3290	1.5460	1.5420	1.2940	1.6850
5 to 3	2.0660	2.2800	1.8300	2.1730	1.9510	1.8880	2.0760
5 to 2	2.5960	3.1820	2.4650	2.8920	2.6120	2.7030	2.6070
5 to 1	3.3660	4.3050	3.0260	3.4230	3.4290	3.3390	3.2940

Air Compressor

	Initial	F.U 0.70	F.U 0.90	SMR 3.0	SMR 3.8	FRR 0.27	FRR 0.33
1 to 2	1.6170	2.1040	2.4450	2.3200	2.4420	2.4440	2.4920
1 to 3	3.6660	2.9690	3.1980	3.8810	2.5590	3.5360	3.1310
1 to 4	5.1280	4.1040	3.7230	5.0250	4.9470	3.9690	3.5550
1 to 5	6.2660	5.0000	6.0000	6.0000	6.0220	6.3030	6.1310
5 to 4	1.6100	1.2270	1.4160	1.6960	1.5860	1.7230	1.6881
5 to 3	2.1430	2.0000	3.0000	2.0600	1.6900	2.0000	1.9620
5 to 2	2.7200	2.4580	4.0000	2.8950	2.5840	2.8220	2.7010
5 to 1	3.3960	4.3300	6.0000	3.5260	3.4690	3.4370	3.3990

Gas Expander

	Initial	F.U 0.70	F.U 0.90	SMR 3.0	SMR 3.8	FRR 0.27	FRR 0.33
1 to 2	2.2270	2.9660	2.4420	2.3170	2.4390	2.4410	2.4890
1 to 3	3.6630	4.1000	3.7200	3.7170	3.6290	3.9660	3.5550
1 to 4	5.1250	4.1000	4.8490	5.0220	4.9440	4.9210	4.8760
1 to 5	6.2630	5.9970	5.9970	6.2530	6.0220	6.3000	6.1280
5 to 4	1.5880	2.0110	1.4160	1.5460	1.5420	1.2940	1.5940
5 to 3	2.2090	2.2800	1.9860	2.1730	1.9510	1.8880	2.0300
5 to 2	2.5960	2.4580	2.5840	3.8060	2.6120	2.7030	2.6070
5 to 1	3.4670	3.9880	3.0260	4.8970	3.4290	3.3390	3.2940

Methane Compressor

	Initial	F.U 0.70	F.U 0.90	SMR 3.0	SMR 3.8	FRR 0.27	FRR 0.33
1 to 2	2.5060	2.9660	2.4420	2.3170	2.4390	2.4410	2.4890
1 to 3	3.6630	4.2080	3.7200	3.8780	3.6320	3.9660	3.5550
1 to 4	5.1250	6.1120	4.8490	5.0220	4.9470	4.9210	4.8730
1 to 5	6.2630	7.3490	6.0660	6.2530	6.0190	6.3000	6.2320
5 to 4	1.5880	2.0110	1.3290	1.5460	1.5420	1.2940	1.6850
5 to 3	2.0660	2.2800	1.8300	2.1730	1.9510	1.8880	2.0760
5 to 2	2.5960	3.1820	2.4650	2.8920	2.6120	2.7030	2.6070
5 to 1	3.3660	4.3050	3.0260	3.4230	3.4290	3.3390	3.2940

HXI

	Initial	F.U 0.70	F.U 0.90	SMR 3.0	SMR 3.8	FRR 0.27	FRR 0.33
1 to 2	2.5090	1.5040	2.4450	2.3200	2.2020	2.4440	3.1310
1 to 3	3.2800	4.2120	4.9020	3.8810	3.6320	4.0550	6.1310
1 to 4	5.1250	6.1020	5.0000	5.0250	4.9470	6.0050	7.1310
1 to 5	6.2800	8.1040	6.0000	6.0000	5.1030	6.0000	11.1310
5 to 4	1.6350	4.0000	1.4160	3.0000	3.0000	1.4370	6.0941
5 to 3	2.6000	5.0000	3.0000	4.0000	3.1030	2.0000	9.1310
5 to 2	2.9560	6.8200	4.0000	5.9430	4.9220	2.0000	9.0940
5 to 1	3.3630	7.4260	6.0000	8.0000	6.2020	4.0000	12.1310

HXII

	Initial	F.U 0.70	F.U 0.90	SMR 3.0	SMR 3.8	FRR 0.27	FRR 0.33
1 to 2	2.5090	2.9690	2.0000	2.3200	2.4420	2.4440	2.3850
1 to 3	3.6660	4.1040	2.4280	3.8810	2.5590	3.5360	3.1310
1 to 4	5.1280	6.1040	3.1980	5.0250	4.9470	3.9690	3.5550
1 to 5	6.2660	7.3520	6.0000	6.0000	6.0220	6.3030	6.1310
5 to 4	2.0800	2.0000	1.4710	1.6960	1.5860	2.0000	1.6881
5 to 3	2.1430	4.0000	1.6690	2.0600	1.6900	4.0000	1.9620
5 to 2	2.7200	5.0000	2.5840	2.8370	2.5840	4.0000	2.7010
5 to 1	3.3960	7.0000	3.2860	3.5260	3.4690	3.4370	3.3990

HXIII

	Initial	F.U 0.70	F.U 0.90	SMR 3.0	SMR 3.8	FRR 0.27	FRR 0.33
1 to 2	2.5060	2.9660	2.4420	2.3170	2.4390	2.4410	2.4890
1 to 3	3.6630	4.2080	3.7200	3.8780	3.6290	3.9660	3.5550
1 to 4	5.0640	6.1000	4.8490	5.0250	4.9470	4.9210	4.8730
1 to 5	6.2630	7.3490	6.0660	6.2530	6.0190	6.3000	6.2320
5 to 4	1.5880	2.0110	1.3290	1.5460	1.5420	1.2940	1.6850
5 to 3	2.0660	2.2800	1.8300	2.1730	1.9510	1.8880	2.0760
5 to 2	2.5960	3.1820	2.4650	2.8920	2.6120	2.7030	2.6070
5 to 1	3.3660	4.3050	3.0260	3.4230	3.4290	3.3390	3.2940

HXIV

	Initial	F.U 0.70	F.U 0.90	SMR 3.0	SMR 3.8	FRR 0.27	FRR 0.33
1 to 2	2.5060	2.9490	2.4420	2.3170	2.4390	2.4410	2.4890
1 to 3	3.6050	5.1000	3.7200	3.8780	3.6290	3.9660	3.5550
1 to 4	5.0640	6.1000	4.8490	5.0220	4.9440	4.9210	4.1280
1 to 5	6.2630	7.9970	5.9080	6.9970	6.0190	6.3000	6.1280
5 to 4	1.5880	1.9690	1.3290	1.5460	1.5420	1.2940	1.5940
5 to 3	2.2090	2.2800	1.8300	2.0600	1.9510	1.8880	2.0760
5 to 2	2.5960	5.9700	2.4650	2.6950	2.5580	2.7030	4.0000
5 to 1	3.3660	8.0000	2.8520	3.4230	3.3680	3.3390	5.0260

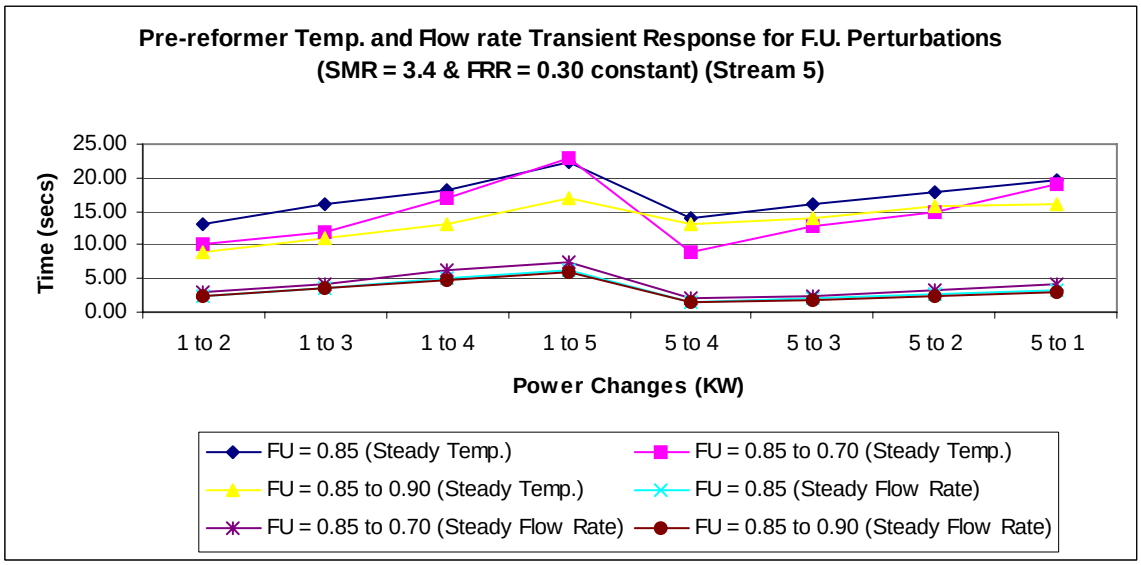
Pre-reformer Temp. and Flow rate Transient Response for F.U. Perturbations
(SMR = 3.4 & FRR = 0.30 constant) (Stream 5)
Time (secs)
25.00
20.00
15.00
10.00
5.00
0.00
1 to 2
1 to 3
1 to 4
1 to 5
5 to 4
5 to 3
5 to 2
5 to 1
Power Changes (KW)
FU = 0.85 (Steady Temp.)
FU = 0.85 to 0.70 (Steady Temp.)
FU = 0.85 to 0.90 (Steady Temp.)
FU = 0.85 (Steady Flow Rate)
FU = 0.85 to 0.70 (Steady Flow Rate)
FU = 0.85 to 0.90 (Steady Flow Rate)

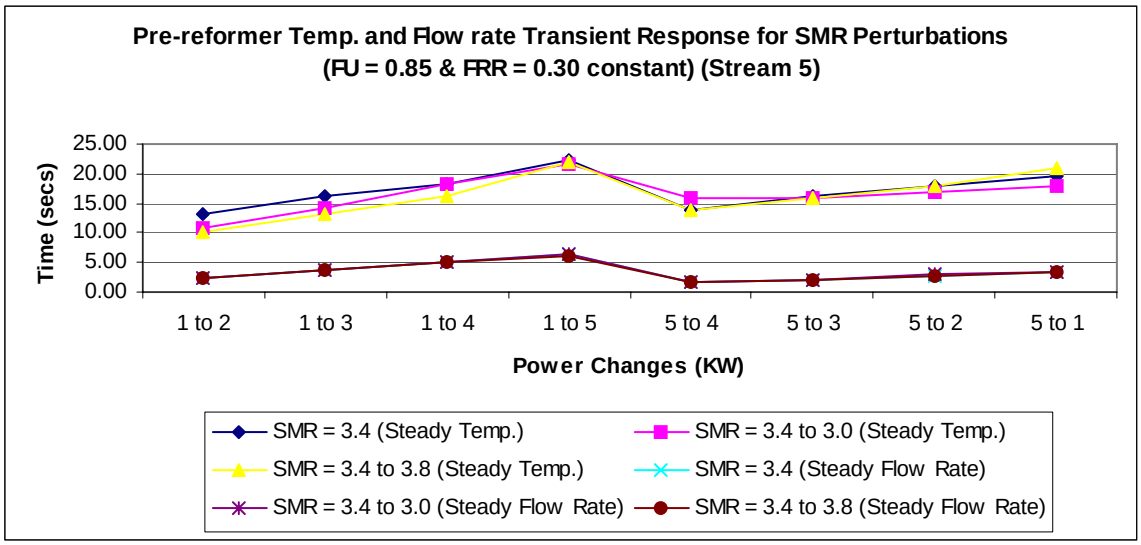
Pre-reformer Temp. and Flow rate Transient Response for SMR Perturbations
(FU = 0.85 & FRR = 0.30 constant) (Stream 5)
Time (secs)
25.00
20.00
15.00
10.00
5.00
0.00
1 to 2
1 to 3
1 to 4
1 to 5
5 to 4
5 to 3
5 to 2
5 to 1
Power Changes (KW)
SMR = 3.4 (Steady Temp.)
SMR = 3.4 to 3.0 (Steady Temp.)
SMR = 3.4 to 3.8 (Steady Temp.)
SMR = 3.4 (Steady Flow Rate)
SMR = 3.4 to 3.0 (Steady Flow Rate)
SMR = 3.4 to 3.8 (Steady Flow Rate)

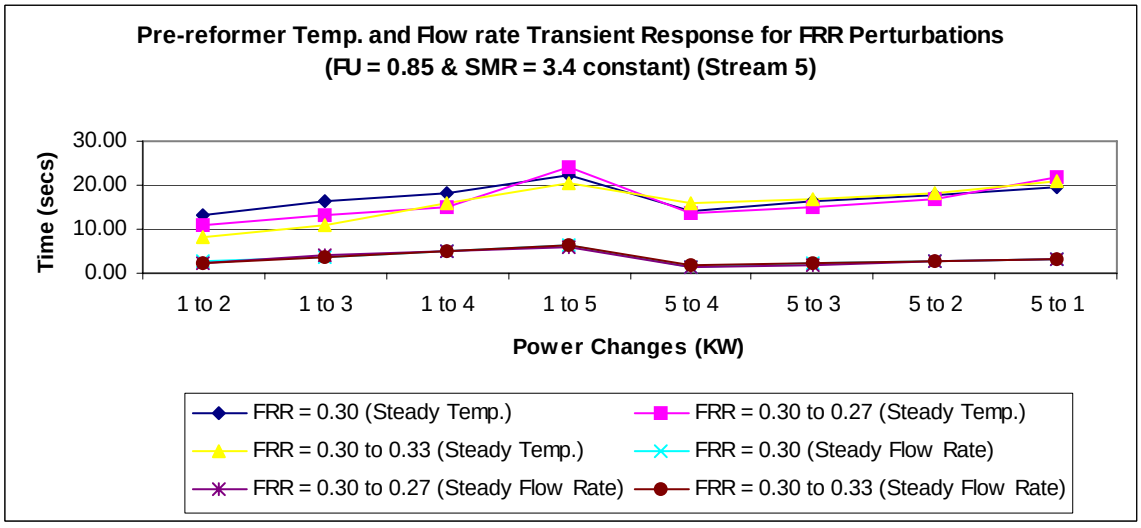
Pre-reformer Temp. and Flow rate Transient Response for FRR Perturbations
(FU = 0.85 & SMR = 3.4 constant) (Stream 5)
Time (secs)
30.00
20.00
10.00
0.00
1 to 2
1 to 3
1 to 4
1 to 5
5 to 4
5 to 3
5 to 2
5 to 1
Power Changes (KW)
FRR = 0.30 (Steady Temp.)
FRR = 0.30 to 0.27 (Steady Temp.)
FRR = 0.30 to 0.33 (Steady Temp.)
FRR = 0.30 (Steady Flow Rate)
FRR = 0.30 to 0.27 (Steady Flow Rate)
FRR = 0.30 to 0.33 (Steady Flow Rate)

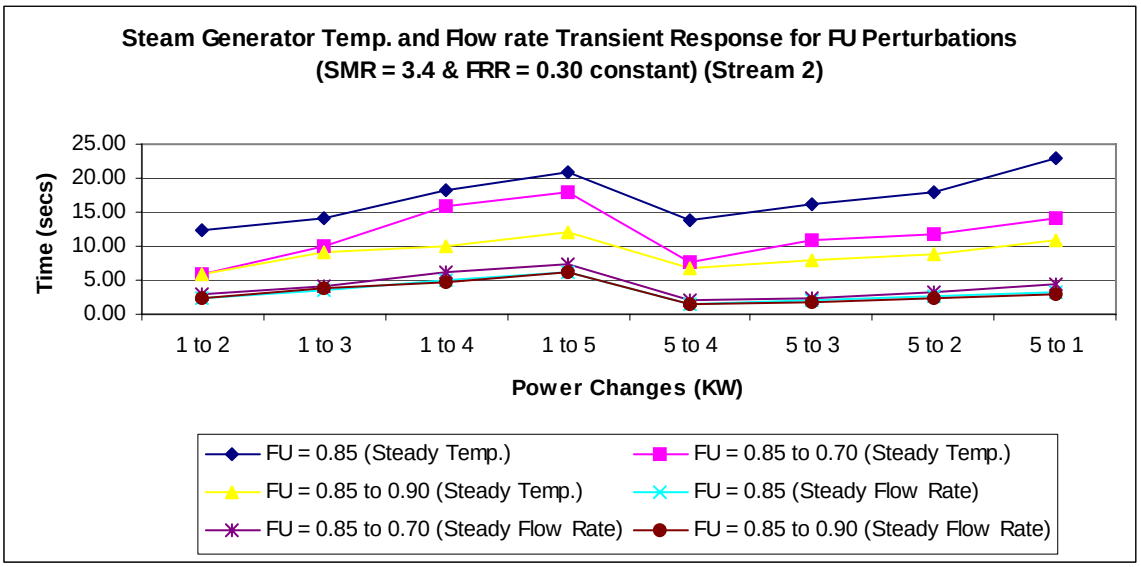
Steam Generator Temp. and Flow rate Transient Response for FU Perturbations (SMR = 3.4 & FRR = 0.30 constant) (Stream 2)
Time (secs)
25.00
20.00
15.00
10.00
5.00
0.00
1 to 2
1 to 3
1 to 4
1 to 5
5 to 4
5 to 3
5 to 2
5 to 1
Power Changes (KW)
FU = 0.85 (Steady Temp.)
FU = 0.85 to 0.70 (Steady Temp.)
FU = 0.85 to 0.90 (Steady Temp.)
FU = 0.85 (Steady Flow Rate)
FU = 0.85 to 0.70 (Steady Flow Rate)
FU = 0.85 to 0.90 (Steady Flow Rate)

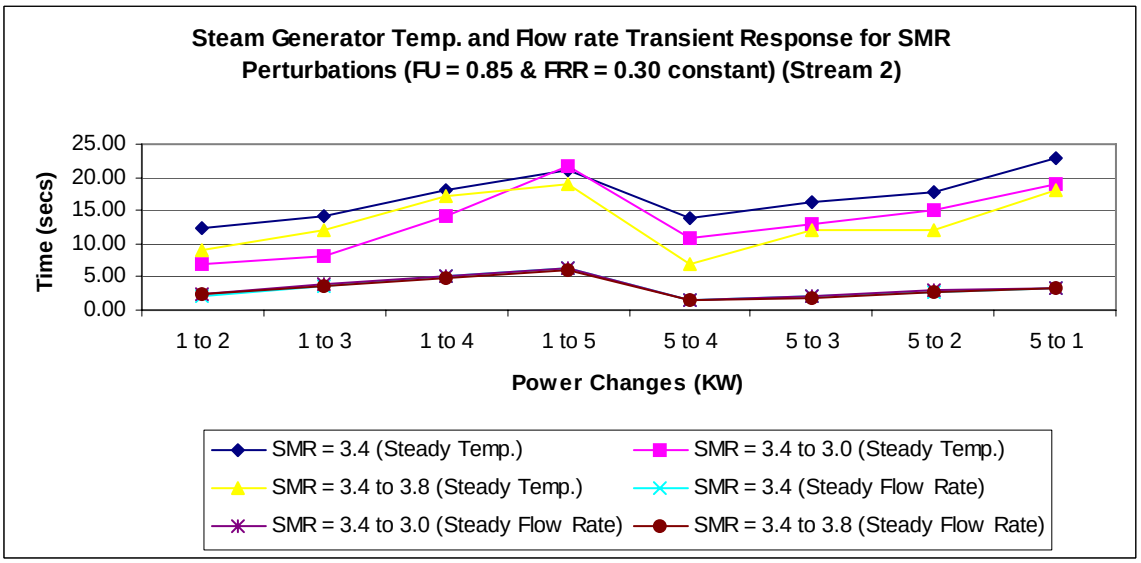
Steam Generator Temp. and Flow rate Transient Response for SMR Perturbations (FU = 0.85 & FRR = 0.30 constant) (Stream 2)
Time (secs)
25.00
20.00
15.00
10.00
5.00
0.00
1 to 2
1 to 3
1 to 4
1 to 5
5 to 4
5 to 3
5 to 2
5 to 1
Power Changes (KW)
SMR = 3.4 (Steady Temp.)
SMR = 3.4 to 3.0 (Steady Temp.)
SMR = 3.4 to 3.8 (Steady Temp.)
SMR = 3.4 (Steady Flow Rate)
SMR = 3.4 to 3.0 (Steady Flow Rate)
SMR = 3.4 to 3.8 (Steady Flow Rate)

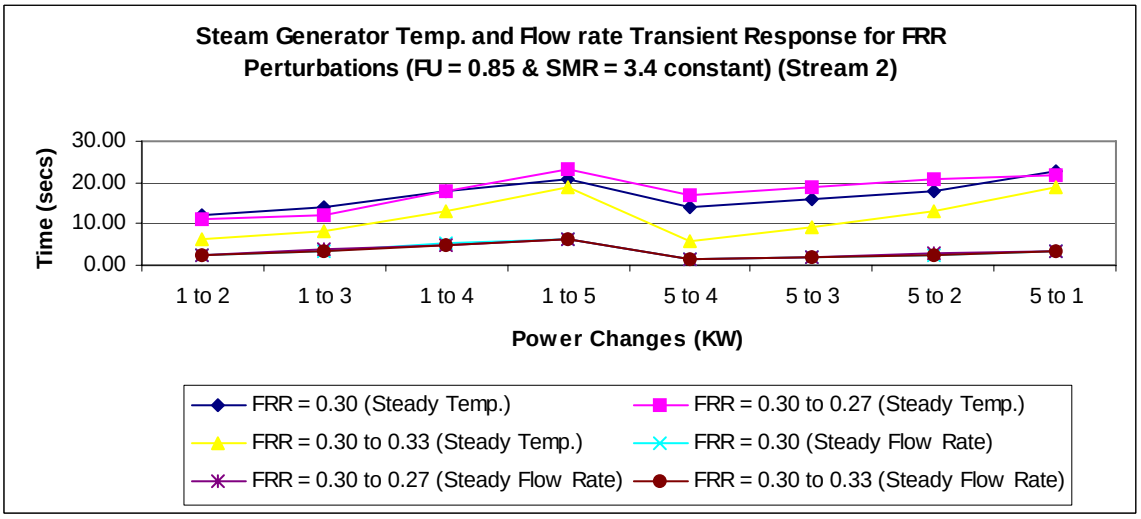
Steam Generator Temp. and Flow rate Transient Response for FRR Perturbations (FU = 0.85 & SMR = 3.4 constant) (Stream 2)
Time (secs)
30.00
20.00
10.00
0.00
1 to 2
1 to 3
1 to 4
1 to 5
5 to 4
5 to 3
5 to 2
5 to 1
Power Changes (KW)
FRR = 0.30 (Steady Temp.)
FRR = 0.30 to 0.27 (Steady Temp.)
FRR = 0.30 to 0.33 (Steady Temp.)
FRR = 0.30 (Steady Flow Rate)
FRR = 0.30 to 0.27 (Steady Flow Rate)
FRR = 0.30 to 0.33 (Steady Flow Rate)

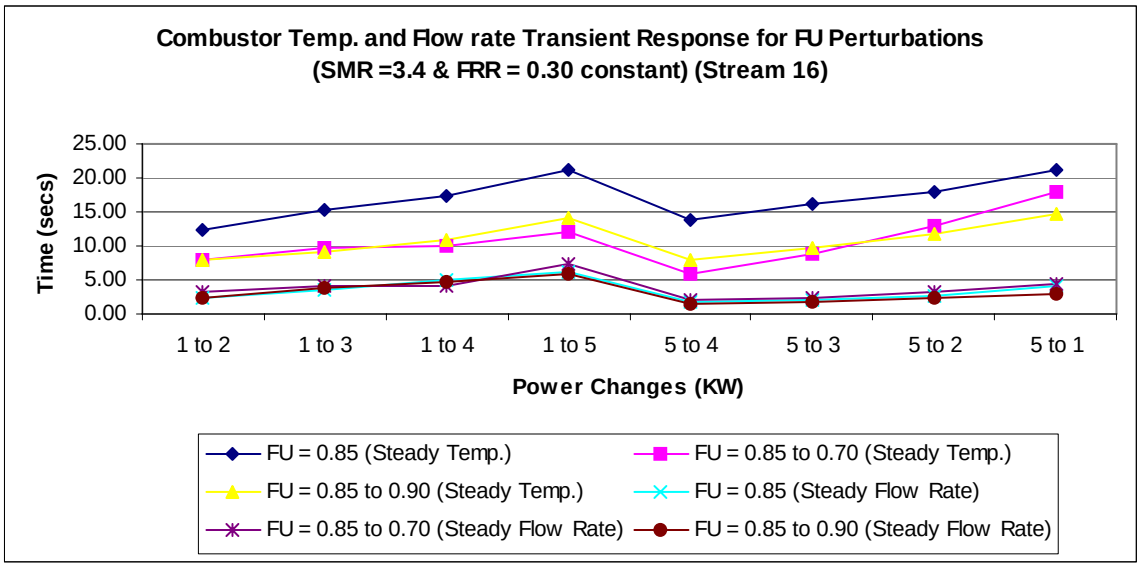
Combustor Temp. and Flow rate Transient Response for FU Perturbations
(SMR =3.4 & FRR = 0.30 constant) (Stream 16)
Time (secs)
25.00
20.00
15.00
10.00
5.00
0.00
1 to 2
1 to 3
1 to 4
1 to 5
5 to 4
5 to 3
5 to 2
5 to 1
Power Changes (KW)
FU = 0.85 (Steady Temp.)
FU = 0.85 to 0.70 (Steady Temp.)
FU = 0.85 to 0.90 (Steady Temp.)
FU = 0.85 (Steady Flow Rate)
FU = 0.85 to 0.70 (Steady Flow Rate)
FU = 0.85 to 0.90 (Steady Flow Rate)

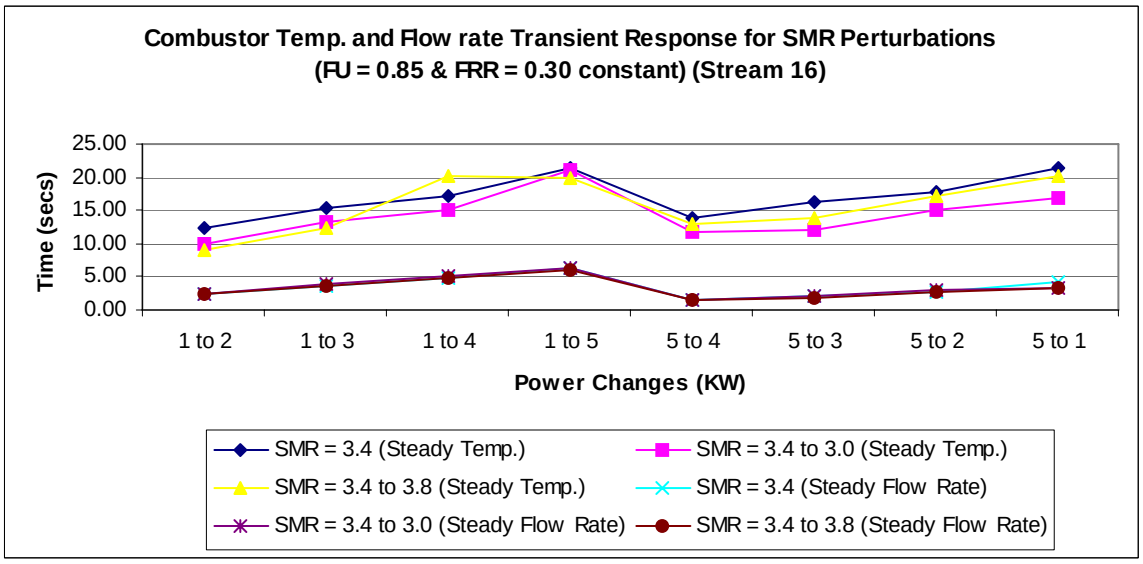
Combustor Temp. and Flow rate Transient Response for SMR Perturbations
(FU = 0.85 & FRR = 0.30 constant) (Stream 16)
Time (secs)
25.00
20.00
15.00
10.00
5.00
0.00
1 to 2
1 to 3
1 to 4
1 to 5
5 to 4
5 to 3
5 to 2
5 to 1
Power Changes (KW)
SMR = 3.4 (Steady Temp.)
SMR = 3.4 to 3.0 (Steady Temp.)
SMR = 3.4 to 3.8 (Steady Temp.)
SMR = 3.4 (Steady Flow Rate)
SMR = 3.4 to 3.0 (Steady Flow Rate)
SMR = 3.4 to 3.8 (Steady Flow Rate)

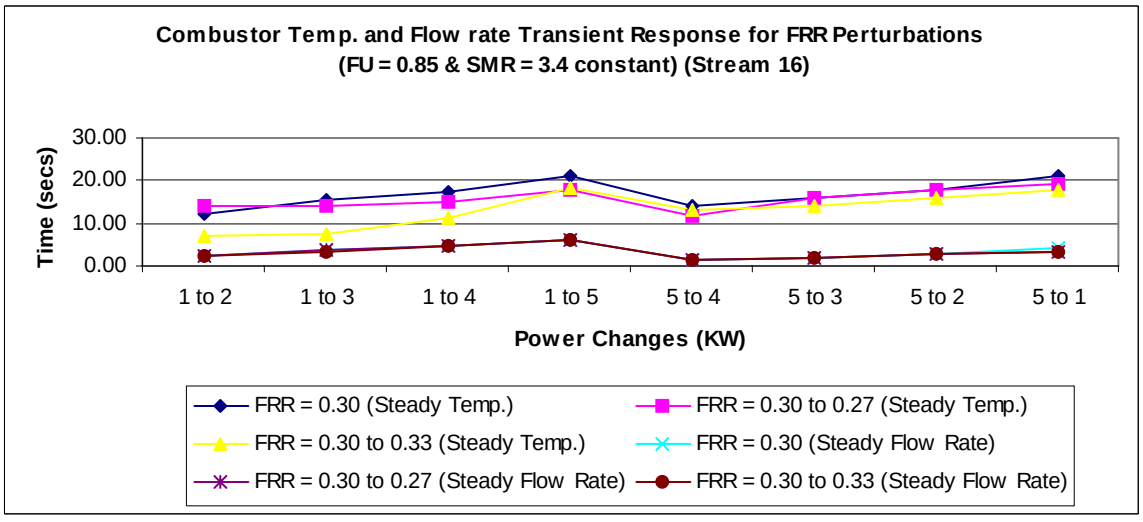
Combustor Temp. and Flow rate Transient Response for FRR Perturbations
(FU = 0.85 & SMR = 3.4 constant) (Stream 16)
Time (secs)
30.00
20.00
10.00
0.00
1 to 2
1 to 3
1 to 4
1 to 5
5 to 4
5 to 3
5 to 2
5 to 1
Power Changes (KW)
FRR = 0.30 (Steady Temp.)
FRR = 0.30 to 0.27 (Steady Temp.)
FRR = 0.30 to 0.33 (Steady Temp.)
FRR = 0.30 (Steady Flow Rate)
FRR = 0.30 to 0.27 (Steady Flow Rate)
FRR = 0.30 to 0.33 (Steady Flow Rate)

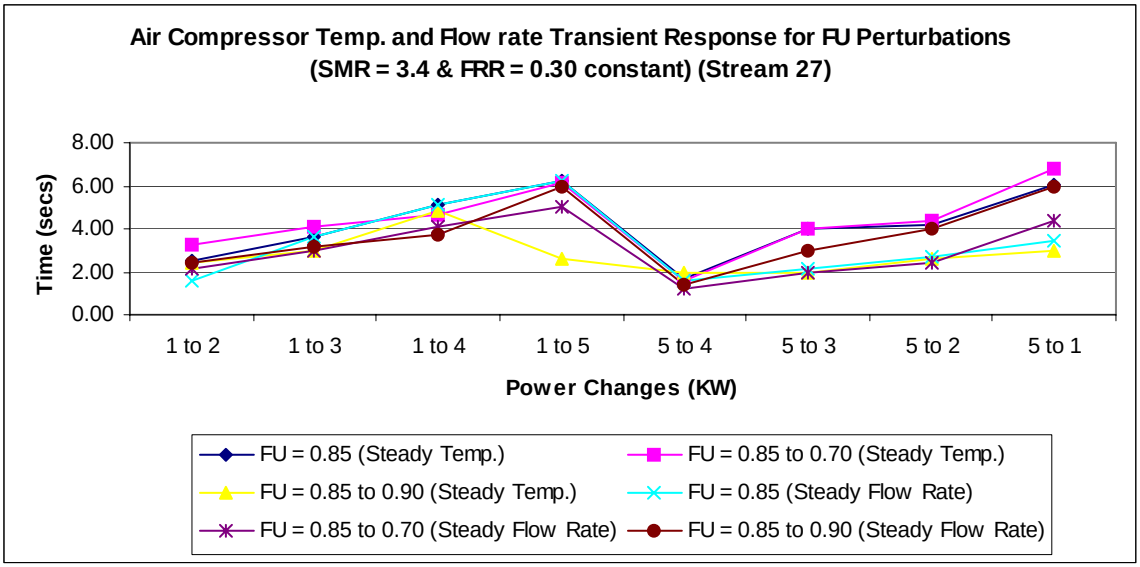
Air Compressor Temp. and Flow rate Transient Response for FU Perturbations
(SMR = 3.4 & FRR = 0.30 constant) (Stream 27)
Time (secs)
8.00
6.00
4.00
2.00
0.00
1 to 2
1 to 3
1 to 4
1 to 5
5 to 4
5 to 3
5 to 2
5 to 1
Power Changes (KW)
FU = 0.85 (Steady Temp.)
FU = 0.85 to 0.70 (Steady Temp.)
FU = 0.85 to 0.90 (Steady Temp.)
FU = 0.85 (Steady Flow Rate)
FU = 0.85 to 0.70 (Steady Flow Rate)
FU = 0.85 to 0.90 (Steady Flow Rate)

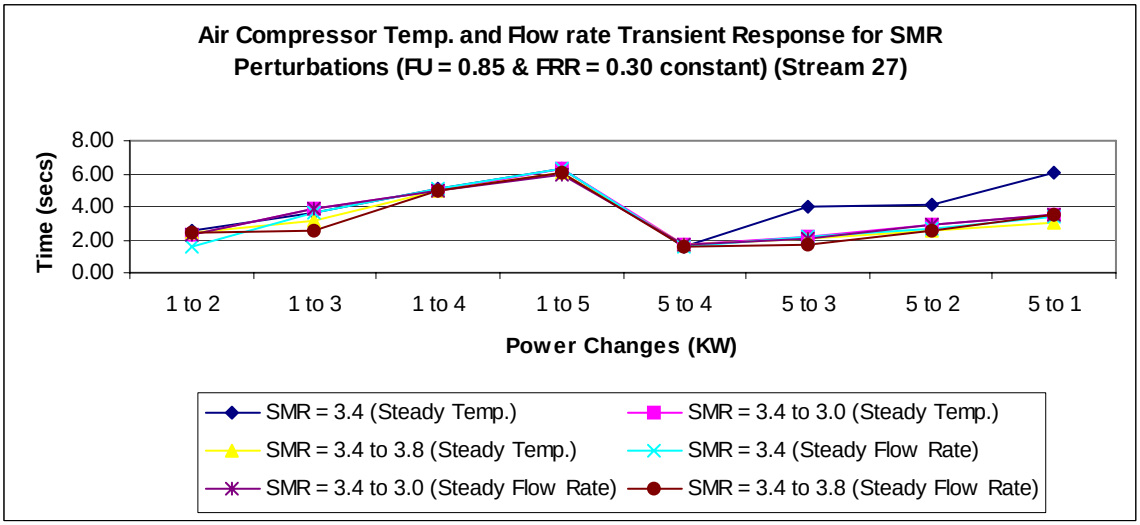
Air Compressor Temp. and Flow rate Transient Response for SMR
Perturbations (FU = 0.85 & FRR = 0.30 constant) (Stream 27)
Time (secs)
8.00
6.00
4.00
2.00
0.00
1 to 2
1 to 3
1 to 4
1 to 5
5 to 4
5 to 3
5 to 2
5 to 1
Power Changes (KW)
SMR = 3.4 (Steady Temp.)
SMR = 3.4 to 3.0 (Steady Temp.)
SMR = 3.4 to 3.8 (Steady Temp.)
SMR = 3.4 (Steady Flow Rate)
SMR = 3.4 to 3.0 (Steady Flow Rate)
SMR = 3.4 to 3.8 (Steady Flow Rate)

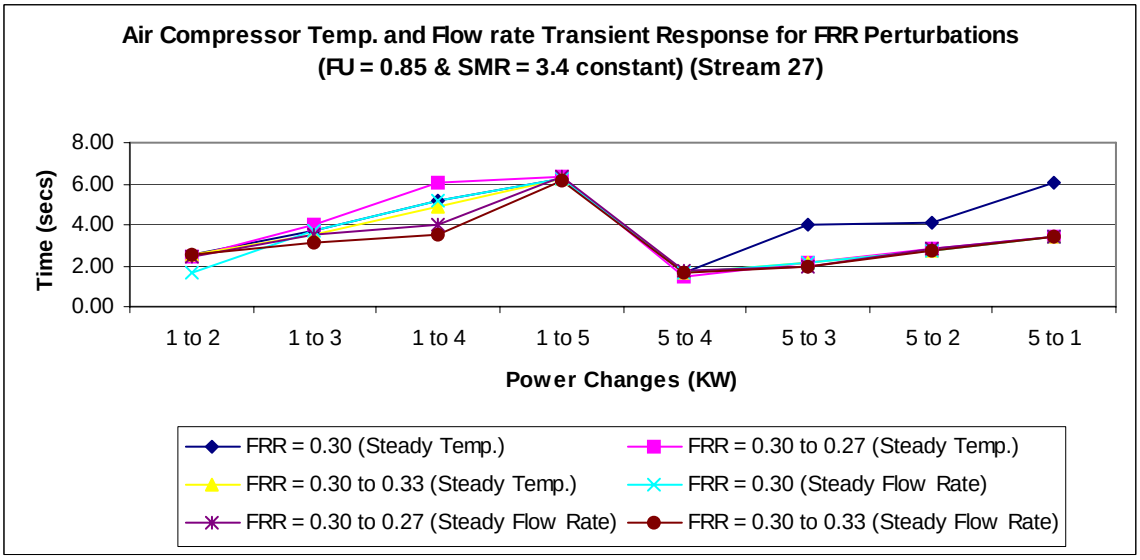
Air Compressor Temp. and Flow rate Transient Response for FRR Perturbations
(FU = 0.85 & SMR = 3.4 constant) (Stream 27)
Time (secs)
8.00
6.00
4.00
2.00
0.00
1 to 2
1 to 3
1 to 4
1 to 5
5 to 4
5 to 3
5 to 2
5 to 1
Power Changes (KW)
FRR = 0.30 (Steady Temp.)
FRR = 0.30 to 0.27 (Steady Temp.)
FRR = 0.30 to 0.33 (Steady Temp.)
FRR = 0.30 (Steady Flow Rate)
FRR = 0.30 to 0.27 (Steady Flow Rate)
FRR = 0.30 to 0.33 (Steady Flow Rate)

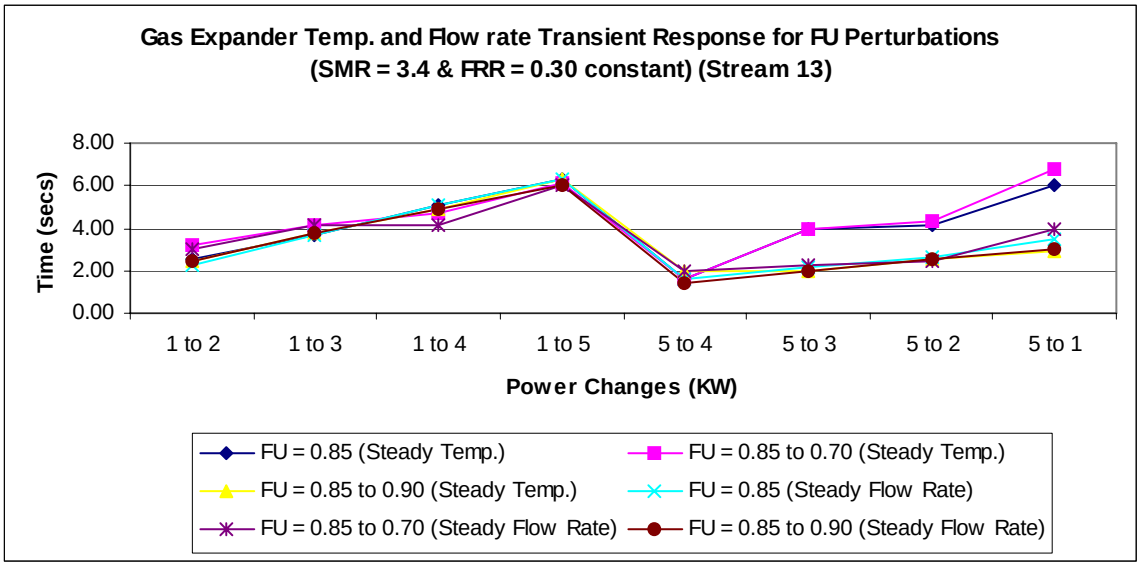
Gas Expander Temp. and Flow rate Transient Response for FU Perturbations
(SMR = 3.4 & FRR = 0.30 constant) (Stream 13)
Time (secs)
8.00
6.00
4.00
2.00
0.00
1 to 2
1 to 3
1 to 4
1 to 5
5 to 4
5 to 3
5 to 2
5 to 1
Power Changes (KW)
FU = 0.85 (Steady Temp.)
FU = 0.85 to 0.70 (Steady Temp.)
FU = 0.85 to 0.90 (Steady Temp.)
FU = 0.85 (Steady Flow Rate)
FU = 0.85 to 0.70 (Steady Flow Rate)
FU = 0.85 to 0.90 (Steady Flow Rate)

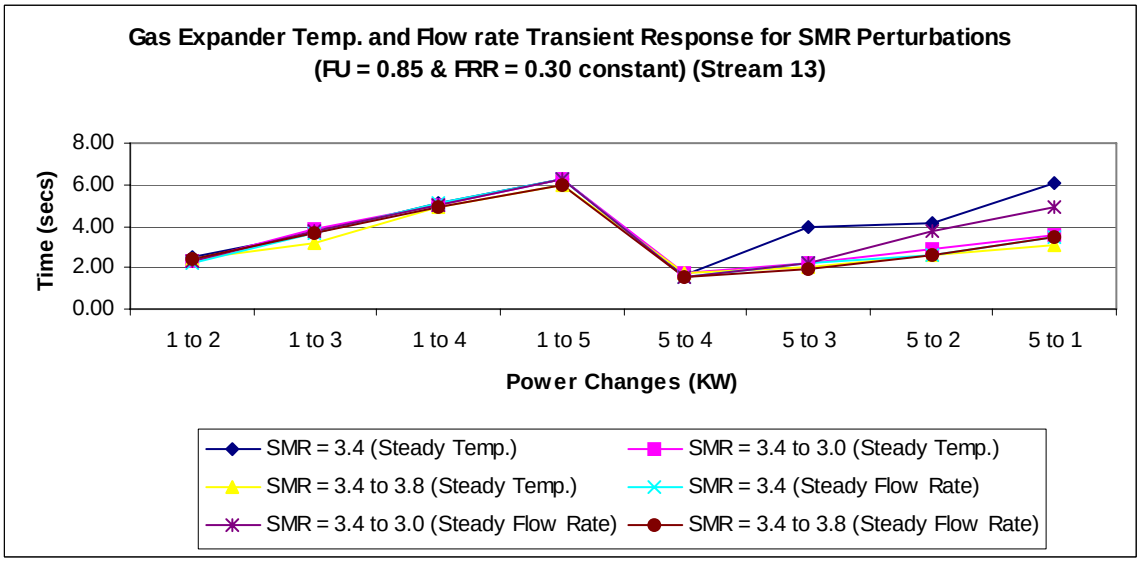
Gas Expander Temp. and Flow rate Transient Response for SMR Perturbations
(FU = 0.85 & FRR = 0.30 constant) (Stream 13)
Time (secs)
8.00
6.00
4.00
2.00
0.00
1 to 2
1 to 3
1 to 4
1 to 5
5 to 4
5 to 3
5 to 2
5 to 1
Power Changes (KW)
SMR = 3.4 (Steady Temp.)
SMR = 3.4 to 3.0 (Steady Temp.)
SMR = 3.4 to 3.8 (Steady Temp.)
SMR = 3.4 (Steady Flow Rate)
SMR = 3.4 to 3.0 (Steady Flow Rate)
SMR = 3.4 to 3.8 (Steady Flow Rate)

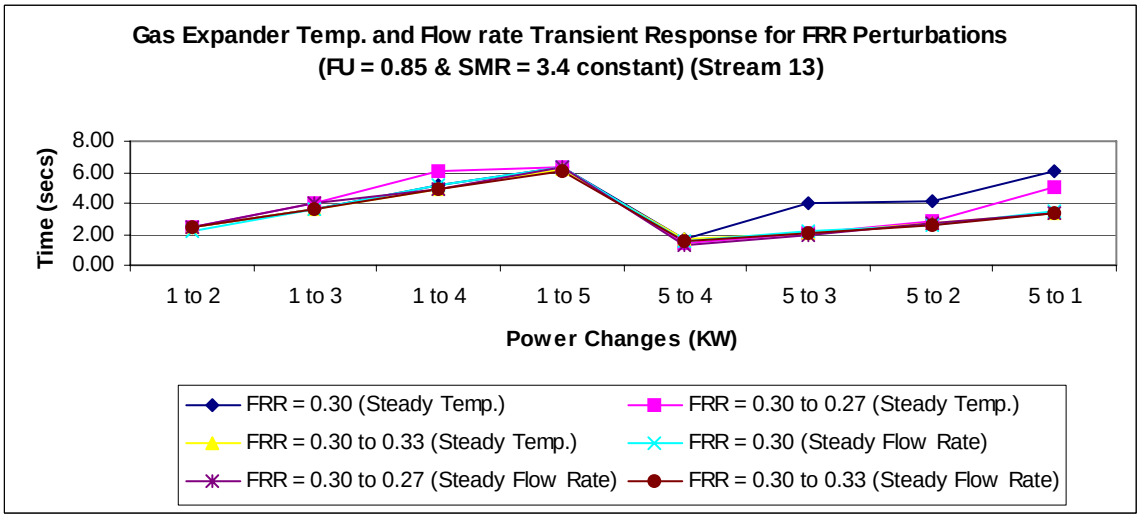
Gas Expander Temp. and Flow rate Transient Response for FRR Perturbations
(FU = 0.85 & SMR = 3.4 constant) (Stream 13)
Time (secs)
8.00
6.00
4.00
2.00
0.00
1 to 2
1 to 3
1 to 4
1 to 5
5 to 4
5 to 3
5 to 2
5 to 1
Power Changes (KW)
FRR = 0.30 (Steady Temp.)
FRR = 0.30 to 0.27 (Steady Temp.)
FRR = 0.30 to 0.33 (Steady Temp.)
FRR = 0.30 (Steady Flow Rate)
FRR = 0.30 to 0.27 (Steady Flow Rate)
FRR = 0.30 to 0.33 (Steady Flow Rate)

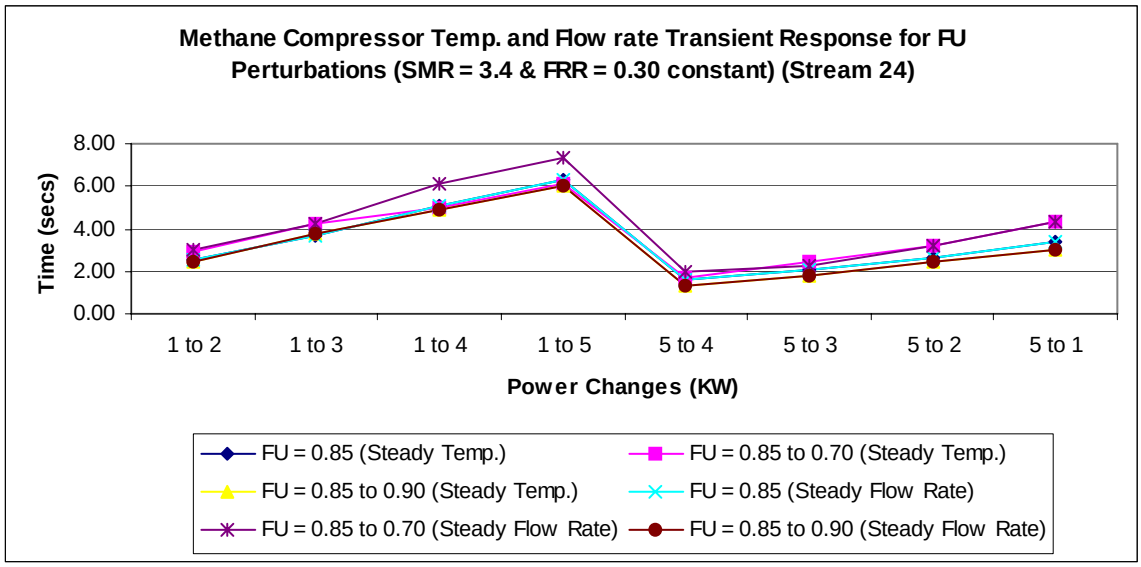
Methane Compressor Temp. and Flow rate Transient Response for FU Perturbations (SMR = 3.4 & FRR = 0.30 constant) (Stream 24)
Time (secs)
8.00
6.00
4.00
2.00
0.00
1 to 2
1 to 3
1 to 4
1 to 5
5 to 4
5 to 3
5 to 2
5 to 1
Power Changes (KW)
FU = 0.85 (Steady Temp.)
FU = 0.85 to 0.70 (Steady Temp.)
FU = 0.85 to 0.90 (Steady Temp.)
FU = 0.85 (Steady Flow Rate)
FU = 0.85 to 0.70 (Steady Flow Rate)
FU = 0.85 to 0.90 (Steady Flow Rate)

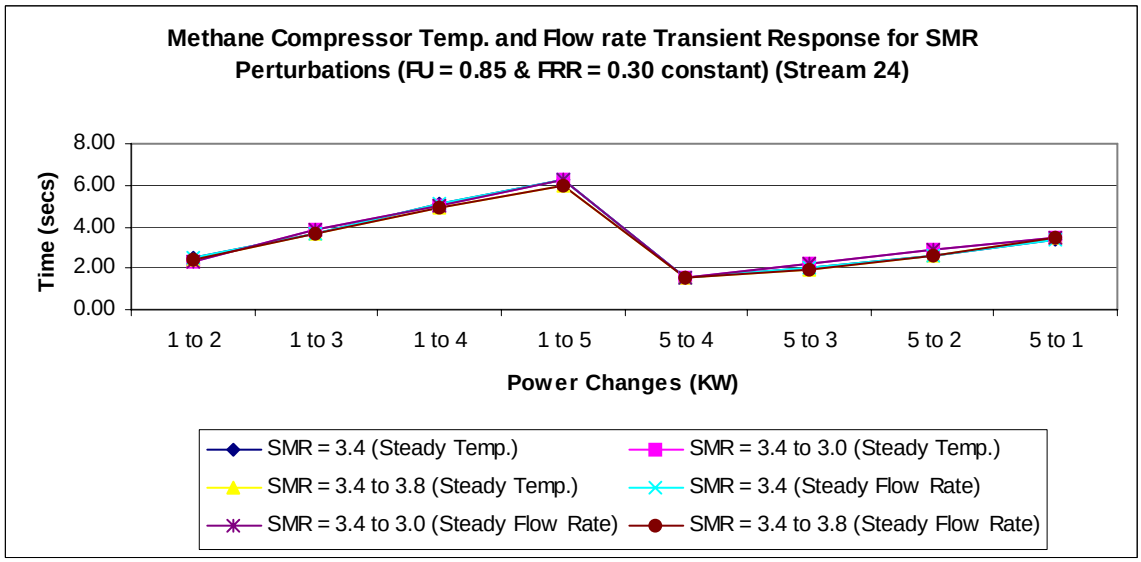
Methane Compressor Temp. and Flow rate Transient Response for SMR Perturbations (FU = 0.85 & FRR = 0.30 constant) (Stream 24)
Time (secs)
8.00
6.00
4.00
2.00
0.00
1 to 2
1 to 3
1 to 4
1 to 5
5 to 4
5 to 3
5 to 2
5 to 1
Power Changes (KW)
SMR = 3.4 (Steady Temp.)
SMR = 3.4 to 3.0 (Steady Temp.)
SMR = 3.4 to 3.8 (Steady Temp.)
SMR = 3.4 (Steady Flow Rate)
SMR = 3.4 to 3.0 (Steady Flow Rate)
SMR = 3.4 to 3.8 (Steady Flow Rate)

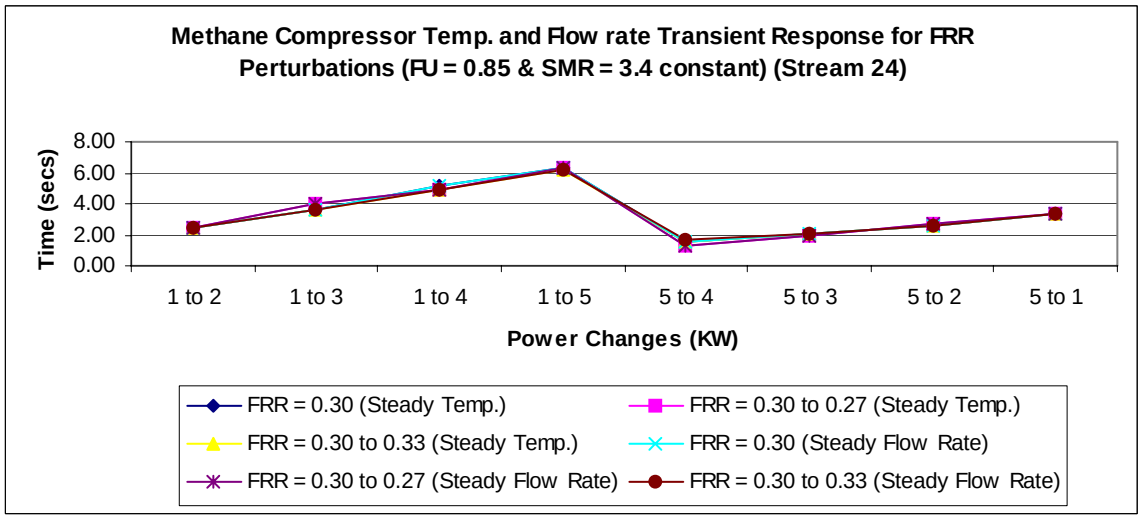
Methane Compressor Temp. and Flow rate Transient Response for FRR Perturbations (FU = 0.85 & SMR = 3.4 constant) (Stream 24)
Time (secs)
8.00
6.00
4.00
2.00
0.00
1 to 2
1 to 3
1 to 4
1 to 5
5 to 4
5 to 3
5 to 2
5 to 1
Power Changes (KW)
FRR = 0.30 (Steady Temp.)
FRR = 0.30 to 0.27 (Steady Temp.)
FRR = 0.30 to 0.33 (Steady Temp.)
FRR = 0.30 (Steady Flow Rate)
FRR = 0.30 to 0.27 (Steady Flow Rate)
FRR = 0.30 to 0.33 (Steady Flow Rate)

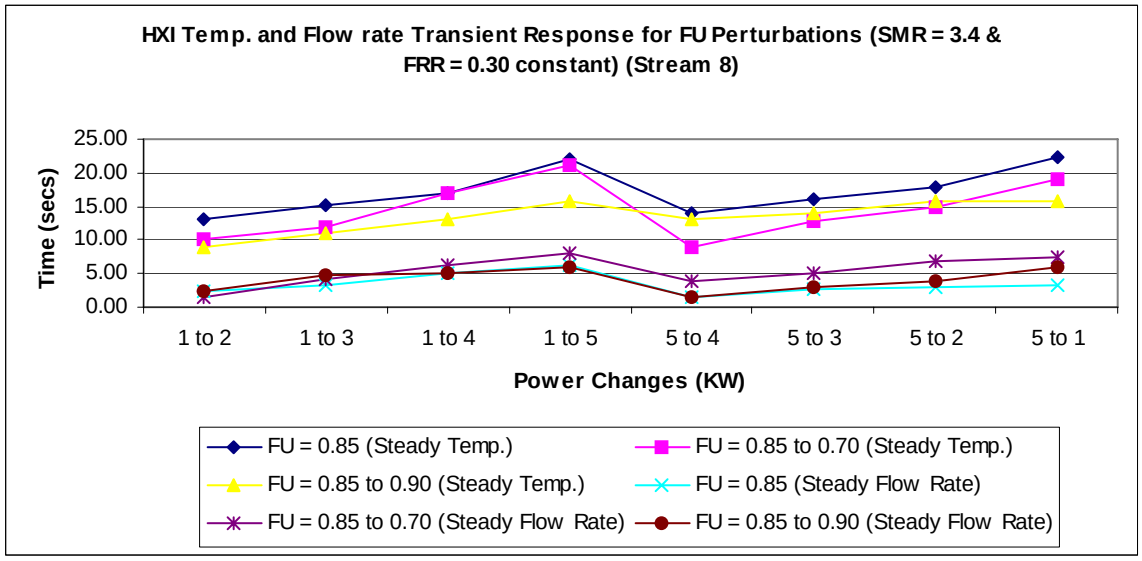
HXI Temp. and Flow rate Transient Response for FU Perturbations (SMR = 3.4 & FRR = 0.30 constant) (Stream 8)
Time (secs)
25.00
20.00
15.00
10.00
5.00
0.00
1 to 2
1 to 3
1 to 4
1 to 5
5 to 4
5 to 3
5 to 2
5 to 1
Power Changes (KW)
FU = 0.85 (Steady Temp.)
FU = 0.85 to 0.70 (Steady Temp.)
FU = 0.85 to 0.90 (Steady Temp.)
FU = 0.85 (Steady Flow Rate)
FU = 0.85 to 0.70 (Steady Flow Rate)
FU = 0.85 to 0.90 (Steady Flow Rate)

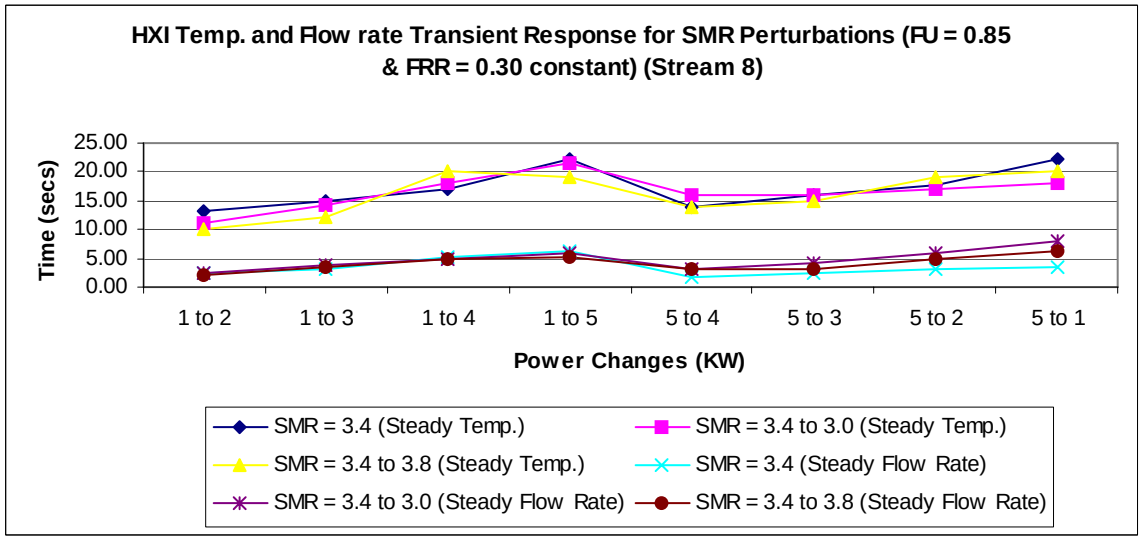
HXI Temp. and Flow rate Transient Response for SMR Perturbations (FU = 0.85 & FRR = 0.30 constant) (Stream 8)
Time (secs)
25.00
20.00
15.00
10.00
5.00
0.00
1 to 2
1 to 3
1 to 4
1 to 5
5 to 4
5 to 3
5 to 2
5 to 1
Power Changes (KW)
SMR = 3.4 (Steady Temp.)
SMR = 3.4 to 3.0 (Steady Temp.)
SMR = 3.4 to 3.8 (Steady Temp.)
SMR = 3.4 (Steady Flow Rate)
SMR = 3.4 to 3.0 (Steady Flow Rate)
SMR = 3.4 to 3.8 (Steady Flow Rate)

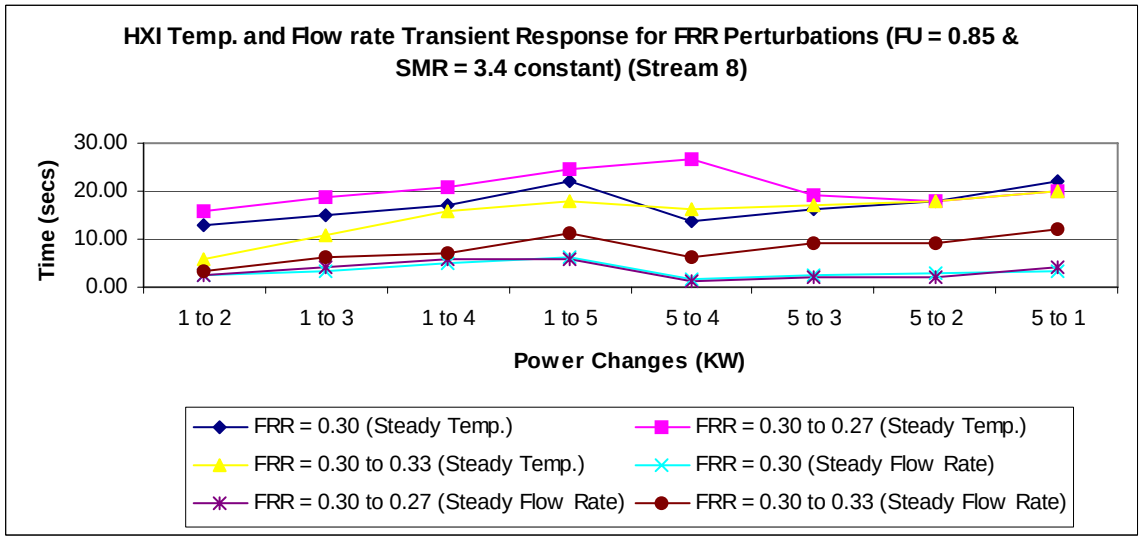
HXI Temp. and Flow rate Transient Response for FRR Perturbations (FU = 0.85 & SMR = 3.4 constant) (Stream 8)
Time (secs)
30.00
20.00
10.00
0.00
1 to 2
1 to 3
1 to 4
1 to 5
5 to 4
5 to 3
5 to 2
5 to 1
Power Changes (KW)
FRR = 0.30 (Steady Temp.)
FRR = 0.30 to 0.27 (Steady Temp.)
FRR = 0.30 to 0.33 (Steady Temp.)
FRR = 0.30 (Steady Flow Rate)
FRR = 0.30 to 0.27 (Steady Flow Rate)
FRR = 0.30 to 0.33 (Steady Flow Rate)

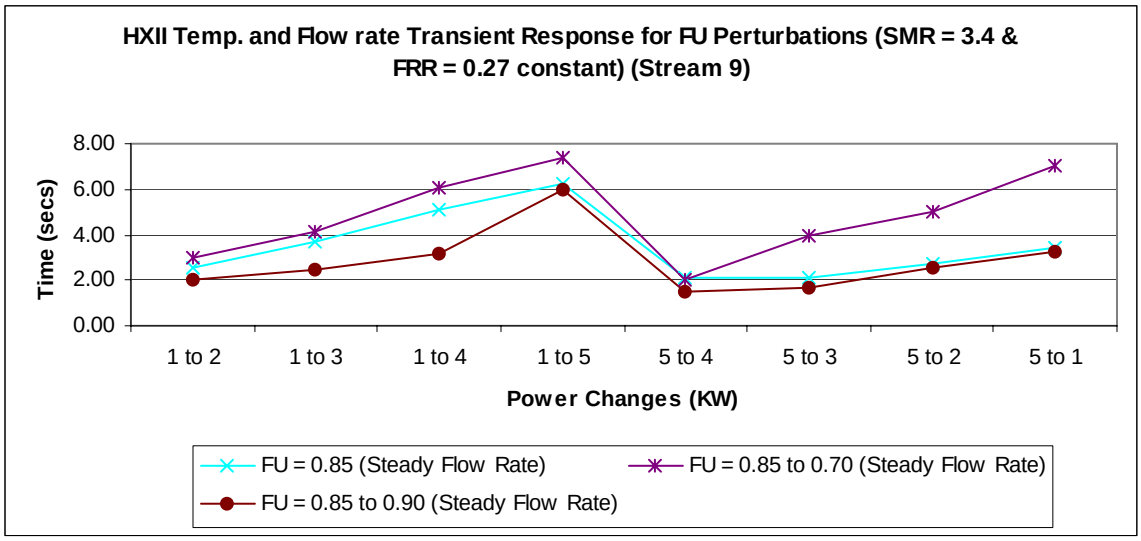
HXII Temp. and Flow rate Transient Response for FU Perturbations (SMR = 3.4 & FRR = 0.27 constant) (Stream 9)
Time (secs)
8.00
6.00
4.00
2.00
0.00
1 to 2
1 to 3
1 to 4
1 to 5
5 to 4
5 to 3
5 to 2
5 to 1
Power Changes (KW)
FU = 0.85 (Steady Flow Rate)
FU = 0.85 to 0.70 (Steady Flow Rate)
FU = 0.85 to 0.90 (Steady Flow Rate)

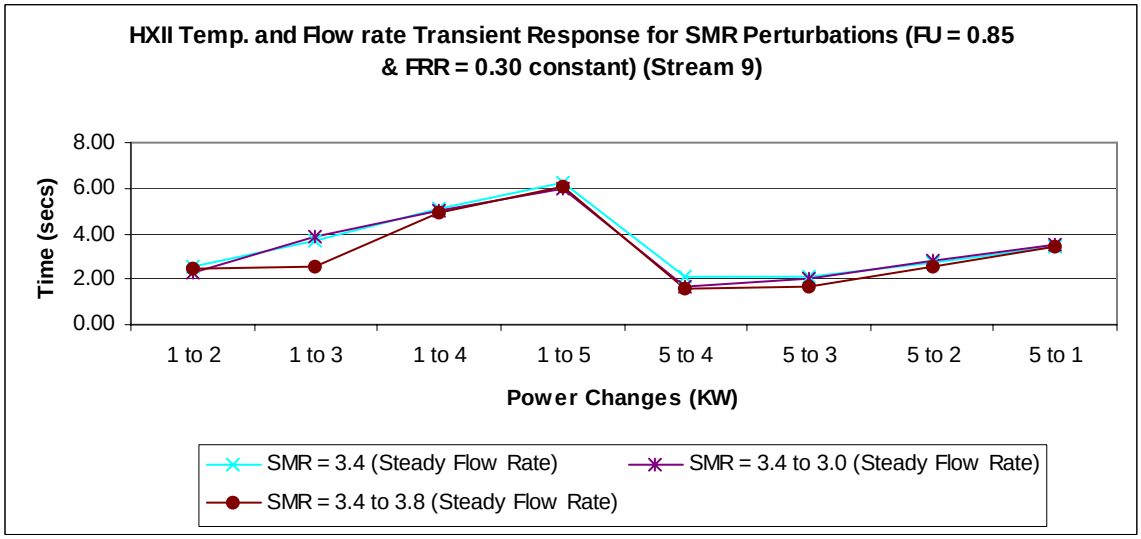
HXII Temp. and Flow rate Transient Response for SMR Perturbations (FU = 0.85 & FRR = 0.30 constant) (Stream 9)
Time (secs)
8.00
6.00
4.00
2.00
0.00
1 to 2
1 to 3
1 to 4
1 to 5
5 to 4
5 to 3
5 to 2
5 to 1
Power Changes (KW)
SMR = 3.4 (Steady Flow Rate)
SMR = 3.4 to 3.0 (Steady Flow Rate)
SMR = 3.4 to 3.8 (Steady Flow Rate)

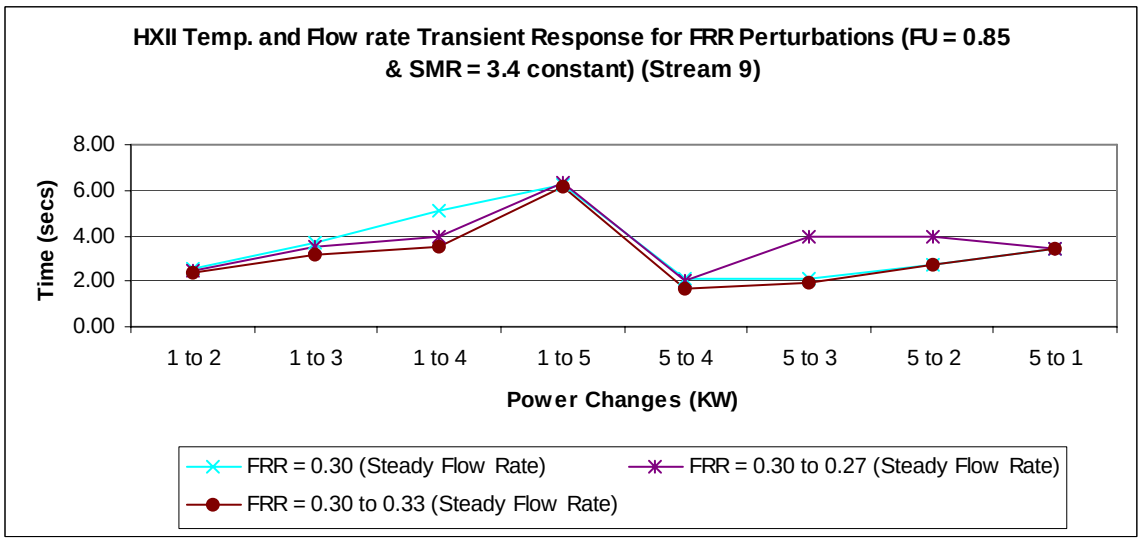
HXII Temp. and Flow rate Transient Response for FRR Perturbations (FU = 0.85 & SMR = 3.4 constant) (Stream 9)
Time (secs)
8.00
6.00
4.00
2.00
0.00
1 to 2
1 to 3
1 to 4
1 to 5
5 to 4
5 to 3
5 to 2
5 to 1
Power Changes (KW)
FRR = 0.30 (Steady Flow Rate)
FRR = 0.30 to 0.27 (Steady Flow Rate)
FRR = 0.30 to 0.33 (Steady Flow Rate)

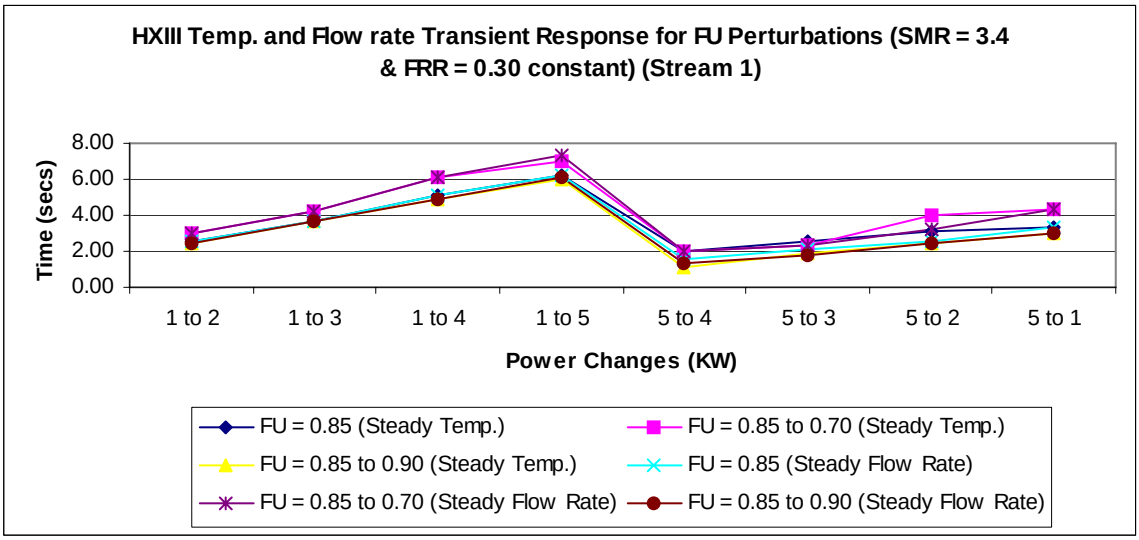
HXIII Temp. and Flow rate Transient Response for FU Perturbations (SMR = 3.4 & FRR = 0.30 constant) (Stream 1)
Time (secs)
8.00
6.00
4.00
2.00
0.00
1 to 2
1 to 3
1 to 4
1 to 5
5 to 4
5 to 3
5 to 2
5 to 1
Power Changes (KW)
FU = 0.85 (Steady Temp.)
FU = 0.85 to 0.70 (Steady Temp.)
FU = 0.85 to 0.90 (Steady Temp.)
FU = 0.85 (Steady Flow Rate)
FU = 0.85 to 0.70 (Steady Flow Rate)
FU = 0.85 to 0.90 (Steady Flow Rate)

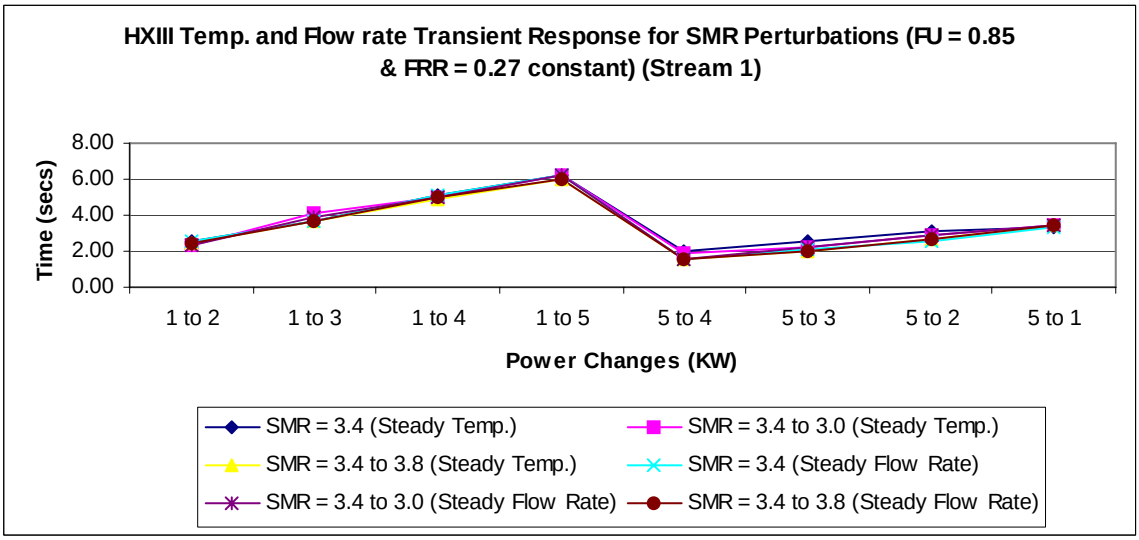
HXIII Temp. and Flow rate Transient Response for SMR Perturbations (FU = 0.85 & FRR = 0.27 constant) (Stream 1)
Time (secs)
8.00
6.00
4.00
2.00
0.00
1 to 2
1 to 3
1 to 4
1 to 5
5 to 4
5 to 3
5 to 2
5 to 1
Power Changes (KW)
SMR = 3.4 (Steady Temp.)
SMR = 3.4 to 3.0 (Steady Temp.)
SMR = 3.4 to 3.8 (Steady Temp.)
SMR = 3.4 (Steady Flow Rate)
SMR = 3.4 to 3.0 (Steady Flow Rate)
SMR = 3.4 to 3.8 (Steady Flow Rate)

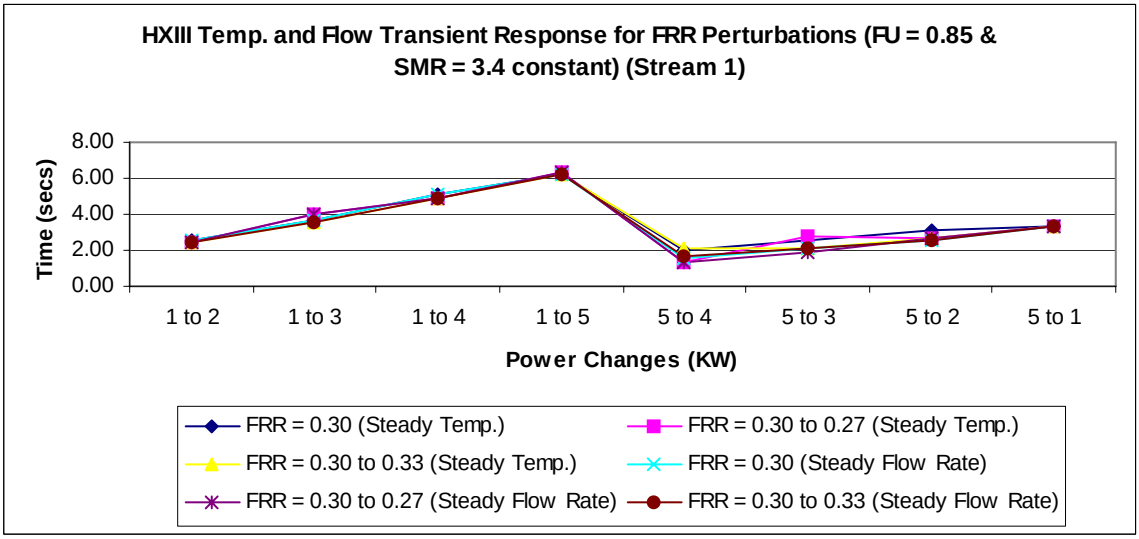
HXIII Temp. and Flow Transient Response for FRR Perturbations (FU = 0.85 & SMR = 3.4 constant) (Stream 1)
Time (secs)
8.00
6.00
4.00
2.00
0.00
1 to 2
1 to 3
1 to 4
1 to 5
5 to 4
5 to 3
5 to 2
5 to 1
Power Changes (KW)
FRR = 0.30 (Steady Temp.)
FRR = 0.30 to 0.27 (Steady Temp.)
FRR = 0.30 to 0.33 (Steady Temp.)
FRR = 0.30 (Steady Flow Rate)
FRR = 0.30 to 0.27 (Steady Flow Rate)
FRR = 0.30 to 0.33 (Steady Flow Rate)

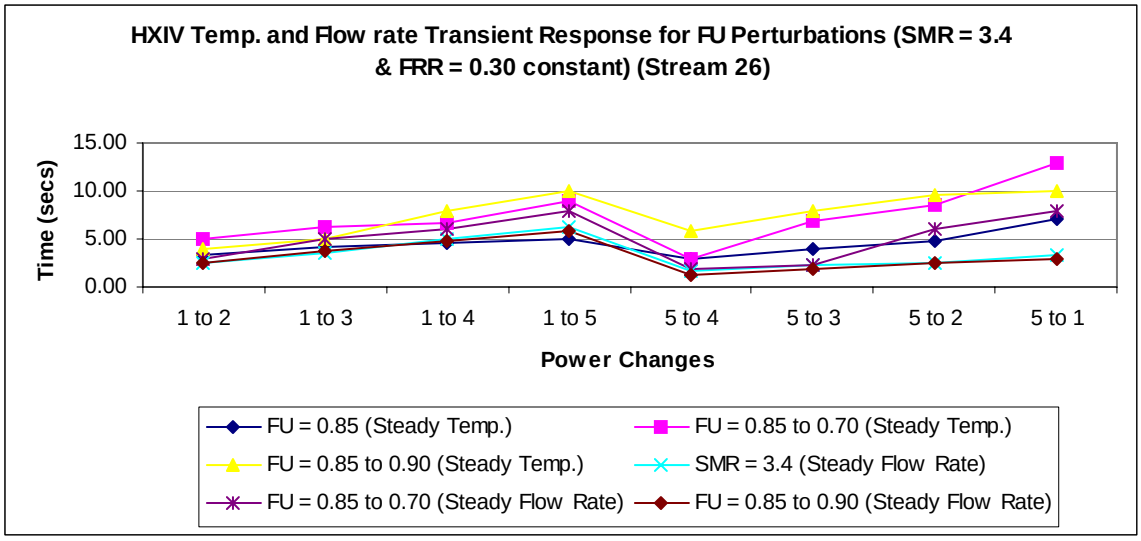
HXIV Temp. and Flow rate Transient Response for FU Perturbations (SMR = 3.4 & FRR = 0.30 constant) (Stream 26)
Time (secs)
15.00
10.00
5.00
0.00
1 to 2
1 to 3
1 to 4
1 to 5
5 to 4
5 to 3
5 to 2
5 to 1
Power Changes
FU = 0.85 (Steady Temp.)
FU = 0.85 to 0.70 (Steady Temp.)
FU = 0.85 to 0.90 (Steady Temp.)
SMR = 3.4 (Steady Flow Rate)
FU = 0.85 to 0.70 (Steady Flow Rate)
FU = 0.85 to 0.90 (Steady Flow Rate)

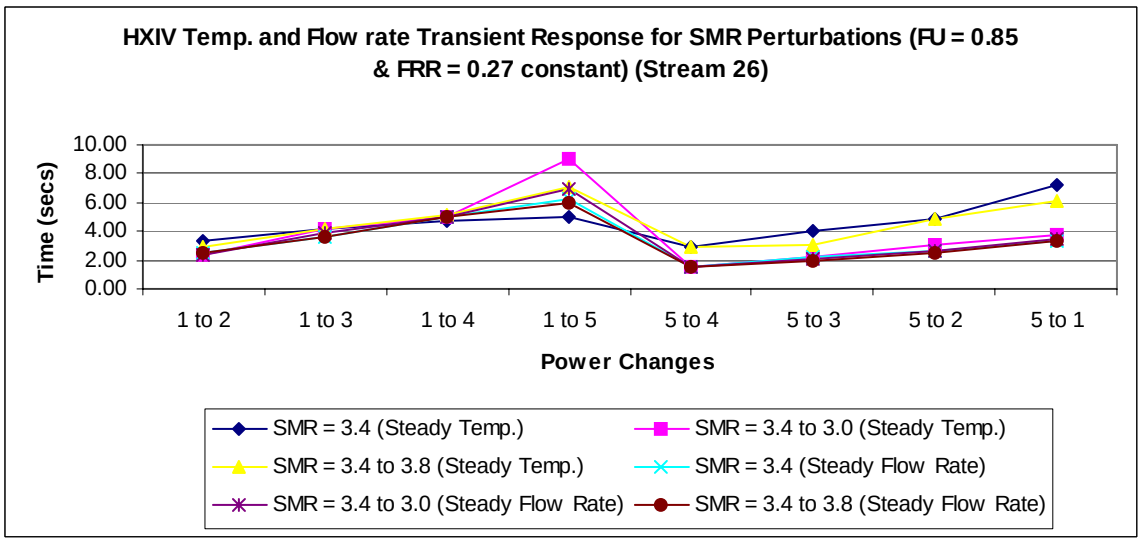
HXIV Temp. and Flow rate Transient Response for SMR Perturbations (FU = 0.85 & FRR = 0.27 constant) (Stream 26)
Time (secs)
10.00
8.00
6.00
4.00
2.00
0.00
1 to 2
1 to 3
1 to 4
1 to 5
5 to 4
5 to 3
5 to 2
5 to 1
Power Changes
SMR = 3.4 (Steady Temp.)
SMR = 3.4 to 3.0 (Steady Temp.)
SMR = 3.4 to 3.8 (Steady Temp.)
SMR = 3.4 (Steady Flow Rate)
SMR = 3.4 to 3.0 (Steady Flow Rate)
SMR = 3.4 to 3.8 (Steady Flow Rate)

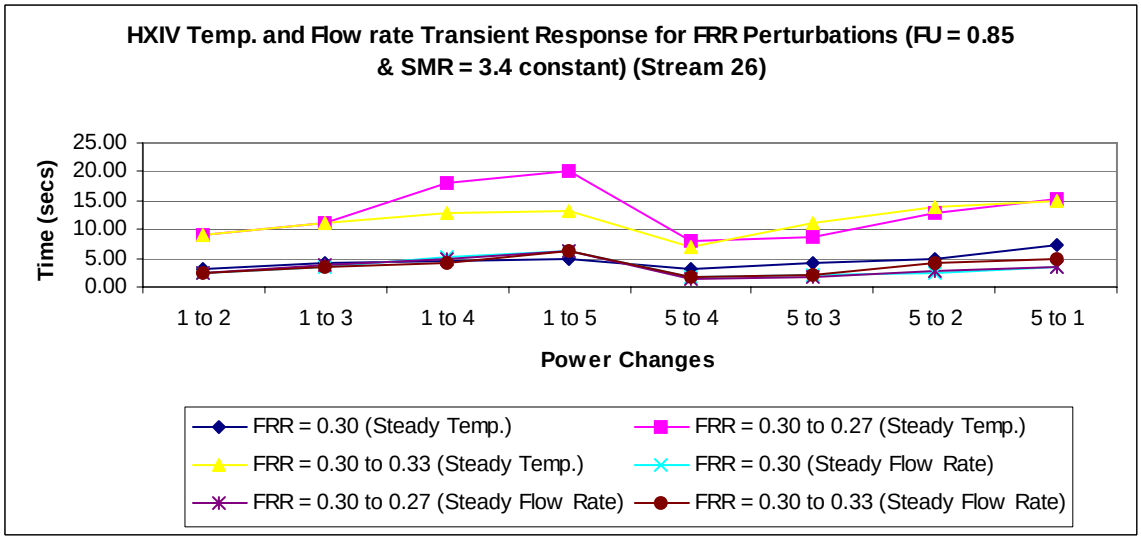
HXIV Temp. and Flow rate Transient Response for FRR Perturbations (FU = 0.85 & SMR = 3.4 constant) (Stream 26)
Time (secs)
25.00
20.00
15.00
10.00
5.00
0.00
1 to 2
1 to 3
1 to 4
1 to 5
5 to 4
5 to 3
5 to 2
5 to 1
Power Changes
FRR = 0.30 (Steady Temp.)
FRR = 0.30 to 0.27 (Steady Temp.)
FRR = 0.30 to 0.33 (Steady Temp.)
FRR = 0.30 (Steady Flow Rate)
FRR = 0.30 to 0.27 (Steady Flow Rate)
FRR = 0.30 to 0.33 (Steady Flow Rate)

Parametric Analysis #1: Component Analysis

Component: Pre-reformer

Stream 5

Power Change (KW)	FU 0.85 SMR 3.4 FRR 0.30	FU 0.70 SMR 3.4 FRR 0.30	FU 0.90 SMR 3.4 FRR 0.30	FU 0.85 SMR 3.0 FRR 0.30	FU 0.85 SMR 3.8 FRR 0.30	FU 0.85 SMR 3.4 FRR 0.27	FU 0.85 SMR 3.4 FRR 0.33
1 to 2	13.1880	10.0000	8.9970	10.8380	10.0100	10.9970	8.0620
1 to 3	16.2010	12.0330	10.9970	14.1160	13.0750	13.0520	11.0000
1 to 4	18.2160	17.0230	12.9970	18.1130	16.1360	15.0000	16.0000
1 to 5	22.2030	22.9970	16.9970	21.6400	22.0230	23.9970	20.6780
5 to 4	13.9530	8.9690	13.0000	15.8500	13.8520	13.8570	16.0910
5 to 3	16.1430	12.8060	13.8440	16.0000	16.0060	14.7820	17.0300
5 to 2	17.8760	15.0000	15.8810	16.9970	18.0000	16.8810	18.0000
5 to 1	19.7380	19.0000	16.0920	17.8970	21.0000	21.9020	21.0000

Stream 6

Power Change (KW)	FU 0.85 SMR 3.4 FRR 0.30	FU 0.70 SMR 3.4 FRR 0.30	FU 0.90 SMR 3.4 FRR 0.30	FU 0.85 SMR 3.0 FRR 0.30	FU 0.85 SMR 3.8 FRR 0.30	FU 0.85 SMR 3.4 FRR 0.27	FU 0.85 SMR 3.4 FRR 0.33
1 to 2	13.1880	11.0170	9.9970	11.9970	9.1990	11.0000	12.0620
1 to 3	16.2190	15.0330	11.9970	14.1160	12.1990	13.0550	14.0680
1 to 4	18.0910	18.0290	14.9970	16.0000	17.1990	15.0520	16.1280
1 to 5	21.0220	23.9970	24.0560	21.9970	19.0230	23.9970	20.0480
5 to 4	13.9530	12.9690	13.8580	12.8500	9.8520	11.8570	13.0910
5 to 3	16.1430	13.8060	14.8440	13.0000	13.0000	13.7820	15.0300
5 to 2	16.8760	17.0000	16.7990	14.9970	15.0770	15.8810	17.0000
5 to 1	19.8390	20.0000	21.7400	19.8970	17.0000	21.9020	21.0220

Overall: Pre-Reformer

Power Change (KW)	FU 0.85 SMR 3.4 FRR 0.30	FU 0.70 SMR 3.4 FRR 0.30	FU 0.90 SMR 3.4 FRR 0.30	FU 0.85 SMR 3.0 FRR 0.30	FU 0.85 SMR 3.8 FRR 0.30	FU 0.85 SMR 3.4 FRR 0.27	FU 0.85 SMR 3.4 FRR 0.33
1 to 2	13.1880	11.0170	9.9970	11.9970	10.0100	11.0000	12.0620
1 to 3	16.2190	15.0330	11.9970	14.1160	13.0750	13.0550	14.0680
1 to 4	18.2160	18.0290	14.9970	18.1130	17.1990	15.0520	16.1280
1 to 5	22.2030	23.9970	24.0560	21.9970	22.0230	23.9970	20.6780
5 to 4	13.9530	12.9690	13.8580	15.8500	13.8520	13.8570	16.0910
5 to 3	16.1430	13.8060	14.8440	16.0000	16.0060	14.7820	17.0300
5 to 2	17.8760	17.0000	16.7990	16.9970	18.0000	16.8810	18.0000
5 to 1	19.8390	20.0000	21.7400	19.8970	21.0000	21.9020	21.0220

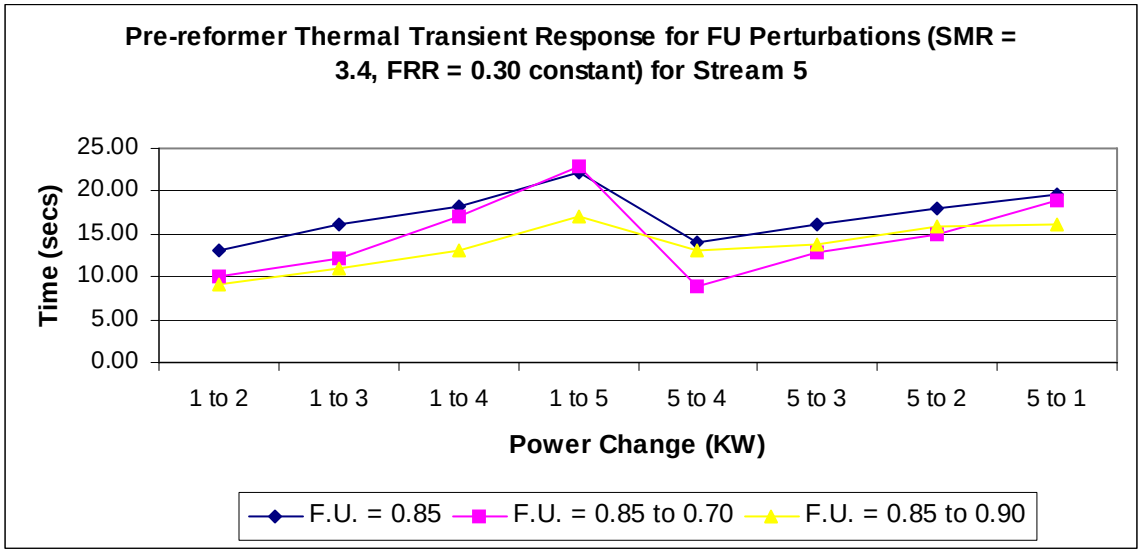
Pre-reformer Thermal Transient Response for FU Perturbations (SMR = 3.4, FRR = 0.30 constant) for Stream 5
Time (secs)
25.00
20.00
15.00
10.00
5.00
0.00
1 to 2
1 to 3
1 to 4
1 to 5
5 to 4
5 to 3
5 to 2
5 to 1
Power Change (KW)
F.U. = 0.85
F.U. = 0.85 to 0.70
F.U. = 0.85 to 0.90

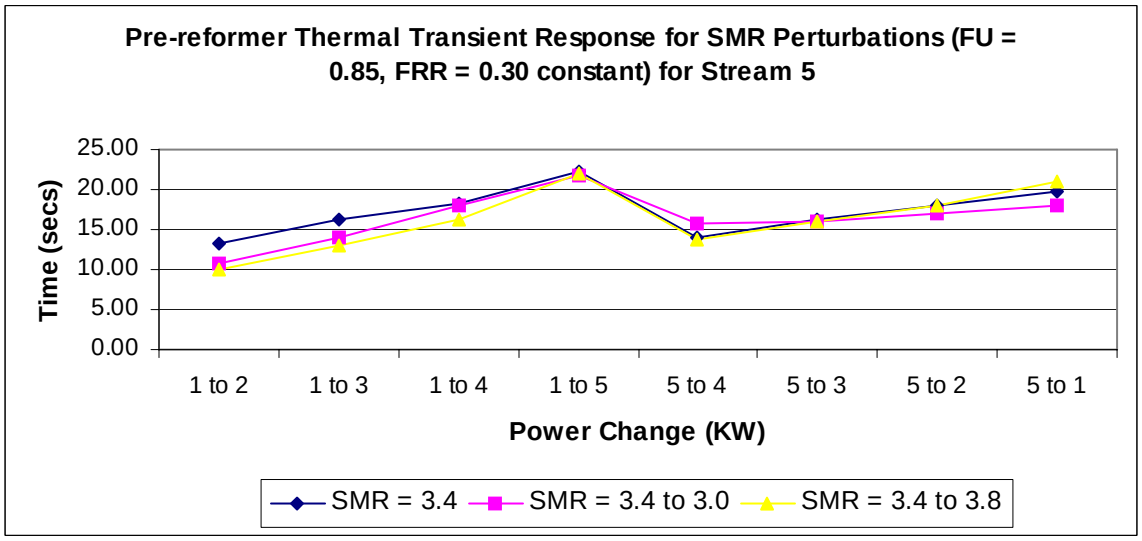
Pre-reformer Thermal Transient Response for SMR Perturbations (FU = 0.85, FRR = 0.30 constant) for Stream 5
Time (secs)
25.00
20.00
15.00
10.00
5.00
0.00
1 to 2
1 to 3
1 to 4
1 to 5
5 to 4
5 to 3
5 to 2
5 to 1
Power Change (KW)
SMR = 3.4
SMR = 3.4 to 3.0
SMR = 3.4 to 3.8

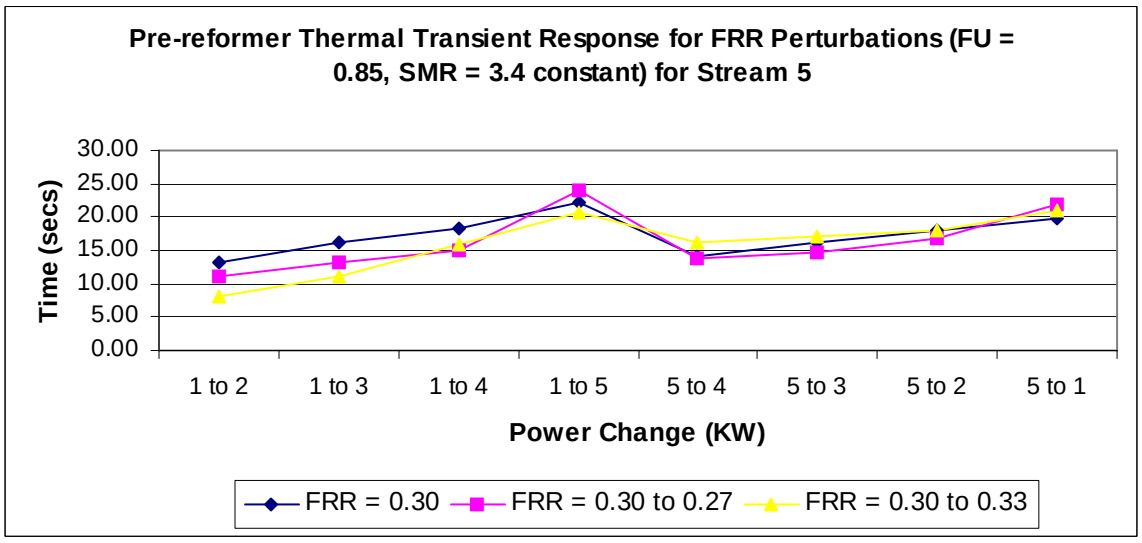
Pre-reformer Thermal Transient Response for FRR Perturbations (FU = 0.85, SMR = 3.4 constant) for Stream 5
Time (secs)
30.00
25.00
20.00
15.00
10.00
5.00
0.00
1 to 2
1 to 3
1 to 4
1 to 5
5 to 4
5 to 3
5 to 2
5 to 1
Power Change (KW)
FRR = 0.30
FRR = 0.30 to 0.27
FRR = 0.30 to 0.33

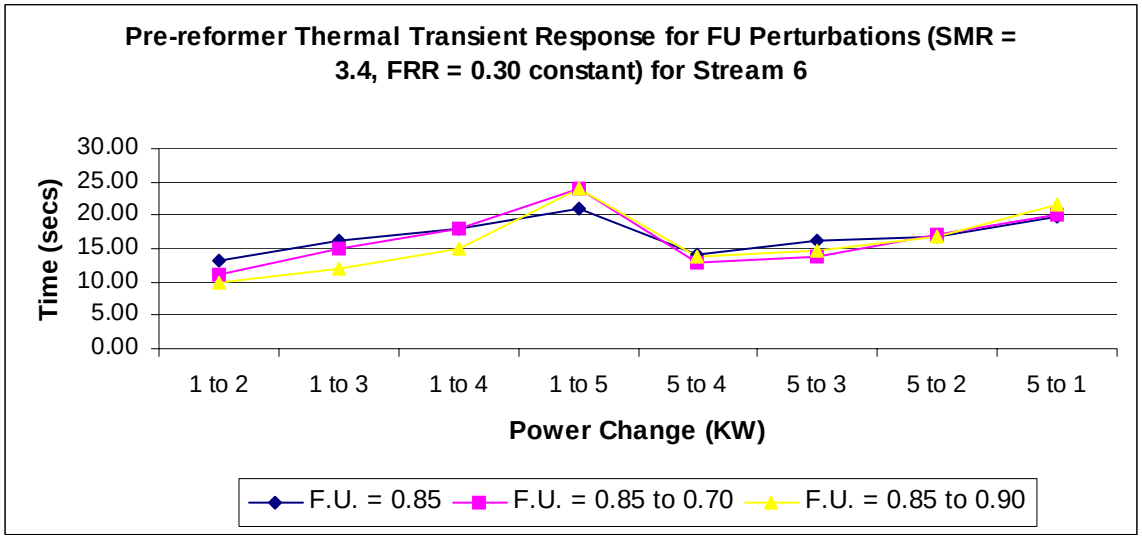
Pre-reformer Thermal Transient Response for FU Perturbations (SMR = 3.4, FRR = 0.30 constant) for Stream 6
Time (secs)
30.00
25.00
20.00
15.00
10.00
5.00
0.00
1 to 2
1 to 3
1 to 4
1 to 5
5 to 4
5 to 3
5 to 2
5 to 1
Power Change (KW)
F.U. = 0.85
F.U. = 0.85 to 0.70
F.U. = 0.85 to 0.90

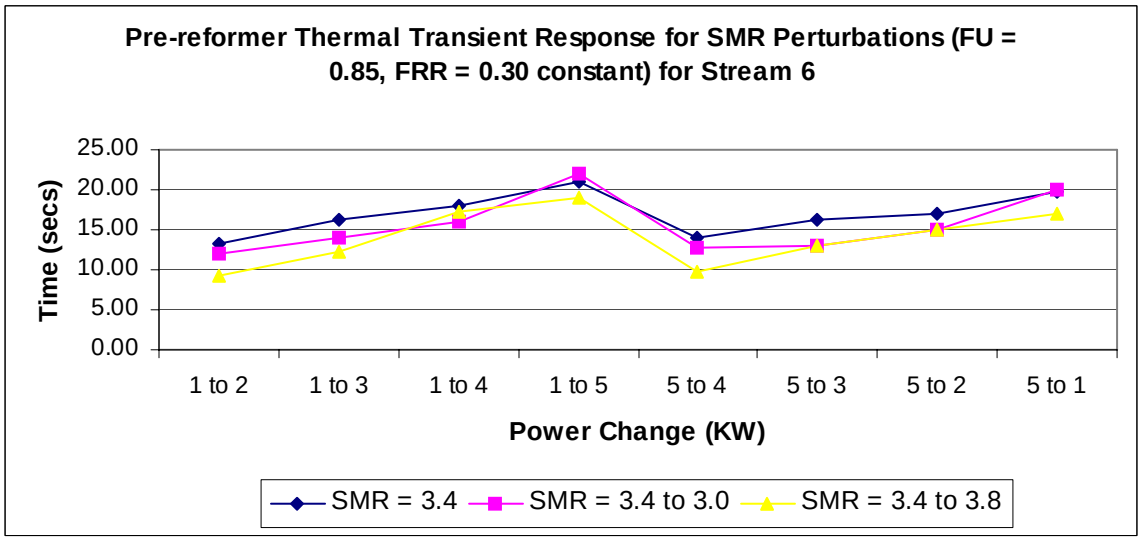
Pre-reformer Thermal Transient Response for SMR Perturbations (FU = 0.85, FRR = 0.30 constant) for Stream 6
Time (secs)
25.00
20.00
15.00
10.00
5.00
0.00
1 to 2
1 to 3
1 to 4
1 to 5
5 to 4
5 to 3
5 to 2
5 to 1
Power Change (KW)
SMR = 3.4
SMR = 3.4 to 3.0
SMR = 3.4 to 3.8

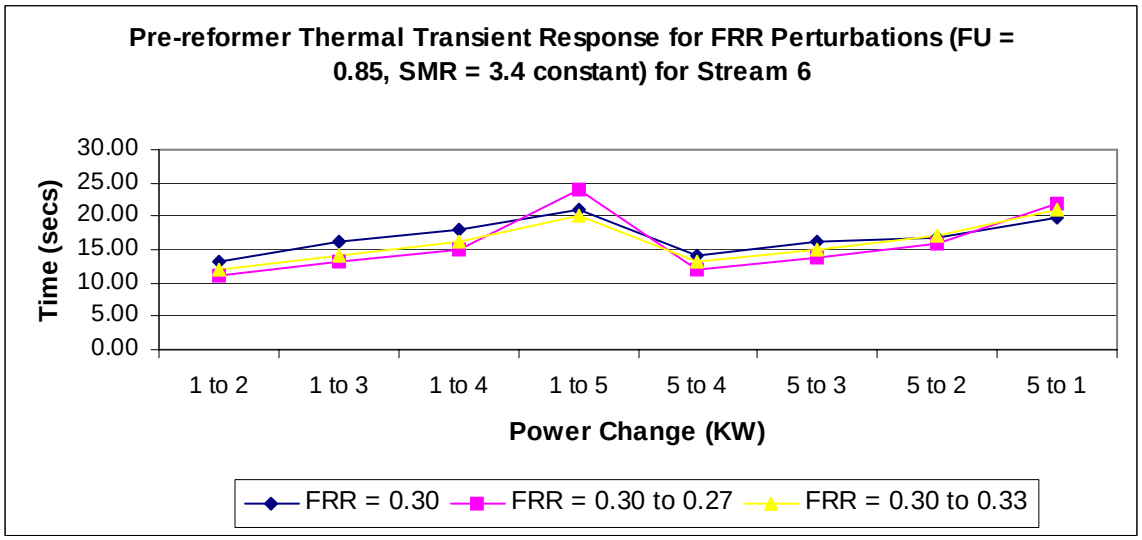
Pre-reformer Thermal Transient Response for FRR Perturbations (FU = 0.85, SMR = 3.4 constant) for Stream 6
Time (secs)
30.00
25.00
20.00
15.00
10.00
5.00
0.00
1 to 2
1 to 3
1 to 4
1 to 5
5 to 4
5 to 3
5 to 2
5 to 1
Power Change (KW)
FRR = 0.30
FRR = 0.30 to 0.27
FRR = 0.30 to 0.33

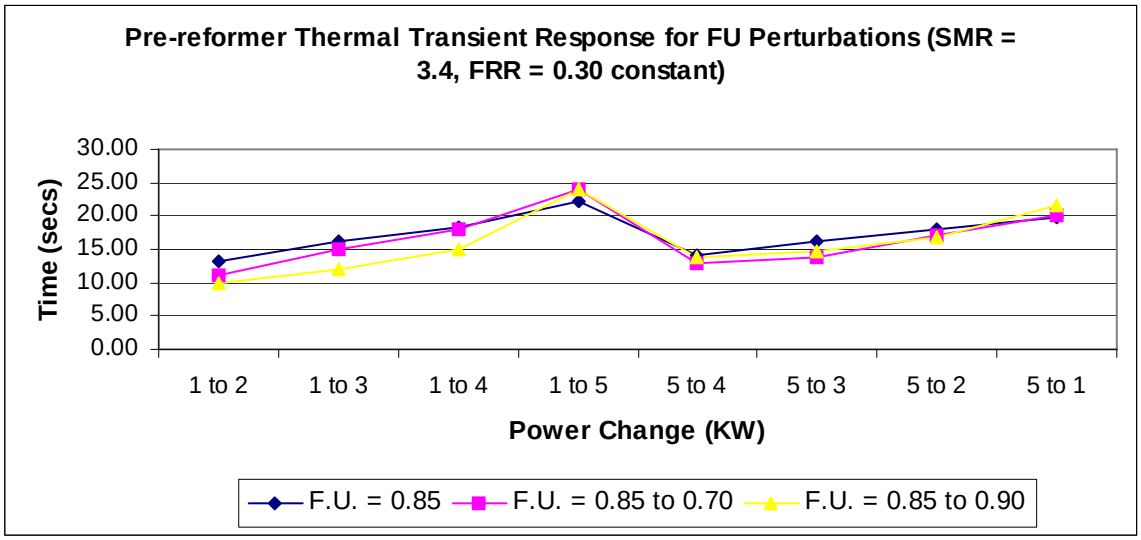
Pre-reformer Thermal Transient Response for FU Perturbations (SMR = 3.4, FRR = 0.30 constant)
Time (secs)
30.00
25.00
20.00
15.00
10.00
5.00
0.00
1 to 2
1 to 3
1 to 4
1 to 5
5 to 4
5 to 3
5 to 2
5 to 1
Power Change (KW)
F.U. = 0.85
F.U. = 0.85 to 0.70
F.U. = 0.85 to 0.90

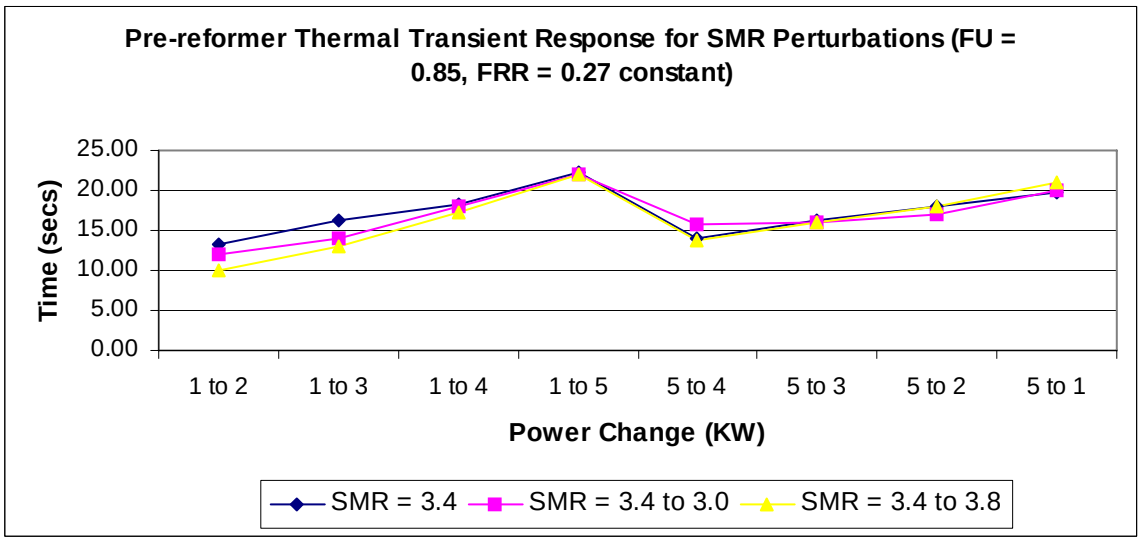
Pre-reformer Thermal Transient Response for SMR Perturbations (FU = 0.85, FRR = 0.27 constant)
Time (secs)
25.00
20.00
15.00
10.00
5.00
0.00
1 to 2
1 to 3
1 to 4
1 to 5
5 to 4
5 to 3
5 to 2
5 to 1
Power Change (KW)
SMR = 3.4
SMR = 3.4 to 3.0
SMR = 3.4 to 3.8

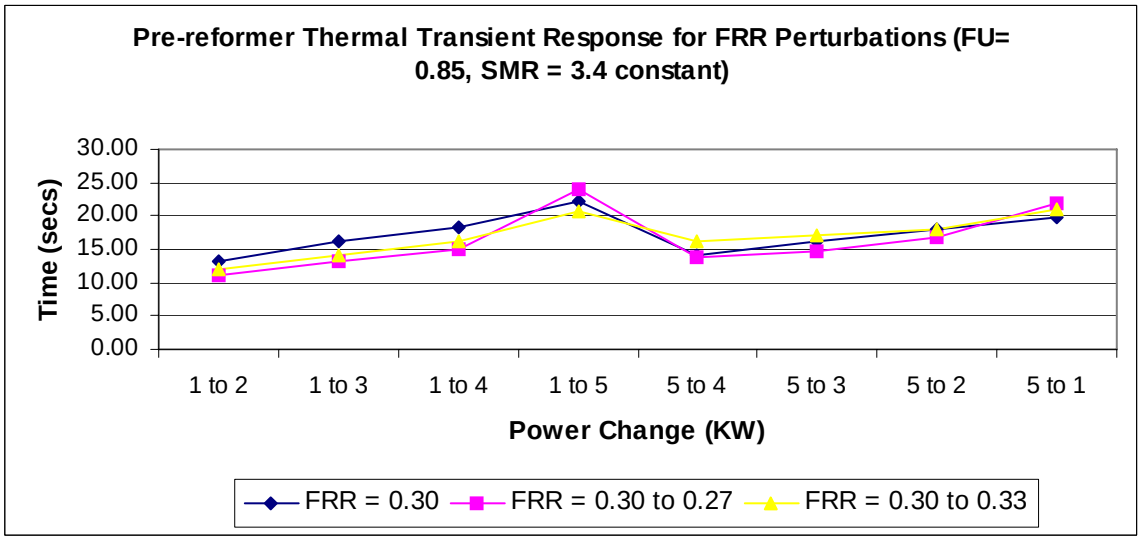
Pre-reformer Thermal Transient Response for FRR Perturbations (FU= 0.85, SMR = 3.4 constant)
Time (secs)
30.00
25.00
20.00
15.00
10.00
5.00
0.00
1 to 2
1 to 3
1 to 4
1 to 5
5 to 4
5 to 3
5 to 2
5 to 1
Power Change (KW)
FRR = 0.30
FRR = 0.30 to 0.27
FRR = 0.30 to 0.33

Component: HXIII

Stream 1

Power Change (KW)	FU 0.85 SMR 3.4 FRR 0.30	FU 0.70 SMR 3.4 FRR 0.30	FU 0.90 SMR 3.4 FRR 0.30	FU 0.85 SMR 3.0 FRR 0.30	FU 0.85 SMR 3.8 FRR 0.30	FU 0.85 SMR 3.4 FRR 0.27	FU 0.85 SMR 3.4 FRR 0.33
1 to 2	2.5060	2.9660	2.4420	2.3170	2.4390	2.4410	2.4890
1 to 3	3.6630	4.2080	3.7200	4.1130	3.6290	3.9660	3.5550
1 to 4	5.1250	6.1000	4.8490	5.0220	4.9440	4.9210	4.8730
1 to 5	6.2630	6.9970	5.9970	6.2530	6.0190	6.3000	6.2320
5 to 4	1.9530	1.9690	1.0590	1.8500	1.5420	1.2940	2.0910
5 to 3	2.5960	2.2800	1.8440	2.1730	1.9510	2.7820	2.0760
5 to 2	3.1400	3.9700	2.4650	2.8920	2.6120	2.7030	2.6800
5 to 1	3.3660	4.3050	3.0260	3.4320	3.4290	3.3390	3.2940

Stream 19

Power Change (KW)	FU 0.85 SMR 3.4 FRR 0.30	FU 0.70 SMR 3.4 FRR 0.30	FU 0.90 SMR 3.4 FRR 0.30	FU 0.85 SMR 3.0 FRR 0.30	FU 0.85 SMR 3.8 FRR 0.30	FU 0.85 SMR 3.4 FRR 0.27	FU 0.85 SMR 3.4 FRR 0.33
1 to 2	2.2120	2.9090	2.4420	2.3200	2.4420	2.4440	2.4920
1 to 3	3.6050	4.1040	3.7230	3.8780	3.2020	3.0220	3.5580
1 to 4	4.2160	6.1160	4.8520	5.0220	4.9470	6.0000	4.8730
1 to 5	6.2630	7.0000	6.0000	6.0000	6.0220	7.0300	6.1520
5 to 4	3.0000	2.6610	1.0590	1.6960	1.5420	1.4370	1.7200
5 to 3	3.8760	2.2800	1.8300	2.1930	1.9510	2.1060	2.1170
5 to 2	4.0000	3.2120	2.5840	2.8920	2.5840	2.8220	2.6800
5 to 1	5.2800	4.3300	2.9630	3.0320	3.0640	3.4370	3.4560

Overall: HX III

Power Change (KW)	FU 0.85 SMR 3.4 FRR 0.30	FU 0.70 SMR 3.4 FRR 0.30	FU 0.90 SMR 3.4 FRR 0.30	FU 0.85 SMR 3.0 FRR 0.30	FU 0.85 SMR 3.8 FRR 0.30	FU 0.85 SMR 3.4 FRR 0.27	FU 0.85 SMR 3.4 FRR 0.33
1 to 2	2.5060	2.9660	2.4420	2.3200	2.4420	2.4440	2.4920
1 to 3	3.6630	4.2080	3.7230	4.1130	3.6290	3.9660	3.5580
1 to 4	5.1250	6.1160	4.8520	5.0220	4.9470	6.0000	4.8730
1 to 5	6.2630	7.0000	6.0000	6.2530	6.0220	7.0300	6.2320
5 to 4	3.0000	2.6610	1.0590	1.8500	1.5420	1.4370	2.0910
5 to 3	3.8760	2.2800	1.8440	2.1930	1.9510	2.7820	2.1170
5 to 2	4.0000	3.2120	2.5840	2.8920	2.6120	2.8220	2.6800
5 to 1	5.2800	4.3300	3.0260	3.4320	3.4290	3.4370	3.4560

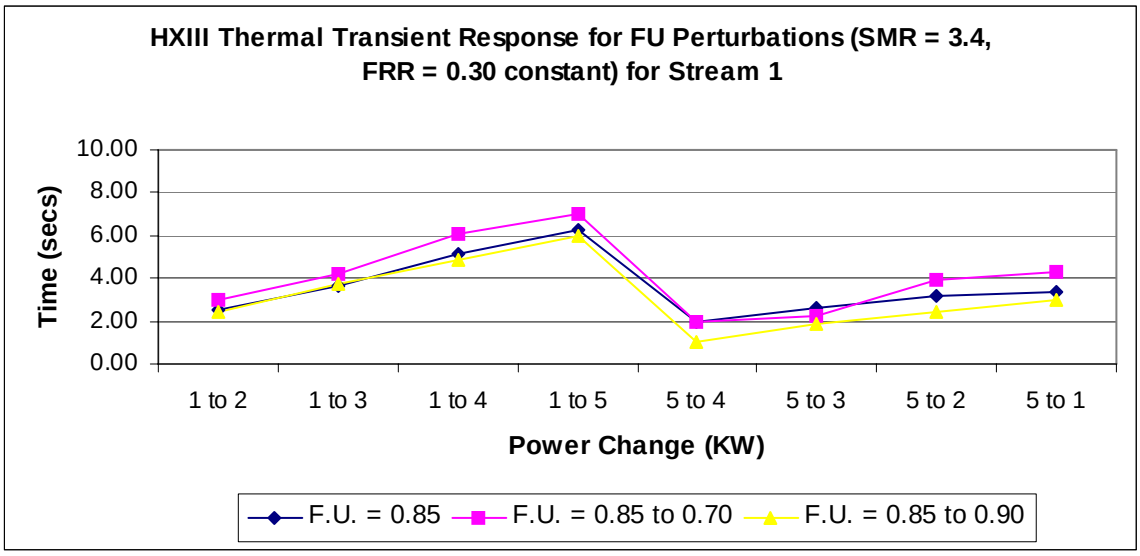
HXIII Thermal Transient Response for FU Perturbations (SMR = 3.4, FRR = 0.30 constant) for Stream 1
Time (secs)
10.00
8.00
6.00
4.00
2.00
0.00
1 to 2
1 to 3
1 to 4
1 to 5
5 to 4
5 to 3
5 to 2
5 to 1
Power Change (KW)
F.U. = 0.85
F.U. = 0.85 to 0.70
F.U. = 0.85 to 0.90

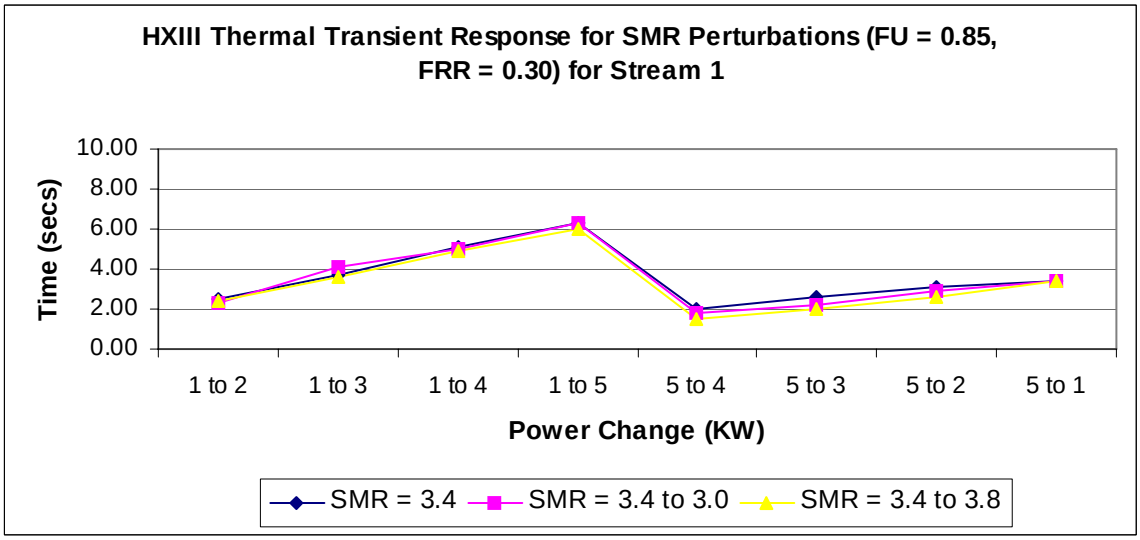
HXIII Thermal Transient Response for SMR Perturbations (FU = 0.85, FRR = 0.30) for Stream 1
Time (secs)
10.00
8.00
6.00
4.00
2.00
0.00
1 to 2
1 to 3
1 to 4
1 to 5
5 to 4
5 to 3
5 to 2
5 to 1
Power Change (KW)
SMR = 3.4
SMR = 3.4 to 3.0
SMR = 3.4 to 3.8

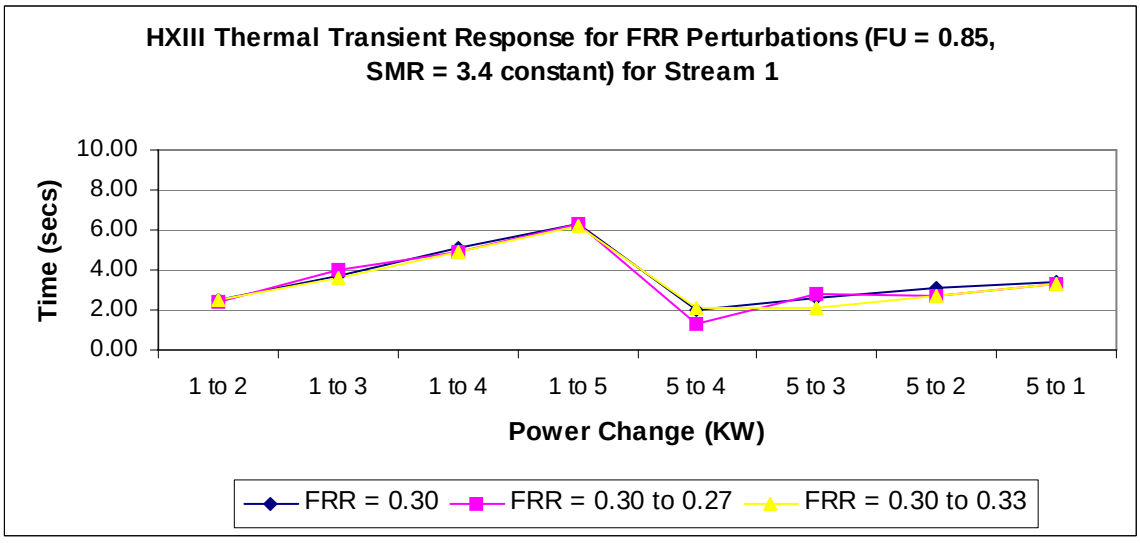
HXIII Thermal Transient Response for FRR Perturbations (FU = 0.85, SMR = 3.4 constant) for Stream 1
Time (secs)
10.00
8.00
6.00
4.00
2.00
0.00
1 to 2
1 to 3
1 to 4
1 to 5
5 to 4
5 to 3
5 to 2
5 to 1
Power Change (KW)
FRR = 0.30
FRR = 0.30 to 0.27
FRR = 0.30 to 0.33

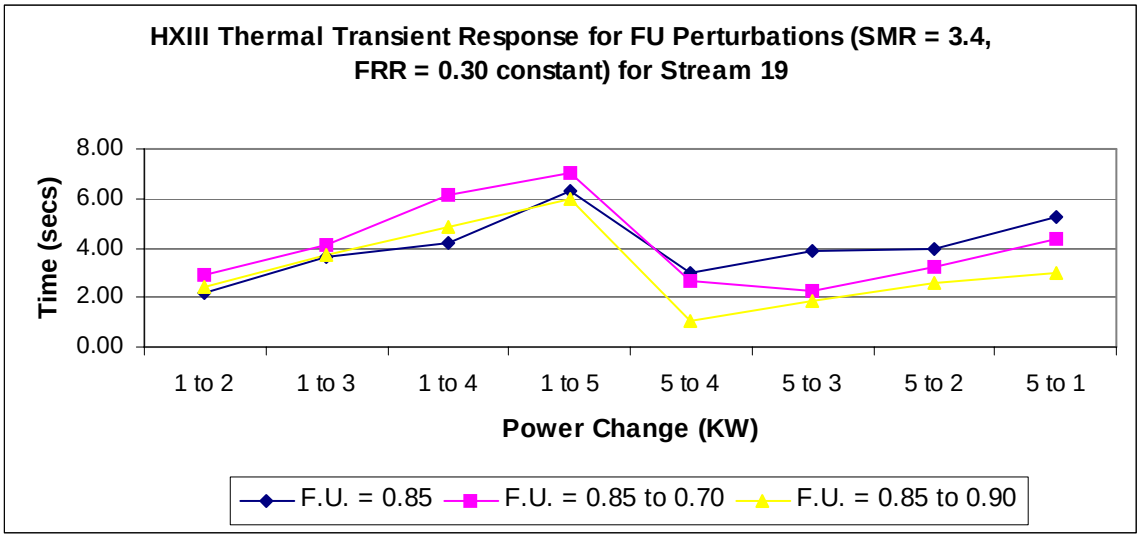
HXIII Thermal Transient Response for FU Perturbations (SMR = 3.4, FRR = 0.30 constant) for Stream 19
Time (secs)
8.00
6.00
4.00
2.00
0.00
1 to 2
1 to 3
1 to 4
1 to 5
5 to 4
5 to 3
5 to 2
5 to 1
Power Change (KW)
F.U. = 0.85
F.U. = 0.85 to 0.70
F.U. = 0.85 to 0.90

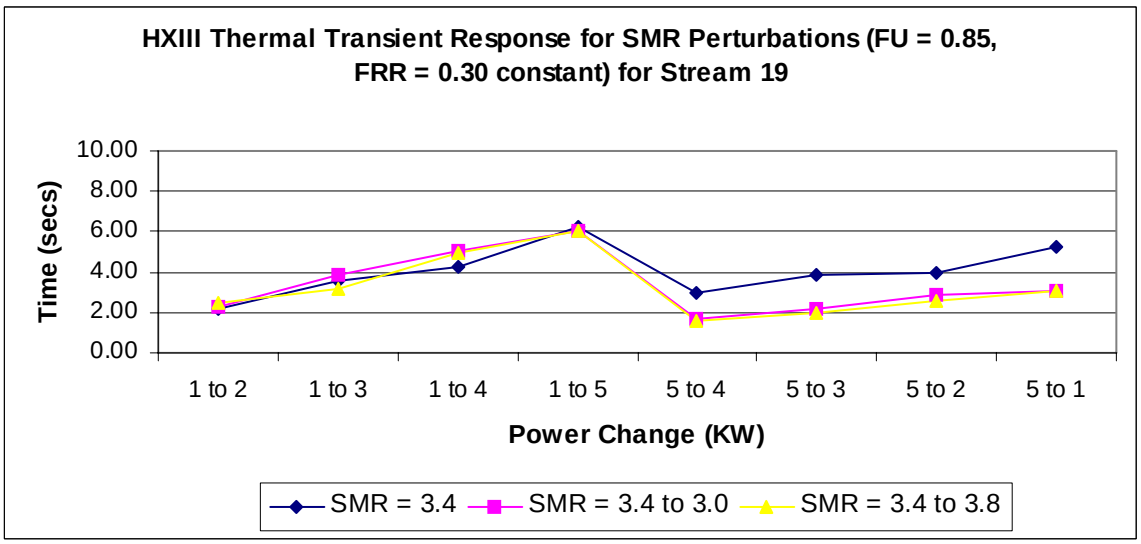
HXIII Thermal Transient Response for SMR Perturbations (FU = 0.85, FRR = 0.30 constant) for Stream 19
Time (secs)
10.00
8.00
6.00
4.00
2.00
0.00
1 to 2
1 to 3
1 to 4
1 to 5
5 to 4
5 to 3
5 to 2
5 to 1
Power Change (KW)
SMR = 3.4
SMR = 3.4 to 3.0
SMR = 3.4 to 3.8

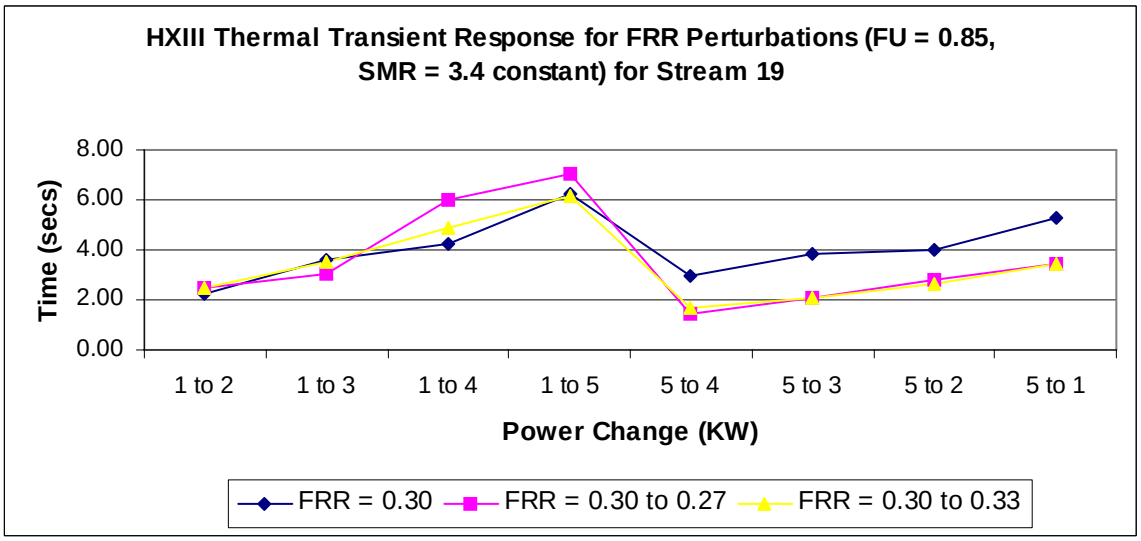
HXIII Thermal Transient Response for FRR Perturbations (FU = 0.85, SMR = 3.4 constant) for Stream 19
Time (secs)
8.00
6.00
4.00
2.00
0.00
1 to 2
1 to 3
1 to 4
1 to 5
5 to 4
5 to 3
5 to 2
5 to 1
Power Change (KW)
FRR = 0.30
FRR = 0.30 to 0.27
FRR = 0.30 to 0.33

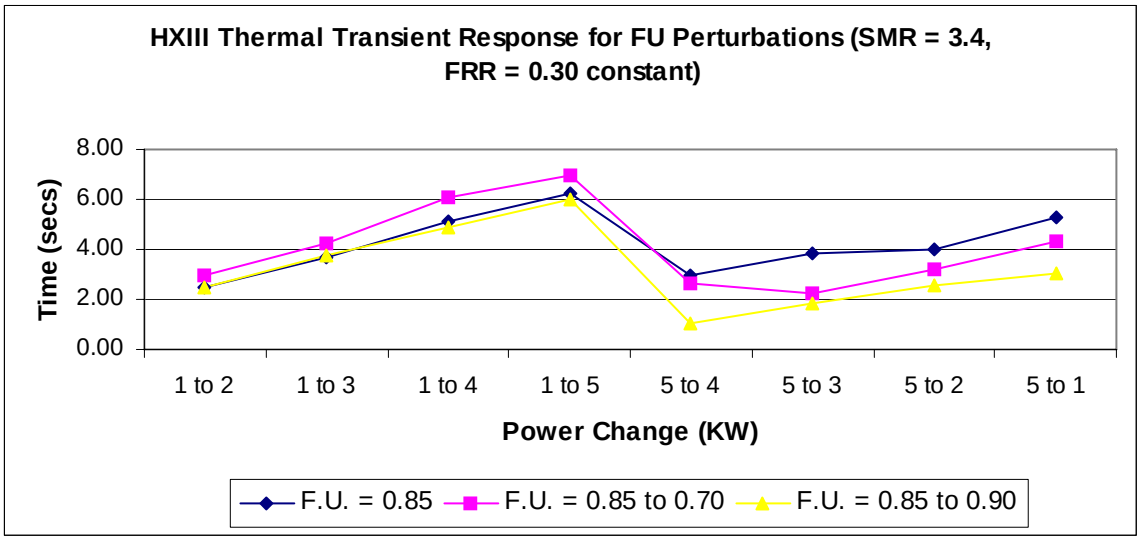
HXIII Thermal Transient Response for FU Perturbations (SMR = 3.4, FRR = 0.30 constant)
Time (secs)
8.00
6.00
4.00
2.00
0.00
1 to 2
1 to 3
1 to 4
1 to 5
5 to 4
5 to 3
5 to 2
5 to 1
Power Change (KW)
F.U. = 0.85
F.U. = 0.85 to 0.70
F.U. = 0.85 to 0.90

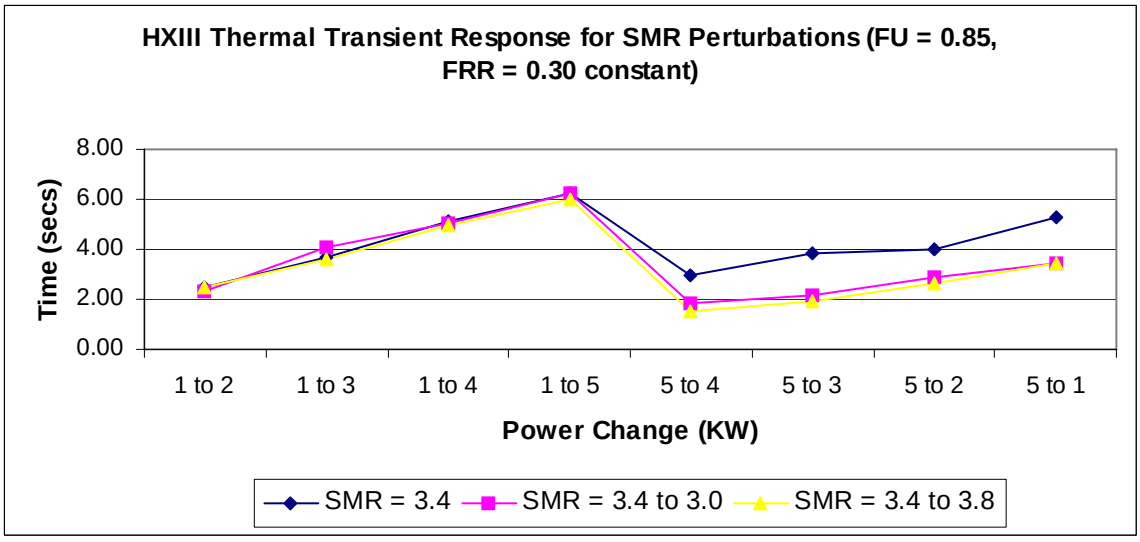
HXIII Thermal Transient Response for SMR Perturbations (FU = 0.85, FRR = 0.30 constant)
Time (secs)
8.00
6.00
4.00
2.00
0.00
1 to 2
1 to 3
1 to 4
1 to 5
5 to 4
5 to 3
5 to 2
5 to 1
Power Change (KW)
SMR = 3.4
SMR = 3.4 to 3.0
SMR = 3.4 to 3.8

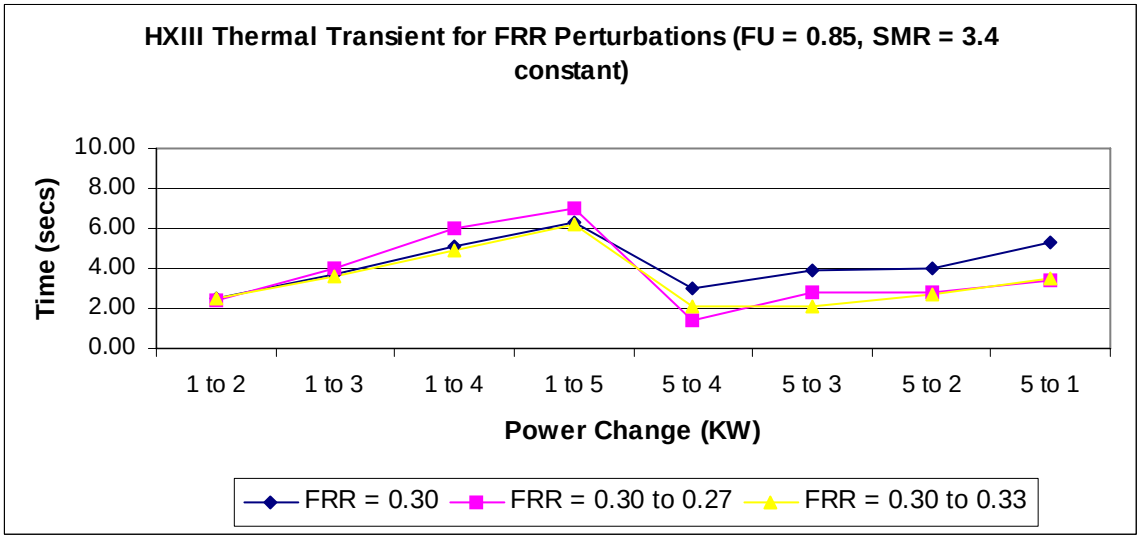
HXIII Thermal Transient for FRR Perturbations (FU = 0.85, SMR = 3.4 constant)
Time (secs)
10.00
8.00
6.00
4.00
2.00
0.00
1 to 2
1 to 3
1 to 4
1 to 5
5 to 4
5 to 3
5 to 2
5 to 1
Power Change (KW)
FRR = 0.30
FRR = 0.30 to 0.27
FRR = 0.30 to 0.33

Component: HXIV

Stream 26

Power Change (KW)	FU 0.85 SMR 3.4 FRR 0.30	FU 0.70 SMR 3.4 FRR 0.30	FU 0.90 SMR 3.4 FRR 0.30	FU 0.85 SMR 3.0 FRR 0.30	FU 0.85 SMR 3.8 FRR 0.30	FU 0.85 SMR 3.4 FRR 0.27	FU 0.85 SMR 3.4 FRR 0.33
1 to 2	3.2770	5.0200	3.9970	2.3170	2.8670	8.9970	9.0000
1 to 3	4.2010	6.3480	4.9970	4.1130	4.1990	11.0520	11.0510
1 to 4	4.6750	6.7700	7.9970	5.0220	5.1990	18.0520	12.9530
1 to 5	5.0090	8.9970	9.9970	8.9970	7.0230	19.9970	13.0480
5 to 4	2.9530	2.9690	5.8580	1.5460	2.8520	7.8570	7.0910
5 to 3	4.0000	6.8060	7.9320	2.1930	3.0060	8.7820	11.0300
5 to 2	4.8760	8.4480	9.5450	3.0320	4.8960	12.8810	14.0000
5 to 1	7.1790	12.9250	10.0000	3.8060	6.1010	15.3850	14.9150

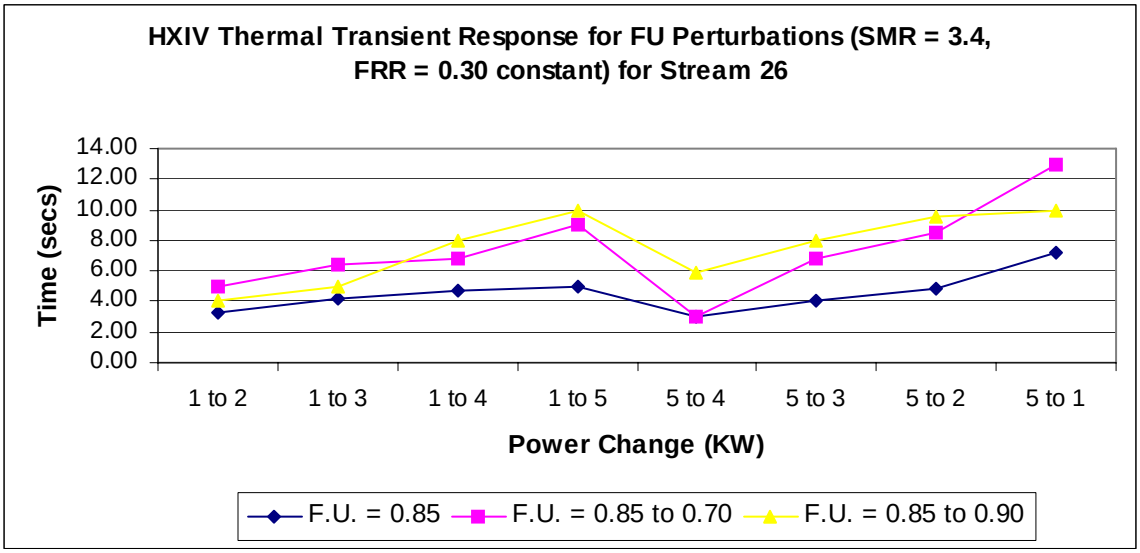
HXIV Thermal Transient Response for FU Perturbations (SMR = 3.4, FRR = 0.30 constant) for Stream 26
Time (secs)
14.00
12.00
10.00
8.00
6.00
4.00
2.00
0.00
1 to 2
1 to 3
1 to 4
1 to 5
5 to 4
5 to 3
5 to 2
5 to 1
Power Change (KW)
F.U. = 0.85
F.U. = 0.85 to 0.70
F.U. = 0.85 to 0.90

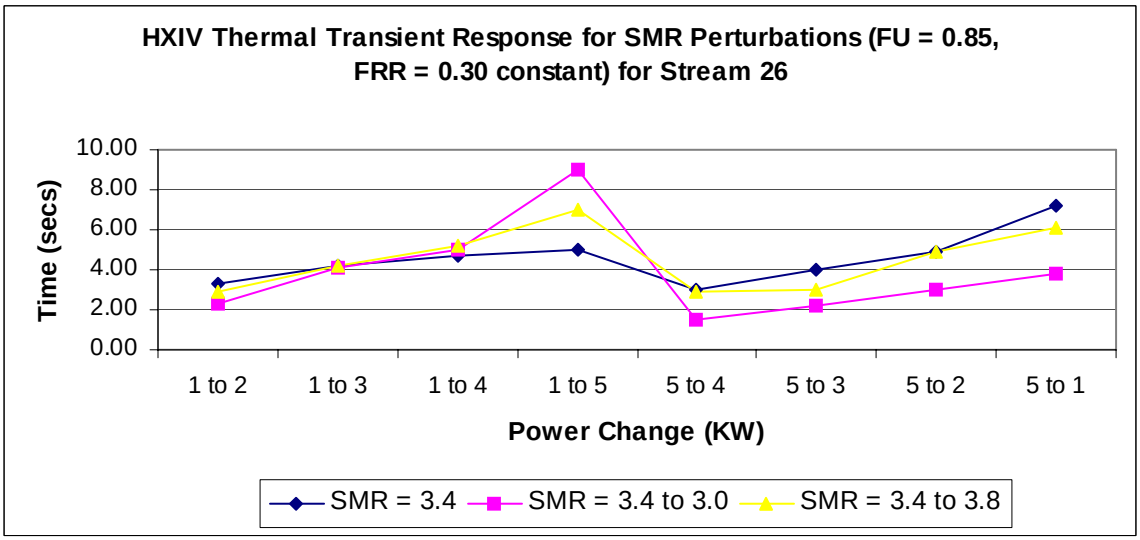
HXIV Thermal Transient Response for SMR Perturbations (FU = 0.85, FRR = 0.30 constant) for Stream 26
Time (secs)
10.00
8.00
6.00
4.00
2.00
0.00
1 to 2
1 to 3
1 to 4
1 to 5
5 to 4
5 to 3
5 to 2
5 to 1
Power Change (KW)
SMR = 3.4
SMR = 3.4 to 3.0
SMR = 3.4 to 3.8

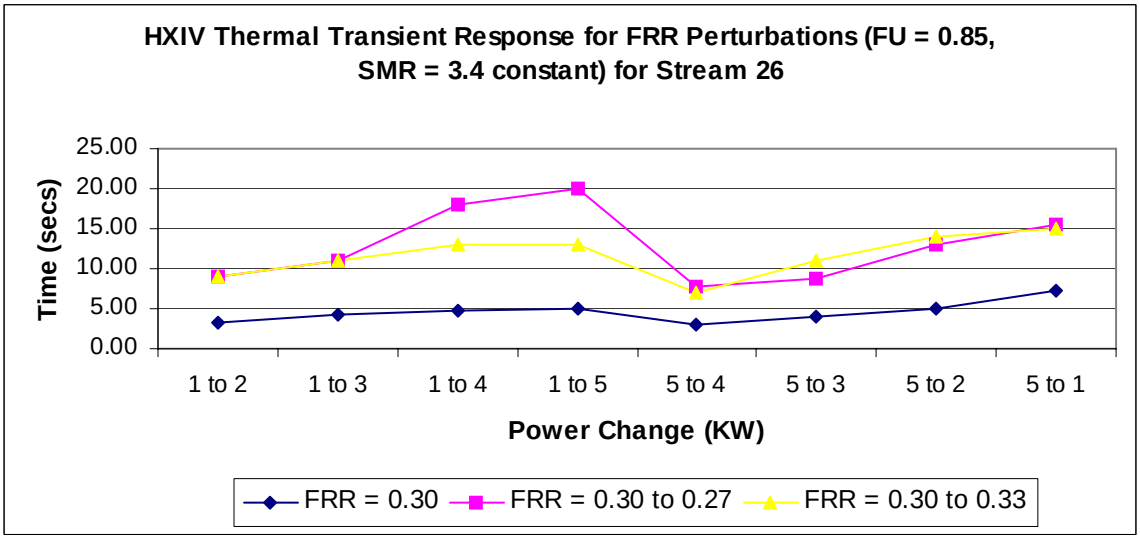
HXIV Thermal Transient Response for FRR Perturbations (FU = 0.85, SMR = 3.4 constant) for Stream 26
Time (secs)
25.00
20.00
15.00
10.00
5.00
0.00
1 to 2
1 to 3
1 to 4
1 to 5
5 to 4
5 to 3
5 to 2
5 to 1
Power Change (KW)
FRR = 0.30
FRR = 0.30 to 0.27
FRR = 0.30 to 0.33

System Thermal Efficiencies: Parametric Analysis #1

For Power increases :

FU Perturbation	System Thermal Efficiency				
	Load (1 KW)	Load (2 KW)	Load (3 KW)	Load (4 KW)	Load (5 KW)
FU 0.85 SMR 3.4 FRR 0.30	0.317377	0.365611	0.392320	0.414220	0.437471
FU 0.70 SMR 3.4 FRR 0.30	0.255898	0.296621	0.321432	0.341744	0.362974
FU 0.90 SMR 3.4 FRR 0.30	0.342342	0.388765	0.416305	0.438456	0.462365

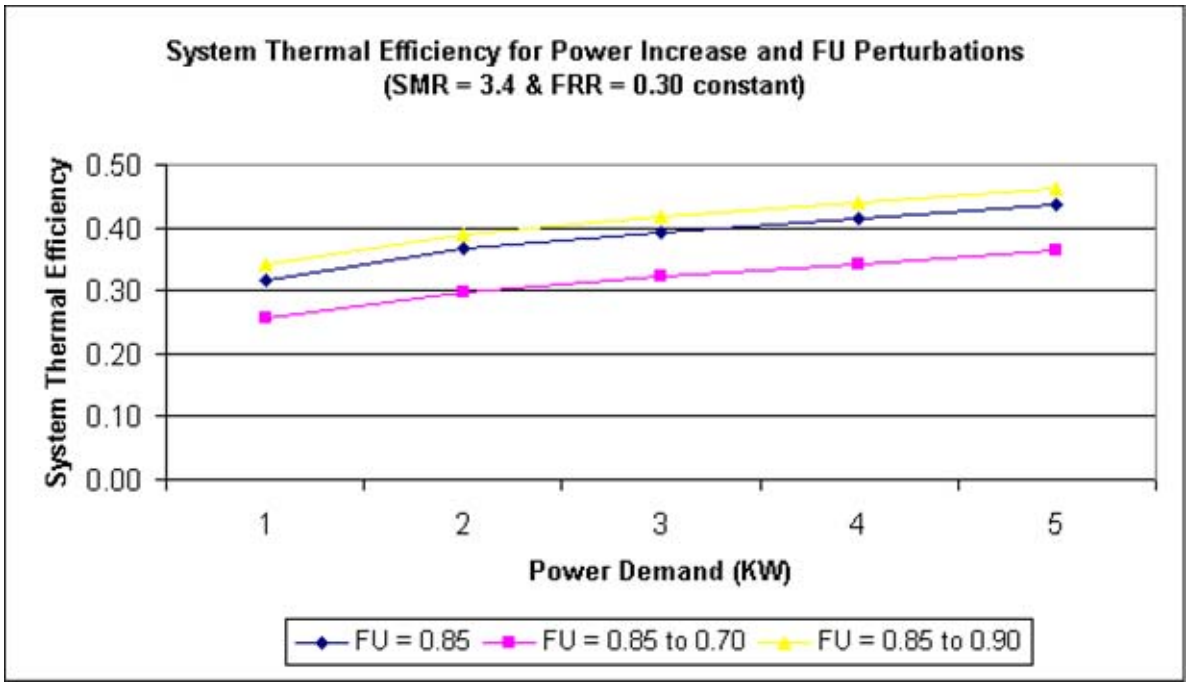

Raising the Fuel Utilization from the pre-determined level of 0.85 to 0.90 increases the System Thermal Efficiency and reducing it to 0.70 decreases it. But the reduction causes a steeper fall in the efficiency as compared with the increase.

SMR Perturbation	System Thermal Efficiency				
	Load (1 KW)	Load (2 KW)	Load (3 KW)	Load (4 KW)	Load (5 KW)
FU 0.85 SMR 3.4 FRR 0.30	0.317377	0.365611	0.392320	0.414220	0.437471
FU 0.85 SMR 3.0 FRR 0.30	0.314374	0.361305	0.387811	0.409837	0.432562
FU 0.85 SMR 3.8 FRR 0.30	0.321336	0.368758	0.394507	0.415592	0.440240

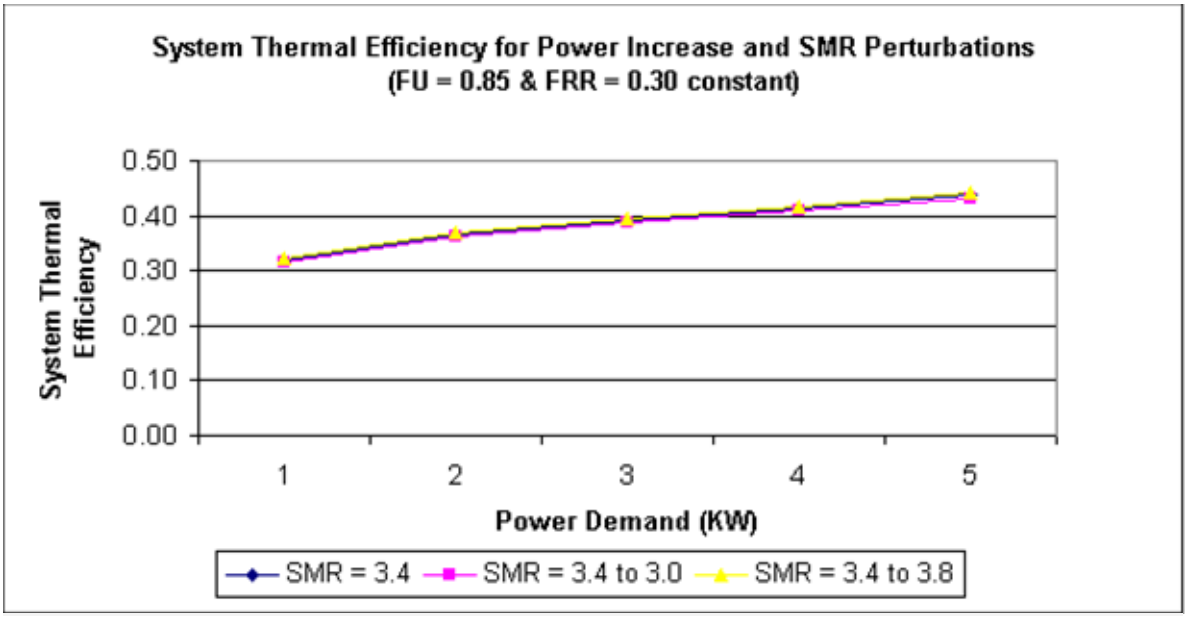

Increase or decrease in Steam to Methane Ratio does not affect the System Thermal Efficiency by a great magnitude. Hence we can infer that for load increases, Steam to Methane Ratio plays a relative subdued role as regards to System Thermal Efficiency.

FRR Perturbation	System Thermal Efficiency				
	Load (1 KW)	Load (2 KW)	Load (3 KW)	Load (4 KW)	Load (5 KW)
FU 0.85 SMR 3.4 FRR 0.30	0.317377	0.365611	0.392320	0.414220	0.437471
FU 0.85 SMR 3.4 FRR 0.27	0.326412	0.376372	0.402782	0.424631	0.448484
FU 0.85 SMR 3.4 FRR 0.33	0.306499	0.355843	0.382294	0.404202	0.427286

0.317377	0.326412	0.306499
0.365611	0.376372	0.355843
0.392320	0.402782	0.382294
0.414220	0.424631	0.404202
0.437471	0.448484	0.427286

Increasing the Fuel Reformate Ratio from 0.30 to 0.33, leads to a slight decrease in System Thermal Efficiency. Decreasing the Fuel Reformate Ratio to 0.27 on the other hand increases the System Thermal Efficiency slightly. Hence, Fuel Reformate Ratio has an inverse effect on the System Thermal Efficiency as regards to its increase or decrease.

For Power decreases :

FU Perturbation	System Thermal Efficiency				
	Load (5 KW)	Load (4 KW)	Load (3 KW)	Load (2 KW)	Load (1 KW)
FU 0.85 SMR 3.4 FRR 0.30	0.428575	0.406349	0.383753	0.356507	0.317377
FU 0.70 SMR 3.4 FRR 0.30	0.356756	0.337026	0.315951	0.290408	0.255898
FU 0.90 SMR 3.4 FRR 0.30	0.455981	0.429477	0.406251	0.379384	0.342342

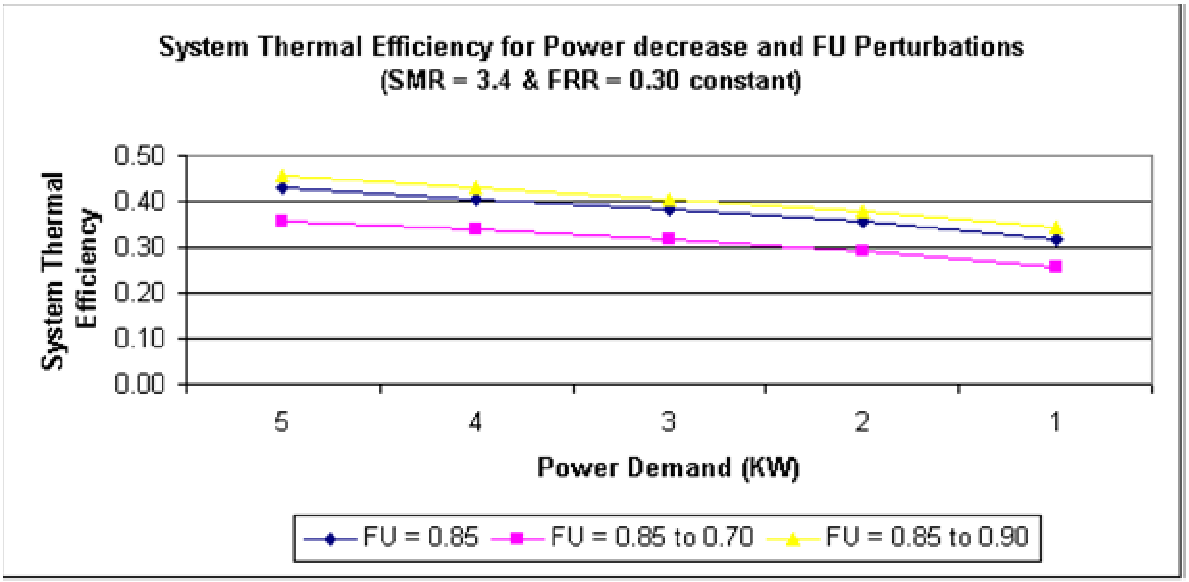

Raising the Fuel Utilization from the pre-determined level of 0.85 to 0.90 increases the System Thermal Efficiency and reducing it to 0.70 decreases it. But the reduction causes a steeper fall in the efficiency as compared with the increase.

SMR Perturbation	System Thermal Efficiency				
	Load (5 KW)	Load (4 KW)	Load (3 KW)	Load (2 KW)	Load (1 KW)
FU 0.85 SMR 3.4 FRR 0.30	0.428575	0.406349	0.383753	0.356507	0.317377
FU 0.85 SMR 3.0 FRR 0.30	0.427353	0.401421	0.378909	0.352590	0.314374
FU 0.85 SMR 3.8 FRR 0.30	0.432051	0.410147	0.389438	0.361779	0.321336

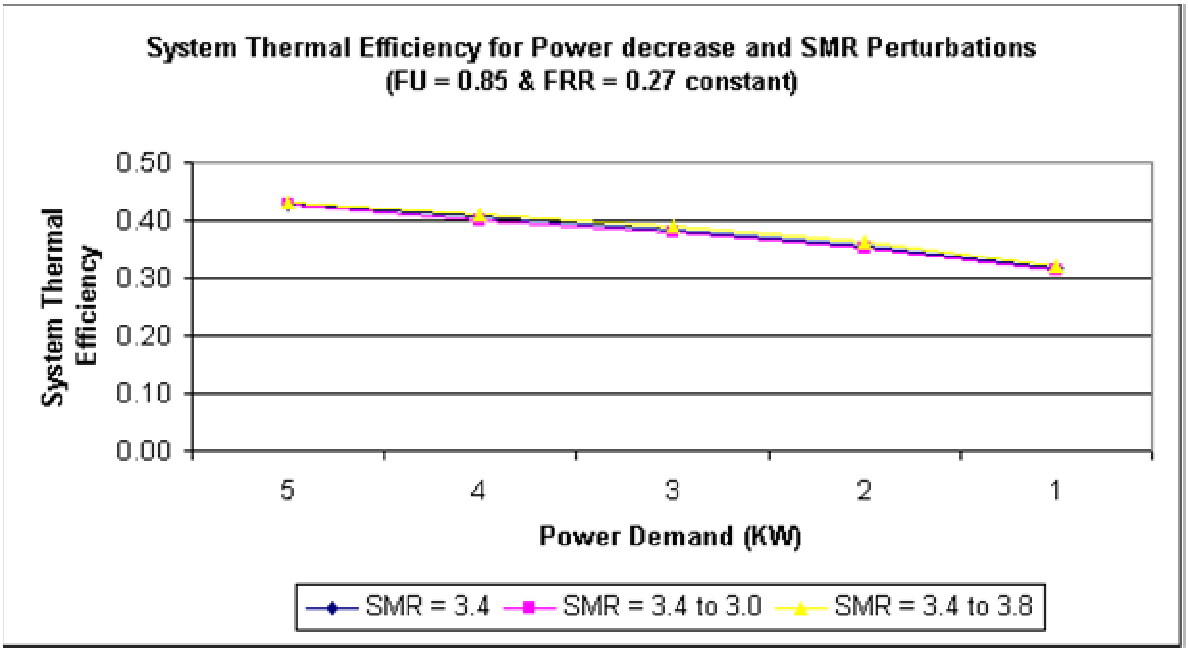

Increase or decrease in Steam to Methane Ratio does not affect the System Thermal Efficiency by a great magnitude. Hence we can infer that for load decreases, Steam to Methane Ratio plays a relative subdued role as regards to System Thermal Efficiency.

FRR Perturbation	System Thermal Efficiency				
	Load (5 KW)	Load (4 KW)	Load (3 KW)	Load (2 KW)	Load (1 KW)
FU 0.85 SMR 3.4 FRR 0.30	0.428575	0.406349	0.383753	0.356507	0.317377
FU 0.85 SMR 3.4 FRR 0.27	0.441306	0.418101	0.394886	0.367254	0.326412
FU 0.85 SMR 3.4 FRR 0.33	0.417750	0.395868	0.374995	0.347551	0.306499

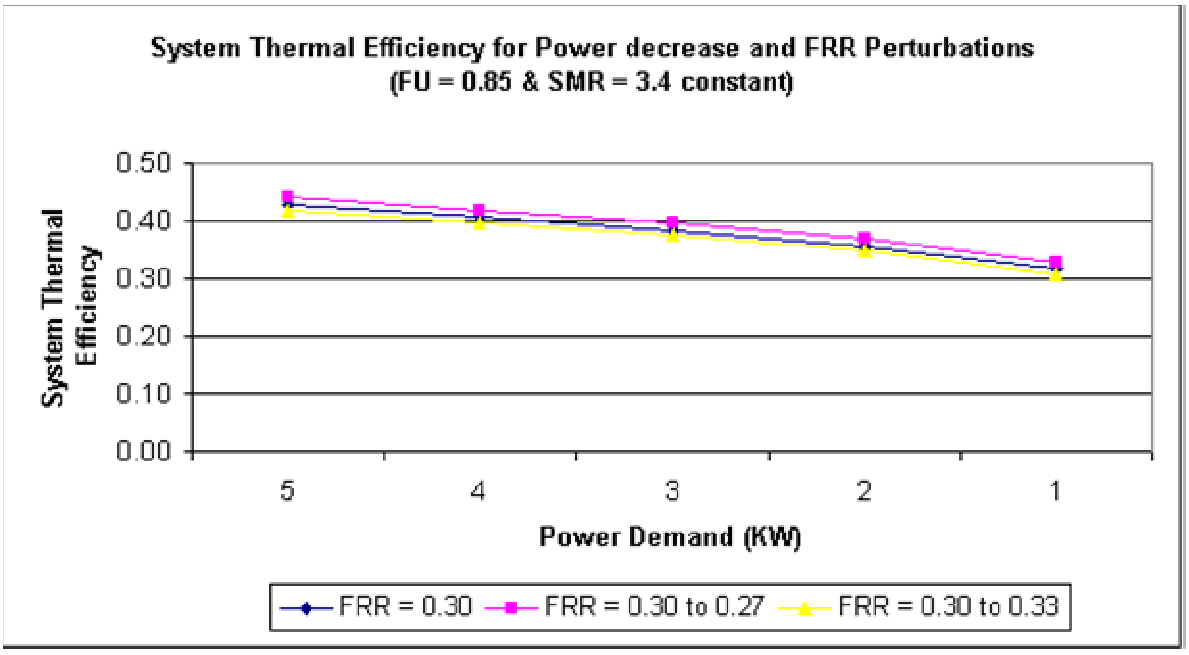

Increasing the Fuel Reformate Ratio from 0.30 to 0.33, leads to a slight decrease in System Thermal Efficiency. Decreasing the Fuel Reformate Ratio to 0.27 on the other hand increases the System Thermal Efficiency slightly. Hence, Fuel Reformate Ratio has an inverse effect on the System Thermal Efficiency as regards to its increase or decrease.

System Energy Efficiencies: Parametric Analysis #1

For Power increases :

FU Perturbation	System Energy Efficiency				
	Load (1 KW)	Load (2 KW)	Load (3 KW)	Load (4 KW)	Load (5 KW)
FU 0.85 SMR 3.4 FRR 0.30	0.308846	0.355784	0.381775	0.403087	0.425712
FU 0.70 SMR 3.4 FRR 0.30	0.249020	0.288648	0.312792	0.332558	0.353218
FU 0.90 SMR 3.4 FRR 0.30	0.333140	0.378315	0.405116	0.426671	0.449937

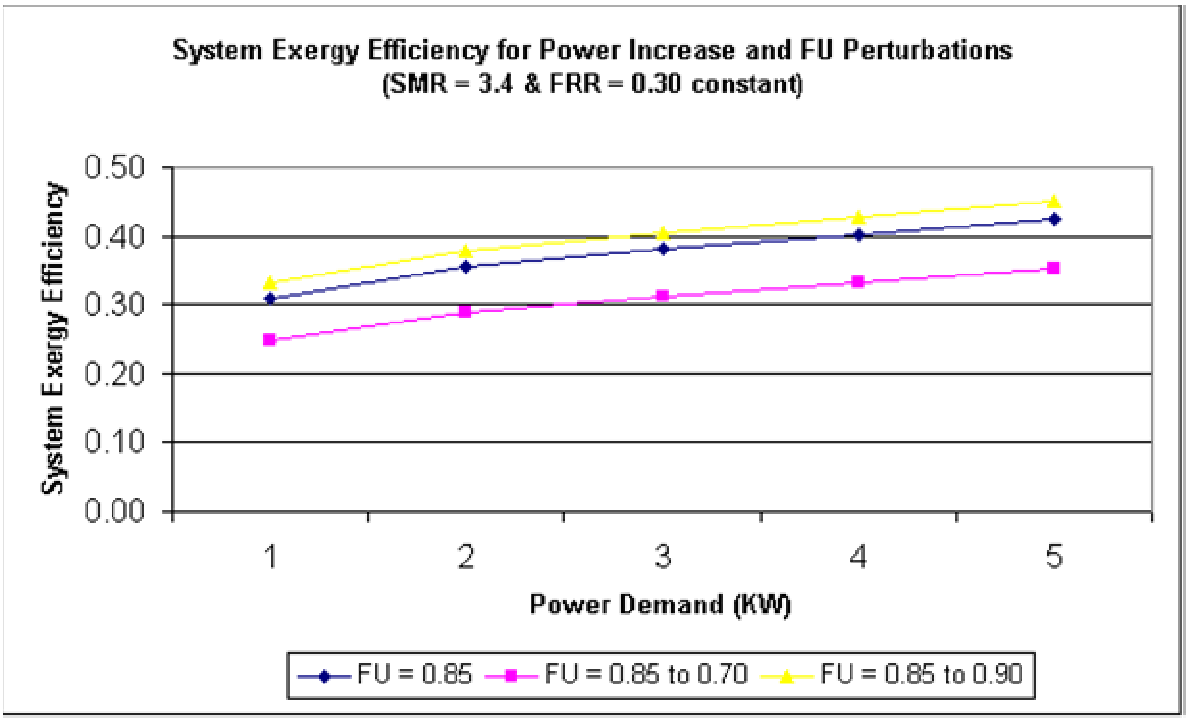

Raising the Fuel Utilization from the pre-determined level of 0.85 to 0.90 increases the System Energy Efficiency and reducing it to 0.70 decreases it. But the reduction causes a steeper fall in the efficiency as compared with the increase.

SMR Perturbation	System Energy Efficiency				
	Load (1 KW)	Load (2 KW)	Load (3 KW)	Load (4 KW)	Load (5 KW)
FU 0.85 SMR 3.4 FRR 0.30	0.308846	0.355784	0.381775	0.403087	0.425712
FU 0.85 SMR 3.0 FRR 0.30	0.305924	0.351594	0.377387	0.398821	0.420935
FU 0.85 SMR 3.8 FRR 0.30	0.312698	0.358846	0.383903	0.404421	0.428407

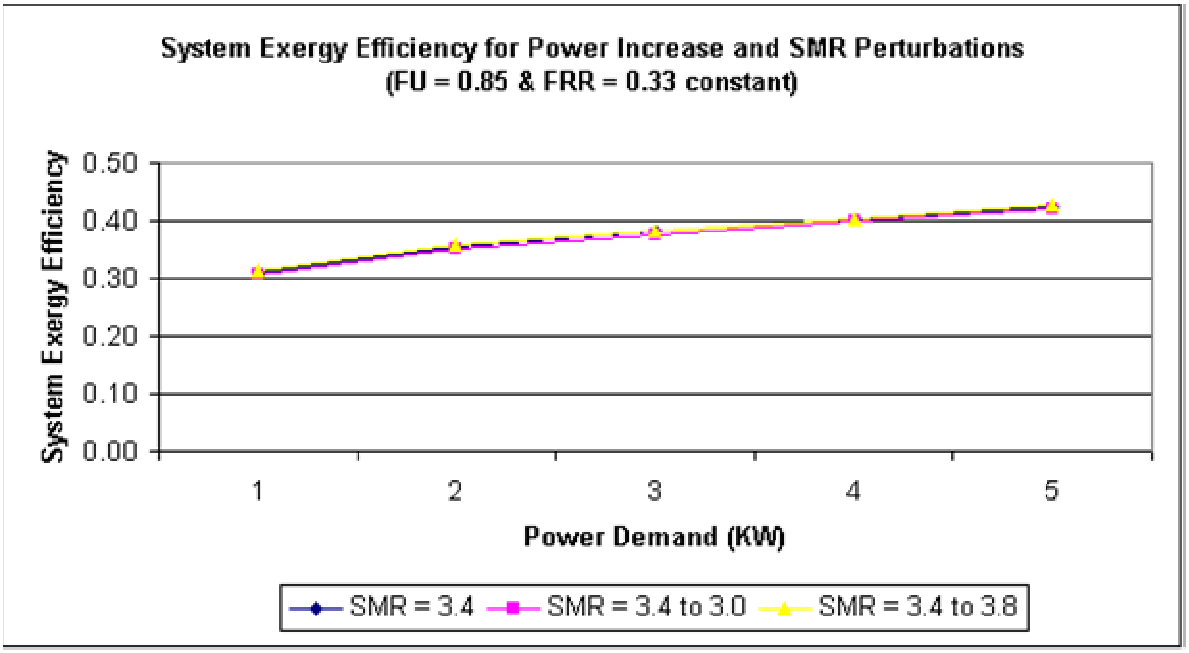

Increase or decrease in Steam to Methane Ratio does not affect the System Energy Efficiency by a great magnitude. Hence we can infer that for load increases, Steam to Methane Ratio plays a relative subdued role as regards to System Energy Efficiency.

FRR Perturbation	System Energy Efficiency				
	Load (1 KW)	Load (2 KW)	Load (3 KW)	Load (4 KW)	Load (5 KW)
FU 0.85 SMR 3.4 FRR 0.30	0.308846	0.355784	0.381775	0.403087	0.425712
FU 0.85 SMR 3.4 FRR 0.27	0.317639	0.366255	0.391956	0.413217	0.436429
FU 0.85 SMR 3.4 FRR 0.33	0.298260	0.346278	0.372019	0.393338	0.415801

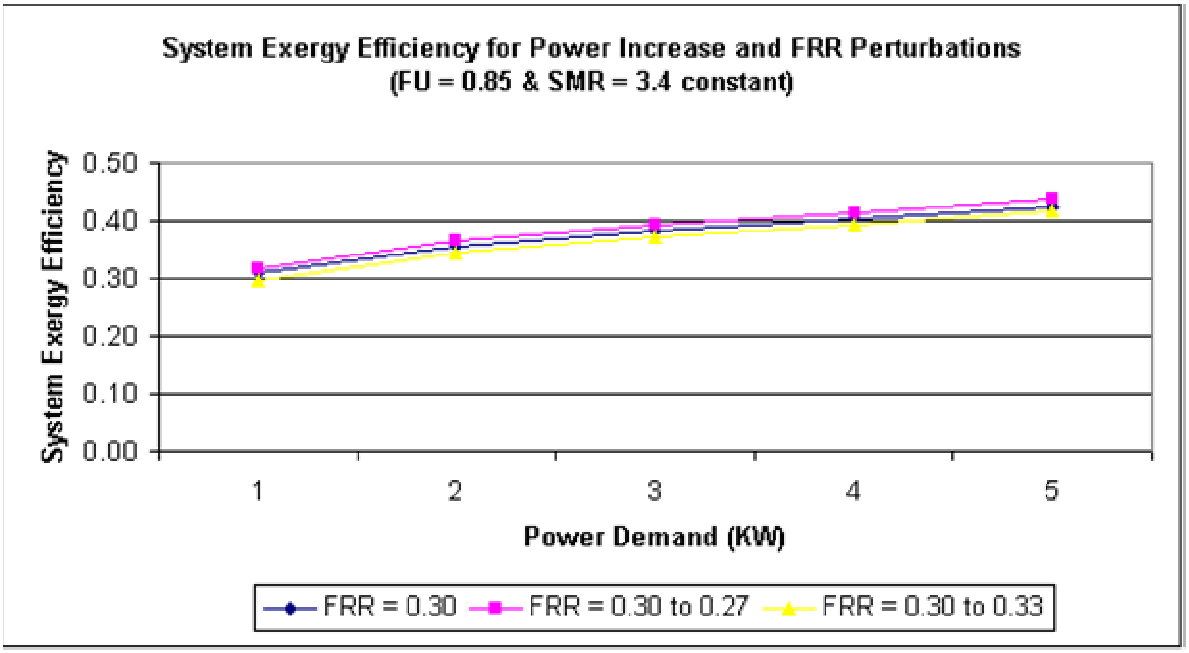

Increasing the Fuel Reformate Ratio from 0.30 to 0.33, leads to a slight decrease in System Energy Efficiency. Decreasing the Fuel Reformate Ratio to 0.27 on the other hand increases the System Energy Efficiency slightly. Hence, Fuel Reformate Ratio has an inverse effect on the System Energy Efficiency as regards to its increase or decrease.

For Power decreases :

FU Perturbation	System Energy Efficiency				
	Load (5 KW)	Load (4 KW)	Load (3 KW)	Load (2 KW)	Load (1 KW)
FU 0.85 SMR 3.4 FRR 0.30	0.417056	0.395426	0.373439	0.346925	0.308846
FU 0.70 SMR 3.4 FRR 0.30	0.347167	0.327967	0.307459	0.282602	0.249020
FU 0.90 SMR 3.4 FRR 0.30	0.443724	0.417933	0.395331	0.369624	0.333140

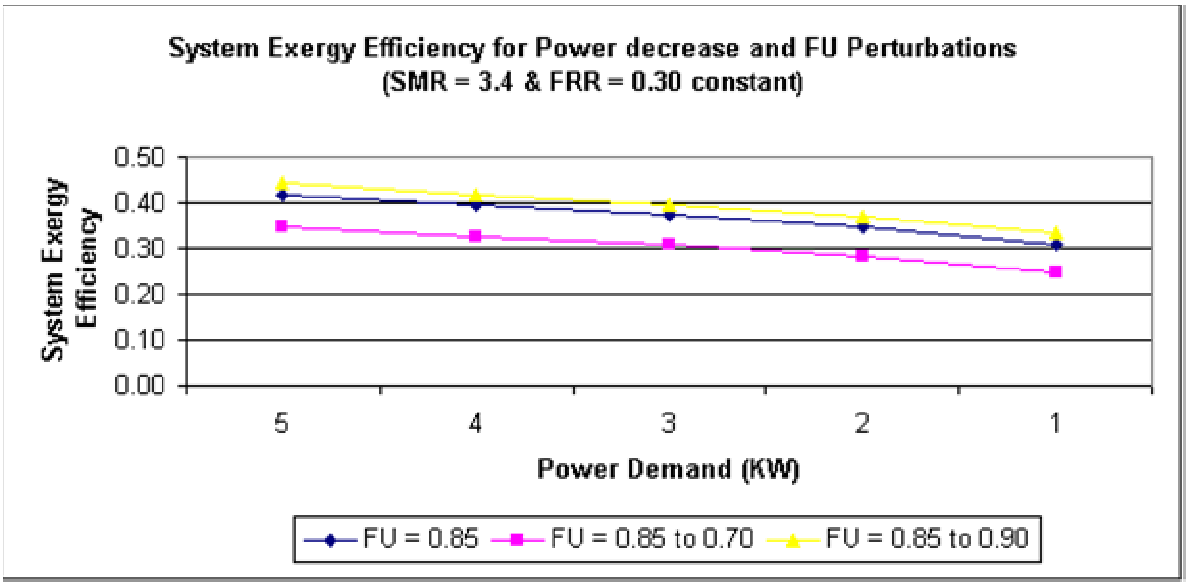

Raising the Fuel Utilization from the pre-determined level of 0.85 to 0.90 increases the System Energy Efficiency and reducing it to 0.70 decreases it. But the reduction causes a steeper fall in the efficiency as compared with the increase.

SMR Perturbation	System Energy Efficiency

	Load (5 KW)	Load (4 KW)	Load (3 KW)	Load (2 KW)	Load (1 KW)
FU 0.85 SMR 3.4 FRR 0.30	0.417056	0.395426	0.373439	0.346925	0.308846
FU 0.85 SMR 3.0 FRR 0.30	0.418562	0.390631	0.368725	0.343113	0.305924
FU 0.85 SMR 3.8 FRR 0.30	0.420438	0.399123	0.378970	0.352055	0.312698

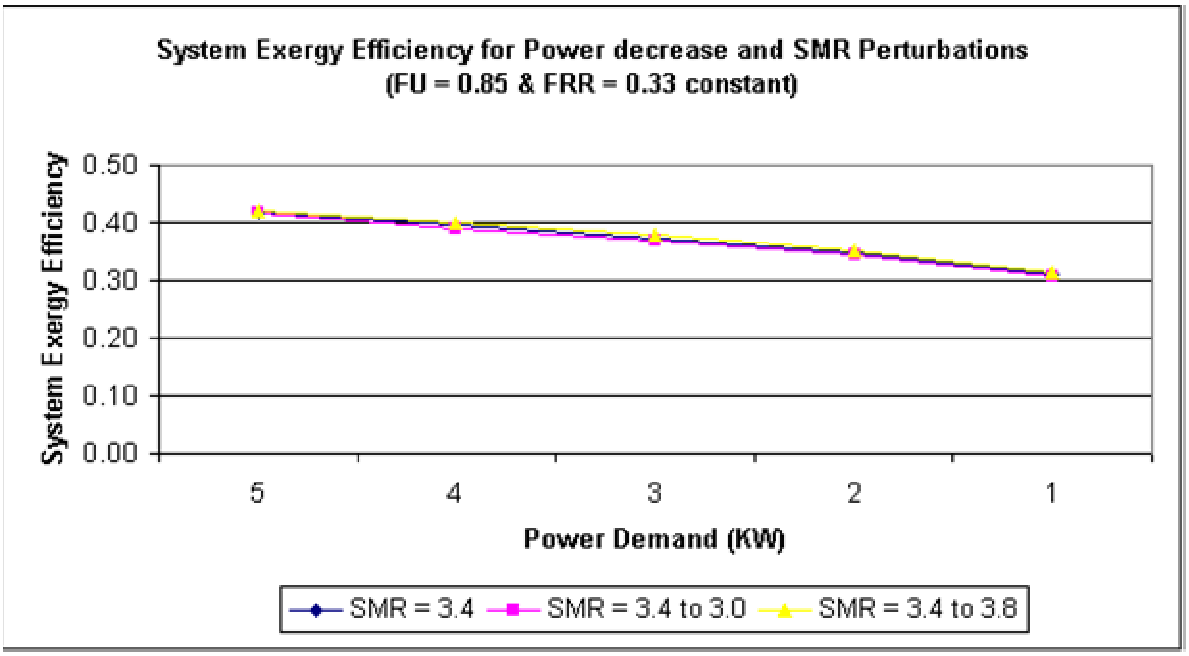

Increase or decrease in Steam to Methane Ratio does not affect the System Energy Efficiency by a great magnitude. Hence we can infer that for load decreases, Steam to Methane Ratio plays a relative subdued role as regards to System Energy Efficiency.

FRR Perturbation

System Energy Efficiency

	Load (5 KW)	Load (4 KW)	Load (3 KW)	Load (2 KW)	Load (1 KW)
FU 0.85 SMR 3.4 FRR 0.30	0.417056	0.395426	0.373439	0.346925	0.308846
FU 0.85 SMR 3.4 FRR 0.27	0.429444	0.406863	0.384272	0.357382	0.326412
FU 0.85 SMR 3.4 FRR 0.33	0.406521	0.385227	0.364916	0.338209	0.298260

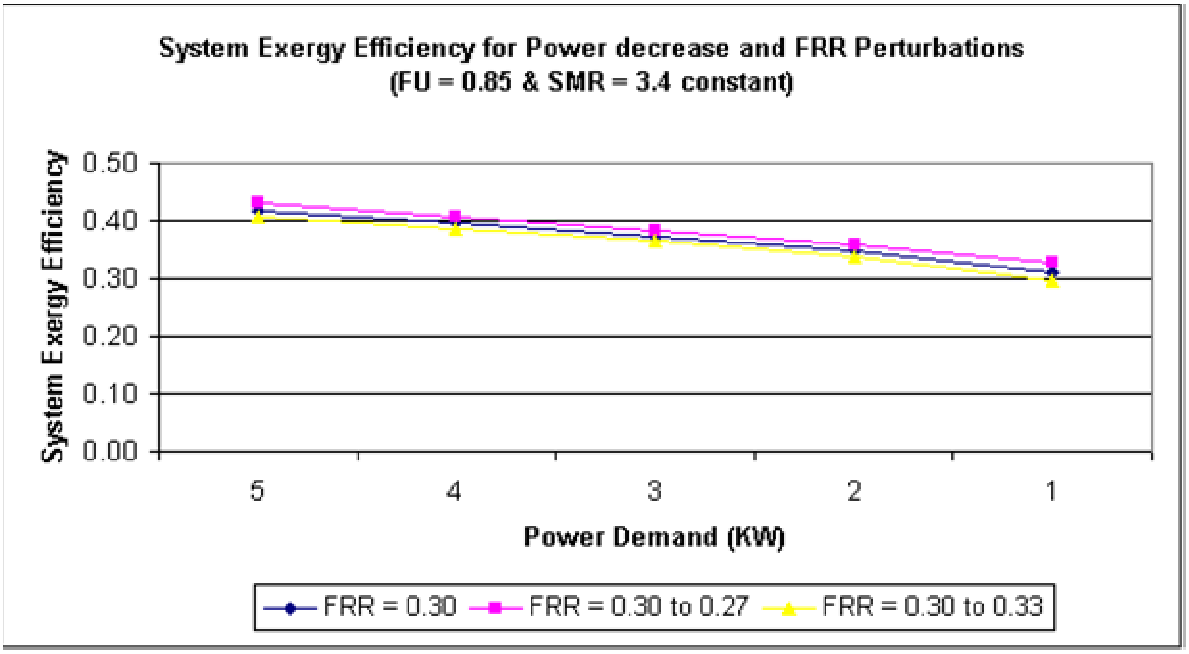

Increasing the Fuel Reformate Ratio from 0.30 to 0.33, leads to a slight decrease in System Energy Efficiency. Decreasing the Fuel Reformate Ratio to 0.27 on the other hand increases the System Energy Efficiency slightly. Hence, Fuel Reformate Ratio has an inverse effect on the System Energy Efficiency as regards to its increase or decrease.

Appendix C.2 PARAMETRIC ANALYSIS #2 OF THE SOFC BASED APU

Perturbations to be performed:

c. As regards to Power

3. **Increase** the Net Power required steadily – Starting from 1000 W, we proceed to 2000 W, 3000 W, 4000 W, 5000 W in steps of 1000 W.
4. **Decrease** the Net Power required steadily – Starting from 5000 W, we proceed to 4000 W, 3000 W, 2000 W, 1000 W in steps of 1000 W.

d. As regards to process parameters

5. Simulate the process with **initial conditions** such as Fuel Utilization: 0.85; Steam to Methane ratio: 3.4, Fuel Reformate ratio: 0.3, Air to Fuel ratio: 20.

6. Simulate the process keeping all the parameters constant and only **changing the Fuel Utilization from:**
   0.85 to 0.70
   0.85 to 0.90

7. Simulate the process this time changing the Steam to Fuel ratio only and keeping the other parameters constant. The **changes in the Steam to Methane ratios are:**
   3.4 to 3.0
   3.4 to 3.8

8. Simulate by changing the Fuel Reformate ratio alone and keeping the other parameters constants. The **changes to the Fuel Reformate ratio were:**
   0.3 to 0.27
   0.3 to 0.33

As regards to parameters, we can also vary the Air to Fuel ratios at the Stack and the Burner.

Note: In the Parametric Analysis #2, unlike the Parametric Analysis #1 where the power perturbations and process parameter perturbations were done separately, both the perturbations are done at the same time. This helps in gauging the effect of dual perturbations on the proposed SOFC System.

Parametric Study Analysis:

The variation of the process variables due to the above said perturbations are analyzed at the following components of the SOFC APU system. The components are:

12. A: Pre-reformer …… @ Stream 5

13. B: Combustor ……@ Stream 16
14. C: Steam Generator ……@ Stream 2
15. D: Air Compressor ……@ Stream 27
16. E: Gas Expander ……@ Stream 13
17. M: Air-Combustion Gas Mixer ……@ Stream 18
18. N: Methane Compressor ……@ Stream 24
19. HXI: Fuel Preheating HX ……@ Stream 8
20. HXII: Air Preheating HX ……@ Stream 9
21. HXIII: Methane Preheating HX ……@ Stream 1
22. HIV: Air Recuperator ……@ Stream 26

The effects of the perturbations on the temperatures and the Mixture Flow rates at these above components are tabulated and analyzed. Based on the time for steady state of the temperatures and the Mixture Flow rates, the time for the system to stabilize is deduced. Also the System Thermal and System Energy efficiencies for the perturbations are also tabulated.

Table showing the components contributing to the attainment of the stability (Temperature) of the System

FU : Fuel Utilization; SMR : Steam to Methane Ratio; FRR : Fuel Reformate Ratio

The Table shows the system components (with their streams in green) contributing to the prolonged stability time (time given in blue), as regards to Stable Temperature, for changes in power requirements and changes in Fuel Utilization, Steam to Methane Ratio and Fuel Reformate Ratio.

S No.	Power Change	Components contributing to increased time for the stability of the system						
		FU 0.85 SMR 3.40 FRR 0.30	**FU 0.70 SMR 3.40 FRR 0.30**	**FU 0.90 SMR 3.40 FRR 0.30**	**FU 0.85 SMR 3.00 FRR 0.30**	**FU 0.85 SMR 3.80 FRR 0.30**	**FU 0.85 SMR 3.40 FRR 0.27**	**FU 0.85 SMR 3.40 FRR 0.33**
1	1000 W to 2000 W	Pre-reformer (5 (13.1880)	Pre-reformer (5 HXI (8) (10)	Pre-reformer (5 (9)	Pre-reformer (5) (13.899)	Pre-reformer (5) (7)	Pre-reformer (5) HXI (8) (10.119)	Pre-reformer (5) HXI (8) (8.5810)
2	1000 W to 3000 W	Pre-reformer (5 (16.2010)	Pre-reformer (5 HXI (8) (11.931)	Steam Generator (2) (9.933)	Pre-reformer (5) (13)	Pre-reformer (5) (14.891)	Pre-reformer (5) (16.119)	Pre-reformer (5) HXI (8) (10.119)
3	1000 W to 4000 W	Pre-reformer (5 (18.2160)	Pre-reformer (5 (20)	Combustor (8) (10.997)	Pre-reformer (5) (17)	HXI (8) (14)	HXI (8) (16.119)	Pre-reformer (5) HXI (8) (13.119)
4	1000 W to 5000 W	Pre-reformer (5 (22.2030)	Pre-reformer (5 (25.682)	Pre-reformer (5 (18)	HXI (8) (17)	HXI (8) (15.894)	Pre-reformer (5) HXI (8) (22.119)	Pre-reformer (5) HXI (8) (18.119)
5	5000 W to 4000 W	Pre-reformer (5 HXI (8), Steam Generator (2) (13.9530)	Pre-reformer (5 (23)	Pre-reformer (5 (14.858)	Pre-reformer (5) HXI (8) (9)	Pre-reformer (5) HXI (8) (11)	Pre-reformer (5) HXI (8) (5.9670)	Pre-reformer (5) (15.966)
6	5000 W to 3000 W	Pre-reformer (5 HXI (8), Steam Generator (2) (16.1430)	Pre-reformer (5 (13)	Pre-reformer (5 HXI (8) (12.844)	Pre-reformer (5) (16)	Pre-reformer (5) (15.903)	Pre-reformer (5) (12.967)	HXI (8) (13.985)
7	5000 W to 2000 W	Pre-reformer (5 HXI (8), Steam Generator (2) (17.8760)	Pre-reformer (5 (15)	Pre-reformer (5 (15.881)	HXI (8) (16)	HXI (8) (13.899)	HXI (8) (12.967)	HXI (8) (15.966)
8	5000 W to 1000 W	Steam Generator (2) (22.8080)	Pre-reformer (5 HXI (8) (19)	Pre-reformer (5 (16.740)	HXI (8) (17)	HXI (8) (15.903)	HXI (8) (15.967)	HXI (8) (18.916)

Table showing the components contributing to the attainment of the stability (Flow rate) of the System

FU : Fuel Utilization; SMR : Steam to Methane Ratio; FRR : Fuel Reformate Ratio

The Table shows the system components (with their streams in green) contributing to the prolonged stability time (time given in blue), as regards to Stable Flow rate, for changes in power requirements and changes in Fuel Utilization, Steam to Methane Ratio and Fuel Reformate Ratio.

S No.	Power Change	Components contributing to increased time for the stability of the system						
		FU 0.85 SMR 3.40 FRR 0.30	**FU 0.70 SMR 3.40 FRR 0.30**	**FU 0.90 SMR 3.40 FRR 0.30**	**FU 0.85 SMR 3.00 FRR 0.30**	**FU 0.85 SMR 3.80 FRR 0.30**	**FU 0.85 SMR 3.40 FRR 0.27**	**FU 0.85 SMR 3.40 FRR 0.33**
1	1000 W to 2000 W	Air Comb. Gas Mixer (18) (5.28)	Combustor (16 (3.211)	Air Comp. (27) HXI (8), Air CombMixer (18 (2.445)	HXI (8) (4.00)	Gas Expander (1 (3.997)	Air Comb. Gas Mixer (18) (5.119)	HXI (8) (5.80)
2	1000 W to 3000 W	Air Comp. (27) HXII (9) (3.666)	HXIV (26) (6.100)	Air Comp. (27) Air CombMixer (18) (3.723)	Air Comb. Gas Mixer (18) (4.137)	HXI (8) (5.00)	Air Comb. Gas Mixer (18) (6.119)	HXIV (26) (8.119)
3	1000 W to 4000 W	Air Comp. (27) HXII (9) (5.128)	HXI (8) (8.104)	HXI (8) (7.00)	Air Comp. (27) HXI (8), HXII (9) (5.091)	Air Comb. Gas Mixer (18) (5.082)	HXI (8) (6.119)	Air Comb. Gas Mixer (18) (5.249)
4	1000 W to 5000 W	Air Comp. (27) HXII (9) (6.266)	HXIII (1) (7.729)	Steam Gen. (2) HXIII (1) (6.066)	Air Comb. Gas Mixer (18) (6.570)	Air Comb. Gas Mixer (18) (6.184)	HXI (8) (9.119)	HXI (8) (7.119)
5	5000 W to 4000 W	HXII (9) (2.080)	HXI (8) (4.00)	Gas Expander (13) (1.858)	HXI (8), HXIV (26) (3.00)	HXI (8) (7.00)	Gas Expander (13) (3.967)	HXI (8) (3.00)
6	5000 W to 3000 W	Air Comp. (27) (2.143)	HXI (8) (4.00)	HXI (8) (3.00)	HXI (8) (4.00)	HXI (8) (4.00)	Gas Expander (13) (2.967)	HXI (8), HXIV (26) (4.00)
7	5000 W to 2000 W	Air Comp. (27) HXII (9), Air CombMixer (18 (2.720)	HXI (8) (6.82)	HXI (8) (6.00)	HXI (8) (7.00)	Gas Expander (1 (4.876)	HXIV (26) (3.892)	HXI (8) (5.00)
8	5000 W to 1000 W	Combustor (16 (4.179)	HXI (8) (9)	HXI (8) (4.00)	HXI (8) (15.00)	HXI (8) (6.00)	HXI (8) (5.00)	HXI (8) (4.00)

Parametric Analysis #2

FU: Fuel Utilization **SMR:** Steam to Methane Ratio **FRR:** Fuel Reformate Ratio

Components and the time taken for steady temperature:

Pre-reformer

	Initial	F.U 0.70	F.U 0.90	SMR 3.0	SMR 3.8	FRR 0.27	FRR 0.33
1 to 2	13.1880	10.0000	9.0000	12.9970	11.8760	10.1250	10.9980
1 to 3	16.2010	11.9310	11.9970	13.8990	14.0000	15.1230	14.9980
1 to 4	18.2160	20.0000	13.9560	17.0000	17.9030	17.2330	16.0000
1 to 5	22.2030	25.6820	18.0000	21.9560	22.9030	22.0190	21.9970
5 to 4	13.9530	9.5690	12.8440	13.0000	11.0000	13.9670	11.9660
5 to 3	16.1430	13.0000	14.5850	16.0000	17.0000	15.2330	12.7700
5 to 2	17.8760	15.0000	15.8810	19.0000	20.0000	16.8180	14.9410
5 to 1	19.7380	19.0000	16.7400	21.4500	22.3900	20.0920	19.8530

Combustor

	Initial	F.U 0.70	F.U 0.90	SMR 3.0	SMR 3.8	FRR 0.27	FRR 0.33
1 to 2	12.2770	6.0170	3.9970	4.9970	6.9970	8.1190	5.1190
1 to 3	15.2770	8.1000	8.9970	5.9970	10.9970	10.9970	6.6680
1 to 4	17.2770	12.1000	10.9970	7.9970	11.9970	11.9970	8.1190
1 to 5	21.2770	12.9970	14.9970	10.9970	12.9970	14.8870	14.1190
5 to 4	13.9530	8.9690	7.8580	6.0000	8.0000	2.0000	8.8130
5 to 3	16.1430	12.0000	9.8440	8.0000	9.9030	5.0000	9.9320
5 to 2	17.8760	11.9700	8.8810	11.0000	10.8760	9.0000	10.0000
5 to 1	21.2800	14.0000	10.7400	13.0000	11.8990	10.8060	11.0000

Steam Generator

	Initial	F.U 0.70	F.U 0.90	SMR 3.0	SMR 3.8	FRR 0.27	FRR 0.33
1 to 2	12.2770	2.9660	3.6580	1.4710	3.3380	3.1190	3.1170
1 to 3	14.2190	10.0330	9.9330	3.8360	4.9970	3.8740	4.0220
1 to 4	18.0910	14.9110	10.0600	4.9970	5.9970	5.0030	5.1170
1 to 5	21.0090	17.0290	11.9080	6.5700	6.1810	15.0330	8.1170
5 to 4	13.9530	7.6610	3.8440	2.6130	1.4910	2.5870	1.9660
5 to 3	16.1430	8.9750	8.8810	3.1200	1.9030	3.4990	4.9660
5 to 2	17.8760	10.8060	11.7400	4.0000	3.1950	3.9670	8.9670
5 to 1	22.8080	11.7620	14.8580	10.0000	5.0000	4.9670	13.5970

Air Compressor

	Initial	F.U 0.70	F.U 0.90	SMR 3.0	SMR 3.8	FRR 0.27	FRR 0.33
1 to 2	2.5090	3.2140	2.4450	2.5620	3.0000	2.3990	2.5100
1 to 3	3.6660	4.1040	3.5980	4.1370	3.6050	5.0030	4.0240
1 to 4	5.1280	4.6720	4.8520	5.0940	5.0820	6.1050	5.1190
1 to 5	6.2660	6.1160	6.0000	6.5700	6.1840	8.1190	6.0910
5 to 4	1.6350	4.0000	1.9860	2.0950	1.4910	1.3780	2.0000
5 to 3	4.0000	4.3300	2.0000	3.0000	2.8330	2.0640	3.3250
5 to 2	4.1430	5.0000	2.5840	3.1010	4.0000	2.7890	5.0000
5 to 1	6.0390	6.8200	2.9630	3.8320	5.0000	3.5320	6.0060

Gas Expander

	Initial	F.U 0.70	F.U 0.90	SMR 3.0	SMR 3.8	FRR 0.27	FRR 0.33
1 to 2	2.5090	3.2140	2.4450	2.5620	3.0000	2.3990	2.5100
1 to 3	3.6660	4.1040	3.5980	4.1370	3.6050	5.0030	4.0240
1 to 4	5.1280	4.6720	4.8520	5.0940	5.0820	6.1050	5.1190
1 to 5	6.2660	6.1160	6.0000	6.5700	6.1840	8.1190	6.0910
5 to 4	1.6350	4.0000	1.9860	2.0950	1.4910	1.3780	2.0000
5 to 3	4.0000	4.3300	2.0000	3.0000	2.8330	2.0640	3.3250
5 to 2	4.1430	5.0000	2.5840	3.1010	4.0000	2.7890	5.0000
5 to 1	6.0390	6.8200	2.9630	3.8320	5.0000	3.5320	6.0060

Methane Compressor

	Initial	F.U 0.70	F.U 0.90	SMR 3.0	SMR 3.8	FRR 0.27	FRR 0.33
1 to 2	2.5060	2.9490	2.4420	2.5590	2.3090	2.3990	2.5100
1 to 3	3.6630	4.2080	3.7200	4.1340	3.6050	3.8740	4.0240
1 to 4	5.1250	4.9970	4.8490	5.0910	5.0000	5.0030	5.2510
1 to 5	6.2630	6.1000	6.0660	6.5670	6.1840	6.1050	6.0910
5 to 4	1.5880	1.7030	1.3290	1.6540	1.4910	1.3780	1.2930
5 to 3	2.0660	2.4740	1.8300	2.0950	1.9930	2.0640	2.0460
5 to 2	2.5960	3.1820	2.4650	2.6460	2.7090	2.7890	2.8130
5 to 1	3.3660	4.3050	3.0260	3.2320	3.3980	3.5320	3.3250

HXI

	Initial	F.U 0.70	F.U 0.90	SMR 3.0	SMR 3.8	FRR 0.27	FRR 0.33
1 to 2	13.0880	10.0000	3.9330	12.0000	4.0000	10.1190	8.5810
1 to 3	15.0530	11.9310	8.8090	13.0000	12.0000	12.1190	10.1190
1 to 4	17.0880	14.6820	10.8190	15.8990	14.0000	16.1190	13.1190
1 to 5	22.1570	20.0000	11.9080	17.0000	15.8910	22.1190	18.1190
5 to 4	13.9530	8.9690	11.7400	9.0000	11.0000	5.9670	12.9670
5 to 3	16.1430	12.8060	12.8440	11.0000	12.8760	10.9670	13.9850
5 to 2	17.8760	13.9700	14.8580	16.0000	13.8990	12.9670	15.9660
5 to 1	22.2800	19.0000	15.8810	17.0000	15.9030	15.9670	18.9160

HXIII

	Initial	F.U 0.70	F.U 0.90	SMR 3.0	SMR 3.8	FRR 0.27	FRR 0.33
1 to 2	2.5060	2.9660	2.4420	2.5590	2.9970	2.0520	2.3830
1 to 3	3.6630	4.2080	3.7200	3.1340	3.6020	3.7070	3.9980
1 to 4	5.1250	6.1000	4.8490	3.9970	4.0000	5.1950	4.9710
1 to 5	6.2630	6.9970	5.9970	4.1810	4.5670	6.1140	5.9970
5 to 4	1.9530	1.9690	1.0590	1.9970	1.9970	1.5770	1.5080
5 to 3	2.5960	3.2800	2.8440	2.2360	2.9170	2.2010	1.8480
5 to 2	3.1400	4.9700	4.4650	2.9970	2.9970	2.6490	2.9410
5 to 1	3.3660	5.3050	5.0260	3.2320	3.8990	3.3600	3.4390

HXIV

	Initial	F.U 0.70	F.U 0.90	SMR 3.0	SMR 3.8	FRR 0.27	FRR 0.33
1 to 2	3.2770	3.2140	3.9330	3.9970	5.5670	2.0520	2.3830
1 to 3	4.2010	6.2630	4.8370	7.9970	8.1700	3.7050	2.6670
1 to 4	4.6750	6.7700	9.9970	8.5600	9.2450	4.2330	2.9980
1 to 5	5.0090	8.9070	10.9080	9.9970	10.1310	5.1630	5.9970
5 to 4	2.9530	2.6610	4.8440	5.0000	6.0000	1.5470	2.9660
5 to 3	4.0000	6.1400	7.6900	7.6080	8.0000	3.2010	4.7700
5 to 2	4.8760	8.2400	8.7400	8.9210	9.0000	4.1100	5.8530
5 to 1	7.1790	11.0000	10.8810	10.0000	11.0000	6.0920	5.9410

Components and the time taken for steady mass flow rate:

Pre-reformer

	Initial	F.U 0.70	F.U 0.90	SMR 3.0	SMR 3.8	FRR 0.27	FRR 0.33
1 to 2	2.5060	2.9660	2.4420	2.5590	2.3060	2.3990	4.0220
1 to 3	3.6050	4.2080	3.7200	4.1340	3.6020	3.8740	4.5110
1 to 4	5.1250	6.1120	4.8490	5.0910	5.0790	5.0030	5.2490
1 to 5	6.2630	7.3490	5.9770	6.5670	6.1810	6.1050	6.0890
5 to 4	1.5880	2.0110	1.4710	1.6550	1.4910	1.3450	1.2590
5 to 3	2.0660	2.2800	1.8300	2.1010	1.9930	2.0310	2.0120
5 to 2	2.5960	3.1820	2.4650	2.6460	2.7090	2.7560	2.7790
5 to 1	3.3660	4.3050	3.0260	3.2320	3.3980	3.5290	3.2920

Combustor

	Initial	F.U 0.70	F.U 0.90	SMR 3.0	SMR 3.8	FRR 0.27	FRR 0.33
1 to 2	2.5060	3.2110	2.4420	2.5590	2.3060	2.3990	3.1190
1 to 3	3.6630	4.1000	3.2200	4.1340	3.3380	3.8740	4.0240
1 to 4	4.8610	5.1000	3.9080	5.0910	4.9970	5.1190	5.1190
1 to 5	6.2630	7.3490	4.8490	6.5670	5.0000	6.1190	6.0890
5 to 4	2.0660	1.7840	1.3290	1.6550	1.4910	1.3780	1.2930
5 to 3	2.5960	2.9690	1.8300	2.0950	1.9930	2.0640	2.0460
5 to 2	2.9530	2.9740	2.4610	2.6130	2.7090	2.7560	3.0000
5 to 1	3.2950	4.3050	3.0260	5.0000	3.3980	3.5320	3.3250

Steam Generator

	Initial	F.U 0.70	F.U 0.90	SMR 3.0	SMR 3.8	FRR 0.27	FRR 0.33
1 to 2	2.5090	2.9660	2.4420	2.5590	2.3060	2.3990	2.5080
1 to 3	3.6630	4.2080	3.7200	4.1340	3.6020	3.8740	4.0220
1 to 4	4.7610	6.1120	4.8510	5.0910	5.0790	5.0030	5.2490
1 to 5	6.2630	7.3490	6.0660	6.5670	6.1810	6.1050	6.0890
5 to 4	1.5880	2.0110	1.3290	1.6550	1.4910	1.3450	1.2590
5 to 3	2.2060	2.2800	1.8300	2.1010	1.9930	2.0310	2.0120
5 to 2	2.5960	3.1820	2.4650	2.6460	2.7090	2.7560	2.7790
5 to 1	3.3660	4.3050	3.0260	3.2320	3.3980	3.5290	3.2920

Air Compressor

	Initial	F.U 0.70	F.U 0.90	SMR 3.0	SMR 3.8	FRR 0.27	FRR 0.33
1 to 2	2.2720	2.1040	2.4450	2.5620	2.3090	2.3990	3.5510
1 to 3	2.5090	2.9690	3.1980	3.8390	3.3410	3.6220	4.0240
1 to 4	4.7610	4.1040	3.7230	5.0000	3.4890	3.8740	5.1190
1 to 5	6.2630	5.0000	6.0000	6.0230	6.0000	4.1190	6.0910
5 to 4	1.7660	1.2270	1.4710	1.6550	1.4910	1.3780	1.2930
5 to 3	2.7200	2.0000	1.6690	2.0950	2.0000	2.0640	2.0000
5 to 2	3.0000	2.9590	2.5840	2.6130	2.7030	2.7890	3.3250
5 to 1	3.4670	4.3300	3.2860	3.2320	3.4990	3.0920	5.0000

Gas Expander

	Initial	F.U 0.70	F.U 0.90	SMR 3.0	SMR 3.8	FRR 0.27	FRR 0.33
1 to 2	3.6630	2.9660	2.4420	2.5590	3.6020	2.3990	3.2610
1 to 3	5.1280	4.1000	2.9970	4.1340	3.9970	3.8740	4.0220
1 to 4	5.2770	5.1000	3.7200	5.0910	4.9970	5.0030	5.2490
1 to 5	6.2630	5.9970	5.2340	6.5670	6.1810	6.1050	6.0910
5 to 4	2.0000	2.0110	1.8300	1.6550	1.4910	2.9670	1.9660
5 to 3	2.5960	2.2200	1.8580	2.0070	1.9930	3.9670	2.0120
5 to 2	2.9530	3.2800	2.4650	3.0000	3.3980	3.4990	2.7790
5 to 1	3.2950	3.9880	3.0260	3.2320	4.8760	3.8590	3.2920

Methane Compressor

	Initial	F.U 0.70	F.U 0.90	SMR 3.0	SMR 3.8	FRR 0.27	FRR 0.33
1 to 2	2.5060	2.9660	2.4420	2.5590	2.3060	2.3990	3.1650
1 to 3	3.6630	4.2080	3.7200	3.9970	3.6020	3.8740	4.0220
1 to 4	5.1250	6.1120	4.8490	5.0910	5.0790	5.0030	5.2490
1 to 5	6.2630	7.3490	6.0660	6.5670	6.1810	6.1050	6.0890
5 to 4	1.5880	2.0110	1.3290	1.6540	1.4910	1.3450	1.2590
5 to 3	2.2060	2.2800	1.8300	2.1010	1.9930	2.0310	2.0120
5 to 2	2.5960	3.1820	2.4650	2.6460	2.7090	2.7560	2.7790
5 to 1	3.3660	4.3050	3.0260	3.2320	3.3980	3.2210	3.2920

HXI

	Initial	F.U 0.70	F.U 0.90	SMR 3.0	SMR 3.8	FRR 0.27	FRR 0.33
1 to 2	2.2800	1.6900	1.3650	2.5650	1.3430	1.5740	1.5790
1 to 3	4.2800	3.2930	2.4450	2.6380	3.0000	3.8740	3.1190
1 to 4	6.2800	4.1040	6.0000	4.0000	3.4890	6.1190	5.8000
1 to 5	9.2800	8.1040	7.0000	5.0000	5.0000	9.1190	7.1190
5 to 4	2.0890	4.0000	1.4160	3.0000	2.1010	2.0000	3.0000
5 to 3	3.0000	4.0000	3.0000	4.0000	4.0000	2.1010	4.0000
5 to 2	3.1020	6.8200	4.0000	7.0000	6.0000	3.2210	4.7560
5 to 1	4.1430	9.0000	6.0000	15.0000	7.0000	5.0000	5.0000

HXII

	Initial	F.U 0.70	F.U 0.90	SMR 3.0	SMR 3.8	FRR 0.27	FRR 0.33
1 to 2	2.5090	2.3050	2.0000	2.5620	1.1450	2.2880	3.5510
1 to 3	3.6660	2.9690	2.4280	3.8390	2.3090	2.9560	4.0240
1 to 4	5.1280	4.1040	3.1980	5.0000	2.4470	3.6220	5.1190
1 to 5	6.2660	5.0000	6.0000	5.6750	2.7620	4.1190	6.0910
5 to 4	2.0800	1.2270	1.4710	1.6510	1.4910	1.3780	1.2930
5 to 3	2.1430	2.0000	1.6690	1.8350	2.0000	2.0640	2.0000
5 to 2	2.7200	4.3300	2.5840	2.6460	1.9930	2.7890	2.7500
5 to 1	3.3960	5.0000	3.2860	3.2320	3.4990	3.5320	3.3250

HXIII

	Initial	F.U 0.70	F.U 0.90	SMR 3.0	SMR 3.8	FRR 0.27	FRR 0.33
1 to 2	2.5060	2.9660	2.4420	2.5590	2.3060	2.3990	2.5080
1 to 3	3.6630	4.2080	3.7200	3.2560	3.6020	3.8740	4.0240
1 to 4	5.0640	6.1000	4.8490	4.1340	5.0790	5.0030	5.2490
1 to 5	6.2630	7.7290	6.0660	6.5670	6.1810	6.1050	6.0890
5 to 4	1.5880	2.0110	1.3290	1.6550	1.4910	1.3450	1.2590
5 to 3	2.0660	2.2800	1.8300	2.1010	1.9930	2.0310	2.0120
5 to 2	2.5960	3.1820	2.4650	2.6460	2.7090	2.7560	2.7500
5 to 1	3.3660	4.3050	3.0260	3.2320	3.3980	3.4990	3.2920

HXIV

	Initial	F.U 0.70	F.U 0.90	SMR 3.0	SMR 3.8	FRR 0.27	FRR 0.33
1 to 2	2.5060	2.9490	2.4420	2.9970	2.3060	2.3990	3.3940
1 to 3	3.6050	3.9970	3.7200	4.1340	3.6020	3.8740	5.2490
1 to 4	5.0640	6.1000	4.8490	5.0910	4.9970	5.0030	6.0910
1 to 5	6.2630	6.1000	5.9080	6.5670	6.1810	6.1050	8.1190
5 to 4	1.5880	1.9690	1.3290	2.0950	3.0000	1.3780	1.2930
5 to 3	2.2090	2.2800	1.8300	2.6460	3.8760	2.0640	3.3250
5 to 2	2.5960	5.9700	2.4650	3.0000	5.0000	3.5320	4.0000
5 to 1	3.3660	7.9750	2.8520	6.0000	4.8990	3.8920	4.3300

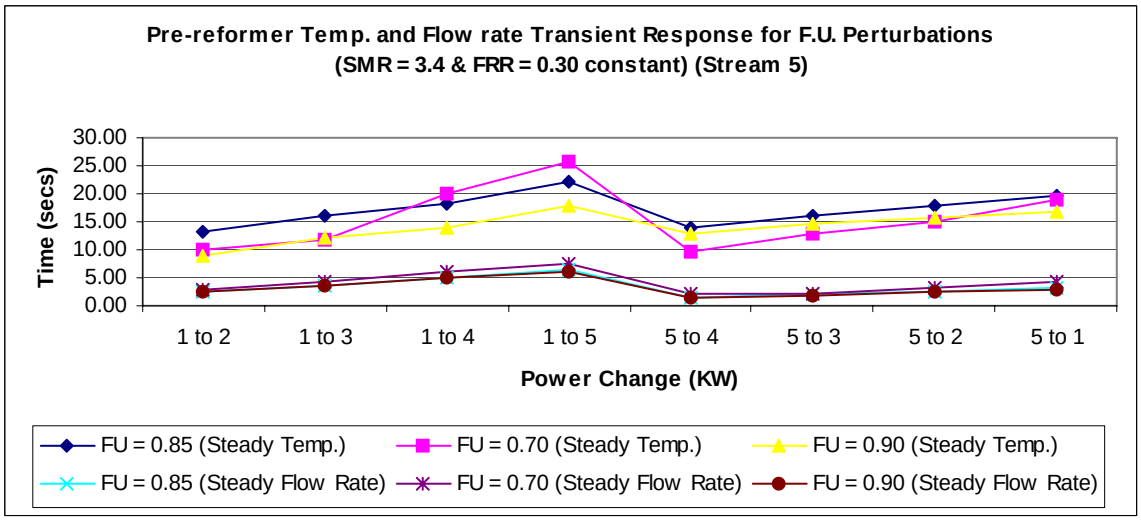
Pre-reformer Temp. and Flow rate Transient Response for F.U. Perturbations
(SMR = 3.4 & FRR = 0.30 constant) (Stream 5)
Time (secs)
30.00
25.00
20.00
15.00
10.00
5.00
0.00
1 to 2
1 to 3
1 to 4
1 to 5
5 to 4
5 to 3
5 to 2
5 to 1
Power Change (KW)
FU = 0.85 (Steady Temp.)
FU = 0.70 (Steady Temp.)
FU = 0.90 (Steady Temp.)
FU = 0.85 (Steady Flow Rate)
FU = 0.70 (Steady Flow Rate)
FU = 0.90 (Steady Flow Rate)

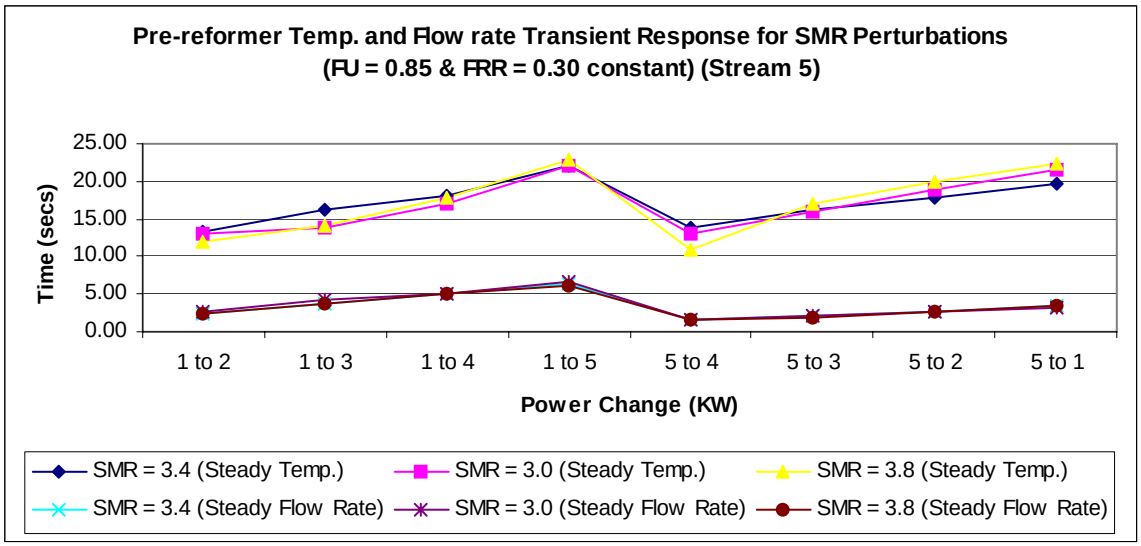
Pre-reformer Temp. and Flow rate Transient Response for SMR Perturbations
(FU = 0.85 & FRR = 0.30 constant) (Stream 5)
Time (secs)
25.00
20.00
15.00
10.00
5.00
0.00
1 to 2
1 to 3
1 to 4
1 to 5
5 to 4
5 to 3
5 to 2
5 to 1
Power Change (KW)
SMR = 3.4 (Steady Temp.)
SMR = 3.0 (Steady Temp.)
SMR = 3.8 (Steady Temp.)
SMR = 3.4 (Steady Flow Rate)
SMR = 3.0 (Steady Flow Rate)
SMR = 3.8 (Steady Flow Rate)

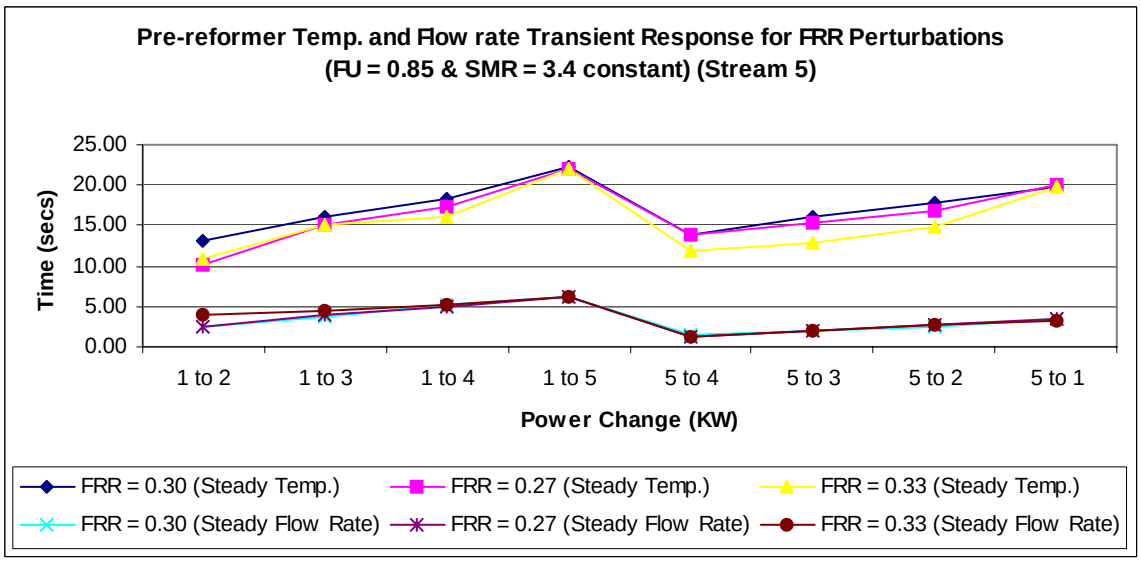
Pre-reformer Temp. and Flow rate Transient Response for FRR Perturbations
(FU = 0.85 & SMR = 3.4 constant) (Stream 5)
Time (secs)
25.00
20.00
15.00
10.00
5.00
0.00
1 to 2
1 to 3
1 to 4
1 to 5
5 to 4
5 to 3
5 to 2
5 to 1
Power Change (KW)
FRR = 0.30 (Steady Temp.)
FRR = 0.27 (Steady Temp.)
FRR = 0.33 (Steady Temp.)
FRR = 0.30 (Steady Flow Rate)
FRR = 0.27 (Steady Flow Rate)
FRR = 0.33 (Steady Flow Rate)

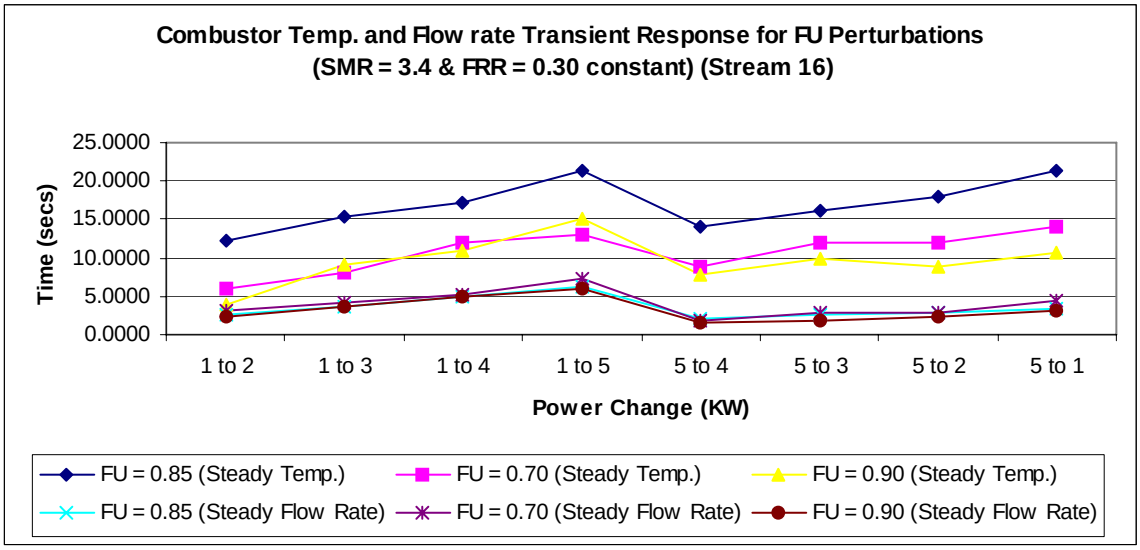
Combustor Temp. and Flow rate Transient Response for FU Perturbations
(SMR = 3.4 & FRR = 0.30 constant) (Stream 16)
Time (secs)
25.0000
20.0000
15.0000
10.0000
5.0000
0.0000
1 to 2
1 to 3
1 to 4
1 to 5
5 to 4
5 to 3
5 to 2
5 to 1
Power Change (KW)
FU = 0.85 (Steady Temp.)
FU = 0.70 (Steady Temp.)
FU = 0.90 (Steady Temp.)
FU = 0.85 (Steady Flow Rate)
FU = 0.70 (Steady Flow Rate)
FU = 0.90 (Steady Flow Rate)

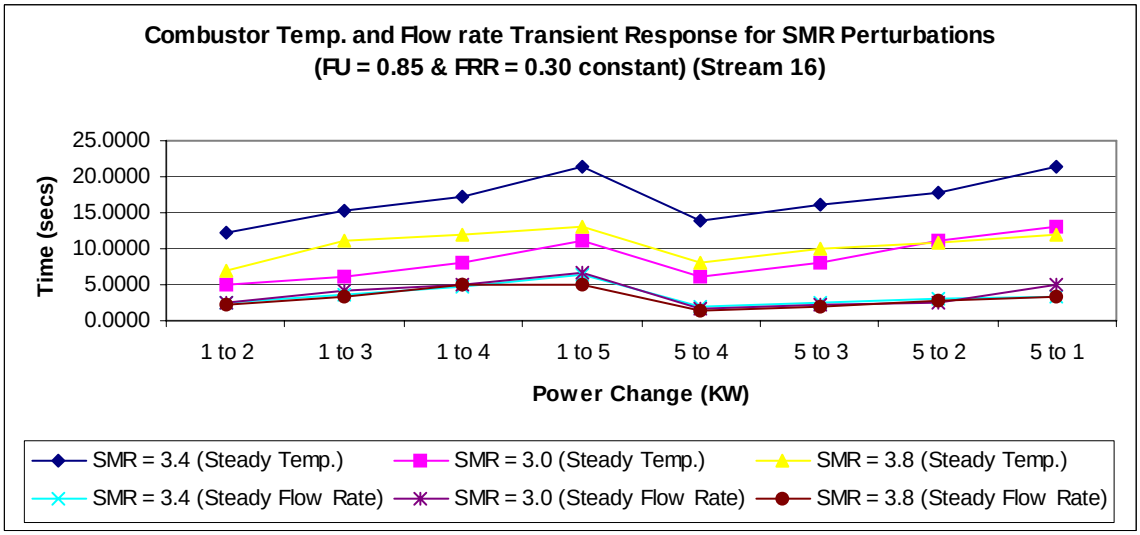
Combustor Temp. and Flow rate Transient Response for SMR Perturbations
(FU = 0.85 & FRR = 0.30 constant) (Stream 16)
Time (secs)
25.0000
20.0000
15.0000
10.0000
5.0000
0.0000
1 to 2
1 to 3
1 to 4
1 to 5
5 to 4
5 to 3
5 to 2
5 to 1
Power Change (KW)
SMR = 3.4 (Steady Temp.)
SMR = 3.0 (Steady Temp.)
SMR = 3.8 (Steady Temp.)
SMR = 3.4 (Steady Flow Rate)
SMR = 3.0 (Steady Flow Rate)
SMR = 3.8 (Steady Flow Rate)

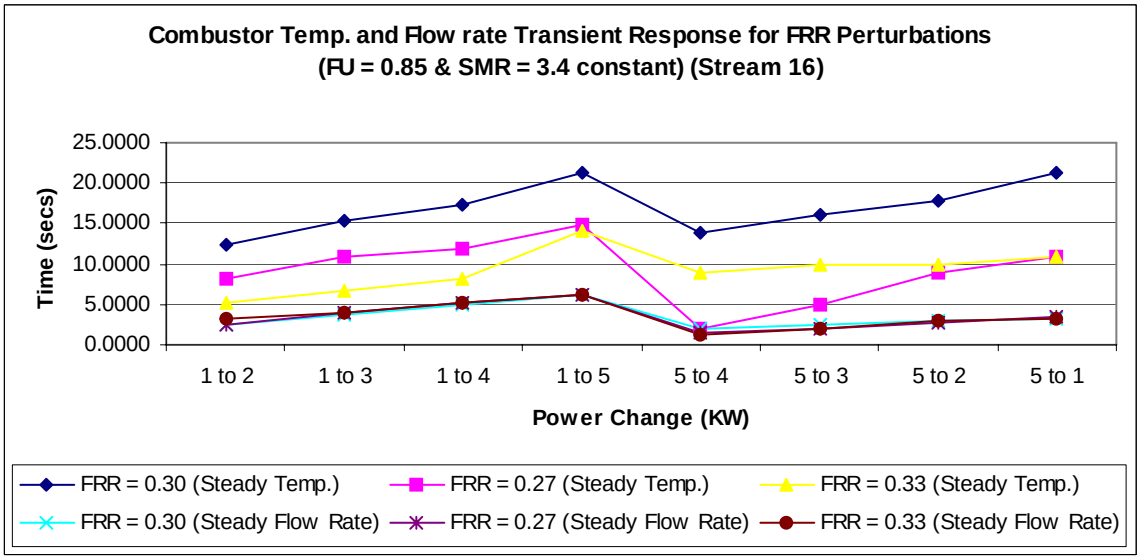
Combustor Temp. and Flow rate Transient Response for FRR Perturbations
(FU = 0.85 & SMR = 3.4 constant) (Stream 16)
Time (secs)
25.0000
20.0000
15.0000
10.0000
5.0000
0.0000
1 to 2
1 to 3
1 to 4
1 to 5
5 to 4
5 to 3
5 to 2
5 to 1
Power Change (KW)
FRR = 0.30 (Steady Temp.)
FRR = 0.27 (Steady Temp.)
FRR = 0.33 (Steady Temp.)
FRR = 0.30 (Steady Flow Rate)
FRR = 0.27 (Steady Flow Rate)
FRR = 0.33 (Steady Flow Rate)

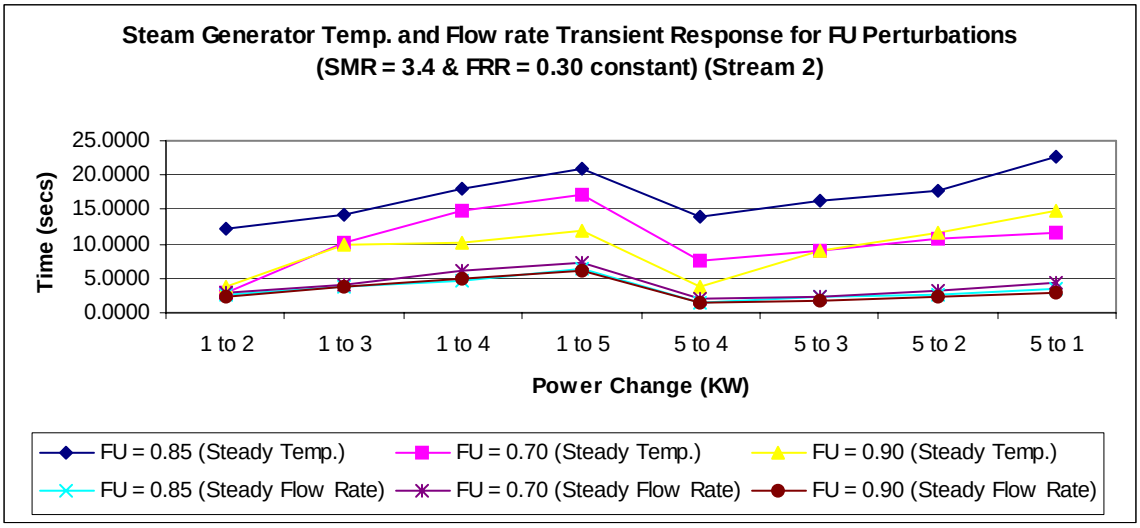
Steam Generator Temp. and Flow rate Transient Response for FU Perturbations
(SMR = 3.4 & FRR = 0.30 constant) (Stream 2)
Time (secs)
25.0000
20.0000
15.0000
10.0000
5.0000
0.0000
1 to 2
1 to 3
1 to 4
1 to 5
5 to 4
5 to 3
5 to 2
5 to 1
Power Change (KW)
FU = 0.85 (Steady Temp.)
FU = 0.70 (Steady Temp.)
FU = 0.90 (Steady Temp.)
FU = 0.85 (Steady Flow Rate)
FU = 0.70 (Steady Flow Rate)
FU = 0.90 (Steady Flow Rate)

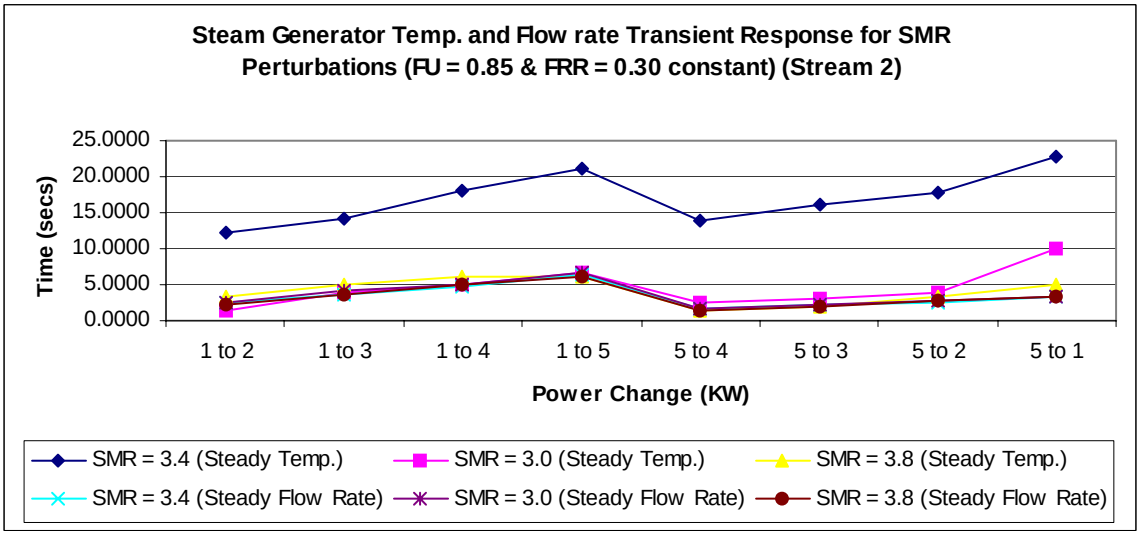
Steam Generator Temp. and Flow rate Transient Response for SMR
Perturbations (FU = 0.85 & FRR = 0.30 constant) (Stream 2)
Time (secs)
25.0000
20.0000
15.0000
10.0000
5.0000
0.0000
1 to 2
1 to 3
1 to 4
1 to 5
5 to 4
5 to 3
5 to 2
5 to 1
Power Change (KW)
SMR = 3.4 (Steady Temp.)
SMR = 3.0 (Steady Temp.)
SMR = 3.8 (Steady Temp.)
SMR = 3.4 (Steady Flow Rate)
SMR = 3.0 (Steady Flow Rate)
SMR = 3.8 (Steady Flow Rate)

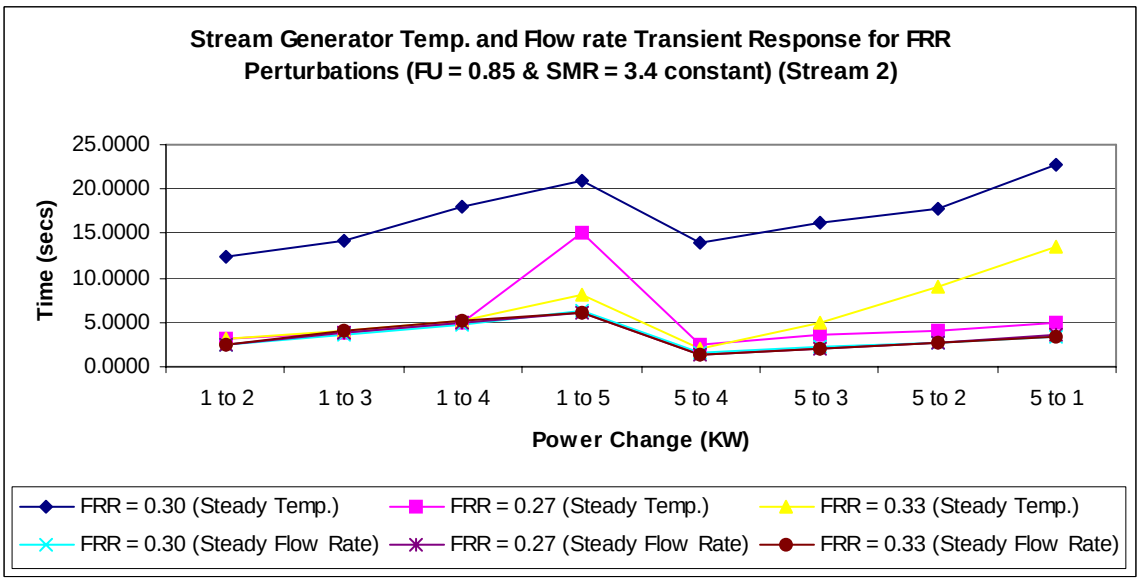
Stream Generator Temp. and Flow rate Transient Response for FRR
Perturbations (FU = 0.85 & SMR = 3.4 constant) (Stream 2)
Time (secs)
25.0000
20.0000
15.0000
10.0000
5.0000
0.0000
1 to 2
1 to 3
1 to 4
1 to 5
5 to 4
5 to 3
5 to 2
5 to 1
Power Change (KW)
FRR = 0.30 (Steady Temp.)
FRR = 0.27 (Steady Temp.)
FRR = 0.33 (Steady Temp.)
FRR = 0.30 (Steady Flow Rate)
FRR = 0.27 (Steady Flow Rate)
FRR = 0.33 (Steady Flow Rate)

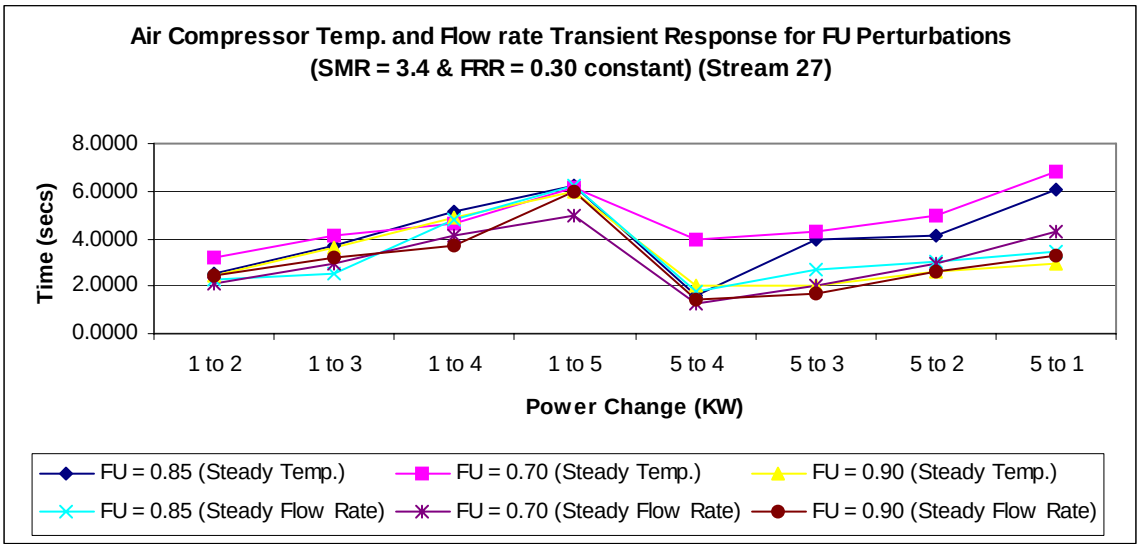
Air Compressor Temp. and Flow rate Transient Response for FU Perturbations
(SMR = 3.4 & FRR = 0.30 constant) (Stream 27)
Time (secs)
8.0000
6.0000
4.0000
2.0000
0.0000
1 to 2
1 to 3
1 to 4
1 to 5
5 to 4
5 to 3
5 to 2
5 to 1
Power Change (KW)
FU = 0.85 (Steady Temp.)
FU = 0.70 (Steady Temp.)
FU = 0.90 (Steady Temp.)
FU = 0.85 (Steady Flow Rate)
FU = 0.70 (Steady Flow Rate)
FU = 0.90 (Steady Flow Rate)

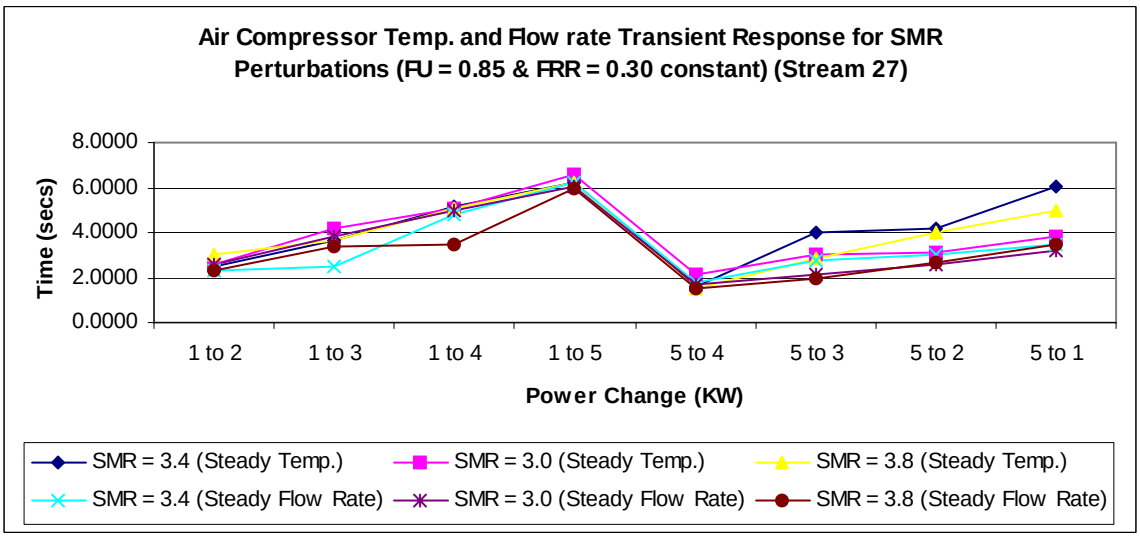
Air Compressor Temp. and Flow rate Transient Response for SMR
Perturbations (FU = 0.85 & FRR = 0.30 constant) (Stream 27)
Time (secs)
8.0000
6.0000
4.0000
2.0000
0.0000
1 to 2
1 to 3
1 to 4
1 to 5
5 to 4
5 to 3
5 to 2
5 to 1
Power Change (KW)
SMR = 3.4 (Steady Temp.)
SMR = 3.0 (Steady Temp.)
SMR = 3.8 (Steady Temp.)
SMR = 3.4 (Steady Flow Rate)
SMR = 3.0 (Steady Flow Rate)
SMR = 3.8 (Steady Flow Rate)

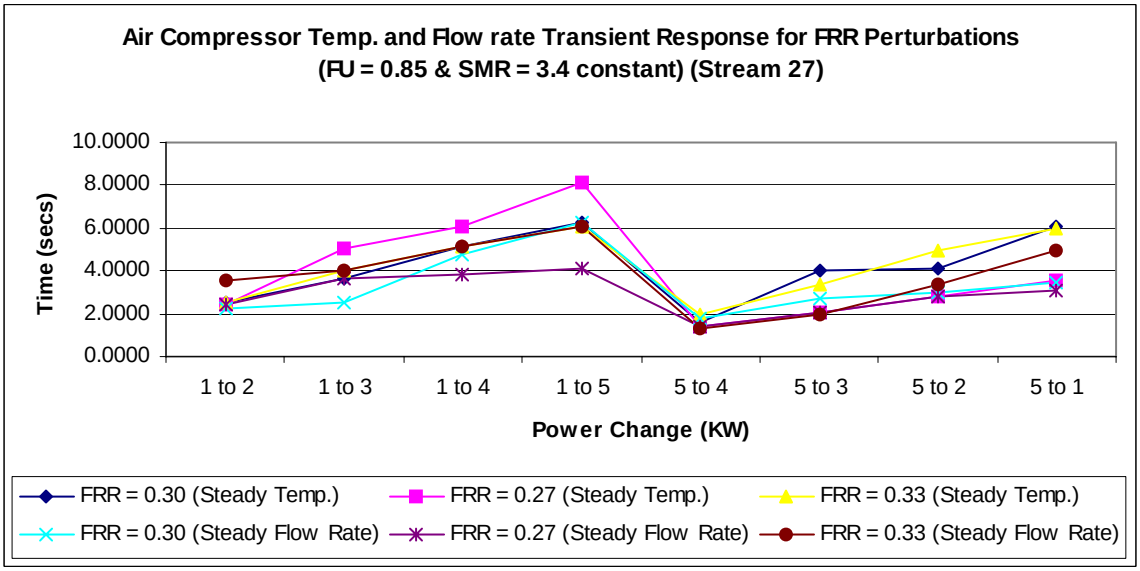
Air Compressor Temp. and Flow rate Transient Response for FRR Perturbations
(FU = 0.85 & SMR = 3.4 constant) (Stream 27)
Time (secs)
10.0000
8.0000
6.0000
4.0000
2.0000
0.0000
1 to 2
1 to 3
1 to 4
1 to 5
5 to 4
5 to 3
5 to 2
5 to 1
Power Change (KW)
FRR = 0.30 (Steady Temp.)
FRR = 0.27 (Steady Temp.)
FRR = 0.33 (Steady Temp.)
FRR = 0.30 (Steady Flow Rate)
FRR = 0.27 (Steady Flow Rate)
FRR = 0.33 (Steady Flow Rate)

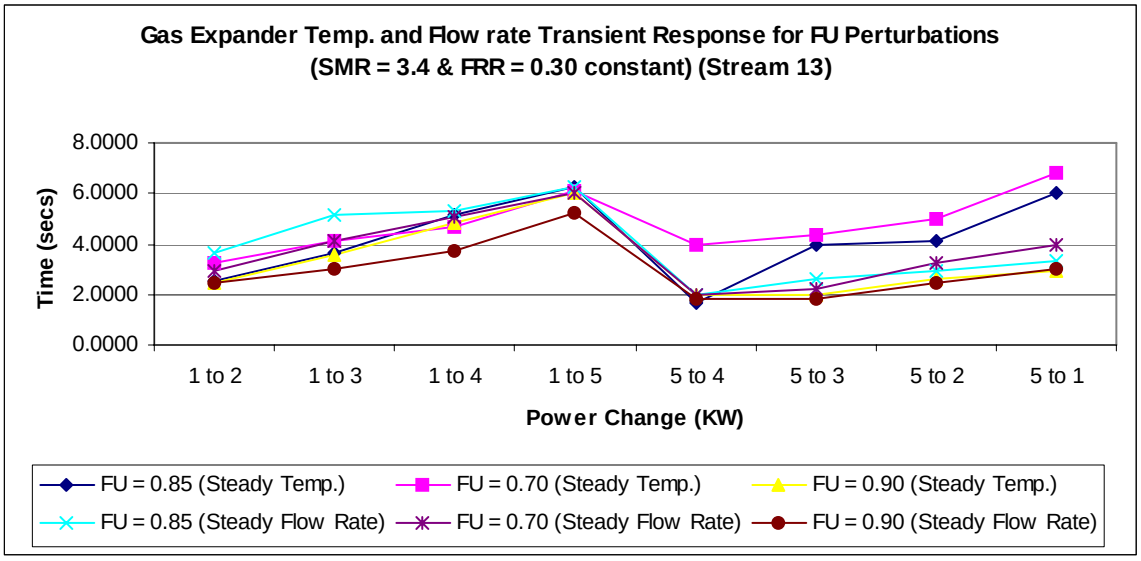
Gas Expander Temp. and Flow rate Transient Response for FU Perturbations
(SMR = 3.4 & FRR = 0.30 constant) (Stream 13)
8.0000
6.0000
4.0000
2.0000
0.0000
Time (secs)
1 to 2
1 to 3
1 to 4
1 to 5
5 to 4
5 to 3
5 to 2
5 to 1
Power Change (KW)
FU = 0.85 (Steady Temp.)
FU = 0.70 (Steady Temp.)
FU = 0.90 (Steady Temp.)
FU = 0.85 (Steady Flow Rate)
FU = 0.70 (Steady Flow Rate)
FU = 0.90 (Steady Flow Rate)

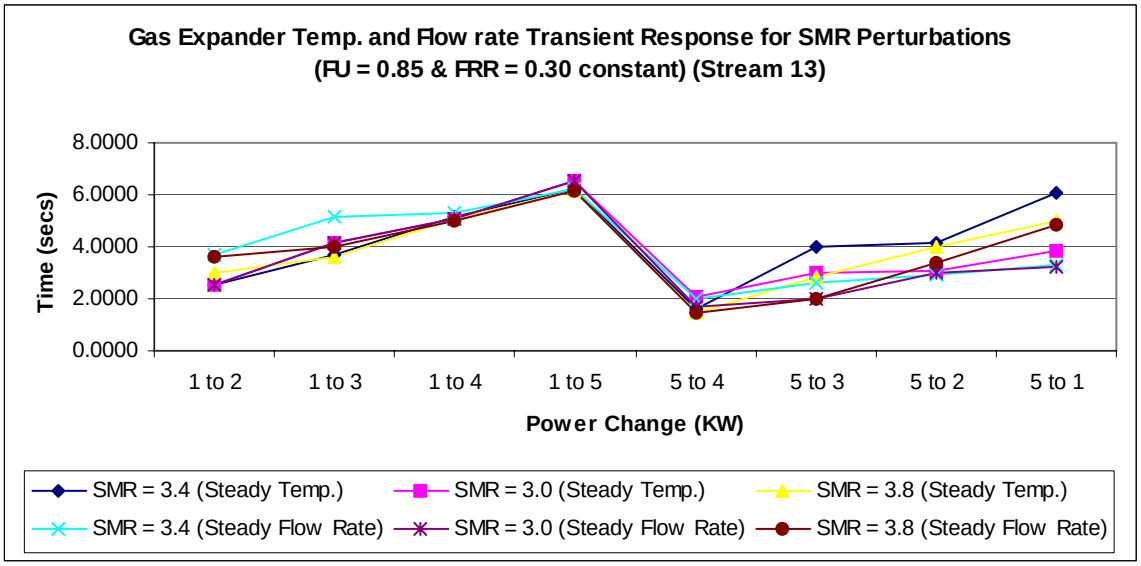
Gas Expander Temp. and Flow rate Transient Response for SMR Perturbations
(FU = 0.85 & FRR = 0.30 constant) (Stream 13)
8.0000
6.0000
4.0000
2.0000
0.0000
Time (secs)
1 to 2
1 to 3
1 to 4
1 to 5
5 to 4
5 to 3
5 to 2
5 to 1
Power Change (KW)
SMR = 3.4 (Steady Temp.)
SMR = 3.0 (Steady Temp.)
SMR = 3.8 (Steady Temp.)
SMR = 3.4 (Steady Flow Rate)
SMR = 3.0 (Steady Flow Rate)
SMR = 3.8 (Steady Flow Rate)

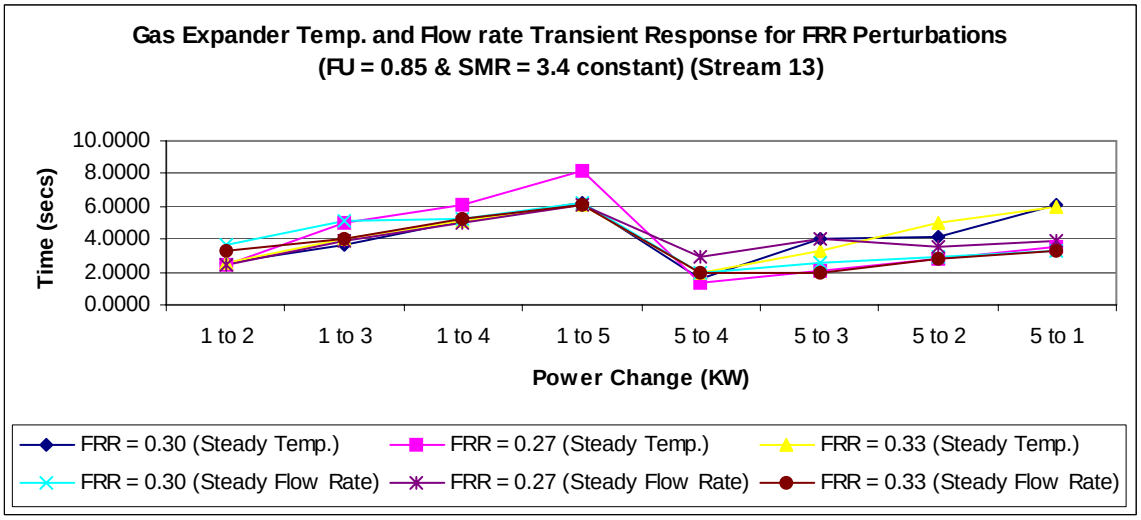
Gas Expander Temp. and Flow rate Transient Response for FRR Perturbations
(FU = 0.85 & SMR = 3.4 constant) (Stream 13)
10.0000
8.0000
6.0000
4.0000
2.0000
0.0000
Time (secs)
1 to 2
1 to 3
1 to 4
1 to 5
5 to 4
5 to 3
5 to 2
5 to 1
Power Change (KW)
FRR = 0.30 (Steady Temp.)
FRR = 0.27 (Steady Temp.)
FRR = 0.33 (Steady Temp.)
FRR = 0.30 (Steady Flow Rate)
FRR = 0.27 (Steady Flow Rate)
FRR = 0.33 (Steady Flow Rate)

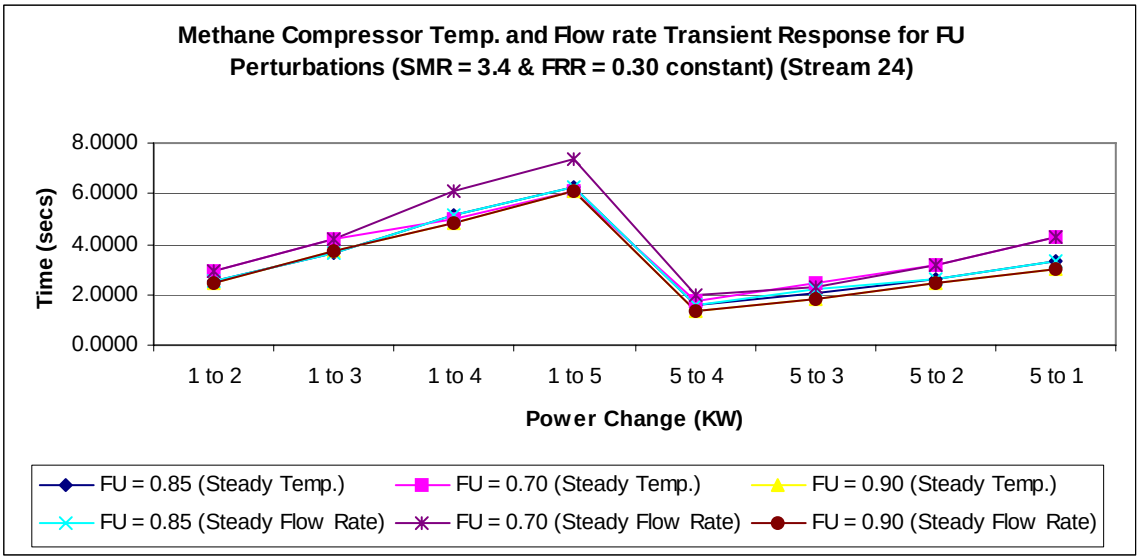
Methane Compressor Temp. and Flow rate Transient Response for FU Perturbations (SMR = 3.4 & FRR = 0.30 constant) (Stream 24)
8.0000
6.0000
4.0000
2.0000
0.0000
Time (secs)
1 to 2
1 to 3
1 to 4
1 to 5
5 to 4
5 to 3
5 to 2
5 to 1
Power Change (KW)
FU = 0.85 (Steady Temp.)
FU = 0.70 (Steady Temp.)
FU = 0.90 (Steady Temp.)
FU = 0.85 (Steady Flow Rate)
FU = 0.70 (Steady Flow Rate)
FU = 0.90 (Steady Flow Rate)

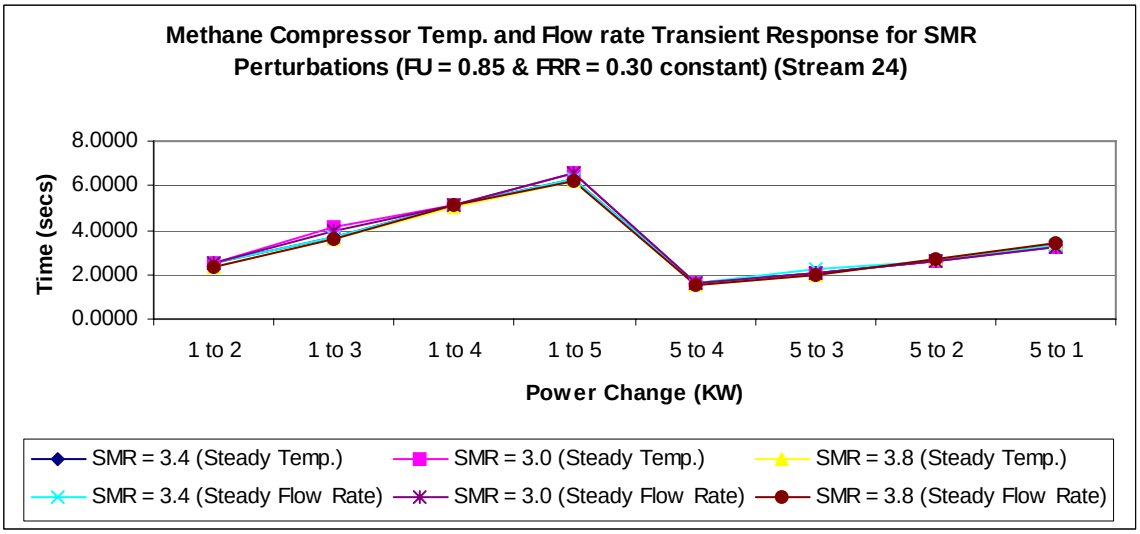
Methane Compressor Temp. and Flow rate Transient Response for SMR Perturbations (FU = 0.85 & FRR = 0.30 constant) (Stream 24)
8.0000
6.0000
4.0000
2.0000
0.0000
Time (secs)
1 to 2
1 to 3
1 to 4
1 to 5
5 to 4
5 to 3
5 to 2
5 to 1
Power Change (KW)
SMR = 3.4 (Steady Temp.)
SMR = 3.0 (Steady Temp.)
SMR = 3.8 (Steady Temp.)
SMR = 3.4 (Steady Flow Rate)
SMR = 3.0 (Steady Flow Rate)
SMR = 3.8 (Steady Flow Rate)

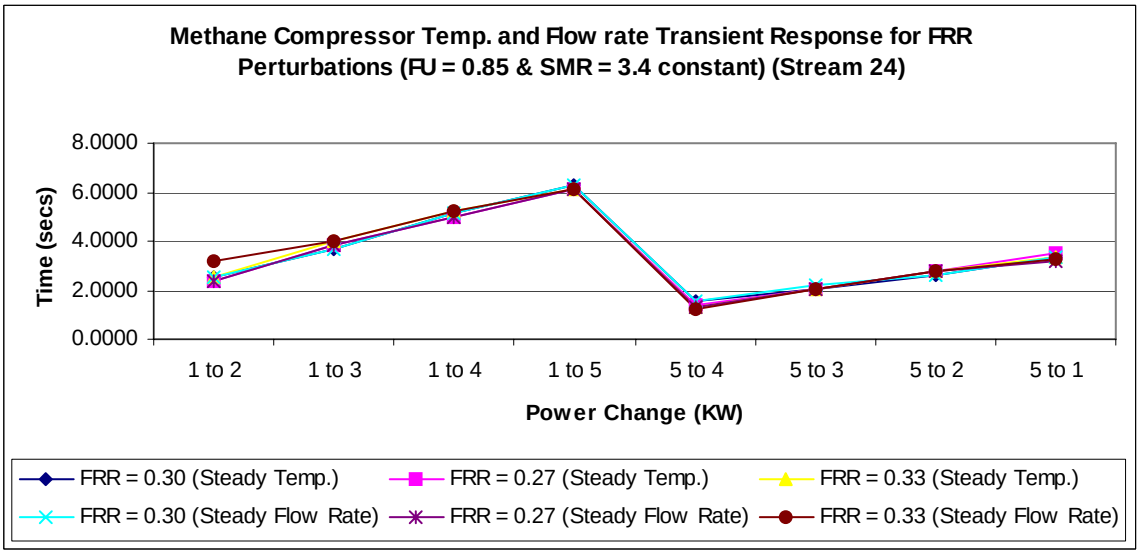
Methane Compressor Temp. and Flow rate Transient Response for FRR Perturbations (FU = 0.85 & SMR = 3.4 constant) (Stream 24)
8.0000
6.0000
4.0000
2.0000
0.0000
Time (secs)
1 to 2
1 to 3
1 to 4
1 to 5
5 to 4
5 to 3
5 to 2
5 to 1
Power Change (KW)
FRR = 0.30 (Steady Temp.)
FRR = 0.27 (Steady Temp.)
FRR = 0.33 (Steady Temp.)
FRR = 0.30 (Steady Flow Rate)
FRR = 0.27 (Steady Flow Rate)
FRR = 0.33 (Steady Flow Rate)

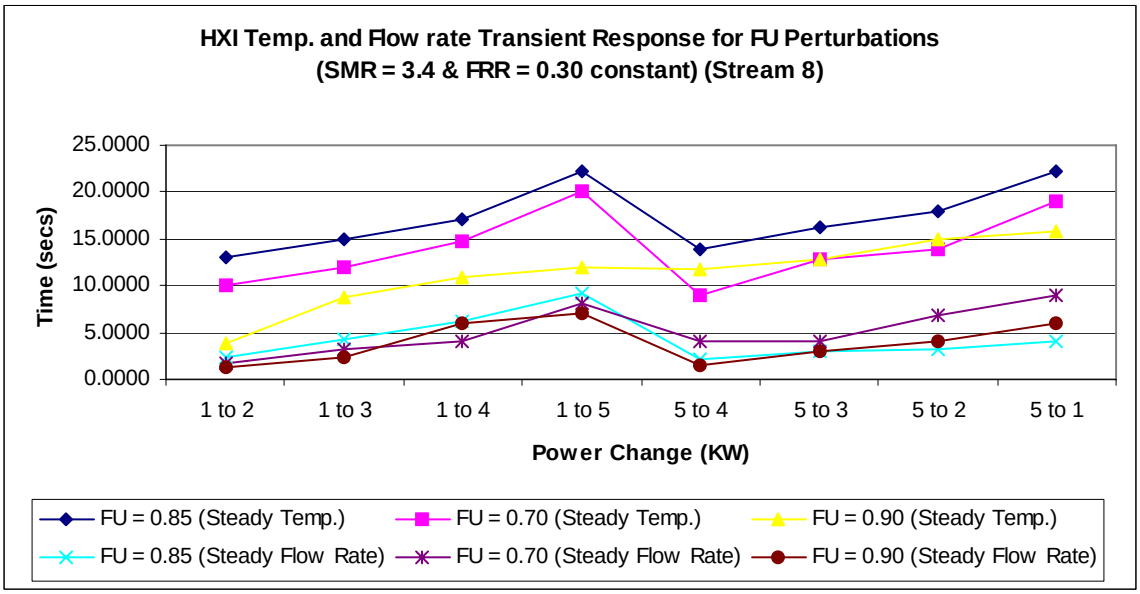
HXI Temp. and Flow rate Transient Response for FU Perturbations
(SMR = 3.4 & FRR = 0.30 constant) (Stream 8)
Time (secs)
25.0000
20.0000
15.0000
10.0000
5.0000
0.0000
1 to 2
1 to 3
1 to 4
1 to 5
5 to 4
5 to 3
5 to 2
5 to 1
Power Change (KW)
FU = 0.85 (Steady Temp.)
FU = 0.70 (Steady Temp.)
FU = 0.90 (Steady Temp.)
FU = 0.85 (Steady Flow Rate)
FU = 0.70 (Steady Flow Rate)
FU = 0.90 (Steady Flow Rate)

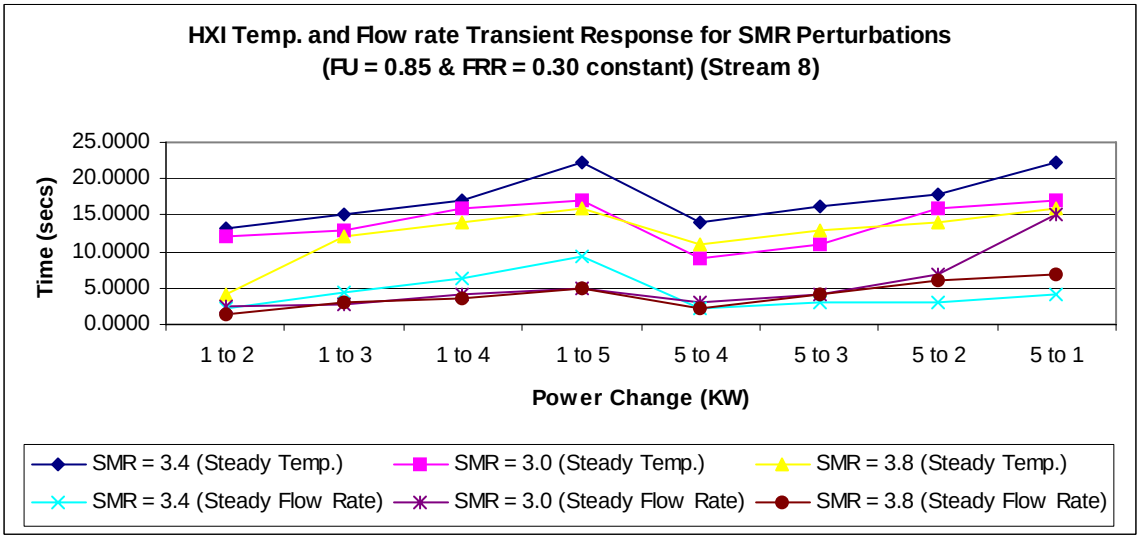
HXI Temp. and Flow rate Transient Response for SMR Perturbations
(FU = 0.85 & FRR = 0.30 constant) (Stream 8)
Time (secs)
25.0000
20.0000
15.0000
10.0000
5.0000
0.0000
1 to 2
1 to 3
1 to 4
1 to 5
5 to 4
5 to 3
5 to 2
5 to 1
Power Change (KW)
SMR = 3.4 (Steady Temp.)
SMR = 3.0 (Steady Temp.)
SMR = 3.8 (Steady Temp.)
SMR = 3.4 (Steady Flow Rate)
SMR = 3.0 (Steady Flow Rate)
SMR = 3.8 (Steady Flow Rate)

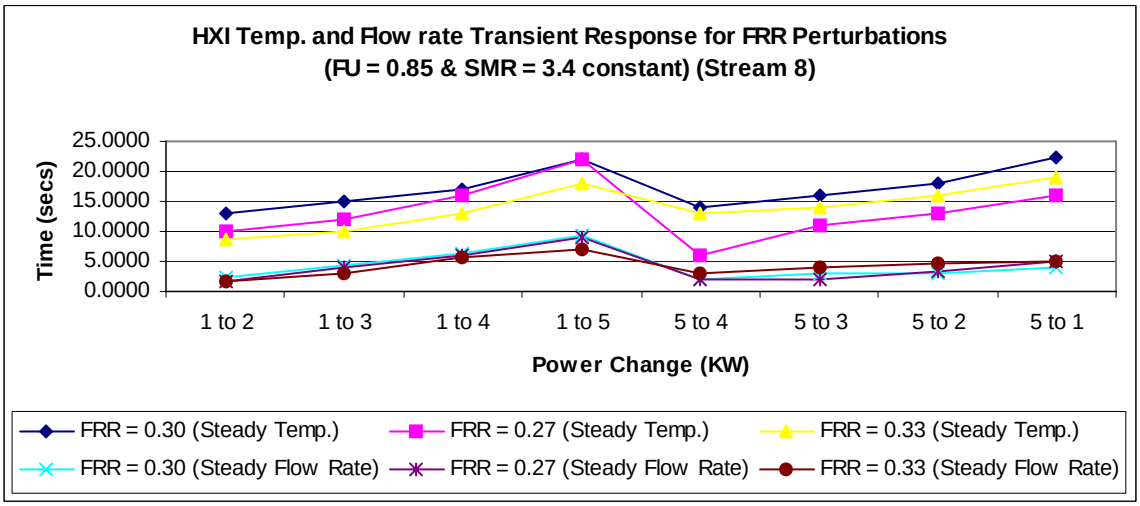
HXI Temp. and Flow rate Transient Response for FRR Perturbations
(FU = 0.85 & SMR = 3.4 constant) (Stream 8)
Time (secs)
25.0000
20.0000
15.0000
10.0000
5.0000
0.0000
1 to 2
1 to 3
1 to 4
1 to 5
5 to 4
5 to 3
5 to 2
5 to 1
Power Change (KW)
FRR = 0.30 (Steady Temp.)
FRR = 0.27 (Steady Temp.)
FRR = 0.33 (Steady Temp.)
FRR = 0.30 (Steady Flow Rate)
FRR = 0.27 (Steady Flow Rate)
FRR = 0.33 (Steady Flow Rate)

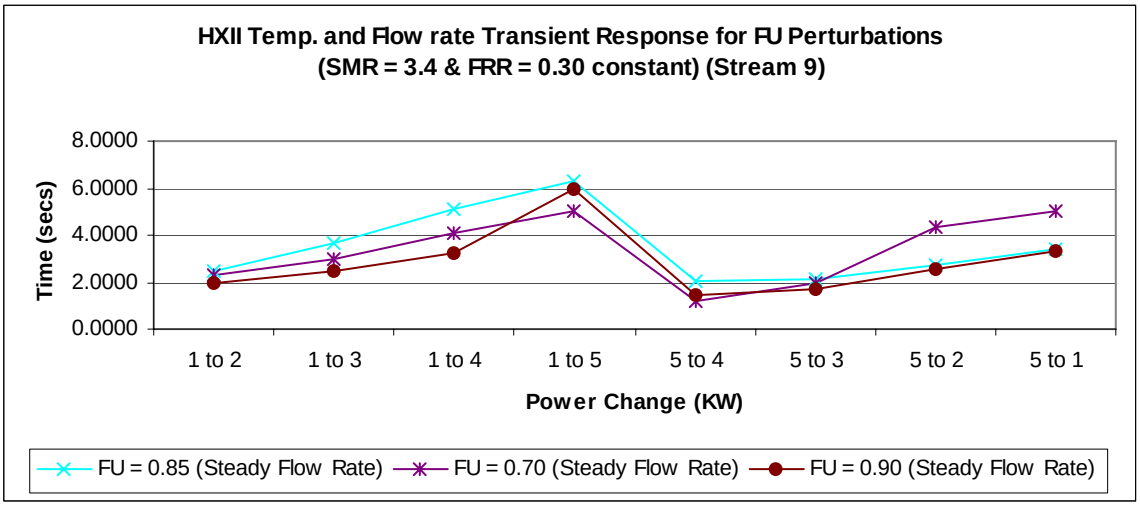
HXII Temp. and Flow rate Transient Response for FU Perturbations
(SMR = 3.4 & FRR = 0.30 constant) (Stream 9)
8.0000
6.0000
4.0000
2.0000
0.0000
Time (secs)
1 to 2
1 to 3
1 to 4
1 to 5
5 to 4
5 to 3
5 to 2
5 to 1
Power Change (KW)
FU = 0.85 (Steady Flow Rate)
FU = 0.70 (Steady Flow Rate)
FU = 0.90 (Steady Flow Rate)

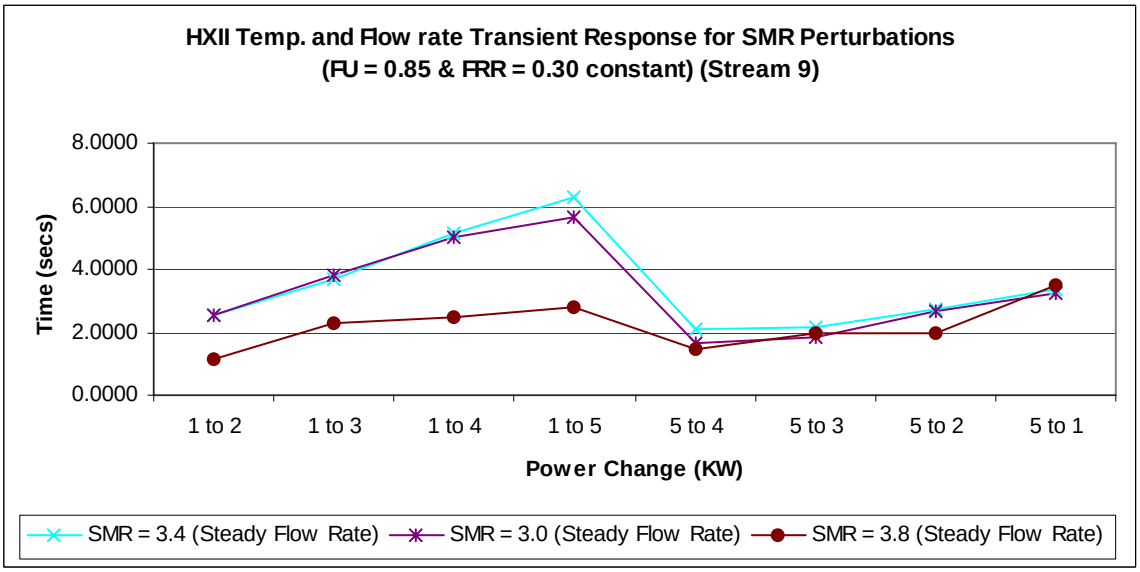
HXII Temp. and Flow rate Transient Response for SMR Perturbations
(FU = 0.85 & FRR = 0.30 constant) (Stream 9)
8.0000
6.0000
4.0000
2.0000
0.0000
Time (secs)
1 to 2
1 to 3
1 to 4
1 to 5
5 to 4
5 to 3
5 to 2
5 to 1
Power Change (KW)
SMR = 3.4 (Steady Flow Rate)
SMR = 3.0 (Steady Flow Rate)
SMR = 3.8 (Steady Flow Rate)

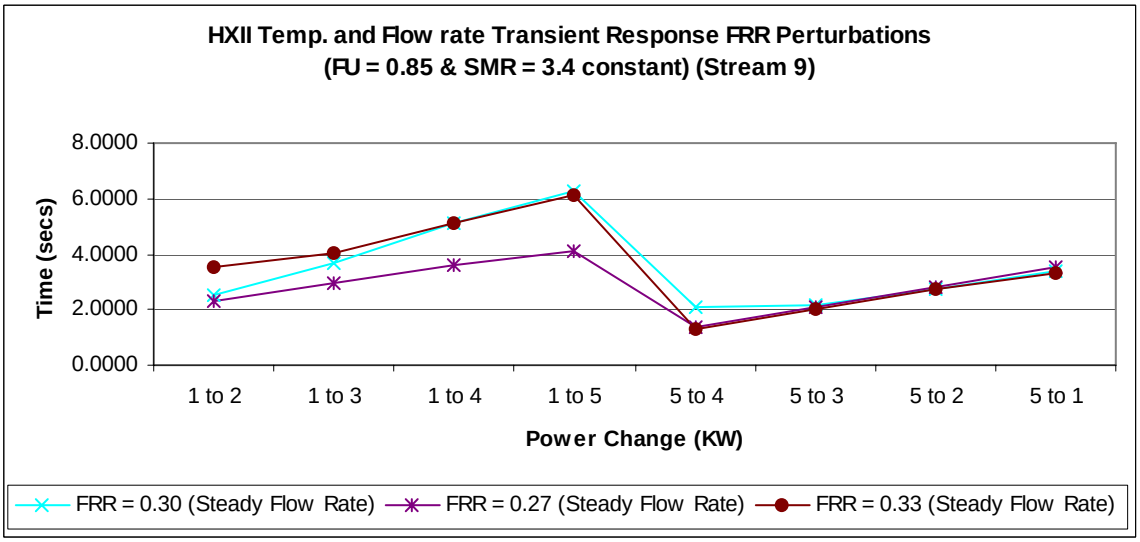
HXII Temp. and Flow rate Transient Response FRR Perturbations
(FU = 0.85 & SMR = 3.4 constant) (Stream 9)
8.0000
6.0000
4.0000
2.0000
0.0000
Time (secs)
1 to 2
1 to 3
1 to 4
1 to 5
5 to 4
5 to 3
5 to 2
5 to 1
Power Change (KW)
FRR = 0.30 (Steady Flow Rate)
FRR = 0.27 (Steady Flow Rate)
FRR = 0.33 (Steady Flow Rate)

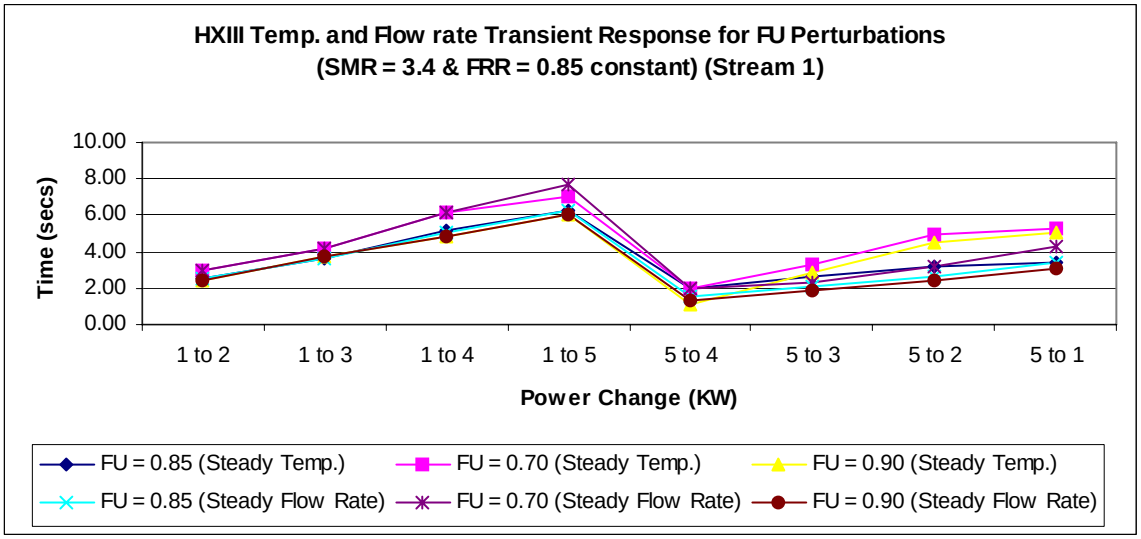
HXIII Temp. and Flow rate Transient Response for FU Perturbations
(SMR = 3.4 & FRR = 0.85 constant) (Stream 1)
Time (secs)
10.00
8.00
6.00
4.00
2.00
0.00
1 to 2
1 to 3
1 to 4
1 to 5
5 to 4
5 to 3
5 to 2
5 to 1
Power Change (KW)
FU = 0.85 (Steady Temp.)
FU = 0.70 (Steady Temp.)
FU = 0.90 (Steady Temp.)
FU = 0.85 (Steady Flow Rate)
FU = 0.70 (Steady Flow Rate)
FU = 0.90 (Steady Flow Rate)

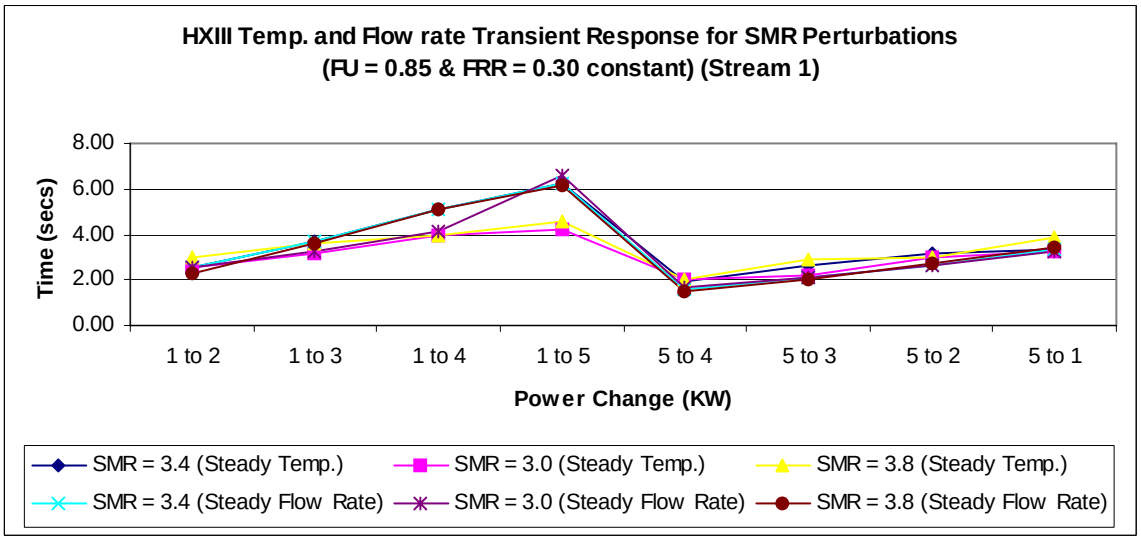
HXIII Temp. and Flow rate Transient Response for SMR Perturbations
(FU = 0.85 & FRR = 0.30 constant) (Stream 1)
Time (secs)
8.00
6.00
4.00
2.00
0.00
1 to 2
1 to 3
1 to 4
1 to 5
5 to 4
5 to 3
5 to 2
5 to 1
Power Change (KW)
SMR = 3.4 (Steady Temp.)
SMR = 3.0 (Steady Temp.)
SMR = 3.8 (Steady Temp.)
SMR = 3.4 (Steady Flow Rate)
SMR = 3.0 (Steady Flow Rate)
SMR = 3.8 (Steady Flow Rate)

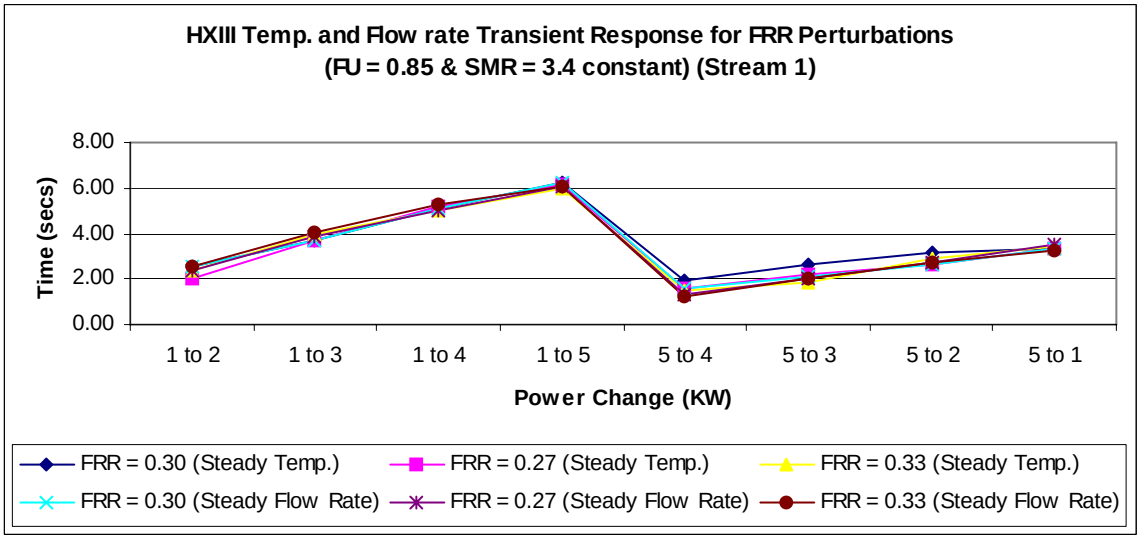
HXIII Temp. and Flow rate Transient Response for FRR Perturbations
(FU = 0.85 & SMR = 3.4 constant) (Stream 1)
Time (secs)
8.00
6.00
4.00
2.00
0.00
1 to 2
1 to 3
1 to 4
1 to 5
5 to 4
5 to 3
5 to 2
5 to 1
Power Change (KW)
FRR = 0.30 (Steady Temp.)
FRR = 0.27 (Steady Temp.)
FRR = 0.33 (Steady Temp.)
FRR = 0.30 (Steady Flow Rate)
FRR = 0.27 (Steady Flow Rate)
FRR = 0.33 (Steady Flow Rate)

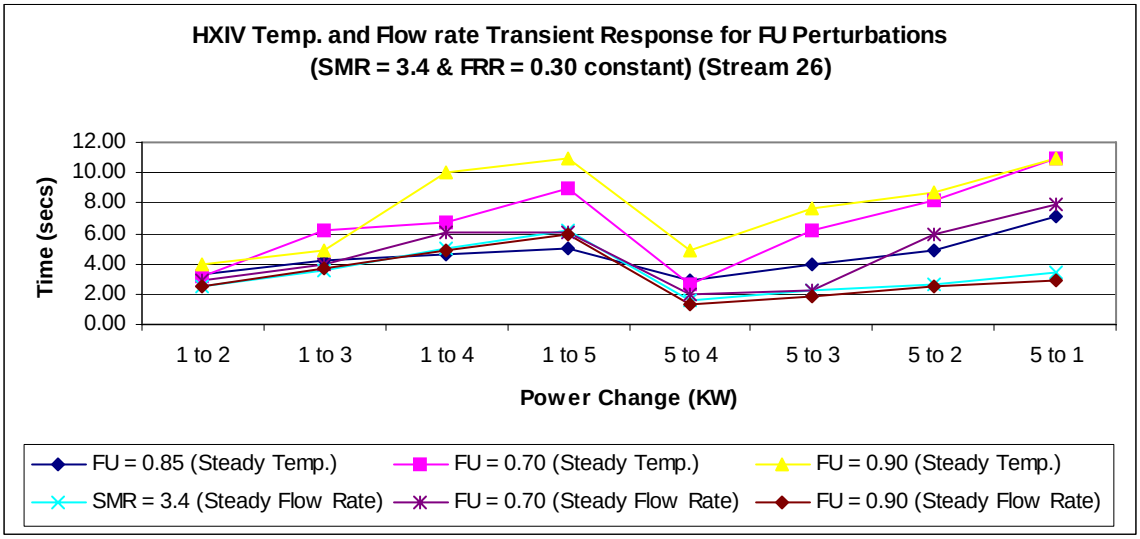
HXIV Temp. and Flow rate Transient Response for FU Perturbations
(SMR = 3.4 & FRR = 0.30 constant) (Stream 26)
Time (secs)
12.00
10.00
8.00
6.00
4.00
2.00
0.00
1 to 2
1 to 3
1 to 4
1 to 5
5 to 4
5 to 3
5 to 2
5 to 1
Power Change (KW)
FU = 0.85 (Steady Temp.)
FU = 0.70 (Steady Temp.)
FU = 0.90 (Steady Temp.)
SMR = 3.4 (Steady Flow Rate)
FU = 0.70 (Steady Flow Rate)
FU = 0.90 (Steady Flow Rate)

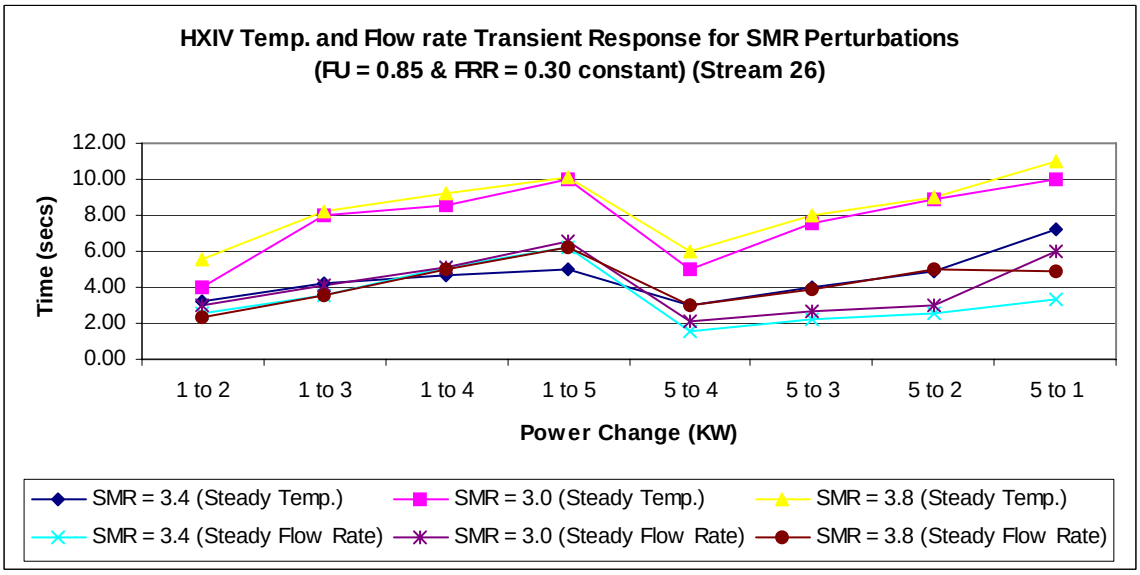
HXIV Temp. and Flow rate Transient Response for SMR Perturbations
(FU = 0.85 & FRR = 0.30 constant) (Stream 26)
Time (secs)
12.00
10.00
8.00
6.00
4.00
2.00
0.00
1 to 2
1 to 3
1 to 4
1 to 5
5 to 4
5 to 3
5 to 2
5 to 1
Power Change (KW)
SMR = 3.4 (Steady Temp.)
SMR = 3.0 (Steady Temp.)
SMR = 3.8 (Steady Temp.)
SMR = 3.4 (Steady Flow Rate)
SMR = 3.0 (Steady Flow Rate)
SMR = 3.8 (Steady Flow Rate)

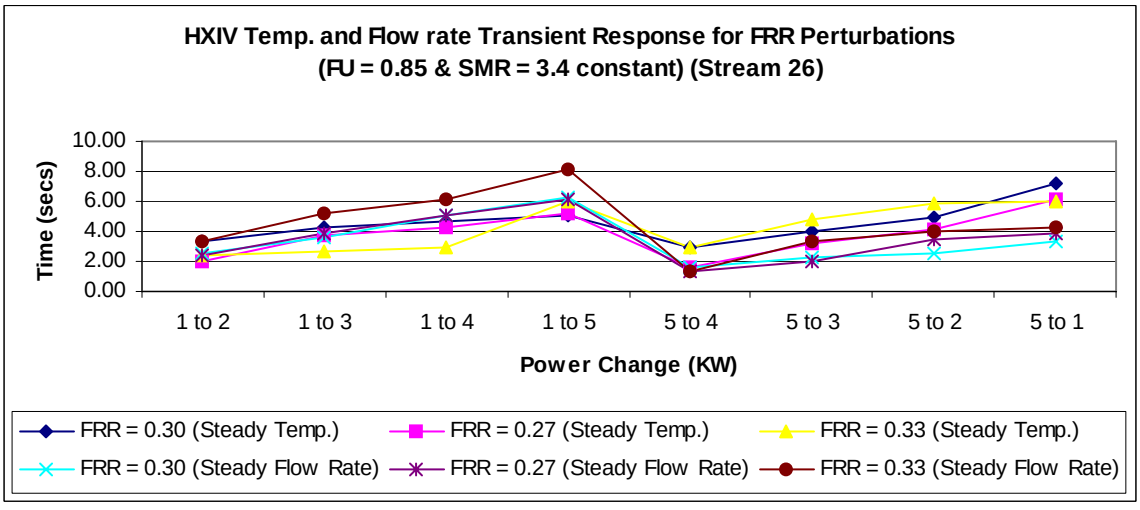
HXIV Temp. and Flow rate Transient Response for FRR Perturbations
(FU = 0.85 & SMR = 3.4 constant) (Stream 26)
Time (secs)
10.00
8.00
6.00
4.00
2.00
0.00
1 to 2
1 to 3
1 to 4
1 to 5
5 to 4
5 to 3
5 to 2
5 to 1
Power Change (KW)
FRR = 0.30 (Steady Temp.)
FRR = 0.27 (Steady Temp.)
FRR = 0.33 (Steady Temp.)
FRR = 0.30 (Steady Flow Rate)
FRR = 0.27 (Steady Flow Rate)
FRR = 0.33 (Steady Flow Rate)

Parametric Analysis #2: Component Analysis

Component: Pre-reformer

Stream 5

Power Change (KW)	FU 0.85 SMR 3.4 FRR 0.30	FU 0.70 SMR 3.4 FRR 0.30	FU 0.90 SMR 3.4 FRR 0.30	FU 0.85 SMR 3.0 FRR 0.30	FU 0.85 SMR 3.8 FRR 0.30	FU 0.85 SMR 3.4 FRR 0.27	FU 0.85 SMR 3.4 FRR 0.33
1 to 2	13.1880	10.0000	9.0000	12.9970	11.8760	10.1250	10.9980
1 to 3	16.2010	11.9310	11.9970	13.8990	14.0000	15.1230	14.9980
1 to 4	18.2160	20.0000	13.9560	17.0000	17.9030	17.2330	16.0000
1 to 5	22.2030	25.6820	18.0000	21.9560	22.9030	22.0190	21.9970
5 to 4	13.9530	9.5690	12.8440	13.0000	11.0000	13.9670	11.9660
5 to 3	16.1430	13.0000	14.5850	16.0000	17.0000	15.2330	12.7700
5 to 2	17.8760	15.0000	15.8810	19.0000	20.0000	16.8180	14.9410
5 to 1	19.7380	19.0000	16.7400	21.4500	22.3900	20.0920	19.8530

Stream 6

Power Change (KW)	FU 0.85 SMR 3.4 FRR 0.30	FU 0.70 SMR 3.4 FRR 0.30	FU 0.90 SMR 3.4 FRR 0.30	FU 0.85 SMR 3.0 FRR 0.30	FU 0.85 SMR 3.8 FRR 0.30	FU 0.85 SMR 3.4 FRR 0.27	FU 0.85 SMR 3.4 FRR 0.33
1 to 2	13.1880	11.0170	9.7560	12.8760	12.3450	11.2340	10.0000
1 to 3	16.2190	15.7130	12.0180	14.0000	14.1350	15.2340	14.0000
1 to 4	18.0910	19.1160	14.8760	18.2330	18.9870	19.2340	17.0000
1 to 5	21.0220	25.9970	19.0560	22.0560	22.7560	23.0190	23.0000
5 to 4	13.9530	10.2120	13.0506	13.7690	11.0000	14.0000	12.0000
5 to 3	16.1430	12.8060	14.8440	17.0000	18.0000	14.2330	14.0000
5 to 2	16.8760	16.1820	17.0000	19.1750	22.0000	15.1430	14.4570
5 to 1	19.8390	20.0000	20.0650	21.3260	23.4560	21.1380	21.7620

Overall: Pre-Reformer

Power Change (KW)	FU 0.85 SMR 3.4 FRR 0.30	FU 0.70 SMR 3.4 FRR 0.30	FU 0.90 SMR 3.4 FRR 0.30	FU 0.85 SMR 3.0 FRR 0.30	FU 0.85 SMR 3.8 FRR 0.30	FU 0.85 SMR 3.4 FRR 0.27	FU 0.85 SMR 3.4 FRR 0.33
1 to 2	13.1880	11.0170	9.9970	12.9970	12.3450	11.2340	10.9980
1 to 3	16.2190	15.7130	11.9970	14.0000	14.1350	15.2340	14.9980
1 to 4	18.2160	20.0000	14.9970	18.2330	18.9870	19.2340	17.0000
1 to 5	22.2030	25.9970	24.0560	22.0560	22.9030	23.0190	23.0000
5 to 4	13.9530	10.2120	13.8580	13.7690	11.0000	14.0000	12.0000
5 to 3	16.1430	13.0000	14.8440	17.0000	18.0000	15.2330	14.0000
5 to 2	17.8760	16.1820	16.7990	19.1750	22.0000	16.8180	14.9410
5 to 1	19.8390	20.0000	21.7400	21.4500	23.4560	21.1380	21.7620

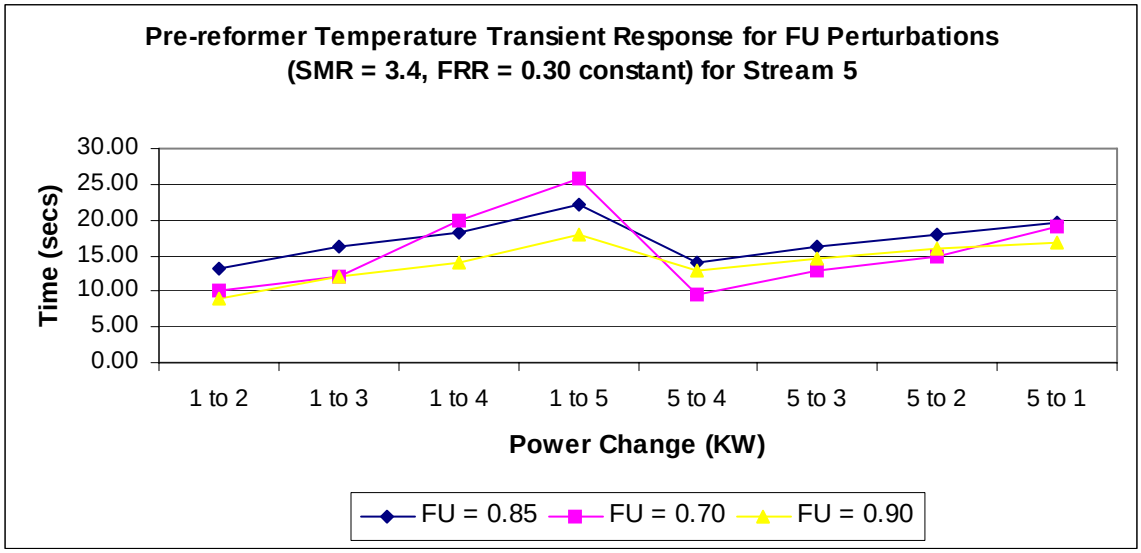
Pre-reformer Temperature Transient Response for FU Perturbations
(SMR = 3.4, FRR = 0.30 constant) for Stream 5
Time (secs)
30.00
25.00
20.00
15.00
10.00
5.00
0.00
1 to 2
1 to 3
1 to 4
1 to 5
5 to 4
5 to 3
5 to 2
5 to 1
Power Change (KW)
FU = 0.85
FU = 0.70
FU = 0.90

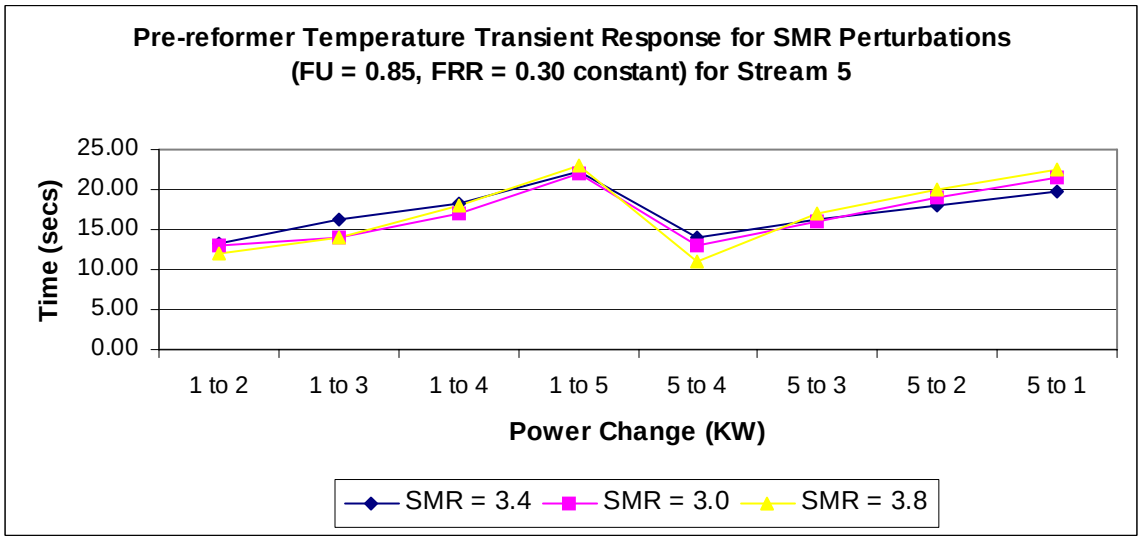
Pre-reformer Temperature Transient Response for SMR Perturbations
(FU = 0.85, FRR = 0.30 constant) for Stream 5
Time (secs)
25.00
20.00
15.00
10.00
5.00
0.00
1 to 2
1 to 3
1 to 4
1 to 5
5 to 4
5 to 3
5 to 2
5 to 1
Power Change (KW)
SMR = 3.4
SMR = 3.0
SMR = 3.8

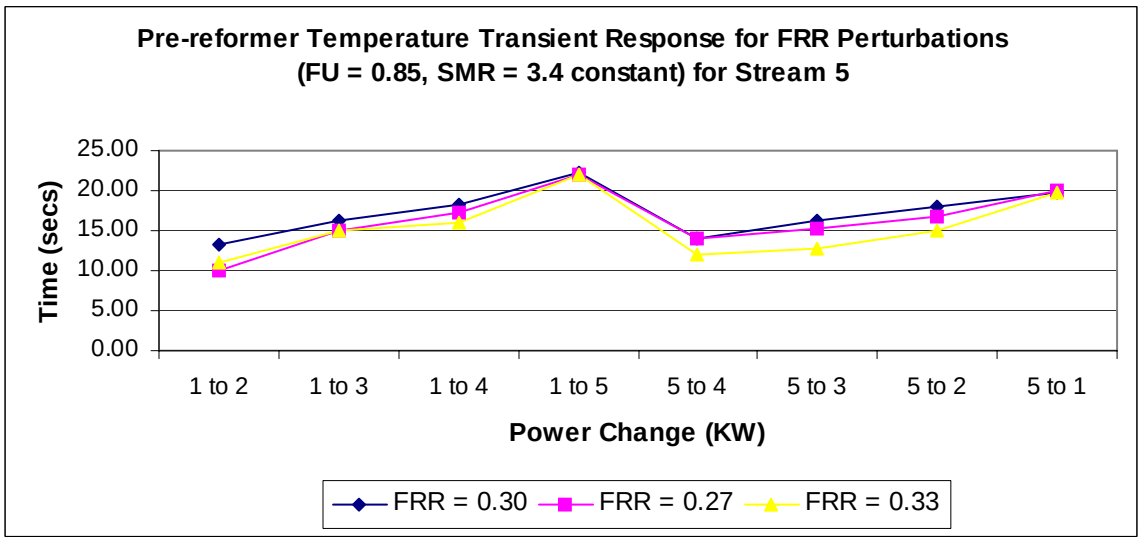
Pre-reformer Temperature Transient Response for FRR Perturbations
(FU = 0.85, SMR = 3.4 constant) for Stream 5
Time (secs)
25.00
20.00
15.00
10.00
5.00
0.00
1 to 2
1 to 3
1 to 4
1 to 5
5 to 4
5 to 3
5 to 2
5 to 1
Power Change (KW)
FRR = 0.30
FRR = 0.27
FRR = 0.33

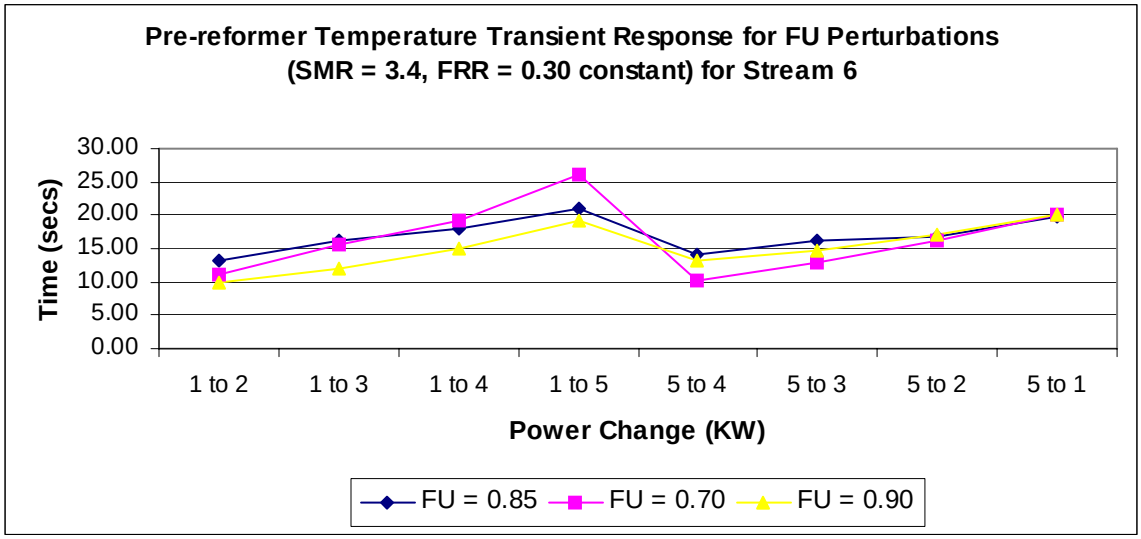
Pre-reformer Temperature Transient Response for FU Perturbations
(SMR = 3.4, FRR = 0.30 constant) for Stream 6
Time (secs)
30.00
25.00
20.00
15.00
10.00
5.00
0.00
1 to 2
1 to 3
1 to 4
1 to 5
5 to 4
5 to 3
5 to 2
5 to 1
Power Change (KW)
FU = 0.85
FU = 0.70
FU = 0.90

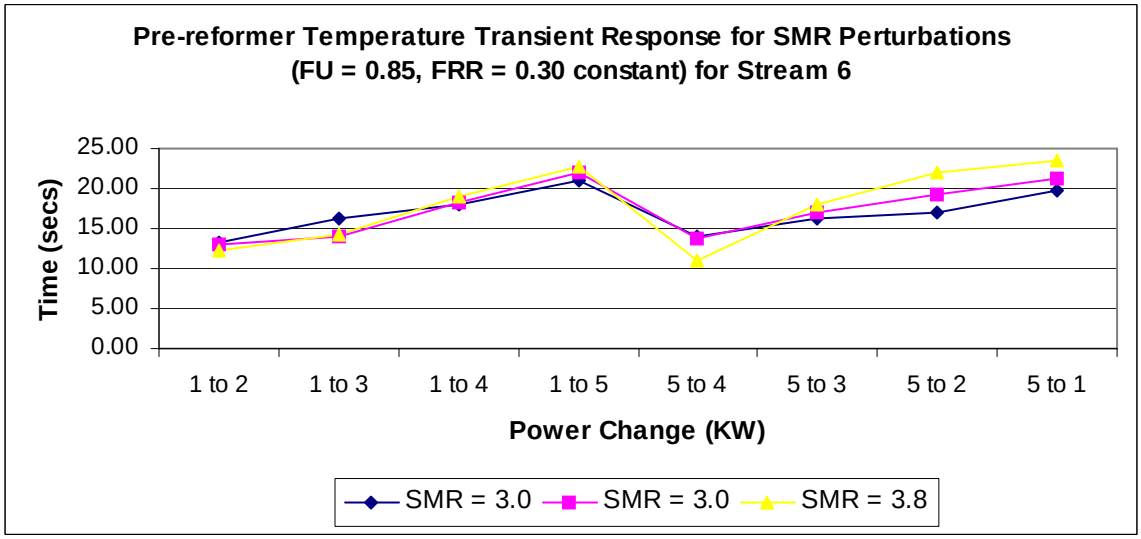
Pre-reformer Temperature Transient Response for SMR Perturbations
(FU = 0.85, FRR = 0.30 constant) for Stream 6
Time (secs)
25.00
20.00
15.00
10.00
5.00
0.00
1 to 2
1 to 3
1 to 4
1 to 5
5 to 4
5 to 3
5 to 2
5 to 1
Power Change (KW)
SMR = 3.0
SMR = 3.0
SMR = 3.8

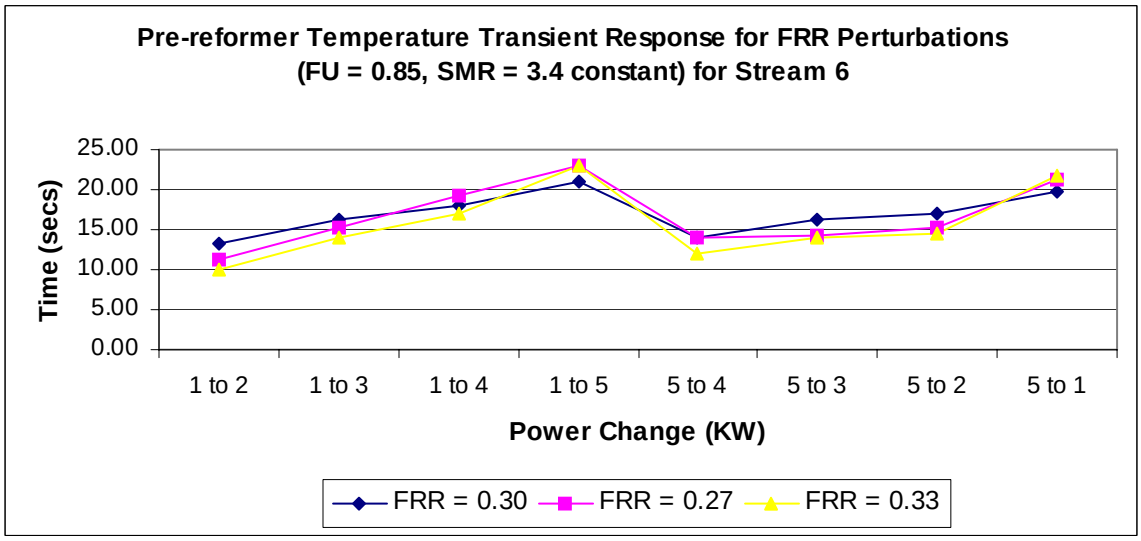
Pre-reformer Temperature Transient Response for FRR Perturbations
(FU = 0.85, SMR = 3.4 constant) for Stream 6
Time (secs)
25.00
20.00
15.00
10.00
5.00
0.00
1 to 2
1 to 3
1 to 4
1 to 5
5 to 4
5 to 3
5 to 2
5 to 1
Power Change (KW)
FRR = 0.30
FRR = 0.27
FRR = 0.33

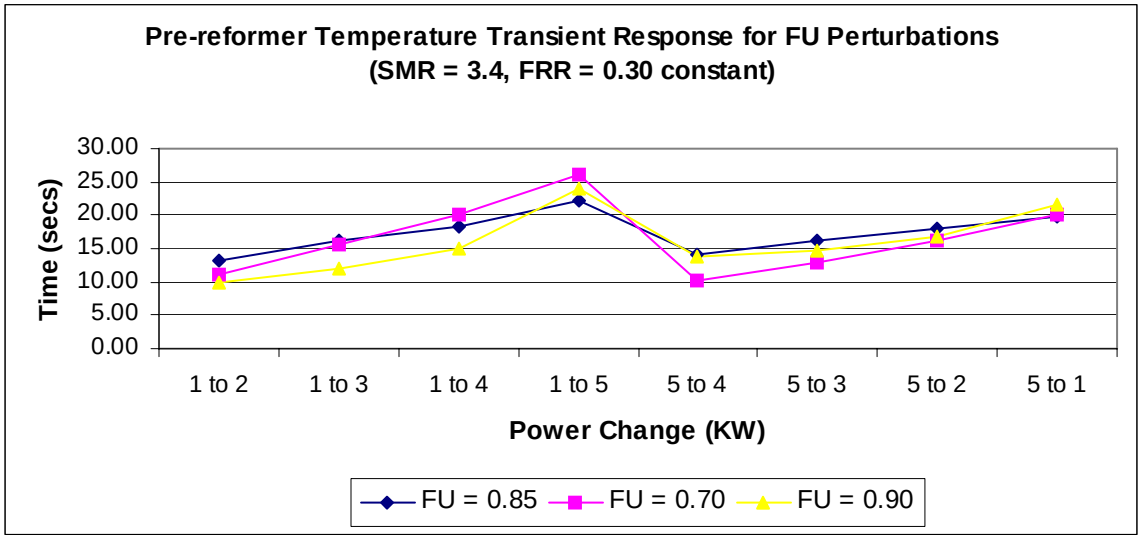
Pre-reformer Temperature Transient Response for FU Perturbations
(SMR = 3.4, FRR = 0.30 constant)
Time (secs)
30.00
25.00
20.00
15.00
10.00
5.00
0.00
1 to 2
1 to 3
1 to 4
1 to 5
5 to 4
5 to 3
5 to 2
5 to 1
Power Change (KW)
FU = 0.85
FU = 0.70
FU = 0.90

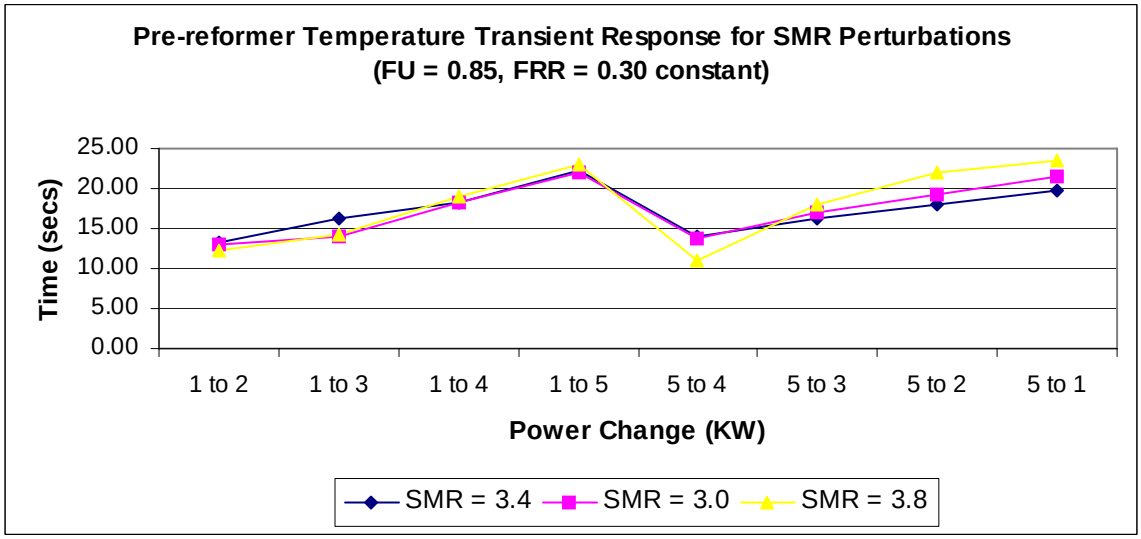
Pre-reformer Temperature Transient Response for SMR Perturbations
(FU = 0.85, FRR = 0.30 constant)
Time (secs)
25.00
20.00
15.00
10.00
5.00
0.00
1 to 2
1 to 3
1 to 4
1 to 5
5 to 4
5 to 3
5 to 2
5 to 1
Power Change (KW)
SMR = 3.4
SMR = 3.0
SMR = 3.8

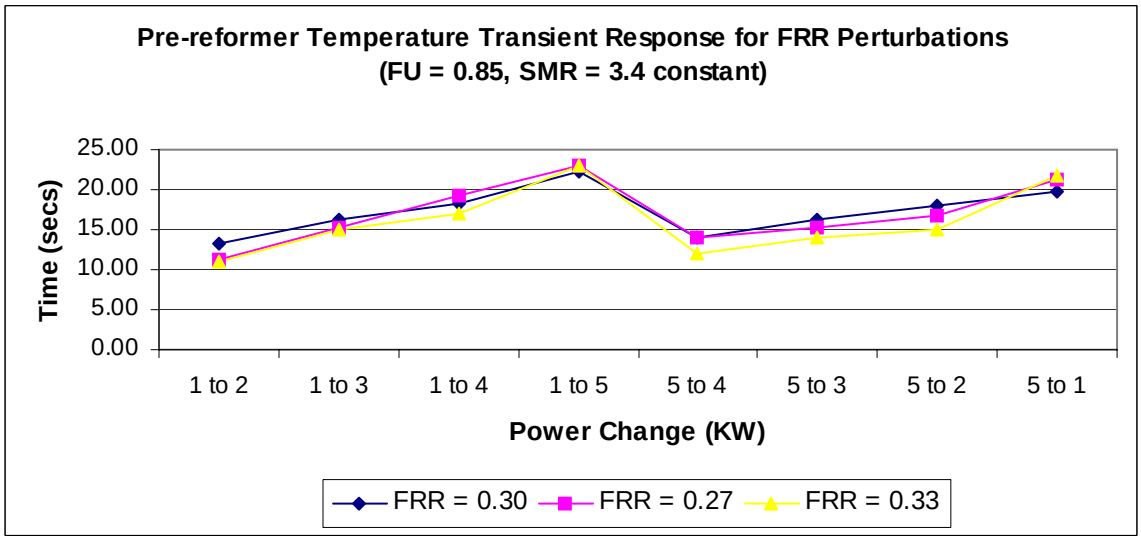
Pre-reformer Temperature Transient Response for FRR Perturbations
(FU = 0.85, SMR = 3.4 constant)
Time (secs)
25.00
20.00
15.00
10.00
5.00
0.00
1 to 2
1 to 3
1 to 4
1 to 5
5 to 4
5 to 3
5 to 2
5 to 1
Power Change (KW)
FRR = 0.30
FRR = 0.27
FRR = 0.33

Component:
HXIII

Stream 1

Power Change (KW)	FU 0.85 SMR 3.4 FRR 0.30	FU 0.70 SMR 3.4 FRR 0.30	FU 0.90 SMR 3.4 FRR 0.30	FU 0.85 SMR 3.0 FRR 0.30	FU 0.85 SMR 3.8 FRR 0.30	FU 0.85 SMR 3.4 FRR 0.27	FU 0.85 SMR 3.4 FRR 0.33
1 to 2	2.5060	2.9660	2.4420	2.5590	2.9970	2.0520	2.3830
1 to 3	3.6630	4.2080	3.7200	3.1340	3.6020	3.7070	3.9980
1 to 4	5.1250	6.1000	4.8490	3.9970	4.0000	5.1950	4.9710
1 to 5	6.2630	6.9970	5.9970	4.1810	4.5670	6.1140	5.9970
5 to 4	1.9530	1.9690	1.0590	1.9970	1.9970	1.5770	1.5080
5 to 3	2.5960	3.2800	2.8440	2.2360	2.9170	2.2010	1.8480
5 to 2	3.1400	4.9700	4.4650	2.9970	2.9970	2.6490	2.9410
5 to 1	3.3660	5.3050	5.0260	3.2320	3.8990	3.3600	3.4390

Stream 19

Power Change (KW)	FU 0.85 SMR 3.4 FRR 0.30	FU 0.70 SMR 3.4 FRR 0.30	FU 0.90 SMR 3.4 FRR 0.30	FU 0.85 SMR 3.0 FRR 0.30	FU 0.85 SMR 3.8 FRR 0.30	FU 0.85 SMR 3.4 FRR 0.27	FU 0.85 SMR 3.4 FRR 0.33
1 to 2	2.2120	2.9490	2.4450	3.0000	3.9970	2.0520	2.3830
1 to 3	3.6050	4.2120	3.6580	6.1700	6.5670	3.8170	2.9980
1 to 4	4.2160	6.1000	4.8520	7.9970	9.9970	5.1950	3.9980
1 to 5	6.2630	7.3520	6.0660	10.7310	11.0000	5.9030	4.9970
5 to 4	3.0000	2.0110	1.3290	4.0000	4.0000	4.9970	1.5080
5 to 3	3.8760	2.7800	1.9860	6.0000	7.0000	5.2010	2.7700
5 to 2	4.0000	4.9590	5.0000	8.0000	9.0000	6.5590	4.9410
5 to 1	5.2800	5.3300	5.2190	9.9670	11.0220	8.0920	5.8530

Overall: HX III

Power Change (KW)	FU 0.85 SMR 3.4 FRR 0.30	FU 0.70 SMR 3.4 FRR 0.30	FU 0.90 SMR 3.4 FRR 0.30	FU 0.85 SMR 3.0 FRR 0.30	FU 0.85 SMR 3.8 FRR 0.30	FU 0.85 SMR 3.4 FRR 0.27	FU 0.85 SMR 3.4 FRR 0.33
1 to 2	2.5060	2.9660	2.4450	3.0000	3.9970	2.0520	2.3830
1 to 3	3.6630	4.2120	3.7200	6.1700	6.5670	3.8170	3.9980
1 to 4	5.1250	6.1000	4.8520	7.9970	9.9970	5.1950	4.9710
1 to 5	6.2630	7.3520	6.0660	10.7310	11.0000	6.1140	5.9970
5 to 4	3.0000	2.0110	1.3290	4.0000	4.0000	4.9970	1.5080
5 to 3	3.8760	3.2800	2.8440	6.0000	7.0000	5.2010	2.7700
5 to 2	4.0000	4.9700	5.0000	8.0000	9.0000	6.5590	4.9410
5 to 1	5.2800	5.3300	5.2190	9.9670	11.0220	8.0920	5.8530

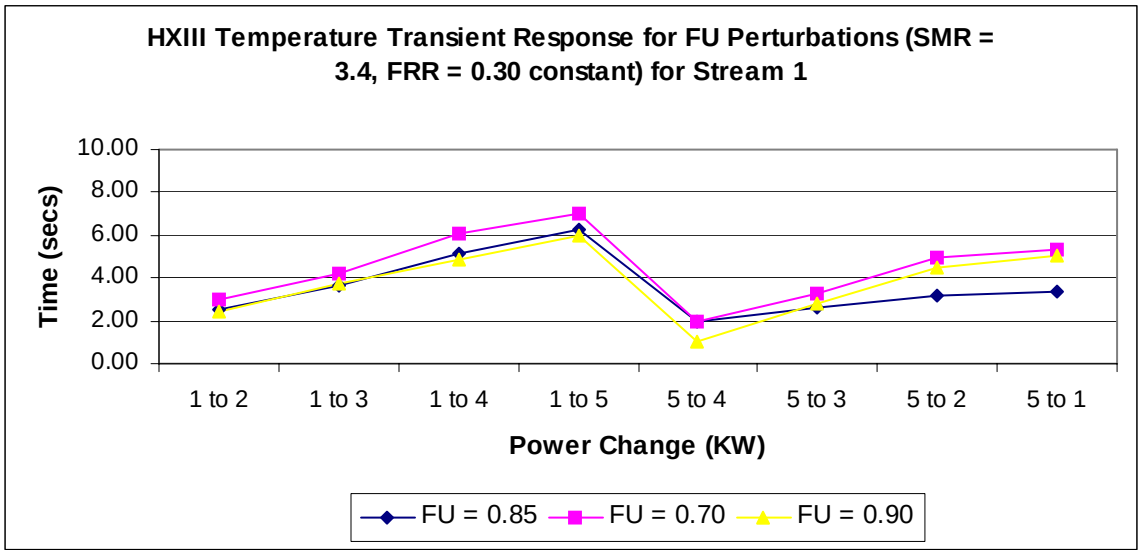
HXIII Temperature Transient Response for FU Perturbations (SMR = 3.4, FRR = 0.30 constant) for Stream 1
Time (secs)
10.00
8.00
6.00
4.00
2.00
0.00
1 to 2
1 to 3
1 to 4
1 to 5
5 to 4
5 to 3
5 to 2
5 to 1
Power Change (KW)
FU = 0.85
FU = 0.70
FU = 0.90

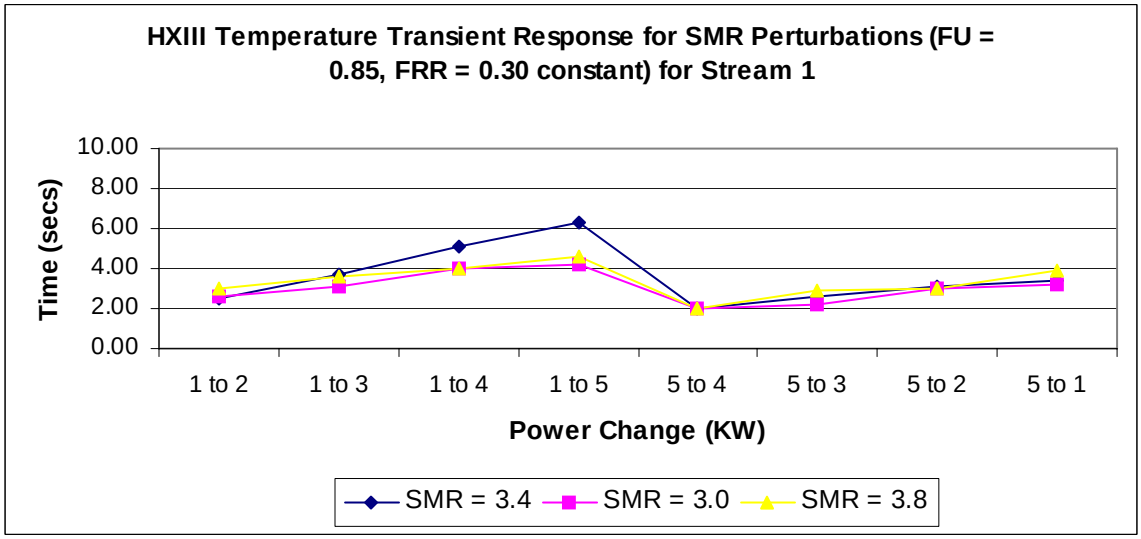
HXIII Temperature Transient Response for SMR Perturbations (FU = 0.85, FRR = 0.30 constant) for Stream 1
Time (secs)
10.00
8.00
6.00
4.00
2.00
0.00
1 to 2
1 to 3
1 to 4
1 to 5
5 to 4
5 to 3
5 to 2
5 to 1
Power Change (KW)
SMR = 3.4
SMR = 3.0
SMR = 3.8

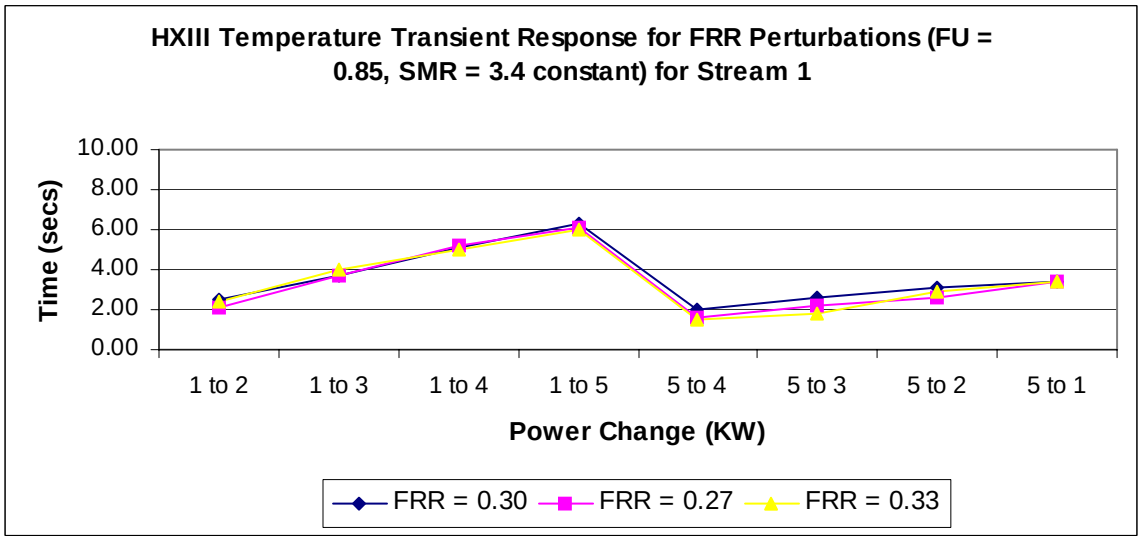
HXIII Temperature Transient Response for FRR Perturbations (FU = 0.85, SMR = 3.4 constant) for Stream 1
Time (secs)
10.00
8.00
6.00
4.00
2.00
0.00
1 to 2
1 to 3
1 to 4
1 to 5
5 to 4
5 to 3
5 to 2
5 to 1
Power Change (KW)
FRR = 0.30
FRR = 0.27
FRR = 0.33

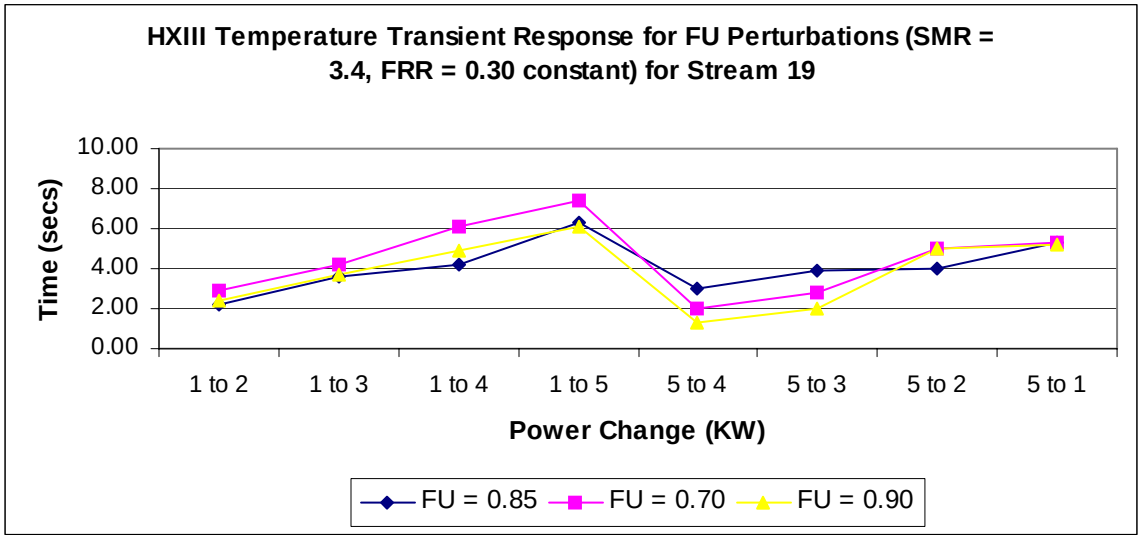
HXIII Temperature Transient Response for FU Perturbations (SMR = 3.4, FRR = 0.30 constant) for Stream 19
Time (secs)
10.00
8.00
6.00
4.00
2.00
0.00
1 to 2
1 to 3
1 to 4
1 to 5
5 to 4
5 to 3
5 to 2
5 to 1
Power Change (KW)
FU = 0.85
FU = 0.70
FU = 0.90

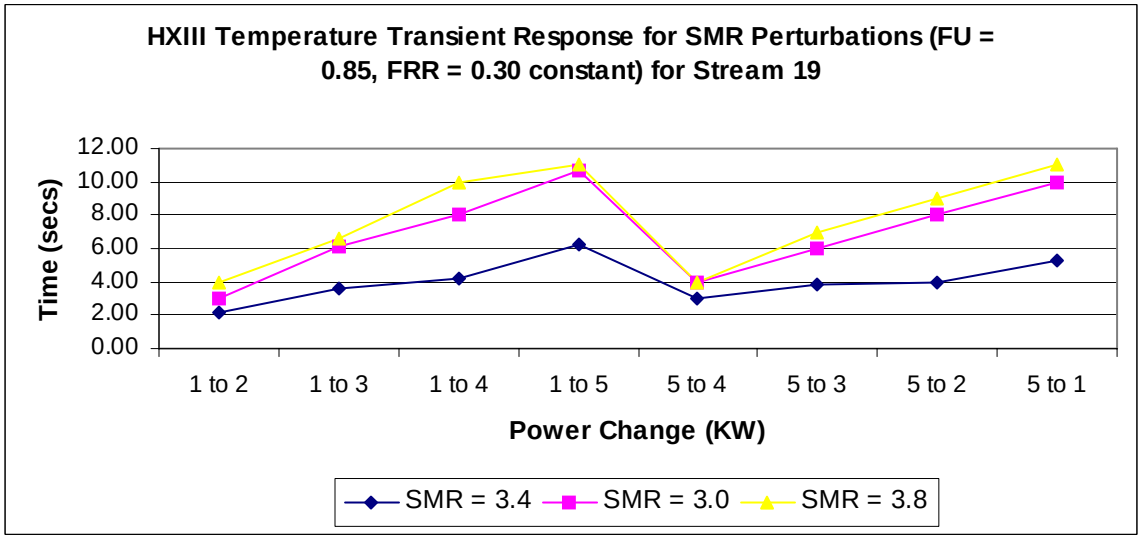
HXIII Temperature Transient Response for SMR Perturbations (FU = 0.85, FRR = 0.30 constant) for Stream 19
Time (secs)
12.00
10.00
8.00
6.00
4.00
2.00
0.00
1 to 2
1 to 3
1 to 4
1 to 5
5 to 4
5 to 3
5 to 2
5 to 1
Power Change (KW)
SMR = 3.4
SMR = 3.0
SMR = 3.8

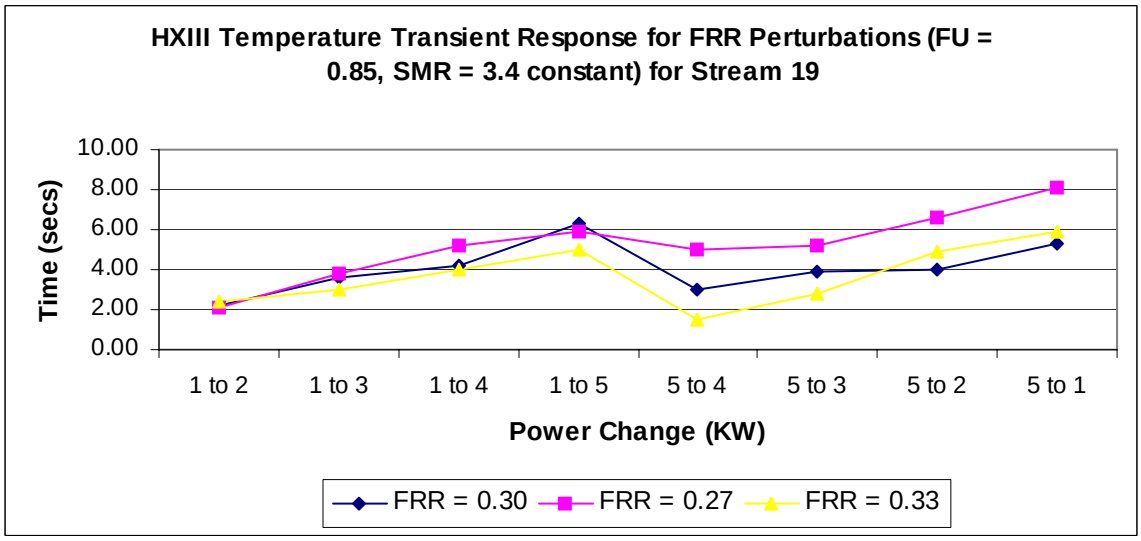
HXIII Temperature Transient Response for FRR Perturbations (FU = 0.85, SMR = 3.4 constant) for Stream 19
Time (secs)
10.00
8.00
6.00
4.00
2.00
0.00
1 to 2
1 to 3
1 to 4
1 to 5
5 to 4
5 to 3
5 to 2
5 to 1
Power Change (KW)
FRR = 0.30
FRR = 0.27
FRR = 0.33

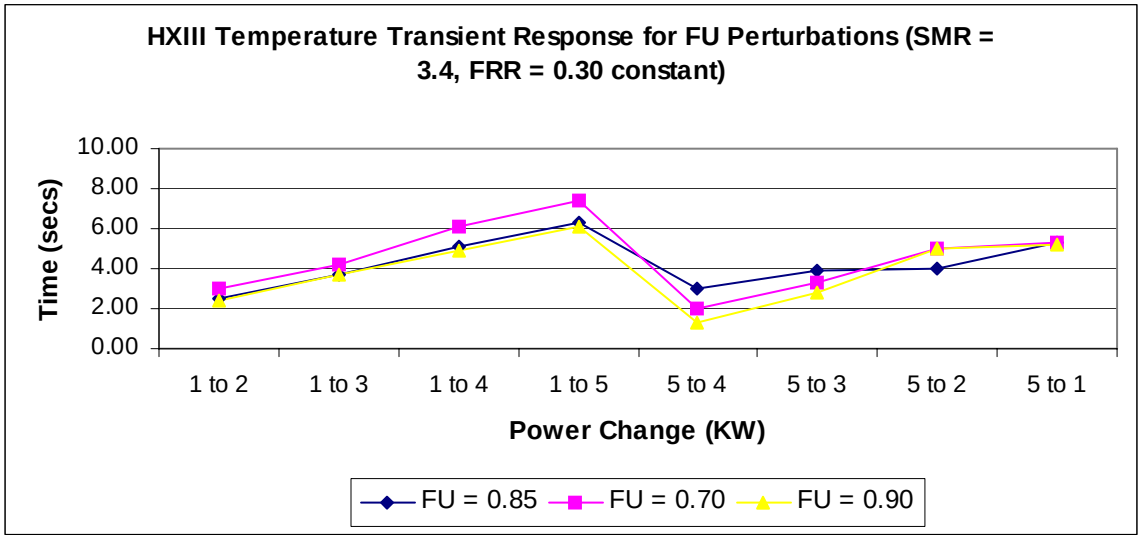
HXIII Temperature Transient Response for FU Perturbations (SMR = 3.4, FRR = 0.30 constant)
Time (secs)
10.00
8.00
6.00
4.00
2.00
0.00
1 to 2
1 to 3
1 to 4
1 to 5
5 to 4
5 to 3
5 to 2
5 to 1
Power Change (KW)
FU = 0.85
FU = 0.70
FU = 0.90

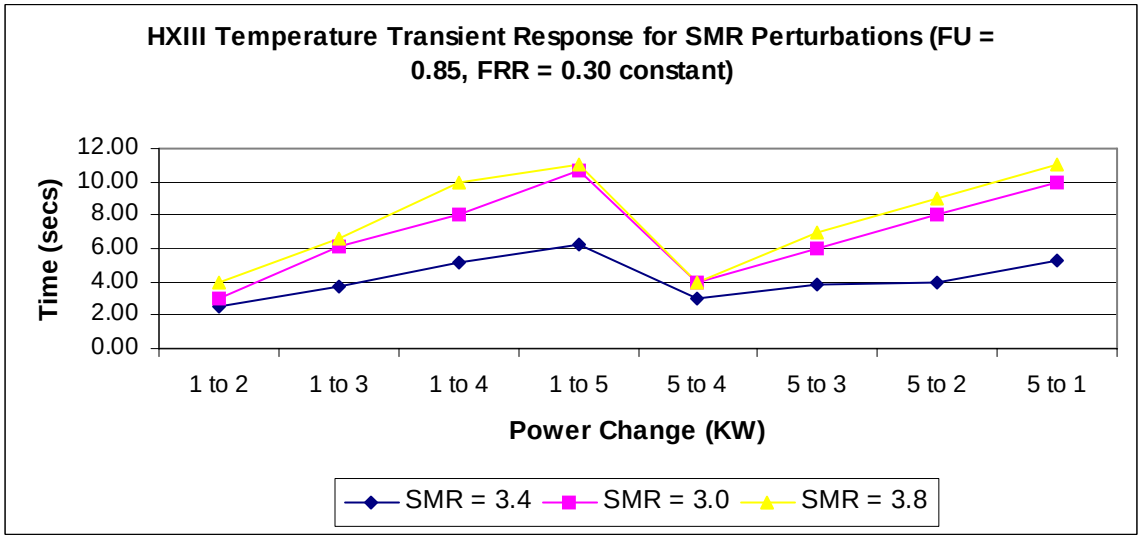
HXIII Temperature Transient Response for SMR Perturbations (FU = 0.85, FRR = 0.30 constant)
Time (secs)
12.00
10.00
8.00
6.00
4.00
2.00
0.00
1 to 2
1 to 3
1 to 4
1 to 5
5 to 4
5 to 3
5 to 2
5 to 1
Power Change (KW)
SMR = 3.4
SMR = 3.0
SMR = 3.8

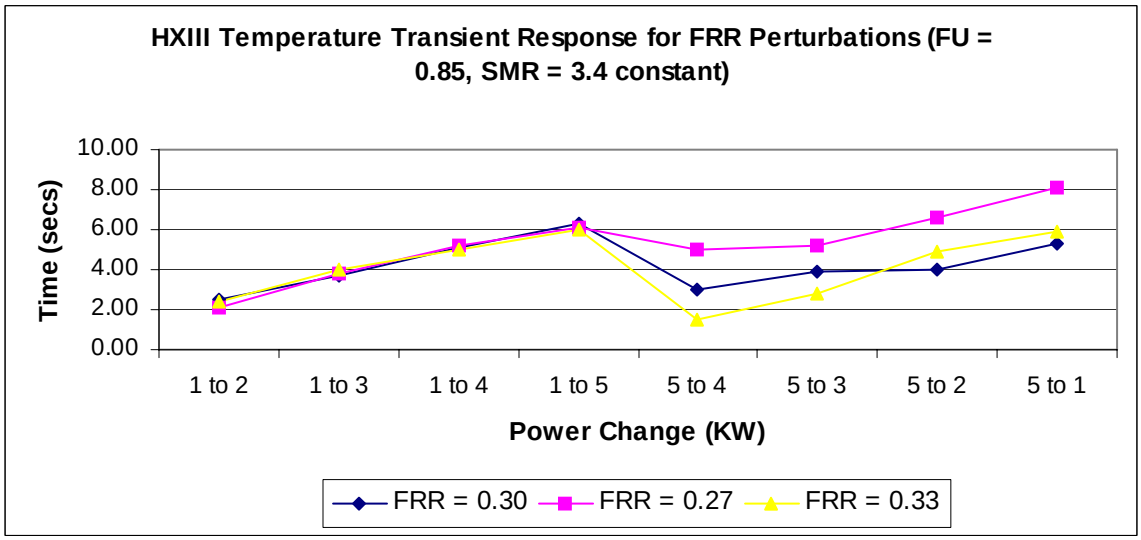
HXIII Temperature Transient Response for FRR Perturbations (FU = 0.85, SMR = 3.4 constant)
Time (secs)
10.00
8.00
6.00
4.00
2.00
0.00
1 to 2
1 to 3
1 to 4
1 to 5
5 to 4
5 to 3
5 to 2
5 to 1
Power Change (KW)
FRR = 0.30
FRR = 0.27
FRR = 0.33

Component: HXIV

Stream 26

Power Change (KW)	FU 0.85 SMR 3.4 FRR 0.30	FU 0.70 SMR 3.4 FRR 0.30	FU 0.90 SMR 3.4 FRR 0.30	FU 0.85 SMR 3.0 FRR 0.30	FU 0.85 SMR 3.8 FRR 0.30	FU 0.85 SMR 3.4 FRR 0.27	FU 0.85 SMR 3.4 FRR 0.33
1 to 2	3.2770	3.2140	3.9330	3.9970	5.5670	2.0520	2.3830
1 to 3	4.2010	6.2630	4.8370	7.9970	8.1700	3.7050	2.6670
1 to 4	4.6750	6.7700	9.9970	8.5600	9.2450	4.2330	2.9980
1 to 5	5.0090	8.9070	10.9080	9.9970	10.1310	5.1630	5.9970
5 to 4	2.9530	2.6610	4.8440	5.0000	6.0000	1.5470	2.9660
5 to 3	4.0000	6.1400	7.6900	7.6080	8.0000	3.2010	4.7700
5 to 2	4.8760	8.2400	8.7400	8.9210	9.0000	4.1100	5.8530
5 to 1	7.1790	11.0000	10.8810	10.0000	11.0000	6.0920	5.9410

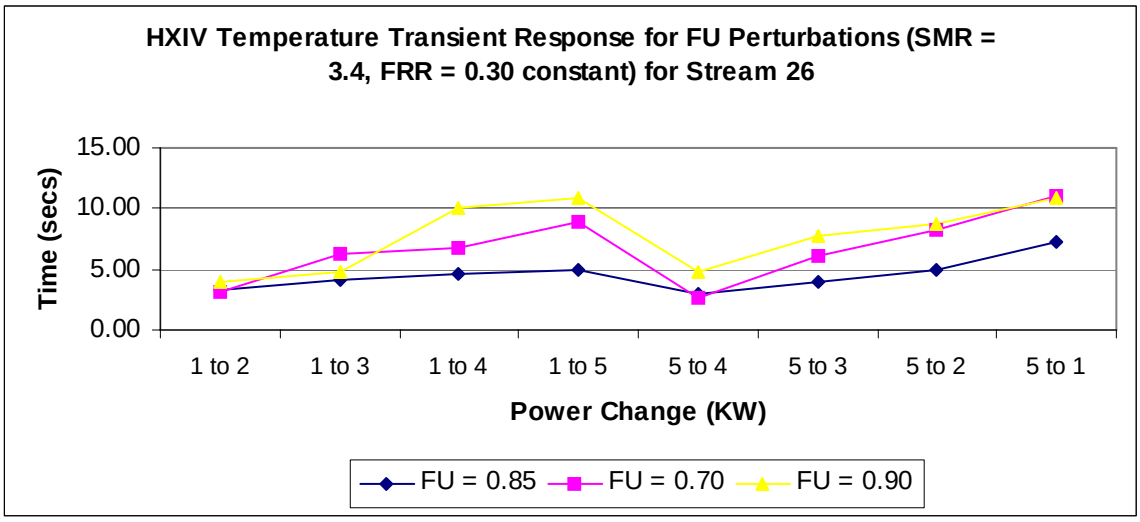
HXIV Temperature Transient Response for FU Perturbations (SMR = 3.4, FRR = 0.30 constant) for Stream 26
Time (secs)
15.00
10.00
5.00
0.00
1 to 2
1 to 3
1 to 4
1 to 5
5 to 4
5 to 3
5 to 2
5 to 1
Power Change (KW)
FU = 0.85
FU = 0.70
FU = 0.90

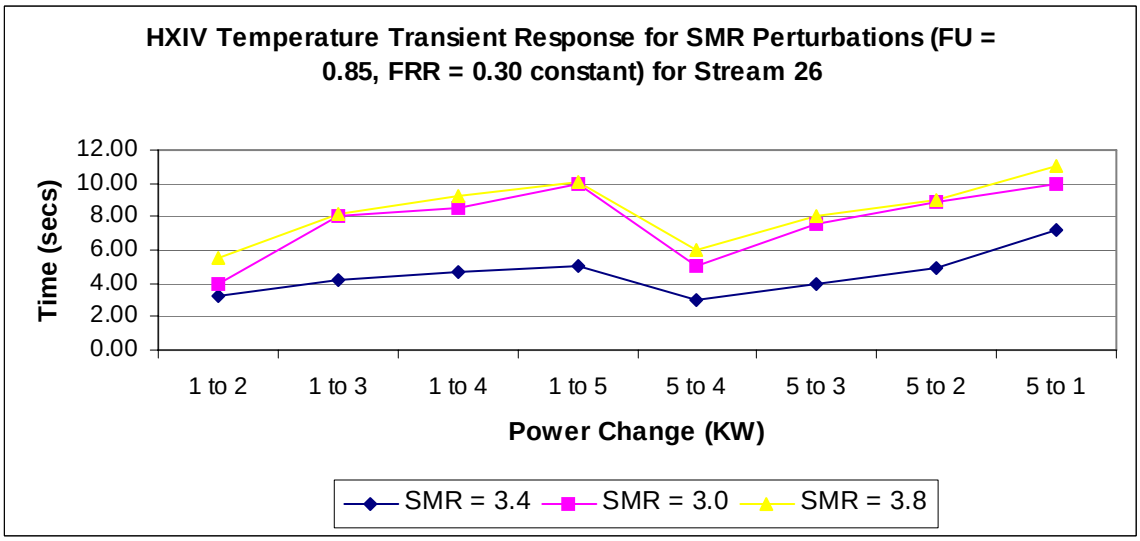
HXIV Temperature Transient Response for SMR Perturbations (FU = 0.85, FRR = 0.30 constant) for Stream 26
Time (secs)
12.00
10.00
8.00
6.00
4.00
2.00
0.00
1 to 2
1 to 3
1 to 4
1 to 5
5 to 4
5 to 3
5 to 2
5 to 1
Power Change (KW)
SMR = 3.4
SMR = 3.0
SMR = 3.8

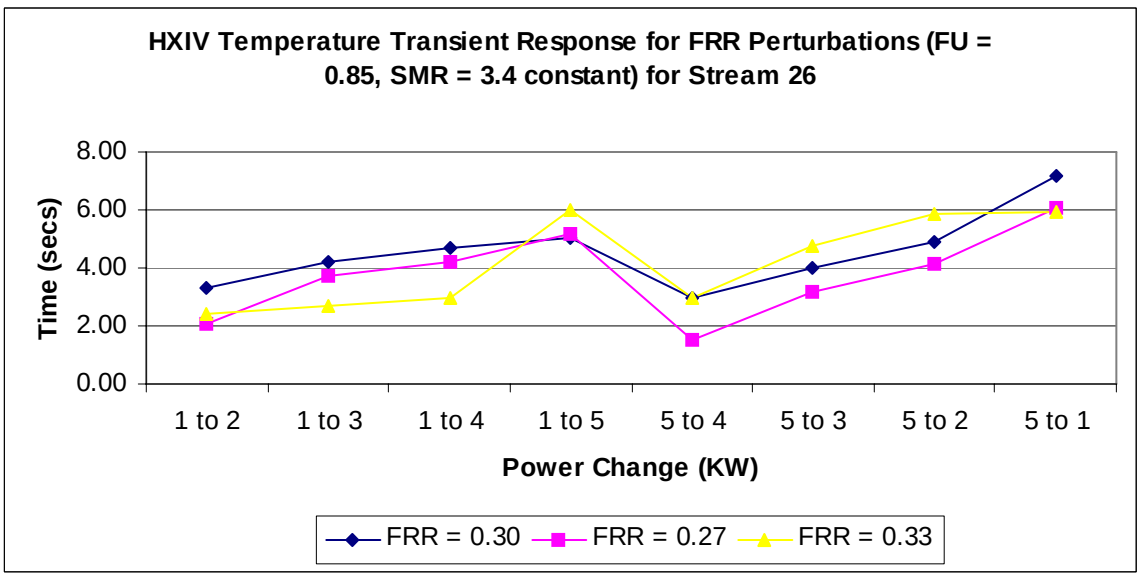
HXIV Temperature Transient Response for FRR Perturbations (FU = 0.85, SMR = 3.4 constant) for Stream 26
Time (secs)
8.00
6.00
4.00
2.00
0.00
1 to 2
1 to 3
1 to 4
1 to 5
5 to 4
5 to 3
5 to 2
5 to 1
Power Change (KW)
FRR = 0.30
FRR = 0.27
FRR = 0.33

System Thermal Efficiencies:

For Power increases :

FU Perturbation	System Thermal Efficiency Load (1 KW)	Load (2 KW)	Load (3 KW)	Load (4 KW)	Load (5 KW)
FU 0.85 SMR 3.4 FRR 0.30	0.317377	0.365611	0.392320	0.414220	0.437471
FU 0.70 SMR 3.4 FRR 0.30	0.255898	0.296621	0.321432	0.341744	0.362974
FU 0.90 SMR 3.4 FRR 0.30	0.342342	0.388765	0.416305	0.438456	0.462365

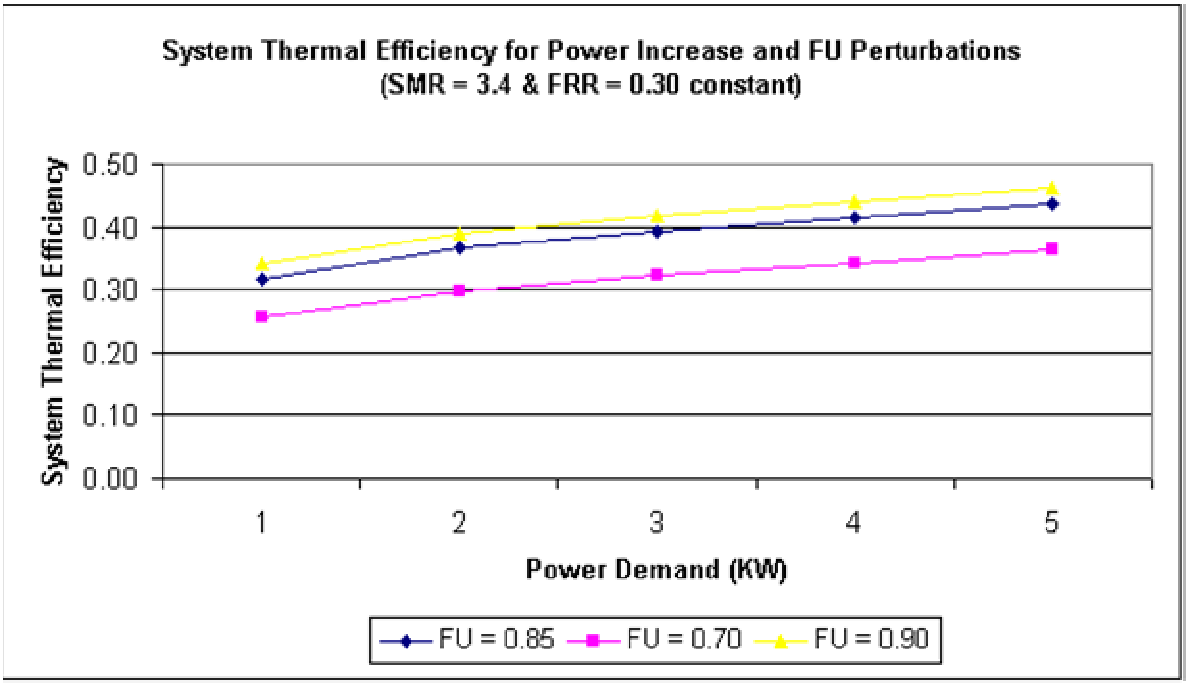

Raising the Fuel Utilization from the pre-determined level of 0.85 to 0.90 increases the System Thermal Efficiency and reducing it to 0.70 decreases it. But the reduction causes a steeper fall in the efficiency as compared with the increase.

SMR Perturbation	System Thermal Efficiency				
	Load (1 KW)	Load (2 KW)	Load (3 KW)	Load (4 KW)	Load (5 KW)
FU 0.85 SMR 3.4 FRR 0.30	0.317377	0.365611	0.392320	0.414220	0.437471
FU 0.85 SMR 3.0 FRR 0.30	0.311043	0.361496	0.388324	0.410663	0.432835
FU 0.85 SMR 3.8 FRR 0.30	0.322150	0.370334	0.397297	0.419428	0.442066

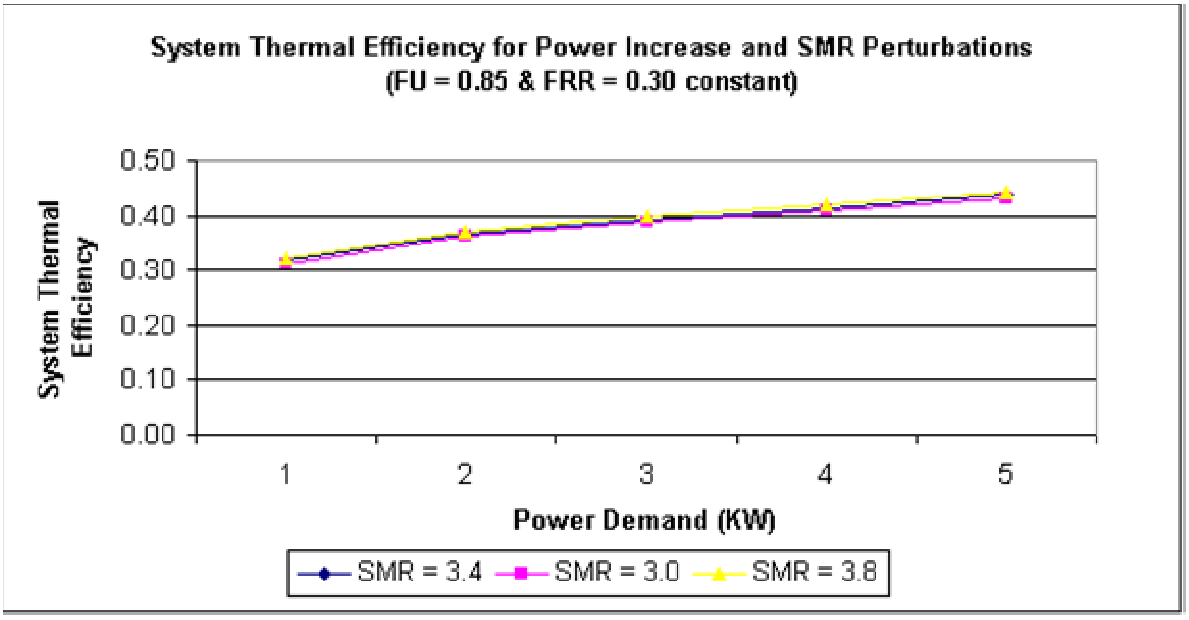

Increase or decrease in Steam to Methane Ratio does not affect the System Thermal Efficiency by a great magnitude. Hence we can infer that for load increases, Steam to Methane Ratio plays a relative subdued role as regards to System Thermal Efficiency.

FRR Perturbation	System Thermal Efficiency				
	Load (1 KW)	Load (2 KW)	Load (3 KW)	Load (4 KW)	Load (5 KW)
FU 0.85 SMR 3.4 FRR 0.30	0.317377	0.365611	0.392320	0.414220	0.437471
FU 0.85 SMR 3.4 FRR 0.27	0.320083	0.376448	0.403765	0.426377	0.449015
FU 0.85 SMR 3.4 FRR 0.33	0.314953	0.356552	0.383443	0.405668	0.427832

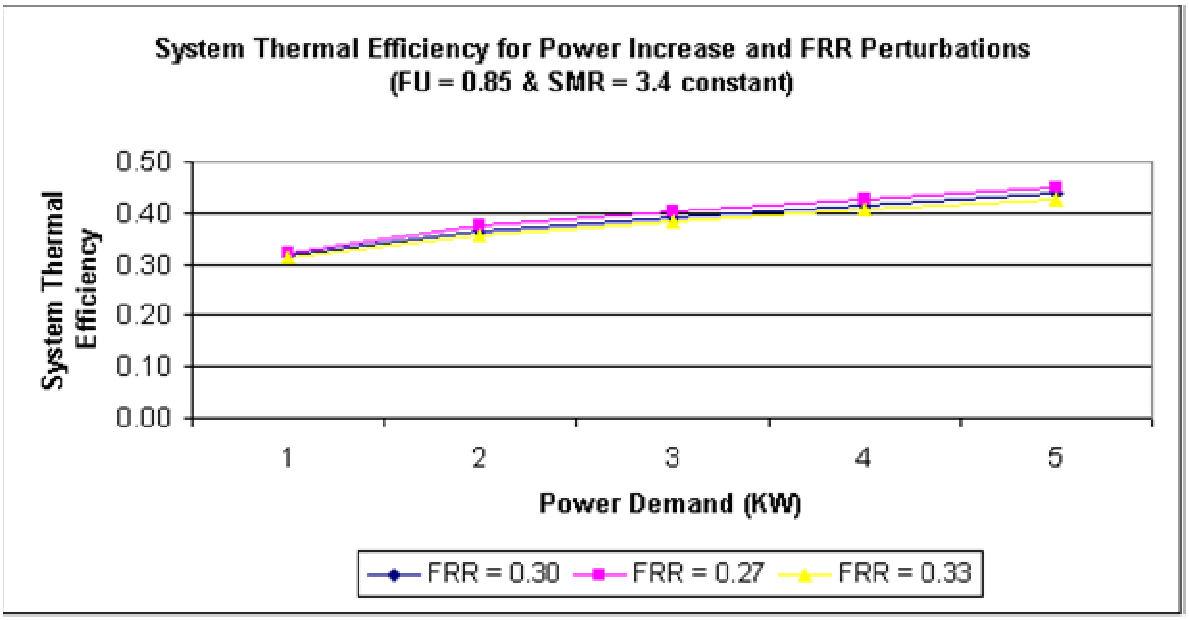

Increasing the Fuel Reformate Ratio from 0.30 to 0.33, leads to a slight decrease in System Thermal Efficiency. Decreasing the Fuel Reformate Ratio to 0.27 on the other hand increases the System Thermal Efficiency slightly. Hence, Fuel Reformate Ratio has an inverse effect on the System Thermal Efficiency as regards to its increase or decrease.

For Power decreases :

FU Perturbation	System Thermal Efficiency				
	Load (5 KW)	Load (4 KW)	Load (3 KW)	Load (2 KW)	Load (1 KW)
FU 0.85 SMR 3.4 FRR 0.30	0.428575	0.406349	0.383753	0.356507	0.317377
FU 0.70 SMR 3.4 FRR 0.30	0.356756	0.337026	0.315951	0.290408	0.255898
FU 0.90 SMR 3.4 FRR 0.30	0.455981	0.429477	0.406251	0.379384	0.342342

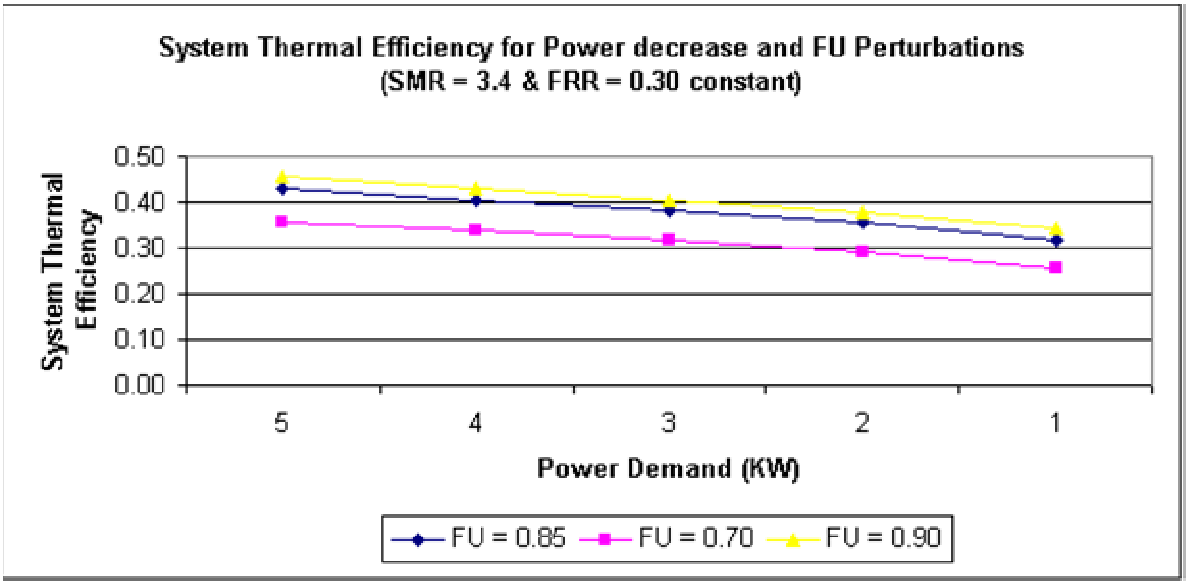

Raising the Fuel Utilization from the pre-determined level of 0.85 to 0.90 increases the System Thermal Efficiency and reducing it to 0.70 decreases it. But the reduction causes a steeper fall in the efficiency as compared with the increase.

SMR Perturbation	System Thermal Efficiency				
	Load (5 KW)	Load (4 KW)	Load (3 KW)	Load (2 KW)	Load (1 KW)
FU 0.85 SMR 3.4 FRR 0.30	0.428575	0.406349	0.383753	0.356507	0.317377
FU 0.85 SMR 3.0 FRR 0.30	0.426286	0.400297	0.377665	0.351748	0.313058
FU 0.85 SMR 3.8 FRR 0.30	0.439126	0.409763	0.388500	0.361881	0.322150

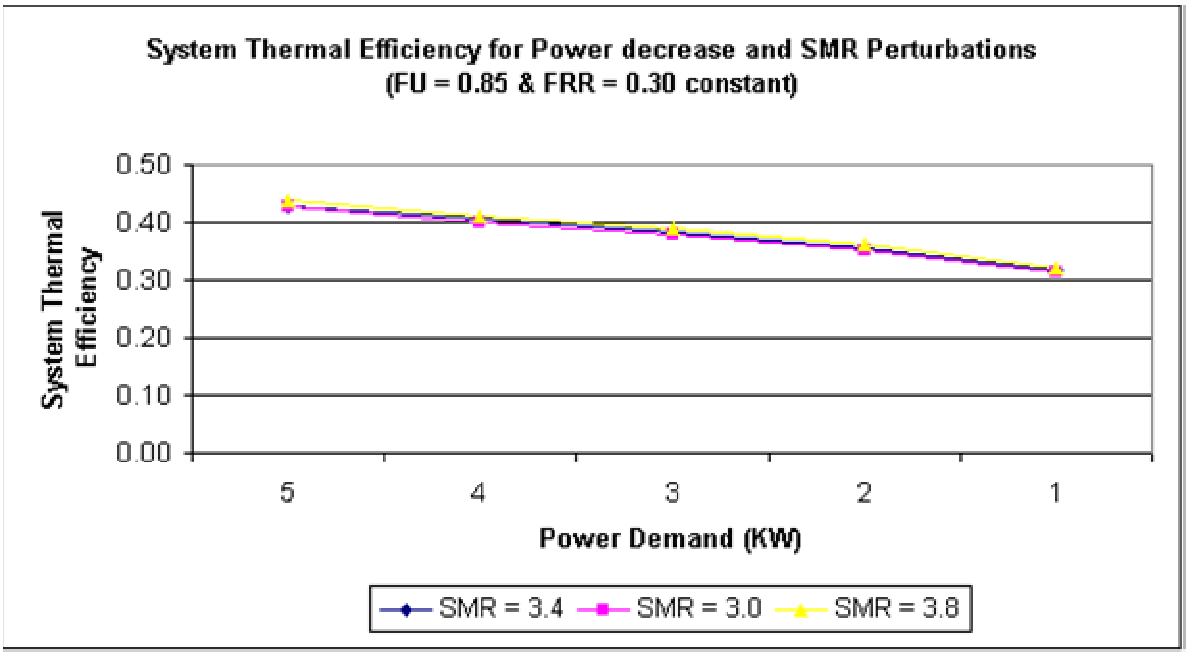

Increase or decrease in Steam to Methane Ratio does not affect the System Thermal Efficiency by a great magnitude. Hence we can infer that for load decreases, Steam to Methane Ratio plays a relative subdued role as regards to System Thermal Efficiency.

FRR Perturbation	System Thermal Efficiency				
	Load (5 KW)	Load (4 KW)	Load (3 KW)	Load (2 KW)	Load (1 KW)
FU 0.85 SMR 3.4 FRR 0.30	0.428575	0.406349	0.383753	0.356507	0.317377
FU 0.85 SMR 3.4 FRR 0.27	0.439126	0.415488	0.394036	0.368938	0.330683
FU 0.85 SMR 3.4 FRR 0.33	0.427286	0.396000	0.374390	0.347113	0.310566

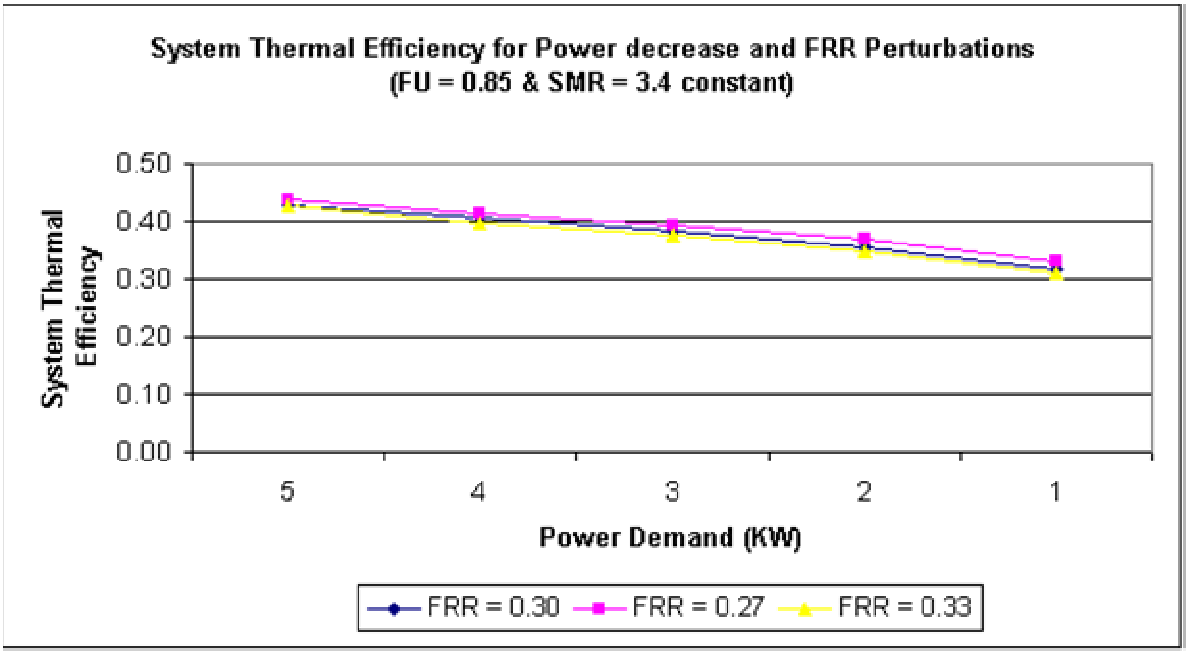

Increasing the Fuel Reformate Ratio from 0.30 to 0.33, leads to a slight decrease in System Thermal Efficiency. Decreasing the Fuel Reformate Ratio to 0.27 on the other hand increases the System Thermal Efficiency slightly. Hence, Fuel Reformate Ratio has an inverse effect on the System Thermal Efficiency as regards to its increase or decrease.

System Energy Efficiencies:

For Power increases :

FU Perturbation	System Energy Efficiency				
	Load (1 KW)	Load (2 KW)	Load (3 KW)	Load (4 KW)	Load (5 KW)
FU 0.85 SMR 3.4 FRR 0.30	0.308846	0.355784	0.381775	0.403087	0.425712
FU 0.70 SMR 3.4 FRR 0.30	0.249020	0.288648	0.312792	0.332558	0.353218
FU 0.90 SMR 3.4 FRR 0.30	0.333140	0.378315	0.405116	0.426671	0.449937

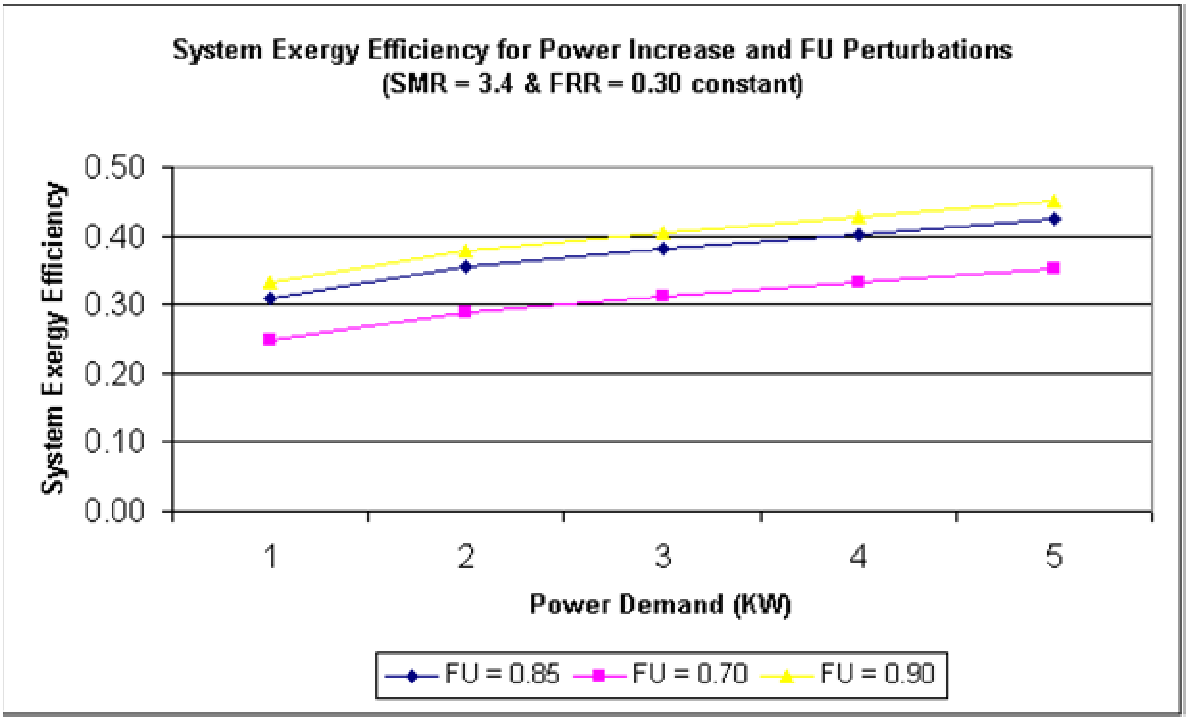

Raising the Fuel Utilization from the pre-determined level of 0.85 to 0.90 increases the System Energy Efficiency and reducing it to 0.70 decreases it. But the reduction causes a steeper fall in the efficiency as compared with the increase.

SMR Perturbation	System Energy Efficiency				
	Load (1 KW)	Load (2 KW)	Load (3 KW)	Load (4 KW)	Load (5 KW)
FU 0.85 SMR 3.4 FRR 0.30	0.308846	0.355784	0.381775	0.403087	0.425712
FU 0.85 SMR 3.0 FRR 0.30	0.302682	0.351780	0.377887	0.399625	0.421201
FU 0.85 SMR 3.8 FRR 0.30	0.313491	0.360380	0.386618	0.408154	0.430184

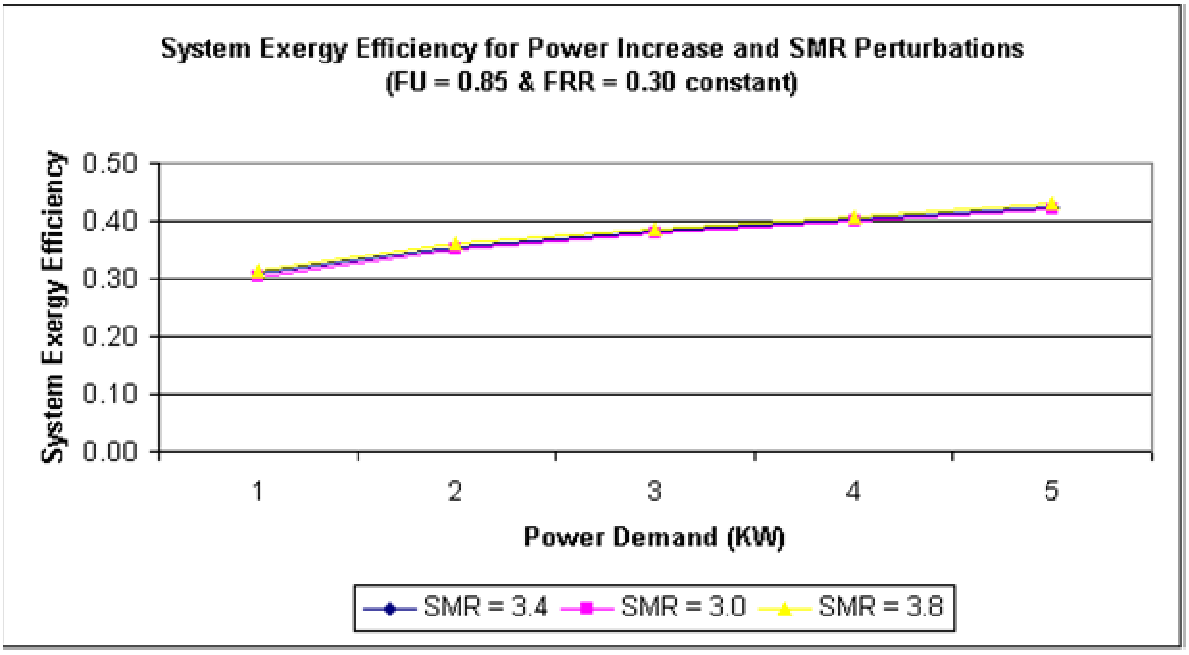

Increase or decrease in Steam to Methane Ratio does not affect the System Energy Efficiency by a great magnitude. Hence we can infer that for load increases, Steam to Methane Ratio plays a relative subdued role as regards to System Energy Efficiency.

FRR Perturbation	System Energy Efficiency				
	Load (1 KW)	Load (2 KW)	Load (3 KW)	Load (4 KW)	Load (5 KW)
FU 0.85 SMR 3.4 FRR 0.30	0.308846	0.355784	0.381775	0.403087	0.425712
FU 0.85 SMR 3.4 FRR 0.27	0.311480	0.366329	0.392912	0.414916	0.436946
FU 0.85 SMR 3.4 FRR 0.33	0.305847	0.346968	0.373137	0.394764	0.416333

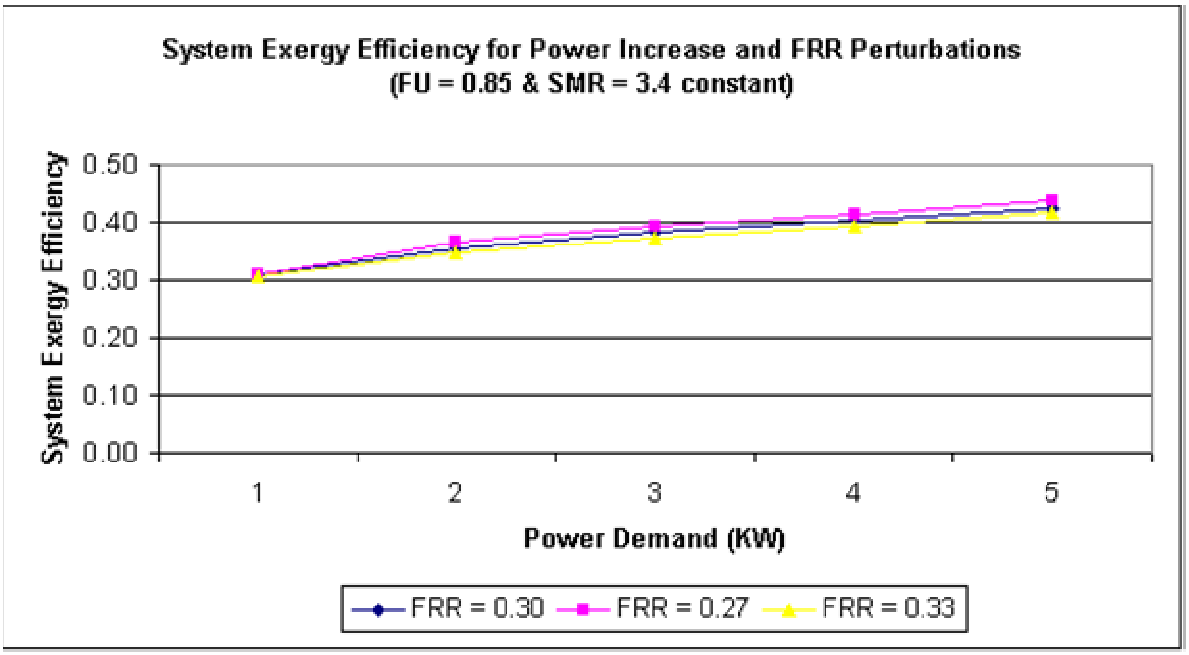

Increasing the Fuel Reformate Ratio from 0.30 to 0.33, leads to a slight decrease in System Energy Efficiency. Decreasing the Fuel Reformate Ratio to 0.27 on the other hand increases the System Energy Efficiency slightly. Hence, Fuel Reformate Ratio has an inverse effect on the System Energy Efficiency as regards to its increase or decrease.

For Power decreases :

FU Perturbation	System Energy Efficiency				
	Load (5 KW)	Load (4 KW)	Load (3 KW)	Load (2 KW)	Load (1 KW)
FU 0.85 SMR 3.4 FRR 0.30	0.417056	0.395426	0.373439	0.346925	0.308846
FU 0.70 SMR 3.4 FRR 0.30	0.347167	0.327967	0.307459	0.282602	0.249020
FU 0.90 SMR 3.4 FRR 0.30	0.443724	0.417933	0.395331	0.369624	0.333140

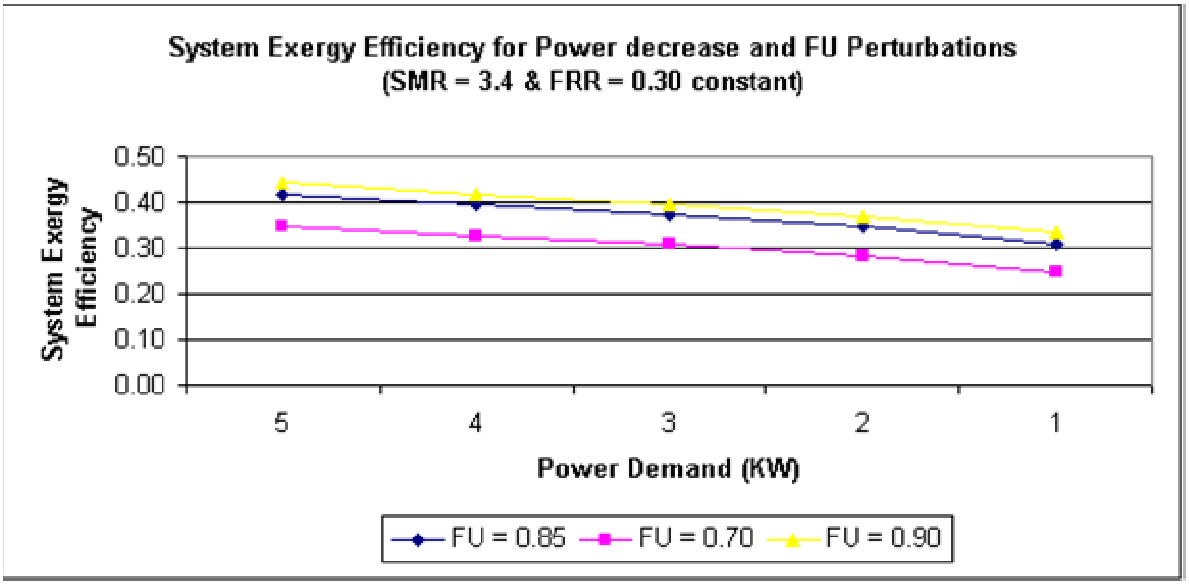

Raising the Fuel Utilization from the pre-determined level of 0.85 to 0.90 increases the System Energy Efficiency and reducing it to 0.70 decreases it. But the reduction causes a steeper fall in the efficiency as compared with the increase.

SMR Perturbation	System Energy Efficiency				
	Load (5 KW)	Load (4 KW)	Load (3 KW)	Load (2 KW)	Load (1 KW)
FU 0.85 SMR 3.4 FRR 0.30	0.417056	0.395426	0.373439	0.346925	0.308846
FU 0.85 SMR 3.0 FRR 0.30	0.415096	0.389537	0.367514	0.342294	0.304643
FU 0.85 SMR 3.8 FRR 0.30	0.427323	0.398747	0.378058	0.352154	0.313491

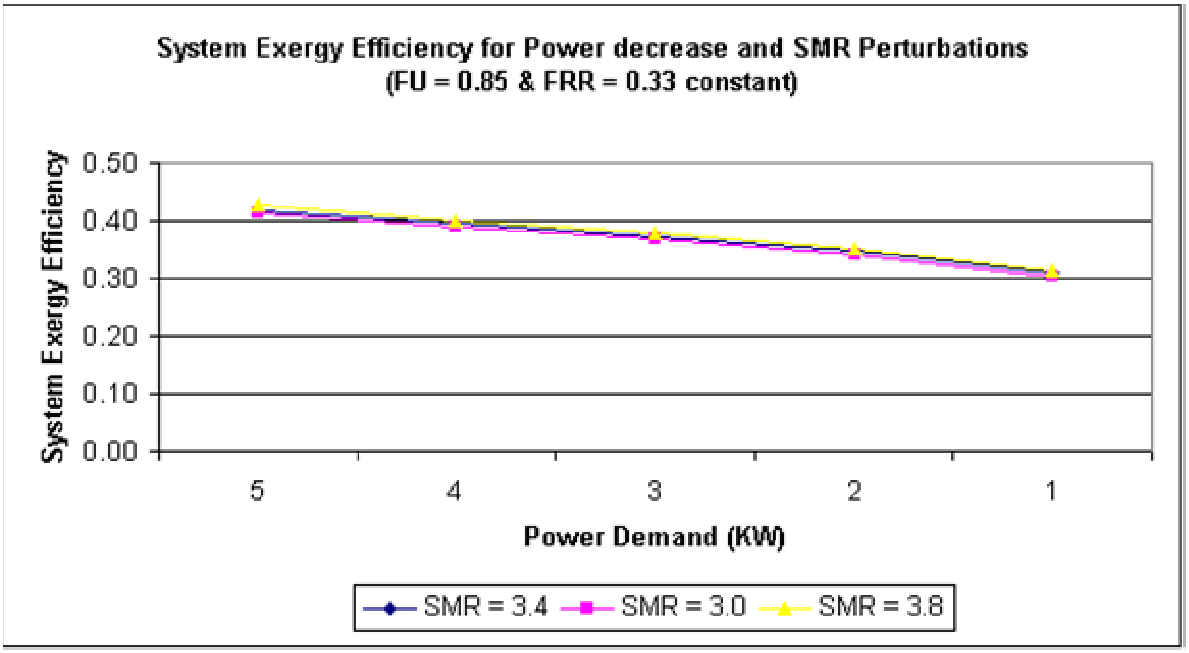

Increase or decrease in Steam to Methane Ratio does not affect the System Energy Efficiency by a great magnitude. Hence we can infer that for load decreases, Steam to Methane Ratio plays a relative subdued role as regards to System Energy Efficiency.

FRR Perturbation	System Energy Efficiency

	Load (5 KW)	Load (4 KW)	Load (3 KW)	Load (2 KW)	Load (1 KW)
FU 0.85 SMR 3.4 FRR 0.30	0.417056	0.395426	0.373439	0.346925	0.308846
FU 0.85 SMR 3.4 FRR 0.27	0.427323	0.404321	0.383445	0.359022	0.321794
FU 0.85 SMR 3.4 FRR 0.33	0.415801	0.385356	0.364327	0.337783	0.302219

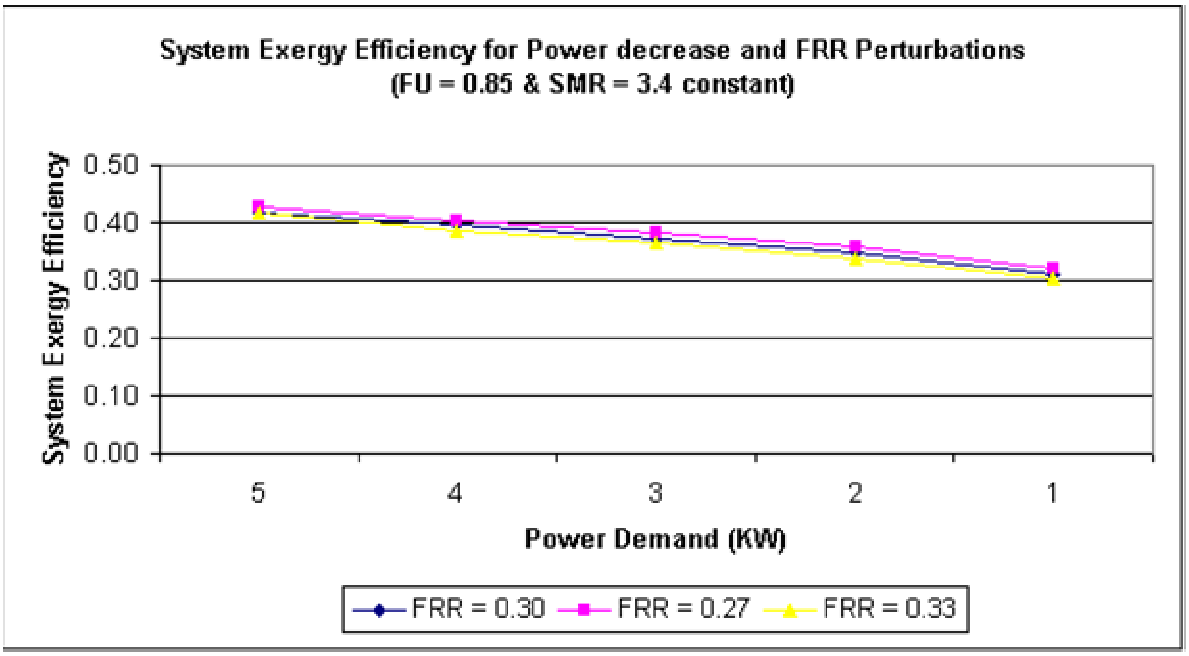

Increasing the Fuel Reformate Ratio from 0.30 to 0.33, leads to a slight decrease in System Energy Efficiency. Decreasing the Fuel Reformate Ratio to 0.27 on the other hand increases the System Energy Efficiency slightly. Hence, Fuel Reformate Ratio has an inverse effect on the System Energy Efficiency as regards to its increase or decrease.

Appendix C.3 PARAMETRIC ANALYSIS #3 OF THE SOFC BASED APU

In the series of parametric studies that have been performed, the emphasis was to determine the effects of perturbations of the system level parameters such as fuel utilization, steam to methane ratio, fuel reformate ratio and air to fuel ratio on the overall system behavior. The effects of these perturbations on the SOFC based APU's overall performance such as the system thermal and energy efficiencies; stability times for temperature and flow rate at the various components of the system are the main cases for study in performing these parametric studies.

In Parametric Analysis 1, for load variations, which are application dependent, the system level parameters were modified and the effect of these variations on the system efficiencies and stability times of the system components were tabulated and analyzed. In Parametric Analysis 2, the load perturbances were introduced along with the system level parameter perturbances and their co-joint effect on the overall performance of the system was observed and studied.

For the Parametric Analysis 3, instead of fixing values for the system parameters, one allows them to float for small load variations. This will allow gauging the impact of floating the system parameters when small power changes are necessitated during the operation of the SOFC based APU. In this parametric study, one fixes the values of the system level parameters such as steam to methane ratio (3.40), fuel reformate ratio (0.30) and air to fuel ratio (20) at their pre-determined level, allowing only the fuel utilization to float. The value of fuel utilization on the other hand depends upon the total amount of hydrogen (H2_Total) entering the SOFC stack subsystem. Hence, in order to allow the value of fuel utilization to float, the amount of the total hydrogen entering the stack subsystem is fixed. One then proceeds to subsequently increment and decrement the net power value in steps of 100 watts from an initial net power (IP), with the total hydrogen value fixed at the initial net power. Based on these perturbances, their effects on the system efficiencies; stability times for temperature and mass flow are observed.

The initial (pre-determined) values of system level parameters in the model (gPROMS code) are as follows: Steam to Methane ratio - 3.40, Fuel Reformate ratio - 0.30, Air to Fuel ratio – 20 and Fuel Utilization – 0.85. In Parametric Analysis 3, one analyses the effect of floating a system level parameter (i.e. Fuel Utilization) to small power changes. Instead of fixing values for the system parameters, one allows them to float for small load variations. This will allow gauging the impact of floating the system parameters when small power changes are necessitated during the operation of the SOFC based APU. In this parametric study, fixing the values of the system level parameters such as Steam to Methane ratio, Fuel Reformate ratio and Air to Fuel ratio at their initial (pre-determined) values, one allows for the value of Fuel Utilization to float. The value of fuel utilization on the other hand depends upon the total amount of hydrogen (H2_Total) entering the SOFC stack subsystem. Hence, in order to allow the value of fuel utilization to float, the amount of the total hydrogen entering the stack subsystem is fixed. One then proceeds to subsequently increment and decrement the net power value in steps of 100 watts from an initial net power, IP (in this case IPs are 1000 watts, 2000 watts,…, 5000 watts), with the total hydrogen value fixed at the initial net power value. Based on these small power perturbances, the effects on the system efficiencies, stability times for temperature and mass flow are observed, tabulated and analyzed.

SUMMARY: What is done in Parametric Analysis 3?

- Load variations are done in small steps of 100 watts from an initial net power (IP). The initial net power values chosen are 1000W, 2000W, 3000W, 4000W and 5000W.
- The amount of the total hydrogen at these initial net power values is kept fixed. The values of H2_Total at each of the IPs are:
- 1000W : 1.00030e-005 Kmol/sec
- 2000W : 1.77030e-005 Kmol/sec
- 3000W : 2.46790e-005 Kmol/sec
- 4000W : 3.10605e-005 Kmol/sec
- 5000W : 3.67564e-005 Kmol/sec
- The above values refer to the total hydrogen values that the Fuel Cell stack requires to produce the respective initial net power. These values of total H2 at their IPs are fixed and small load variations are introduced allowing Fuel Utilization to float.
- With these fixed hydrogen values, small load variations (in steps of 100W) are introduced. Both increasing and decreasing load variations from the initial power value are done.
- The value of fuel utilization, which is fixed at 0.85 at the initial power value, is allowed to float during every load variation introduced.
- The maximum power that a fixed fuel (hydrogen) rate can sustain from an initial power value is a point of interest in this analysis. Also, the minimum power that the same fuel rate can sustain is also noted.
- The stability times of the components of the SOFC based APU as regards to the molar flow rate and temperature through them is also recorded and used for further analysis of the system.

The different components of the SOFC based APU taken into consideration in the analysis and their respective streams (given in brackets) are given below:

1. Pre-reformer (streams 5 and 6)
2. Combustor (stream 16)
3. Steam generator (streams 2 and 22)
4. Air Compressor (stream 27)
5. Gas Expander (stream 13)
6. Air Combustion Gas Mixer (stream 18)
7. Methane Compressor (stream 24)
8. Heat Exchanger I (stream 8)
9. Heat Exchanger II (streams 9 and 11)
10. Heat Exchanger III (streams 1 and 19)
11. Heat Exchanger IV (streams 12 and 26)

The analysis is done graphically for the range of powers that were possible for the fixed hydrogen amount at the different initial net powers. Graphs were drawn for the power ranges with respect to the changes in the fuel utilization value, system thermal and energy efficiency, time for stable temperature and molar flow rate for each component and the streams taken into consideration.

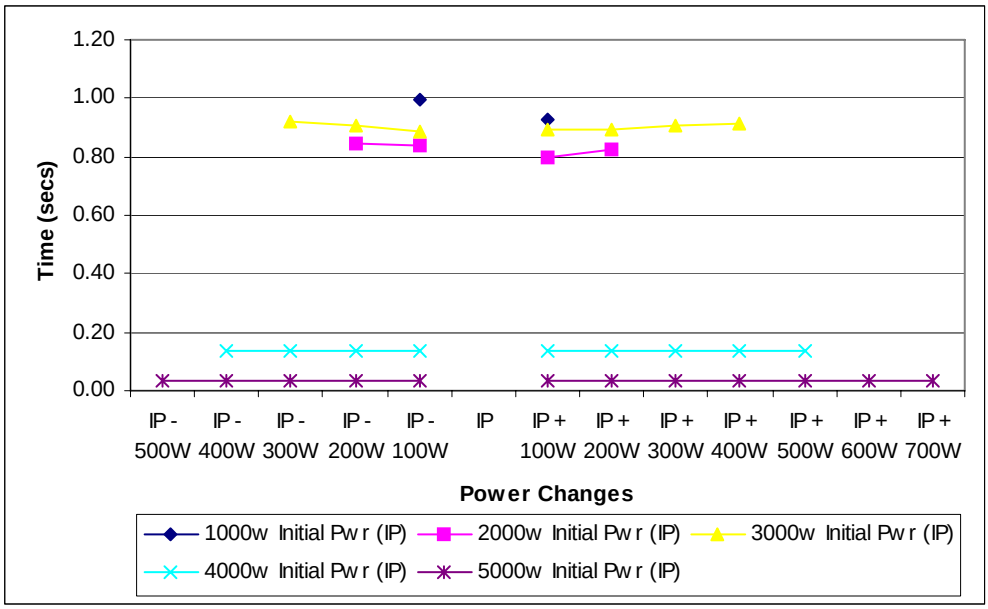

Air Compressor Thermal Transient Response for small Power changes for constant H2 at IP (Stream 27)

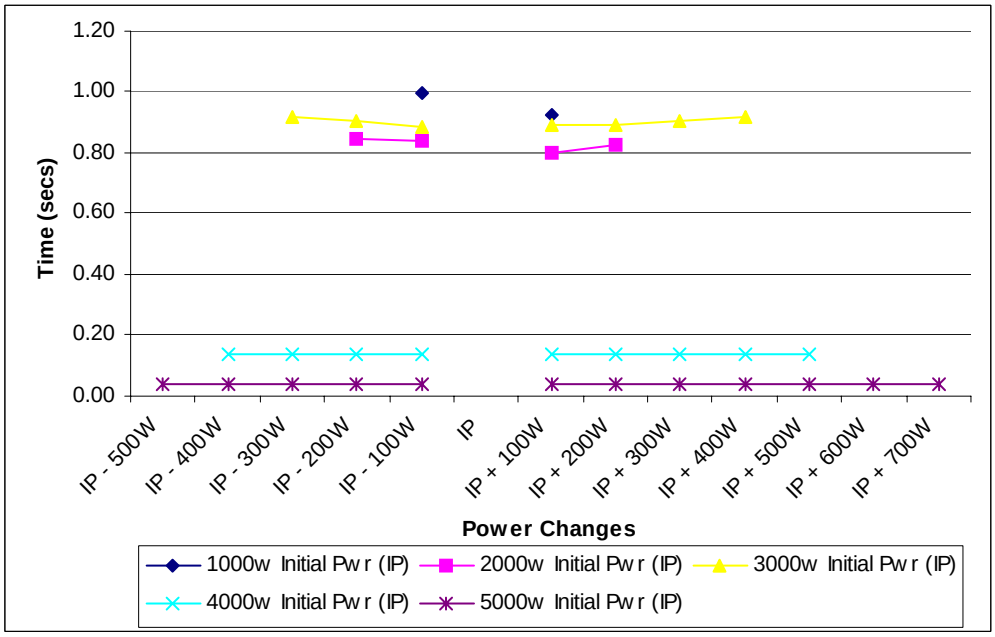

Air Compressor Thermal Transient Response for small Power changes for constant H2 at IP (Stream 13)

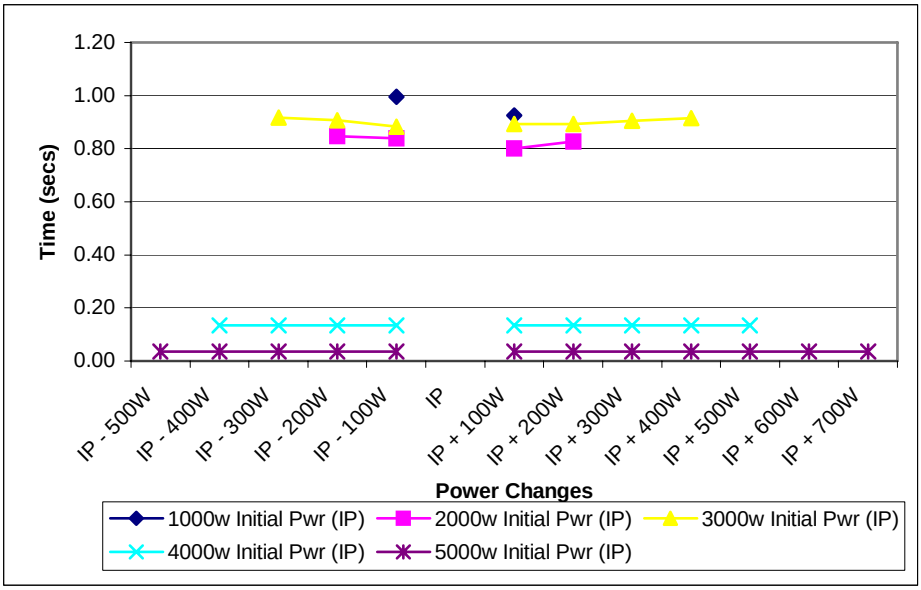

Gas Expander Thermal Transient Response for small Power changes for constant H2 at IP (stream 18)

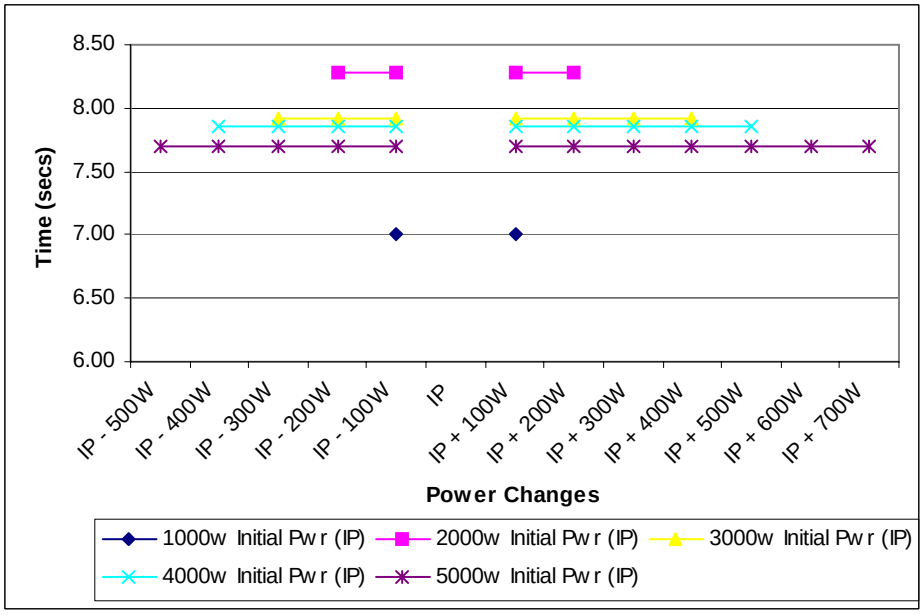

Pre-reformer Thermal Transient Response for small Power changes for constant H2 at IP (stream 5)

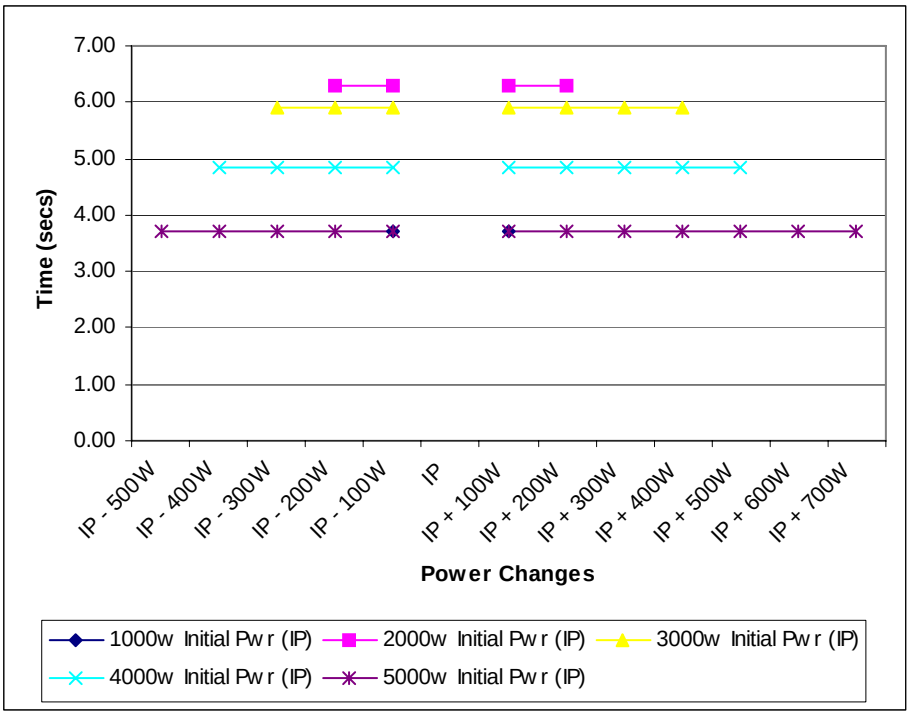

Pre-reformer Thermal Transient Response for small Power changes for constant H2 at IP (stream 6)

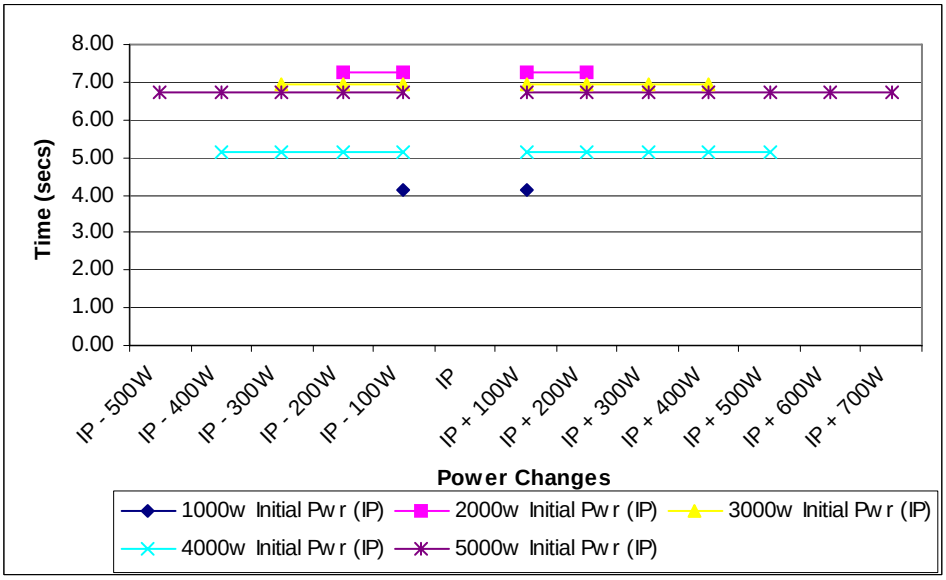

Combustor Thermal Transient Response for small Power changes for constant H2 at IP (stream 16)

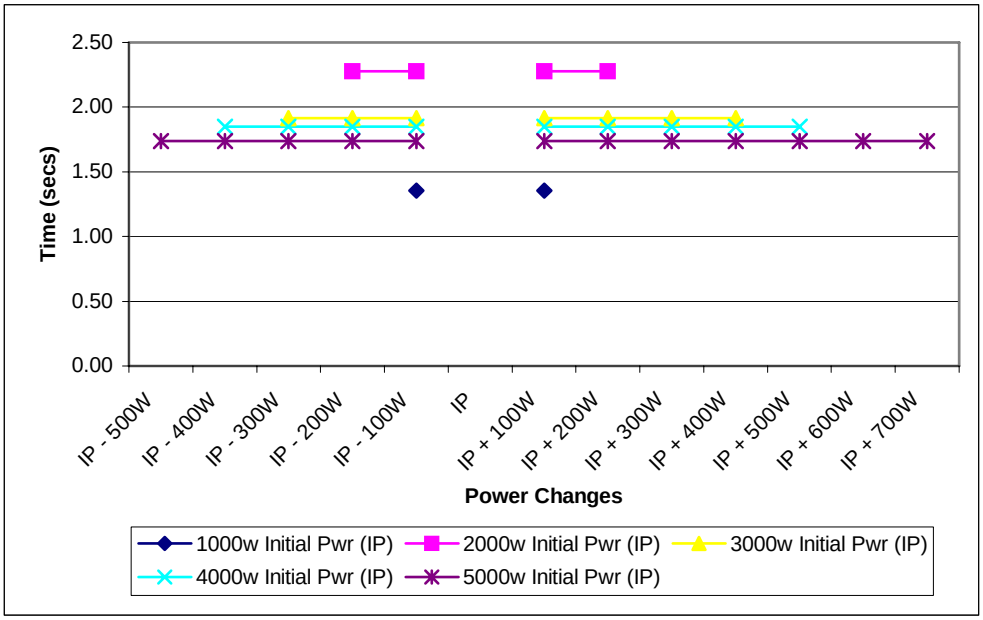

Steam Generator Thermal Transient Response for small Power changes for constant H2 at IP (stream 2)

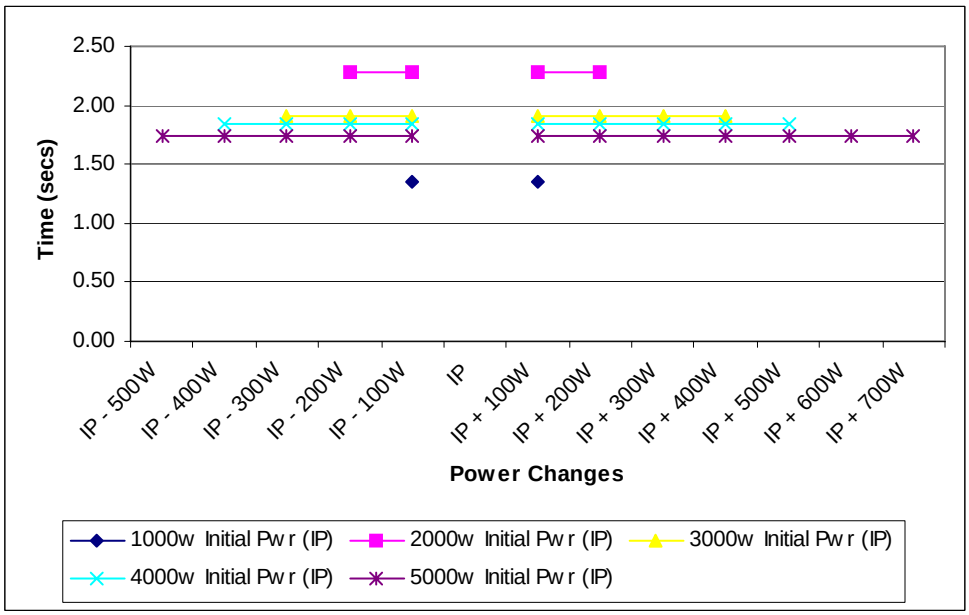

Steam Generator Thermal Transient Response for small Power Change for constant H2 at IP (stream 22)

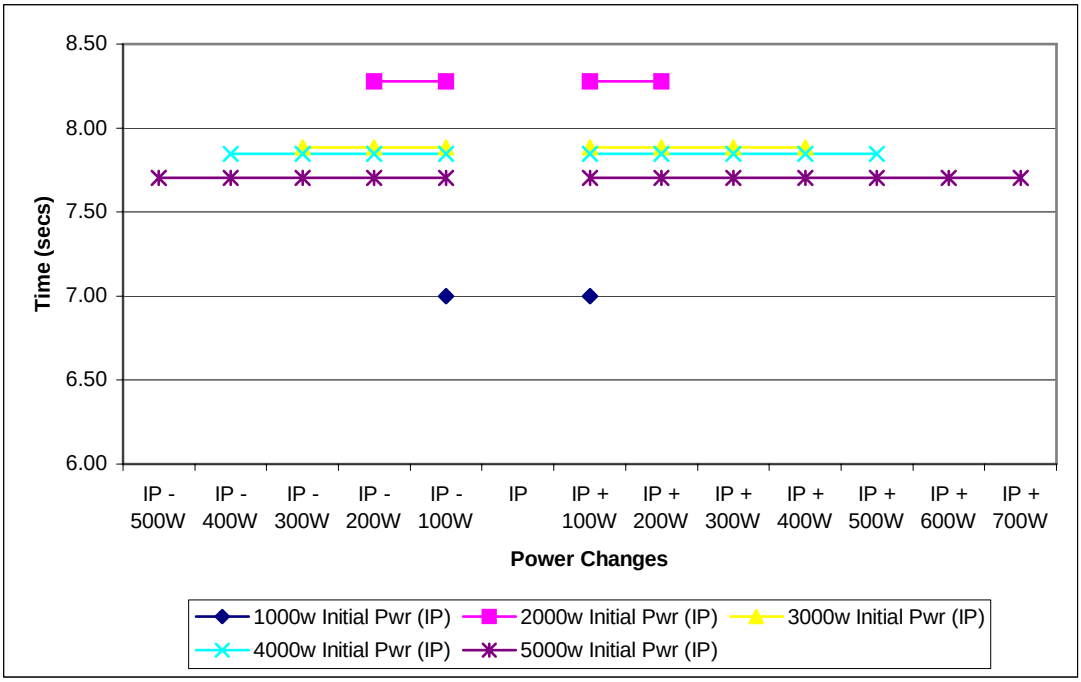

HXI Thermal Transient Response for small Power changes for constant H2 at IP (stream 8)

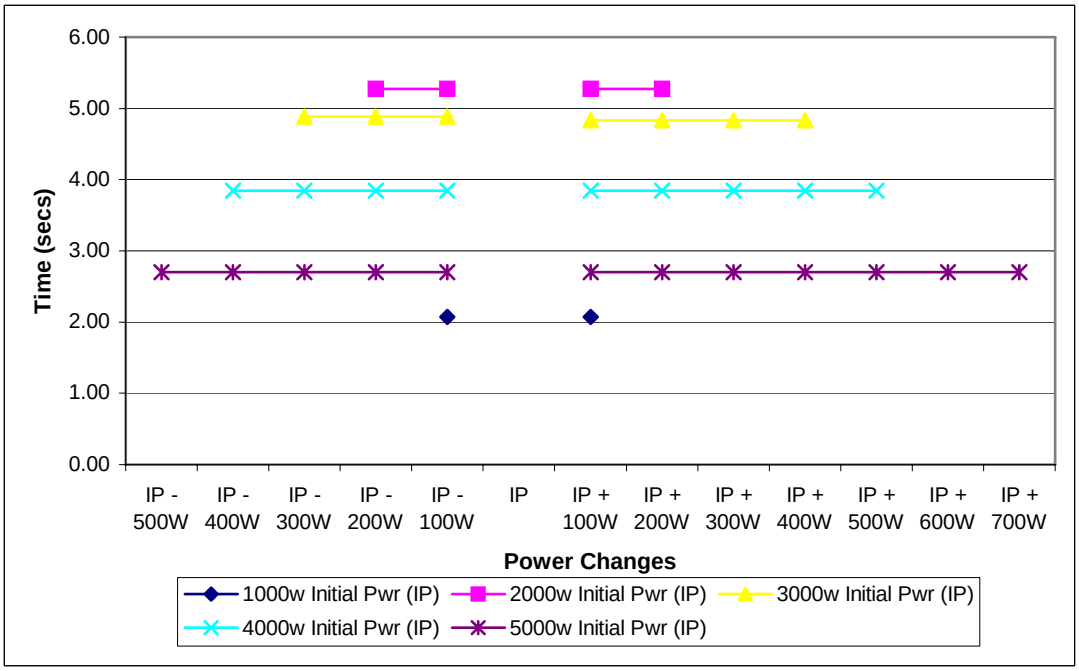

HXII Thermal Transient Response for small Power changes for constant H2 at IP (stream 19)

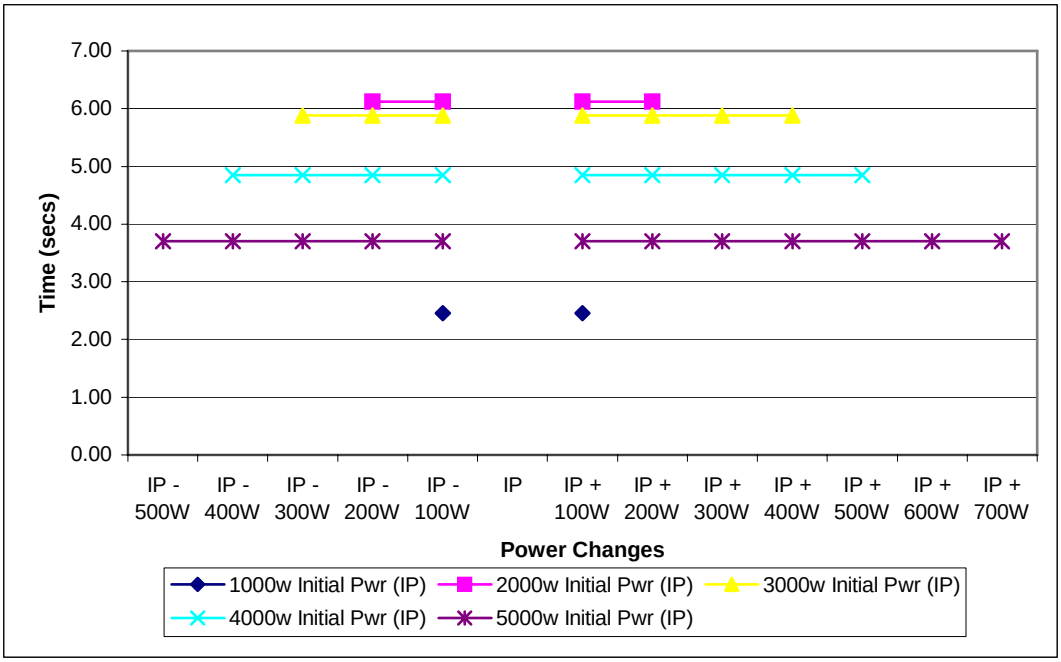

HXIV Thermal Transient Response for small Power changes for constant H2 at IP (stream 26)

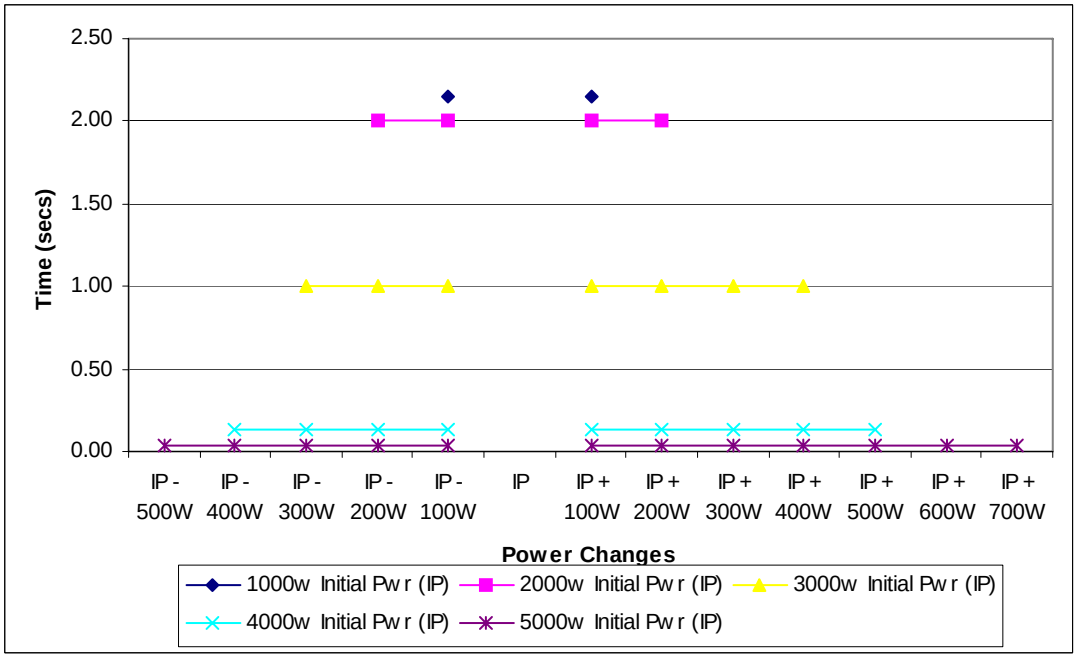

Air Compressor Flow rate Transient Response for small Power changes for constant H2 at IP (stream 27)

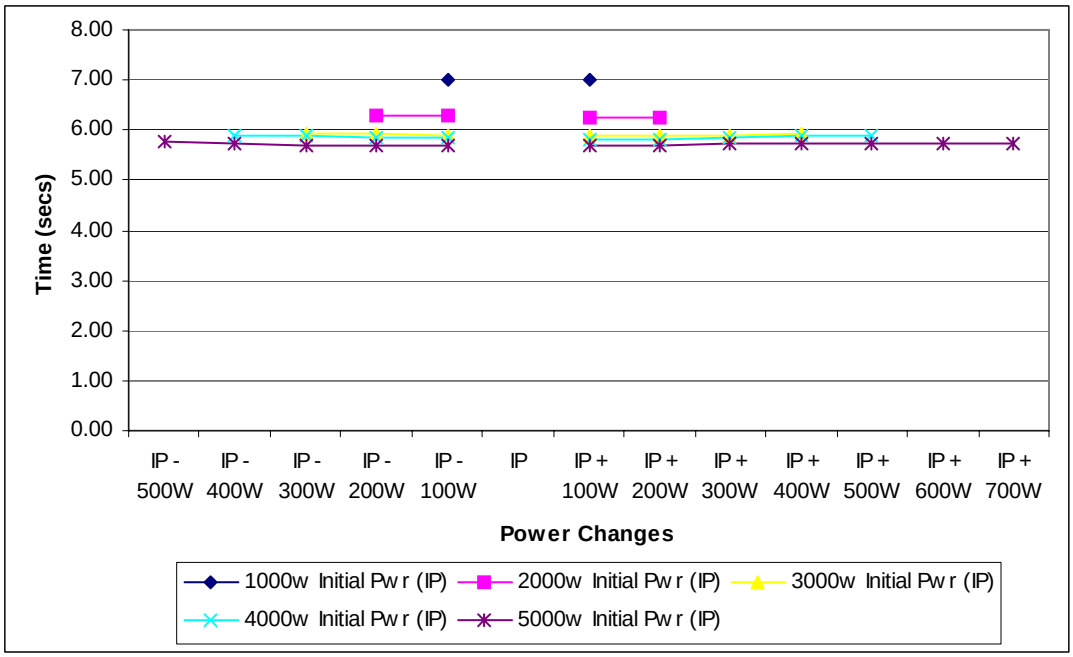

Gas Expander Flow rate Transient Response for small Power changes for constant H_2 at IP (stream 13)

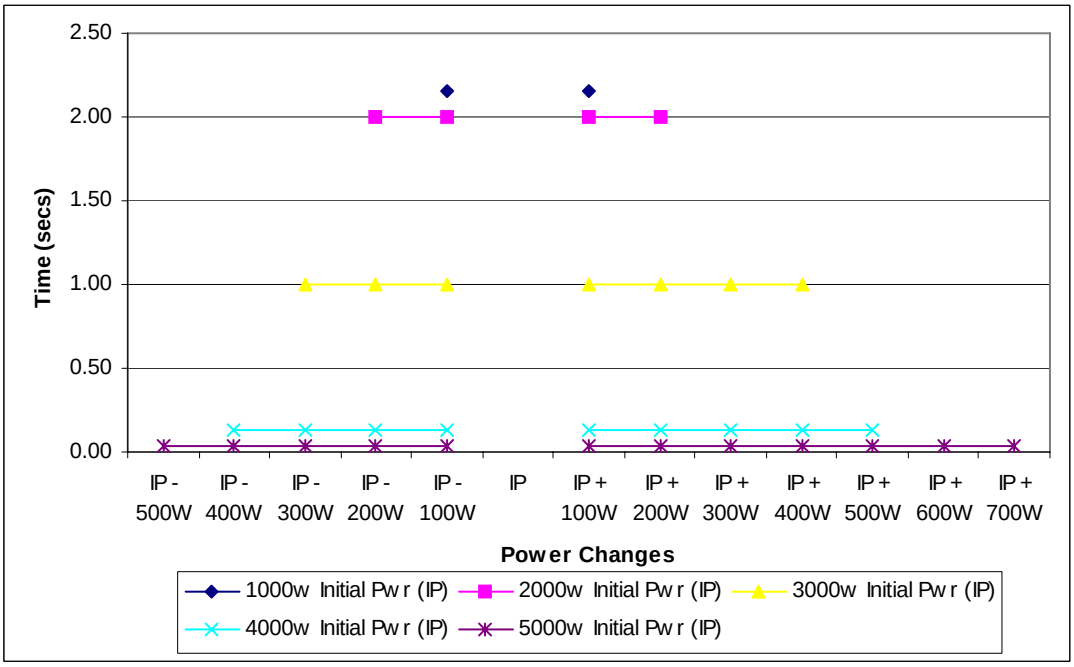

Air Comb. Gas Mixer Flow rate Transient Response for small Power changes for constant H_2 at IP (stream 18)

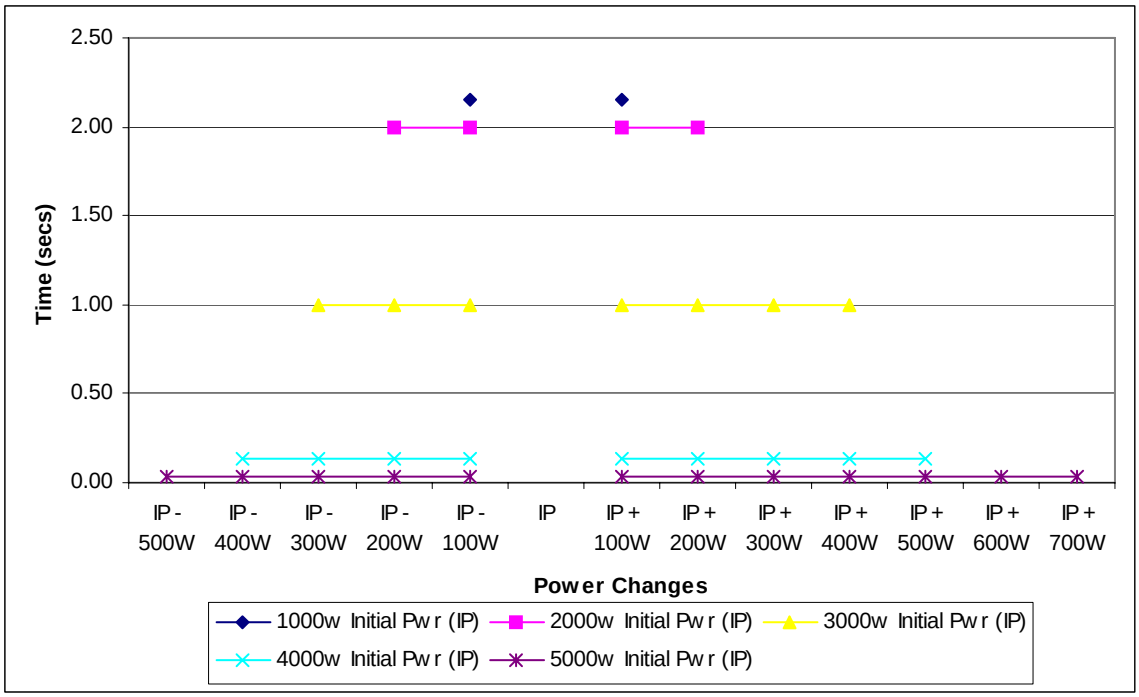

HXII Flow rate Transient Response for small Power changes for constant H_2 at IP (stream 9)

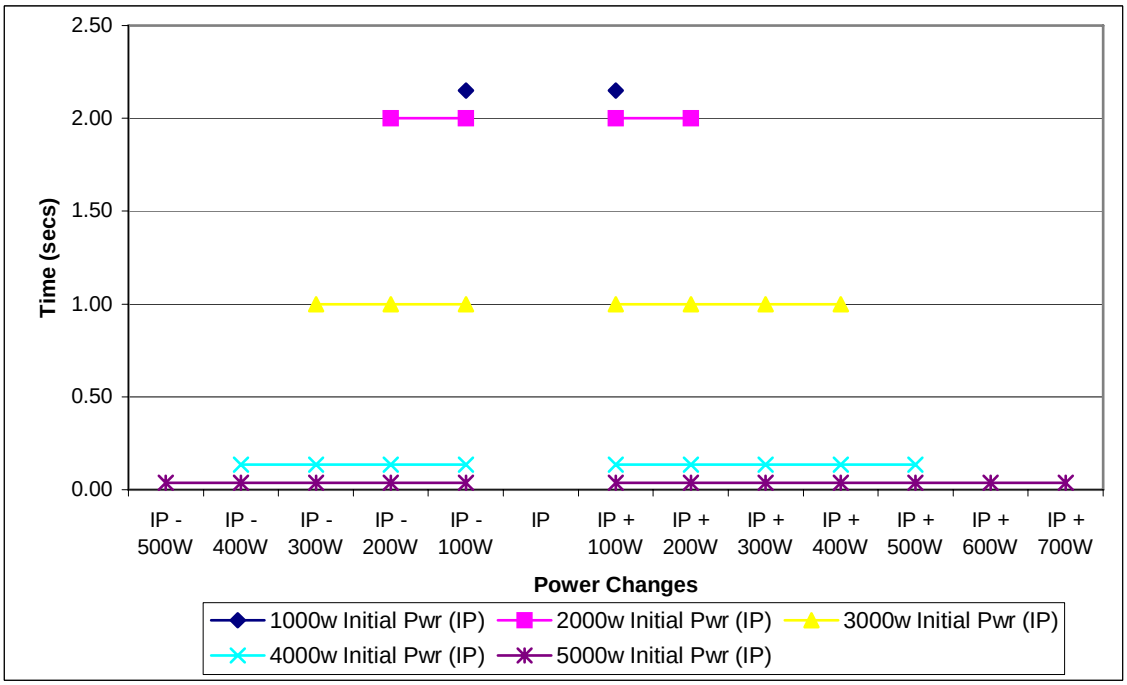

HXII Flow rate Transient Response for small Power changes for constant H_2 at IP (stream 11)

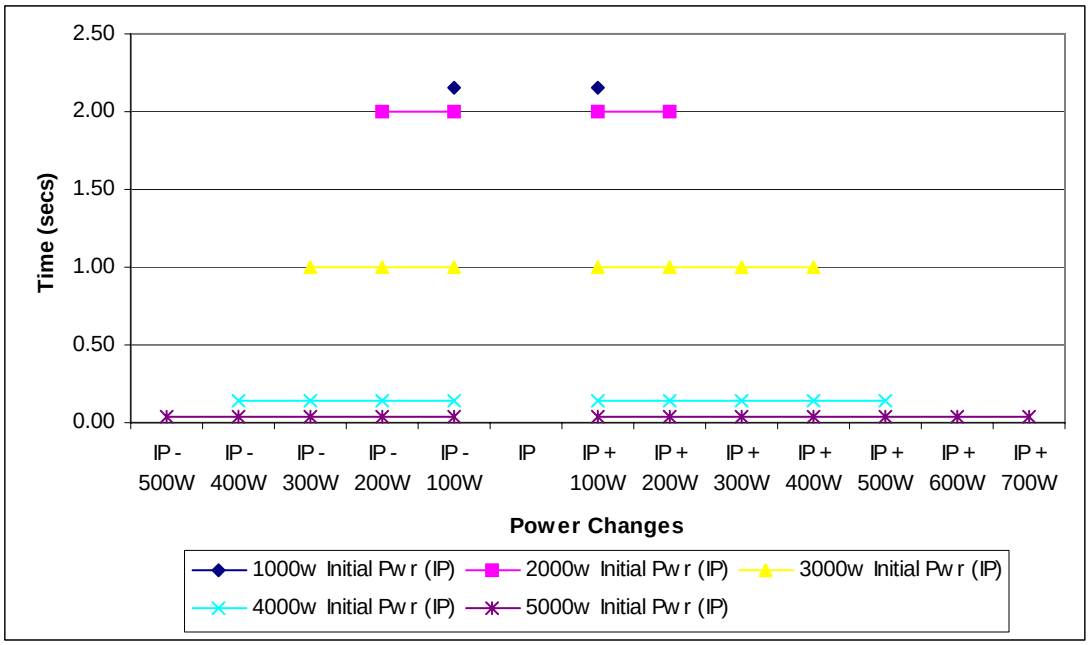

HXIV Flow rate Transient Response for small Power changes for constant H_2 at IP (stream 12)

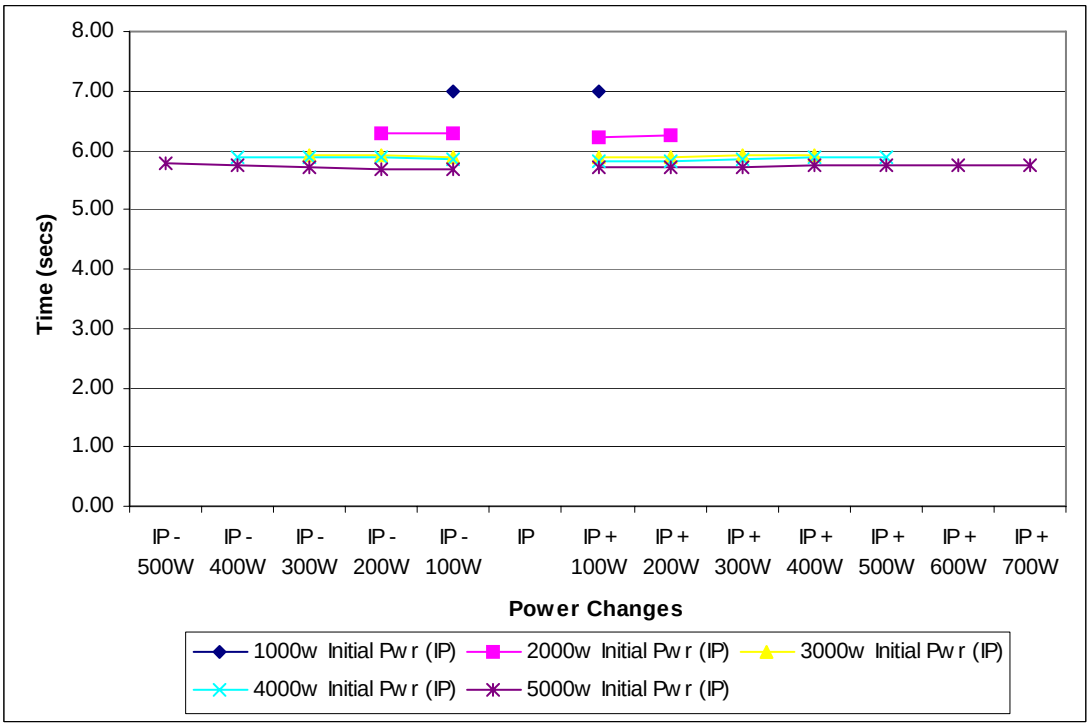

HXIV Flow rate Transient Response for small Power changes for constant H_2 at IP (stream 26)

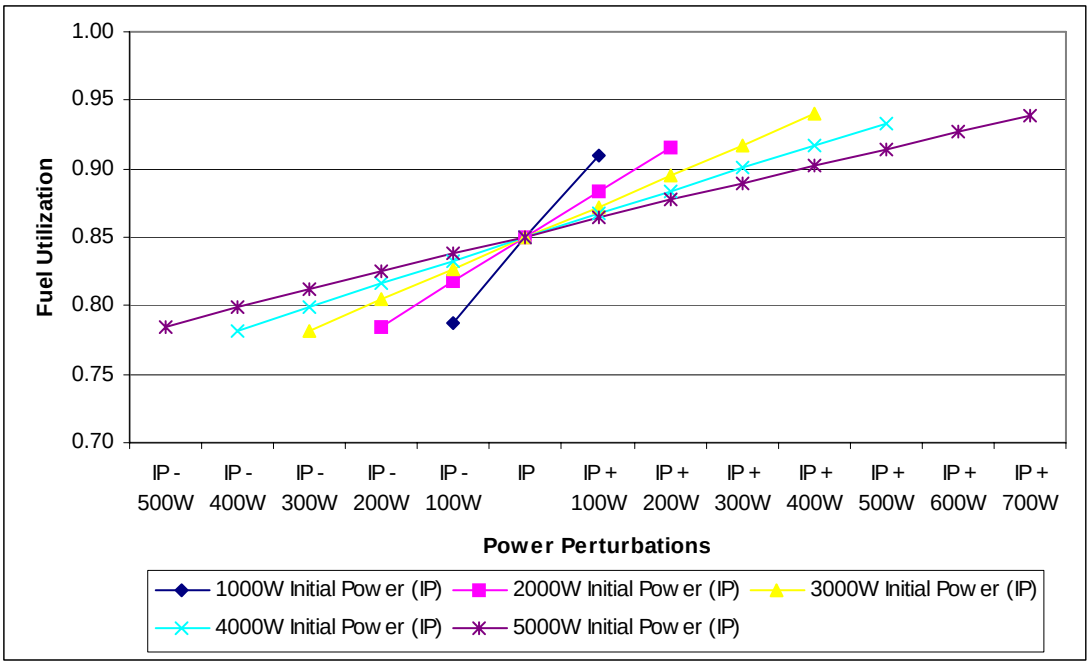

Fuel Utilization Changes for small power changes for constant H_2 at IP

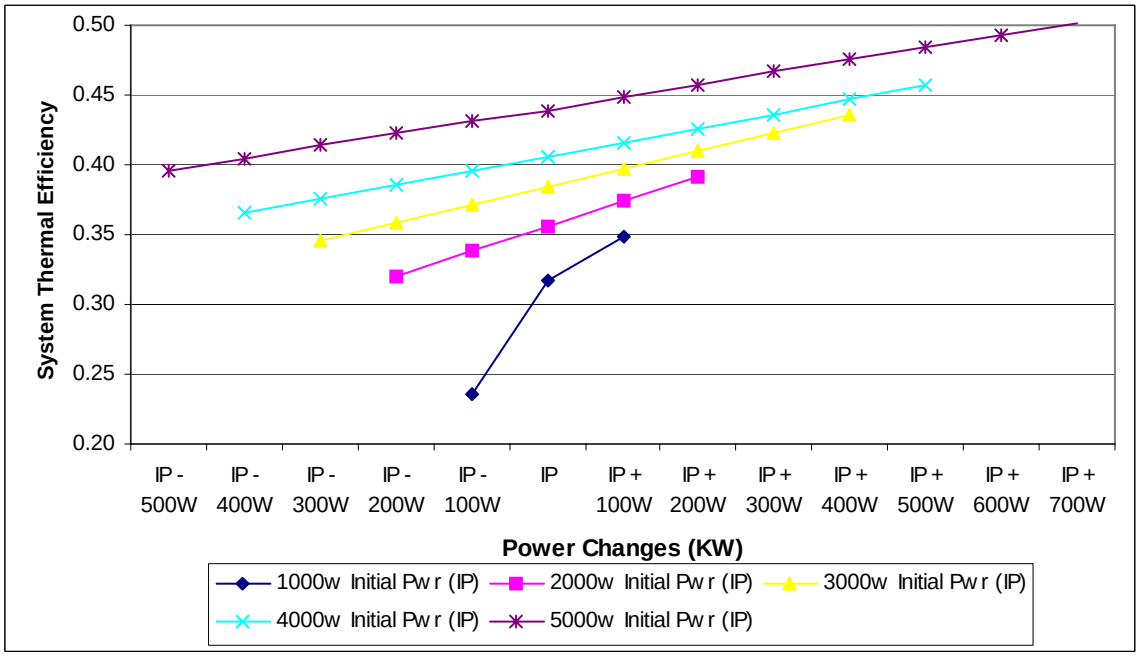

System Thermal Efficiencies for small power changes for constant H_2 at IP

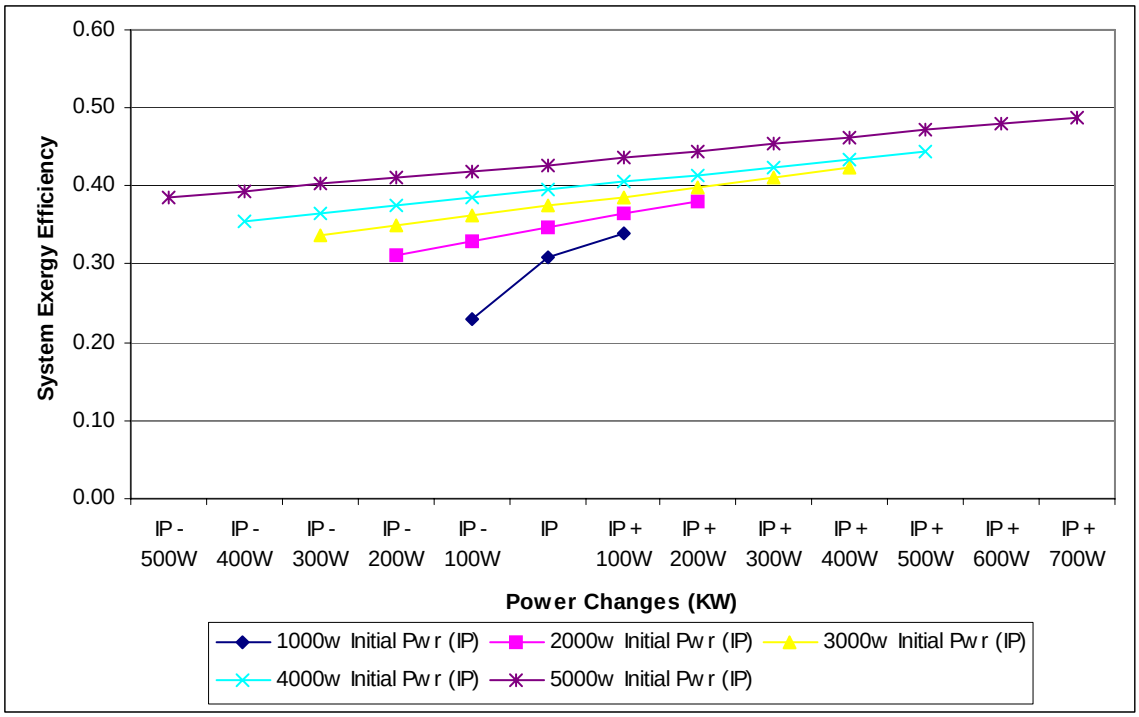

System Energy Efficiency for small power changes for constant H_2 at IP

Appendix C.4 PARAMETRIC ANALYSIS #4 OF THE SOFC BASED APU

This is the final analysis in the series of parametric analysis that was performed. In this parametric study the primarily concentration was on the Pre-reformer component. The previous three parametric studies had shown that the Pre-reformer to be the component leading to extended system stabilization times, thus this interest.

In this parametric study, temperature control effects on the Pre-reformer temperature, mass flow stabilization times and system thermal and energy efficiencies were studied. The Pre-reformer component has four streams: Inlet steam-methane stream (3), Outlet steam-methane stream (5), Inlet combustion gas stream (4) and Outlet combustion gas stream (6) associated with it. The inlet combustion gas stream is used to heat up the inlet steam-methane stream entering the Pre-reformer. The outlet combustion gas stream is in turn used to pre-heat the inlet methane to the system at Heat exchanger III, steam in the Steam generator and the air at Heat exchanger IV. This parametric study is divided into 5 segments:

Analysis 4a: Perturbation of the inlet combustion gas stream temperature, T4.

Analysis 4b: Perturbation of the inlet steam-methane temperature, T3.

Analysis 4c: Perturbation of the inlet steam temperature.

Analysis 4d: Perturbation of molar flow rate of steam generator inlet combustion gas stream, F3.

The effects of the 4 above-mentioned perturbations on the Pre-reformer streams are analyzed and inferences derived.

Analysis 4a –

Here the inlet combustion gas stream temperature, T4 is perturbed. The rest of the temperatures of the streams of the Pre-reformer are dependent on T4.

As per the gPROMS code, the value for T4 is fixed at a value of 1200K. The effects on temperature and mass flow stabilization times for the remaining three streams and the system thermal and energy efficiencies for changes in T4 is analyzed graphically. The values of T4 considered are: 1120K, 1150K, 1200K, 1300K, 1400K, 1500K, 1550K and 1570K. The effects of this temperature perturbation are summarized below.

Temperature Transient Response

Temperature transient response of streams 3, 5 and 6 (as mentioned above) for stream 4 temperature perturbations is observed for increasing and decreasing load variations. For different inlet combustion gas temperature variation, the temperature transient response times are noted. The objective is to maintain the inlet combustion gas temperature that will minimize the thermal transient response. A lower thermal response time would mean lowered thermal response time for the APU system as a whole as the Pre-reformer is the component taking the longer stabilization time in the system.

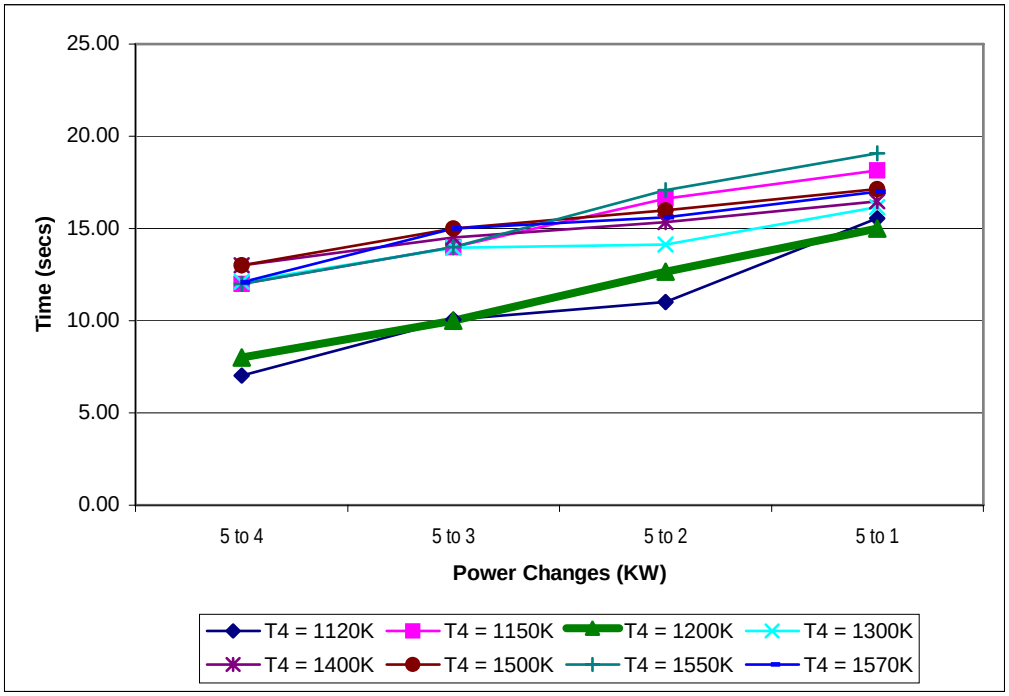

Thermal transient response of Pre-reformer Inlet Steam-Methane stream(3) for perturbations of inlet Gas stream temperature(T4) for Power decreases

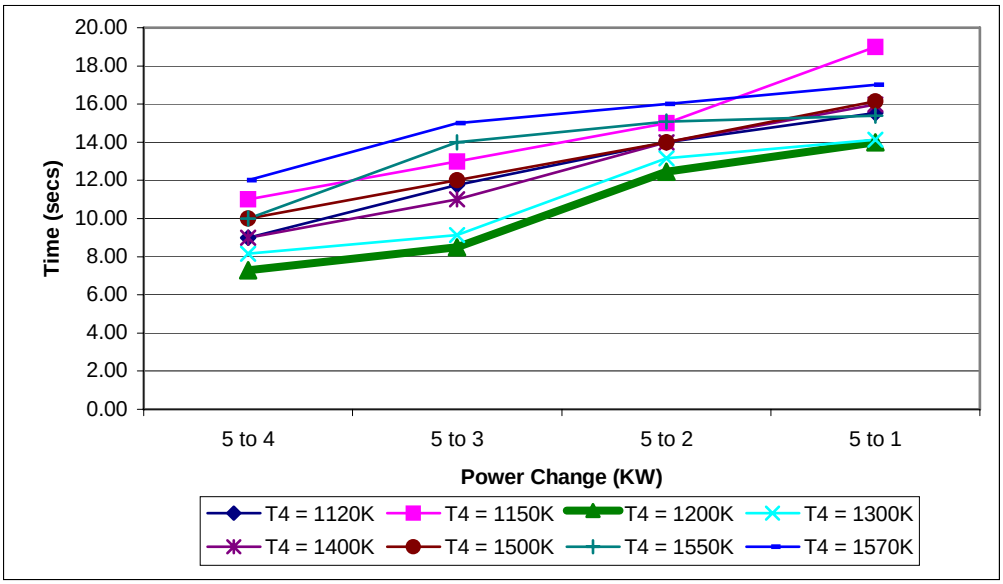

Thermal transient response of Pre-reformer Outlet Steam-Methane stream(5) for perturbations of Inlet Gas stream temperature(T4) for Power decreases

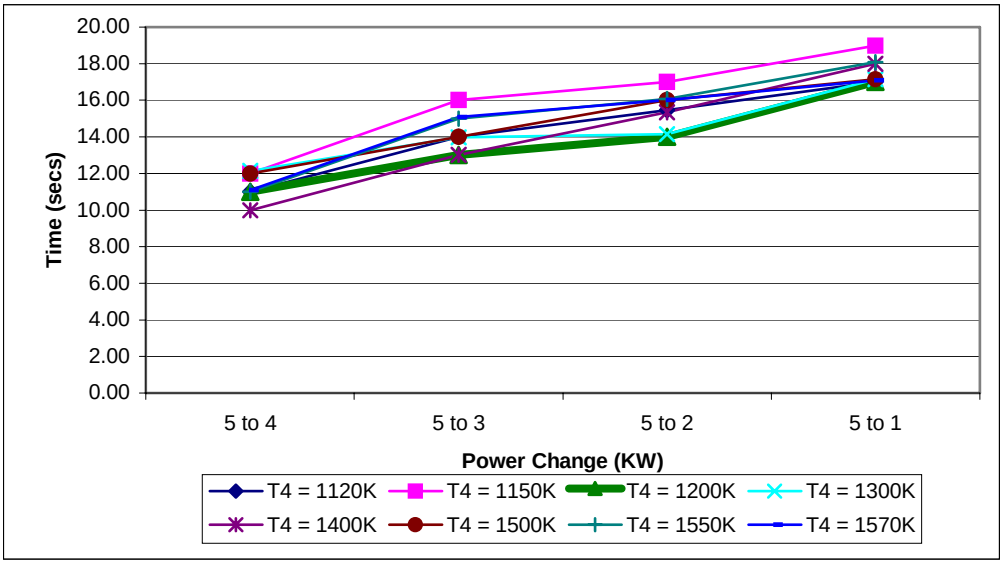

Thermal transient response of Pre-reformer Outlet Gas stream(6) for perturbations of Inlet Gas stream temperature(T4) for Power decreases

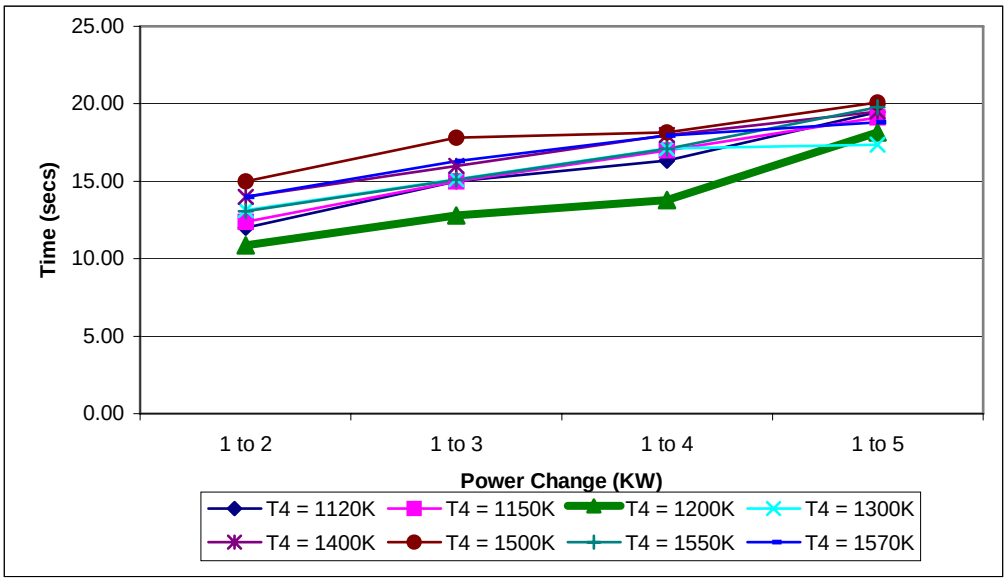

Thermal transient response of Pre-reformer Inlet Steam-Methane stream(3) for perturbations of Inlet Gas stream temperature(T4) for power increases

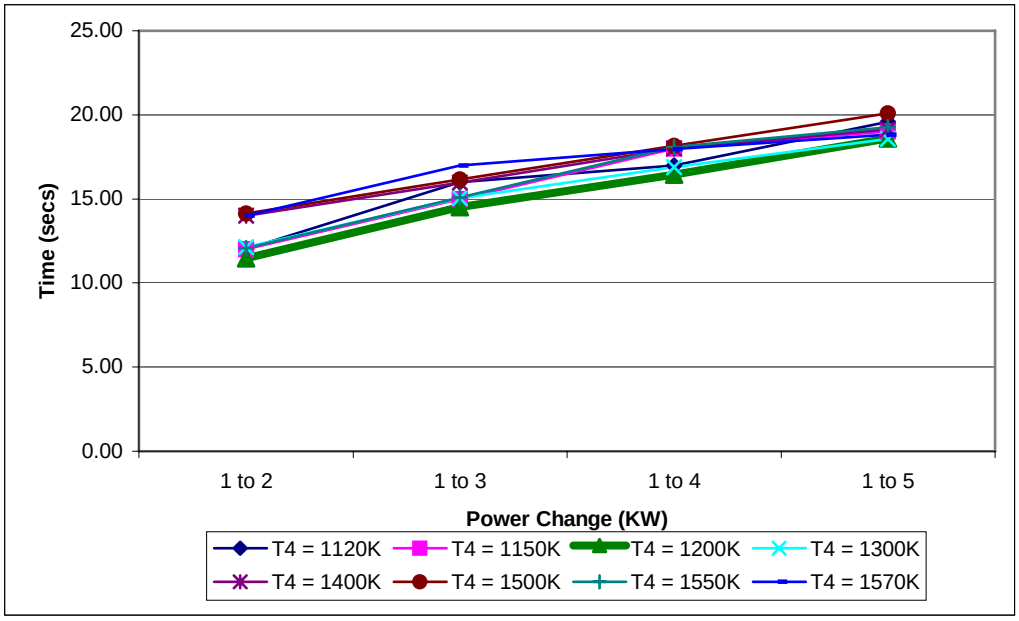

Thermal transient response of Pre-reformer Outlet Steam-Methane stream(5) for perturbations of Inlet Gas temperature(T4) for Power increases

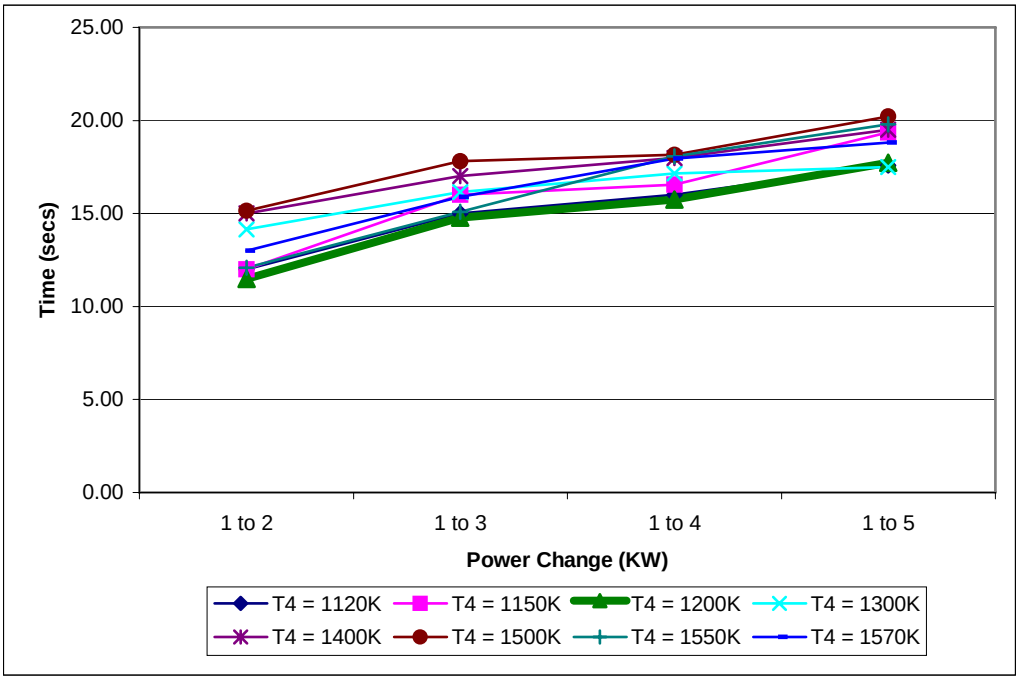

Thermal transient response of Pre-reformer Outlet Gas stream(6) for perturbations of Inlet Gas temperature (T4) for Power increases

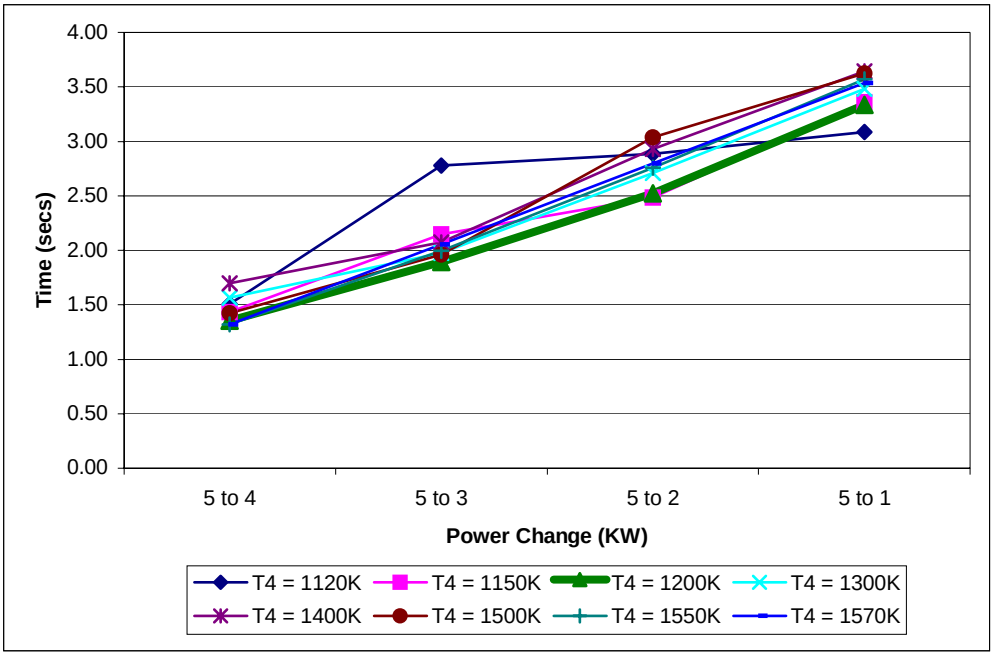

Molar Flow rate transient response for Pre-reformer Steam-Methane and Outlet Gas streams for perturbations of Inlet Gas stream temperature (T4) for Power decreases

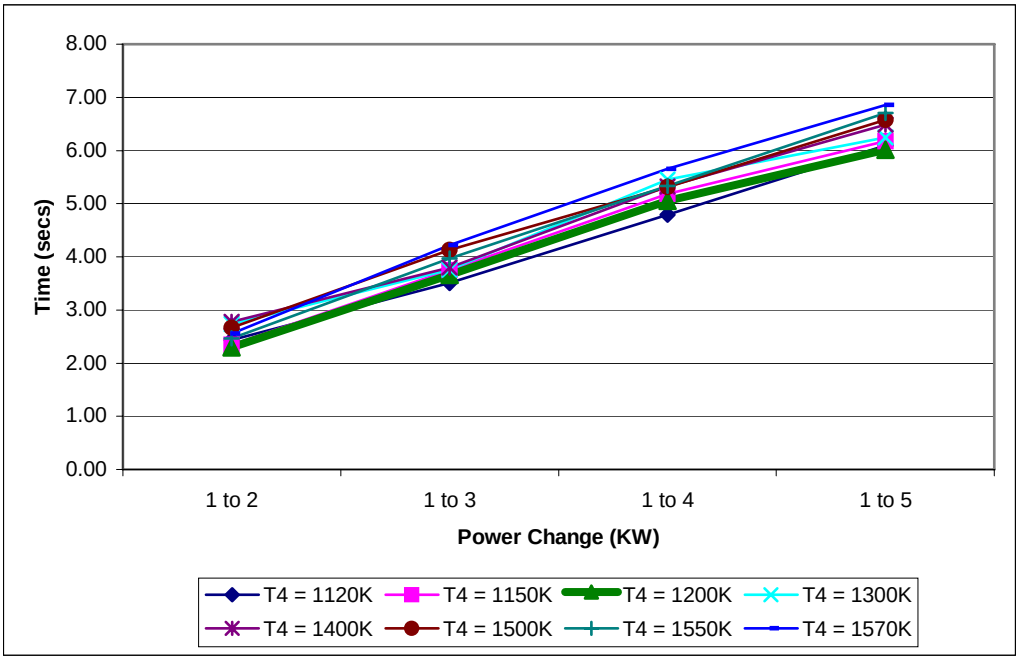

Molar Flow rate transient response for Pre-reformer Steam-Methane and Outlet Gas streams for perturbations of Inlet Gas stream temperature (T4) for Power increases

(P.T.O)

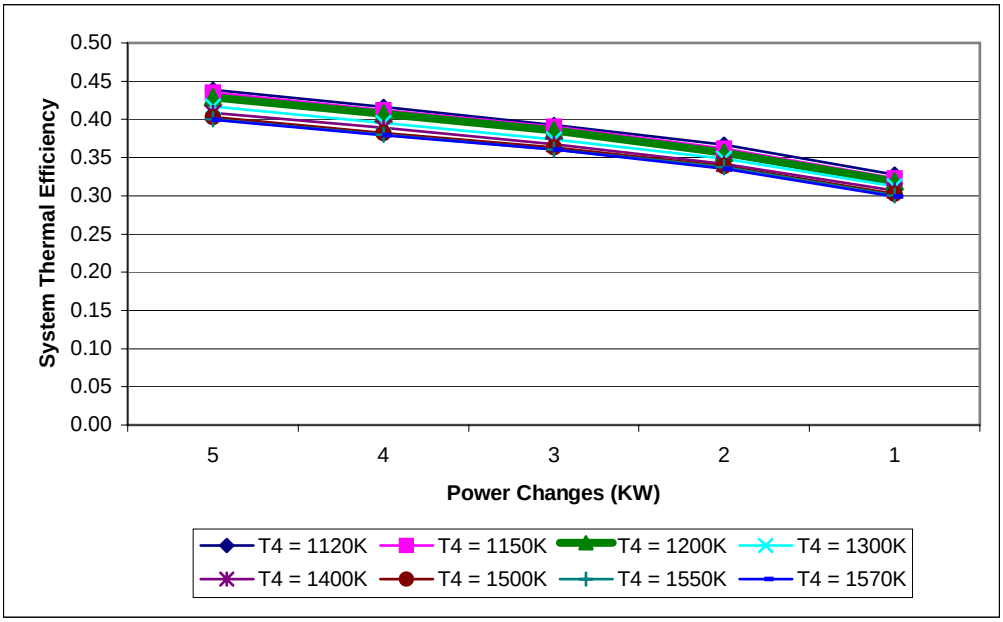

System Thermal Efficiency for Pre-reformer Inlet Gas temperature perturbations for Power decreases

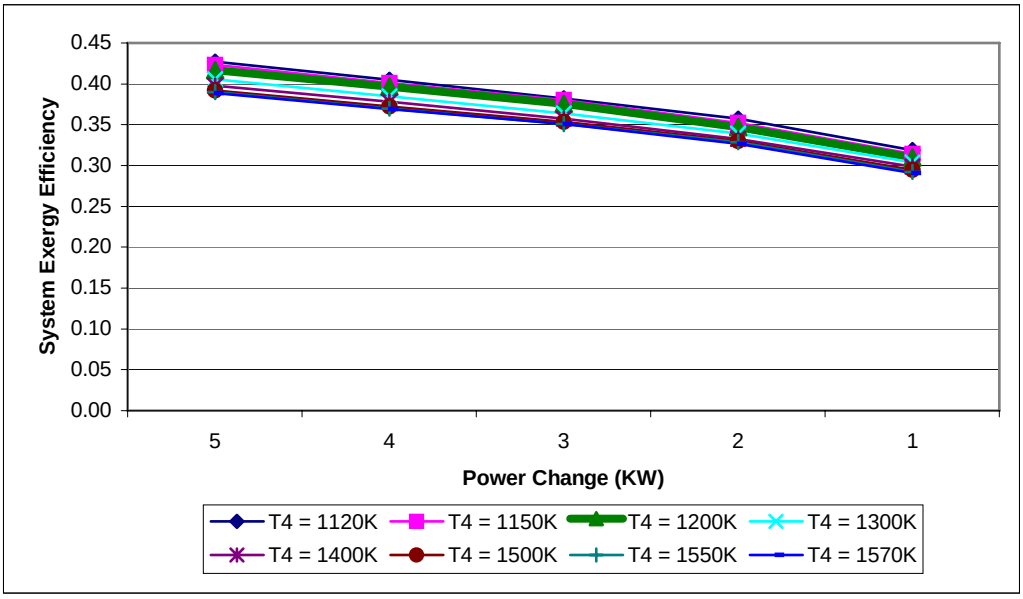

System Energy Efficiency for Pre-reformer Inlet Gas temperature perturbations for Power decreases

Analysis 4b –

In addition to varying the inlet combustion gas temperature, T4 (which was fixed initially at 1200K), one also tries to see the thermal, flow rate and efficiency responses of the Pre-reformer streams for fixed values of inlet steam-methane temperature, T3. The possible values for T3 keeping T4 constant at 1200K were 800K and 870K. The responses at these temperatures will be compared with the system where T3 is not fixed and T4 is fixed at 1200K. This will show the impact of fixing T3 on the responses. The analysis in this case is done similar to the previous analysis i.e. for both increasing and decreasing power.

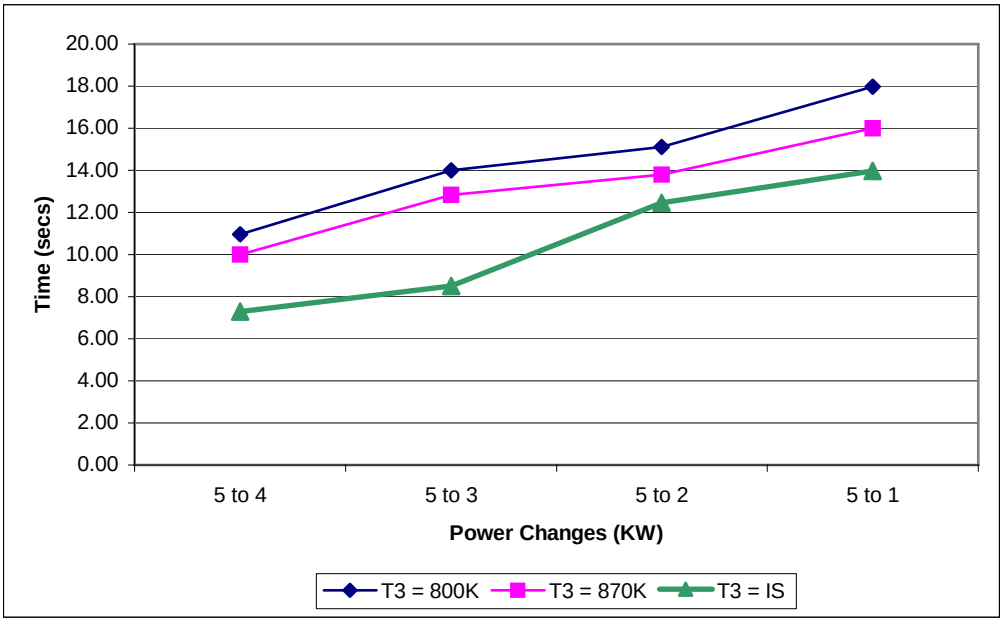

Thermal transient response of Pre-reformer Outlet Steam-Methane stream(5) for perturbations of the Inlet Steam-Methane stream(3) temperature for Power decreases

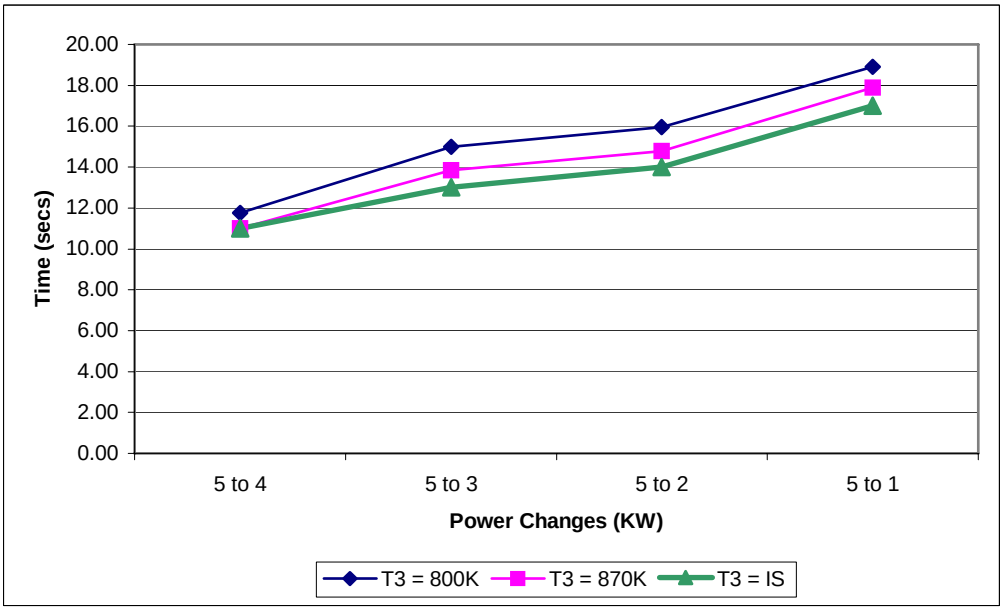

Thermal Transient response of Pre-reformer Outlet Gas stream(6) for perturbations of the Inlet Steam-Methane stream(3) temperature for power decreases

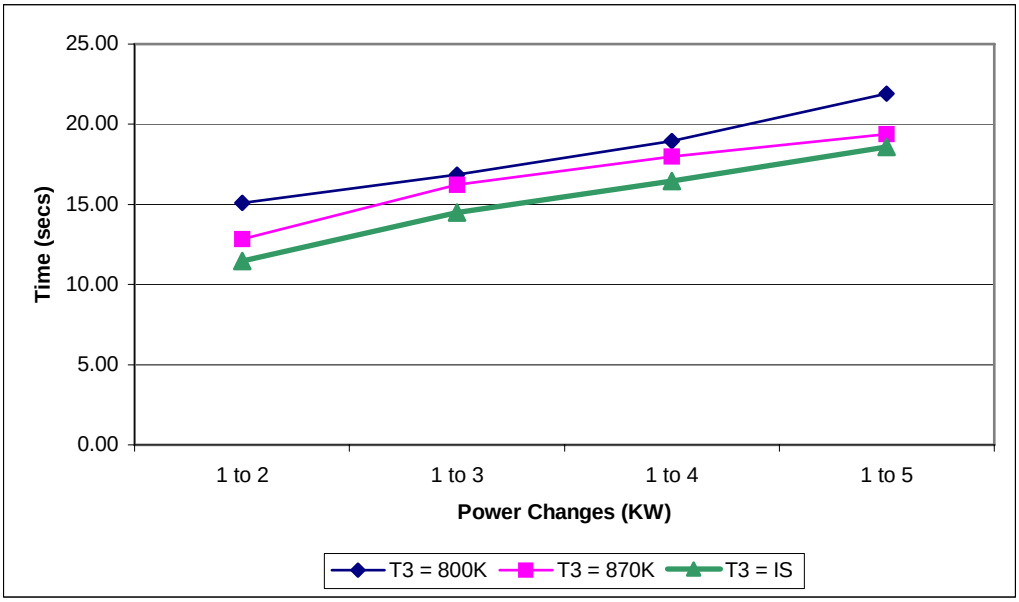

Thermal Transient response of Pre-reformer Outlet Steam-Methane stream(5) for perturbations of the Inlet Steam-Methane stream(3) temperature for power increases

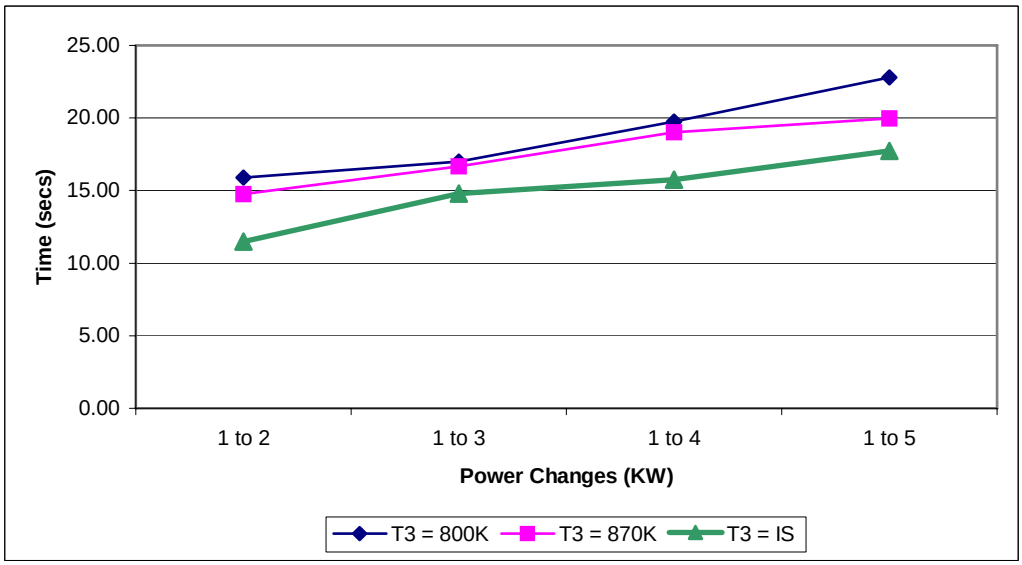

Thermal transient response of Pre-reformer Outlet Gas stream (6) for perturbations of the Inlet Steam-Methane stream(3) temperature for power increases

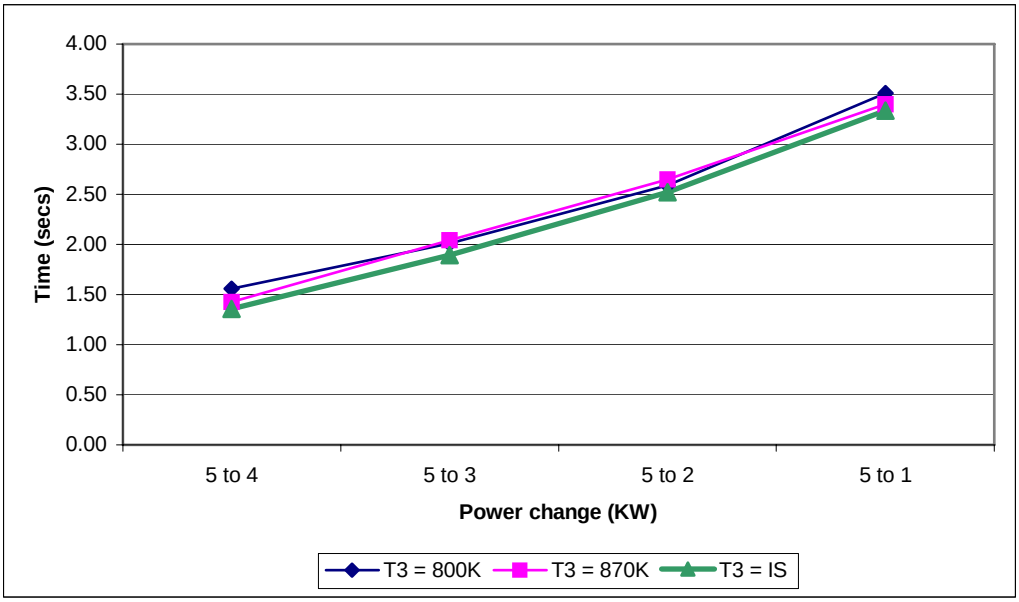

Molar flow transient response of Pre-reformer Steam-Methane streams for perturbations of Inlet Steam-Methane stream (3) temperature for Power decreases

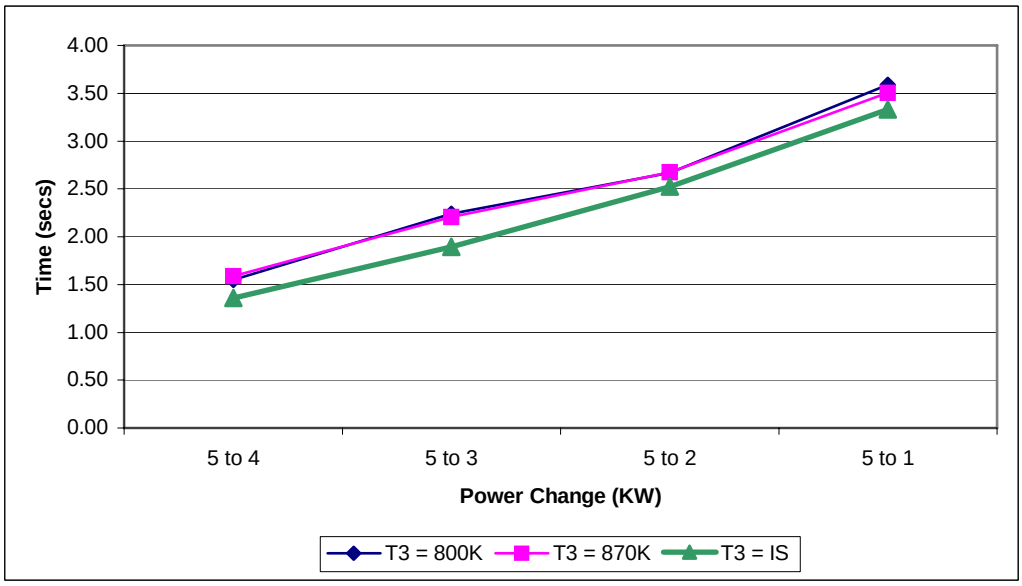

Molar flow transient response for Pre-reformer Gas stream for perturbations of Inlet Steam-Methane stream(3) temperature for Power decreases

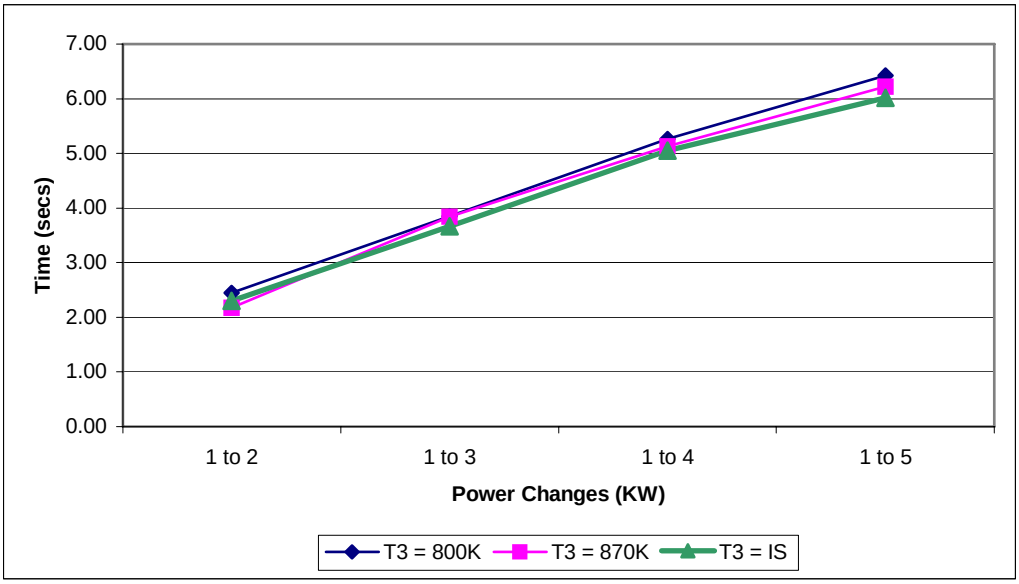

Molar flow rate transient response for Pre-reformer Steam-Methane streams for perturbations of Inlet Steam-Methane stream(3) temperature for Power increases

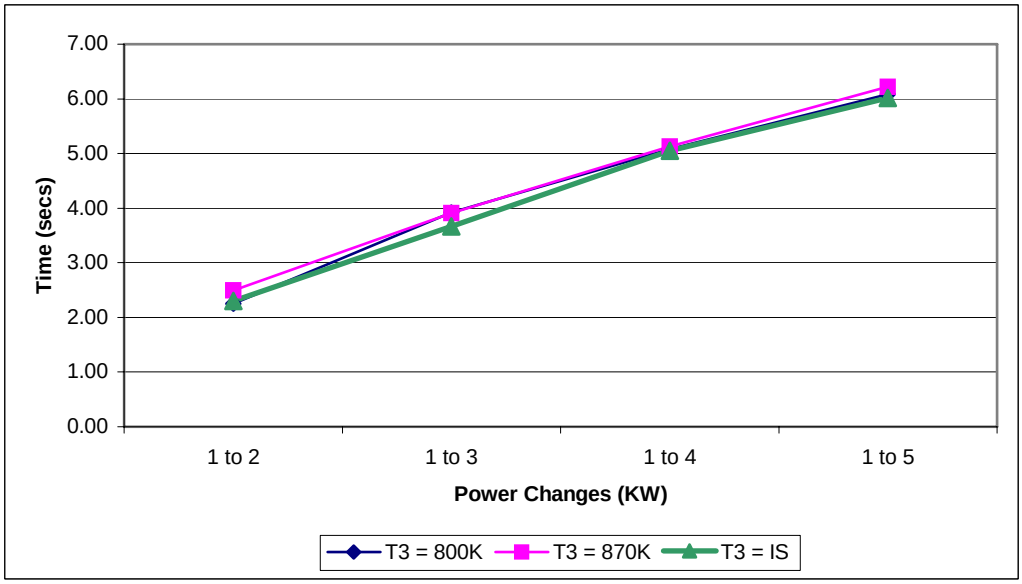

Molar flow rate transient response of Pre-reformer Gas stream for perturbations of Inlet Steam-Methane stream(3) temperature for Power increases

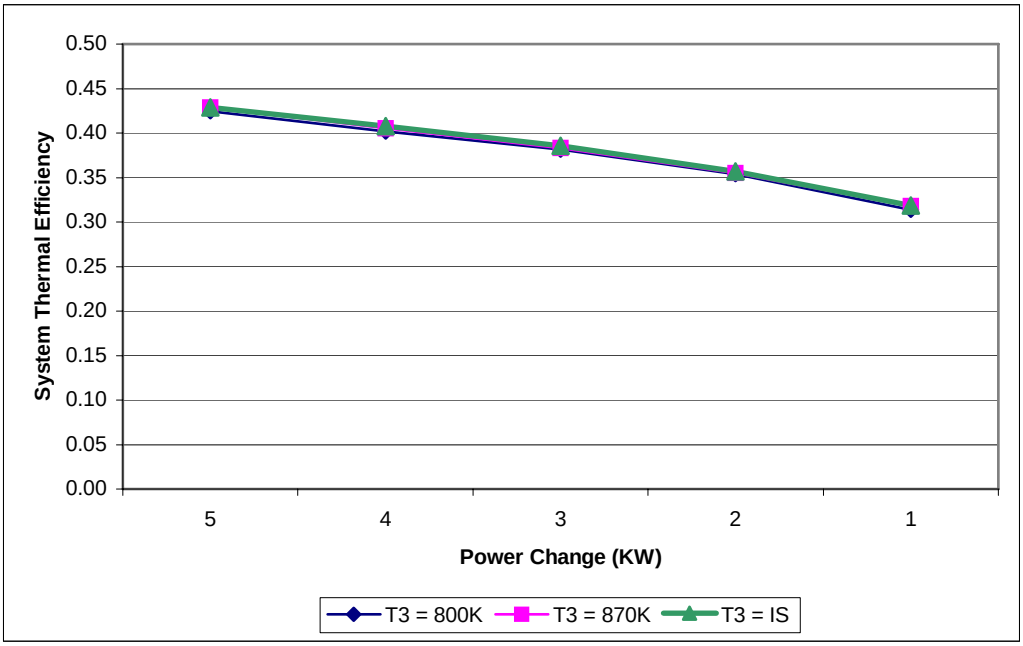

System Thermal Efficiency for Pre-reformer Inlet Steam-Methane temperature perturbations for Power decreases

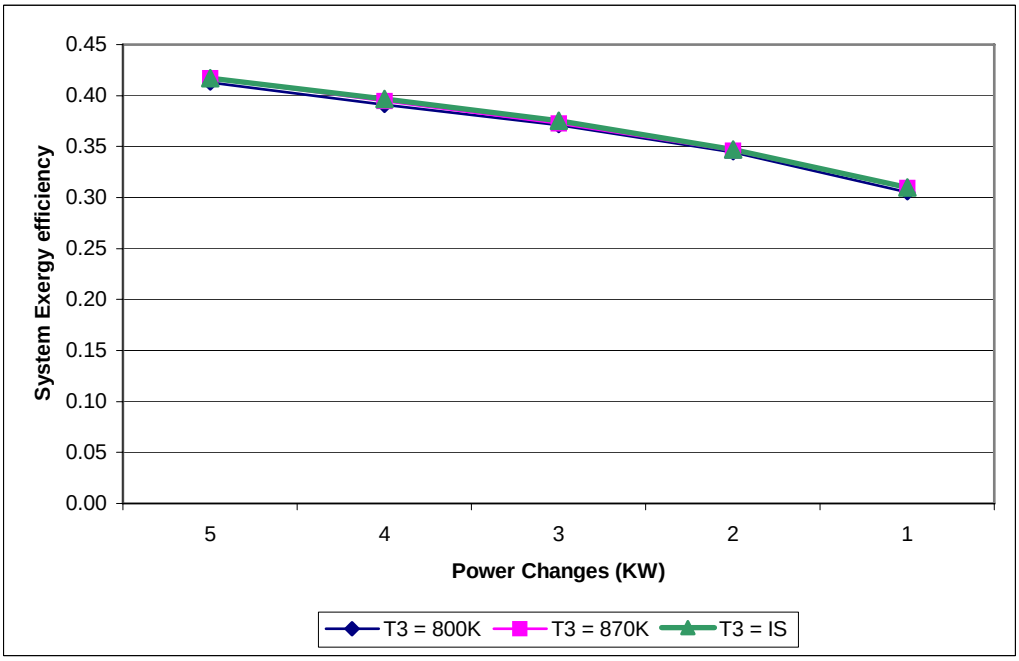

System Energy efficiency for Pre-reformer Inlet Steam-Methane temperature perturbations for Power decreases

Analysis 4c

In this parametric study, temperature control effects on the Pre-reformer temperature, mass flow stabilization times and system thermal and energy efficiencies were studied. The Pre-reformer component has four streams: Inlet steam-methane stream (3), Outlet steam-methane stream (5), Inlet combustion gas stream (4) and Outlet combustion gas stream (6) associated with it. The inlet combustion gas stream is

used to heat up the inlet steam-methane stream entering the Pre-reformer. The outlet combustion gas stream is in-turn used to pre-heat the inlet methane to the system at Heat exchanger III, steam in the Steam generator and the air at Heat exchanger IV. In this particular study (analysis 4c), the inlet steam temperature entering the steam generator is perturbed. Perturbing the inlet steam generator will in-turn affect the thermal and molar flow rate transients of the Pre-reformer streams (3, 5 and 6). Analysis procedure: The default value of the inlet steam temperature with which the SOFC system acts is 293K. This is the value provided in the gPROMS code too. It can be observed that in the analysis one varies this value of inlet steam entering the steam generator and gauges its impact on the system thermal and energy efficiencies; temperature and molar flow transient responses of Pre-reformer streams. The values of the inlet steam temperatures considered are: 150K, 200K, 293K (default), 350K and 450K. The effects of the above temperature perturbations are given below.

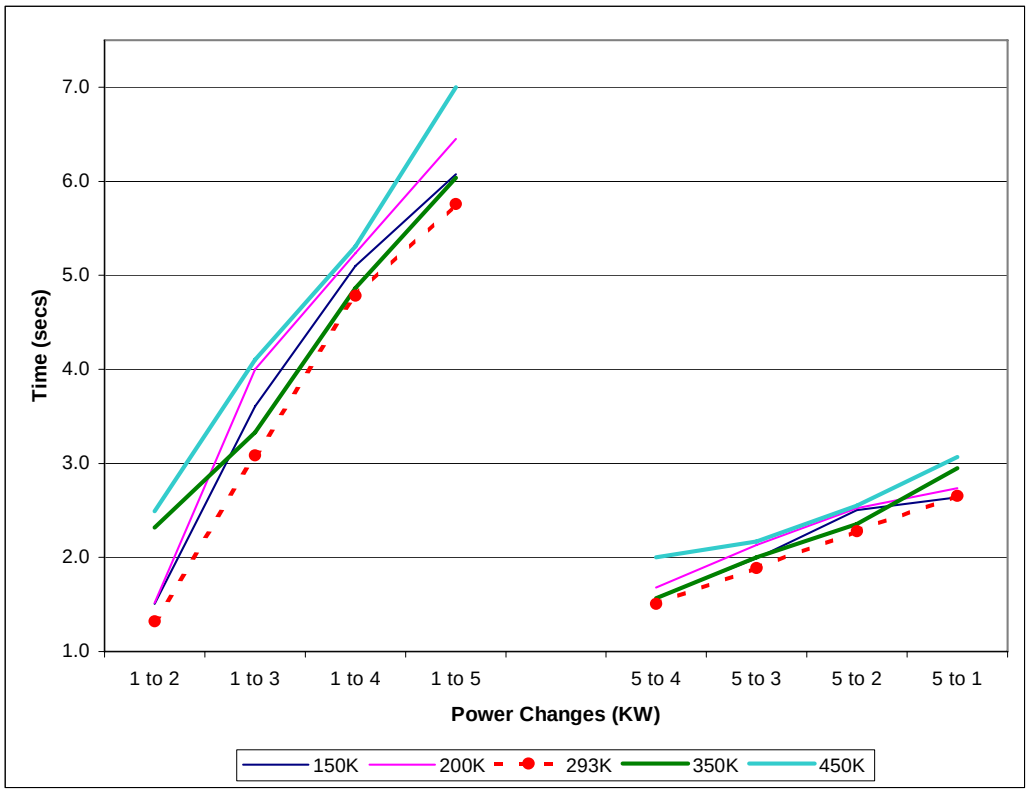

System Thermal transient response of Pre-reformer inlet Methane stream (3) for perturbations of inlet Steam temperature

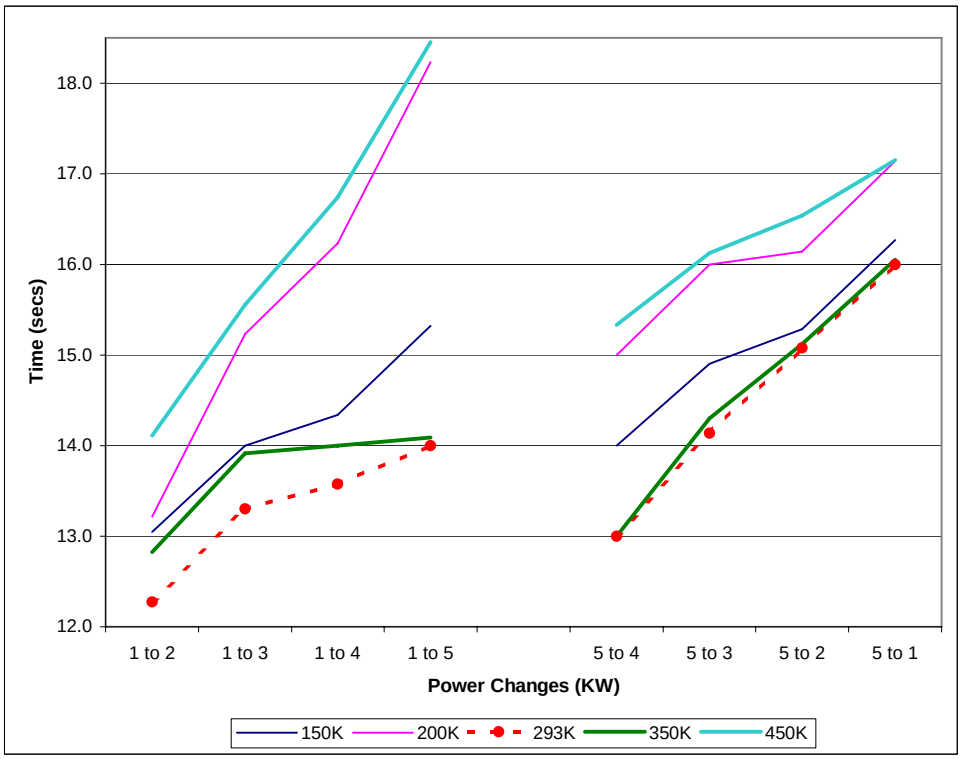

System Thermal transient response of Pre-reformer outlet methane stream (5) for perturbations of inlet Steam temperature

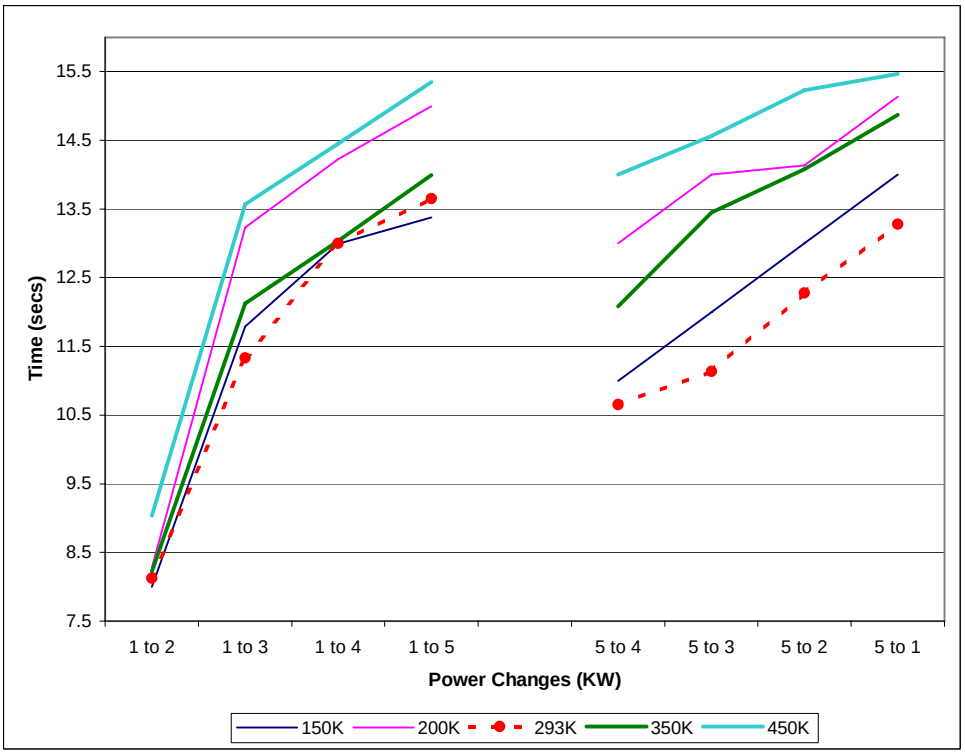

System Transient response for Pre-reformer outlet combustion Gas stream (6) for perturbations of inlet Steam temperature

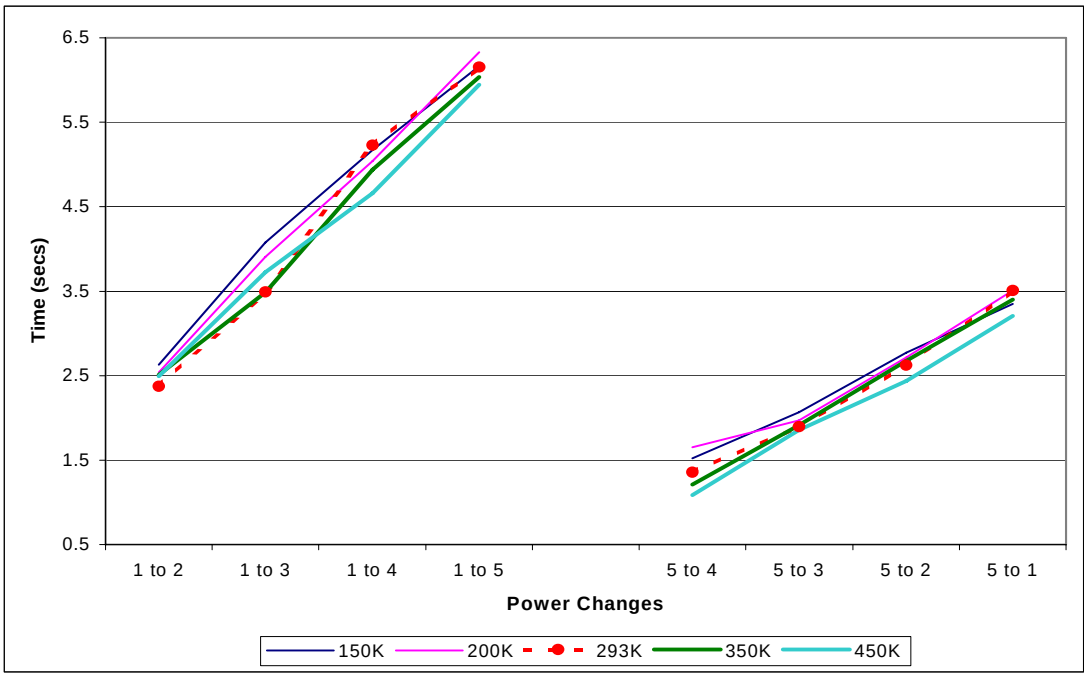

Molar Flow rate times of Pre-reformer streams (3, 5 and 6) for perturbations of inlet Steam temperature

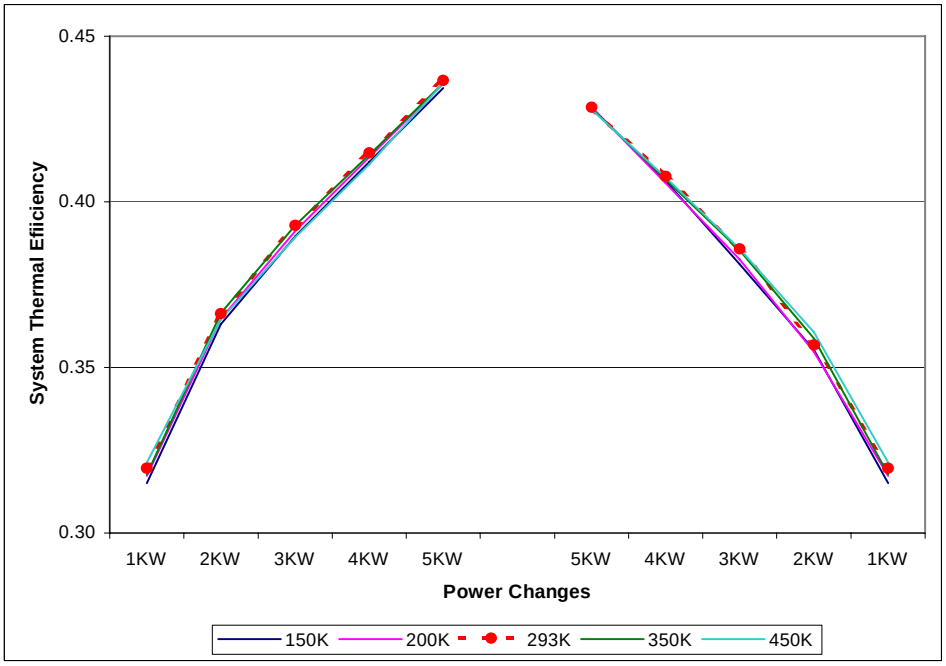

System Thermal Efficiency for perturbations of inlet Steam temperature for Power increases and decreases

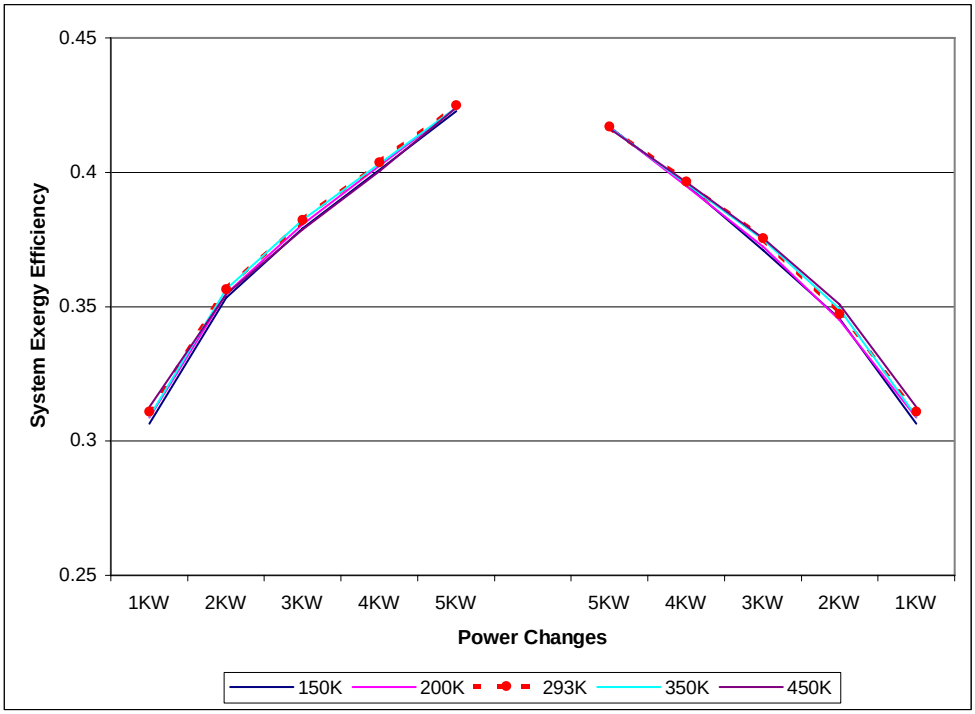

System Energy Efficiency for perturbations of inlet Steam temperature for power increases and decreases

Analysis 4d -

In this parametric study, the Steam generator inlet combustion gas flow rate control effects on the Pre-reformer temperature, mass flow stabilization times and system thermal and energy efficiencies were studied. The Pre-reformer component has four streams: Inlet steam-methane stream (3), Outlet steam-methane stream (5), Inlet combustion gas stream (4) and Outlet combustion gas stream (6) associated with it. The inlet combustion gas stream is used to heat up the inlet steam-methane stream entering the Pre-reformer. The outlet combustion gas stream is in-turn used to pre-heat the inlet methane to the system at Heat exchanger III, steam in the Steam generator and the air at Heat exchanger IV. In this particular study (analysis 4c), the flow rate of the inlet combustion gas entering the steam generator is perturbed. Perturbing the flow rate of the inlet combustion gas will in-turn affect the thermal and molar flow rate transients of the Pre-reformer streams (3, 5 and 6).

Analysis procedure: The default amount of the inlet combustion gas flow rate entering the steam generator of the SOFC system is 0.427 times the total outlet combustion gas stream (6) flow rate. This is the value provided in the gPROMS code too. In the analysis inlet combustion gas flow rate entering the steam generator (as a function of Fmix6 - total outlet combustion gas stream (6) flow rate) is varied and its impact on the system thermal and energy efficiencies; temperature and molar flow transient responses of Pre-reformer streams is gauged.

The values of the inlet steam temperatures considered are: 0.30 times Fmix6, 0.35 times Fmix6, 0.427 times Fmix6 (default), 0.50 times Fmix6 and 0.55 times Fmix6. The effects of the above flow rate perturbations are given below.

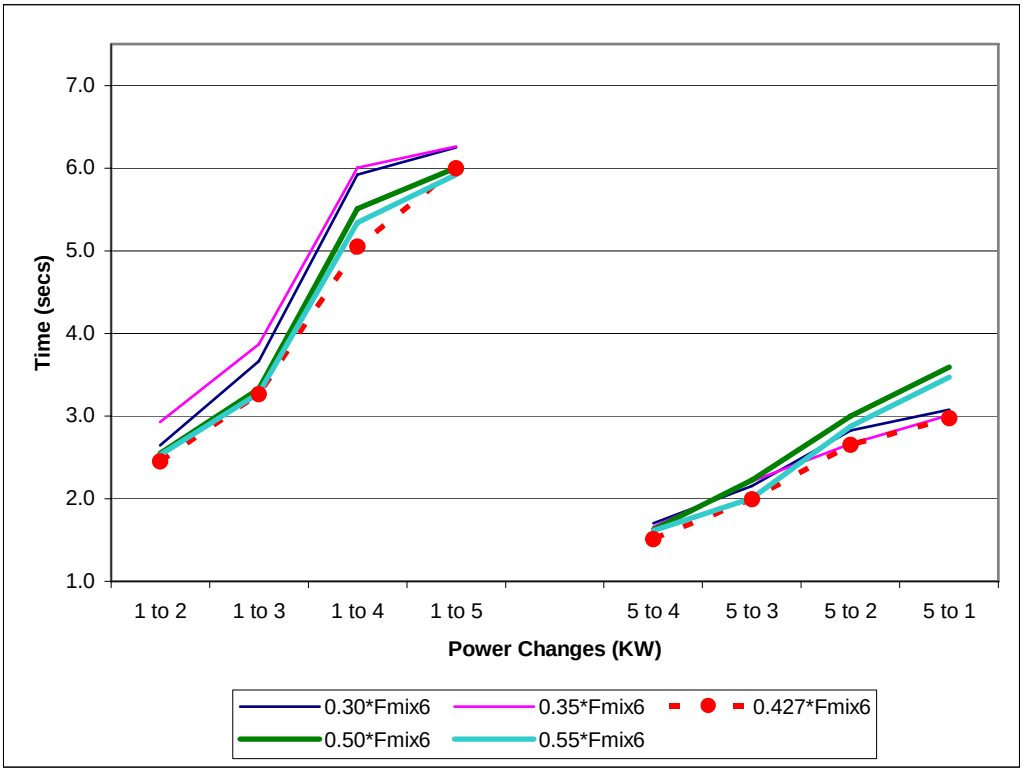

System Thermal transient response of Pre-reformer inlet Methane stream (3) for perturbations of inlet Combustion gas flow rate entering the Steam generator for Power increases and decreases

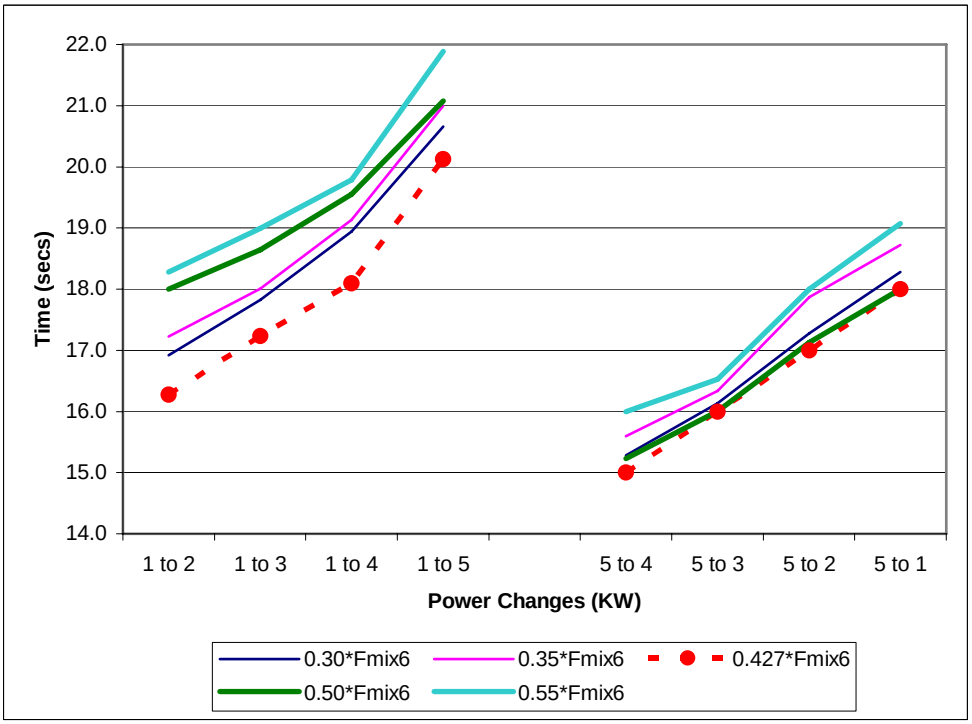

System Thermal transient response of Pre-reformer outlet methane stream (5) for perturbations of inlet Combustion gas flow rate entering the Steam generator for Power increases and decreases

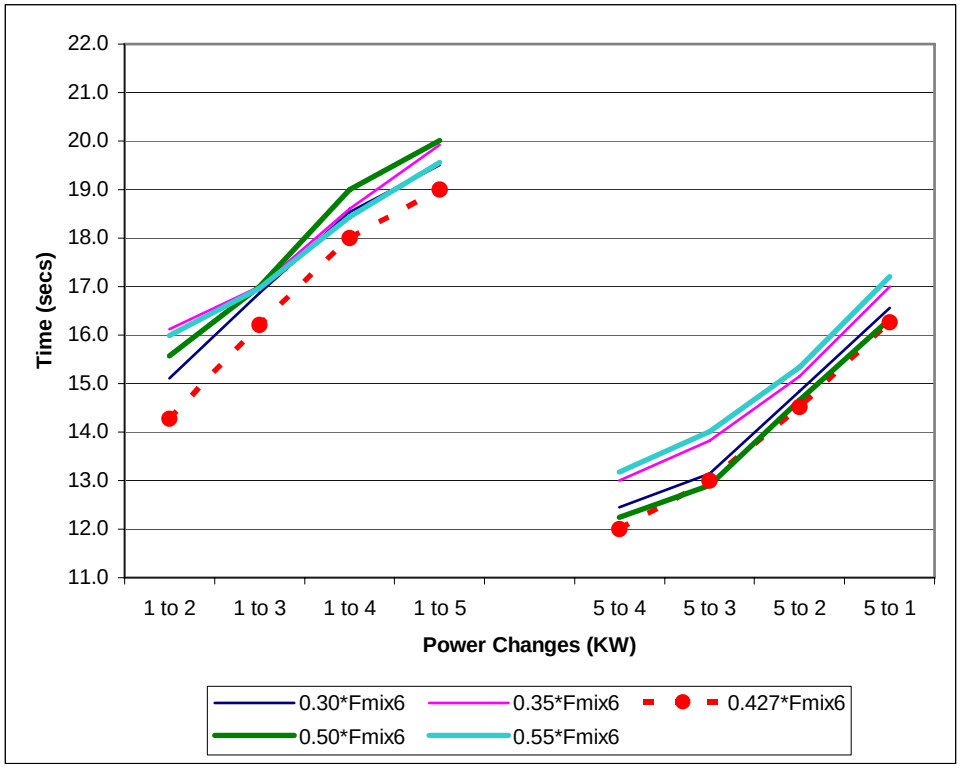

System Transient response for Pre-reformer outlet combustion Gas stream (6) for perturbations of inlet Combustion gas flow rate entering the Steam generator for Power increases and decreases

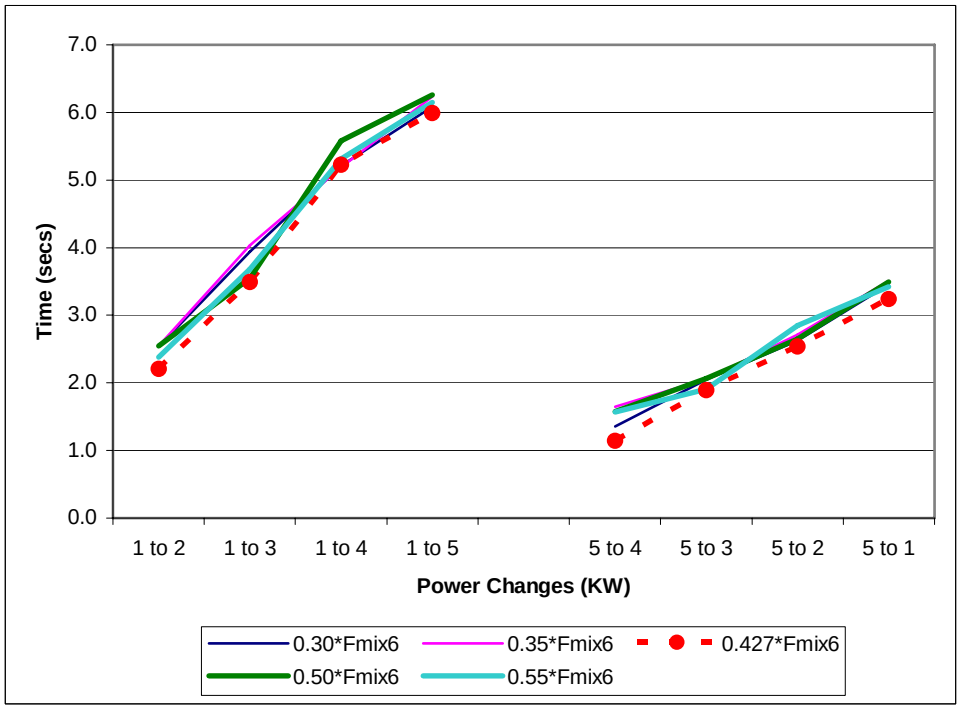

Molar Flow rate times of Pre-reformer streams (3, 5 and 6) for perturbations of inlet Combustion gas flow rate entering the Steam generator for Power increases and decreases

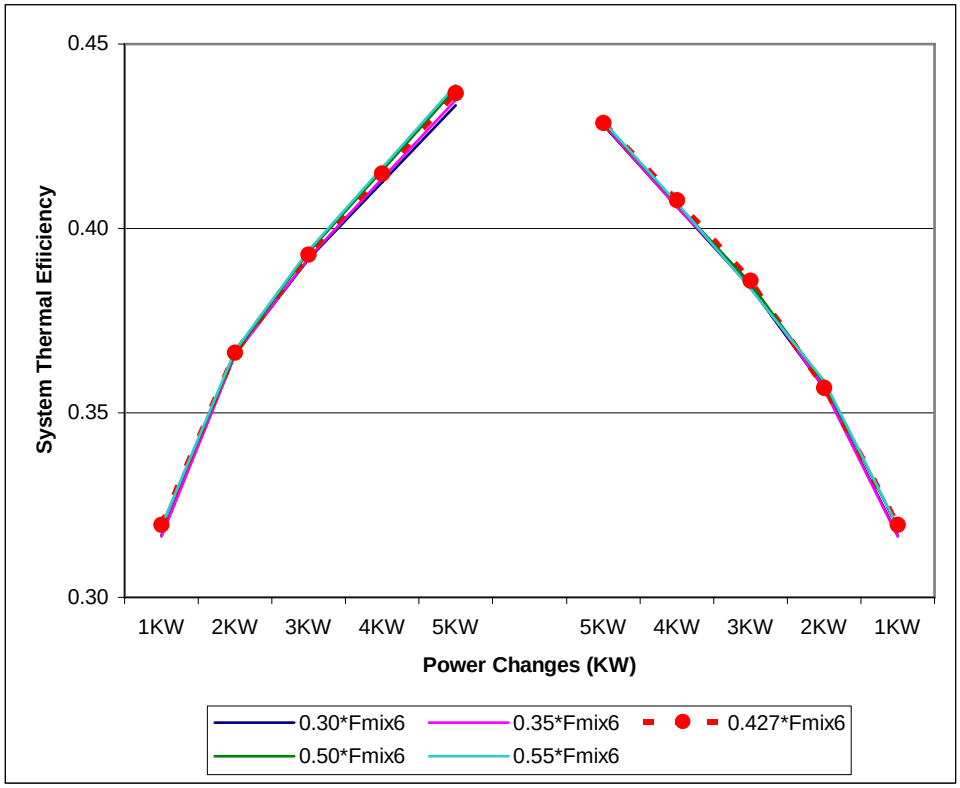

System Thermal Efficiency for perturbations of inlet Combustion gas flow rate for Power increases and decreases

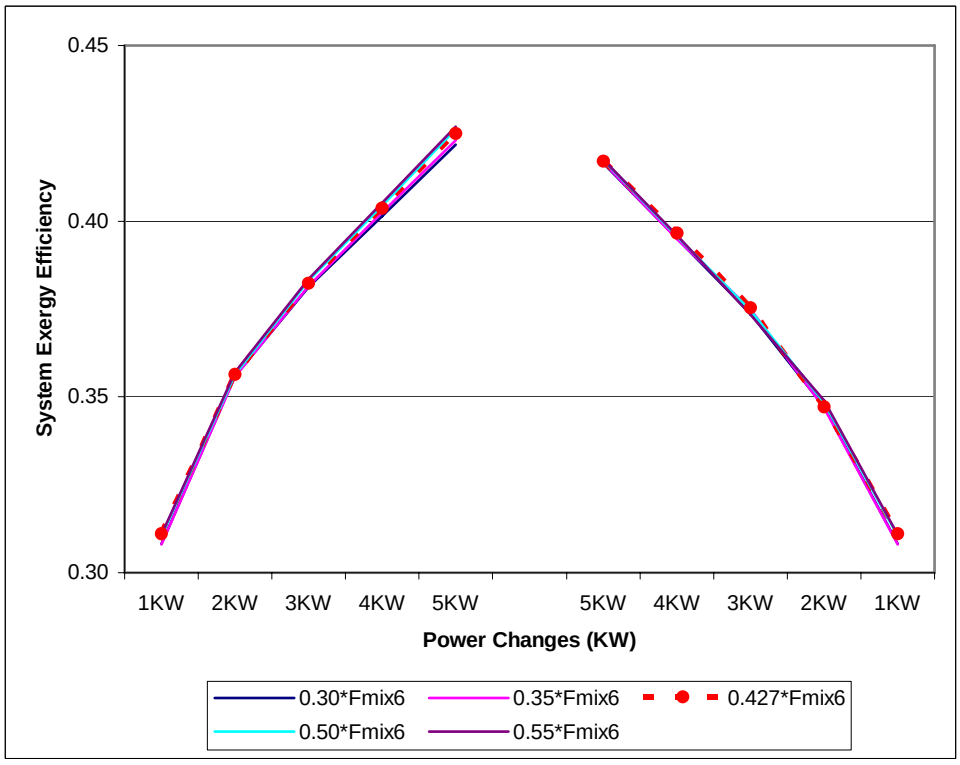

System Energy Efficiency for perturbations of inlet Combustion gas flow rate for Power increases and decreases